



UNIVERSITY OF
LIVERPOOL

**Cellular mechanisms of oxygen sensing in human coronary
artery smooth muscle cells (HCASMCs)**

Thesis submitted in accordance with the requirements of the University of Liverpool
for the degree of Doctor in Philosophy

By

Mingming Yang

September 2016

Contents

Abstract	VI
Acknowledgements	VII
List of Figures	VIII
List of Tables	VIX
List of Abbreviations	XX

Chapter 1	1
1.1 General introduction.....	2
1.2 Human cardiovascular system.....	3
1.3 Human coronary circulation.....	4
1.3.1 Structure and function of coronary circulation.....	4
1.3.2 Anatomy of human coronary arteries.....	6
1.4 O ₂ delivery.....	8
1.4.1 O ₂ carrier.....	8
1.4.2 O ₂ tension, exchange and gradient.....	8
1.5 O ₂ sensing mechanisms: a role for O ₂ sensors.....	10
1.5.1 Overview.....	10
1.5.2 Carotid body.....	10
1.5.3 O ₂ sensitive ion channels.....	11
1.5.4 Mitochondria.....	13
1.5.5 Hypoxia-inducible factor (HIF).....	14
1.5.6 Other O ₂ sensors.....	16
1.6 Metabolic/hypoxic vasodilation.....	17
1.6.1 Definitions.....	17
1.6.2 Indirect vasodilatory effect of hypoxia on SMCs.....	18
1.6.3 Direct vasodilatory effect of hypoxia on VSMCs.....	19
1.7 Vascular tone and contraction.....	19
1.7.1 Vascular tone.....	19
1.7.2 SMC contraction.....	20
1.7.3 Ca ²⁺ sensitization.....	22
1.8 Ion channels in VSMCs.....	23
1.8.1 K ⁺ channels in VSMCs.....	23
1.8.2 Ca ²⁺ channels in VSMCs.....	26
1.9 K _{ATP} channels.....	28
1.9.1 Structure and distribution of K _{ATP} channels.....	28

1.9.2 Nucleotide sensitivity and K_{ATP} channel gating	32
1.9.3 Cellular function of K_{ATP} channels in vascular smooth muscle	34
1.9.4 Pharmacological regulation of K_{ATP} channel.....	35
1.9.5 Cell membrane microenvironment and K_{ATP} channels.....	35
1.10 Cellular metabolism	37
1.10.1 ATP Production.....	37
1.10.2 Mitochondria as ATP consumers	39
1.10.3 Methods to study cellular metabolism.....	42
1.11 Hypothesis.....	44
Chapter 2.....	46
2.1 Materials.....	47
2.1.1 Cell culture	47
2.1.2 Antibodies	48
2.1.3 Plasmids DNA.....	49
2.1.4 Primers	49
2.1.5 Fluorescent probes.....	51
2.1.6 Agonists.....	51
2.1.7 Antagonists.....	51
2.1.8 Reagents	51
2.2 Cell culture	52
2.2.1 Routine passage of HCASMCs	52
2.2.2 Freezing and storing of HCASMCs	52
2.2.3 Resuscitation of HCASMCs.....	53
2.2.4 Culturing of HEK293 and HEK293T cells.....	53
2.3 Cell transfection	53
2.3.1 Transient transfection	53
2.3.2 Lentivirus based biosensors.....	54
2.4 Cell-based assays	57
2.4.1 CellTiter Glo [®] Luminescent Cell Viability Assay	57
2.4.2 ATP:ADP ratio microplate assay	58
2.4.3 MTT assay.....	58
2.4.4 Scratch-wound assay	58
2.4.5 Transwell migration assay	59
2.5 Seahorse XF [®] 96 analyses of oxygen consumption rate and extracellular acidification rate	62
2.5.1 Mitochondrial stress test.....	64
2.5.2 Glycolytic stress test.....	65
2.5.3 Comparison of bioenergetic phenotype of HCASMCs	66
2.5.4 Normalization of OCR and ECAR data	67
2.6 FACS analysis of cell cycle.....	67
2.6.1 Cell preparation.....	67
2.6.2 Sample preparation for flow cytometric analysis	67
2.6.3 Analysis on flow cytometer	68

2.7 Western blot.....	68
2.7.1 Sample preparation.....	68
2.7.2 BCA protein assay.....	69
2.7.3 Preparing polyacrylamide gels.....	70
2.7.4 Running polyacrylamide gels.....	71
2.7.5 Coomassie brilliant blue staining.....	71
2.7.6 Western blotting.....	71
2.7.7 Developing the photographic film.....	72
2.7.8 Re-blotting.....	73
2.8 Immunocytochemistry.....	73
2.8.1 Plating HCAECs and HCASMCs.....	73
2.8.2 Fixing, quenching and permeabilising of cells.....	74
2.8.3 Labelling with antibodies.....	74
2.8.4 Confocal microscopy (immunocytochemistry imaging).....	75
2.9 Confocal microscopy (live cell imaging).....	75
2.9.1 Intracellular ATP:ADP ratio and pH.....	76
2.9.2 Ca ²⁺ measurement.....	77
2.9.3 Membrane potential measurement.....	77
2.9.4 Mitochondrial localization and mitochondrial membrane potential measurements.....	77
2.10 Total Internal Reflection Fluorescence (TIRF) Microscopy.....	78
2.11 Bacterial transformation, growth and stock.....	78
2.11.1 Preparation of ampicillin stock.....	78
2.11.2 Preparation of LB agar plates.....	78
2.11.3 Amplification of competent <i>E.coli</i> cell.....	79
2.11.4 Transformation.....	80
2.11.5 Glycerol stocks.....	80
2.11.6 Plasmid preparation.....	81
2.12 Cloning, PCR and DNA amplification.....	81
2.12.1 Preparation of the vector.....	81
2.12.2 Design of the primer.....	81
2.12.3 Sub-cloning by PCR.....	82
2.12.4 Verification of constructed plasmids.....	84
2.13 Statistical analysis.....	84

Chapter 3.....85

3.1 Introduction.....	86
3.2 Aims.....	89
3.3 Methods and preliminary results.....	89
3.3.1 Optimization of the cell transfection.....	89
3.3.2 Transfection of HCASMCs with Perceval/PercevalHR and/or pHRed.....	95
3.4 Results.....	98
3.4.1 Bioenergetic profile of HCASMCs.....	98
3.4.2 ATP content in HCASMCs.....	111

3.4.3 Effect of metabolic inhibitors and hypoxia on ATP:ADP ratio	117
3.4.4 Metabolic inhibition and mitochondrial membrane potential	135
3.3.5 Microplate based ATP:ADP ratio measurement	161
3.4 Discussion	162
Chapter 4.....	172
4.1 Introduction.....	173
4.1.1 PiggyBac™ transposon vector system	173
4.1.2 Lentivirus-mediated gene delivery	174
4.1.3 Other alternatives	178
4.2 Aims	180
4.3 Methods.....	181
4.3.1 Plasmid production, amplification and isolation	181
4.3.2 Production of lenti-psuedoviral particles.....	181
4.3.3 Transduction	182
4.3.4 Cell permeabilisation.....	182
4.3.5 Making FUGW-pHRed and Lyn-FUGW-PercevalHR	184
4.3.6 Analysis of cell morphology using Fiji	184
4.3.7 Cell volume measurement using Fiji.....	185
4.3.8 Ratiometric image analysis using Fiji	186
4.4 Results.....	187
4.4.1 PiggyBac™ transposon vector system	187
4.4.2 Transfection of HCASMCs with FUGW-PercevalHR	187
4.4.3 Morphological comparison between transfection with lentivirus and transfection reagents	188
4.4.4 Intracellular calibration of FUGW-PercevalHR	191
4.4.5 Metabolic inhibitors and intracellular ATP:ADP ratio	199
4.4.6 Constructing FUGW-pHRed	213
4.4.7 Transfection of HCASMCs with FUGW-pHRed	215
4.4.8 Effect of metabolic inhibitors on intracellular pH.....	215
4.4.9 Ratiometric measurement of intracellular pH	220
4.4.10 Simultaneous imaging of intracellular ATP:ADP ratio and pH.....	227
4.4.11 PercevalHR fluorescence and mitochondria.....	230
4.4.12 Membrane targeting PercevalHR/Lyn-FUGW-PercevalHR.....	231
4.4.13 TIRF imaging of FUGW-PercevalHR.....	238
4.5 Discussion	241
4.5.1 Lentivirus transduction and other alternatives	241
4.5.2 Reporting intracellular ATP:ADP ratio using FUGW-PercevalHR.....	245
4.5.3 Investigation of cellular metabolism in plasma membrane microdomains	247
4.5.4 Gene delivery in cardiovascular system	247
4.6 Conclusion.....	248
Chapter 5.....	249
5.1 Introduction.....	250

5.2 Aims	251
5.3 Results	251
5.3.1 Effect of hypoxia on Ca ²⁺ homeostasis in single HCASMCs	251
5.3.2 Effect of hypoxia on membrane potential of single HCASMCs	265
5.4 Discussion	283
Chapter 6.....	288
6.1 Introduction	289
6.2 Aims	290
6.3 Results	290
6.3.1 Cell growth and morphology	290
6.3.2 Coomassie blue staining	293
6.3.3 WB and ICC	293
6.3.4 Effect of hypoxia on cell number determined by cell counting.....	295
6.3.5 Assessing HCASMC proliferation with MTT assay	297
6.3.6 Effect of hypoxia on HCASMC migration.....	304
6.3.7 Effect of metabolic inhibitors and hypoxia on HCASMC cell cycle	306
6.4 Discussion	313
Chapter 7.....	317
7.1 Introduction	318
7.2 K ⁺ channels as cellular targets in hypoxic vasodilation	319
7.3 K _{ATP} channels in hypoxic vasodilation	320
7.4 Other K ⁺ channels in hypoxic vasodilation	326
7.5 VDCCs in hypoxic vasodilation	327
7.6 Limitations and future work	328
7.7 Conclusion remarks	329

Abstract: Cellular mechanisms of oxygen sensing in human coronary artery smooth muscle cells (HCASMCs)

Hypoxic coronary vasodilation is an important mechanism that ensures adequate oxygenated blood is provided to metabolically active heart. Although it is beyond doubt that this phenomenon plays a central role in matching oxygen supply and increased demand of cardiac myocytes, the underlying mechanisms have proved difficult to disentangle. This study investigated the cellular targets of hypoxic coronary vasodilation with testing the main hypothesis that K_{ATP} channels play an important role in hypoxic vasodilation by coupling cellular metabolism to cell excitability.

Seahorse experiments showed HCASMCs preferentially rely on oxidative phosphorylation (OXPHOS) to generate ATP (~54.53%), in which O_2 acts as the final electron acceptor of electron transport chain (ETC). Intracellular ATP was measured by CellTiter Glo Luminescent Assay and ATP:ADP ratio was examined by genetically encoded biosensors Perceval/PercevalHR. FUGW-pHRed was also used to monitor pH. Either inhibiting glycolysis or OXPHOS with metabolic inhibitors caused a reduction in intracellular ATP and ATP:ADP ratio. A further change was observed when blocking both glycolysis and OXPHOS. There was no obvious change of ATP:ADP ratio reported using PercevalHR in cells infected with lentivirus under hypoxia (1% O_2). Rhodamine123, a mitochondrial membrane potential (ψ_m) sensitive dye showed hypoxia didn't cause a significant change in ψ_m further indicated that low level O_2 in this study did not change ATP:ADP ratio.

Live cell imaging with HCASMCs loaded with Fluo-4 and DiBAC4(3) was used to assess the changes in intracellular Ca^{2+} ($[Ca^{2+}]_i$) and membrane potential, respectively. Using K^+ channel modulators, it was characterized the presence of K_{ATP} , BK_{Ca} , SK_{Ca}/IK_{Ca} and K_v channels in HCASMCs, and of those, K_{ATP} and K_{ir} channels play an essential role in setting resting membrane potential. Application of metabolic inhibitors (e.g. rotenone and antimycin) of OXPHOS caused hyperpolarization, and the effects were inhibited by either 10 μM glibenclamide or 60 mM K^+ , indicating a role of K_{ATP} channels. Hypoxia caused a decrease in spontaneous Ca^{2+} oscillations and oscillations induced by vasoconstrictors. Exposure to hypoxia resulted in membrane hyperpolarization which was completely abolished by 60 mM K^+ , but not by a single K^+ channel inhibitor.

ATP:ADP ratio in the close vicinity of K_{ATP} channels may be more important than its global level which PercevalHR reports. Further experiments were designed to examine ATP:ADP ratio in the cell membrane microdomains using a membrane targeted PercevalHR and TRIF imaging. Preliminary experiments showed successful measurement of ATP:ADP ratio in the cell membrane microdomains.

Taken together, hypoxia may cause coronary artery smooth muscle relaxation by modulating $[Ca^{2+}]_i$ and K^+ channels. The identity of K^+ channels involved in hypoxia induced hyperpolarization is unknown.

Acknowledgements

First, I would like to express my most sincere thanks to my primary supervisor Dr John Quayle, for the continued support, motivation and encouragement throughout my four years PhD. My thanks also go to my secondary supervisor Dr Caroline Dart, for taking care of me during my stay in Lab D and giving me invaluable advices for my microbiology work. I would like to particularly thank Dr Tomoko Kamishima for helping me with the lab, giving me advices throughout the project and correcting the thesis. I also thank my project advisors Professor Judy Coulson, Dr Alec Simpson and Dr Laura Swan for assessing the development of my research.

I would like to express my gratitude to Dr Rachael Quinn for her help and patience in showing me basic lab skills when I started lab. I would like to acknowledge Dr Owain Roberts for teaching me key molecular biology techniques. I would like to thank Dr Joanna Wardyn and really appreciated for her advice in lentivirus transduction. I am also indebted to Dr Amy Chadwick for her selfless in helping with Seahorse experiments and Dr Sandra Cachinho with cell cycle experiments. Thanks go to Centre for Cell Imaging for help with confocal microscopy and TIRF. Thanks also go to members in Cellular and Molecular physiology and Lab D, especially Dr Dominic Byrne and Christopher Clarke for all the help during my work in Lab D.

Thanks to my friends in China for encouragement and amazing people I met here for making my stay in UK an enjoyable and wonderful one.

My PhD was founded by China Scholarship Council and university of Liverpool, without which my studies would never have happened.

Finally, special thanks to my mum and dad, for their love and support.

List of Figures

Chapter 1

Figure 1.1	Human cardiovascular system	4
Figure 1.2	Distribution of main coronary arteries	5
Figure 1.3	Branch patterns of human coronary artery	6
Figure 1.4	Structure of the artery wall	7
Figure 1.5	Micrographs of canine coronary artery (A) and arterioles (B&C)	7
Figure 1.6	Structure of Hb	8
Figure 1.7	Regional distribution of O ₂ partial pressure from airways to cytosol	9
Figure 1.8	Graphical representation of a simplified diffusion equation and typical barriers	10
Figure 1.9	Redox mechanism for O ₂ sensing	14
Figure 1.10	Structure and regulation of HIF-1	16
Figure 1.11	Ca ²⁺ channels and transporters in VSMCs	21
Figure 1.12	VSMC actin-myosin cross-bridge	22
Figure 1.13	K ⁺ channels subunits	25
Figure 1.14	Voltage-gated Ca ²⁺ channels	28
Figure 1.15	Organization of K _{ATP} channels	31
Figure 1.16	K _{ATP} channel regulation by intracellular ATP	33
Figure 1.17	Flow diagram of key cellular energy metabolic pathways	39
Figure 1.18	Schematic presentation of mitochondrial ETC and ATP synthase	41
Figure 1.19	Chemical structure of metabolic inhibitors	43
Figure 1.20	Metabolic inhibition of ETC	43
Figure 1.21	K _{ATP} channel modal for hypoxic vasodilation	45

Chapter 2

Figure 2.1	Scratch-wound Assay	59
Figure 2.2.1	Transwell cell culture plate	60
Figure 2.2.2	Transwell cell migration assay	61
Figure 2.3	Seahorse XF Analyzer machinery and an illustration of its working principle	63
Figure 2.4	Mitochondrial stress test	65
Figure 2.5	Glycolysis stress test	66
Figure 2.6	Cell bioenergetics phenotype profile	67

Chapter 3

Figure 3.1	PercevalHR detects ATP:ADP ratio	88
Figure 3.2	Cell number optimization of HEK293 cells for transfection	90
Figure 3.3	Optimization of pHRed transfection using different reagents	91
Figure 3.4	HEK293 transfection with pEGFP-N1 after 24 hrs	92
Figure 3.5	Optimization of Perceval transfection	93
Figure 3.6	Optimization of pHRed transfection	94
Figure 3.7	Co-transfection of Perceval and pHRed in HEK293 cells	95
Figure 3.8	Cell number optimization for transfection of HCASMCs	96
Figure 3.9	Perceval/PercevalHR and pHRed transfection of HCASMCs	97
Figure 3.10	Optimization of FCCP and oligomycin concentrations	99
Figure 3.11	Determination of oligomycin concentration	100
Figure 3.12	Mitochondrial stress test	102
Figure 3.13	Cellular bioenergetics of HCASMCs during culture	103
Figure 3.14	Glycolysis stress test	104
Figure 3.15	ATP production rate from glycolysis and OXPHOS	106
Figure 3.16	Effect of oligomycin after blocking ETC	107
Figure 3.17	Effect of oligomycin after dissipating ETC	108
Figure 3.18	2-DG abolished the reverse mode of ATP synthase	108

Figure 3.19	Bioenergetic phenotype in response to metabolic inhibitors	110
Figure 3.20	Percent change in OCR and ECAR in response to metabolic inhibitors	111
Figure 3.21	CellTiter-Glo luminescent viability assay	112
Figure 3.22	Effect of vasoconstrictors on intracellular ATP	113
Figure 3.23	Inhibition of glycolysis with 2-DG caused a decrease in ATP level	115
Figure 3.24	Inhibition of OXPHOS caused a decrease in ATP level	115
Figure 3.25	Effects of metabolic inhibitors on cellular ATP	116
Figure 3.26	Combined inhibition of glycolysis and OXPHOS by 2-DG and oligomycin caused further reduction in cellular ATP	117
Figure 3.27	The effect of 2-DG on Perceval signal	118
Figure 3.28	Glucose removal caused a decrease in Perceval signal	119
Figure 3.29	Reduction in Perceval signal after glucose removal is reversible	120
Figure 3.30	Time control study with HCASMC expressing Perceval	121
Figure 3.31	Application of 2-DG decreases Perceval signal	121
Figure 3.32	The effect of 2-DG on pHRed signal in bicarbonate buffered PSS	122
Figure 3.33	The effect of 2-DG in HEPES buffered PSS	122
Figure 3.34	Inhibiting ETC by antimycin causes a decrease in ATP:ADP ratio	123
Figure 3.35	pHRed reports changes in cellular pH	123
Figure 3.36	O ₂ concentration in the chamber and medium during hypoxia	125
Figure 3.37	Measurement of dissolved O ₂ during perfusion	125
Figure 3.38	Effect of hypoxia (1% O ₂) on Perceval signal	126
Figure 3.39	Transient hypoxia caused a reversible change in ATP:ADP ratio signal	127
Figure 3.40	Effect of 10% and 5% O ₂ on Perceval signal	128

Figure 3.41	Effect of hypoxia on pH	129
Figure 3.42	Effect of hypoxia on pHRed ratio fluorescence	129
Figure 3.43	Vehicle control of PercevalHR fluorescence	130
Figure 3.44	Effect of rotenone on ATP:ADP ratio signal	131
Figure 3.45	Effect of antimycin on ATP:ADP ratio signal	132
Figure 3.46	Effect of oligomycin on ATP:ADP ratio signal	133
Figure 3.47	Effect of CCCP on ATP:ADP ratio signal	134
Figure 3.48	Effect of sequential application of rotenone and antimycin on ATP:ADP ratio signal	134
Figure 3.49	Effect of hypoxia on PercevalHR signal	135
Figure 3.50	Staining mitochondrial with MitoTracker	136
Figure 3.51	Measurement of mitochondrial membrane potential	137
Figure 3.52	Effect of DMSO on mitochondrial membrane potential of cells kept in 10 mM glucose PSS	139
Figure 3.53	Effect of rotenone on mitochondrial membrane potential	139
Figure 3.54	Effect of antimycin on mitochondrial membrane potential	140
Figure 3.55	Effect of oligomycin on mitochondrial membrane potential	141
Figure 3.56	Effect of CCCP on mitochondrial membrane potential	142
Figure 3.57	Effect of hypoxia on mitochondrial membrane potential	143
Figure 3.58	Effect of metabolic inhibitors on mitochondrial membrane potential	144
Figure 3.59	Effect of hypoxia on mitochondrial membrane potential in the presence of metabolic inhibitors	145
Figure 3.60	Time control of mitochondrial membrane potential signal in 60K ⁺ PSS	147
Figure 3.61	Vehicle control of mitochondrial membrane potential signal in 60K ⁺ PSS	147
Figure 3.62	Effect of rotenone on mitochondrial membrane potential in 60K ⁺ PSS	148

Figure 3.63	Effect of antimycin on mitochondrial membrane potential in 60K ⁺ PSS	149
Figure 3.64	Effect of oligomycin on mitochondrial membrane potential in 60K ⁺ PSS	150
Figure 3.65	Effect of CCCP on mitochondrial membrane potential in 60K ⁺ PSS	151
Figure 3.66	Effect of hypoxia on mitochondrial membrane potential in 60K ⁺ PSS	152
Figure 3.67	Effect of sequential application of metabolic inhibitors on mitochondrial membrane potential in 60K ⁺ PSS	153
Figure 3.68	Effect of combined application of metabolic inhibitors on mitochondrial membrane potential signal in 60K ⁺ PSS	154
Figure 3.69	Depolarization of mitochondrial membrane potential by rotenone in 0 mM glucose PSS	156
Figure 3.70	Depolarization of mitochondrial membrane potential by antimycin in 0 mM glucose PSS	157
Figure 3.71	Hyperpolarization of mitochondrial membrane potential by oligomycin in 0 mM glucose PSS	158
Figure 3.72	Depolarization of mitochondrial membrane potential by CCCP in 0 mM glucose PSS	159
Figure 3.73	Effect of hypoxia on mitochondrial membrane potential in 0 mM glucose PSS	160
Figure 3.74	Effect of sequential application of metabolic inhibitors and hypoxia in 0 mM glucose PSS	161
Figure 3.75	Microplate based ATP:ADP ratio measurement under hypoxia	162
Figure 3.76	Metabolic inhibitors cause a decrease ATP:ADP ratio signal measured in microplate	162
Figure 3.77	Summary of mitochondrial bioenergetics profile	165

Figure 3.78	pH regulation by ion transporters in SMC	169
Chapter 4		
Figure 4.1	PiggyBac TM transposon vector systems	174
Figure 4.2	Schematic representation of HIV-1 genome	176
Figure 4.3	Schematic illustration of HIV-1 derived lentivirus	177
Figure 4.4	Production of lentivirus	182
Figure 4.5	Analysis of cell morphology using Fiji	185
Figure 4.6	Modal for ratiometric image analysis of a cell expressing PercevalHR or pHRed	186
Figure 4.7	Transfection of PB vector containing AGR2	187
Figure 4.8	FUGW-PercevalHR transfected HCASMCs	188
Figure 4.9	Cell transfection using different methods	189
Figure 4.10	Comparison of cell size between different transfection methods with Fiji	190
Figure 4.11	Comparison of cell morphology between different transfection methods using Fiji	190
Figure 4.12	Cell permeabilisation with ESCIN	191
Figure 4.13	α -toxin causes SMC contraction	192
Figure 4.14	Poly D-Lysine coating helps cells adhere to the glass	193
Figure 4.15	PercevalHR signal measured using α -toxin permeabilised HCASMCs	195
Figure 4.16	Dose-response curve of PercevalHR fluorescence as a function of ATP concentrations	197
Figure 4.17	Effect of ADP on PercevalHR fluorescence	198
Figure 4.18	2-DG caused decrease in PercevalHR signal	200
Figure 4.19	Transient glucose removal caused a transient decrease in PercevalHR signal	201
Figure 4.20	Time control of PercevalHR fluorescence	202

Figure 4.21	Vehicle control of PercevalHR fluorescence	203
Figure 4.22	Metabolic inhibition of mitochondrial complex I caused a decrease in PercevalHR signal	204
Figure 4.23	Metabolic inhibition of mitochondrial complex III caused a decrease in PercevalHR signal	205
Figure 4.24	Blocking ATP synthase caused a decrease in PercevalHR signal	206
Figure 4.25	Application of proton ionophore resulted in a reduction in PercevalHR signal	207
Figure 4.26	Effect of hypoxia on PercevalHR signal	208
Figure 4.27	Interrelationship of mitochondrial complex I and complex III	209
Figure 4.28	Interrelationship of ETC and ATP synthase	209
Figure 4.29	HCASMCs expressing FUGW-PercevalHR	210
Figure 4.30	Time control of ratiometric imaging	211
Figure 4.31	Vehicle control of ratiometric imaging	212
Figure 4.32	Effect of rotenone on PercevalHR ratiometric signal	213
Figure 4.33	Schematic diagram of constructing FUGW-pHRed	214
Figure 4.34	Agarose gel verification of FUGW-pHRed	214
Figure 4.35	HCASMCs expressing FUGW-pHRed	215
Figure 4.36	Time control of FUGW-pHRed fluorescence	216
Figure 4.37	Vehicle control of FUGW-pHRed fluorescence signal	217
Figure 4.38	Effect of rotenone on pHRed signal	217
Figure 4.39	Effect of oligomycin on pHRed signal	218
Figure 4.40	Effect of antimycin on cellular pH in the presence of rotenone	219
Figure 4.41	Effect of CCCP on pHRed signal in the presence of oligomycin	220
Figure 4.42	HCASMCs expressing FUGW-pHRed	221
Figure 4.43	Time control of FUGW-pHRed fluorescence	221

Figure 4.44	Vehicle control of FUGW-pHRed fluorescence	222
Figure 4.45	Effect of rotenone on FUGW-pHRed ratio fluorescence	223
Figure 4.46	Effect of antimycin on FUGW-pHRed ratio fluorescence	224
Figure 4.47	Effect of oligomycin on FUGW-pHRed ratio fluorescence	225
Figure 4.48	Effect of CCCP on FUGW-pHRed ratio fluorescence	226
Figure 4.49	FUGW-pHRed ratio fluorescence in response to antimycin and subsequent application of CCCP	227
Figure 4.50	HCASMCs expressing both PercevalHR and pHRed	228
Figure 4.51	Concurrent measurement of intracellular ATP:ADP ratio and pH	229
Figure 4.52	Distribution of PercevalHR and MitoTracker	231
Figure 4.53	Designing of Lyn-FUGW-PercevalHR by PCR cloning	233
Figure 4.54	Designing of Lyn-FUGW-PercevalHR by In-Fusion cloning	233
Figure 4.55	Agarose gel verification of Lyn-FUGW-PercevalHR	234
Figure 4.56	HEK293 cells transfected with Lyn-FUGW-PercevalHR	235
Figure 4.57	3D reconstruction of HEK293 cells transfected with Lyn-FUGW-PercevalHR	235
Figure 4.58	HCASMC transfected with Lyn-FUGW-PercevalHR	236
Figure 4.59	Lifted HCASMC expressing Lyn-FUGW-PercevalHR	237
Figure 4.60	Metabolic inhibition lead to a change in Lyn-FUGW-PercevalHR signal	238
Figure 4.61	Diagram of TIRF imaging	239
Figure 4.62	Images obtained using epifluorescence and TIRF	240
Figure 4.63	TIRF imaging of the effect of 1 μ M antimycin on cellular metabolism	241
Figure 4.64	Representative components of a gene delivery vector	243
Figure 4.65	Schematic illustration of viral and non-viral delivery systems for gene delivery	244
Figure 4.66	The evolution of heart gene delivery research	248

Chapter 5

Figure 5.1	Ca ²⁺ measurement with Fluo-4	252
Figure 5.2	Ca ²⁺ oscillations	253
Figure 5.3	Analysis of Ca ²⁺ oscillations with Matalab	254
Figure 5.4	Effect of A23187 on intracellular Ca ²⁺	256
Figure 5.5	Effect of PDGF-BB on intracellular Ca ²⁺	256
Figure 5.6	Effect of PE on intracellular Ca ²⁺	257
Figure 5.7	Effect of PGF2 α on intracellular Ca ²⁺	257
Figure 5.8	Effect of U46619 on intracellular Ca ²⁺	258
Figure 5.9	Effect of high K ⁺ on intracellular Ca ²⁺	258
Figure 5.10	Effect of hypoxia on Ca ²⁺ oscillations	260
Figure 5.11	Effect of hypoxia on PDGF-BB induced Ca ²⁺ oscillations	261
Figure 5.12	Effect of hypoxia on PGF2 α induced Ca ²⁺ oscillations	261
Figure 5.13	Effect of hypoxia on U46619 induced Ca ²⁺ oscillations	262
Figure 5.14	Effect of hypoxia on basal and spontaneous Ca ²⁺ oscillations	263
Figure 5.15	Effect of PDGF-BB on intracellular Ca ²⁺ in the presence of pinacidil	264
Figure 5.16	Effect of nimodipine on basal Ca ²⁺ and spontaneous Ca ²⁺ oscillations	264
Figure 5.17	Effect of hypoxia on high K ⁺ induced Ca ²⁺ oscillations	265
Figure 5.18	Distribution of DiBAC4(3) according to membrane potential	267
Figure 5.19	Characterization of DiBAC4(3) fluorescence	267
Figure 5.20	Changes of DiBAC4(3) fluorescence in control studies	269
Figure 5.21	Effects of K ⁺ channels in regulating resting membrane potential of HCASMCs	270
Figure 5.22	Effect of adenosine on plasma membrane potential	272
Figure 5.23	Effect of K _{ATP} channel modulators on membrane potential	273
Figure 5.24	Effect of NS1619 on membrane potential	274
Figure 5.25	Effect of NS11021 on membrane potential	275

Figure 5.26	Effect of IK_{Ca} and SK_{Ca} channel modulators on membrane potential	276
Figure 5.27	Effect of rotenone on membrane potential	278
Figure 5.28	Effect of antimycin on membrane potential	279
Figure 5.29	Effect of oligomycin and CCCP on membrane potential	280
Figure 5.30	Effect of hypoxia on membrane potential	281
Figure 5.31	Role of K^+ channels in hypoxia induced hyperpolarization	282
Figure 5.32	Mechanisms of VSMC contraction	285
 Chapter 6		
Figure 6. 1	Morphology of HCASMCs	291
Figure 6.2	Comparison of cell size between different passages	292
Figure 6.3	Comparison of cell morphology between different passages	292
Figure 6.4	Coomassie blue staining of electrophoretically separated protein sample from P7-P13	293
Figure 6.5	Western blot of α -SMA and calponin in HCASMCs	294
Figure 6.6	Immunocytochemistry of α -SMA, calponin and MHC expression	295
Figure 6.7	Effect of serum deprivation on cell number after 48 hours	296
Figure 6.8	Effect of 6 μ M oligomycin on cell number	297
Figure 6.9	Effect of hypoxia and high glucose on cell number	297
Figure 6.10	Colormetric change of MTT in reaction	298
Figure 6.11	Cell number and 570 nm absorbance of MTT assay	298
Figure 6.12	Effect of PDGF-BB on HCASMC proliferation	299
Figure 6.13	Effect of high glucose on HCASMC proliferation	299
Figure 6.14	Effect of hypoxia on HCASMC proliferation	300
Figure 6.15	Effect of K_{ATP} channel modulators on HCASMC proliferation	301
Figure 6.16	Effect of BK_{Ca} channel modulators on HCASMC	302

	proliferation	
Figure 6.17	Effect of IK_{Ca} / SK_{Ca} channel modulators on HCASMC proliferation	302
Figure 6.18	Effect of K_{ir} channel inhibitors on HCASMC proliferation	303
Figure 6.19	Effect of K_v channel inhibitor on HCASMC proliferation	303
Figure 6.20	Effect of ion channel inhibitors on hypoxia induced HCASMC proliferation	304
Figure 6.21	The effect of PDGF-BB on HCASMC migration	305
Figure 6.22	The effect of hypoxia on HCASMC migration	306
Figure 6.23	Hypoxia induces HCASMC migration in transwell assay	306
Figure 6.24	Staining of HCASMCs with Reastain Diff kit	307
Figure 6.25	Schematic presentation of cell division cycle	308
Figure 6.26	Negative control with unstained HCASMCs	309
Figure 6.27	Cell cycle analysis	310
Figure 6.28	Effect of serum deprivation on HCASMC cell cycle	311
Figure 6.29	Cell cycle profiles of HCASMCs in hypoxia	312
Figure 6.30	Effect of glibenclamide on HCASMCs cell cycle	312
Figure 6.31	The role that K_{Ca} channels play in regulating SMC plasticity	316
Chapter 7		
Figure 7. 1	Relationship between O_2 consumption and coronary blood flow	319
Figure 7.2	Regulation of vascular K_{ATP} channels	322
Figure 7.3	Hypothesised mechanisms of metabolic/hypoxic vasodilation of HCASMCs	330

List of Tables

Chapter 1

Table 1.1	Different combinations of K_{ATP} channels subunits in various tissues	30
Table 1.2	K_{ATP} channel subunit genes	30

Chapter 2

Table 2.1	HCASMC inventory	48
Table 2.2	Primary antibodies	48
Table 2.3	Secondary antibodies	49
Table 2.4	Summary of primers and oligonucleotides	50
Table 2.5	Transfection reagents used in the study	54
Table 2.6	Preparation of transfection mixture	55
Table 2.7	Transfection mixture for one 10 cm dish using transfection reagent	56
Table 2.8	Ligation protocol with T4 DNA ligase	84

Chapter 3

Table 3.1	Summary of HEK293 cell transfection efficiency of pHRed	91
Table 3.2	Transfection reagents optimized in HCASMCs	98

Chapter 4

Table 4.1	Retroviridae family	175
Table 4.2	Comparison of 2 nd and 3 rd generation lentiviral systems	178
Table 4.3	Basic properties of main viral vectors and non-viral vectors	180
Table 4.4	Advantages and disadvantages of different gene delivery systems	244
Table 4.5	Development of improved recombinant lentivectors	245

Chapter 5

Table 5.1	The effects of vasoconstrictors and high K^+ on $[Ca^{2+}]_i$	255
-----------	---	-----

List of Abbreviations

2-DG	2-Deoxy-D-glucose
4-PA	4-aminopyridine
α-SMA	Smooth muscle α -actin
θ_c	Critical angle
ψ_m	Mitochondrial membrane potential
AA	Arachidonic acid
AAV	Adeno-associated viruses
ABC	ATP-binding cassette
Ad	Adenovirus
ADP	Adenosine diphosphate
AGR2	Anterior gradient protein 2
AK	Adenylate kinase
AKAP	A-kinase anchor protein
AMPK	AMP-activated protein kinase
AP-1	Activator-protein 1
APS	Ammonium persulfate
AR	Aspect ratio
ARD1	Arrest defective-1
ARNT	Aryl hydrocarbon nuclear translocator
ATP	Adenosine triphosphate
[ATP]_i	Intracellular ATP level
AUC	Area under curve
BCA	Bicinchonic acid
bHLH	Basic helix-loop-helix
BK_{Ca}	Ca ²⁺ and voltage-activated K ⁺ channel
BP	Blood pressure
BSA	Bovine serum albumin
[Ca²⁺]_i	Intracellular Ca ²⁺ concentration
cAMP	Cyclic AMP
CCB	Ca ²⁺ channel blocker
CCCP	Carbonyl cyanide <i>m</i> -chlorophenyl hydrazone
CCI	Center for Cell Imaging suite
CCICR	Ca ²⁺ -channel-induced Ca ²⁺ release
cGMP	Cyclic GMP
CHI	Congenital hyperinsulinism
Circ	Circularity
CK	Creatine kinase
CNS	Central nervous system
COX	Cytochrome c oxidase
CP	Coupling efficiency
DAPI	4',6'-diamidino-2-phenylindole
DiBAC4(3)	Bis-(1,3-dibutylbarbituric acid) trimethine oxonol

DM	Diabetes mellitus
DMEM	Dulbecco's modification of Eagle's medium
DPBS	Dulbecco's phosphate buffered saline
EC	Endothelial cell
ECAR	Extracellular acidification rate
E_K	K ⁺ equilibrium potential
E_m	Membrane potential
Egr-1	Early growth response factor
eNOS	Endothelial NO synthase
EPAC	Exchange protein activated by cAMP
ETC	Electron transport chain
EtOH	Ethanol
FACS	Fluorescence-activated cell sorting
FADH₂	Flavin adenine dinucleotide
FBS	Fetal bovine serum
FC	Fat cell
FCCP	Carbonyl cyanide <i>p</i> -trifluoromethoxyphenylhydrazone
FIH	Factor inhibiting HIF
FRET	Fluorescence resonance energy transfer
FSC	Forward scatter (FACS)
GLUT	Glucose transporter
G protein	Guanosine-5'-triphosphate-binding protein
G_s	G-protein (stimulatory)
GSH	Glutathione
GSSG	Oxidized glutathione
Hb	Hemoglobin
HCAEC	Human coronary artery endothelial cell
HCASMC	Human coronary artery smooth muscle cell
HepesBSS	HEPES buffered saline solution
HK	Hexokinase
hPDGF-BB	Human platelet-derived growth factor BB
HIF	Hypoxia-inducible factor
H₂O₂	Hydrogen peroxide
HO-2	Haem oxygenase-2
HRE	Hypoxia responsive element
HRP	Horseradish peroxidase
hUBCpro-F	Human Ubiquitin C (UbC) promoter, forward primer
HVA	High voltage activated
IAA	Iodoacetate
IbTX	Iberitoxin
ICC	Immunocytochemistry
IK_{Ca}/SK_{Ca}	Intermediate/small conductance Ca ²⁺ -sensitive K ⁺ channel
IP₃R	Inositol trisphosphate receptor
ITRs	Inverted terminal repeat sequences

K2P	Two-pore domain K ⁺ channel
K_{ATP}	ATP sensitive K ⁺ channel
KCO	K _{ATP} channel openers
K_{ir}	Inward rectifier K ⁺ channel
[K⁺]_o	Extracellular K ⁺ concentration
K_v	Voltage-gated K ⁺ channel
LAD	Left anterior descending
LC	Left circumflex
LCA	Left coronary artery
LDH	Lactate dehydrogenase
LF2000	Lipofectamin TM 2000
LMCA	Left main coronary artery
LVA	Low voltage activated
MCU	Mitochondrial calcium uniporter
MEM	Minimum essential media
MHC	Myosin heavy chain
MLC₂₀	Regulatory light chain of myosin (20 kDa)
MLCK	Myosin light chain kinase
MQ water	Milli q water
MTP	Mitochondrial permeability transition pore
MTT	3-(4,5 dimethylthiazol-2-yl)-2,5-diphenyltetrazolium bromide
MYPT	Myosin phosphatase target subunit
NADH	Nicotinamide adenine dinucleotide
NADPH	Nicotinamide adenine dinucleotide phosphate
NBD	Nucleotide binding domain
N(/C)TAD	N(/C)-terminal two transactivation domain
NCX	Na ⁺ -Ca ²⁺ exchanger
NEAA	Non-essential amino acids
NF-κB	Nuclear factor-κB
NLS	Nuclear localizing signal
NO	Nitric oxide
OCR	Oxygen consumption rate
O.D.	Optical density
ODD	Oxygen-dependent degradation
ORF	Open reading frame
OXPHOS	Oxidative phosphorylation
PAS	Per Arnt Sim domain
PCR	Polymerase chain reaction
PDL	Poly D-lysine
PE	Phenylephrine
PFA	Paraformaldehyde
PFK	Phosphor-fructo-kinase
PGF2α	Prostaglandin F2α
PHD	Prolyl-hydroxylase

P_i	Inorganic phosphate
PMF	Proton motive force
PIP₂	Phosphatidylinositol (4,5)-bisphosphate
PK	Pyruvate kinase
PKA	Protein kinase A
PKC	Protein kinase C
PKG	Protein kinase G
PLC	Phospholipase C
PO₂	Partial pressure of O ₂
PcO₂	Capillary PO ₂
PiO₂	Intracellular PO ₂
P_o	Open possibility
P/O ratio	Phosphate/oxygen ratio
PP2B	Protein phosphatase 2B
PsO₂	Cell surface PO ₂
PSS	Physiological saline solution
RBC	Red blood cell
ROC	Receptor-operated Ca ²⁺ channel
PPR	Proton production rate
RCA	Right coronary artery
RCR	Respiratory control ratio
RO water	Reverse osmosis water
ROS	Reactive oxygen species
RRE	Rev-responsive element
RT-PCR	Reverse transcription polymerase chain reaction
SDS-PAGE	Sodium dodecyl sulphate polyacrylamide gel electrophoresis
SEM	Standard error of mean
SERCA	Sarcoplasmic reticulum/endoplasmic reticulum Ca ²⁺ -ATPase
SGLT	Sodium-dependent glucose transporter
SOD	Superoxide dismutase
SOC	Store-operated Ca ²⁺ channel
SR	Sarcoplasmic reticulum
SSC	Sodium citrate buffer
SSC	Side scatter (FACS)
SUR	Sulphonylurea
TASK-1	Twin pore acid-stimulated K ⁺ channel
TCA cycle	Tricarboxylic acid cycle
TEA	Tetraethylammonium
TIRF	Total internal reflection fluorescence
TMD	Transmembrane domain
TNS	Trypsin neutralizing solution
TRP	Transient receptor potential family of channels
TTFA	Thenoyltrifluoroacetone
UHQ water	Ultra high quality water

VDCC	Voltage-dependent Ca ²⁺ channel
VHL	Von Hippel-Lindau
VSMC	Vascular smooth muscle cell
VSV-G	Vesicular stomatitis virus glycoprotein
VV	Vasa vasora
W_{A/B}	Walker A/B motif
WB	Western blot
WPRE	Woodchuck hepatitis virus (WHP) posttranscriptional regulatory element
WPRE-R	5' end of WPRE, reverse primer
WR	Working reagent

Units conversion for O₂

$$1 \text{ kPa} = 7.5 \text{ Torr}$$

$$1 \text{ Torr} = 1 \text{ mmHg}$$

$$760 \text{ mmHg} = 21\% \text{ O}_2$$

$$1\% \text{ O}_2 = 10 \text{ } \mu\text{M O}_2$$

Chapter 1

Introduction

1.1 General introduction

Oxygen (also referred as O_2 in this thesis) is an absolute requirement for multicellular organisms that generally require higher level of energy. In vertebrates, it is transported throughout the body by hemoglobin (Hb) in red blood cells (RBCs) so that every cell can perform aerobic energy production. Shortage and lack of O_2 , hypoxia and anoxia, could result in serious and irreversible damage to vital organs. Sensing and responding appropriately to O_2 deprivation is therefore of great importance and required for survival of all forms of aerobic life. Ensuring appropriate O_2 supply is particularly important for energy hungry organs such as heart, brain and kidney [1], and acute O_2 deficiency is usually resolved by increasing blood flow. Thus, hypoxia causes arteries to dilate, increasing blood supply. An exception to this is the pulmonary artery which constricts and shunts the blood to better ventilated areas of the lung to maintain the ventilation perfusion ratio. Despite the above well-established phenomenon in the vasculature, the underlying mechanisms have proved to be complicated and difficult to disentangle [2].

Hypoxic vasodilation of coronary arteries is a physiologically protective response to match blood flow to increased O_2 demand of the heart. For most of the tissues, O_2 extraction is no more than 25%. However, myocardium extracts a high proportion (65-75%) of O_2 in coronary blood at baseline conditions [1]. Therefore, O_2 reserve of the heart is small, leaving little spare for further extraction [1, 3, 4]. When there is an increase in cardiac workload, the coronary blood flow may increase more than 5 fold almost instantly [1, 2]. A number of processes may be involved and work in concert in metabolic vasodilation, thus link cell metabolism to cell viability and function [2].

Although coronary artery vasodilation during hypoxia is a well-known phenomenon for many years, its mechanism is still controversial, and this thesis aims to shed light on this fundamental yet unresolved question. Combination of molecular and cellular techniques was used, and attempts were made to permit mechanistic and quantitative investigations wherever possible. Experiments were performed using smooth muscle cells (SMCs) obtained from human coronary artery. As a cardiologist,

this is a cell model of my interest, and I begin the introduction discussing human cardiovascular system.

1.2 Human cardiovascular system

The cardiovascular system, also called the circulatory system, is a network comprised of heart, blood and blood vessels. The heart is a hollow muscular organ with four chambers: left atrium, right atrium, left ventricle and right ventricle. De-oxygenated blood returns to right atrium through superior and inferior vena cava and then right ventricle and travels to the lung through pulmonary trunks. Blood is oxygenated in the lung via a short and low pressure circulation (the pulmonary circulation) [1] (**Figure 1.1**) and goes to left atrium, and then left ventricle. Left ventricle pumps the oxygenated blood out of the heart to arterial vessels, and delivers O_2 and energetic substrates to the tissues of the body at high pressure (the general/systemic circulation). Pulmonary circulation is different from that of systemic circulation as pulmonary artery carries deoxygenated blood and pulmonary vein carries oxygenated blood. Blood delivers O_2 , nutrients (e.g. glucose), electrolytes, enzymes, hormones to the organs, tissues, and cells of the body. Subsequent metabolic waste products (e.g. CO_2 , H^+) are removed at the same time.

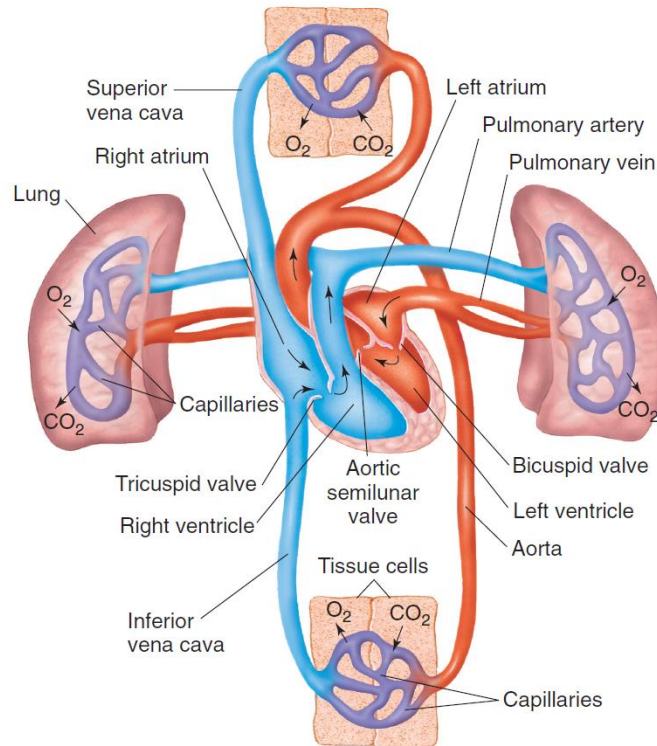


Figure 1.1: Human cardiovascular system. Systemic circulation and pulmonary circulation.

(Source: highered.mheducation.com/sites/dl/free/0073403490/578766/sample_chapter10.pdf).

1.3 Human coronary circulation

1.3.1 Structure and function of coronary circulation

The chambers of the heart contain blood, but ironically cardiac muscle is unable to obtain O_2 directly from it. This is because diffusion distance of O_2 is very short, and so the heart requires its own circulation where blood is provided by coronary arteries. Left main and right coronary arteries (LMCA and RCA) branch off the ascending aorta just above the aortic valve, and LMCA is further divided into left anterior descending (LAD) and left circumflex (LCX) as LMCA is very short (**Figure 1.2**). Thus, it is LAD, LCX and RCA that extend over the heart's surface as they traverse away from the aorta. Three main coronary arteries branch out into progressively smaller arteries which penetrate the epicardium to supply transmural myocardium with O_2 and nourishment. Ultimately, blood is channeled to capillaries,

and the cardiac myocyte is unusual in the body in having a cell to capillary ratio of 1 to 1 [1]. Various branches of coronary arteries were summarized and divided into different patterns based on the arteries distribution [5] as shown in **Figure 1.3**. Because of the compressive force taking place during systole, the transmural blood supply is received mainly during ventricular relaxation in the left ventricle.

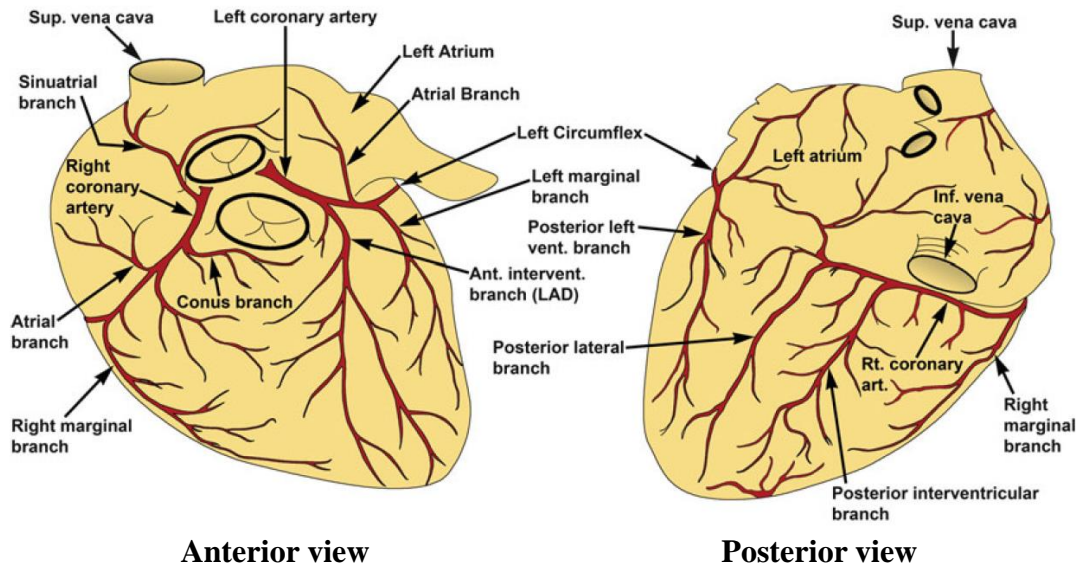


Figure 1.2: Distribution of main coronary arteries. The major human coronary arteries of the heart from both anterior and posterior, most of them are epicardial vessels (Reproduced from Robert J. Tomanek, 2013 [5]).

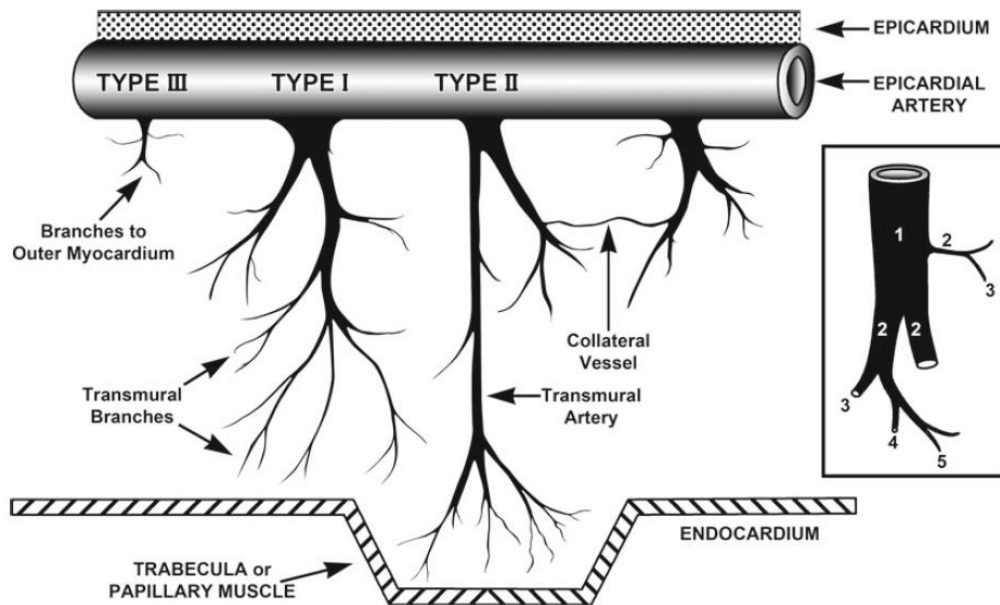


Figure 1.3: Branch patterns of human coronary artery. Type I: Intramural branches; Type II: Branches directed mainly to the subendocardial myocardium; Type III: Short branches supplying subepicardial myocardium. The figure in the inset shows the generations of branches (2, 3, 4, 5). (Reproduced from Tomanek, 2013 [5])

1.3.2 Anatomy of human coronary arteries

Blood pressure (BP) and blood flow are controlled in the body through constricting and dilating of the vessels. With the exception of capillaries, the wall of blood vessels is comprised of three layers [1, 5]. The tunica intima (inner coat) of the vessel is formed with a single layer of squamous endothelial cells (ECs) and separates vascular SMCs (VSMCs) from the plasma. Multiple layers of spindle shaped SMCs form the tunica media (middle coat), providing the contractile machinery of the vessels. The tunica adventitia (outer coat) mainly consists of connective tissue with a variety of cells such as nerves within. Even though the three layers are separated physically from each other by internal and external elastic lamina, the signal from intima can be transmitted to media by the myo-endothelial junction. **Figure 1.4** represents the main components of a coronary artery. **Figure 1.5** shows the structure of canine coronary artery under electron micrographs [5].

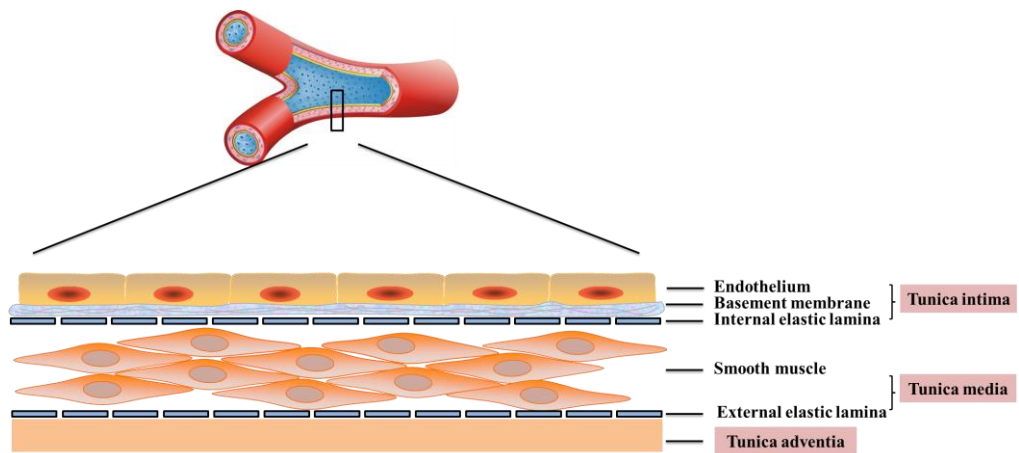


Figure 1.4: Structure of the artery wall. The three layers of the artery wall: Intima (endothelium and subendothelium); media (external elastic lamina and smooth muscle); and adventitia.

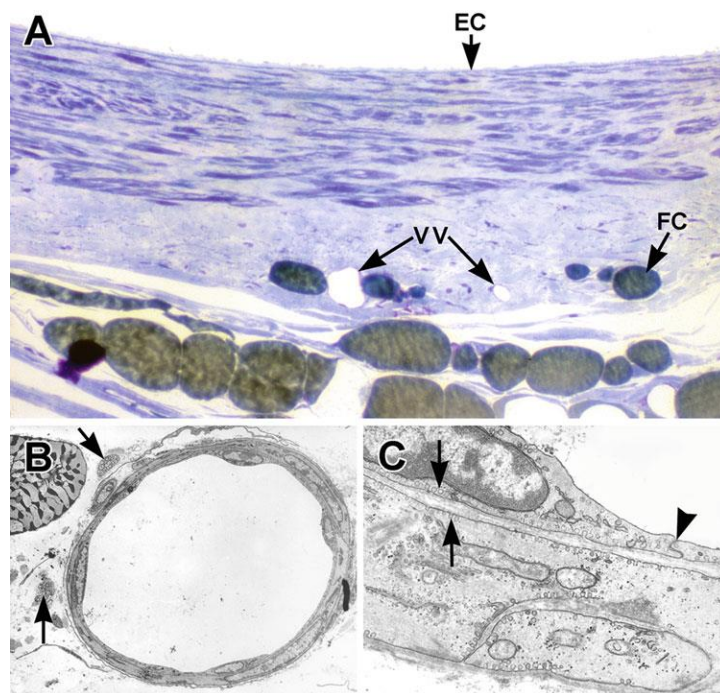


Figure 1.5: Micrographs of canine coronary artery (A) and arterioles (B&C). (A) Epicardial artery with a media consisting of SMCs (blue elongated structures) and connective tissue (light blue). VV: vasa vasora; FC: fat cells; EC: endothelial cell. (B) A small arteriole with an endothelium and one layer of smooth muscle. The arrows indicate the nerve bundle in the adventitia. (C) Arrows indicate plasma membrane vesicles or caveolae. Arrowhead indicates a gap junction. (Reproduced from Tomanek, 2013 [5])

1.4 O₂ delivery

1.4.1 O₂ carrier

In vertebrates, there are three main steps for the O₂ delivery to the cells: breathing of O₂ by the lung, transporting of O₂ in the blood and delivering of O₂ to cells. Passively dissolving O₂ to blood is completely inadequate for the purpose, and a more efficient way to ferry around O₂ is required. It is Hb in RBCs that acts as O₂ carrier binding to O₂ in the lung and releasing it to tissues upon arriving to capillaries where the partial pressure of O₂ (PO₂) is very low. In a normal individual, a RBC has a lifespan of ~115 days, varying between 70 and 140 days [6]. RBCs maintain a relatively constant number of about 5×10^{11} cells/dL [7], and equilibrium in number is achieved between the scavenging activity by macrophages and RBC production [8]. RBCs can produce polypeptide chains (α - and β -globin) and protoporphyrin, and these and Fe²⁺ form a functional adult Hb molecule. At the places where O₂ level is high (e.g. lung), Hb binds to O₂ with a structure change from T state to R state (one pair of $\alpha\beta$ subunits shifts with respect to the other by a rotation of 15 degrees) [9, 10] (Figure 1.6).

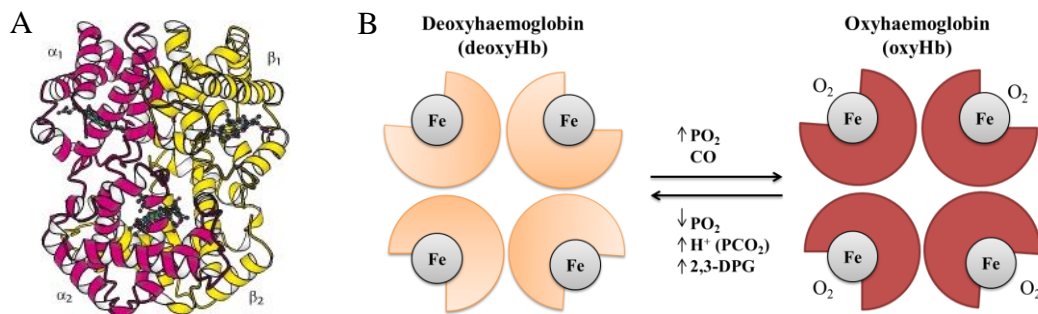


Figure 1.6: Structure of Hb. (A) Quaternary structure of Hb. Hb consists of two α chains and two β chains, and functions as a pair of $\alpha\beta$ dimers (Reproduced from Berg et al., 2002 [10]). (B) Switches of Hb between T state (left) and R state (right).

1.4.2 O₂ tension, exchange and gradient

Once O₂ is delivered to the cells, it acts as the final electron acceptor of electron transport chain (ETC), the final step of cellular respiration. The PO₂ at sea level is

approximately 21 KPa, corresponding to ~21% of atmospheric pressure. Due to longitudinal and radial gradients during delivery from trachea to the cells, PO₂ decreases dramatically [11-14] (**Figure 1.7**). It is suggested that the median PO₂ is approximately 7 KPa (~7%) in systemic arteries, and 3-4 Kpa (~3-4%) in arterioles and capillaries [11]. Many investigations have consistently shown that a great amount of O₂ is lost from arterioles while the change in the capillaries is small. This has been suggested to be related to the metabolic state of the organ [14]. Possible reasons for the loss of O₂ in arterioles include O₂ consumption by nearby parenchymal cells, diffusion of O₂ to neighboring microvessels, increased O₂ solubility in cell membrane as well as O₂ consumption by SMCs and ECs in the vessel wall [11, 14-16]. The destination of O₂ is mitochondria, and to reach there from a microvessel, O₂ needs to pass through a series of structures (e.g. cell membrane, cytosol) [12] (**Figure 1.8**). Such barriers may further contribute to O₂ gradients that shift according to change in metabolic demand. Myoglobin microspectrophotometry identified a gradient of O₂ across the sarcolemma of cardiac myocyte [17]. Studies in human skeletal muscle showed an intracellular PO₂ (PiO₂) of ~32 mmHg at rest that decreased to ~3-6 mmHg during moderate to heavy exercise [18, 19].

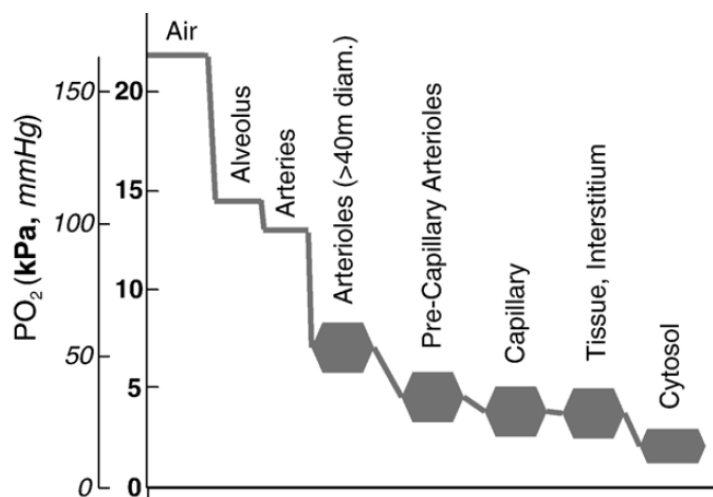


Figure 1.7: Regional distribution of O₂ partial pressure from airways to cytosol. The thickness of the line represents the variation of the value. (Reproduced from Ward, 2008 [11])

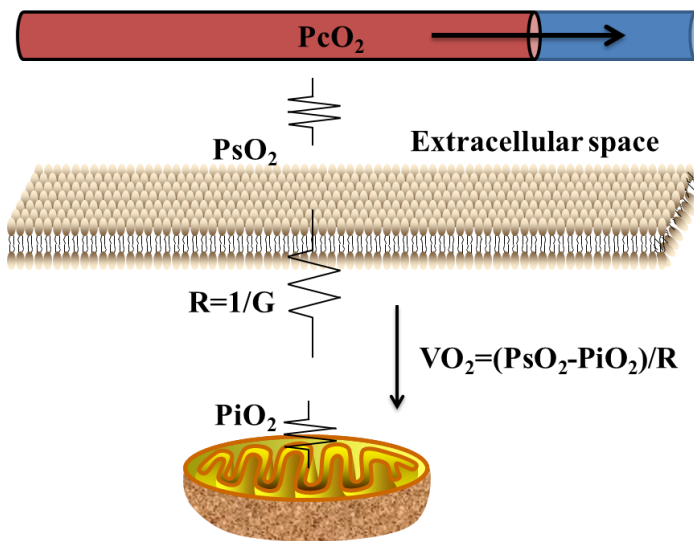


Figure 1.8: Graphical representation of a simplified diffusion equation and typical barriers. O_2 diffuses from capillaries to mitochondria through a series of barriers including extracellular fluid, plasma membrane, cytosol and mitochondria membrane. P_{cO_2} , capillary PO_2 ; P_{sO_2} , cell surface PO_2 ; P_{iO_2} , intracellular PO_2 ; R is resistance to diffusion, inverse of conductance, G . (Modified from Clanton et al., 2013 [12])

1.5 O_2 sensing mechanisms: a role for O_2 sensors

1.5.1 Overview

Adequate O_2 supply is of utmost importance for cell function and survival. A deficit of O_2 , though a useful trigger for many physiological processes, could lead to pathogenesis of many diseases if it becomes harmful [20-24]. Understanding how altered O_2 causes adaptive changes in the cells requires knowledge of how the cells sense O_2 in the first place. A number of mechanisms have been suggested in the cardiovascular system which assess and sense the concentration of O_2 [2, 11, 12, 21, 22, 25].

1.5.2 Carotid body

Carotid body is made of chemoreceptors that are responsible for fast, cardiorespiratory, and circulatory systemic reflexes (e.g. hyperventilation or

sympathetic activation). Chemoreceptors respond to a decrease in PO_2 and rise in partial pressure of CO_2 and H^+ . When hypoxia occurs, chemoreceptors respond immediately, increasing O_2 uptake [26-28]. Chemoreceptors are classified into two categories, central and peripheral chemoreceptors, and the carotid body belongs to the latter. Central receptors are in the medulla oblongata and respond to the changes in pH and CO_2 [29]. In addition to carotid body, peripheral chemoreceptors are located in aortic bodies, neuroepithelial bodies and adrenomedullary chromaffin bodies, and they are more important in sensing global O_2 tension. Peripheral chemoreceptors have neurosecretory cells which can release neurotransmitters when PO_2 decrease (<60 mmHg). Although many chemoreceptors exist, carotid body is the major arterial chemoreceptor that controls the hyperventilatory response to hypoxia, and therefore I will focus on the carotid body [21, 28].

The pair of carotid bodies are located near the bifurcation of the carotid arteries and contain glomus cells (Type I cell) which respond to hypoxia. O_2 sensitive, neuron-like glomus cells are innervated by sensory fibers, and they can transmit the signal to central nervous system when O_2 tension changes in the artery. O_2 sensitive cells in arterial chemoreceptors and other organs are important in homeostatic O_2 sensing system, and well known for their ability in adaption to acute perturbation of environmental PO_2 . However, the mechanisms by which these chemoreceptors sense O_2 tension remain controversial, and possibly more than one pathway may be working in concert [12, 27, 30]. It is acknowledged that hypoxia activation of glomus cells of all mammalian species is correlated with the O_2 sensitive K^+ channels. A decrease in K^+ channel conductance results in cell depolarization and subsequent Ca^{2+} influx, releasing neurotransmitters to activate the nerve fibers [28, 31]. However, more work remains to be done to shed light on the molecular mechanisms in the regulation of ion channel conductance in different tissues when O_2 tension changes.

1.5.3 O_2 sensitive ion channels

1.5.3.1 K^+ channels

Since the initial finding of an O_2 sensitive K^+ channel in rabbit carotid body

[32], many studies have been carried out to investigate O₂ sensitive K⁺ channels in a wide range of tissues. It is now known that many K⁺ channel subtypes alter their activity with acute hypoxia, and changes in the expression level of different K⁺ channels were observed under prolonged hypoxia [21]. ATP-sensitive K⁺ channels (K_{ATP}) are activated by intracellular ADP and inhibited by ATP. Due to their sensitivity to intracellular nucleotides, K_{ATP} channels can couple cellular metabolism to cell excitability, possibly making them uniquely positioned in the process of hypoxic vasodilation in systemic arteries [33, 34]. However, it is still under debate whether hypoxia causes a sufficient change in cellular nucleotides for activation of K_{ATP} channels [33]. It is also uncertain whether the effect on K⁺ channels is a direct effect from hypoxia, or secondary from other molecules produced during hypoxia. Evidence on excised membrane patch and recombinant systems has suggested hypoxia may modulate K⁺ channels directly [35-37]. However, other studies suggested an indirect effect on K⁺ channels from intracellular O₂ sensitive signaling molecules such as reactive oxygen species (ROS) and haem oxygenase (HO) [21, 22, 38, 39].

1.5.3.2 Ca²⁺ channels

Ca²⁺ enters VSMCs mainly through voltage dependent Ca²⁺ channels (VDCCs) where an increase in intracellular free Ca²⁺ concentration ([Ca²⁺]_i) results in SMC contraction. VDCCs are a group of voltage-gated Ca²⁺ channels which are regulated by membrane potential. Hypoxia causes an increase in [Ca²⁺]_i and pulmonary artery SMC contraction while it causes a decrease in [Ca²⁺]_i and systemic artery SMC relaxation [40]. The relationship between changes of membrane potential and increase in open probability (P_o) of VDCCs is very steep where a few millivolts (mV) depolarization will cause several fold change in [Ca²⁺]_i [41-43]. As the membrane potential in VSMC is thought to be determined primarily by K⁺ channels, the changes in [Ca²⁺]_i may be secondary to changes in activity of K⁺ channels. On the other hand, there is also evidence for a direct effect of hypoxia on [Ca²⁺]_i independent of membrane potential [44, 45].

1.5.4 Mitochondria

The mitochondrion is a double membrane organelle existing in most cells. It is where the biochemical process of O₂ respiration happens, generating the bulk of ATP in cells. Due to their crucial and ubiquitous task in producing ATP, it is recognized as the energy factory of the cell. However, mitochondria appear increasingly multi-tasking organelles with other roles including cell signaling, cell differentiation, cell cycle and cell death [46, 47]. To generate ATP via oxidative phosphorylation (OXPHOS), it requires mitochondria to use O₂ as the final electron acceptor. Thus, mitochondrial F1F0-ATPase works in a forward mode and consumes proton motive force (PMF) to produce ATP. On the other hand, when hypoxia/anoxia prevails, ETC is ceased and cells begin to utilize energy from glycolysis. Based on these, mitochondria are well positioned as promising candidates for cellular O₂ sensing [11, 47]. However, because the main O₂ sensitive enzyme cytochrome oxidase has a low apparent concentration for 1/2 maximum velocity (K_m) for O₂, it is still saturated until O₂ tension decreases to a very low level (<1 mm Hg). The O₂ level at which respiratory rate is 50% of maximum (P50) of cytochrome aa3 is ~0.07 kPa PO₂ (~0.7 μM), which was measured in systemic cells [48]. Therefore mitochondria may function well as a sensor of anoxia but are unable to sense a moderate change in O₂ tension in the cells [49]. If true, mitochondria cannot be a major player in hypoxic vasodilation that occurs at much higher O₂ levels [2]. It should be noted, however, that the measurement of the O₂ concentration at K_m is usually carried out in isolated enzyme, so it is very likely to be different in the whole intact cell especially when taking into consideration of O₂ longitudinal and radial gradients (See **Figure 1.7 and 1.8**).

Although this thesis does not address the issue experimentally, by-products of cellular metabolism may be important when considering hypoxic response. The redox state and mitochondrial ROS production resulting from mitochondrial inhibition are usually unrelated to energy state of the cells. During electron transport in the ETC, ROS in the form of superoxide can be formed at several sites when single electrons are lost to O₂. Studies also suggested about 3% of O₂ consumed is

not reduced effectively and there is evidence indicating electron lost at the same time [50, 51]. The formation of ROS needs O_2 as substrate, so the question would be whether there is enough O_2 to make ROS during hypoxia. However, even at an intracellular PO_2 of 1 Torr, there is still $\sim 1.4 \mu\text{mol/L } O_2$ in the cytosol and $\sim 5\text{-}7 \mu\text{mol/L } O_2$ in the cell membrane [12]. Increased mitochondrial redox state and ROS production during hypoxia/anoxic conditions may therefore act as a signaling mediator [11, 12, 26] (Figure 1.9).

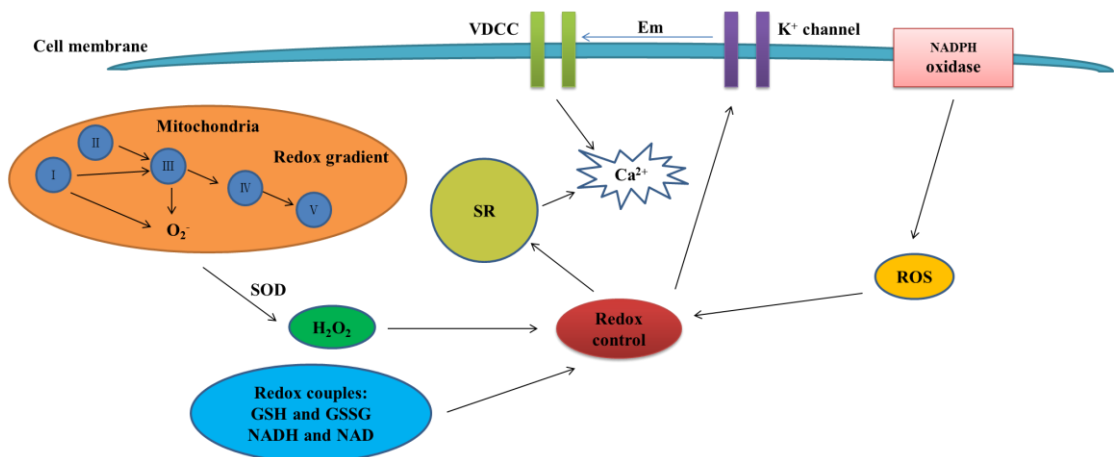


Figure 1.9: Redox mechanism for O_2 sensing. ROS are produced from mitochondria, NADPH oxidase and redox couples. Redox signaling may regulate K^+ channels on the cell membrane and Ca^{2+} entry. The same redox signaling may control Ca^{2+} in the sarcoplasmic reticulum. SOD: superoxide dismutase; H_2O_2 : hydrogen peroxide; GSH: glutathione; GSSG: oxidized glutathione. (Modified from Weir et al., 2005 [26])

1.5.5 Hypoxia-inducible factor (HIF)

Response to hypoxia is not restricted to an acute one such as relaxation of systemic artery. Chronic hypoxia can initiate adaptive mechanisms. One such example is hypoxia-inducible factor (HIF) which is a transcription factor. HIF is a dimer composed of one of the HIF α subunits (1α , 2α , or 3α) and a β subunit. Among three subtypes (HIF-1, HIF-2 and HIF-3), HIF-1 is most studied [52]. HIF 1β , also named aryl hydrocarbon receptor nuclear translocator (ARNT), is constitutively

expressed. HIF 1 α is responsible for O₂ dependent prolyl and asparaginyl hydroxylation that causes increasing angiogenic gene expression [53]. Under normoxia, HIF 1 α is hydroxylated by prolyl-hydroxylase (PHD), taking an ubiquitin dependent degradation pathway. Hypoxia inactivates and stabilizes PHD. Together with HIF 1 β , HIF 1 α binds to hypoxia responsive element (HRE), leading to activation of genes responsible for erythropoiesis, angiogenesis, expression of ion channels and activation of glycolytic energy production [11, 22, 54]. O₂ sensitivity of HIF 1 α is presented in **Figure 1.10**. Together with other transcriptional factors such as early growth response factor (Egr-1), nuclear factor- κ B (NF- κ B), as well as activator-protein 1 (AP-1), HIF-1 protects cells from injuries during prolonged hypoxia [55-57]. HIF 1 α deficient (HIF 1 α ^{-/-}) mouse embryos die at mid-gestation with defects in the cardiovascular system [53]. Pulmonary artery SMCs from wild type mice respond to hypoxia with increased [Ca²⁺]_i and decreased voltage-gated K⁺ currents while these effects were lost in HIF1 α ^{+/-} mice [58]. In the same study, it has been shown that even though carotid bodies isolated from Hif 1 α ^{+/-} mice maintained normal histology, they are unable to respond to hypoxia [58].

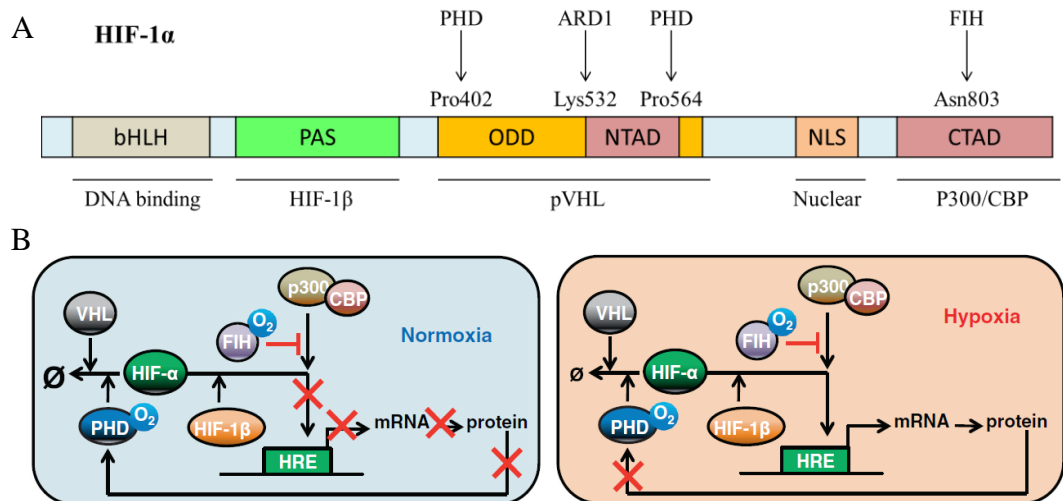


Figure 1.10: Structure and regulation of HIF-1. (A) HIF 1 α structure (Modified from Yeom et al., 2011 [59]). (B) Pathways of HIF-1 regulation under normoxia and hypoxia (Reproduced from Cavadas et al., 2013 [60]). HIF: hypoxia-inducible factor; PHD: prolyl-hydroxylase; ARD1: arrest defective-1; FIH: factor inhibiting HIF; bHLH: basic helix-loop-helix; PAS: Per Arnt Sim domain; ODD: oxygen-dependent degradation; N(C)TAD: N(C)-terminal two transactivation domain; NLS: nuclear localizing signal; VHL: von Hippel-Lindau; HRE: hypoxia responsive element.

1.5.6 Other O₂ sensors

Besides what are generally considered to be major mechanisms mentioned above, many other mediators (e.g. NADPH oxidase, HO, cytochrome P-450 4A, pentose phosphate pathway) may play a role in O₂ sensing [11, 22, 38, 61]. Mitochondria are not the only ROS production site. NADPH oxidase on the cell membrane is an enzyme that can catalyze the production of superoxide anion radical (O²⁻) from O₂ and NADPH (Figure 1.9). Haem oxygenase-2 has been reported as an O₂ sensor in carotid body activation by hypoxia [62], and its deletion in mouse caused impaired immunity and abnormal O₂ sensing [63]. Compared to other cells, mitochondria in glomus cells and pulmonary artery SMCs showed much higher sensitivity to low O₂ [11, 39], and the opposite responses of systemic artery and pulmonary artery may rise from a fundamental difference in their mitochondria [64]. It should be noted that some O₂ sensors may be more important in some specialized

cells than others, and the ways via which O₂ sensors transduce signal to their ultimate effector can be different [11].

In summary, over physiological hypoxia, a wide range of O₂ sensors are activated to serve different functions with shared goals to provide more O₂, enhance the efficiency to use available O₂, and protect cell viability and function.

1.6 Metabolic/hypoxic vasodilation

1.6.1 Definitions

Even though the PO₂ in the air is ~21%, it decreases to 3-4% when reaching arterioles and capillaries [11] and lower still in the cytosol [12]. Therefore, hypoxia is a relative term, indicating conditions in which failure of delivery and/or use of O₂ (O₂ starvation) affect the function of the tissue. Hypoxia is different from ischemia as the latter is a decrease in blood flow to the tissue, and so resulting inadequate oxygenation is secondary. Ischemia can always cause hypoxia, but hypoxia can occur without ischemia (e.g. high altitude, anemia). Depending on the causes, hypoxia may be classified as four subtypes according to the primary origin of the defect: hypoxic hypoxia occurs when the PO₂ of arterial blood falls, anemic hypoxia occurs when there is a decrease in the oxygen carrying ability of the blood, stagnant hypoxia occurs when the blood flow is abnormally low, and histotoxic hypoxia occurs when mitochondrial ATP production decreases due to a defect in O₂ usage [65]. Hypoxia can also be divided into acute and sustained (continuous and intermittent) as discussed earlier, and this causes different response and insults of the tissue. A general reduction of O₂ in the arteries usually causes activation of sympathetic system that would lead to a rapid increase in BP. The local responses to hypoxia is a different matter altogether and may vary widely, such as acute vasodilation and vasoconstriction.

Hypoxic vasodilation is a conserved adaptive response to match blood supply to local metabolic demand in response to an acute reduction in arterial PO₂. The restoration of O₂ delivery re-balances the acute O₂ supply-demand mismatch, thus protecting the cells from O₂ deficit and subsequent malfunction. This highly

conserved physiological response was first depicted by Roy and Brown in 1880 where they found a temporary cessation of local blood resulted in dilation of arterioles, capillaries and veins along with an increased blood flow [66]. On the other hand, pulmonary arteries constrict in hypoxia (~20-60 mmHg PO₂) in order to maintain the ventilation-perfusion ratio [67]. Although hypoxic vasodilation of systemic arteries is beyond debate, the fundamental physiological processes in sensing hypoxia still remain uncertain [2]. In general, the effects of hypoxia on systemic arteries can be ascribed to indirect effects (e.g. vasodilator metabolites from adjacent tissues) and direct effects (e.g. SMC K⁺ channel activation) on arterial VSMCs.

1.6.2 Indirect vasodilatory effect of hypoxia on SMCs

Increases in systemic blood flow confer cellular protection against hypoxia. One of the major hypotheses accounting for hypoxic vasodilation is the release of vasodilating metabolites from adjacent tissues. Blood vessels are innervated and thus receive the input from neuroendocrine system. During exercise, sympathetic β -adrenoceptor mediated arteriolar vasodilation contributes ~25% of the increased coronary blood flow through the activation of β 2-adrenoceptors on coronary vascular myocytes [1]. Meantime, α -adrenoceptors (α 1 and α 2) mediates vasoconstriction of medium to large coronary arteries, the significance of this being maintenance of blood flow to the vulnerable sub-endocardium [68]. Thus, apparently opposite effects (contraction and dilation) serve to achieve shared goal, supplying blood to sub-endocardium, the area where vast majority of cardiac ischemic injury arises. More importantly from the point of this thesis, studies also suggested that hypoxia is capable of increasing local blood flow in isolated organs, therefore this phenomenon can happen independently of neural-mediated reflex mechanisms [69, 70]. The cross-talk communication between cellular metabolites from cardiac myocytes and VSMCs may play a crucial role here. Under hypoxia, cardiac myocytes produce adenosine, H⁺ and a rise in extracellular K⁺, resulting in SMC relaxation, in part through the activation of K⁺ channels [71-73]. In addition to vasodilator metabolites

from cardiac myocytes, ECs and erythrocytes also release vasodilator substrates including NO, prostaglandins and endothelium derived hyperpolarizing factor. The identity of the last item is currently unknown but candidates include CO, H₂O₂, or ONOO⁻ [74-76].

1.6.3 Direct vasodilatory effect of hypoxia on VSMCs

Besides the events mediated by cardiac myocytes and ECs, hypoxia can exert direct effects on VSMCs [77, 78]. Even though there is difference between different arteries, hypoxia has been shown to activate a series of K⁺ channels in VSMCs, resulting in membrane potential hyperpolarization, a decrease in [Ca²⁺]_i and vasodilation [21, 34, 38]. This is because the concentration of intracellular K⁺ ([K⁺]_i ~140 mM) is much higher than that of extracellular ([K⁺]_o ~5 mM) making K⁺ equilibrium potential (E_K) calculated from Nernst equation in SMCs very negative (-88.7 mV). However, membrane potential (E_m) of SMC is almost always positive to E_K, and opening of K⁺ channels therefore leads to hyperpolarization due to net K⁺ efflux. When membrane potential is hyperpolarized, VDCCs will close, leading to decrease in [Ca²⁺]_i. When [K⁺]_o is elevated (80 mM and above), E_K will shift to a more positive value where opening of K⁺ channels will no longer cause hyperpolarization as net K⁺ efflux no longer occurs. Although K⁺ channels are likely to be involved in hypoxia induced vasodilation, other mechanisms are almost certainly involved, ensuring the proper blood supply is ensured. Smani et al. (2002) showed that hypoxia (~20 mmHg) relaxed vascular smooth muscle in the presence of high [K⁺]_o, suggesting relaxation is independent of K⁺ channels [77]. The study by Calderón-Sánchez et al. (2009) suggested that besides a reduction of Ca²⁺ entry via VDCCs, a mechanism in which a Ca²⁺ channel-induced Ca²⁺ release (metabotropic CCICR) from sarcoplasmic reticulum (SR) is involved [79].

1.7 Vascular tone and contraction

1.7.1 Vascular tone

The myogenic response of vasculature was first described by Sir William

Bayliss in 1902 (Bayliss effect) [80]. Myogenic tone is independent of central nervous system, and artery muscles respond to a stretching force by contraction and diminution of tension by relaxation [80]. Myogenic tone is intrinsic to smooth muscle and by doing so, small arteries and arterioles maintain the flow constant when BP changes. Without such a mechanism, blood flow to the brain where the constant and stable blood supply is crucial may change all the time (e.g. standing from lying down). The microcirculation of coronary arterioles with a diameter of 50-200 μm was reported to account for ~60% of the coronary resistance [81]. However, myogenic tone is not substantial in medium to large arteries and in veins [81, 82].

Myogenic response has been observed both *in vivo* and *in vitro*. However, the regulation of vasomotor tone is not homogenous, involving different mediators at different sites of specific microcirculation. Various membrane receptors and ion channels in both ECs and VSMCs coordinate together to modulate microcirculation vasomotor tone.

1.7.2 SMC contraction

1.7.2.1 Ca^{2+} regulation

In arteries, vasomotor tone is determined by contraction of VSMCs in the vessel wall, and contraction is generally triggered by an increase in $[\text{Ca}^{2+}]_i$. The force of the vessel is developed by cross-bridge cycling in VSMCs where Ca^{2+} plays an important role [83]. In general, the increase in $[\text{Ca}^{2+}]_i$ of SMCs is dependent on two sources: (i) Ca^{2+} entry from extracellular space (e.g. VDCCs); (ii) Ca^{2+} release from intracellular stores, principally the SR. VDCCs are the major route of Ca^{2+} entry, but Ca^{2+} influx also occurs via voltage-independent, receptor-operated Ca^{2+} channels. The increases in $[\text{Ca}^{2+}]_i$ can occur by release from the SR via inositol 1,4,5-trisphosphate receptors (IP_3Rs) and ryanodine receptors (RyRs).

The force of systemic arteries, particularly small resistance arteries and arterioles, has a close relationship with $[\text{Ca}^{2+}]_i$. Notwithstanding the level of Ca^{2+} is very high in the extracellular space (~2 mM), $[\text{Ca}^{2+}]_i$ is considerably lower and very

tightly controlled [83, 84]. The main routes for Ca^{2+} removal are plasma membrane Ca^{2+} ATPase (PMCA), SR Ca^{2+} -ATPase (SERCA) and sarcolemmal Na^+ - Ca^{2+} exchanger (NCX). **Figure 1.11** shows the routes through which Ca^{2+} is modulated in SMCs.

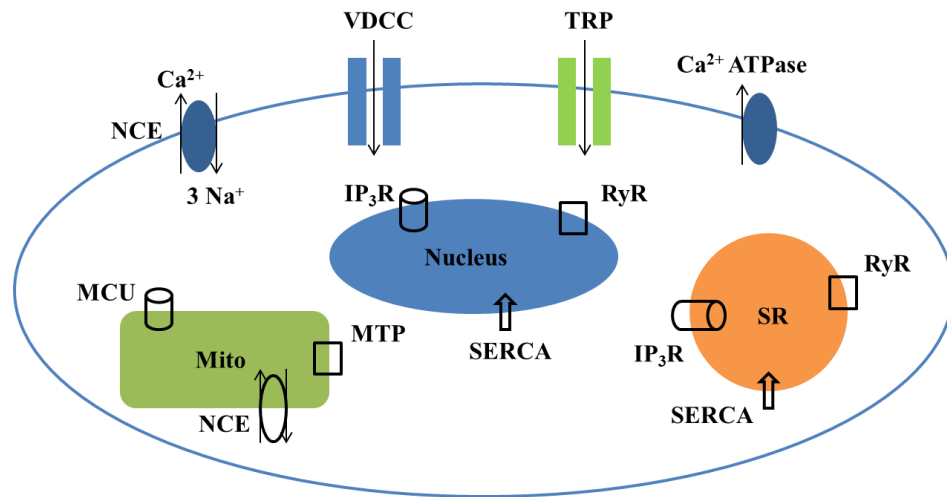


Figure 1.11: Ca^{2+} channels and transporters in VSMCs. Mito: mitochondria; SR: sarcoplasmic reticulum; MCU: mitochondrial Ca^{2+} uniporter; MTP: mitochondrial permeability transition pore; NCE: Na^+ - Ca^{2+} exchanger; SERCA: sarcoplasmic reticulum ATPase; TRP: transient receptor potential family of channels; VDCC: voltage dependent Ca^{2+} channel.

1.7.2.2 Cross-bridge and cell contraction

Like striated muscle, the contraction of SMCs is caused by the interaction between thin and thick, actin and myosin, contractile filaments. In VSMCs, the thin filaments are rooted in dense bands instead of Z lines in the case of cardiac myocytes. Because these dense bodies are patchy plaques and not regularly and systematically aligned, VSMCs lack the striated banding pattern found in cardiac and skeletal muscle [1]. Furthermore, unlike cardiac and skeletal muscle, VSMCs do not normally fire action potentials, and as a result, the contraction is graded, sustained and tends to be small. Although there are some differences from striated muscles, contractile force in SMCs does depend on the formation of cross-bridges between

thick myosin and thin actin filaments (**Figure 1.12**).

In addition to $[Ca^{2+}]_i$ entry through VDCCs, release of Ca^{2+} from SR is also responsible for increase in $[Ca^{2+}]_i$. An increase in $[Ca^{2+}]_i$ enhances Ca^{2+} binding to calmodulin, four Ca^{2+} ions bind to four EF-hand motifs of calmodulin and form Ca^{2+} /calmodulin complex. The interaction between Ca^{2+} and calmodulin subsequently causes the activation of the enzyme myosin light chain kinase (MLCK), which phosphorylates one of the two myosin light chains (MLCs). This process involves the hydrolysis of ATP, and transfer of an inorganic phosphate (P_i) to MLC. Phosphorylating MLC of myosin causes the cycling of cross-bridges and thus contraction, and de-phosphorylation will cause relaxation [85], the latter is mediated by myosin light chain phosphatase (MLCP).

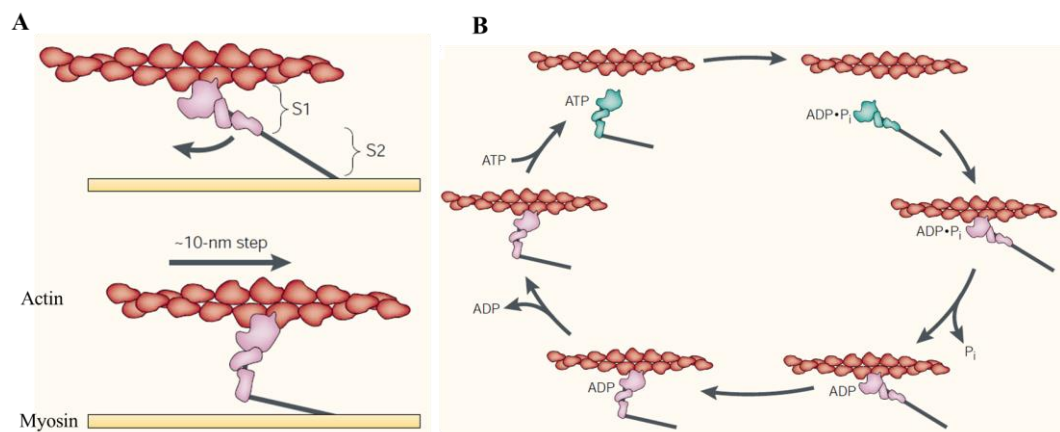


Figure 1.12: VSMC actin-myosin cross-bridge. (A) Sliding movement of actin filaments and cross-bridge formation. (B) Actin-activated myosin ATPase cycle involves association and disassociation of ATP to myosin heads (Adapted from Spudich, 2001 [86]).

1.7.3 Ca^{2+} sensitization

Ca^{2+} sensitization is the mechanism by which contraction can occur in the absence of increase in $[Ca^{2+}]_i$. This mechanism is directly related to the RhoA/Rho kinase pathway, in which de-phosphorylation of MLC by MLCP is inhibited by Rho-kinase-dependent phosphorylation, and thus vascular force is maintained [87].

Therefore, the contractile state of VSMCs is dependent on the concentration of $[Ca^{2+}]_i$, as well as the sensitivity of the contractile proteins. Given the major roles of MLCK and MLCP in MLC phosphorylation/de-phosphorylation, either Ca^{2+} removal or myosin phosphatase activation will lead to VSMCs relaxation.

1.8 Ion channels in VSMCs

1.8.1 K^+ channels in VSMCs

1.8.1.1 Classification of K^+ channels

In evolutionary terms, K^+ channels are the first ion channel to emerge. They are expressed in every cell of the body forming the largest ion channel family and influence processes as diverse as cognition, cell excitability, cell cycle and proliferation. In SMCs, K^+ channels dominate membrane conductance at rest, and therefore determine E_m . K^+ channels are also involved in cell volume and cell cycle regulation, giving them an important role in cell proliferation and apoptosis. The controlling of vascular tone by K^+ channels is essential in determining the contractile force of VSMCs. A small change in membrane potential can lead to several fold change in Ca^{2+} entry through VDCCs and therefore SMC contraction [43]. As E_m is normally more positive to E_K , the opening of K^+ channels will cause K^+ efflux in VSMCs. The outward K^+ current causes SMC hyperpolarization, a closure of VDCCs, and systemic artery vasodilation with a subsequent increased blood flow to meet the high demand of the tissue.

In VSMCs, there are traditionally four types of K^+ channels identified according to their electrophysiological and pharmacological features [43, 88]. They are voltage-activated K^+ (K_v) channels, Ca^{2+} -dependent K^+ (K_{Ca}) channels, K_{ATP} channels and inward rectifier K^+ (K_{ir}) channels. Ca^{2+} -dependent K^+ channels can be further divided into three different subtypes according to their conductance, large conductance K^+ (BK_{Ca}) channels, intermediate conductance K^+ (IK_{Ca}) channels and small conductance K^+ (SK_{Ca}) channels. Besides the above four classical K^+ channels, a new family of K^+ channels, two-pore domain K^+ channels (K2P) were found in mid-1990s. They are background leak channels and may be involved in setting

resting membrane potential [89-91]. These K^+ channels are not modulated by traditional K^+ channel activators and inhibitors, and lack of specific inhibitors particularly hampered the understanding role of K2P channels.

1.8.1.2 Properties of K^+ channels

It is almost always the case that cells express more than one type of K^+ channel. Classical K^+ channels have distinctive characteristics, and their fingerprints can be detected by manipulation of membrane potential combined with use of pharmacological agents in patch clamp experiments. Such traditional classification of ion channels is further enforced and clarified by molecular biology techniques, uncovering many more subtypes than perhaps anticipated. For example, more than 40 K_v channel subunits have been identified, and they are expressed in a variety of vascular tissues [92]. Activation of K_v channels allows a K^+ outward current in response to depolarization. Thus, K_v channels may act as a break when membrane potential depolarizes from resting state. K_{Ca} channels are divided into three main subtypes based on single channel conductance: BK_{Ca} (100-300 pS), IK_{Ca} (25-100 pS) and SK_{Ca} (2-25 pS), pS (pico Siemens) being the unit for conductance. BK_{Ca} channels in VSMCs have a conductance ranging 100-250 pS and are the most abundant K^+ channels and their activity increases with depolarization (-60 to -30 mV) or a rise in $[Ca^{2+}]_i$ (100-600 nM) [43, 93, 94]. Although both K_v and BK_{Ca} are activated by depolarization, activity of BK_{Ca} channel is less sensitive to voltage when compared to other voltage dependent K^+ channels [95]. IK_{Ca} and SK_{Ca} are generally not at all or very poorly expressed in contractile phenotype SMCs, but their expression increases dramatically in synthetic phenotype [96, 97]. K_{ATP} channels were first reported in cardiac myocytes, and then identified in a variety of vascular beds [98]. They are activated by intracellular ADP and inhibited by ATP. As mentioned earlier, the nucleotide sensitivity of K_{ATP} channels couples cellular metabolism to cell excitability. K_{ir} channels are named so as they allow current/ K^+ more easily in the inward direction (into the cell) than outward direction. Moreover, it is the only K^+ channel whose P_o is increased when there is a small rise in $[K^+]_o$.

over physiological E_m in VSMCs [1]. Electrophysiological studies have suggested the existence of K_{ir} channel in cerebral, mesenteric and coronary arteries, especially in resistance small arteries [93, 99].

K_v channels and BK_{Ca} channels have similar structures, comprising four pore forming α -subunits, each with an ancillary β -subunit ($\alpha:\beta$, 1:1). A-subunit of K_v channels have 6 transmembrane domains (S1-S6) and BK_{Ca} channels have 7 (S0-S6), where S4 is the voltage sensor, and the pore-forming re-entrant P-loop is situated between S5 and S6 (**Figure 1.13**). K_{ir} channels form as tetramers, each subunit has only two transmembrane domains with one pore loop (**Figure 1.13**). In hetero-octameric K_{ATP} channels, four K_{ir} (6.1/6.2) subunits form the pore in the middle with four sulphonylurea (SUR) receptors associated to each pore forming subunit. SUR serves as regulatory subunit where ATP and sulphonylurea such as glibenclamide bind. More detailed information regarding K_{ATP} channels structure will be discussed in **section 1.9.1**. Different from the aforementioned K^+ channels, $K2P$ channels are formed as dimers with each subunit having two pore loops (**Figure 1.13**).

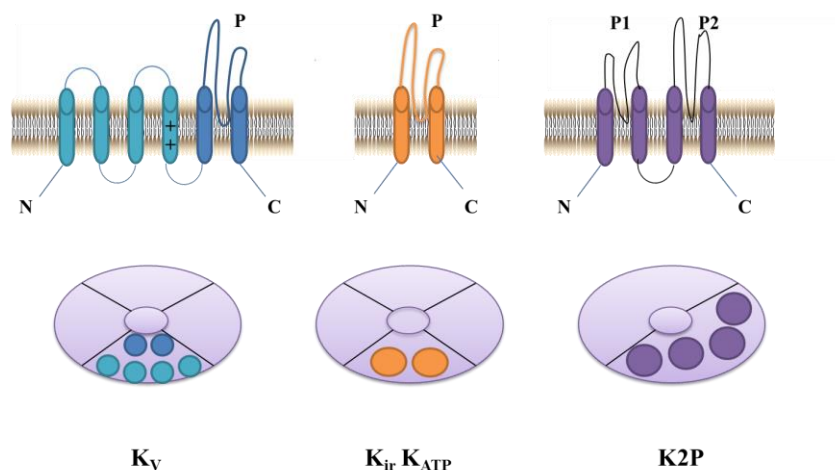


Figure 1.13: K^+ channels subunits. The typical structure of six transmembrane segments and one pore domain (left), two transmembrane segments and one pore domain (middle), four transmembrane segments and two pore domains (right). (Modified from Es-Salah-Lamoureux et al., 2010 [100])

1.8.1.3 Modulation of K⁺ channels

K⁺ channels in the cell membrane are regulated by a wide variety of vasoactive substances. Vasoconstrictors (e.g. angiotension, endothelin) act on cell membrane receptors and cause activation of protein kinase C (PKC) isoforms with subsequent inhibition of K⁺ channel activity [94, 101]. Besides PKC, it has been reported that activation of the novel cyclic AMP (cAMP) sensor, exchange protein activated by cAMP (EPAC), inhibits K_{ATP} channels in VSMCs [102]. Many vasodilators (e.g. adenosine, β-adrenergic agonists) induce vasodilation through the activation of cAMP dependent protein kinase A (PKA) while others (e.g. NO, atrial natriuretic factor) increase cyclic GMP (cGMP), activating cGMP dependent protein kinase G (PKG) and causing subsequent K⁺ channel opening [43, 92, 94, 101].

Although electrophysiological properties of ion channels can reveal their identity in patch clamp experiments, pharmacological agents are invaluable tools in investigating K⁺ channels. K_{ATP} channels are activated by many drugs such as diazoxide, pinacidil, nicorandil, cromakalim [43, 93]. K_{ATP} channels in vascular smooth muscle are inhibited by sulfonylurea agents (e.g. glibenclamide, tolbutamine), U-37883A and external Ba²⁺, and glibenclamide is thought to be the ‘gold standard’ [43, 94]. NS004 and NS1619 have been shown to open BK_{Ca} channels [103, 104]. A novel BK_{Ca} channel activator NS11021 was also reported with better specificity and higher potency [105]. Tetraethylammonium (TEA), charybdotoxin and iberiotoxin all inhibit BK_{Ca} channels with variable specificity, and iberiotoxin is considered to be the most specific [43, 92, 94]. IK_{Ca} and SK_{Ca} channels have been proposed to be affected by tram34 and apamin, respectively [106-108]. K_{ir} channels are blocked by low concentration of extracellular Ba²⁺ and Cs⁺ [43]. K_v channels are inhibited by 4-aminopyridine (4-AP), TEA and Ba²⁺, and 4-AP is suggested to be the most selective of these relatively non-selective inhibitors [43, 92]. A potent and selective inhibitor of K_v7 channels, XE991, was used in our project [109].

1.8.2 Ca²⁺ channels in VSMCs

There are two main types of Ca²⁺ channels: (i) VDCCs such as L-type VDCC

and T-type VDCC; (ii) voltage independent Ca^{2+} channels, such as receptor-operated Ca^{2+} channels (ROCs) and store-operated Ca^{2+} channels (SOCs). In recent years, a novel class of voltage-independent, non-selective cation channels named transient receptor potential (TRP) channels have been studied, and moreover they have also been suggested to participate in the formation of functional ROC and SOC in vasculature [110].

Based on their electrophysiological and pharmacological features, VDCCs can be further classified broadly into two groups according to voltage dependence of activation. High voltage activated (HVA) channels includes L-type, P-type, N-type channels; low voltage activated (LVA) channels are T-type Ca^{2+} channels (**Figure 1.14**) [111, 112]. Both L-type and T-type VDCCs have been identified in various vascular beds, such as aorta, mesenteric artery, coronary artery, and renal arteries [113-116].

L-type Ca^{2+} channels are specific differentiation markers of VSMCs [117], and have been indicated as the major Ca^{2+} influx pathways from extracellular environment [118]. They can be activated directly by a depolarization of membrane potential (e.g. high K^+) or indirectly by agonists (e.g. noradrenaline) [42, 43]. Different from T-type, L-type VDCCs are very sensitive to dihydropyridines, such as nifedipine, felodipine, as well as other organic and inorganic Ca^{2+} antagonists [112]. Ca^{2+} channel blockers targeting L-type VDCCs have been widely prescribed as antihypertensive drugs for many years [113]. Bay K8644 is a structural analogue of the 1,4-dihydropyridines and a selective activator of L-type VDCC in its S enantiomer, causing vasoconstriction [119].

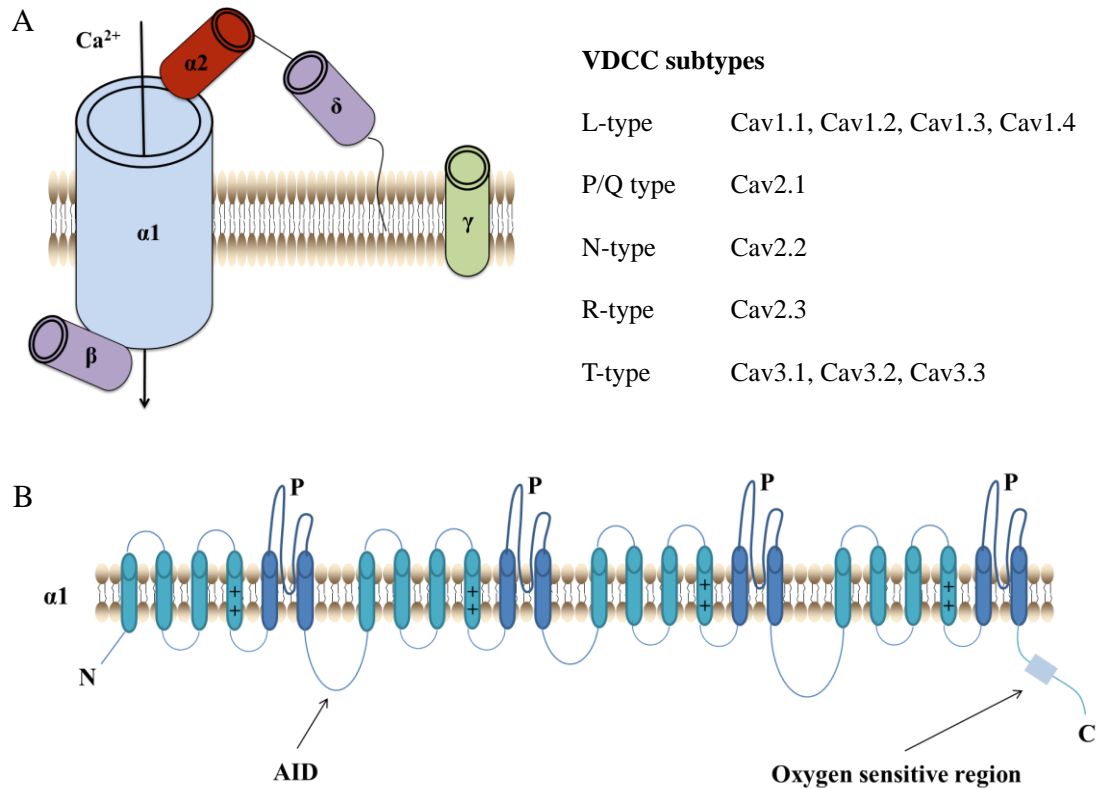


Figure 1.14: Voltage-gated Ca^{2+} channels. (A) Schematic VDCC structure. VDCCs are comprised of four homologous domains of $\alpha 1$ subunit, and auxiliary β , γ , $\alpha 2\delta$ subunits. (B) Structure of $\alpha 1$ subunit. AID: α interacting domain, by which α subunit interact with β subunit. (Modified from Bourinet et al., 2014, and Hool et al., 2007 [111, 120])

1.9 K_{ATP} channels

1.9.1 Structure and distribution of K_{ATP} channels

It has been over 3 decades since K_{ATP} currents was first described in guinea pig cardiac myocytes by Noma, who also showed the channel activity was inhibited by an increase in intracellular ATP level ($[\text{ATP}]_i$) [98]. Since this initial finding, K_{ATP} channels have been shown to play an important role in a variety of cell functions including pancreatic β -cell insulin secretion, vascular smooth muscle relaxation, and skeletal muscle excitability [43, 121, 122]. Perhaps unique among channels expressed in plasmalemma, K_{ATP} channels also have been reported to express in mitochondrial and nuclear membranes (mito and nuclear K_{ATP} channels) [122, 123].

K_{ATP} channels are weak inwardly rectifying K^+ channels and their hallmark sensitivity to intracellular nucleotides makes K_{ATP} channel a target sensor in coupling cellular metabolic change to excitability. Regulation of K_{ATP} channels has been studied for a number of years, yet many fundamental questions remain unanswered.

K_{ATP} channels are hetero-octameric complexes composed of two different subunits, $K_{ir}6x$ pore-forming and sulphonylurea receptor (SURx) regulatory subunits (**Figure 1.15**). Pore forming subunits $K_{ir}6.1$ and $K_{ir}6.2$ of mammalian species have two transmembrane domains encoded by KCNJ8 and KCNJ11 genes respectively [[122](#), [123](#)]. Recently, another $K_{ir}6.x$ isoform $K_{ir}6.3$ was found and characterized in zebra fish [[124](#)]. The regulatory SUR subunits are encoded by two important SUR genes, ABCC8 (SUR1) and ABCC9 (SUR2) [[123](#)], the latter SUR2 has two splice variants, SUR2A and SUR2B. VSMCs mainly express $K_{ir}6.1/SUR2B$ isoform, and isoforms of K_{ATP} channels in other tissues are summarized in **Table 1.1 and 1.2**. Auxiliary SUR proteins belong to the superfamily of ATP-binding cassette (ABC) proteins. However, instead of transporting various molecules across cell membranes as other ABC proteins at the expense of ATP hydrolysis, SUR is part of the functional K_{ATP} channel and possesses intracellular nucleotide binding domains. Both of the nucleotide binding domains (NBD1 and BND2) are not surprisingly on the cytoplasmic side, one is between transmembrane domain 1 (TMD1) and TMD2 and the other is at the C-terminal. It is generally recognized that the pore forming $K_{ir}6$ subunit mainly confers selectivity, inward rectification and unitary conductance, and the SUR subunit is primarily associated with the nucleotide sensitivity and pharmacological modulation [[125](#), [126](#)].

Table 1.1: Different combinations of K_{ATP} channels subunits in various tissues.

Tissue	Subunit composition
Cardiovascular tissues:	
Ventricle	$K_{ir}6.2/SUR2A$
Conduction system	$K_{ir}6.1/Kir6.2/SUR2B$
Atrium	$K_{ir}6.2/SUR1/SUR2A$
Vascular smooth muscle	$K_{ir}6.1/SUR2B$
Endothelium	$K_{ir}6.1/K_{ir}6.2/SUR2B$
Mitochondria	$K_{ir}1.1$ and/or $SUR2A-55$
Other tissues:	
pancreatic β -cell/neuronal	$K_{ir}6.2/SUR1$
Non-vascular smooth muscle	$K_{ir}6.2/SUR2B$
Skeletal myocytes	$K_{ir}6.2/SUR2A$

(Modified from Foster et al., 2016 [[123](#)])

Table 1.2: K_{ATP} channel subunit genes.

Protein	Gene	Chromosome
$K_{ir}6.1$	KCNJ8	12p11.23
$K_{ir}6.2$	KCNJ11	11p15.1
SUR1	ABCC8	11p15.1
SUR2	ABCC9	12p12.1

(Modified from Foster et al., 2016 [[123](#)])

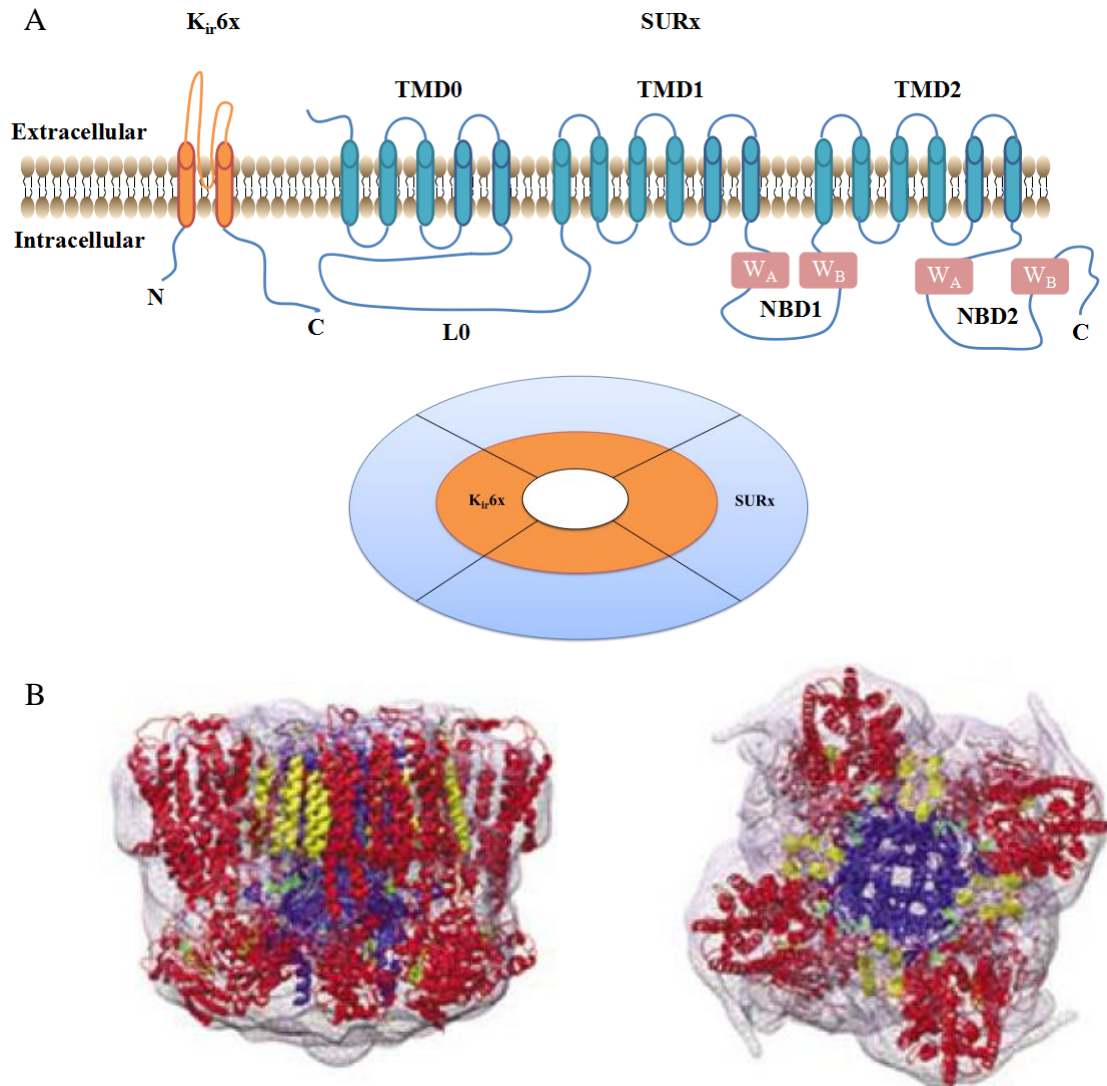


Figure 1.15: Organization of K_{ATP} channels. (A) Topology of K_{ATP} channel. Four pore forming subunits (top orange) and four auxiliary SUR subunits (top blue) form hetero-octameric (4:4 stoichiometry) K_{ATP} channels (bottom). TMD0 domain and the linker region of SURx interact closely and modulate gating of K_{ir6} . NBDs are ATP binding sites and responsible for the reaction of ATP hydrolysis. (B) 3D structure model of K_{ATP} channel. Side (left) and top (right) views of K_{ATP} channel complex structural details, respectively (Reproduced from Mikhailov et al., 2005 [127]). NBD: nucleotide binding domain; TMD: transmembrane domain; W_A : Walker A motif; W_B : Walker B motif. $K_{ir6.2}$ is indicated in blue, SUR1 minus TMD0 in red, TMD0 in yellow, and ATP molecules are shown in green.

1.9.2 Nucleotide sensitivity and K_{ATP} channel gating

K_{ATP} channels are named due to their response to cytoplasmic concentration of ATP [98] (Figure 1.16). In traditional electrophysiology, sensitive is the term used for inhibitory effector while dependent usually means activated by. The changes in the open probability (P_o) of K_{ATP} channels provide a unique feedback between cellular metabolism and cell electrical activity [33, 43]. The optimal concentration of $[ATP]_i$ required to inhibit K_{ATP} channels is determined by various factors (e.g. K_{ATP} channel types, species) [128]. In the cardiovascular system, it is reported that ATP sensitivity of atrium and ventricle are highest, followed by smooth muscle, cardiac conduction system and mitochondria [123].

Although SURs are ABCs and so regarded as the nucleotide binding site, it is now shown that both $K_{ir}6.0$ and SUR subunits provide binding sites for nucleotides and cause the conformational changes during channels opening or closure [129]. ATP exerts an inhibitory effect on the channels by binding to the intracellular sites of K_{ir} subunits, while the activity of the channels are increased when nucleotides bind to NBDs of SUR subunits in the presence of Mg^{2+} [130]. Under physiological concentrations, $[ATP]_i$ is in millimolar range and stable, negatively regulating K_{ATP} channels at rest against other substances which activate the channels [1, 131, 132]. Although full length $K_{ir}6$ subunit alone does not express functionally, Tunker et al. (1997) found that truncated $K_{ir}6.2$ ($K_{ir}6.2\Delta C26$, $K_{ir}6.2\Delta C36$) produced ATP sensitive currents in a Mg^{2+} independent manner, indicating the existence of ATP binding site in $K_{ir}6.2$ subunit with intrinsic ATP inhibitory effect [133]. ATP interacts with $K_{ir}6.2$ without Mg^{2+} , and non-hydrolysable ATP analogues also cause inhibition indicating ATP hydrolysis is not required [134]. In addition to ATP, other nucleotides (e.g. ADP, CTP, GTP, AMP) can also exhibit an inhibitory effect when binding to $K_{ir}6.2$ subunit, but with much less potency compared with ATP [123]. However, it is still not completely known how ATP binding is translated into the closure of K_{ir} pore.

SUR subunits are generally responsible for the increase of K_{ATP} activity to Mg^{2+} -nucleotides as mutation in NBD2 abolished the effect of $MgATP$ and caused persistent hyperinsulinemic hypoglycemia of infancy (PHHI) [130, 135]. When

compared to channels consisting of truncated $K_{ir}6.2$ alone ($K_{ir}6.2\Delta C26$), co-expressing with SUR1 increased channel sensitivity to ATP by ~10 times (IC_{50} : ~10-20 μM of $K_{ir}6.2/SUR1$ vs ~140 μM of $K_{ir}6.2$) [133, 136]. ATP occupies both of the NBDs, in which Walker A and Walker B motifs provide the binding sites with ATPase activity. Studies have suggested that MgATP bound to NBD2 is hydrolyzed to MgADP, and a much higher ATPase activity was reported for purified NBD2 than NBD1 of SUR2 [123, 137, 138]. On the other hand, NBD1 can bind to ATP without Mg^{2+} and has much less ATPase activity therefore hydrolysing ATP very slowly [123, 139]. More recent studies have suggested that the hydrolysis is not necessary for channel activation [140]. Therefore hydrolyzed MgADP may have a direct access to NBD2 and the trapping of nucleotides causes channel activation [123]. The initial conformational change in NBD2 by binding of MgADP causes subsequent conformational change in NBD1 stabilizing its ATP binding. Mirroring this, removal of MgADP from NBD2 resulted in ATP dissociation from NBD1 and a subsequent reduction in K_{ATP} channel activity [141]. It has been suggested that the regulation of $K_{ir}6.2$ gating by SUR is through TMD0 domain and the linker region L0 [136], the latter is in close proximity to the N-terminal of $K_{ir}6.2$ [127]. The conformational ‘activated’ state that overrides ATP inhibition at the $K_{ir}6.2$ subunit results in channel activation.

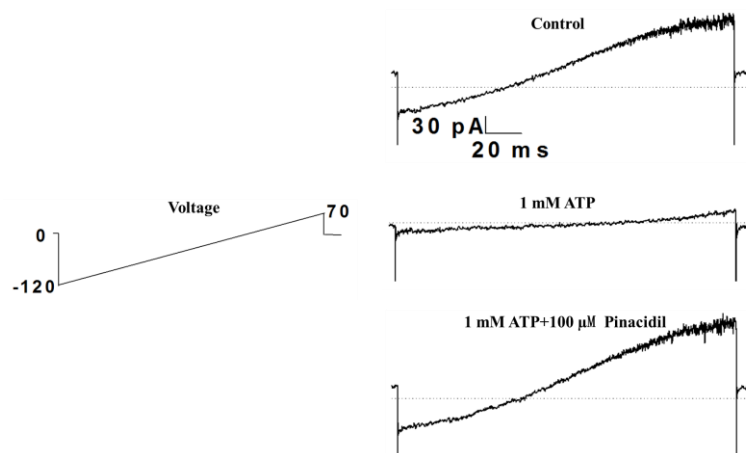


Figure 1.16: K_{ATP} channel regulation by intracellular ATP. (Data by John Quayle, Used with permission)

1.9.3 Cellular function of K_{ATP} channels in vascular smooth muscle

Different from classical K_{ATP} channels in the heart and pancreas, the predominant vascular smooth muscle K_{ATP} channel subtypes are inactive in isolated membrane patches, and their P_o increases when there are nucleotide diphosphate and Mg^{2+} [33]. Studies with transgenic mice with ATP insensitive K_{ATP} channels showed that the channels were persistently opened in pancreatic β -cells [142], but closed in cardiac cells [143]. Amongst all the K_{ATP} channel subtypes, the physiological role of those in insulin-secreting pancreatic β -cell are the best studied. In human β -cells, glucose metabolism is coupled to insulin secretion that is governed by K_{ATP} channel activity [144]. When blood glucose increases, it causes an increase in $[ATP]_i$, or more precisely an increase in ATP:ADP ratio. This causes K_{ATP} channels to close, resulting in membrane depolarization and activation of VDCCs. Increase in $[Ca^{2+}]_i$ causes exocytosis of insulin-containing granules and therefore insulin secretion. Once blood insulin level goes up, blood glucose level will go down, leading to a decrease in $[ATP]_i$. Reduced $[ATP]_i$ will lead to the removal of K_{ATP} channel inhibition, completing the cycle of events. The opening of K_{ATP} channels under conditions of metabolic inhibition, such as ischemia and hypoxia, has a protective effect to cardiac myocytes [98, 145, 146]. This protective effect comes from the shortening of the action potential duration by activation of K_{ATP} channels, and therefore contraction will be shorter which conserves energy. Several years after the discovery of the channel and its role in heart protection, an important phenomenon, ischemic preconditioning, was reported by Murry [147]. Ischemic preconditioning is a process in which exposing the heart to transient brief episodes of ischemia has been shown to protect it from subsequent episodes of prolonged ischemia. However, there is still debate lying in whether plasma membrane or mitochondrial K_{ATP} channels are important in ischemic preconditioning. Although there is much less density of K_{ATP} channel expression in VSMCs (~ 300 K_{ATP} channels/cell, ~ 1 channel/ $10 \mu m^2$) than that in cardiac myocytes ($\sim 50,000$ K_{ATP} channels/cell, ~ 100 channel/ $10 \mu m^2$) [43, 72, 148], K_{ATP} channels play an important role in both resting membrane potential and regulation of vascular tone [1, 43]. For example, genetically modified mice ($Kir6.1^{-/-}$

or SUR2^{-/-}) have exhibited incidences of coronary vasospasm, resembling human Prinzmetal angina [33, 123].

1.9.4 Pharmacological regulation of K_{ATP} channel

K_{ATP} channels can be pharmacologically manipulated by a number of compounds, including a group of K_{ATP} channel openers (KCOs) and inhibitors [43]. However, the effects of pharmacological agents differ among subtypes of K_{ATP} channels and those in different tissues. Examples of KCOs include pinacidil, cromakalim, minoxidil sulfate, nicorandil, dizoxide, RP-49356. However, they may come into effect through different means. Some of them such as pinacidil and cromakalim, increase channel P_o at a given concentration of [ATP]_i by reducing the channel sensitivity to ATP. Others require intracellular ADP for activity, in which nicorandil is used clinically for treating angina and diazoxide for hyper-secretion of insulin associated with congenital hyperinsulinism (CHI) [123, 130]. Pharmacological agents that inhibit K_{ATP} channels are antidiabetic sulfonylurea drugs (e.g. tolbutamide, glibenclamide), as well as U-37883A and external Ba²⁺ (K_i of ~100 μM at -80 mV) [43, 94]. Other K⁺ channel inhibitors (e.g. apamin, charybdotoxin, IbTX, TEA) do not inhibit K_{ATP} channels [43, 149]. Both antidiabetic sulphonylureas and KCOs act on SUR subunits with only a few exceptions, for example U37883A, which exhibits an inhibitory effect through the K_{ir} pore and is more selective for K_{ir}6.1 than K_{ir}6.2 [150-152]. The effectiveness of K_{ATP} channel modulators varies depending on the state of ATP:ADP ratio. Pancreatic β-cell K_{ATP} channel activation by diazoxide is related to intracellular Mg²⁺ and MgATP/MgADP, therefore dependent on the ATPase activity of NBD2 domain [123]. The inhibiting effect of K_{ATP} channels by glibenclamide was also relieved during metabolic inhibition [153, 154].

1.9.5 Cell membrane microenvironment and K_{ATP} channels

The distinct lipid structures of cell membrane containing over 2000 species of lipids are generally constituted of liquid-disordered phase (Ld) micro-domains and

liquid-ordered phase (Lo) micro-domains, the latter is also called ‘lipid raft’ [155]. Phospholipids, sphingolipids with saturated acyl chains and cholesterol pack together and form lipid rafts [155, 156]. There has been an increasing accumulation of evidence suggesting a wide range of ion channel localization in lipid rafts [157-159]. Thus, far from being a simple fluid mosaic model originally proposed by Singer and Nicolson [160], cell membrane has a very sophisticated structure where many signaling molecules are compartmentalized. Furthermore, it is reported ion channels are modulated by some structures in the lipid rafts (e.g. cholesterol, caveolin) [159, 161]. The role of phosphatidylinositol 4,5-bisphosphate (PIP₂) has been well described, its application increases K_{ATP} channel P_o through competing with the binding of ATP [33, 162]. After gene transcription, K_{ATP} channel subunits are synthesized by ribosomes in ER into functional (K_{ir}6/SUR)₄ and destined for the plasma membrane. When K_{ir}6 and SUR subunits come together, the ER retention sequences (arginine-lysine-arginine, RKR sequence) in both of them are masked, and therefore trafficked to cell membrane to exert function [163]. Caveolae are recognized as a subtype of lipid raft with identifiable morphology [159]. K_{ATP} channels have been shown to be localized to caveolae and its function is modulated by proteins tucked within these specialized microdomains [157, 159, 161, 164]. Co-localization of K_{ATP} channels and protein kinases in caveolae appears vital for channel modulating signaling pathways [157, 159, 165]. Although [ATP]_i is usually high enough to inhibit K_{ATP} channels, they may not sense global cytosolic ATP ([ATP]_c). Instead, local concentrations of nucleotides in the area of membrane microdomains close to K_{ATP} channels are crucial, and it is conceivable that subcellular nucleotide concentrations dynamically change due to the activities of membrane ATPases and phosphotransfer enzymes. The ATP binding site on K_{ir}6.2 subunit has estimated to be ~2 nm below the membrane and at the interface between adjacent K_{ir}6.2 [166]. Studies in intact cells suggested that local submembrane nucleotide concentrations are modulated by metabolic enzymes including adenylate kinase (AK), creatine kinase (CK), AMP-activated protein kinase (AMPK) and lactate dehydrogenase (LDH) [33, 123, 167]. K_{ATP} channel protein complex has also

been suggested to include other metabolically active protein subunits such as AK, CK and LDH [168-170]. A model integrating two major phosphotransfer enzymes, CK and AK was analyzed and described in cardiac K_{ATP} channels, indicating local nucleotide level is modified when bulk ATP was transmitted over diffusional barrier into sub-membrane space [167]. The interactions between the channel and metabolic enzymes may therefore enable the channels to be more sensitive to small changes in cellular ATP [171].

1.10 Cellular metabolism

1.10.1 ATP Production

Energy storing molecule ATP fuels a variety of cell functions such as maintaining the cell structure, generating transmembrane ionic gradients, cell proliferation and migration, and muscle contraction. ATP is also an important non-adrenergic, non-cholinergic neurotransmitter. It also acts as an intracellular signaling molecule which coordinates pathophysiological responses to cellular energy status. ATP is a nucleotide comprised of three parts, adenosine, a ribose and a triphosphate. Due to its two phosphoanhydride bonds, a large amount of free energy is liberated when ATP is hydrolyzed into ADP/AMP and phosphate(s) [172]. Cellular metabolic processes are linked directly or indirectly to the free energy through hydrolysis of ATP. Dysfunction in cellular metabolism is therefore involved in many diseases such as diabetes mellitus, inherited mitochondrial disorders and metabolic syndrome.

In general, the supply of ATP is maintained through two metabolic pathways: (i) Glycolysis: where cytoplasmic reactions proceed without the need for O_2 ; (ii) OXPHOS: reactions proceed in mitochondria and O_2 is required [173] (**Figure 1.17**). Except for a few exceptions (eg. immune cells, erythrocytes) [174], OXPHOS is the preferential pathway to synthesize ATP in cells [175]. Amongst all the substrates, monosaccharide glucose ($C_6H_{12}O_6$), present in most dietary carbohydrates, is the key source for ATP generation. In mammalian cells, glucose enters the cytosol through facilitated diffusion via glucose transporters (GLUTs) and sodium-dependent glucose

transporters (SGLT). Glycolysis happens in the cytoplasm where one molecular glucose is converted into two molecules of pyruvate with the concomitant release of two H^+ and a net production of two molecules of ATP [172]. Glycolysis in the cytoplasm does not need O_2 , in which the reactions are conducted by a series of enzymes. The rate of glycolysis is regulated by the intracellular level of three glycolytic enzymes hexokinase (HK), phosphor-fructo-kinase (PFK) and pyruvate kinase (PK), among them PFK is considered to be the key controlling point (**Figure 1.17**).

In the presence of enough O_2 , pyruvate generated from glycolysis is decarboxylated into acetyl coenzyme A (AcCoA) in mitochondria, then together with AcCoA generated from other substrates (fatty acids, amino acids) enters tricarboxylic acid (TCA) cycle (or Krebs cycle) to produce ATP. However, in hypoxia or anoxia, pyruvate is converted into lactate and H^+ , the nicotinamide adenine dinucleotide (NAD^+) yielded in the process is returned back to be recycled in glycolysis. As the final common route for substrate (carbohydrates, fatty acids and amino acids) oxidation, AcCoA undergoes a stepwise oxidation controlled by a series of enzymes, resulting in the production of CO_2 [172]. During the TCA cycle, high energy electrons are harvested and used to form eight reduced nicotinamide adenine dinucleotide (NADH) and two reduced flavin adenine dinucleotide ($FADH_2$) per one molecule glucose. Two ATP are generated in TCA cycle per one molecule glucose. The free energy stored within NADH and $FADH_2$ is finally used to generate PMF, thus drive ATP synthase to convert ADP to ATP [172, 176]. Altogether, thirty six molecules of ATP can be generated per one molecule glucose consumed in optimal conditions, including thirty two molecules of ATP from OXPHOS, two from TCA cycle and a further two from glycolysis. However, it has been reported that there is an approximately ~20% of mitochondrial proton leak in a range of vertebrate and invertebrate species [173, 177]. Therefore, proton leak across the inner membrane determines the coupling efficiency between respiration and ATP synthesis [172, 178].

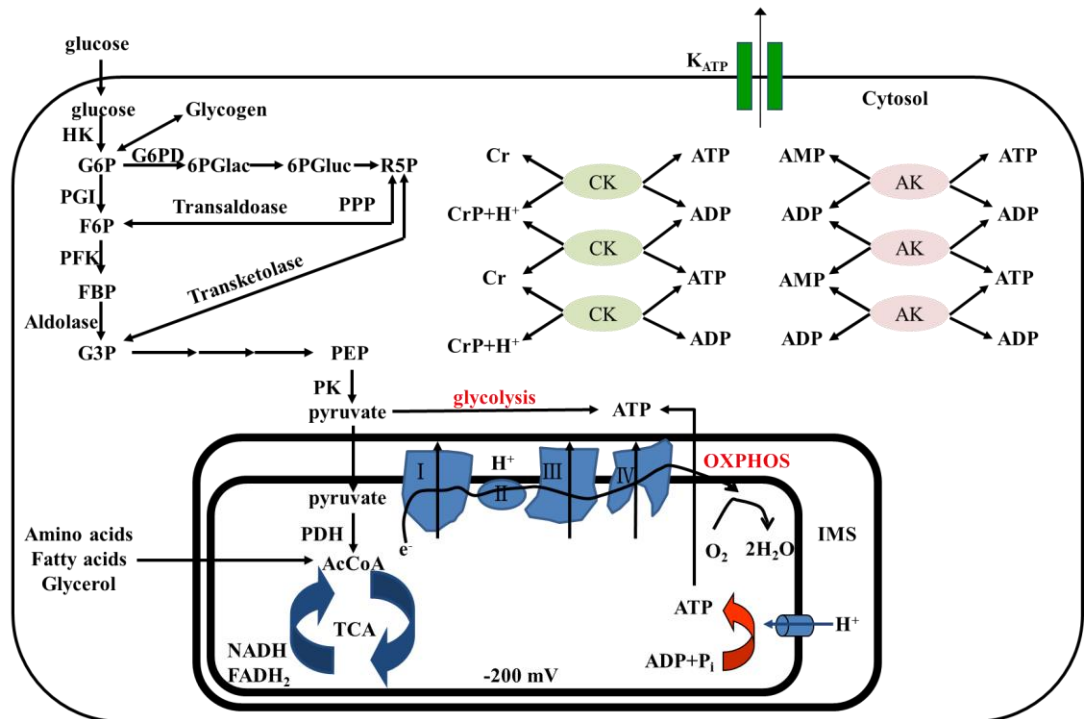


Figure 1.17: Flow diagram of key cellular energy metabolic pathways. Glucose enters the cells and produces ATP through glycolysis. Pyruvate generated from glycolysis is catalyzed into lactate or converted into AcCoA in mitochondria. Together with AcCoA from other pathways, AcCoA proceeds into OXPHOS and more ATP is generated. AK, adenylate kinase; CK, creatine kinase; FADH₂, reduced flavin adenine dinucleotide; FBP, fructose-1,6-biphosphate; G3P, glyceraldehyde-3-phosphate; G6P, glucose-6-phosphate; G6PD, glucose-6-phosphate dehydrogenase; HK, hexokinase; IMS: mitochondrial intermembrane space; NADH, reduced nicotinamide adenine dinucleotide; 6PGlac, 6-P-gluconolactone; 6PGLuc, 6-P-gluconate; PFK, phosphor-fructo-kinase; PGI, phosphoglucose isomerase; PK, pyruvate kinase; PDH, pyruvate dehydrogenase; PPP, pentose phosphate pathway; PEP, phosphoenol pyruvate; R5P, ribose-5-phosphate. (Modified from Liemburg-Apers et al., 2011, and Flagg et al., 2010 [33, 176])

1.10.2 Mitochondria as ATP consumers

The primary role of mitochondria is to couple respiration to ATP synthesis. ETC is central to mitochondria function by generating an electrochemical proton gradient as electrons jump from one carrier to another, which establishes the PMF, i.e. the

sum of mitochondrial membrane potential (ψ_m) and pH gradient. Four major protein complexes (complex I-IV) are bound to the inner membrane of the mitochondria, which transfer high energy electrons from TCA to O_2 (**Figure 1.18A**). Complex I and complex II receive electrons from reduced nicotinamide adenine dinucleotide (NADH) and reduced flavin adenine dinucleotide ($FADH_2$) respectively and pass them to Coenzyme Q (CoQ). The continual regeneration of ψ_m ensures ATP synthase to run in a direction of net ATP synthesis (**Figure 1.18B**). When mitochondrial homeostasis is compromised (e.g. inhibition of ETC), ATP synthase works in reverse and consumes ATP from glycolysis in favor of maintaining ψ_m (**Figure 1.18C**). Therefore, ATP synthase functions as an ATPase and hydrolyzes ATP during mitochondrial dysfunction [178, 179]. The ‘null-point’ assay has been suggested as a convenient means to assess mitochondria function, in which oligomycin, an ATP synthase inhibitor, causes ψ_m hyperpolarization when ATP synthase is generating ATP from ADP while if ATP synthase works in a reverse mode, the reverse will occur (depolarization of ψ_m) [178]. This is because there is a small proton leak when ATP synthase works in forward mode, causing a small depolarization, prevention of which will lead to a small hyperpolarization.

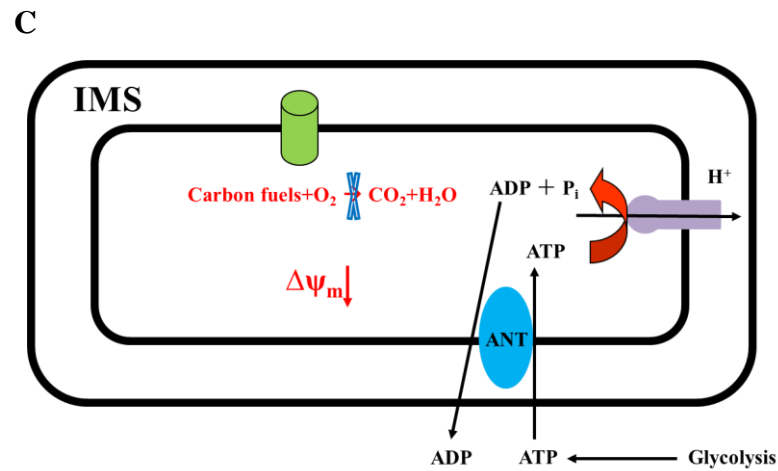
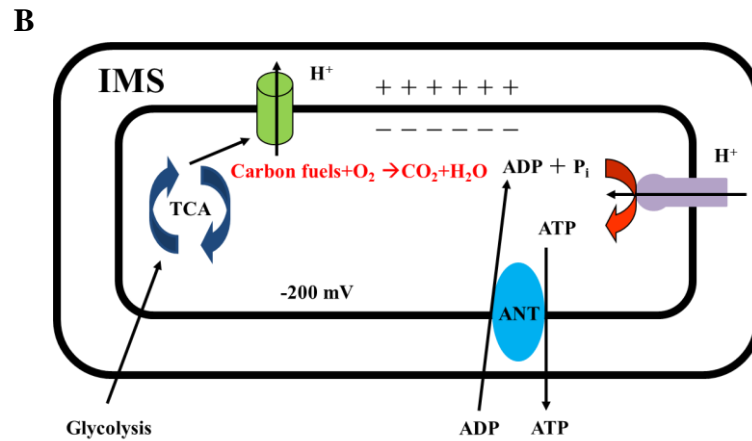
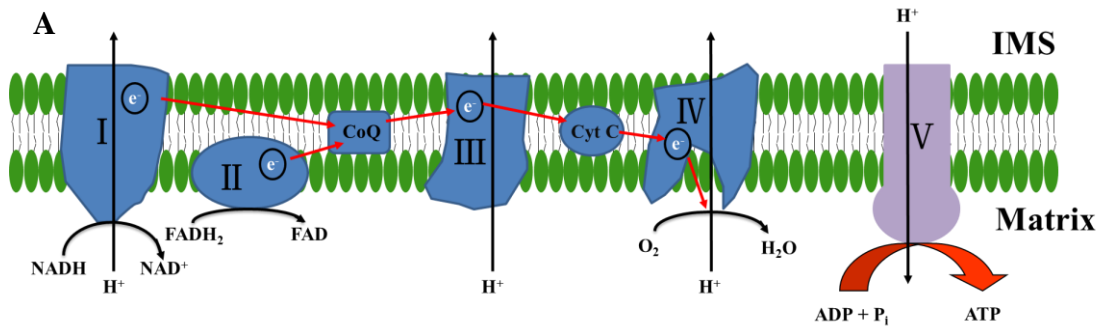


Figure 1.18: Schematic presentation of mitochondrial ETC and ATP synthase. (A) Electron transport in ETC. (B) Forward mode of ATP synthase. (C) Reverse mode of ATP synthase. (Modified from Berg et al., 2015 and Campanella et al., 2009 [172, 179])

1.10.3 Methods to study cellular metabolism

1.10.3.1 Metabolic inhibitors

With access to a wide range of metabolic inhibitors, it is possible to study the cellular metabolism of glycolysis and OXPHOS by inhibiting different sites of the pathways. 2-Deoxy-D-glucose (2-DG) and iodoacetate (IAA) are typical inhibitors of glycolysis. Rotenone, antimycin A, thenoyltrifluoroacetone (TTFA) and cyanide are important inhibitors which block different sites of ETC. Oligomycin B inhibits ATP synthase. Protonophores such as carbonyl cyanide *m*-chlorophenyl hydrazone (CCCP) and carbonyl cyanide *p*-trifluoromethoxyphenylhydrazone (FCCP) cause metabolic inhibition indirectly. In this project, 2-DG, rotenone, antimycin A, oligomycin B, FCCP and CCCP were applied to investigate cell metabolism (**Figure 1.19**). 2-DG is a glucose analog with the 2-hydroxyl group replaced by hydrogen. When entering the cell, 2-DG is phosphorylated by HK, but the product 2-deoxyglucose-6-phosphate cannot undergo further glycolysis. The product from 2-DG is then trapped in the cell and cannot be metabolized, and therefore acts as a competitive inhibitor of phosphoglucosomerase resulting in a decrease in $[ATP]_i$. Rotenone inhibits complex I of ETC, therefore its application will lead to the block of respiration with NAD-linked substrates, but the FAD-linked respiration can still proceed. Antimycin A is the inhibitor of complex III, which blocks both NAD-linked and FAD-linked respiration (**Figure 1.20**). Oligomycin B is an inhibitor of ATP synthase which blocks its proton channel (F_o subunit), and therefore prevents state 3 respiration and stops OXPHOS of ADP to ATP. CCCP is an uncoupling agent which belongs to the group of carbonyl cyanide phenylhydrazones. Application of CCCP causes unstrained O_2 consumption without ADP until O_2 is run out. However, no ATP is produced during the above oxidation process, as the energy is dissipated as heat. The effects of rotenone and antimycin A are not affected by CCCP, because they act directly on mitochondrial ETC.

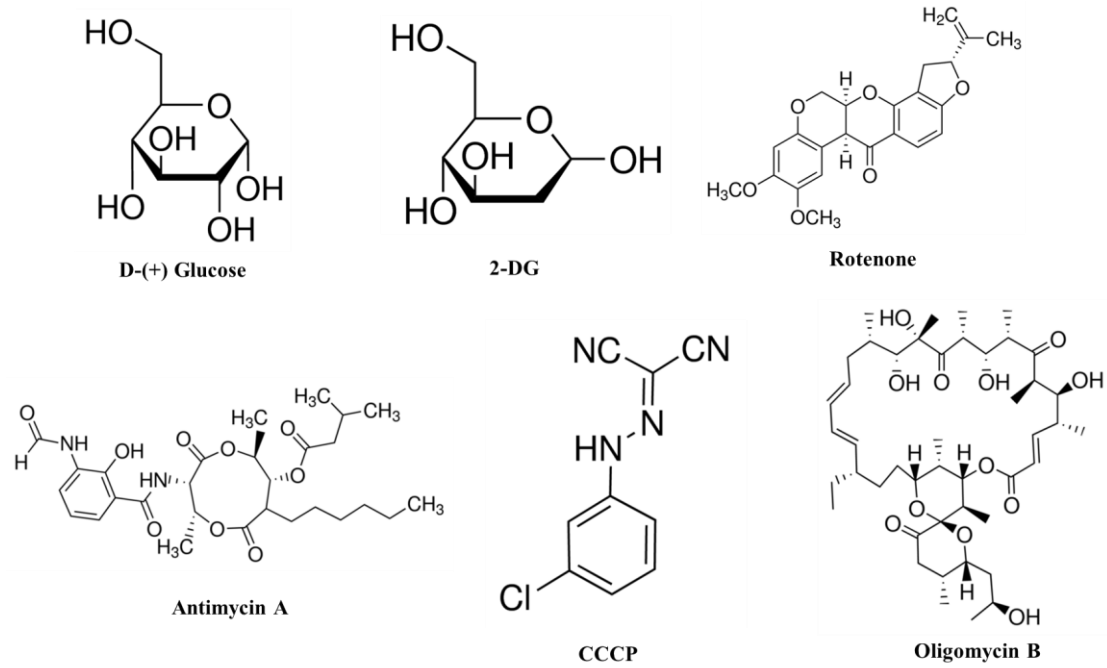


Figure 1.19: Chemical structure of metabolic inhibitors.

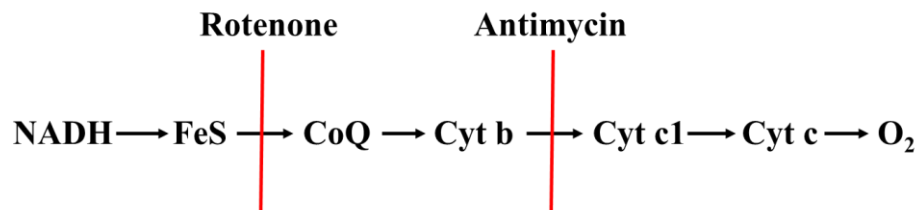


Figure 1.20: Metabolic inhibition of ETC. CoQ, coenzyme Q; Cyt b, cytochrome b; Cyt c, cytochrome c; Cyt c1, cytochrome c1; FeS, iron-sulphur; NADH, reduced nicotinamide adenine dinucleotide.

1.10.3.2 Cell based assay and molecular probes

Cell bioenergetics and changes in $[\text{ATP}]_i$ can be characterized by a variety of methods such as cell based assays and fluorescent tools. Seahorse technique is designed to monitor cell oxygen consumption rate (OCR) and extracellular acidification rate (ECAR) simultaneously. This highly sensitive and rapid analysis allows real time quantification of both glycolysis and OXPHOS [180, 181]. Luciferase-based bioluminescent assay is a well-established method and has been used widely to report ATP levels in the cells under various pathophysiological

conditions [182]. CellTiter-Glo luminescent viability assay was applied in this project, the luminescence generated was proportional to ATP and the number of viable cells [183]. Recombinant luciferase can be introduced to the cells by transient transfection, and it can be targeted to specific areas, so not only bulk ATP levels but ATP in the subcellular compartments can be examined [182, 184]. Fluorescent and fluorescent resonance energy transfer (FRET) based probes allow the measurement of ATP and ATP:ADP ratio in the cells [185-187]. Unlike enzyme based assays, these probes do not consume ATP, and ratiometric measurement enables the analysis to be independent of biosensor concentration in the cells [187]. By introducing a specific targeting sequence to the biosensor, it permits the measuring of ATP:ADP ratio in related cellular compartments [188]. For example, a palmitoylation and myristoylation modification sequence will favor the protein to be localized in the lipid rafts of cell membrane [188, 189]. Most recently, total internal reflection fluorescence microscopy (TIRF) imaging allows the fluorophores to be selectively imaged in the plasmalemmal surface and subplasmalemmal zone [190, 191], thus it directly reports ATP or ATP:ADP ratio in K_{ATP} channel microenvironment.

1.11 Hypothesis

The overall aim of this study is to investigate cellular mechanisms underlying direct hypoxic vasodilation of human coronary artery SMCs (HCASMCs). We tested the main hypothesis that hypoxia would lead to a decrease in $[ATP]_i$ and a rise in ADP concentration, thus activating K_{ATP} channels and resulting in membrane potential hyperpolarization and vasodilation (**Figure 1.21**). In addition, we also tested the possible effect of hypoxia on other K^+ channels, including K_{ir} , BK_{Ca} , K_v channels. It could be argued that this is an ambitious project for a PhD thesis when hypoxic vasodilation very much remains as a conundrum despite the efforts of many investigators. However, the subject is very much of my core interest, and my goal was to make small contributions to the understanding of coronary hypoxic vasodilation.

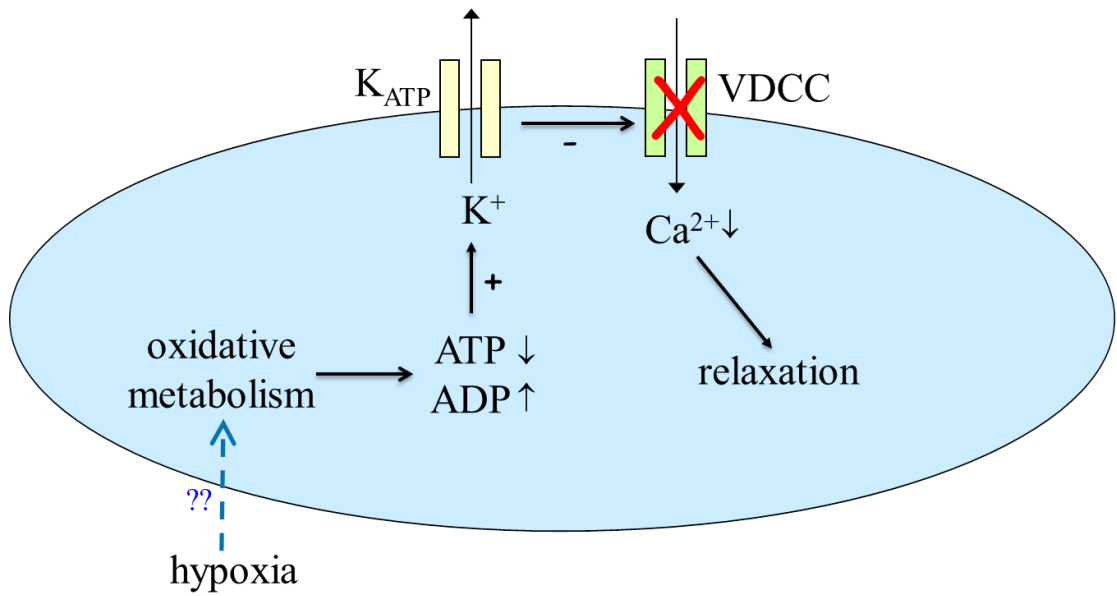


Figure 1.21: K_{ATP} channel modal for hypoxic vasodilation. Hypoxia causes activation of K_{ATP} channels through the inhibition of OXPHOS, followed by membrane potential hyperpolarization and a closure of VDCCs, thus SMC relaxation.

Chapter 2

Materials and Methods

2.1 Materials

2.1.1 Cell culture

Cryopreserved HCASMCs (Cat no. C12511, Lot no. 9052004.5 and 3100203.10) were purchased from Promocell (Heidelberg, Germany) at passage 2 (P2) (**Table 2.1**). HCASMCs were cultured in Promocell smooth muscle cell growth medium 2 (Cat no. C-22062) supplemented with Promocell smooth muscle cell growth medium 2 supplement mix (Cat no. C-39267) with a final supplement concentration of (per ml): 5% v/v fetal calf serum, 0.5 ng epidermal growth factor (recombinant human), 2 ng basic fibroblast growth factor (recombinant human) and 5 µg insulin (recombinant human).

HEK293 cells were cultured in minimum essential media (MEM) supplemented with GlutaMAX™-I and Earle's salts (Cat no. 41090-028, Gibco, Life Technologies) and 10% (v/v) fetal bovine serum (FBS) (Cat no. 10500-064, Gibco, Life Technologies)

HEK293T cells were obtained from Christina Parkes (University of Liverpool) and cultured in Dulbecco's modification of Eagle's medium (DMEM) with 4.5 g/l glucose and non-essential amino acids (NEAA) (Cat no. 10938-025, Gibco, Life Technologies). FBS was added to the medium with a final concentration of 10% (v/v).

Penicillin/streptomycin (Cat no. 15140-122, Gibco, Life Technologies) was added to all cell culture medium with a final concentration of 100 U/ml and 100 µg/ml respectively, unless otherwise stated.

Table 2.1: HCASMC inventory. Lot and donor specific information of HCASMCs used in this project.

Catalogue #	Lot #	Age	Gender	Race	Viability*	Population doubling time (h)
C-12511	9052004.5	54	Male	Caucasian	80%	46.0
C-12511	3100203.10	32	Male	Caucasian	93%	35.4

*Adherence of cells could vary (data provided by Promocell).

2.1.2 Antibodies

Tables 2.2 and 2.3 summarize the primary antibodies and secondary antibodies used in Western blot (WB) and immunocytochemistry (ICC).

Table 2.2 Primary antibodies

Primary Antibody	Company	Type	Isotype	Dilutions	
				WB	ICC
Anti-human vWF	Dako, Denmark (Cat no. A0082)	Polyclonal	Rabbit IgG		1:300
Anti-human CD31	Dako, Denmark (Cat no. M0823)	Monoclonal	Mouse IgG		1:300
Anti α -actin	Sigma-Aldrich (Cat no. A 2547)	Monoclonal	Mouse IgG	1:500	1:300
Anti-calponin	Sigma-Aldrich (Cat no. C2687)	Monoclonal	Mouse IgG	1:500	1:300
Anti-MHC	Novocastra (Cat no. NCL-MHCs)	Monoclonal	Mouse IgG		1:300
Anti actin	Sigma-Aldrich (Cat no. A 4700)	Monoclonal	Mouse IgG	1:500	
Anti-Anterior Gradient 2	Abcam (Cat no. ab56703)	Monoclonal	Mouse IgG		1:200

Table 2.3 Secondary antibodies

Secondary Antibody	Company	Produced in	Conjugate	Dilutions	
				WB	ICC
Anti-mouse	Fitzgerald Industries International (Cat no. 43C-CB1569-FIT, Stratech, Suffolk, England)	Goat	HRP	1:10,000	
Anti-rabbit	Molecular Probes, USA (Cat no. A-11034)	Goat	Alexa fluor 488		1:500
Anti-mouse	Molecular Probes, USA (Cat no. A-11029)	Goat	Alexa fluor 488		1:500

2.1.3 Plasmids DNA

pEGFP-N1 plasmid was provided by Dr. Owain Llyr Roberts (University of Liverpool), GW1CMV-Perceval (Cat no. 21737), GW1-PercevalHR (Cat no. 49082), FUGW-PercevalHR (Cat no. 49083) and GW1-pHRed (Cat no. 31473) were obtained from Addgene. FUGW-pHRed was constructed by ligation of pHRed with the lentiviral vector from FUGW-PercevalHR. Lyn-FUGW-PercevalHR was made by inserting a 5' myristoylation and palmitoylation lipid modification sequence (GCIKSKRKDK) into FUGW-PercevalHR. Rev, Rev-responsive element (RRE) and vesicular stomatitis virus glycoprotein (VSV-G) were given by Joanna Wardyn (University of Liverpool).

2.1.4 Primers

All primers and oligonucleotides used for the studies were purchased from Sigma and summarized in **Table 2.4**.

Table 2.4 Summary of primers and oligonucleotides

Primer/oligonucleotide	Sequence	Tm (°C)	Purpose
hUBCpro-F (Human Ubiquitin C (UbC) promoter, forward primer)	TGAAGCTCCGGTTTTGAAC T	63.6	Sequencing primer for FUGW-pHRed and Lyn-FUGW-PercevalHR
WPRE-R (5' end of WPRE, reverse primer)	CATAGCGTAAAAGGAGCAA CA	61.7	Sequencing primer for FUGW-pHRed and Lyn-FUGW-PercevalHR
PercevalHR Forward	TGCCTGAGGCCTCTAGAAT G	64.4	Sequencing primer for Lyn-PercevalHR
PercevalHR Reverse	GACCTGATTCCTAAGGTGA AGATC	62.9	Sequencing primer for Lyn-PercevalHR
Lyn-PercevalHR and Lyn-FUGW-PercevalHR Forward	TCTAGAATGGGCTGCATCA AGAGCAAGCGCAAGGACA AGATGAAAAAGGTTGAATC CATC	88.6	PCR cloning
Lyn-PercevalHR and Lyn-FUGW-PercevalHR Reverse	GAATTCTCACAGTGCTTCC TTGCC	68.9	PCR cloning
Oligonucleotide 1 (Lipid raft targeting sequence 1)	GCAGGTCGACTCTAGAATG GGCTGCATCAAGAGCAAG CGCAAGGACAAGCACTAG ACCACCATGAA	92.5	Membrane targeting
Oligonucleotide 2 (Lipid raft targeting sequence 2)	TTCATGGTGGTCTAGTGCTT GTCCTTGCGCTTGCTCTTG ATGCAGCCCATTCTAGAGT CGACCTGC	92.5	Membrane targeting

2.1.5 Fluorescent probes

Bis-(1,3-Dibutylbarbituric Acid) Trimethine Oxonol (DiBAC4(3)) (Cat no. B-438), Fluo-4 AM (Cat no. F14201), Fura-Red AM (Cat no. F3021), MitoTracker (Cat no. M7512), rhodamine123 (Cat no. R302), and 4',6'-diamidino-2-phenylindole (DAPI) (Cat no. D3571) were purchased from Molecular Probes and used following manufacture's instruction.

2.1.6 Agonists

Human platelet-derived growth factor BB (PDGF-BB) (Cell Signaling, USA, Cat no. 8912), (R)-(-)-phenylephrine hydrochloride (Sigma, Cat no. P-6126), prostaglandin F₂ α tris salt (PGF₂ α) (Sigma, Cat no. P0424), U46619 (Tocris Bioscience, Cat no. 1932), pinacidil monohydrate (Sigma, Cat no. P154), NS1619 (Sigma, Cat no. N170), SKA31 (Sigma, S5576), and adenosine (Sigma, Cat no. A9251) were used in this study. NS11021 was kindly given by Bo Hjorth Bentzen (University of Copenhagen, Denmark).

2.1.7 Antagonists

2-Deoxy-D-glucose (2-DG) (Calbiochem, Cat no. 25972), rotenone (Sigma, R8875), antimycin A (Sigma, A8674), oligomycin B (Abcam Biochemicals, Cat no. AB143424), CCCP (Sigma, Cat no. C-2759), nimodipine (Sigma, Cat no. N-149), glibencamide (Sigma, G0639), iberitoxin (Sigma, Cat no. I2141), penitrem A (Alomone labs, Israel, Cat no. P-650), BaCl₂ (Sigma, Cat no. B-0750), XE991 (Tocris Bioscience, Cat no. 2000), apamin (Tocris Bioscience, Cat no. 1652), and tram34 (Sigma, Cat no. T6700) were used in this study.

2.1.8 Reagents

Standard reagents were purchased from Sigma-Aldrich (Gillingham), BDH (Poole) or Fisher Scientific (Loughborough) unless otherwise stated. Solutions were made using ultra high quality (UHQ) or Milli-Q (MQ) water with a minimum resistance of 18.2 M Ω .

2.2 Cell culture

2.2.1 Routine passage of HCASMCs

HCASMCs were grown in T75 cm² flasks with 15 ml fully supplemented smooth muscle growth medium 2 in a 5% CO₂ humidified incubator at a temperature of 37 °C. Cells were routinely passaged every 48-72 hours when reaching about 70-80% confluency. Cell culture medium was aspirated, and the cells were washed with 15 ml pre-warmed Dulbecco's Phosphate Buffered Saline (DPBS, no Ca²⁺/Mg²⁺, Cat no. 14190-144, Gibco) or HEPES Buffered Saline Solution (HepesBSS). Cells were then trypsinised with 1.5 ml versene (Gibco) containing 0.025% trypsin (Gibco) or 100 µl per cm² Trypsin/EDTA Solution (0.04%/0.03%) for approximately 1 min. Enzyme was neutralized by addition of 8 ml fully supplemented cell culture medium or 100 µl per cm² Trypsin Neutralizing Solution (TNS). HepesBSS, Trypsin/EDTA Solution and TNS were all contained in Promocell DetachKit (Cat no. C-41200). Cells were then re-suspended in fully supplemented fresh cell culture medium and cultured in T75 cm² flasks at a volume of 15 ml or 10 cm cell culture dishes at a volume of 10 ml.

2.2.2 Freezing and storing of HCASMCs

Cells were grown to 70-80% confluency, harvested and counted using either a hemocytometer or Z1 Coulter[®] Particle Counter (Beckman Coulter). Cell suspensions were centrifuged at 220 g for 3 minutes, and supernatant was removed. Pelleted cells were re-suspended in Cryo-SFM (Promocell, Cat no. C-29910) or in-house freezing medium (90% (v/v) FBS, 10% (v/v) DMSO) at a density of ~1.2 million cells/ml. 1 mL cell suspension was aliquoted into each cryovial (Star Lab, Cat no. E3090-6222). Cryovials were placed into Nalgene Mr. Frosty[®] Cryo 1 °C Freezing Container (Thermo Scientific) or CoolCell (Biocision) and frozen at -80 °C overnight. Cells were kept at -135 °C or liquid nitrogen (-196 °C) for long-term storage.

2.2.3 Resuscitation of HCASMCs

A frozen vial was taken out and placed on dry ice for transport. Cells were quickly thawed in 37 °C water bath by gently swirling the vial for about 1 minute or until ~90% thawed. Cells were completely thawed by the time when the vial was cleaned and taken into the hood where they were gently pipetted into a T75 cm² flask containing 15 ml pre-warmed medium or 10 cm cell culture dish with 10 ml pre-warmed medium. Medium was replaced with fully supplemented fresh medium after 16-24 hours once cells were adhered to surface.

2.2.4 Culturing of HEK293 and HEK293T cells

Cells were rapidly thawed in a 37 °C water bath by gently swirling or until ~90% thawed and plated into 10 ml fully supplemented medium in a 10 cm cell culture Petri dish. After 24 hours, the medium was replaced with fully supplemented fresh growth medium. Cells were sub-cultured every 48-72 hours when they reached about 70-80% confluence. The cells were washed with 10 ml DPBS and incubated with 1 ml trypsin solution (0.025% in versene) for about 1 minute in a 37 °C incubator until all cells became detached. Trypsin was neutralized by addition of 3 ml fully supplemented cell culture medium, and the cells were seeded into 10 cm Petri dishes with a total of 10 ml pre-warmed medium at a ratio of 1:8 to 1:16 as required.

2.3 Cell transfection

2.3.1 Transient transfection

Cells were transfected with the transfection reagents listed in the **Table 2.5**. Cells were seeded 24 hours prior to transfection normally at a density of 2.0×10^6 for HEK293 and HEK293T cells and 1.25×10^5 for HCASMCs per well in 6-well cell culture plates or 35 mm glass-bottom dishes (see cell number optimization for transfection in **chapter 3.3.1**). Note that cell seeding number may be modified according to the passage of the cells and the growth rate of the cells. On the day of transfection, cells were transfected following the protocols provided by the

manufacturer.

Table 2.5 Transfection reagents used in the study

Name	Company
Lipofectamin TM 2000 (LF2000)	Invitrogen (Cat no. 11668-027)
FuGENE [®] 6	Promega (Cat no. E2691)
FuGENE [®] HD	Promega (Cat no. E2313)
X-tremeGENE 9 DNA	Roche (Cat no. 06 366 511001)
X-tremeGENE HP DNA	Roche (Cat no. 06 365 752001)
TransIT [®] -LT1	Cambridge Bioscience (Product no. MIR 2310)
TransIT-X2 [®] Dynamic Delivery System	Cambridge Bioscience (Product no. MIR 6010)
Promofectin	Promocell (Cat No. PK-CT-2000-100)

2.3.2 Lentivirus based biosensors

2.3.2.1 Production of lentivirus third generation virus stocks

Lentivirus based biosensors were prepared in two ways, calcium precipitation method and transfection reagent method.

In calcium chloride method, HEK293T cells were maintained in DMEM high glucose medium, and cells at early passages were used. Cells were seeded a day before the transfection at a density of 6.0×10^6 into 15 cm dishes and left overnight in a 37 °C/5%CO₂ incubator. Next day, cells were fed with 20 ml fully supplemented medium 2 hours before transfection. Transfection mixture for five 15 cm dishes was prepared as shown in **Table 2.6** using a 50 ml sterile falcon tube, and was left at room temperature for 5-30 mins for incubation. 2.25 ml of the mixture was then added to each 15 cm dish. The dishes were left in a 37 °C/5%CO₂ incubator overnight. Early next morning the medium was discarded and replaced with 16 ml fresh DMEM medium or smooth muscle cell growth medium 2, and incubated in 37 °C/5%CO₂

incubator. After 24 hours incubation, medium was collected and spun down in a centrifuge at the speed of 500 g for 5 minutes, and the supernatant was stored at 4 °C. Cells were incubated for another 24 hours in 16 ml fresh DMEM or smooth muscle cell growth medium 2. On next morning, the second batch of medium was collected and spun down at the speed of 500 g for 5 minutes. The supernatant was reserved, and the cells were discarded. The above two batches of medium were combined and filtered twice through 0.22 µm PES filter (Merck Millipore, Cat no. SLGP033RS). Filtered medium was then aliquoted and kept in -80°C freezer.

Table 2.6 Preparation of transfection mixture

0.1x TE buffer	3.3 ml
FUGW-PercevalHR/Lyn- FUGW-PercevalHR	112.5 µg
pCMV-VSV-G	39.5 µg
pMDLg/pRRE	73 µg
pRSV-Rev	73 µg
Buffered water	1.75 ml
2.5 M CaCl ₂	565 µl
2x HEBS buffer	5.7 ml

Note: Volume should be scaled according to the number of dishes needed

Buffered water	2.5 M CaCl₂
50 ml MQ water	9.18 g CaCl ₂ •2H ₂ O (Sigma, Cat no. C3881)
125 µl 1 M HEPES	
pH 7.3	25 ml MQ water
Filter sterile	Filter sterile
Store up to 6 months at 4°C	Store at 4°C

Lentivirus could also be produced by using transfection reagents such as LF2000 and Promofectin. HEK293T cells were cultured in DMEM high glucose

medium, and cells at early passages were used. Cells were seeded a day before the transfection at a density of 2.0×10^6 into 10 cm dishes and left overnight in a 37 °C/5%CO₂ incubator. Transfection was performed on the following day. In general, 45.0 µl of LF2000 was gently mixed with 1.5 ml Opti-MEM medium (Gibco, Cat no. 51985-034) and incubated at room temperature for about 5 minutes. 9.0 µg vector plasmid (FUGW-PercevalHR or FUGW-pHRed or Lyn-FUGW-PercevalHR), 4.5 µg pMDLg/pRRE, 1.8 µg pRSV-Rev and 2.7 µg pCMV-VSV-G were gently mixed into another 1.5 ml Opti-MEM medium. DNA and LF2000 mixture were then gently mixed together and incubated at room temperature for 20 minutes to allow DNA and lipid to form complexes. During incubation, cell culture medium of HEK293T cells was replaced with 5.0 ml DMEM medium containing 10% FBS without antibiotics. 3.0 ml DNA-LF2000 complexes was added to 10 cm HEK293T cell dish. Same procedure was performed when using Promofectin to transfect the cells. Transfection conditions were summarized in the **Table 2.7**. Virus collection and freezing were performed in the same way as calcium precipitation method.

Table 2.7 Transfection mixture for one 10 cm dish using transfection reagent

FUGW-PercevalHR/FUGW-pHRed/Lyn- FUGW-PercevalHR	9.0 µg
Gag-Pol expression vector (pMDLg/pRRE)	4.5 µg
Rev expression vector (pRSV-Rev)	1.8 µg
VSV-G expression vector (pCMV-VSV-G)	2.7 µg
Total plasmid DNA	18 µg
Lipofectamine™2000/ Promofectin	45 µl/36 µl
Total Opti-MEM	3 ml
Vol. of DMEM	5 ml

2.3.2.3 Infection of the cells with lentivirus

HCASMCs were plated at a density of 2.0×10^4 in 35 mm glass-bottom dishes or 6 well plates about 24 hour prior to transduction. On the day of transduction, cells

were fed with fresh medium 2 hours before being treated with lentivirus. For the transduction of 10 cm dishes, cells that reached about 40-50% confluence were fed with fresh medium 2 hours before lentivirus treatment. After 2 hours, 2 ml of media containing lentivirus was added to 35 mm dishes or wells of the 6 well plate, and 10 ml of media containing lentivirus was added to the 10 cm dishes. Cells were incubated in a 37 °C/5%CO₂ incubator for around 16 hours. Early next morning, the medium was changed with fresh smooth muscle growth medium 2. Counting the discarding of lentivirus containing media as day one, cells are normally imaged from day 3 onwards. In some cases such as when the concentration of lentivirus was low, cells were infected twice in order to boost transfection efficiency.

2.4 Cell-based assays

CellTiter-Glo[®] Luminescent Cell Viability Assay (Promega, Cat no. G7572) was used to measure intracellular ATP level. Proliferation of HCASMCs was assessed using a 3-(4,5 dimethylthiazol-2-yl)-2,5-diphenyltetrazolium bromide (MTT, Sigma, Cat no. M2128) assay, and cell migration was characterized by scratch-wound assay and transwell migration assay.

2.4.1 CellTiter Glo[®] Luminescent Cell Viability Assay

HCASMCs were grown to 70-80% confluence on the day of seeding for assay. After lifting, cells were counted with the Z1 Coulter[®] particle counter and resuspended at the density of 25,000 cells/ml. 100 µl of the cell suspension was then plated into each well of a 96-well flat bottom black polystyrene plate (Costar, Cat No. 3916) and left in a 37 °C/5%CO₂ incubator for 24-48 hours. On the day of assay, test compounds were added to experimental wells for the allocated time. 100 µl of CellTiter-Glo[®] reagent (equal to the volume of cell culture medium present in each well) was added to each well, and cell lysis was induced by 2 minutes of incubation on an orbital shaker. The plate was allowed to incubate further at room temperature for 10 minutes to stabilize luminescent signal and luminescence was recorded in a plate reader (FLUOstar Omega, BMG LABTECH).

2.4.2 ATP:ADP ratio microplate assay

FUGW-PercevalHR was transduced into HCASMCs by 3rd generation lentivirus. Cells expressing FUGW-PercevalHR were seeded into a 96-well black polystyrene plate at a density of 2,500 cells per well. Fluorescence was recorded every 1 minute with a plate reader (FLUOstar Omega, BMG LABTECH) with the excitation of 485 nm and emission of 520 nm.

2.4.3 MTT assay

Cells were seeded into 96-well cell culture plates (Costar, Cat no. 3596) at a density of 2500 cells/well in 100 µl medium. In order to synchronize the cell cycle, medium was replaced next day with 100 µl low serum medium where Promocell smooth muscle cell growth medium 2 supplement mix was reduced to 0.1% for 48 hours. Inclusion of a small amount of supplement mix was necessary as HCASMCs did not tolerate complete elimination of supplement. Cells were then treated with test chemicals or exposed to hypoxia, and incubated according to culture protocol. 5 µl of MTT (5 mg/ml in DPBS) was then added to each well, and the plate was shaken with a shaker for 1 minute, and cells were incubated in the 37 °C/5%CO₂ incubator for four hours. Next, 50 µl of stop solution (10% SDS in 0.01 M HCl) was added to each well and mixed on an orbital shaker for 1 minute. The plate was incubated further in the 37 °C/5%CO₂ incubator overnight. The plate was read at absorption of 570 nm on the following day.

2.4.4 Scratch-wound assay

Cells were plated into 6-well plates and left overnight to reach around 80-90% confluence. On the following day, a scratch was made using a 1000 µl blue tip in the mid-line of the well. The gap would gradually close as cells at the edges of the wound migrate to scratched area (**Figure 2.1**) [192, 193]. Chemicals of interest such as PGDF-BB can be added to the scratched wells, or the plates can be placed into hypoxic chambers with different oxygen levels. Images were captured using a DC5000 CMEX microscope camera (Euromex) with a 4x objective. Pictures were

analyzed using Fiji software, and the degree of migration was determined as migration rate where '1' corresponds to the complete closure of the wound, and each condition was repeated in 3 wells.

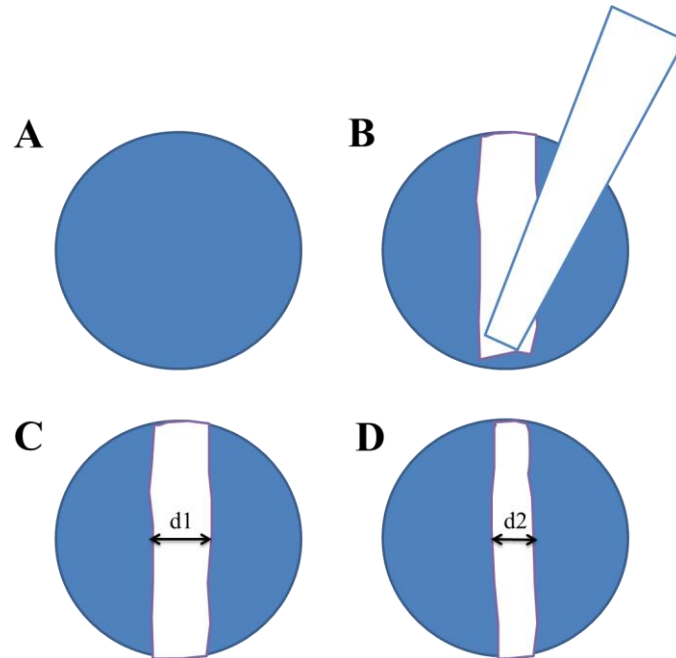


Figure 2.1 Scratch-wound Assay. A wound was made to the cell monolayer of each well (A) by drawing a line using a 1000 μ l blue tip (B). The denuded area is imaged to measure the boundary of the wound before migration (C) and after cells have migrated inward to fill the gap (D). Migration rate was calculated as $(d1-d2)/d1$.

2.4.5 Transwell migration assay

When HCASMCs reached about 70% confluent, medium was replaced with low serum medium and incubated for 48 hours in a 37 $^{\circ}$ C/5%CO₂ incubator to synchronize the cell cycle. Cells were then collected in low serum medium and resuspended at a density of 2.0×10^5 /ml. 100 μ l of cell suspension (2.0×10^4 cells) were seeded to the upper chamber of the transwell insert with 8.0 μ m pore size (VWR, Cat no. 734-1574). Inserts with cells were put into the 24-well plates containing 600 μ l fully supplemented medium, and cells were allowed to migrate for 8 hours in 37 $^{\circ}$ C/5%CO₂ incubators with different levels of O₂. A Reastain Quick Diff kit

(Reagent, Cat no. 102164) was used to stain migrated cells, which were subsequently counted using a microscope and images were taken using a DC5000 CMEX microscope camera. Cells from three areas of each insert membrane were randomly chosen and counted and each condition was repeated in triplicate. The procedure of this assay is briefly summarized in **Figure 2.2**.

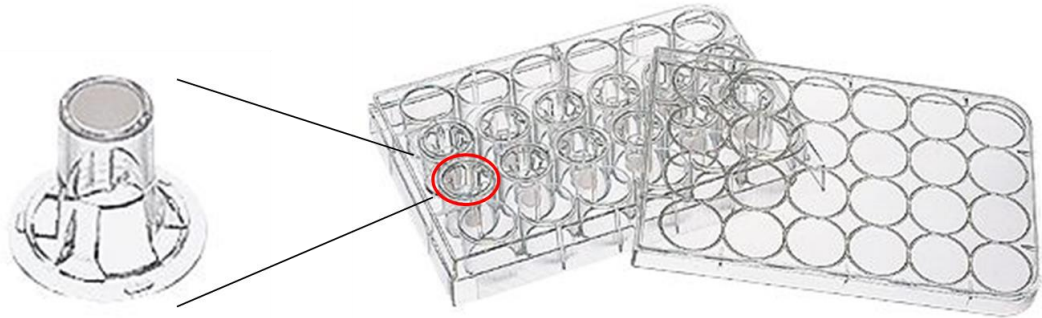
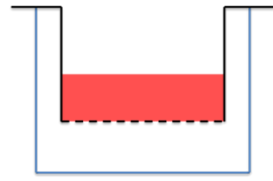


Figure 2.2.1 Transwell cell culture plate. Transwell insert with 8.0 μm pores for investigation of cell migration. An example of transwell membrane was shown by leaving the transwell cell culture insert upside down (see **Figure 2.2.2**). (Reproduced from <http://www.coleparmer.com/>)



Saturate the membrane with low serum medium

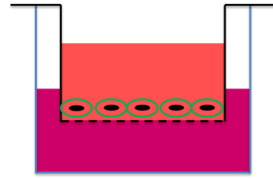
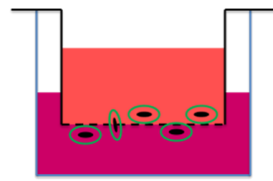
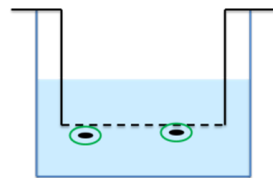


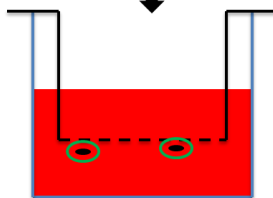
Plate 2.0×10^4 cells to the top part of the transwell



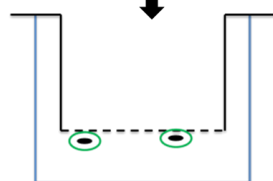
Incubate cells in experimental conditions for a required time



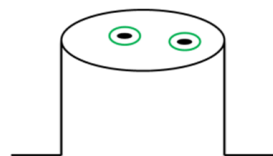
Fixing cells



Stain cells



Wash off excess dye



Count under microscope

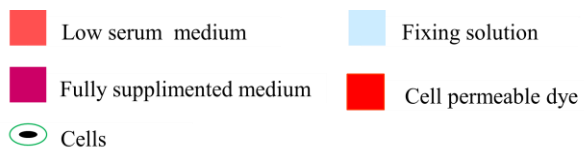


Figure 2.2.2: Transwell cell migration assay.

2.5 Seahorse XF⁹⁶ analyses of oxygen consumption rate and extracellular acidification rate

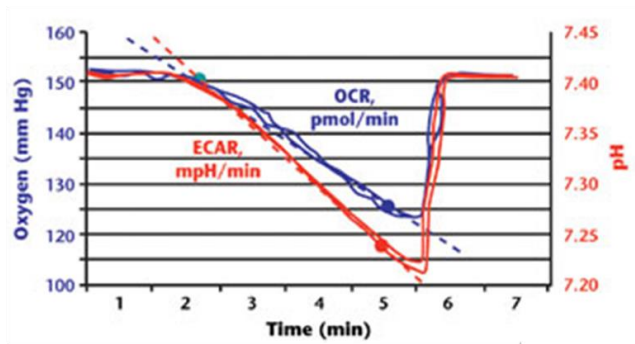
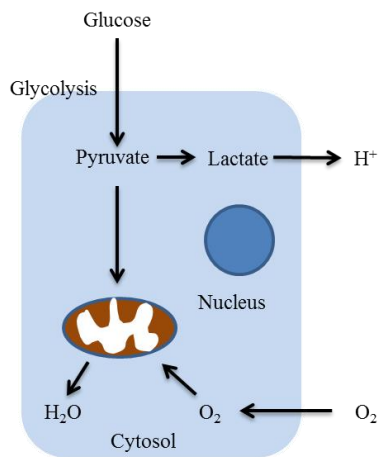
Seahorse XF⁹⁶ Analyser (**Figure 2.3**) was used to continually monitor both aerobic and glycolytic components of cellular bioenergetics. It allows rapid measurements of oxygen consumption and lactate production, the former a measure of oxidative phosphorylation and the latter, a measure of glycolysis. Seahorse technique determines OCR and ECAR from fluorescence intensity of two probes, one reading oxygen concentration and the other proton content. All measurements were made in an unbuffered XF Base Medium Minimal DMEM assay medium (Seahorse Bioscience, Cat no. 102353-100) [183].

HCASMCs were plated into Seahorse 96-well XF Cell Culture Microplates (Seahorse Bioscience, Cat no. 101085-004) at a density of 2.0×10^4 per well and left to form the monolayer overnight. The day before assay, 200 μ l of XF Calibrant Solution (Seahorse Bioscience, Cat no. 100840-000) was added to each well of XF⁹⁶ FluxPaks (Seahorse Bioscience, Cat no. 102416-100) and incubated overnight at 37 °C in a CO₂ free incubator to hydrate the sensor cartilage. On the day of assay, the media of the wells for mitochondrial stress test was replaced with unbuffered minimal DMEM containing 1 mM sodium pyruvate, 25 mM D-glucose and 2 mM L-glutamine (pH 7.4). Medium for glycolytic stress test was replaced with unbuffered minimal DMEM containing 1 mM sodium pyruvate and 2 mM L-glutamine (pH 7.4). The cell plate was then incubated at 37 °C in a CO₂ free environment for a minimum period of 1 h before measurement.

A



B



C

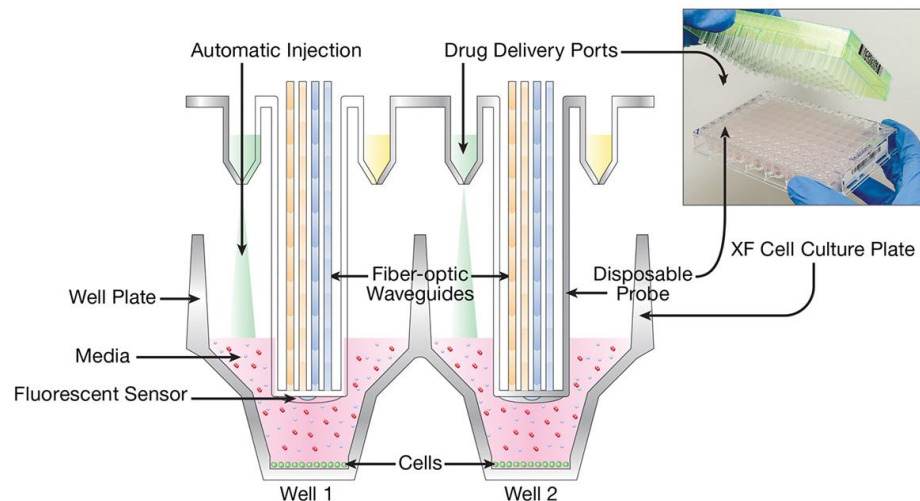


Figure 2.3: Seahorse XF Analyzer machinery and an illustration of its working principle. (A) The Seahorse XF Analyzer. (B) OCR and ECAR calculation. (C) Working Seahorse XF Analyzer plate. (Reproduced from www.seahorsebio.com)

2.5.1 Mitochondrial stress test

Mitochondrial stress test was performed by sequentially adding pharmacological inhibitors of OXPHOS using Seahorse technology [180, 181]. First, the basal O₂ consumption was established corresponding to the total O₂ consumption including mitochondria as well as other oxidases. Cells were first treated with oligomycin (oligo), an ATP synthase inhibitor that causes a cessation of oxidative energy generation shutting down the O₂ consumption independent of proton leak. To estimate the maximal potential respiration of the cells, a proton ionophore FCCP (Sigma, Cat no. C2920) was used. O₂ consumption increases with uncoupler as the mitochondrial inner membrane becomes permeable to protons, eliminating the proton gradient. Thus, the difference between application of oligomycin and FCCP is the latter measures mitochondrial reserve capacity, calculated by subtracting the basal OCR from FCCP-stimulated rate. Finally rotenone and antimycin (R+A) were applied to inhibit oxygen consumption related to the activity of complex I and complex III. Such pharmacological inhibition of electron transport typically inhibits the majority of O₂ consumption in the cell, and we attribute the remaining O₂ consumption to non-mitochondrial oxidases in the cell (**Figure 2.4**).

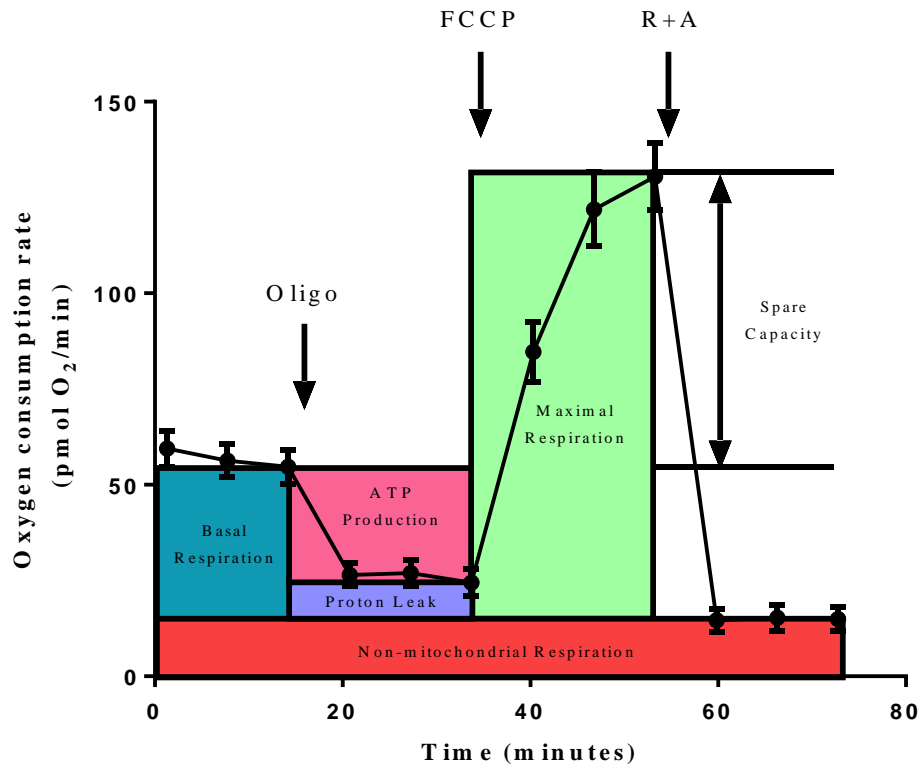


Figure 2.4: Mitochondrial stress test. A typical experiment of mitochondrial stress test. The basal O₂ consumption of the cells is established first, then sequential application of oligomycin, FCCP, and combination of rotenone and antimycin A are applied to dissect the relative contribution of ATP synthase-linked O₂ consumption, non-mitochondrial respiration, proton leak, and the reserve capacity of the cells

2.5.2 Glycolytic stress test

During glycolysis, the breakdown of one glucose molecule into two pyruvate anions generates two H⁺. Therefore, change in glycolytic function can be assessed by determining ECAR in response to the addition of glycolysis modulating compounds [180, 181]. In this assay, glucose was first added to the cells in glucose free unbuffered minimal DMEM Seahorse medium. Next, oligomycin was applied to cause a loss of mitochondrial ATP production leading to near maximal level of glycolytic rate. Finally, non-glycolytic extracellular acidification can be measured by introducing 2-DG as a pseudosubstrate of glucose to determine ECAR due to non-glycolytic mechanisms. (Figure 2.5)

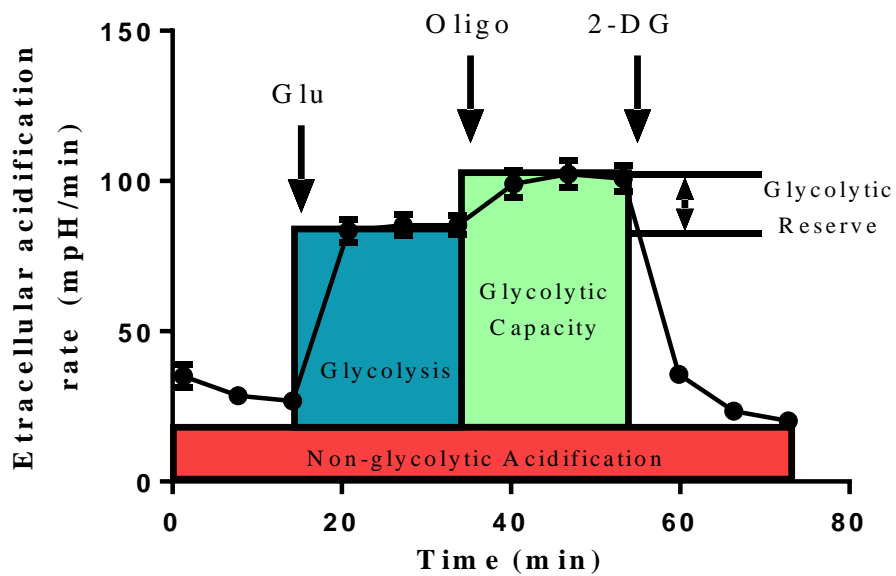


Figure 2.5: Glycolysis stress test. A typical glycolysis stress test. After basal ECAR is allowed to stabilize in the absence of glucose, glucose is added. Next oligomycin is added causing near maximal glycolytic rate. The addition of 2-DG at the end allows the measurement of non-glycolytic extracellular acidification.

2.5.3 Comparison of bioenergetic phenotype of HCASMCs

In order to assess the bioenergetic phenotype of the cells and how it may shift in response to mitochondrial toxicants, OCR and ECAR were plotted before and after treatments. As shown in **Figure 2.6**, the relative phenotype of the cells can be classified as aerobic, energetic, quiescent and glycolytic, based on the possible 4 combination outcomes of OCR and ECAR measurements.

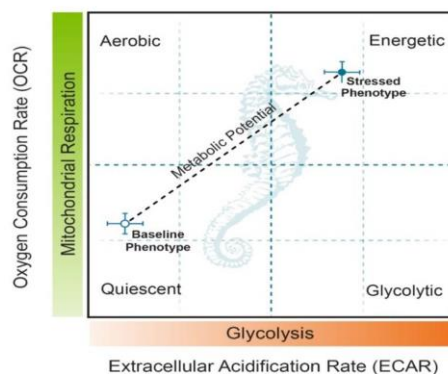


Figure 2.6 Cell bioenergetic phenotype profile. Four cell bioenergetic phenotypes characterized from OCR and ECAR measurements. Graph shows an example of cell bioenergetic phenotype shifting from a baseline quiescent phenotype (open circle) to a stressed energetic phenotype (filled circle). (Reproduced from www.seahorsebio.com)

2.5.4 Normalization of OCR and ECAR data

At the end of each mitochondrial and glycolytic stress test, solution in the wells was removed and 20 μ l of somatic cell ATP releasing reagent (Sigma, Cat no. FLSAR-1VL) was added to each well, followed by 5 minutes vortex in order to fully lyse the cells. The total amount of protein in each well was determined by BCA assay in a microplate, OCR and ECAR rates were then normalized to μ g protein.

2.6 FACS analysis of cell cycle

2.6.1 Cell preparation

HCASMCs were seeded into 10 cm dishes and incubated for 24 hours to allow adhesion. The following day, the cell culture medium was replaced with low serum medium, and all plates were incubated for 48 hours. After this starving period, all plates were treated as designed (metabolic inhibitors, hypoxia etc.) for a required period.

2.6.2 Sample preparation for flow cytometric analysis

At the end of each treatment, cells were collected, centrifuged at 1000 rpm for 5

mins, and the pellet was re-suspended in 0.5 ml PBS. The cells were fixed by transferring the cell suspension to 4.5 ml of 70% ice cold ethanol, and kept at 4 °C for a minimum period of 30 minutes. Ethanol-suspended cells were centrifuged for 5 minutes at 2000 rpm, and the pellet was washed with 5 ml PBS. Cells were then permeabilised by adding 1 ml of saponin (0.5% in PBS) (Calbiochem, Cat no. 558255) for 5 minutes. Cells were washed with PBS and centrifuged at 2000 rpm for 30s twice. 1 ml of DAPI solution (1µg/ml in PBS) was added to each sample for FACS analysis.

2.6.3 Analysis on flow cytometer

All samples were analyzed on the FACSCanto II Flow Cytometer (BD biosciences), and a population of 15,000 events was used for each analysis. Percentages of cells in each cell cycle were calculated with BD FACSDiva software v6.1.3.

2.7 Western blot

Western blot analysis was used to detect specific proteins in human coronary artery endothelial cell (HCAEC) and HCASMC lysates.

2.7.1 Sample preparation

HCASMC were cultured in 10 cm cell culture petri dishes in 10 ml fully-supplemented media until 80-90% confluent, approximately 48-72 hours. The dish was then placed on crushed ice, the media was removed and washed with 5 ml ice-cold DPBS. The DPBS was removed and replaced with 500 µl ice-cold 1% v/v protease inhibitor cocktail (Sigma, Cat no. P8340)/lysis buffer solution (20 mM Trizma HCl, 250 mM NaCl, 3 mM EDTA, 3 mM EGTA, 0.5% v/v Triton X-100, pH adjusted to 7.6) for 5 minutes, tilting the dish gently to ensure that it covers the whole surface area evenly. A 25 cm cell scraper (Sarstedt, Cat no. 83.1830) was used to dislodge the cells by scraping across whole surface. Lysates were then collected in a pre-chilled 1.5 ml microcentrifuge tube (Eppendorf) and centrifuged at 18,200 g for

10 minutes at 4°C. Usually, 150 µl of the supernatant was reserved and frozen at -20°C for the BCA assay. The volume of remaining supernatant was measured and appropriate amount of x2 sample buffer (Sigma, Cat no. S3401) was added and gently mixed, and heated at 98°C in a dry heating block for 10 minutes. Cell lysate was cooled down on crushed ice before aliquoting into 0.5 ml microcentrifuge tubes (Eppendorf) and stored at -20°C for up to 4 months if not required immediately. HCAEC lysates were provided by Rachael Quinn (University of Liverpool).

2.7.2 BCA protein assay

Protein concentrations of the sample lysates were determined by a Pierce Bicinchoninic Acid (BCA) assay kit (Thermo Scientific, Cat no. 23227). All standards and protein lysates were tested by either test-tube procedure or microplate procedure.

2.7.2.1 Test-tube procedure (Sample to WR ratio = 1:20)

The standard protein solutions, bovine serum albumin (BSA) 2000, 1500, 1000, 750, 500, 250, 125, 25 and 0 µg/ml, were made according to manufacture's protocol using lysis buffer. Working Reagent (WR) was prepared by mixing 50 parts reagent A and 1 part reagent B. 50 µl of each protein solution was added to 1.5 ml microcentrifuge tubes, followed by 1 ml of WR, and the mixture was vortexed. Each condition was duplicated. Tubes were incubated in a water bath at 37°C for 30 minutes. After cooling down to room temperature, the protein concentration was measured using a Jenway spectrophotometer (Genova, 1690) at the absorbance of 562 nm.

2.7.2.2 Microplate procedure (Sample to WR ratio = 1:20)

In the microplate procedure, 10 µl of each sample was added to a 96 well plate (Thermo Scientific, Cat no. 15041) in duplicates, followed by 200 µl of WR. The plate was mixed thoroughly on a plate shaker for about 30 seconds and incubated in a 37°C incubator for 30 minutes. After being cooled down to room temperature, the

plate was read at 562 nm in a plate reader (SPECTRAmax, Molecular Devices).

2.7.3 Preparing polyacrylamide gels

Proteins were separated according to their size by sodium dodecyl sulphate polyacrylamide gel electrophoresis (SDS-PAGE). 10% resolving gel was cast using 1 mm spacer thick glass plates in a vertical casting apparatus (Bio Rad), topped up with isopropanol to flatten the gel surface and prevent from drying out, and then allowed to polymerize at room temperature for approximately 45 minutes. Once set, isopropanol was poured out, and space between glass plates was washed using UHQ water. The stacking gel was added onto the resolving gel, and a comb was inserted to form 10 wells for the loading. The stacking gel was allowed to set for approximately 45 minutes at room temperature.

10% Resolving gel	
30% w/v Acrylamide (Biorad, 16100158)	4.3 ml
Resolving buffer (2 M Trizma base, pH 8.8)	3.3 ml
87% v/v glycerol	930 μ l
10% SDS	130 μ l
UHQ water	4.4 ml
10% w/v ammonium persulfate (APS)	60 μ l
TEMED	13 μ l

4% Stacking gel	
30% w/v Acrylamide	840 μ l
Stacking buffer (0.5 M Trizma base, pH 6.8)	1.5 ml
10% SDS	60 μ l
UHQ water	3.8 ml
10% w/v ammonium persulfate (APS)	53 μ l
TEMED	11 μ l

2.7.4 Running polyacrylamide gels

The cell lysates were briefly mixed by vortex and heated in the dry heating block at 98°C for 5 minutes to ensure complete denaturing of the proteins. 7.0 µl of rainbow protein mass marker (Amersham full-range rainbow MW marker, Cat no. RPN800E) and 25 µl of each lysate were added to the wells. Gels were placed in a vertical gel electrophoresis tank (Bio Rad) and submerged in SDS running buffer (25 mM Tris base, 192 mM Glycine and 3.5 mM SDS). Gels were run at 120 V for 1 hour until the rainbow ladder had been fully separated.

2.7.5 Coomassie brilliant blue staining

Electrophoresed gels were gently removed from the glass plates, and rinsed twice in reverse osmosis (RO) water. Gels were then put into Coomassie brilliant blue stain solution, and left on an oscillating platform for at least 30 minutes at room temperature. The gels were washed again with RO water several times in order to remove excess stain. Gels were left in destaining buffer until the protein bands became visible and background was reduced. Gels were scanned using an ImageScanner III gel scanner (GE Life Sciences).

Coomassie brilliant blue stain solution	Destaining buffer
0.1% (w/v) Coomassie brilliant blue stain	20% (v/v) methanol
50% (v/v) methanol	10% (v/v) glacial acetic acid
7% (v/v) glacial acetic acid	

2.7.6 Western blotting

Separated proteins were transferred from polyacrylamide gel onto nitrocellulose membrane (Amersham Hybond ECL, Cat no. RPN303D) in transfer buffer (25 mM Trizma base, 192 mM Glycine and 20% (v/v) methanol) at 110 V for 1 hour in a low temperature by placing the tank containing a blue ice pillow into a bucket filled with crushed ice. After proteins were transferred, membranes were washed twice in Tris

buffered saline with TWEEN 20 (TBST, 20 mM Trizma base, 137 mM NaCl, 0.1% v/v TWEEN 20, pH 7.6). As an optional step, the membranes were submerged in Ponceau S solution (Sigma, Cat no. P7170) for 5 minutes to check the transfer efficiency of the protein, Ponceau S can be washed away by washing the blots with TBST on the rocker (Labnet rocker 25) for 5 minutes. Membranes were trimmed and blocked for 1 hour at room temperature on the rocker using TBST containing 5% or 1% w/v non-fat powdered milk (Marvel). Membranes were then put into a continuous bag where 1.0 ml of diluted primary antibody was added (see the dilution factor in **Table 2.2**), and bags were heat sealed. The primary antibodies were diluted in TBST with 5% or 1% w/v non-fat milk, and incubated overnight at 4°C.

Next day, the membranes were quickly washed twice in TBST, followed by further three washes with TBST on the rocker (10 minutes each). Horseradish peroxidase (HRP)-conjugated secondary antibodies were used at a 10,000 fold dilution (anti-mouse) or a 5,000 fold dilution (anti-rabbit) in TBST with non-fat milk (5% or 1% w/v). Nitrocellulose membranes were then incubated with HRP-conjugated secondary antibodies for over one hour and up to two hours at room temperature on the rocker. After incubation with secondary antibody, membranes were washed a couple of times with TBST, followed by further three washes on the rocker, 10 min each. During wash, enhanced chemiluminescence solution mixture was prepared by combining equal volume of ECL solutions 1 and 2 (ECL, Amersham, Cat no. RPN2109). The membranes were then incubated in the ECL solutions for one minute. Care was taken to ensure that whole membrane was well covered with solution by repeatedly spraying it using a 1,000 µl pipette. After removing the excess ECL solution, the membranes were carefully put into plastic wallets (Lyreco) and fixed onto the hypercassette (Amersham Biosciences) with tapes.

2.7.7 Developing the photographic film

All procedures were carried out in a dark room. Photographic film (Amersham hyperfilm ECL high performance chemiluminescence film, Cat no. 28906836) was

overlayed onto the membrane in the hypercassette and exposed for 5 mins, 10 mins, 30 mins or longer if required. The photographic film was processed using Kodak photographic solutions (Kodak GBX fixer and developer). After the films were dried, bands were sized by referencing to the rainbow ladder. To semi-quantify the darkness of the bands, densitometric analysis was processed using Image J software.

2.7.8 Re-blotting

Even with care, equal loading of wells could not be guaranteed, making semi-quantitative comparison difficult. In order to ensure the protein expression difference did not arise from uneven loading, expression of housekeeping protein (actin) was examined by re-blotting. Used nitrocellulose membranes were re-hydrated with TBST for 0.5-1.0 hour, followed by stripping of previous antibodies with stripping solution (100 mM β -mercaptoethanol, 2% w/v SDS, and 62.5 mM Tris base, pH 6.7) for 10 mins on a rocker, repeated twice. Membranes were then blocked using non-fat milk in TBST as before and incubated with primary and secondary antibodies as normal Western blotting procedure.

2.8 Immunocytochemistry

Western blot technique is useful in detecting proteins by virtue of known protein size. However, Western blotting does not provide useful information about the localization of proteins. Immunocytochemistry is a useful parallel technique to Western blotting as the spatial information of expression can be obtained.

2.8.1 Plating HCAECs and HCASMCs

Flame-sterilized size 1 coverslips (diameter, 13 mm) were coated with 1% v/v poly D-lysine (Millipore, Cat no. A-003-E) and incubated for 1-2 hours in a 37 °C/5% CO₂ incubator. HCAECs were provided by Rachael Quinn (University of Liverpool). After incubation, coverslips were washed twice with UHQ water and dried in the hood before being placed in a 24-well cell culture plate.

Cells were trypsinised and counted with Z1 Coulter[®] particle counter. HCAECs

were seeded onto coverslips with a density of 100,000 cells per well and HCASMCs with a density of 125,000 cells per well, both in 2 ml fully-supplemented cell culture medium (Promocell). Empty wells at the edges of the 24-well plate were filled with UHQ water to create a humidified environment. Cells were cultured at 37°C/5%CO₂ typically overnight.

2.8.2 Fixing, quenching and permeabilising of cells

Culture medium was removed, and cells were washed with 1 ml DPBS. After removing DPBS, 1 ml of 2% w/v paraformaldehyde in PBS (in mM: 2.7 KCl, 1.5 KH₂PO₄, 137 NaCl, 8.0 Na₂HPO₄, pH 7.4) was added into each well to fix the cells. After incubating for 10 minutes at room temperature, the fixative was removed and replaced with 1 ml 100 mM glycine solution (pH 7.4) for 10 minutes at room temperature to quench the excess fixative. Cells could then be stored in 4°C fridge in DPBS containing 10 mM sodium azide for future use. Glycine solution/DPBS was removed, and a fine-ended glass Pasteur pipette (SLS select, PIP4101) was used to add 3 ml permeabilisation solution (0.1% v/v Triton X-100 in PBS, pH adjusted to 7.4 using 1 M NaOH). Cells were incubated for 10 minutes at room temperature in order to make the intracellular space accessible to antibody.

2.8.3 Labelling with antibodies

Permeabilised cells were rinsed with 2 ml PBS 3 times, 5 minutes each. Next, the cells were incubated with 200 µl antibody diluting solution (see below) for 30 minutes at room temperature to block non-specific binding. After taking off antibody diluting solution, 200 µl of diluted primary antibody (see **Table 2.2**) was added to the wells. Cells were incubated with primary antibodies at 4°C overnight. On the following day, the primary antibody was removed and the cells were washed with 1 ml antibody wash solution (see below) at room temperature three times, 10 minutes each. Primary antibodies were indirectly stained using fluorescent Alexa Fluor 488-conjugated goat anti-rabbit or anti-mouse IgG secondary antibodies at the dilution of 1:500. To prevent photo-bleaching, the plate with coverslips was

incubated in the dark for a period of at least 1 hour but no more than 2 hours at room temperature. The cells were then washed with antibody wash solution three times at room temperature, 10 minutes each. Coverslips were taken out of the wells, washed quickly with UHQ water twice and left to air dry in the dark. When dry, coverslips were mounted onto glass slides with 20 μ l mounting medium (Dako, S3023) containing 5 nM DAPI for counter staining of the nuclei. Air bubbles were avoided during this procedure. Finally, the slides were allowed to dry at room temperature in the dark before imaging.

Sodium citrate buffer (SSC)	
NaCl	250 mM
Na ₃ Citrate	15 mM

Antibody diluting solution (pH 7.2)	Antibody wash solution (pH 7.2)
SSC with	SSC with
2% v/v goat serum	0.05% v/v Triton X-100
0.05% v/v Triton X-100	
1% w/v bovine serum albumin	

2.8.4 Confocal microscopy (immunocytochemistry imaging)

A LSM510 multiphoton laser-scanning confocal microscope was used to visualize the labelled cells. Alexa Fluor 488 was excited at 488 nm using an argon-ion laser, and emission light was collected at 500-550 nm. For the detection of DAPI nuclear staining, a Mai Tai infra-red laser (Spectra-Physics) on LSM510 multiphoton was used for two-photon excitation at a wavelength of 810 nm, providing the working excitation of 405 nm.

2.9 Confocal microscopy (live cell imaging)

Fluorescence signal was collected with LSM510, LSM510 multiphoton or

LSM780 confocal microscopy, all of them allowed control of CO₂, humidity and temperature. Environmental O₂ can be changed in LSM510 and LSM 780, allowing cells to be exposed to hypoxic conditions. Software analysis of the data from LSM510 and LSM510 multiphoton were carried out by region of interest analysis using AIM software, version 3.2 SP2 (Carl Zeiss AG, Oberkochen, Germany). Data from LSM780 confocal microscopy were analyzed with Zen SP1 software (Carl Zeiss AG, Oberkochen, Germany).

2.9.1 Intracellular ATP:ADP ratio and pH

GW1CMV-Perceval/GW1-PercevalHR, fluorescent reporters of ATP:ADP ratio, were transiently transfected into HEK293 cells or HCASMCs. FUGW-PercevalHR and Lyn-FUGW-PercevalHR were transfected into the cells via a 3rd generation lentivirus based system to measure intracellular or near membrane ATP:ADP ratio. Cells expressing GW1CMV-Perceval, GW1-PercevalHR, FUGW-PercevalHR or Lyn-FUGW-PercevalHR were excited with 488 nm light from an argon laser, and emitted fluorescence was collected at 500-550 nm. In the experiments of ratio-metric excitation measurement, cells expressing FUGW-PercevalHR were excited at 458 nm and 488 nm, and emission signal was collected at 500-550 nm.

GW1-pHRed, a genetically encoded pH sensor, was transiently transfected into HEK293 cells or HCASMCs. FUGW-pHRed was transfected into the cells via a 3rd generation lentivirus based system. Cells expressing FUGW-pHRed was excited at 458 nm and emission signal over 575 nm was collected. For ratiometric measurement, FUGW-pHRed was excited at 458 or 561 nm, and emission signal was collected at over 575 nm or 575-630 nm respectively.

With the cells co-transfected with FUGW-PercevalHR and FUGW-pHRed, FUGW-PercevalHR were excited at 488 nm, emission signal was collected at 500-550 nm, FUGW-pHRed were stimulated at 458 or 561 nm, emission signal was collected at over 575 nm or 575-630 nm respectively.

2.9.2 Ca²⁺ measurement

HCASMCs were plated into 35 mm glass-bottom dishes (Greiner bio-one, Material no. 627861) at a density of 1.0×10^5 - 1.25×10^5 in 2 ml cell culture medium and placed in the incubator overnight. On the following day, cells were washed twice with 2 ml PBS and incubated with 5 μ M Fluo-4 AM or Fura-Red AM in bicarbonate buffered physiological saline solution (PSS) containing [mM]: 120 NaCl, 5 KCl, 1 MgCl₂, 2 CaCl₂, 0.42 Na₂HPO₄, 0.44 NaH₂PO₄, 24 NaHCO₃, 10 Glucose for 20 minutes at 37 °C in the dark. Excess dye was then washed off by PSS and the cells were incubated for another 20 minutes at 37 °C in the dark to achieve de-esterification. Cells were viewed using a Carl Zeiss LSM510 high-speed confocal laser-scanning microscope. Fluo-4 loaded cells were excited with 488 nm light from an argon ion laser and the emitted fluorescence was captured at 500-550 nm. Fura-Red was excited at 488 nm and the emission signal was collected over 585nm.

2.9.3 Membrane potential measurement

HCASMCs were plated into 35 mm glass-bottom dishes a day before experiments, as described above. Next day, cells were washed twice with 2 ml PBS, then incubated with 1 μ M DiBAC4(3) in PSS for 15 minutes in a 37 °C/5%CO₂ incubator. Cells were then used without washing the dye as the continued presence of the dye in the extracellular media was required for this experiment. DiBAC4(3) labelled cells were excited with 488 nm light from an argon ion laser and the emitted fluorescence signal was captured at 500-550 nm.

2.9.4 Mitochondrial localization and mitochondrial membrane potential measurements

HCASMCs were plated into 35 mm glass-bottom dishes. To visualize mitochondria, cells were washed with 2 ml PBS twice, then incubated in PBS containing 500 nM MitoTracker for 20 mins in a 37 °C/5%CO₂ incubator. The cells were then washed twice with calcium/magnesium containing PBS. The dye was excited at 561 nm, and the emission signal over 575 nm was collected.

In order to measure the change in ψ_m , cells were washed with bicarbonate buffered PSS twice, and then incubated with 10 $\mu\text{g/ml}$ rhodamine123 in PSS for 15 minutes in a 37 $^{\circ}\text{C}/5\%\text{CO}_2$ incubator. After incubation cells were washed with PSS twice. The dye was excited at 514 nm, and emission was collected at 520-555 nm.

2.10 Total Internal Reflection Fluorescence (TIRF) Microscopy

HCASMCs transduced with FUGW-PercevalHR, Lyn-FUGW-PercevalHR, or FUGW-pHRed were seeded into 35 mm glass-bottom dishes in 2 ml cell culture medium. Cells were then incubated in the 37 $^{\circ}\text{C}/5\%\text{CO}_2$ incubator overnight to allow attachment. Cells expressing FUGW-PercevalHR or Lyn-FUGW-PercevalHR were excited with 488 nm laser, and emission signal was collected by a 525/50 band pass filter. Cells expressing FUGW-pHRed were excited at 561nm, and emission signal was collected by a 630/95 band pass filter. All images were taken using a 100x oil immersion objective lens.

2.11 Bacterial transformation, growth and stock

2.11.1 Preparation of ampicillin stock

Stock of 100 mg/ml ampicillin (Sigma, Cat no. A9518) in MQ water was filter sterilized through a 0.22 μm filter (Merck, Cat no. SLGP033RS) and aliquoted into 1.5 ml centrifuge tubes and stored at -20 $^{\circ}\text{C}$.

2.11.2 Preparation of LB agar plates

LB agar (MERCK, Cat no. 1.10283.0500) in MQ water (w/v 3.7%) was autoclaved and then cooled at room temperature to approximately hand warm. Ampicillin was added to sterilized warm LB agar at a final concentration of 100 $\mu\text{g/ml}$. After mixing with ampicillin, agar was immediately dispensed into 10 cm Petri dishes (Sarstedt, Cat no. 82.1473) and allowed to set at room temperature in a hood. The dishes were used when the agar was set, and spare plates were sealed with parafilm (Bemis, Supplier no. PM-992) and kept at 4 $^{\circ}\text{C}$ for no longer than 4 weeks.

LB agar
1% (w/v) tryptone
0.5% (w/v) yeast extract
1% (w/v) NaCl
1.5% (w/v) Agar

2.11.3 Amplification of competent *E.coli* cell

On day 1, One-shot[®] Top10 chemically competent *E.coli* cells (Invitrogen, Cat no. C4040-10) was streaked onto LB agar plate without antibiotics. Cells were placed in an incubator at 37 °C overnight. On day 2, a single colony was picked and grown in 100 ml antibiotic free LB broth (MERCK, Cat no. 1.10285.0500) overnight in a 37 °C incubator. On day 3, 2.5 ml of the culture was diluted into 250 ml antibiotic free LB broth and placed in a 37 °C incubator with agitation at 250 rpm for about 2 hours, from this point optical density (O.D.) at 600 nm was measured until it reached a value between 0.6-0.8. Culture was aliquoted into 50 ml Falcon tubes and centrifuged at 5000 *g* at 4 °C for 5 minutes, and each pelleted bacteria were re-suspended in 20 ml ice-cold filter sterilized TFB1 buffer, followed by further 5 minutes incubation on ice. The cells were then centrifuged again at the same condition for another 5 minutes and each cell pellet was re-suspended in 2 ml ice-cold TFB2. The cells were incubated in ice-cold filter-sterilized TFB2 on crushed ice for 30 minutes before being aliquoted into autoclaved sterile pre-chilled tubes.

TFB1 (pH 5.8)	TFB2 (pH 6.5)
RbCl 100 mM	MOPS 10 mM
KOAc 30 mM	CaCl ₂ 2H ₂ O 75 mM
CaCl ₂ 2H ₂ O 10 mM	RbCl 10 mM
MnCl ₂ 4H ₂ O 50 mM	Glycerol 15% (v/v)
Glycerol 15% (v/v)	

2.11.4 Transformation

One-shot[®] Top10 chemically competent *E.coli* cells or Stellar[™] competent cells (Clontech, Cat no. 636767) were used for the expression of plasmid DNA. Competent cells were thawed on crushed ice, and 50 µl was used to incubate with plasmid DNA on crushed ice for 20 minutes before being heat shocked at 42 °C in a water bath (Grant) for 45 seconds. The cells were put back immediately on ice for about 4 minutes after heat shock. After being chilled, 250 µl of SOC medium was added and mixed with the cells, and the cells were agitated at 240 rpm for 1 hour at 37 °C on the shaker (New Brunswick Scientific, Innova[™] 4000). 50 µl and 100 µl of transformation mixture were then spread onto LB agar plates, respectively, and incubated overnight in a humidified incubator at 37 °C. On the following day, single colonies were picked from the agar plates and inoculated into 5 ml LB broth with required antibiotics as the starter culture. The starter was cultured and agitated at 240 rpm overnight at 37 °C.

SOC medium	LB broth
2% vegetable peptone	1% (w/v) tryptone
0.5% yeast extract	0.5% (w/v) yeast extract
10 mM NaCl	1% (w/v) NaCl
2.5 mM KCl	
10 mM MgCl ₂	
10 mM MgSO ₄	
20 mM glucose	

2.11.5 Glycerol stocks

1 ml of overnight bacterial culture suspension was added to 667 µl 50% glycerol (w/v) in a cryovial, and mixed by gentle pipetting. All the cryovials were frozen and stored at -80 °C.

2.11.6 Plasmid preparation

Many methods have been developed to purify plasmid DNA from competent cells, and these methods invariably involve three steps: growth of the bacterial culture, harvest and lysis of the bacteria, and purification of plasmid DNA. QIAprep Spin Miniprep Kit (Qiagen, Cat no. 27104), Plasmid Midi Kit (Qiagen, Cat no. 12143) and HiSpeed Plasmid Maxi Kit (Qiagen, Cat no. 12662) were used in this project to extract plasmid DNA from competent cells according to manufacturer's protocols.

2.12 Cloning, PCR and DNA amplification

2.12.1 Preparation of the vector

A lentiviral based mammalian expression vector was prepared from FUGW-PercevalHR to which the gene of interest was inserted. FUGW-PercevalHR was firstly digested with XbaI (New England Biolabs, Cat no. R0145s) and EcoRI-HFTM (New England Biolabs, Cat no. R3101s) enzymes in a 37 °C water bath for a minimum period of 1 hour as instructed by the manufacturer. After the parental plasmids had been fully digested, reaction mix was run on a 1.0% (w/v) agarose gel to separate the vector from the insert. The vector was excised and purified using a QIAQuick Gel Extraction kit (Qiagen, Cat no. 28704) following the manufacturer's protocol. After the concentration of the vector was determined by NanoDrop ND-1000, it was stored at -20 °C.

2.12.2 Design of the primer

Some of the commonly used primers for sequence verification are suggested by the addgene website (<https://www.addgene.org/>) such as hUBCpro-F and WPRE-R. Primers for PCR cloning were designed using the Invitrogen OligoPerfectTM Designer. After the primers have been determined, we tended to create a 3' ending with either guanine or cytosine by editing the sequence manually, in order to help the primer anchor to the template. In order to make our primers more efficient, sometimes a 5' XbaI restriction site was added ahead of the forward primers and a 5'

EcoRI restriction site was added to the reverse primer respectively as suggested by New England Biolabs. In some conditions, further guanine and/or cytosine nucleosides were added to the 5' end of the restriction site to have a better digestion of the sequence.

2.12.3 Sub-cloning by PCR

The open reading frame (ORF) containing PercevalHR was amplified from FUGW-PercevalHR using the primers containing a membrane targeting sequence derived from Lyn kinase (detail in **Table 2.4**). With the purpose of achieving high fidelity proof reading, KOD Hot Start DNA Polymerase (Novagen, Cat no. 71086) was used with the method provided by the manufacture.

After the amplification procedure, the PCR product was run on a 1.0% (w/v) agarose gel to separate the amplified insert containing the membrane targeting Lyn sequence. The insert was then cut under UV and purified using a Qiagen QIAQuick Gel Extraction kit according to the protocol described by the manufacturer. The concentration of the insert was determined by NanoDrop ND-1000. Purified digested vector and insert were then mixed at the ratio of 1:1, 1:3, 1:5 and 1:7 in microcentrifuge tubes and ligated using T4 DNA ligase (New England Biolabs, Cat no. M0202) at room temperature overnight. The ligation protocol was carried out as described by the manufacture (**Table 2.8**), and all molar ratios were calculated using NEBioCalculator.

PCR reaction mix

10x Buffer for KOD Hot Start DNA Polymerase	5 μ l
25 mM MgSO ₄	3 μ l
dNTPs (2 mM each)	5 μ l
PCR Grade Water	32.5 μ l
Sense(5') Primer (10 μ M)	1.5 μ l
Anti-Sense (3') Primer (10 μ M)	1.5 μ l
Template DNA (FUGW-PercevalHR)	0.5 μ l
KOD Hot Start NAN Polymerase (1 U/ μ l)	1.0 μ l
Total reaction volume	50 μ l

Reaction setup

Step	Temperature and time
1. Polymerase activation	95 °C for 2 min
2. Denature	95 °C for 20 s
3. Annealing	48 °C for 10 s
4. Extension	70 °C for 4 s
Repeat steps 2-4	30 cycles
5. Final elongation	70 °C 6 min
6. Hold	4 °C

Table 2.8: Ligation protocol with T4 DNA ligase

Component	20 µl reaction
10xT4	2 µl
Vector DNA	0.020 pmol
Insert DNA	0.060 pmol
Nuclease-free water	to 20 µl
T4 DNA Ligase	1 µl

This example table shows a ligation using a molar ratio of 1:3 (vector to insert). Ligation at other vector to insert ratios could be calculated in the same way by taking this table as a reference.

2.12.4 Verification of constructed plasmids

Plasmids produced from cloning were verified by running an agarose gel after cutting by appropriate restriction enzymes followed by DNA sequencing performed by GATC Biotech (European Genome and Diagnostics Centre, Germany).

2.13 Statistical analysis

All values are expressed as a mean \pm standard error of mean (SEM) as represented through error bars on graphs. N indicates number of cells, wells or plates unless otherwise stated. Statistical analyses were performed using SPSS software package, version 20.0 (IBM). Statistical significance was evaluated with a Student's *t*-test (paired and un-paired) or by using ANOVA with Tukey's test for post hoc analysis. Results were deemed significant when p-value was smaller than 0.05. Significance in the plots is represented as: * equivalent to $P < 0.05$, ** equivalent to $P < 0.01$ and *** equivalent to $P < 0.001$.

Chapter 3

**Effect of Hypoxia and Metabolic
Inhibitors on Cellular Metabolism
of Single HCASMCs**

3.1 Introduction

Metabolic vasodilation is the widening of arteries caused by increased oxygen consumption of surrounding tissues. It is an important phenomenon in the heart, as if coronary blood flow is insufficient to meet the metabolic demands it will lead to pathologies including anginal pain and a pre-disposition to cardiac arrhythmia. It is not surprising, therefore, that there are several pathways for coronary artery metabolic vasodilation to ensure adequate cardiac perfusion. This includes multiple triggering factors that can induce coronary artery dilation including hypoxia, change in pH and various metabolites. However, it has proven difficult to elucidate the exact mechanisms by which coronary arteries dilate [2].

In terms of vascular energy status, ATP concentration and ATP:ADP ratio are important indicators. ATP not only serves as the main energy currency, but also links metabolic changes to electrical activity, calcium signaling and contractility of VSMCs [33, 34, 43]. K_{ATP} channels of VSMCs are reported to be sensitive to intracellular metabolic change and therefore may play an important role in hypoxic vasodilation [43, 101]. One major unresolved issue here is whether relatively mild hypoxia (i.e. $PO_2 \sim 30$ mmHg) known to cause vasodilation can indeed change intracellular nucleotide levels sufficiently to activate K_{ATP} channels. The lack of methods to tackle this fundamental question has prevented investigations in this area.

Recent development and improvement of bioluminescent and fluorescent tools have made it finally possible to address this question directly in live cells. Luciferase-based bioluminescence assays allow dynamic measurements of ATP content in isolated cells [182]. Recombinant luciferase can be introduced into cells by transient transfection, allowing measurement of ATP levels in response to hypoxia. Luciferase can be targeted to plasma membrane or mitochondria, giving the potential to fully define the metabolic effects of hypoxia in subcellular ATP compartments [182, 184]. Recently, FRET based probes have been developed for measurement of ATP and ATP:ADP ratio [185-187, 194]. These probes have unique advantages over luciferase in that they do not consume cellular ATP and are less sensitive to other factors such as H^+ . Mitochondrial membrane potential can be measured by

cell-permeant, fluorescent lipophilic cationic dyes such as rhodamine123, tetramethylrhodamine methyl (TMRM) and ethyl (TMRE) [195]. Thus, cellular and subcellular energy status of single cells as well as effect of hypoxia and metabolic modulators can be now investigated.

In this chapter, cellular nucleotide levels were measured using bioluminescent and fluorescent probes (Perceval/PercevalHR). As well as manipulating O₂ tension in a custom made micro-imaging chamber, metabolic inhibitors were used: glycolysis was inhibited with 2-DG, mitochondrial respiratory chain with rotenone, antimycin A, and oligomycin B, and electron transfer was uncoupled from ATP generation using protonophores such as CCCP. Combined application of these pharmacological agents allowed further dissection of cellular metabolism of HCASMCs. The goal of this chapter was to determine the relative importance of mitochondrial ATP and glycolytic ATP in HCASMCs, and whether hypoxia has any effects on cellular metabolism.

Perceval is a fluorescent biosensor of adenylate nucleotides [185]. It is constructed by integrating a yellow cpFP, circularly permuted monomeric Venus (cpmVenus), into the T loop of ATP binding bacterial protein GlnK1. ATP and ADP bind to the same site of Perceval with very high affinity, so the binding site is always occupied at physiological ATP and ADP concentrations. The competition between ATP and ADP makes the sensor a reporter of intracellular ATP:ADP ratio [185], although at least one paper reported that signal is only dependent on ATP, not ADP [196]. PercevalHR is an improved fluorescent biosensor derived from Perceval by performing a structure-guided protein engineering strategy and is tuned to sense the ATP:ADP ratios expected in healthy mammalian cells [186]. The principle of PercevalHR sensing cellular ATP:ADP ratio is illustrated in **Figure 3.1**. One potential issue in using Perceval/PercevalHR, as in the case of other green fluorescent protein derived biosensors, is its sensitivity to pH where apparent change in signal may not originate from change in ATP:ADP ratio but from pH. Ideally, monitoring of pH should be carried out simultaneously with Perceval/PercevalHR fluorescence recording, but if not, pH should be measured separately using identical

conditions. A genetically encoded pH sensor, pHRed, made by mutagenesis of the red fluorescent protein mKeima is a ratiometric biosensor and used in this study [197].

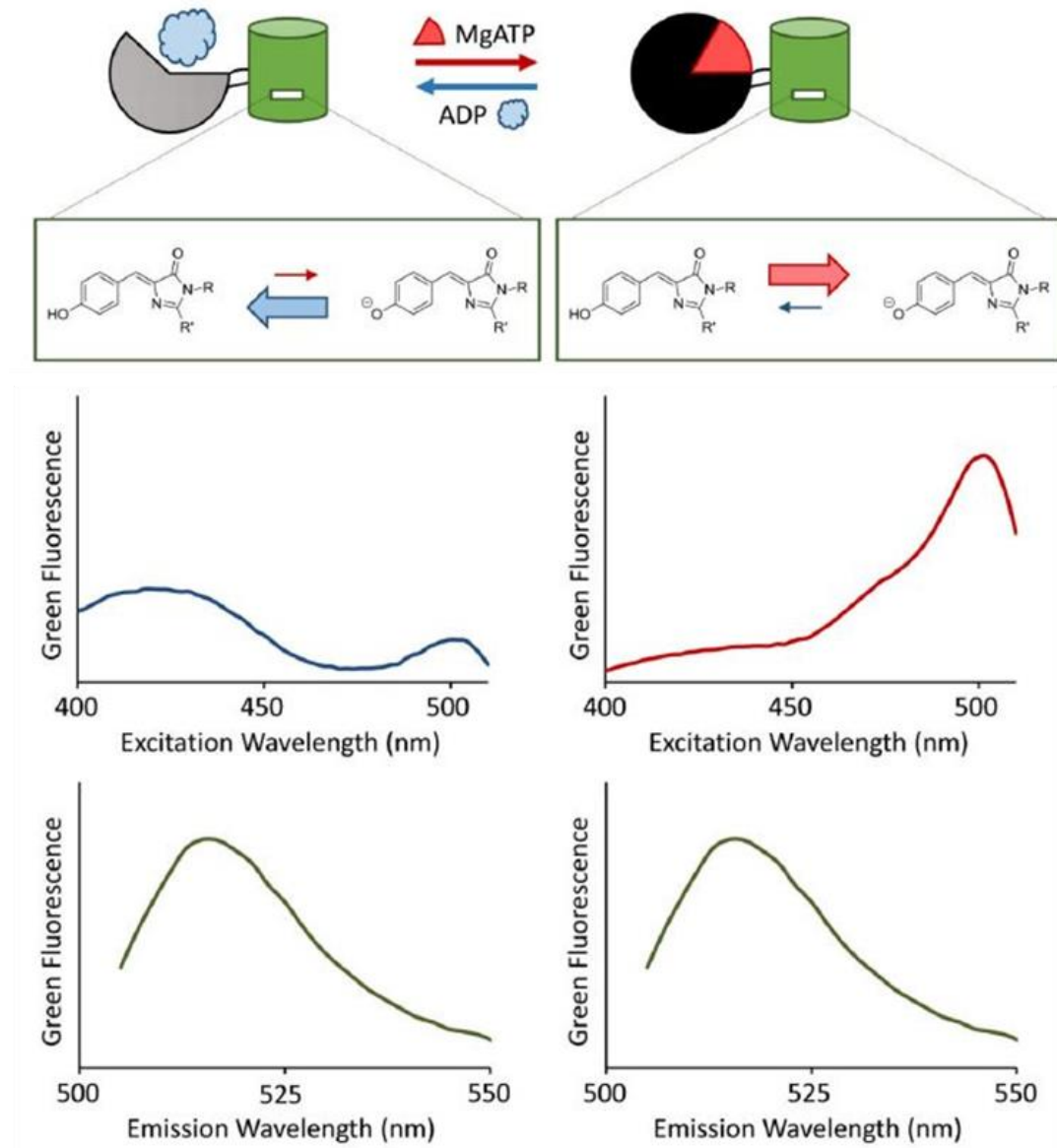


Figure 3.1: PercevalHR detects ATP:ADP ratio. Binding of ADP to GlnK domain (grey partial circle) of PercevalHR shifts the Venus (Green) chromophore charge state equilibrium (box), favoring the neutral protonated state. ATP binding, on the other hand, shifts protein conformation to the anionic deprotonated state. The emission spectrum is not significantly different between the two states. (Reproduced from Tantama et al., 2014 [187])

3.2 Aims

The overall aim of this chapter was to evaluate the effect of hypoxia and metabolic inhibitors on HCASMC cellular energy status. First, OCR and ECAR were determined by Seahorse technology to characterize oxidative and glycolytic contribution to cellular energy status. Second, intracellular ATP level was detected in HCASMC populations by bioluminescence assay. Third, ATP:ADP ratio was measured in single HCASMCs by genetically encoded biosensor Perceval/PercevalHR. Finally, mitochondrial membrane potential was examined by rhodamine123.

3.3 Methods and preliminary results

3.3.1 Optimization of the cell transfection

Initial optimization of the transfection was carried out using an established cell line, HEK293 cells. For the best results, cell density should be ~70% confluent at the point of transfection. Thus, cell seeding at $0.8-1.0 \times 10^6$ cells per well of 6-well plate was optimal for transfection after 24 hours (**Figure 3.2**). In preliminary studies, 1 μg , 2 μg , 4 μg pEGFP-N1, Perceval, and pHRed were transiently transfected to HEK293 cells using LP2000 according manufacturer's protocol. Transfection efficiency of pEGFP-N1, Perceval, and pHRed was checked after 24 and 48 hours of transfection (data not shown). pEGFP-N1 transfection of HEK293 cells showed good transfection efficiency both after 24 hours and 48 hours. Although some cells were transfected with Perceval after 24 hours, a larger proportion of cells were positive after 48 hours. However, very few cells were transfected with pHRed after 24 hours, and there was little improvement after 48 hours. Since our aim was to co-transfect the cells with Perceval and pHRed, it was necessary to improve the transfection efficiency of pHRed. Transfection of pHRed with five different transfection reagents showed that Fugene 6 gave the best efficiency after 24 hours (**Figure 3.3 and Table 3.1**). Fugene 6 was selected as the transfection reagent, and transfection with pEGFP-N1, Perceval, and pHRed was optimized with different plasmid concentrations and transfection times. 4 μg pEGFP-N1 gave optimal transfection efficiency after 24 hours (**Figure**

3.4). 48 hour transfection using 4 μg Perceval gave the best efficiency (**Figure 3.5**). 4 μg pHRed gave the best efficiency, and a longer time increased the expression of pHRed (**Figure 3.6**). For subsequent experiments, Fugene 6 was used for the co-transfection of Perceval and pHRed (**Figure 3.7**).

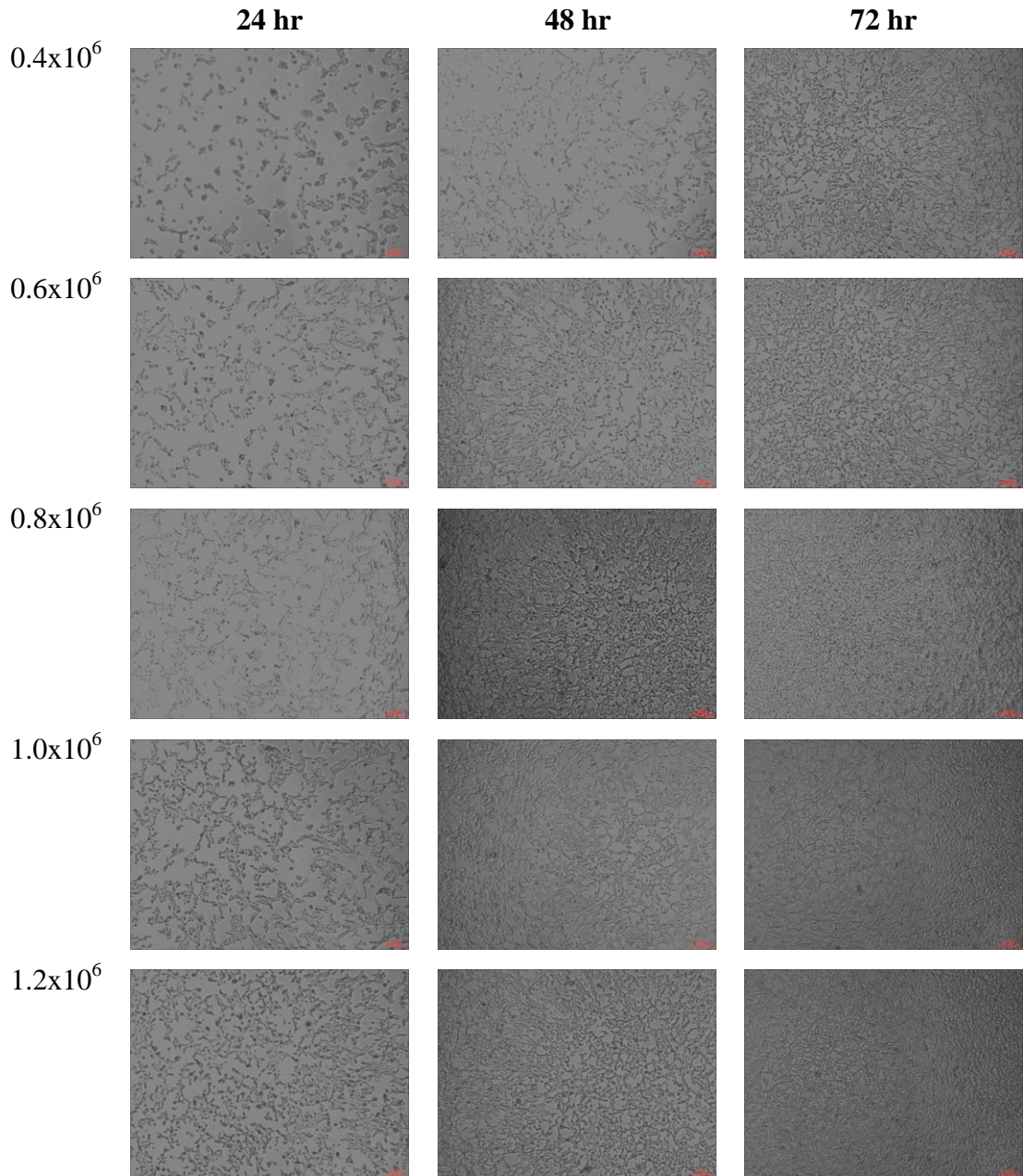


Figure 3.2: Cell number optimization of HEK293 cells for transfection. Seeding density of $0.8\text{-}1.0 \times 10^6$ of HEK293 cells was optimal for transfection after 24 hours.

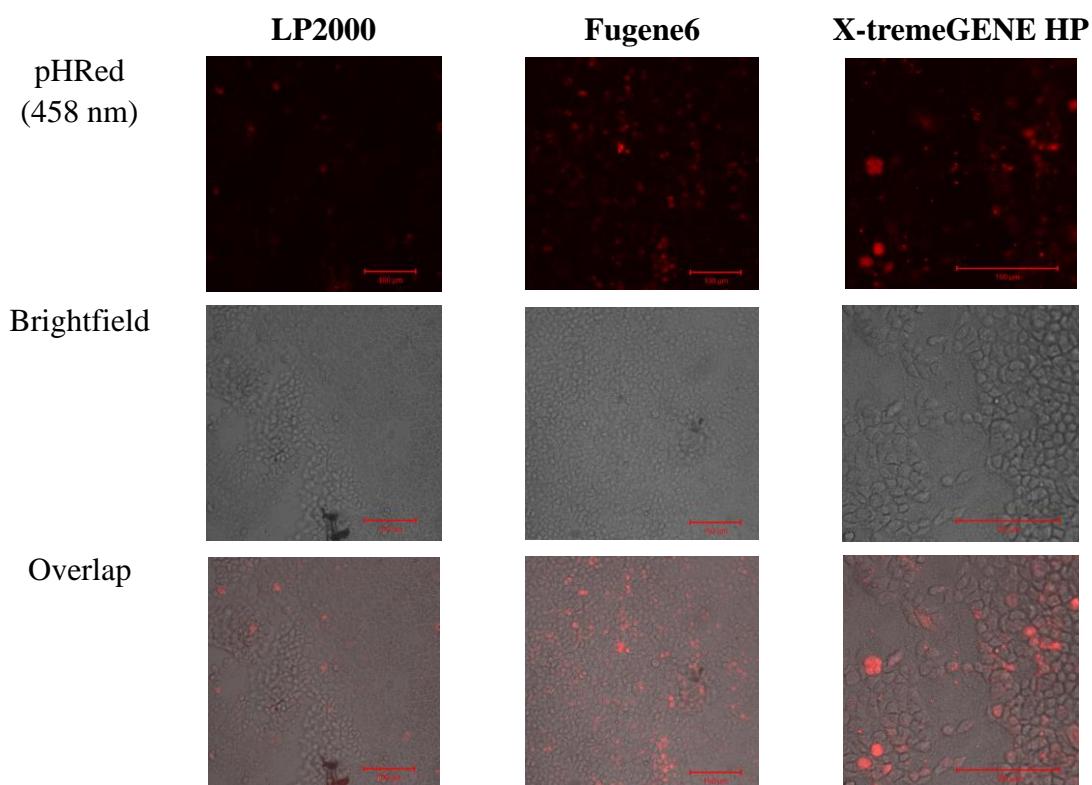


Figure 3.3: Optimization of pHRed transfection using different reagents. 24 hours transfection of HEK293 cells with pHRed using five different reagents showed that Fugene 6 gave the best transfection efficiency. Results from three reagents are shown here with a larger magnification for X-tremeGENE HP (right panels). Scale bar is 100 μ m.

Table 3.1: Summary of HEK293 cell transfection efficiency of pHRed

Transfection Reagent	Transfection Efficiency
Lipofectamine 2000	~ 1-5%
FuGENE 6	~ 15-20%
FuGENE 6 HD	~1-3%
X-tremeGENE 9	0%
X-tremeGENE HP	~5-10%

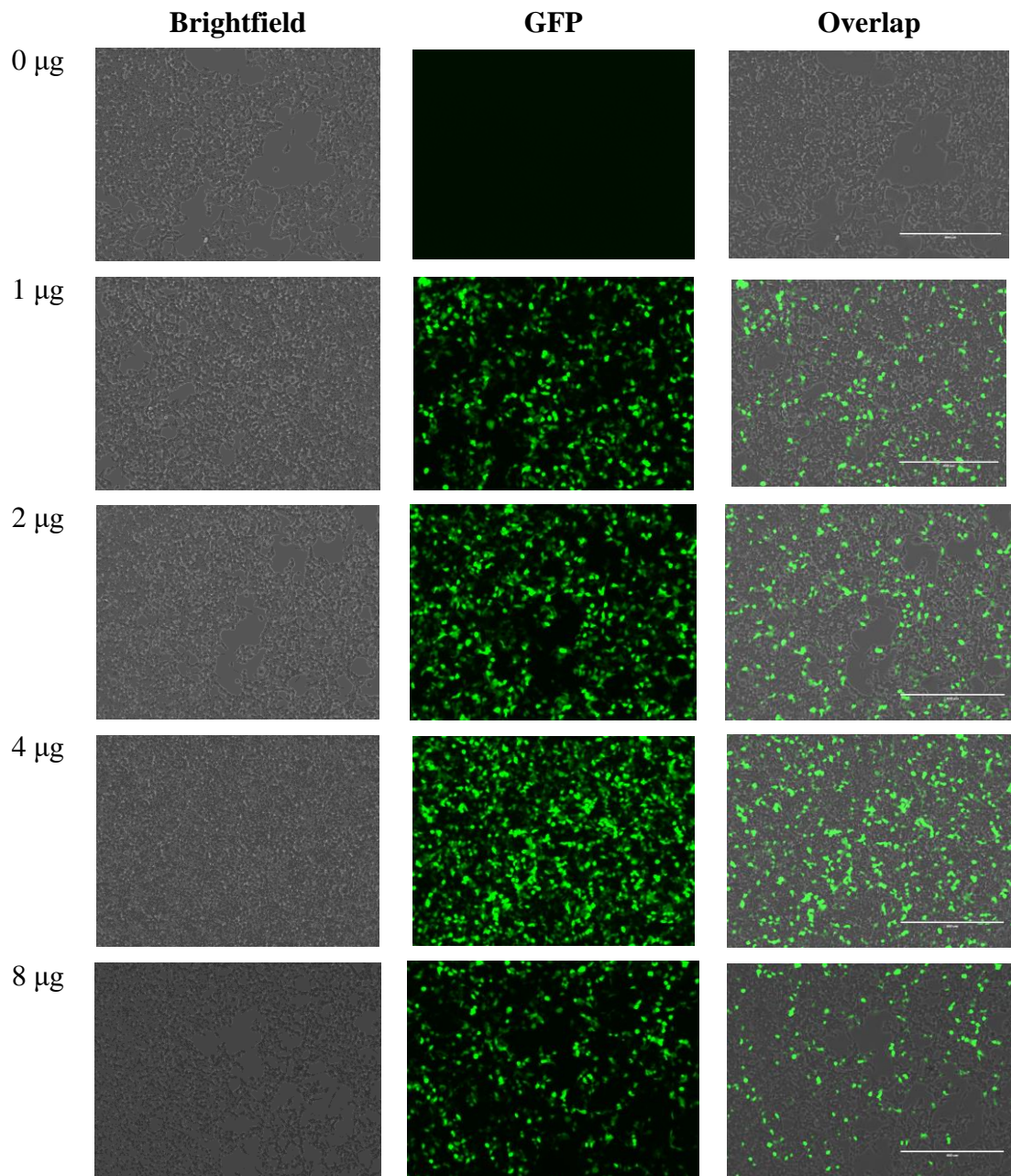


Figure 3.4: HEK293 transfection with pEGFP-N1 after 24 hrs. HEK293 cell transfection with pEGFP-N1 showed that 4 μg pEGFP-N1 gave optimal transfection efficiency after 24 hours. Scale bar is 400 μm .

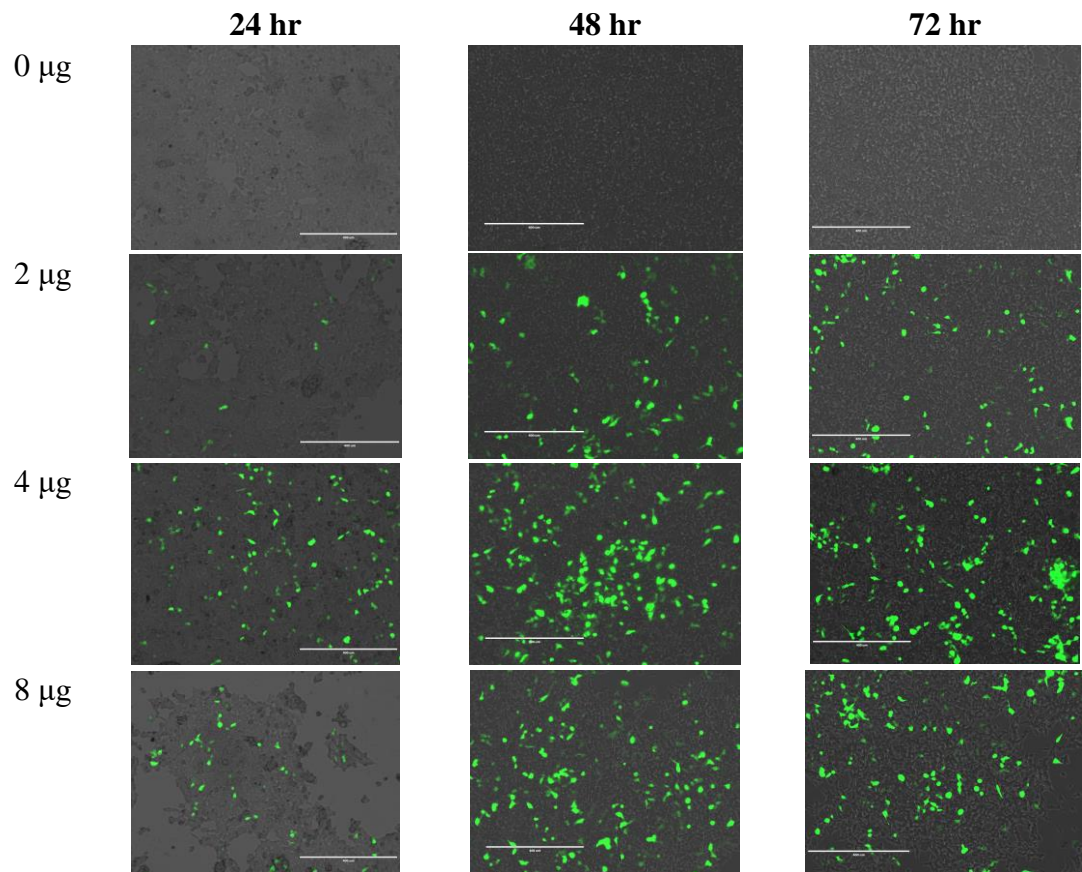


Figure 3.5: Optimization of Perceval transfection. Time course of Perceval transfection with different amount of plasmid showed that 48 hour transfection using 4 μg Perceval gave the best efficiency. Scale bar is 400 μm .

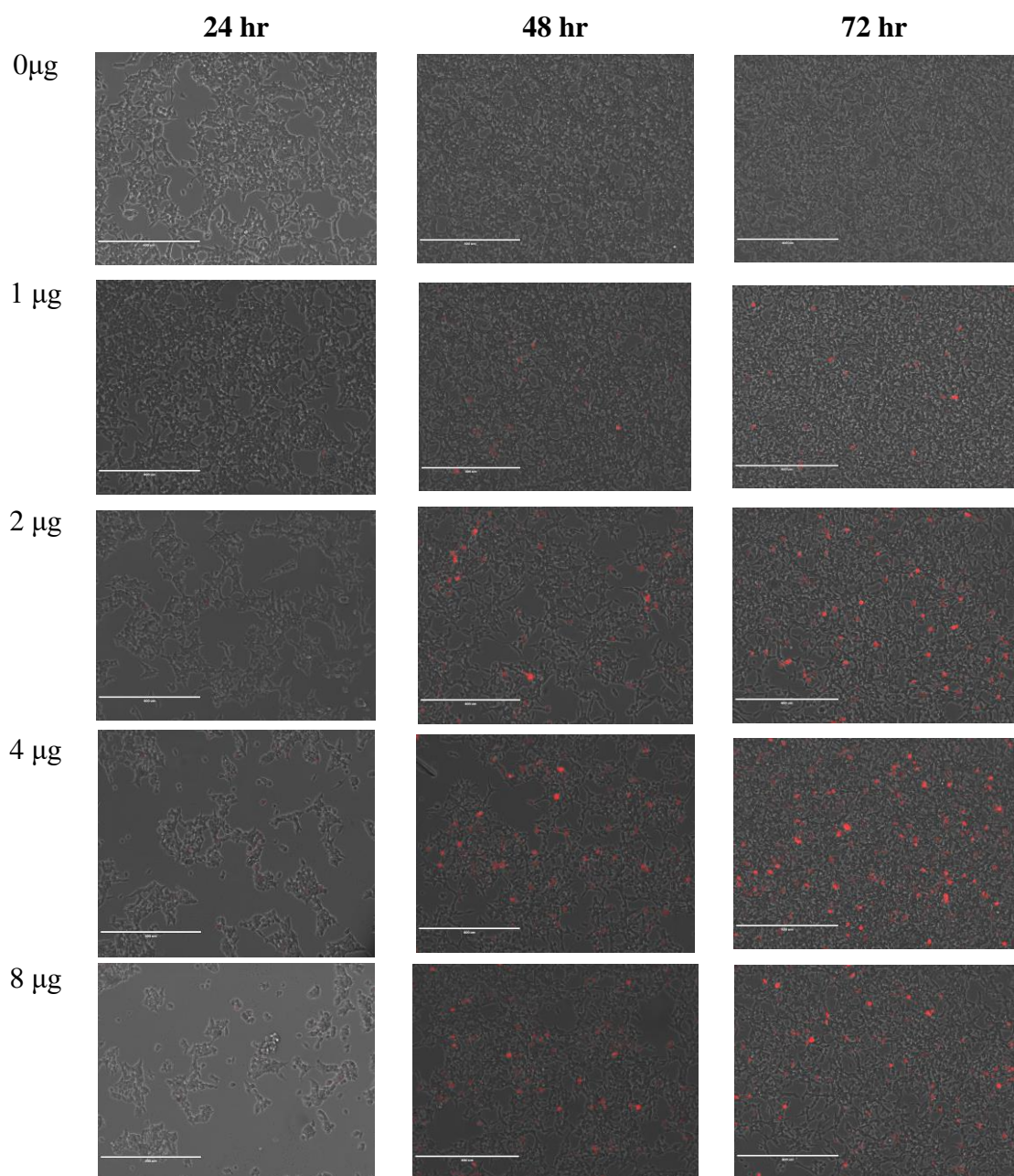


Figure 3.6: Optimization of pHRed transfection. Using 4 μg gave the best efficiency for pHRed transfection with continued increase in expression during the course of observation. Scale bar is 400 μm .

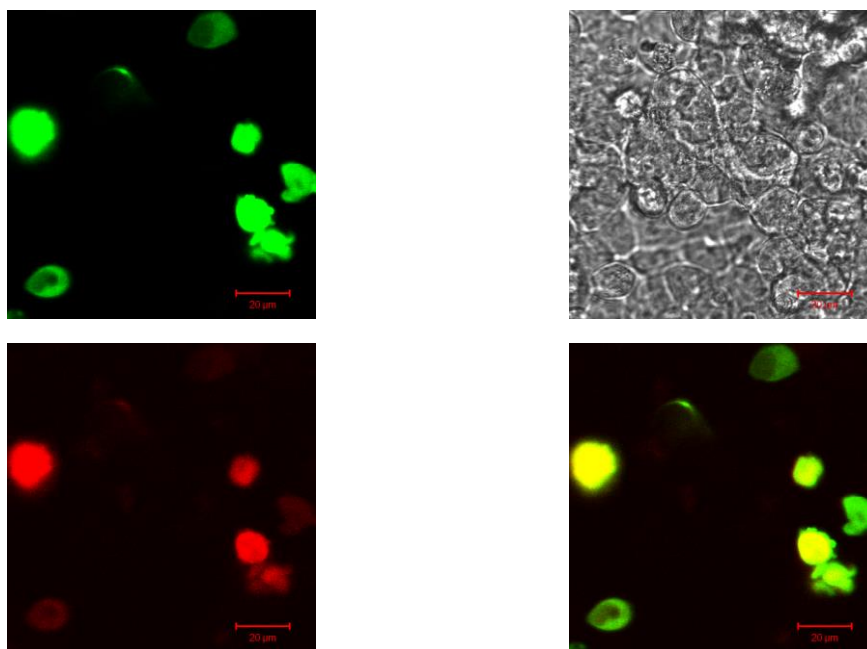


Figure 3.7: Co-transfection of Perceval and pHRed in HEK293 cells.

Co-transfection of HEK293 cells with Perceval (green) and pHRed (red) using Fugene 6. Yellow cells (bottom right) indicate co-expression. Scale bar is 20 μm .

3.3.2 Transfection of HCASMCs with Perceval/PercevalHR and/or pHRed

Transfection of HEK293 cells proved to be successful using Fugene 6. Next, we transfected HCASMCs with Perceval/PercevalHR and pHRed. Cell number optimization showed that plating at the density of $1.25\text{-}1.75 \times 10^5$ is optimal for transfection after 24 hours (**Figure 3.8**). In addition to Fugene 6, Promofectin, LT1 and LTX2 can be used successfully for the transfection of HCASMCs (**Figure 3.9, Table 3.2**).

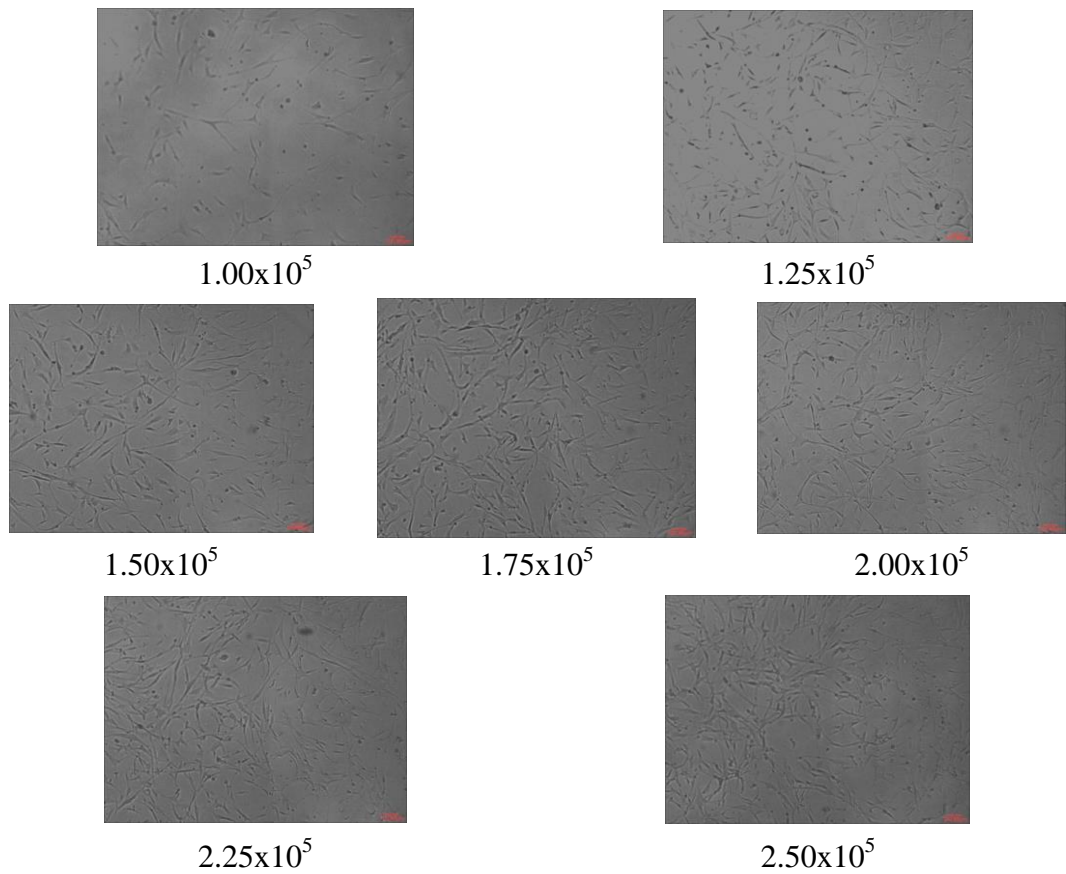


Figure 3.8: Cell number optimization for transfection of HCASMCs. A seeding density about $1.25\text{-}1.75 \times 10^5$ of HCASMCs was optimal for transfection after 24 hours.

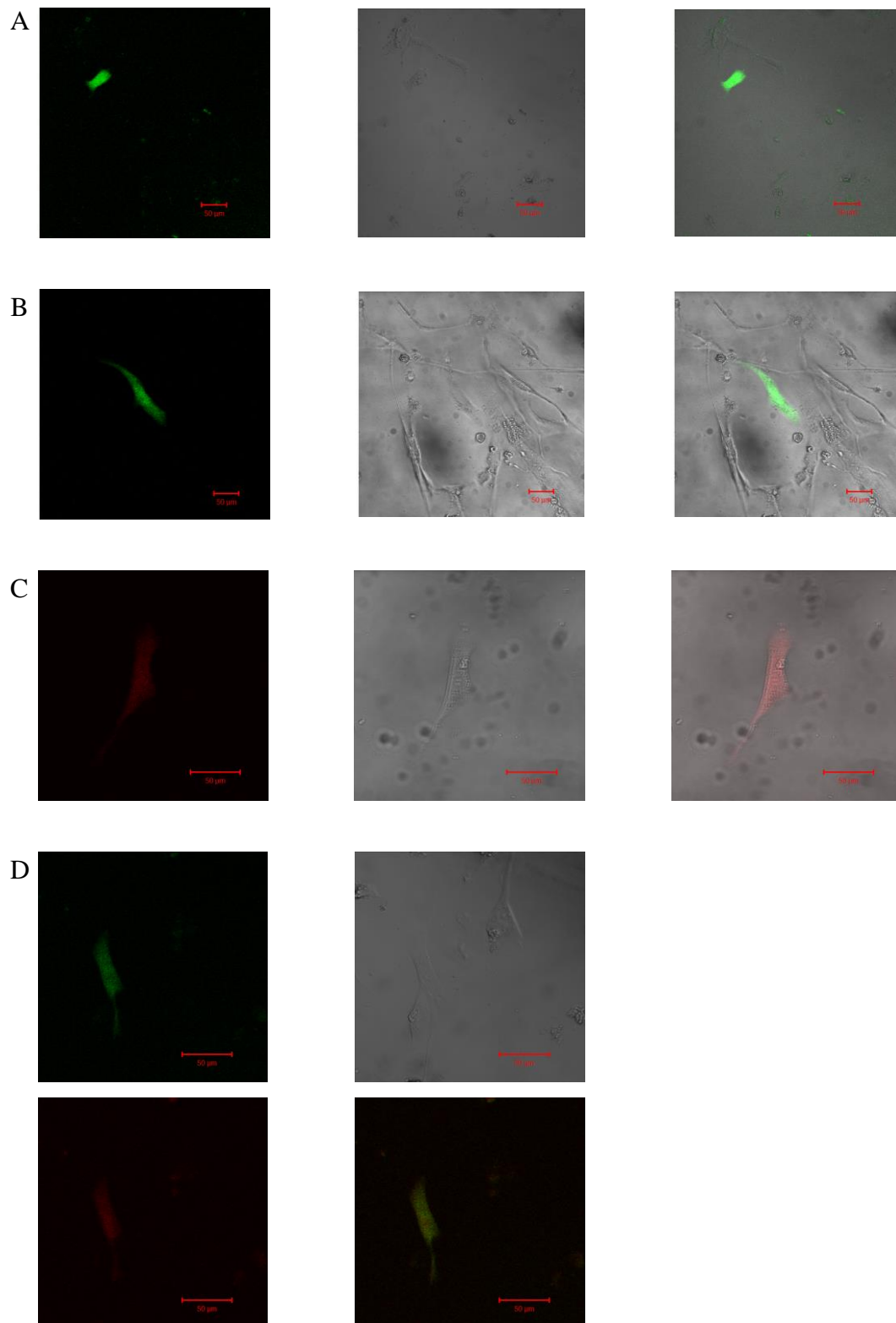


Figure 3.9: Perceval/PercevalHR and pHRed transfection of HCASMCs. (A) HCASMC expressing Perceval (Fugene 6). (B) HCASMC expressing PercevalHR (LTX2). (C) HCASMC expressing pHRed (Fugene 6). (D) HCASMC expressing Perceval and pHRed (Fugene 6). Scale bar is 50 μm .

Table 3.2: Transfection reagents optimized in HCASMCs

	Perceval	PercevalHR	pHRed	Co-transfection
LP2000	✓	✓	-	-
Fugene 6	✓	✓	✓	✓
Promofectin	-	✓	-	-
LT1	-	✓	-	-
LTX2	-	✓	-	-

✓: Reagents used in HCASMC transfection.

3.4 Results

3.4.1 Bioenergetic profile of HCASMCs

3.4.1.1 Determination of the optimal concentrations of FCCP and oligomycin

In Seahorse assay, OCR is a measure of OXPHOS and ECAR is a measure of glycolysis. Both OCR and ECAR can be compartmentalized by a sequential application of OXPHOS inhibitors provided concentrations are carefully chosen [180, 181, 183]. While oligomycin concentration must be high enough to fully inhibit ATP synthase, it is known that a supramaximal dose of oligomycin will continue to increase OCR [183]. This OCR component is therefore ATP synthase independent and could be due to an increased proton leak related oxygen consumption [198]. The stimulation of OCR with FCCP is bell-shaped [180, 183], indicating that FCCP first stimulates and then inhibits OCR in a dose-dependent manner. For this reason, titration of oligomycin and FCCP is necessary, and the results of this experiment are shown in **Figure 3.10 and 3.11**. Oligomycin and FCCP at a concentration of 1.0 μM and 0.75 μM were chosen to study the cellular bioenergetics of HCASMCs.

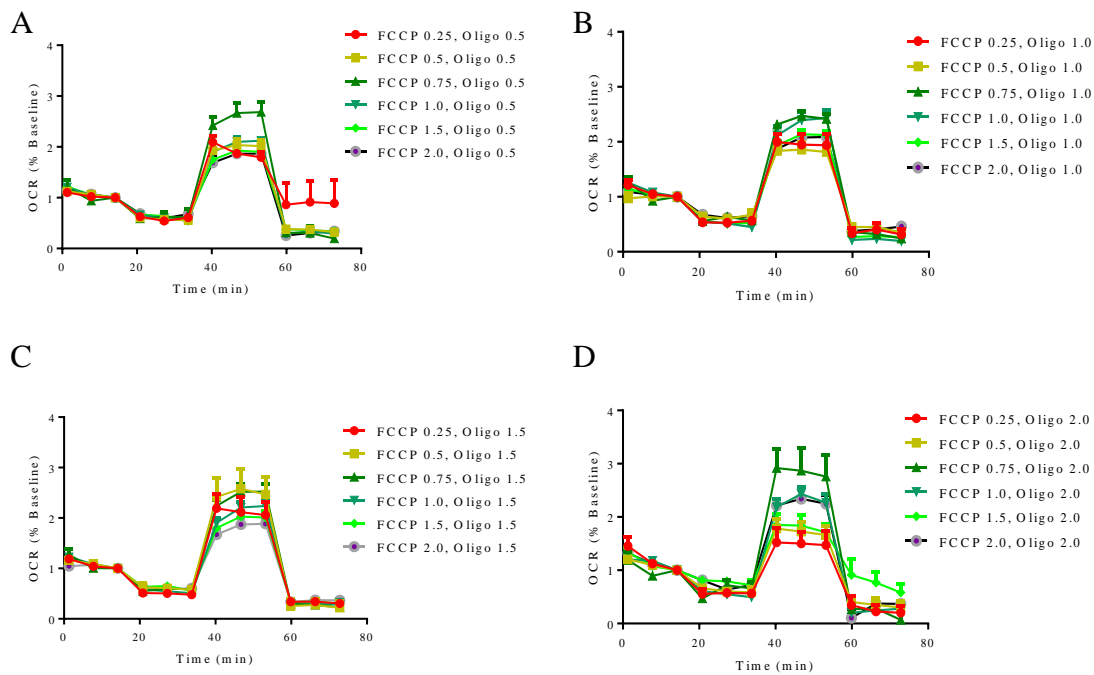


Figure 3.10: Optimization of FCCP and oligomycin concentrations. OCR determined with different FCCP concentrations is plotted for given oligomycin concentration. FCCP shows a bell-shaped concentration response, and a concentration of 0.75 μM is optimal to cause maximal effect at all oligomycin concentrations tested ($n=4$). Metabolic inhibitors were added sequentially as shown in **Figure 2.4** (see **section 2.5.1**).

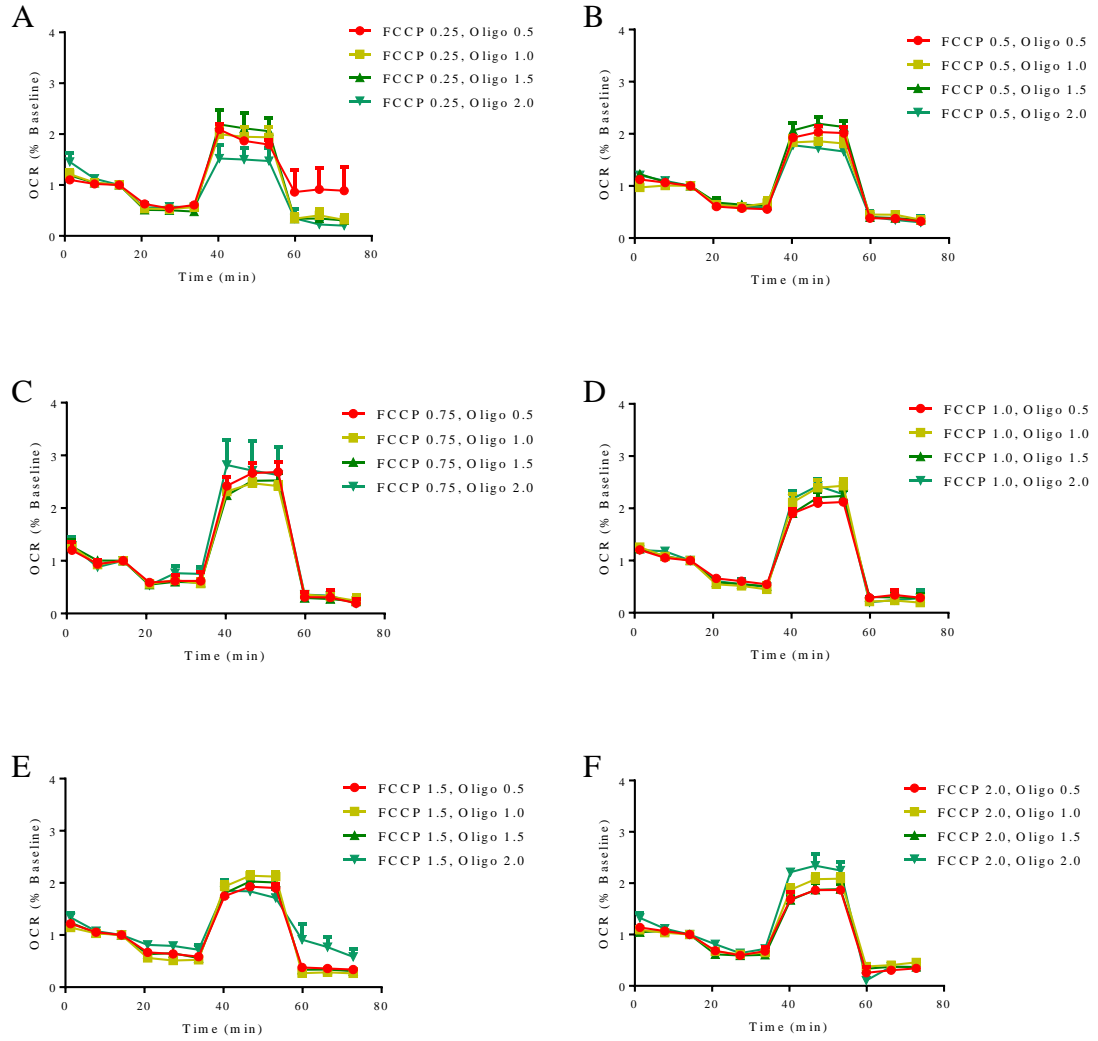


Figure 3.11: Determination of oligomycin concentration. OCR changes at different concentrations of oligomycin plotted while FCCCP concentration is kept constant. At optimal FCCCP concentration (0.75 μM), oligomycin at 0.5, 1.0 and 1.5 μM caused a similar effect. However, increasing oligomycin concentration to 2.0 μM lead to maximal inhibition of OCR initially, followed by a progressive increase in OCR over time. Oligomycin concentration of 1.0 μM was chosen (n=4). Metabolic inhibitors were added sequentially as shown in **Figure 2.4** (see **section 2.5.1**).

3.4.1.2 Microplate based OCR measurement (Mitochondrial stress test)

In a mitochondrial stress test (**Figure 3.12**), basal OCR was 54.69 ± 4.56 pmol/min per 2×10^4 cells (initial cell count) and 5.93 ± 0.43 pmol/min per μg protein respectively (see **Section 2.5.1**). Application of oligomycin reduced OCR to 24.48 ± 3.52 pmol/min per 2×10^4 cells and 2.66 ± 0.36 pmol/min per μg protein, suggesting that ATP synthase-linked O_2 consumption accounts for 55.24% of basal respiration. FCCP brought cell OCR to 130.49 ± 8.75 pmol/min per 2×10^4 cells and 14.20 ± 0.85 pmol/min per μg protein (**Figure 3.12**). This indicates the high mitochondrial reserve capacity that presumably plays a crucial role in response to acute insults. Rotenone plus antimycin decreased OCR to 14.98 ± 3.18 pmol/min per 2×10^4 cells and 1.65 ± 0.34 pmol/min per μg protein. This remaining OCR reflects non-mitochondrial oxygen consumption including substrate oxidation as well as cell surface O_2 consumption [199]. Therefore, basal oxygen consumption of HCASMCs comprises of 72.60% of mitochondrial O_2 consumption and 27.40% of non-mitochondrial O_2 consumption, and in the former 76.09% of O_2 consumption is coupled to ATP synthase and 23.91% is due to proton leak. When normalized internally, HCASMCs have a coupling efficiency of $56.41 \pm 3.34\%$ ($100\% \times [(\text{ATP synthase linked respiration})/\text{basal}]$), $\text{state}_{\text{apparent}} (=4 - (\text{basal-oligo})/(\text{FCCP-oligo}))$ of 3.71 ± 0.01 , $\text{RCR}_{\text{basal}} (= (\text{basal-R/A})/(\text{Oligo-R/A}))$ of 4.31 ± 0.25 , $\text{RCR}_{\text{max}} (= (\text{FCCP-R/A})/(\text{oligo-R/A}))$ of 12.79 ± 1.26 .

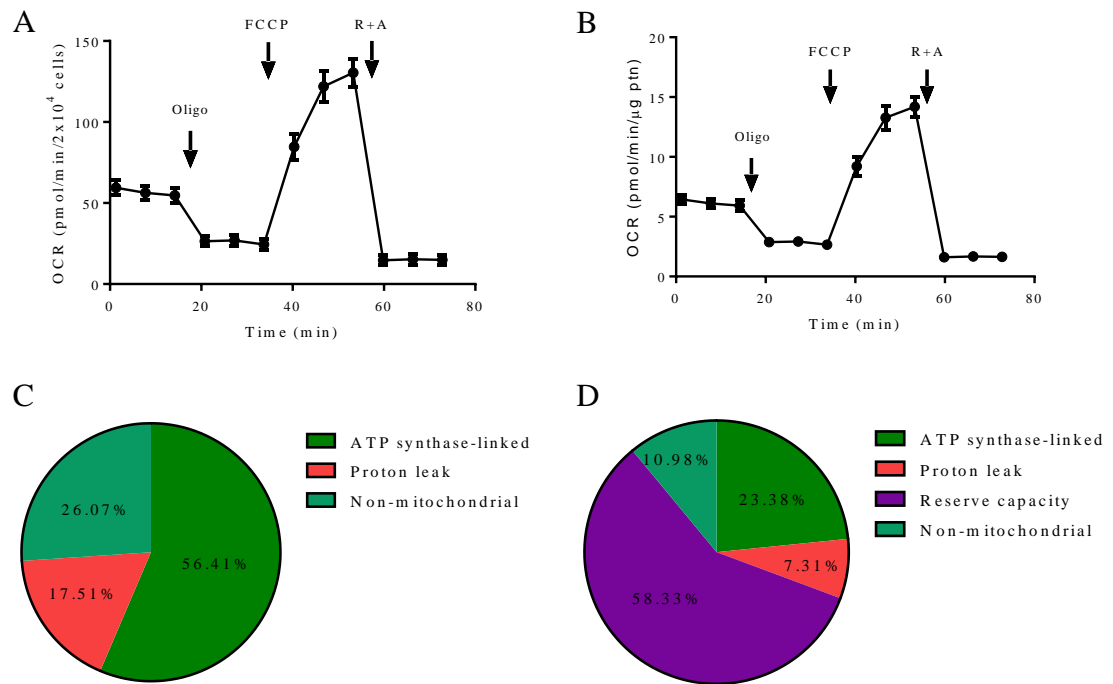


Figure 3.12: Mitochondrial stress test. Indices of mitochondrial function were compartmentalized by a sequential application of pharmacological inhibitors, and the changes in OCR of intact cells in real time (A) was calibrated to μg protein (B). The proportion of ATP synthase-linked O_2 consumption, proton leak related O_2 consumption, non-mitochondrial O_2 consumption, and reserve capacity are quantified in two ways by taking basal OCR (C) or maximal OCR (D) as 100% (n=8).

3.4.1.3 Changes of bioenergetic profile during cell culture

As phenotype of primary cells is known to change during cell culture, the bioenergetic function of HCASMCs at different cell passages was analyzed *in vivo*. **Figure 3.13** shows that HCASMCs rely mainly on mitochondrial ATP generation. With an increase in passage number, HCASMCs showed less sensitivity to oligomycin, increased non-mitochondrial O_2 consumption and less reserve capacity. These are indications of cells switching from a contractile phenotype to a proliferative and migratory phenotype.

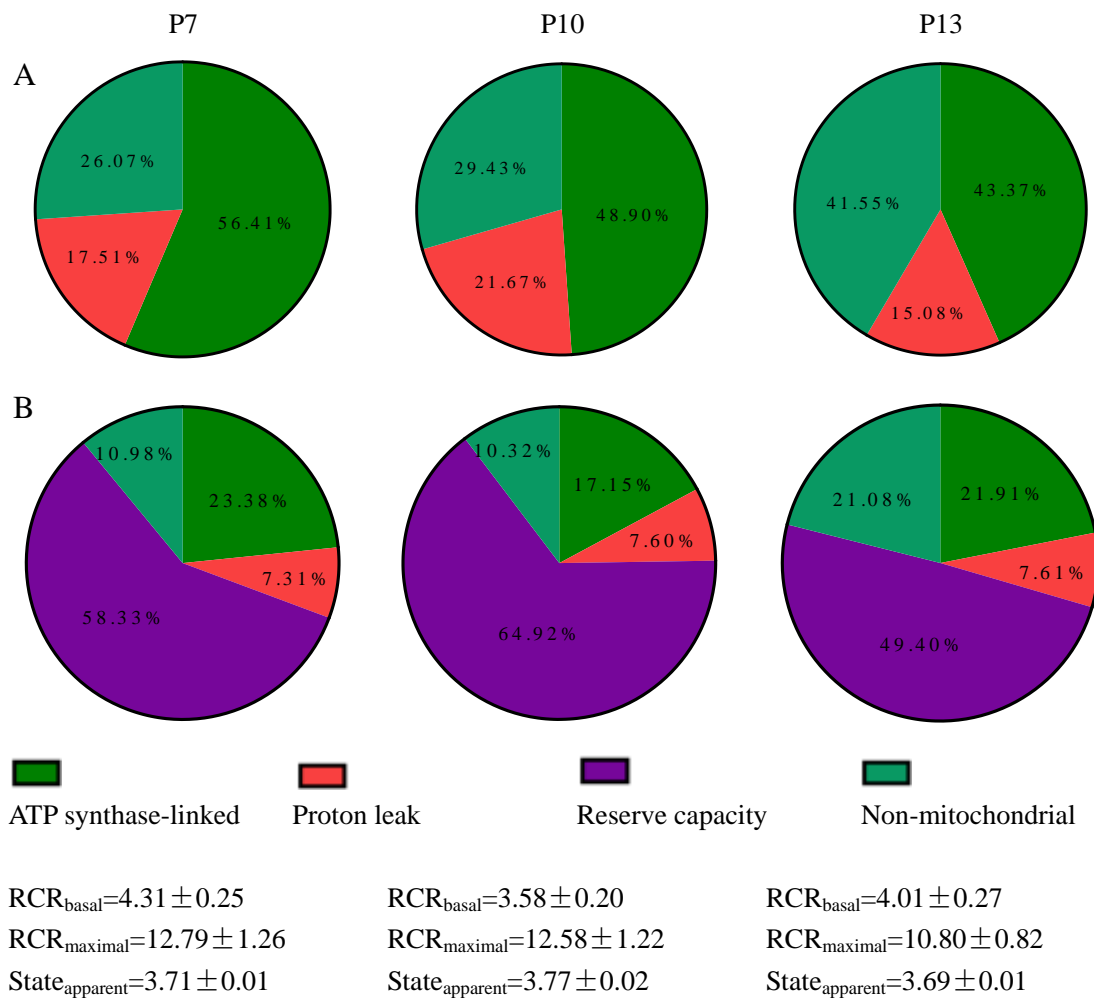


Figure 3.13: Cellular bioenergetics of HCASMCs during culture. (A) The proportion of ATP synthase-linked O₂ consumption, proton leak related O₂ consumption, non-mitochondrial O₂ consumption were quantified when basal OCR is taken as 100%. (B) Above parameters in (A) and reserve capacity were quantified when maximal OCR was taken as 100%. State_{apparent}, as well as respiratory control ratio (RCR) for basal and maximal OCR were also calculated for different passages of HCASMCs (n=8).

3.4.1.4 Microplate based ECAR measurement (Glycolysis stress test)

Basal ECAR in glucose free unbuffered minimal DMEM Seahorse medium was 26.78 ± 1.50 mpH/min per 2×10^4 cells (initial cell count) and 3.24 ± 0.18 mpH/min per μg protein (**Figure 3.14**). Application of 10 mM glucose increased ECAR to 85.27 ± 3.22 mpH/min per 2×10^4 cells and 10.31 ± 0.40 mpH/min per μg protein.

Oligomycin application caused a loss of mitochondrial ATP production and lead to a maximal glycolytic rate of 101.14 ± 4.35 mpH/min per 2×10^4 cells and 12.18 ± 0.50 mpH/min per μg protein. Finally non-glycolytic acidification was estimated by inhibiting glycolysis with 2-DG, which brought ECAR down to 20.24 ± 1.12 mpH/min per 2×10^4 cells and 2.45 ± 0.15 mpH/min per μg protein.

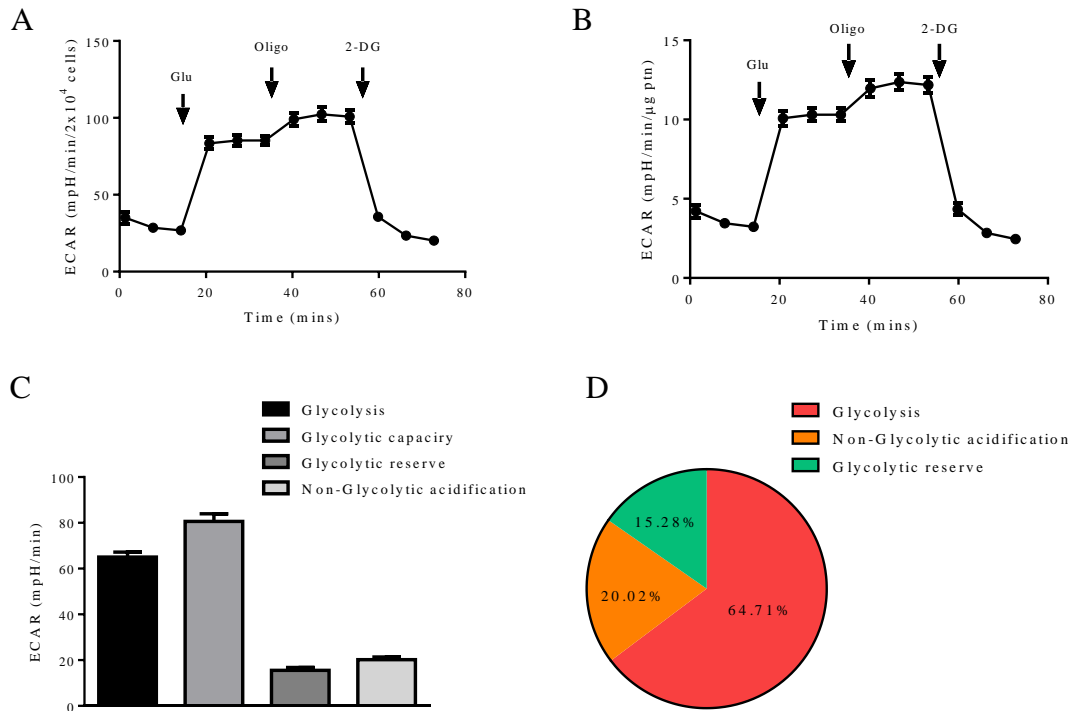


Figure 3.14: Glycolysis stress test. Evaluation of glycolysis was made by a sequential application of pharmacological inhibitors for OXPHOS and glycolysis, and change in ECAR of intact cells in real time (A) was calibrated to μg protein (B). The contribution of each element to ECAR is shown in (C), and the pie chart gives percentages of glycolysis, non-glycolytic acidification and glycolytic reserve when maximal ECAR value was taken as 100% (D) (n=8).

3.4.1.5 ATP production rate from glycolysis and OXPHOS

In order to estimate proportions of ATP generated by glycolysis and OXPHOS in HCASMCs, we next assessed oligomycin sensitive O_2 consumption and proton production rate (PPR). The former reflects OXPHOS while the latter is an indicator of glycolysis. Glycolytic rate can be measured by PPR where acidification of assay

medium is used as the measure of lactate and CO₂ production [181, 200, 201]. During glycolysis, one glucose molecule breaks down into two pyruvates (pK_a 2.5), releasing two protons. When glucose-derived pyruvate is linked to OXPHOS, pyruvate enters the TCA cycle and CO₂ is released. For one pyruvate molecule, three molecules of CO₂ are generated, one from pyruvate dehydrogenase (PDH), the other two from the oxidation of 6-carbon molecules through isocitrate dehydrogenase and α-ketoglutarate dehydrogenase. CO₂ is hydrated to carbonic acid and released as HCO₃⁻ and H⁺. A parallel study measuring PPR (**Figure 3.15B**) was carried out along with the mitochondrial stress test (**Figure 3.15A**). By inhibiting PPR using oligomycin in the presence of 2-DG, the remaining PPR represents non-glycolytic acidification, and this accounted for 23.74% of the total PPR (36.00/151.64) (**Figure 3.15B**). In general, generation of 2 ATP from one glucose molecule releases two lactate anions (pK_a 3.9) and two H⁺ into the assay medium. The relationship between PPR and ATP production is 1:1 [201, 202]. ATP production from OXPHOS was calculated from oligomycin sensitive O₂ consumption using a phosphate/oxygen ratio (P/O ratio) of 2.31 [173]. Our results showed that HCASMCs cultured in high glucose DMEM containing 1 mM sodium pyruvate and 2 mM L-glutamate generate ATP at a rate of 115.87 ± 3.33 pmol/min per 2x10⁴ cells or 12.69 ± 0.50 pmol/min per μg protein from glycolysis, and 138.93 ± 8.88 pmol/min per 2x10⁴ cells or 15.04 ± 0.59 pmol/min per μg protein from OXPHOS. These results indicate that the cells rely on ~54.53% of the total ATP from OXPHOS (**Figure 3.15E and 3.15F**).

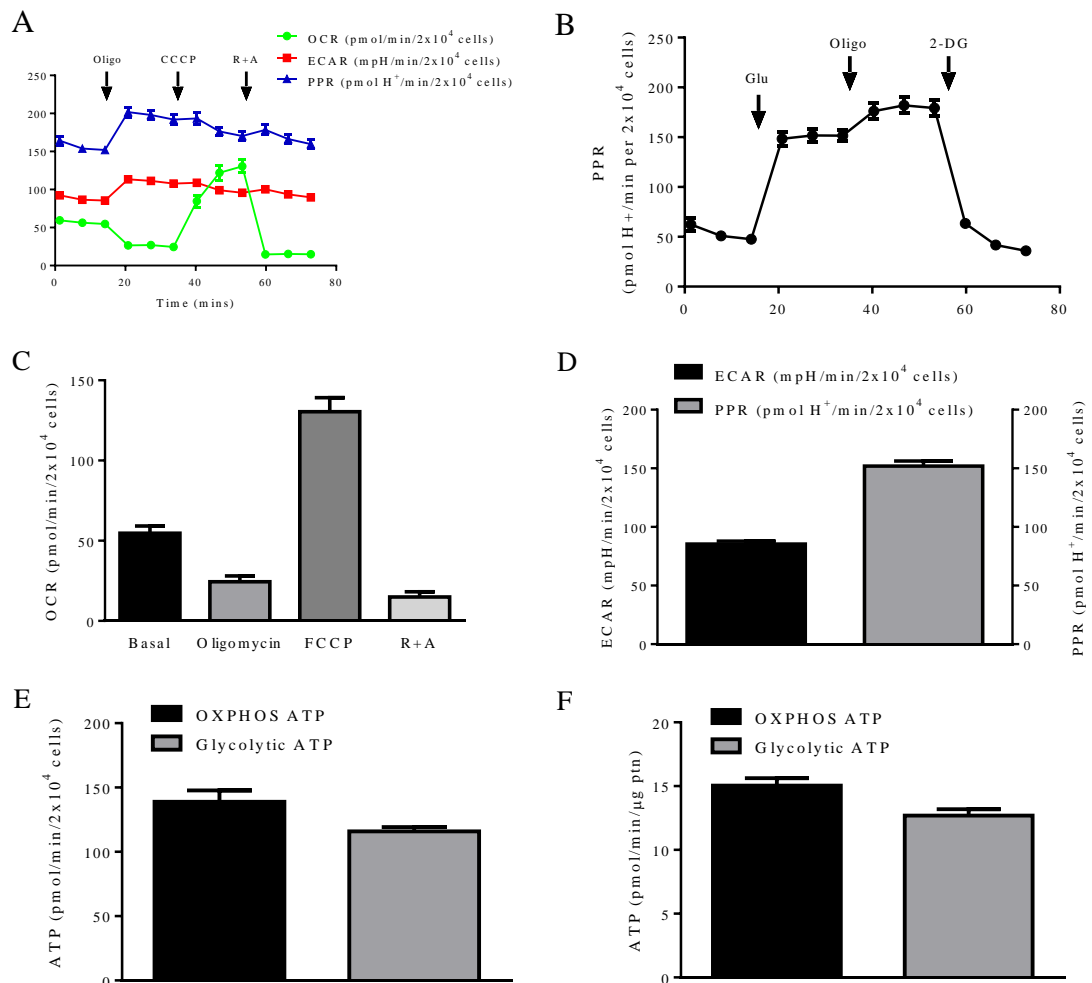


Figure 3.15: ATP production rate from glycolysis and OXPHOS. (A) Mitochondrial stress test (n=8). (B) Glycolysis stress test (n=8). (C) Quantitative analysis of OCR of HCASMCs. (D) Basal ECAR and PPR of HCASMCs. (E) ATP production rate from OXPHOS and glycolysis normalized to cell number. (F) ATP production rate from OXPHOS and glycolysis normalized to total protein content.

3.4.1.6 Interplay between glycolysis and OXPHOS

The results above suggest that cultured HCASMCs have active mitochondrial respiration and depend on ATP from OXPHOS more than ATP generated from glycolysis pathway. The bioenergetics of the cells is regulated by many factors such as energy requirements, substrate availability, and overall quality of the mitochondrial population. Blocking ETC with R+A decreased OCR, making cells to rely more on glycolysis as indicated by increased ECAR. Application of oligomycin had no further effect on OCR indicating that R+A stop ETC effectively (**Figure 3.16**).

When PMF was dissipated with application of FCCP, OCR increased dramatically along with an increase in ECAR (**Figure 3.17**). Oligomycin still increased OCR slightly in the presence of FCCP (**Figure 3.17**). As oligomycin reduced ECAR in the presence of R+A or CCCP, inhibition of ETC caused ATP synthase to work in a reverse mode in favor of maintaining the $\Delta\psi_m$ at a cost of ATP consumption (see **Figure 1.18B & C, Section 1.10.2**). Moreover, application of 2-DG blocked this effect (**Fig 3.18**) further supporting the hypothesis that the ATP synthase is working in a reverse mode in the presence of FCCP, utilizing ATP generated by glycolysis.

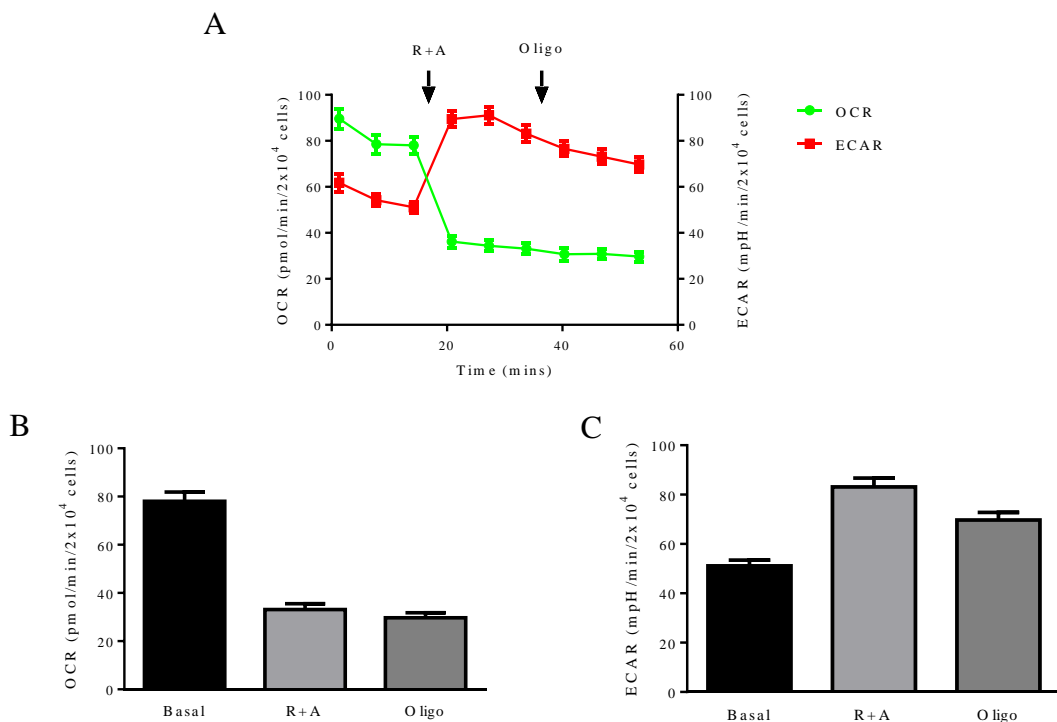


Figure 3.16: Effect of oligomycin after blocking ETC. (A) R+A decreased HCASMC oxygen consumption rate, and oligomycin had little effect on OCR in the presence of R+A. (B) Mean \pm SEM of OCR. (C) Mean \pm SEM of ECAR. (n=8)

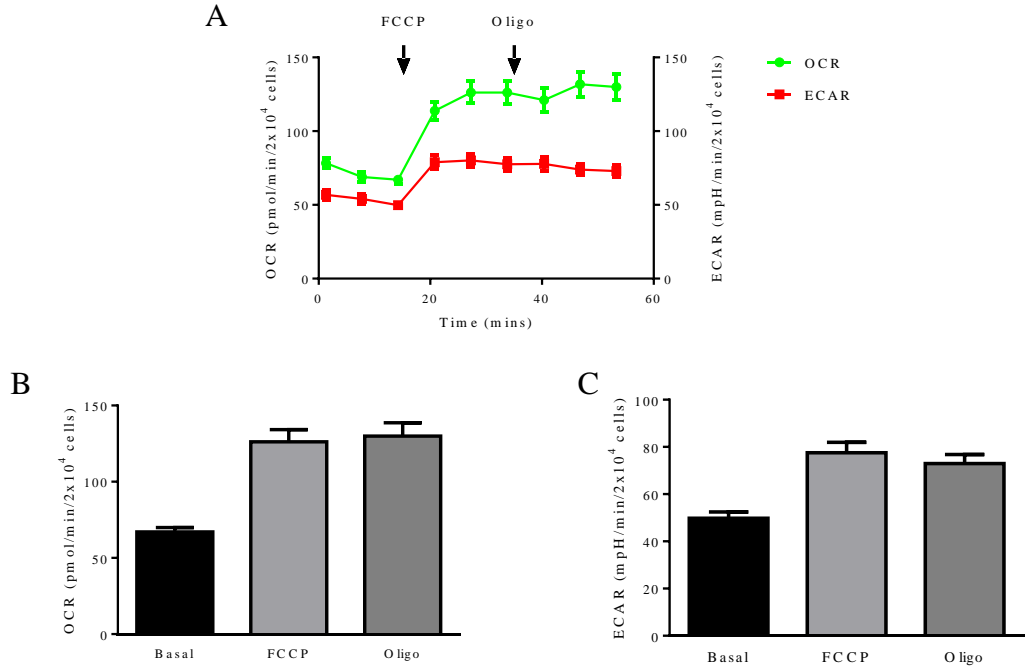


Figure 3.17: Effect of oligomycin after dissipating ETC. (A) FCCP increased HCASMC oxygen consumption, and oligomycin had little effect on OCR in the presence of FCCP. (B) Mean \pm SEM of OCR. (C) Mean \pm SEM of ECAR. (n=8)

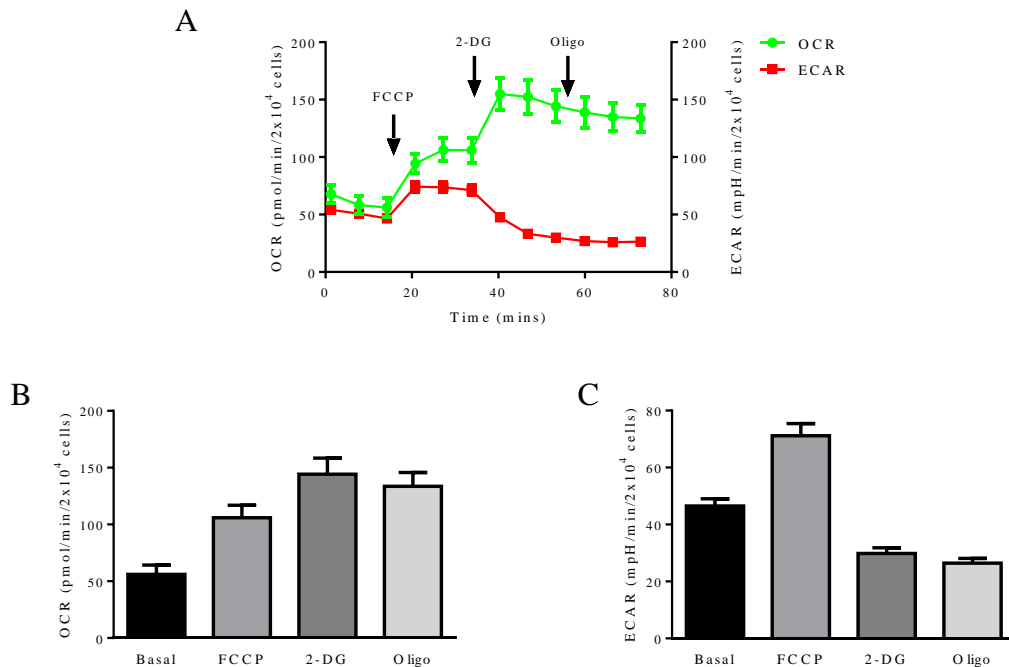


Figure 3.18: 2-DG abolished the reverse mode of ATP synthase. (A) FCCP increased ECAR which was decreased by 2-DG, and final application of oligomycin had no effect. (B) Mean \pm SEM of OCR. (C) Mean \pm SEM of ECAR. (n=8)

3.4.1.7 Impact of metabolic inhibitors on mitochondrial bioenergetic phenotype

Mitochondrial function is important in energy production and cell signaling, and altered bioenergetics by metabolic inhibitors and hypoxia can cause cell malfunction. Seahorse technology was used to determine the bioenergetic phenotype of cultured HCASMCs in response to glucose and metabolic inhibitors. Addition of glucose to glucose-free DMEM shifted relative HCASMC bioenergetic phenotype from aerobic to glycolytic (**Figure 3.19A**). 2-DG shifted HCASMC bioenergetic phenotype to be more aerobic (**Figure 3.19B**). Rotenone, antimycin and oligomycin caused the cells to become a more glycolytic bioenergetic phenotype (**Figure 3.19C&D&E**), indicating that glycolysis allows compensatory production of ATP when OXPHOS is inhibited. FCCP shifted relative HCASMC bioenergetic phenotype from quiescent to energetic indicated by a large increase in O₂ consumption (**Figure 3.19F**). When compared to basal level, OCR decreased by $33.30 \pm 0.55\%$ after addition of glucose (in glucose-free DMEM), increased by $7.55 \pm 3.48\%$ in response to 2-DG, decreased by $58.15 \pm 1.69\%$ in response to rotenone, by $52.19 \pm 2.27\%$ in response to antimycin, by $47.84 \pm 2.38\%$ in response to oligomycin, and increased by $84.10 \pm 4.33\%$ in response to FCCP (**Figure 3.20A**). When compared to basal level, ECAR increased by $221.18 \pm 7.84\%$ after addition of glucose (to glucose-free DMEM), decreased by $37.34 \pm 1.88\%$ in response to 2-DG, increased by $67.94 \pm 5.58\%$ in response to rotenone, increased by $75.14 \pm 3.74\%$ in response to antimycin, increased by $51.66 \pm 3.58\%$ in response to oligomycin, and increased by $63.12 \pm 1.78\%$ in response to FCCP (**Figure 3.20B**).

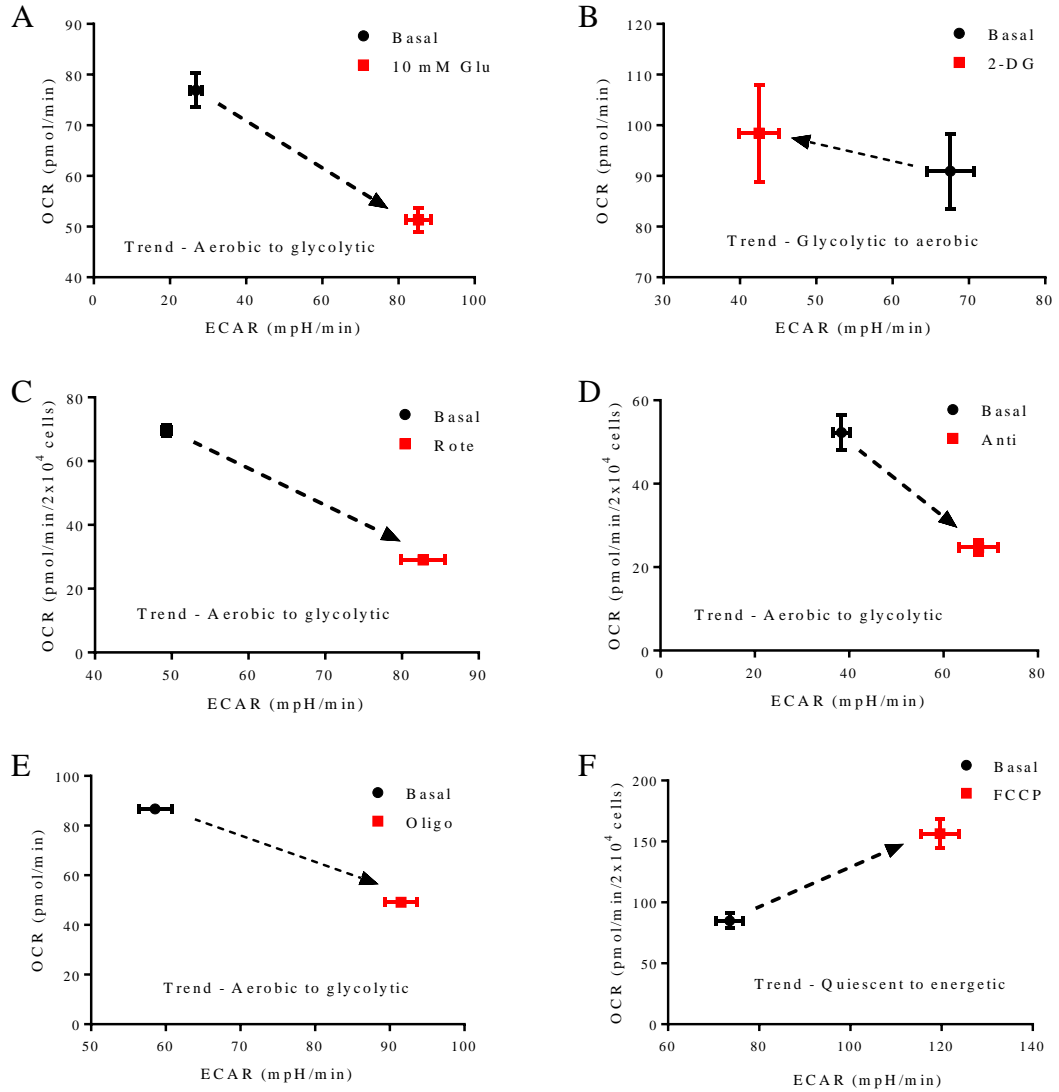


Figure 3.19: Bioenergetic phenotype in response to metabolic inhibitors. The shift of bioenergetic phenotype of HCASMCs after exposure to 10 mM glucose (in glucose-free medium) (A, n=8), 5 mM 2-DG (B, n=8), 1 μ M rotenone (C, n=8), 1 μ M antimycin (D, n=7), 1 μ M oligomycin (E, n=7) and 0.75 μ M FCCP (F, n=8).

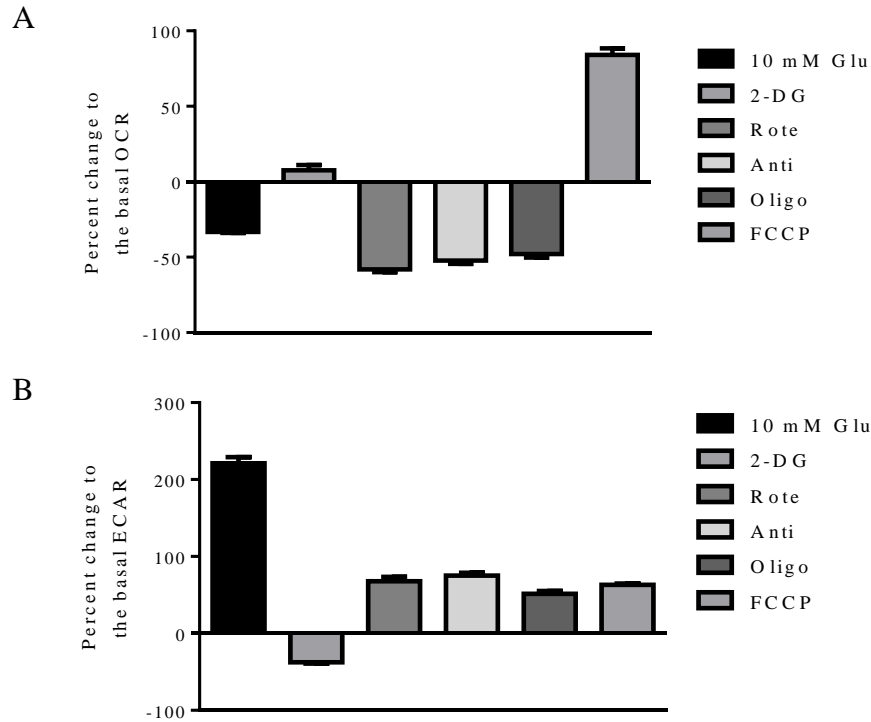


Figure 3.20: Percent change in OCR and ECAR in response to metabolic inhibitors. Percent change of OCR (top panel) and ECAR (bottom panel) against the basal measurement after exposure to, from left to right, 10 mM glucose (in glucose-free DMEM) (n=8), 5 mM 2-DG (n=8), 1 μ M rotenone (n=8), 1 μ M antimycin (n=7), 1 μ M oligomycin (n=7) and 0.75 μ M FCCP (n=8).

3.4.2 ATP content in HCASMCs

3.4.2.1 ATP in cultured HCASMC

Intracellular ATP was determined by CellTiter-Glo luminescent viability assay. The luciferase reaction for the assay is shown in **Figure 3.21A** where luminescent signal generated is proportional to the amount of ATP. An ATP standard curve was generated by using serial tenfold dilutions of ATP in cell culture medium (1 μ M to 10 nM) according to manufacturer's protocol (**Figure 3.21B**). High concentrations of ATP caused a saturation of the signal (**data not shown**). Luminescence signal and cell number followed a linear relationship (**Figure 3.21C**). HCASMCs contained an estimated $(1.48 \pm 0.03) \times 10^{-14}$ mole ATP per cell. The volume of HCASMCs was estimated to be $\sim 13.43 \pm 2.90$ pL (n=10, see **section 4.3.7**). Assuming this is equal to the intracellular space where ATP is dissolved (the upper end of cell volume), the

ATP concentration in HCASMCs is therefore calculated to be ~1.10 mM (the lower end of ATP concentration).

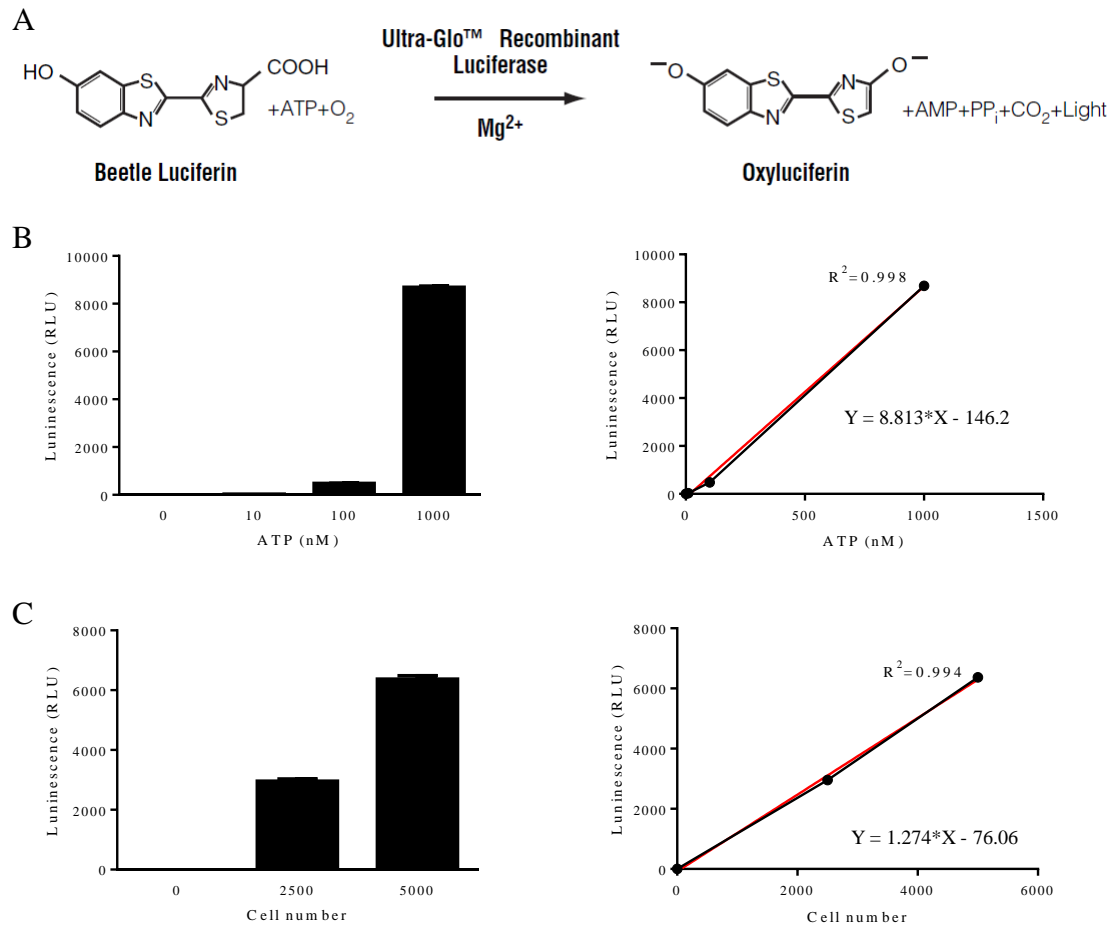


Figure 3.21: CellTiter-Glo luminescent viability assay. (A) Luciferase reaction. Mono-oxygenation of luciferin is catalyzed by luciferase in the presence of Mg^{2+} , ATP and molecular oxygen. (B) ATP standard curve was made by reading luminescence output at a serial tenfold dilutions of ATP in cell culture medium (n=6). (C) Cell number correlates with luminescence output (n=6, $r^2=0.994$).

3.4.2.2 Effect of vasoconstrictors on intracellular ATP

The ATP level in the cells was measured in cell culture medium as well as 10 glucose PSS and 0 glucose PSS. Using buffers instead of medium made the experiments more flexible and comparable to the condition used for confocal experiments. We first tested whether an increase in ATP consumption will cause a change in intracellular ATP. PDGF-BB and PGF2 α are known vasoconstrictors, and

more ATP is hydrolyzed in working cells. *In vivo*, ATP is consumed during SMC contraction, but even if the cultured cells may not be contractile phenotype, if the agonists elevate intracellular Ca^{2+} ($[\text{Ca}^{2+}]_i$), this would lead to increased ATP consumption due to the enhanced activities of Ca^{2+} ATPase. PDGF-BB and $\text{PGF}2\alpha$ increased $[\text{Ca}^{2+}]_i$ in HCASMCs (refer to **section 5.3.1.3**), but both had little effect on cellular ATP in PSS containing 10 mM glucose. PDGF-BB did not change ATP in 0 glucose PSS, $\text{PGF}2\alpha$ slightly decreased cellular ATP, but not significantly (**Figure 3.22**). We postulate that the cells generate enough ATP for various functions, and a high reserve capacity guarantees energy generation when the demand for ATP increases at least in the short term.

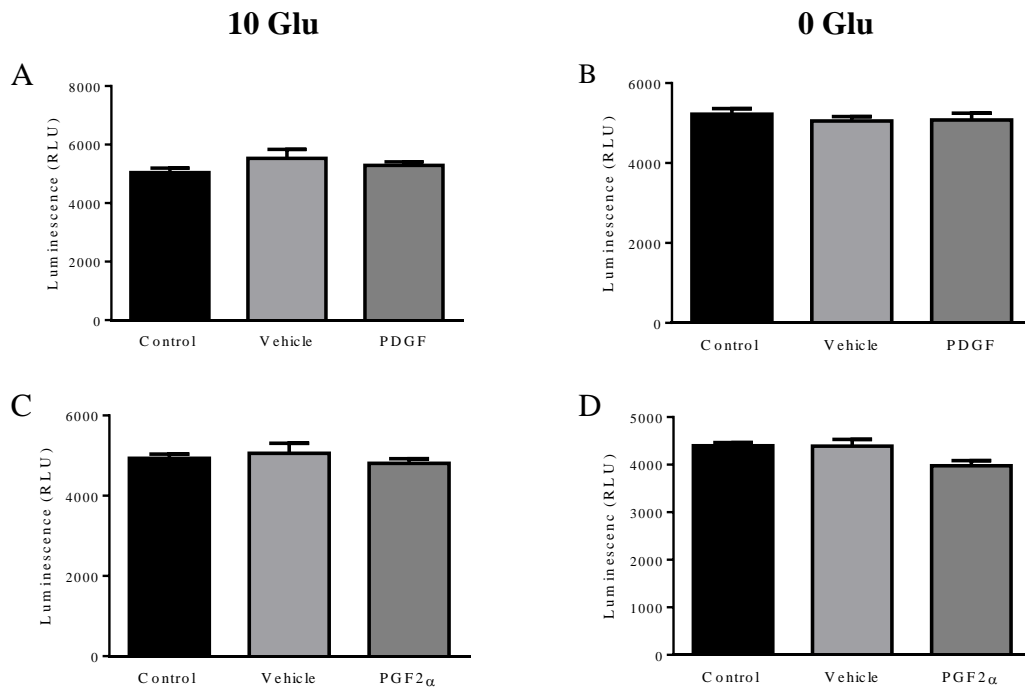


Figure 3.22: Effect of vasoconstrictors on intracellular ATP. (A) Luminescent signal changes in response to PDGF-BB in PSS containing 10 mM glucose (n=4, vehicle control vs. PDGF P=0.483). (B) Luminescent signal changes in response to PDGF-BB in 0 mM glucose PSS (n=4, vehicle control vs. PDGF, P=0.907). (C) Luminescent signal changes in response to $\text{PGF}2\alpha$ in PSS containing 10 mM glucose (n=4, vehicle vs. $\text{PGF}2\alpha$ P=0.394). (D) Luminescent signal changes in response to $\text{PGF}2\alpha$ in 0 mM glucose PSS (n=4, vehicle vs. $\text{PGF}2\alpha$, P=0.062).

3.4.2.3 Effect of metabolic inhibitors on intracellular ATP

In cell culture medium containing 5.55 mM glucose, blocking glycolysis using 5 mM 2-DG caused $55.24 \pm 0.49\%$ reduction in ATP level. A similar effect of 2-DG was observed in PSS in the presence and absence of 10 mM glucose (**Figure 3.23**). After inhibiting cellular oxidative phosphorylation with oligomycin, cellular ATP level decreased as shown in **Figure 3.24**. A summary of ATP levels determined in the presence of various metabolic inhibitors is shown in **Figure 3.25**. In cell culture medium, ATP level was reduced by $9.16 \pm 0.56\%$ (1 μM rotenone), $7.26 \pm 3.41\%$ (1 μM antimycin), $13.31 \pm 2.76\%$ (6 μM oligomycin), and $17.96 \pm 1.86\%$ (1 μM CCCP). In 10 mM glucose PSS, ATP level was reduced by $8.93 \pm 1.61\%$ (1 μM rotenone), $14.39 \pm 1.96\%$ (1 μM antimycin), $13.72 \pm 1.76\%$ (6 μM oligomycin), and $22.73 \pm 1.53\%$ (1 μM CCCP). In 0 glucose PSS, ATP level was reduced by $32.33 \pm 1.34\%$ (1 μM rotenone), $36.08 \pm 2.69\%$ (1 μM antimycin), $28.93 \pm 1.05\%$ (6 μM oligomycin), and $60.14 \pm 0.86\%$ (1 μM CCCP). The co-application of 2-DG and oligomycin caused a larger inhibition than those caused by either of the inhibitors alone (**Figure 3.26**).

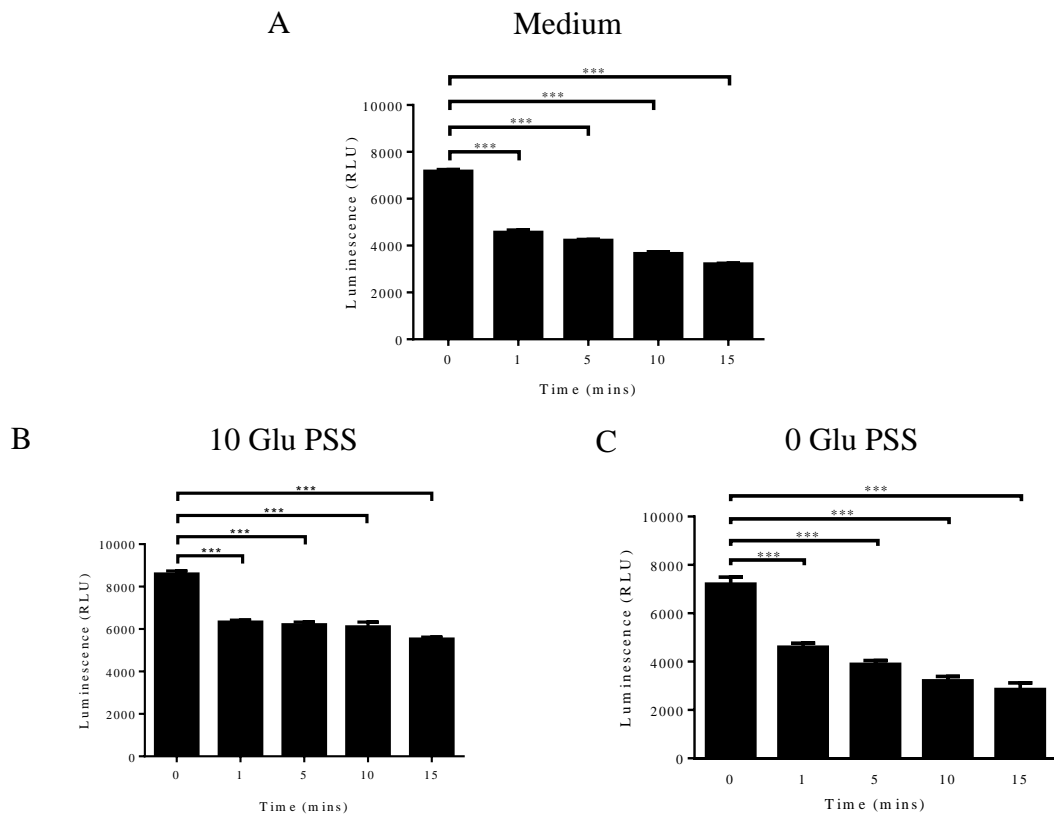


Figure 3.23: Inhibition of glycolysis with 2-DG caused a decrease in ATP level.

Blocking glycolysis using 5 mM 2-DG reduced cellular ATP level in cell culture medium (A), 10 mM glucose PSS (B), and 0 mM glucose PSS (C) (n=4). Time 0 represents before 2-DG application.

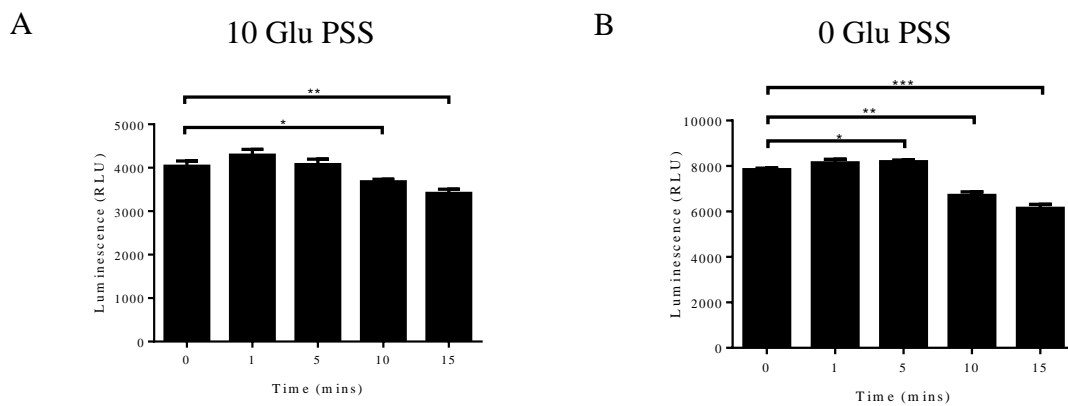


Figure 3.24: Inhibition of OXPHOS caused a decrease in ATP level. Inhibiting

OXPHOS with 6 μ M oligomycin decreased ATP level in PSS with (A) and without (B) 10 mM glucose (n=4). Time 0 represents reading before oligomycin application.

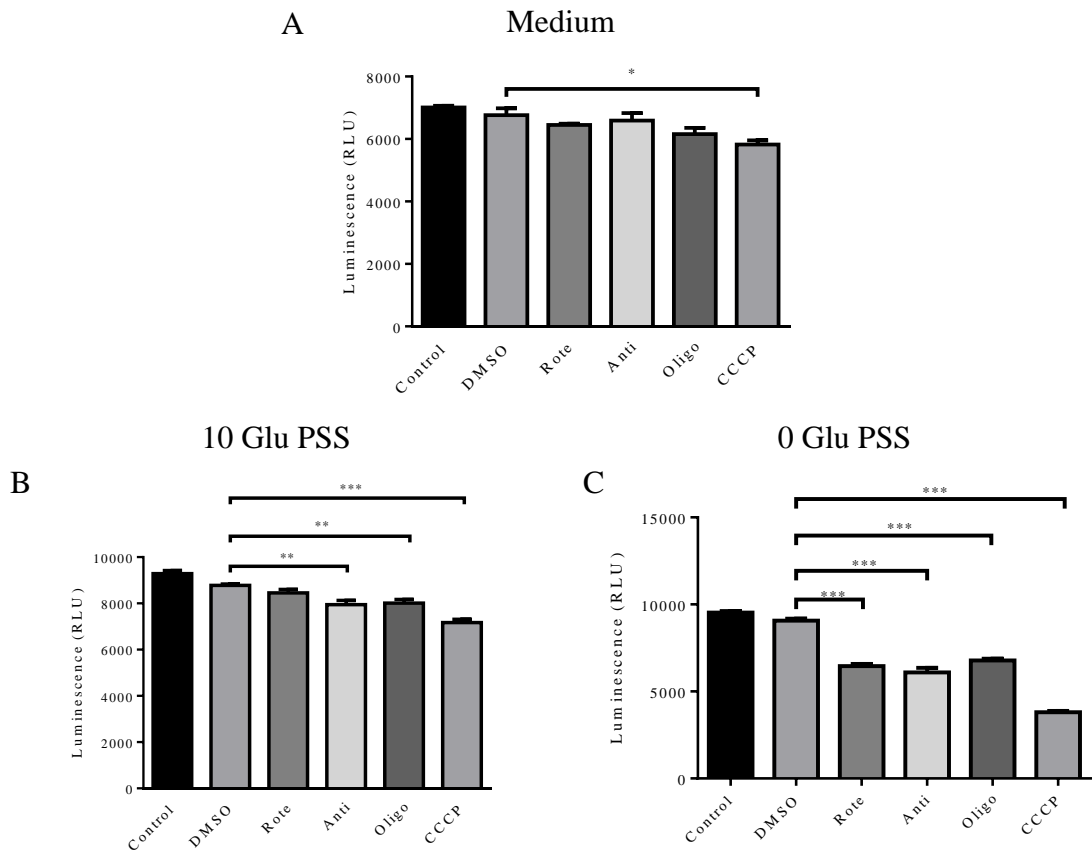


Figure 3.25: Effects of metabolic inhibitors on cellular ATP. Effect of metabolic inhibitors on cellular ATP in cell culture medium (A), 10 mM glucose PSS (B), and 0 mM glucose PSS (C) after 10 minutes (n=4). Statistical comparisons were made against vehicle control (DMSO). Control represents medium or 10 mM glucose PSS or 0 mM glucose PSS.

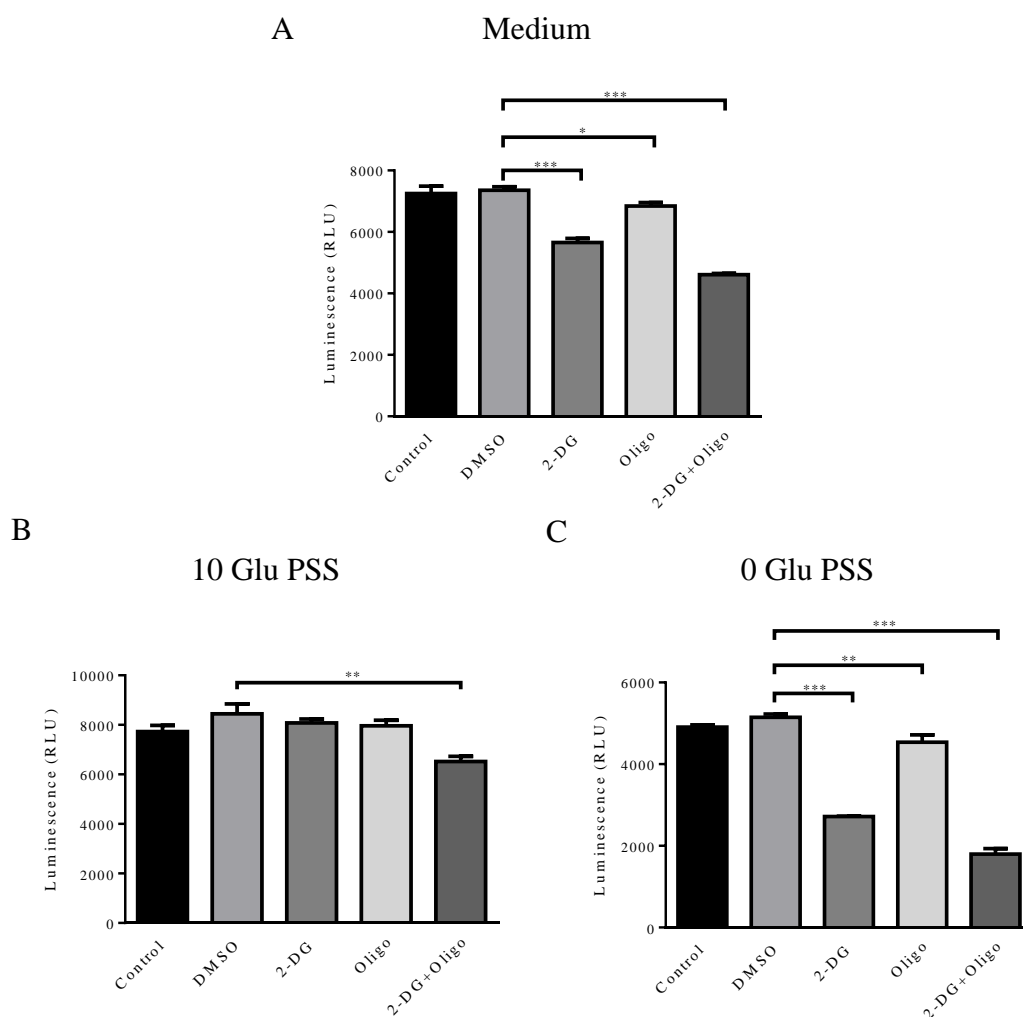


Figure 3.26: Combined inhibition of glycolysis and OXPHOS by 2-DG and oligomycin caused further reduction in cellular ATP. Effect of 5 mM 2-DG and 6 μ M oligomycin on ATP in culture medium (A), 10 mM glucose PSS (B), and 0 mM glucose PSS (C) after 10 minutes (n=4). Statistics was done against vehicle control (DMSO). Control represents medium or 10 mM glucose PSS or 0 mM glucose PSS.

3.4.3 Effect of metabolic inhibitors and hypoxia on ATP:ADP ratio

3.4.3.1 Transfection of HEK293 cell with Perceval

HEK293 cells expressing Perceval was initially used to examine whether Perceval fluorescence signal changes with glycolysis inhibition. Application of 5 mM 2-DG caused a decrease in Perceval signal by $17.28 \pm 4.54\%$ (**Figure 3.27**). Raising concentration of 2-DG from 5 mM to 50 mM caused further decrease in Perceval signal (n=2, data not shown). A preliminary study using HEK293 cells expressing

pHRed showed that application of 5 mM 2-DG did not change intracellular pH suggesting that observed reduction in Perceval signal was not due to acidification (data not shown).

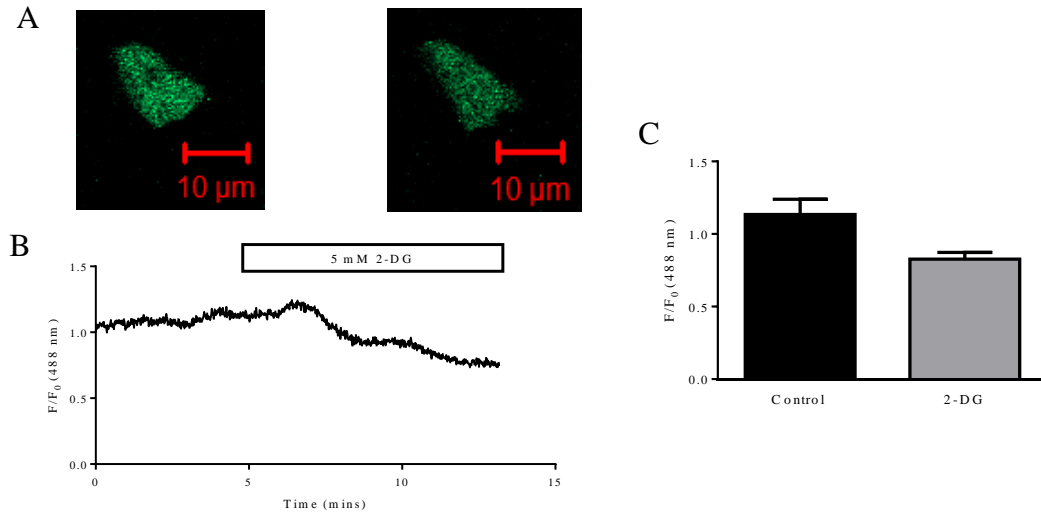


Figure 3.27: The effect of 2-DG on Perceval signal. (A) Images of HEK293 cell expressing Perceval before (left) and after (right) application of 5 mM 2-DG. (B) Fractional fluorescence of the cell in (A) decreased with application of 5 mM 2-DG. (C) Mean \pm SEM of fractional fluorescence showing Perceval signal just before (control) and after the application of 5 mM 2-DG ($P=0.084$, $n=3$).

3.4.3.2 Effect of glucose deprivation on ATP:ADP ratio in HCASMCs

Perceval experiments were next carried out using HCASMCs. Removing glucose from extracellular solution resulted in a decrease in ATP:ADP signal by $25.67 \pm 8.33\%$ (**Figure 3.28**). This was not due to the loss of focus as the response was reversible (**Figure 3.29**).

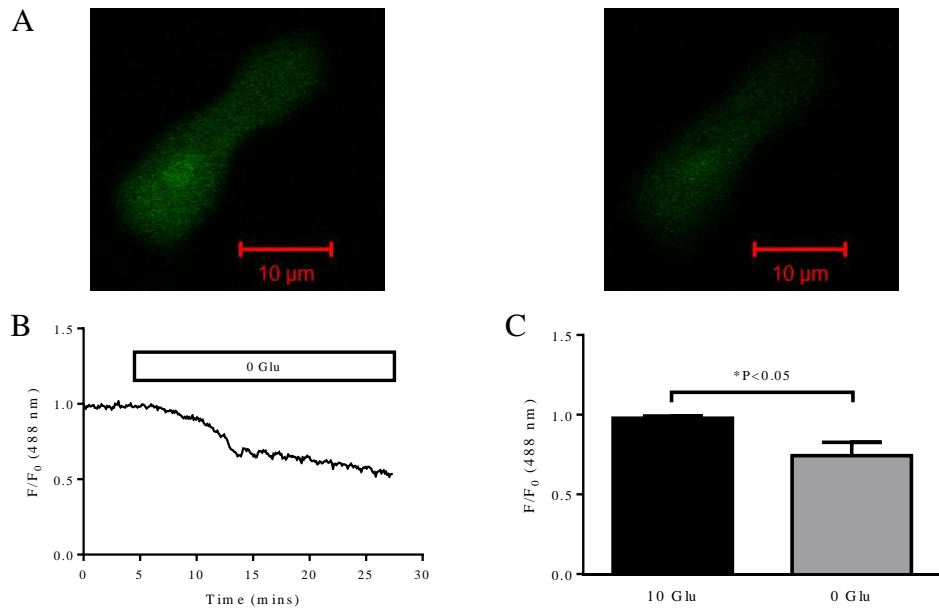


Figure 3.28: Glucose removal caused a decrease in Perceval signal. (A) Images of HCASMC expressing Perceval under control condition (left) and after glucose removal (right). (B) Time course of fractional fluorescence change induced by glucose removal. (C) Mean \pm SEM of fractional fluorescence of Perceval just before (10 Glu) and after (0 Glu) glucose removal (n=6, including 3 cells from Figure 3.29).

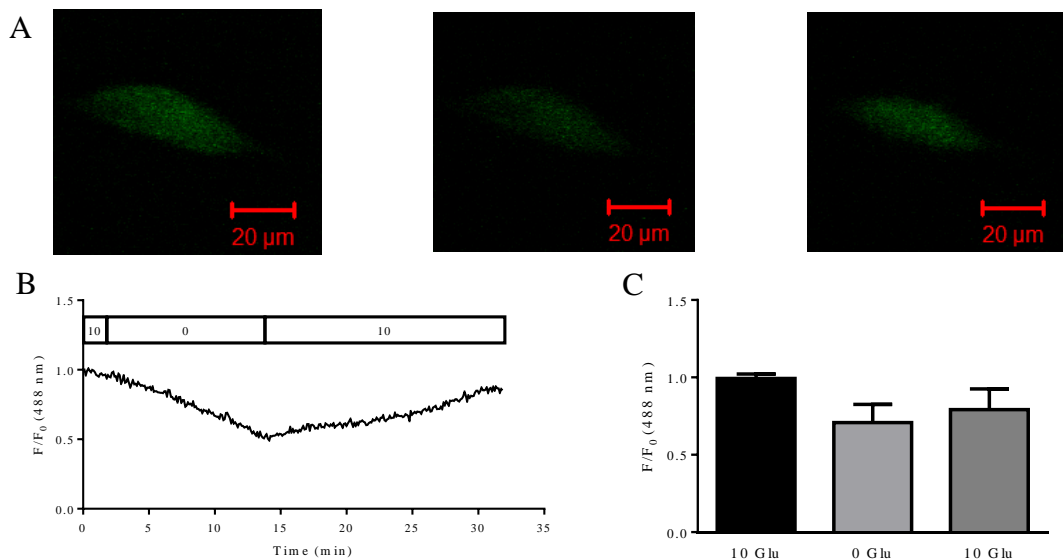


Figure 3.29: Reduction in Perceval signal after glucose removal is reversible. (A) Images of HCASMC expressing Perceval under control condition (left), after 12 minutes of glucose removal (middle), and after glucose re-administration (right). (B) Time course of fractional fluorescence caused by glucose removal and re-administration. (C) Mean \pm SEM of fractional fluorescence for control, 0 mM glucose and 10 mM glucose (n=3).

3.4.3.3 Effect of metabolic inhibitors on ATP:ADP ratio in HCASMCs

Continuous perfusion with PSS for about 40 minutes showed little change in Perceval fluorescence signal (**Figure 3.30**). When 5 mM 2-DG was substituted for 10 mM glucose, Perceval fluorescence signal was reduced by $54.02 \pm 15.29\%$ (**Figure 3.31**). The effect of 2-DG was not reversible (data not shown). Experiments with cells expressing pHRed showed that 2-DG effect is unlikely to be caused by change in pH in bicarbonate buffered PSS as the brief change in the signal was transient (**Figure 3.32**). When HEPES buffered PSS was used, however, application of 2-DG caused a change in pHRed signal (**Figure 3.33**). Inhibiting ETC by application of antimycin decreased ATP:ADP ratio signal by $\sim 45\%$ (**Figure 3.34**). We also tested the effect of 20 mM NH_4Cl on pHRed that produced predicted change in signal in a reversible manner (**Figure 3.35**).

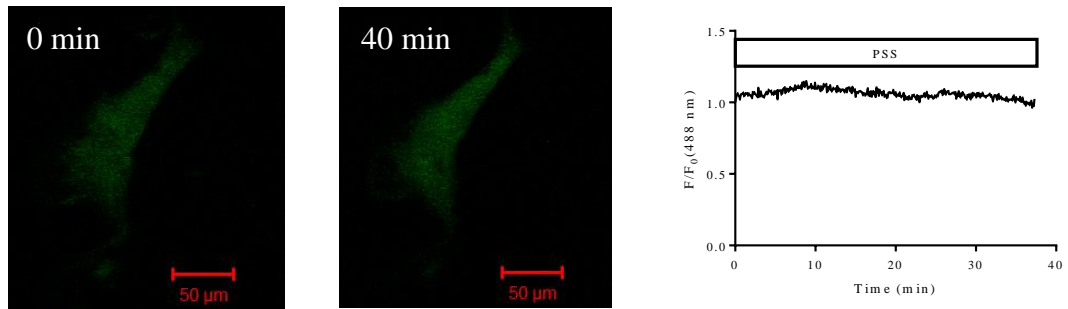


Figure 3.30: Time control study with HCASMC expressing Perceval. Perfusion with PSS for a period of 40 minutes caused little change in Perceval fluorescence signal (n=1).

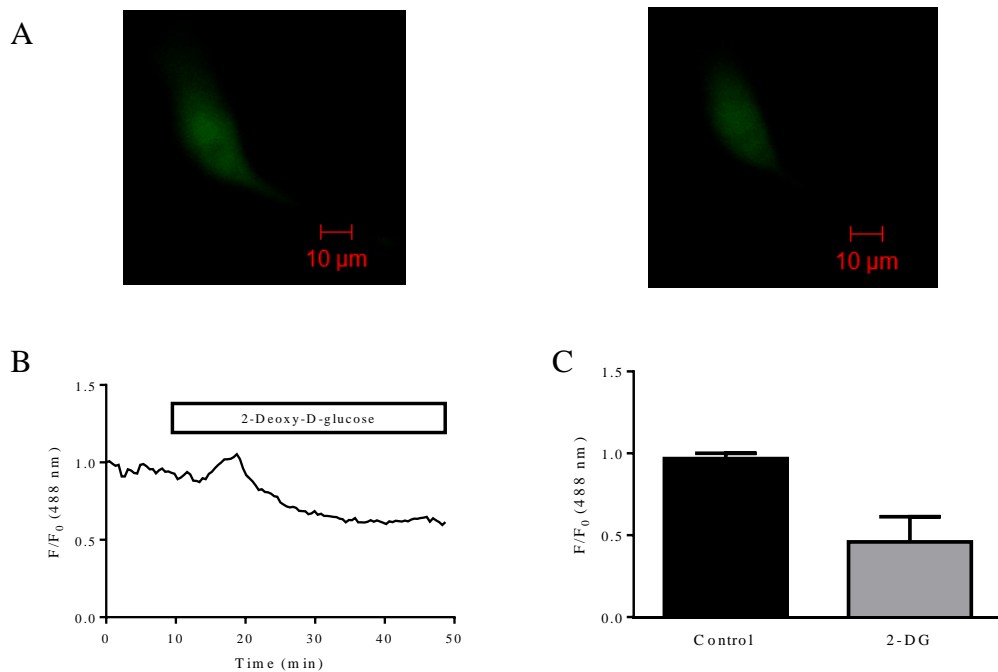


Figure 3.31: Application of 2-DG decreases Perceval signal. (A) Images of HCASMC expressing Perceval before (left) and after the application of 2-DG (right). (B) Time course of fractional fluorescence change caused by application of 2-DG. (C) Mean \pm SEM of fractional fluorescence of Perceval just before (control) and after administration of 2-DG (P=0.112, n=3).

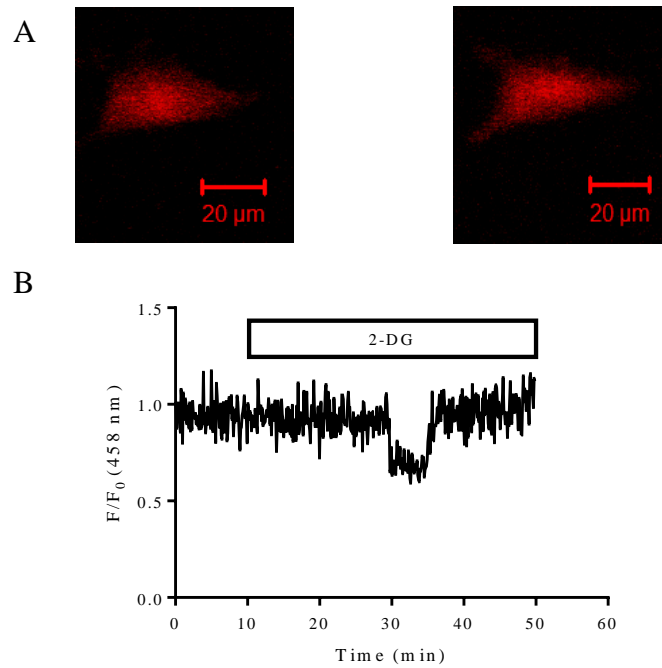


Figure 3.32: The effect of 2-DG on pHRed signal in bicarbonate buffered PSS.

(A) Images of HCASMC expressing pHRed before (left) and after application of 2-DG (right). (B) Time course of fractional fluorescence during application of 2-DG.

This experiment was repeated twice with a similar result.

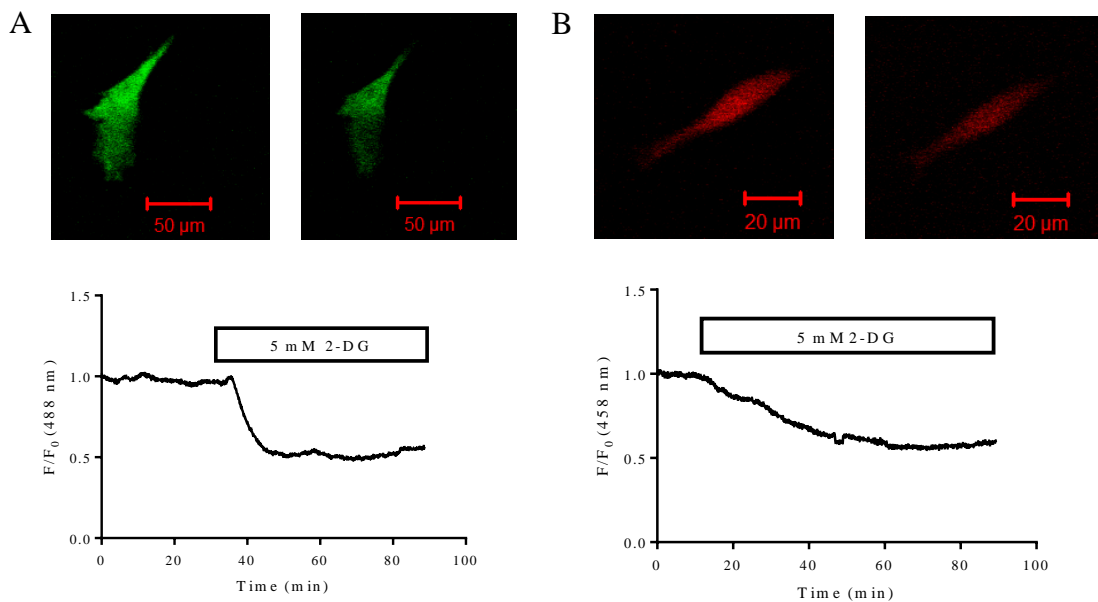


Figure 3.33: The effect of 2-DG in HEPES buffered PSS. In HEPES buffered PSS,

5 mM 2-DG caused a reduction in Perceval signal (A, n=1), as well as in pHRed signal (B, n=2).

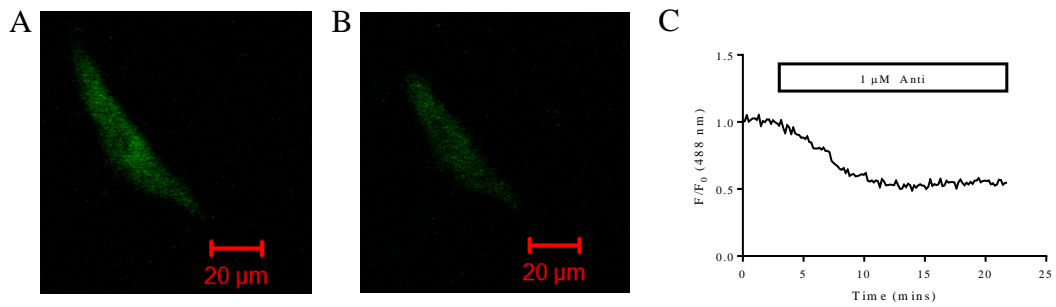


Figure 3.34: Inhibiting ETC by antimycin causes a decrease in ATP:ADP ratio.

Images of HCASMC expressing Perceval before (A) and after (B) application of 1 μM antimycin. (C) Time course of fractional fluorescence showing $\sim 45\%$ decrease by antimycin (n=1).

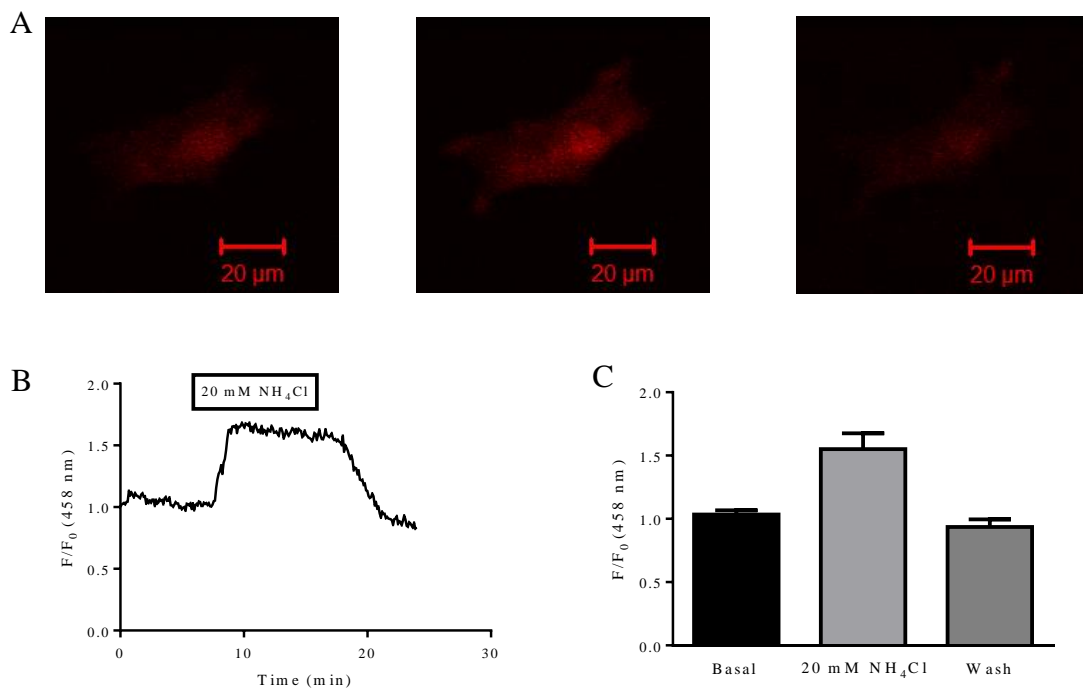


Figure 3.35: pHRed reports changes in cellular pH. (A) A representative

HCASMC transfected with pHRed before (left) and after (middle) application of NH_4Cl . Right panel shows the image after washing of NH_4Cl . (B) Time course of experiment shown in (A).

(C) Average fractional fluorescence of pHRed at basal (measured just before the application of NH_4Cl), 20 mM NH_4Cl (measured at the end of NH_4Cl application) and after wash (measured at the end of the experiment) (n=3).

3.4.3.4 Effect of hypoxia on intracellular ATP:ADP ratio.

It is crucial to know the exact hypoxia level experienced by the cells. This is particularly important for acute experiments attempted in this thesis as the gas already dissolved in the experimental media may be slow to exchange with atmospheric gas where the O₂ tension was manipulated. In addition, it is highly likely that the hypoxia effect on ATP:ADP ratio in resting HCASMCs, if any, will occur at a very low O₂ tension, probably close to near anoxia [203]. The following experiments were carried out to address these issues.

Manipulating O₂ tension in the custom made micro-imaging chamber (atmospheric gas) was achieved by an O₂ controller (# 0508.000, PeCon GmbH, Germany), which also allows the control of CO₂/humidity/temperature. A fiber optic oxygen meter (PHIboard number: v1212143, PM number: 20060308, Serial number: TX3-AOT-03-0297, PeCon GmbH, Germany) was used to measure the dissolved O₂ level in the medium of the imaging dish. We first tested the dissolved O₂ level in the cell culture medium when atmospheric O₂ in the chamber was changed to 1%. When switched to hypoxia, O₂ concentration in the chamber decreased from ~20% to 1% within 3 minutes. The O₂ in cell culture medium also reached to near lowest level. However, the concentration of dissolved O₂ in the medium (lowest at 2.87%) is not as low as that in the chamber (1%) as shown in **Figure 3.36**. In order to see whether O₂ level changes during perfusion, dissolved O₂ was examined while the cells were perfused with HCO₃⁻-buffered PSS. In the hypoxic chamber (1% O₂), reading of fiber optic oxygen meter showed exchange of O₂ dissolved in PSS reached an equilibrium under perfusion followed by a continuous decrease by stopping perfusion (**Figure 3.37**). Therefore, we were unable to do hypoxia experiments with perfusion in this system as the dissolved O₂ was still high during perfusion. One way to overcome this would be to have the perfusion solution gassed with nitrogen first to achieve hypoxia.

In cell culture medium, hypoxia (1% O₂) resulted in a decrease in ATP:ADP ratio signal by $10.99 \pm 2.13\%$ (**Figure 3.38**). The change in Perceval signal caused by hypoxia was reversible (**Figure 3.39**). There was no change in Perceval signal

when mild hypoxia (10% and 5% O₂) was tested (**Figure 3.40**). There was no change in intracellular pH after exposure to hypoxia as reported by pHRed (**Figure 3.41**). Ratiometric measurement (F₅₄₃/F₄₅₈) of pHRed signal from three HCASMCs also showed no change by hypoxia (**Figure 3.42**).

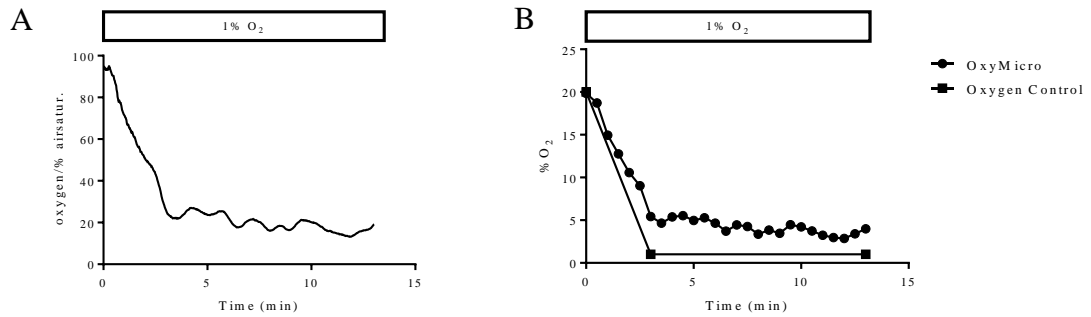


Figure 3.36: O₂ concentration in the chamber and medium during hypoxia. (A) Dissolved O₂ in the medium measured by fiber optic O₂ meter. (B) O₂ concentration in the medium converted into percentage (OxyMicro, filled circle) and O₂ concentration in the custom made micro-imaging chamber (atmospheric gas, Oxygen Control, filled square).

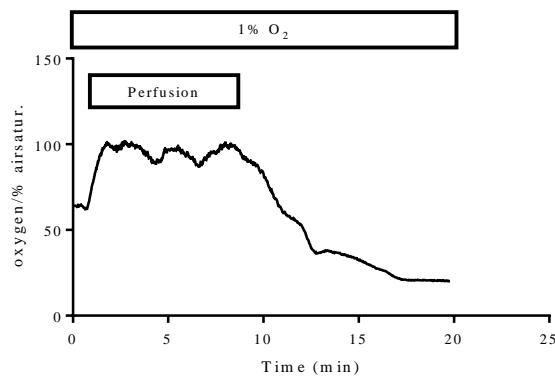


Figure 3.37: Measurement of dissolved O₂ during perfusion. In the hypoxic imaging chamber (1% O₂), perfusion brought dissolved O₂ level in HCO₃⁻-buffered PSS to a higher level near normoxia. When perfusion was stopped, the dissolved O₂ level in the solution continuously decreased. Note: The perfusion was started before equilibrium was reached the lowest level.

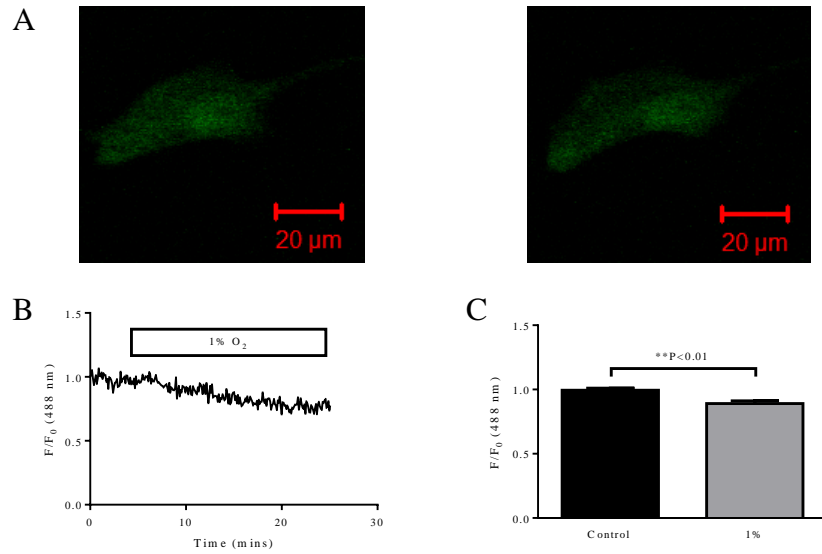


Figure 3.38: Effect of hypoxia (1% O₂) on Perceval signal. (A) Images of HCASMC expressing Perceval under control condition (left) and hypoxia (right). (B) Time course of fractional fluorescence of the cell shown in (A). (C) Mean \pm SEM of fractional fluorescence of Perceval before and after hypoxia (n=8, including 5 cells from Figure 3.39).

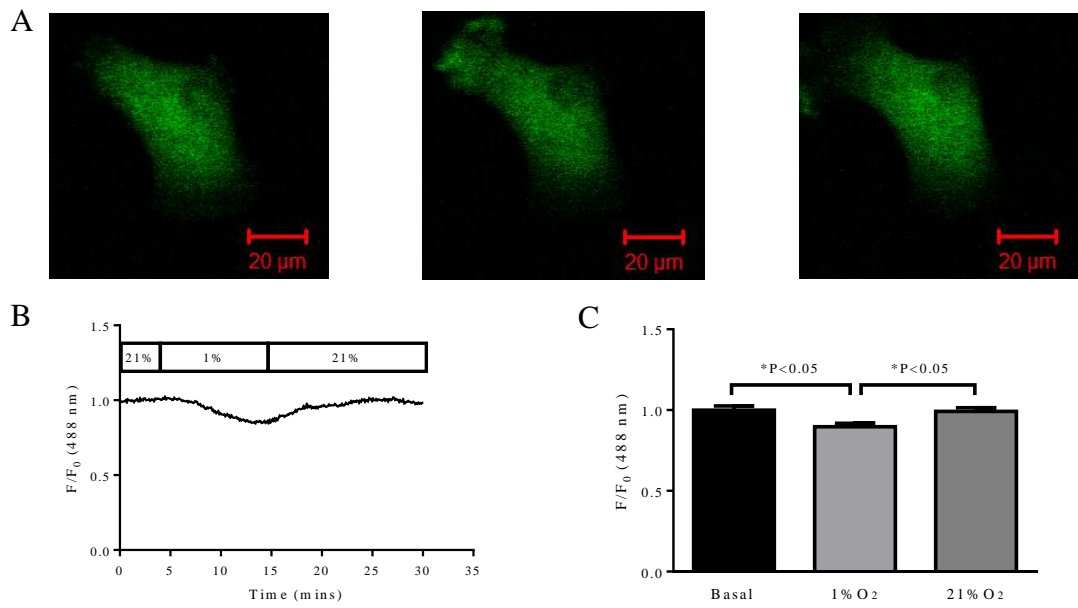


Figure 3.39: Transient hypoxia caused a reversible change in ATP:ADP ratio signal. (A) Images of HCASMC expressing Perceval under control condition (left), after 10 minutes exposure to hypoxia (middle), and recovery after re-oxygenation (right). (B) Time course of fractional fluorescence of the cell shown in (A). (C) Mean \pm SEM of fractional fluorescence of ATP:ADP ratio signal under control, hypoxia and O₂ re-administration (n=5).

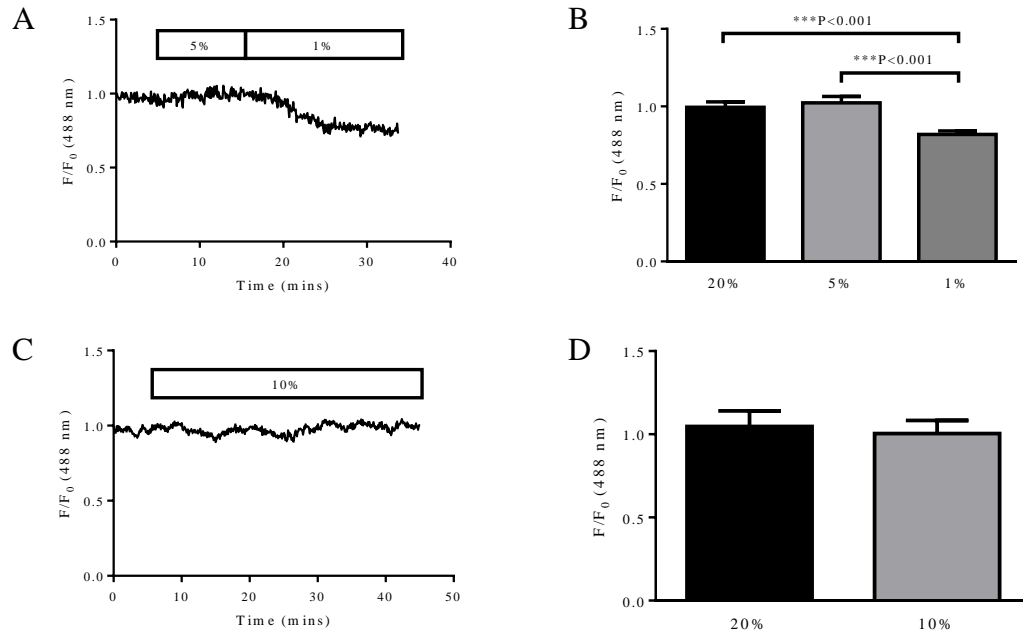


Figure 3.40: Effect of 10% and 5% O₂ on Perceval signal. (A) Time course of fractional fluorescence of Perceval showed little change during exposure to 5% O₂ followed by a significant decrease under 1% O₂. (B) Mean \pm SEM of fractional fluorescence of ATP:ADP ratio signal under normoxia, 5% O₂ and 1% O₂ (n=4). (C) Time course of fractional fluorescence of Perceval showed little change during exposure to 10% O₂. (D) Mean \pm SEM of fractional fluorescence of ATP:ADP ratio signal under normoxia and 10% O₂ (n=4).

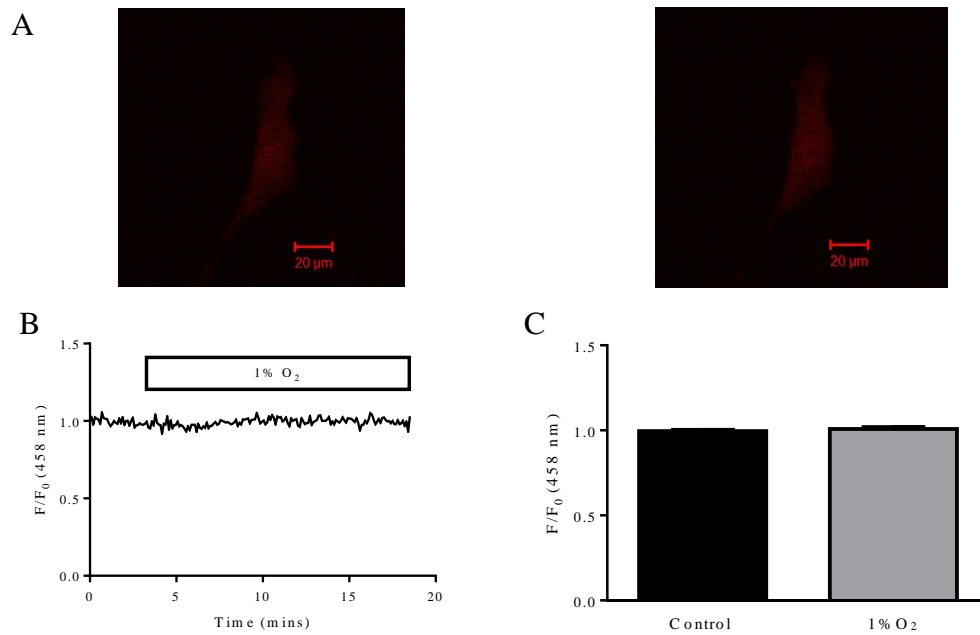


Figure 3.41: Effect of hypoxia on pH. (A) Images of HCASMC expressing pHRed under control condition (left) and during exposure to 1% O₂ (right). (B) Time course of fractional fluorescence of the cell showed little change with exposure to 1% O₂. (C) Mean \pm SEM of fractional fluorescence of pHRed during control condition and 1% O₂ (n=5).

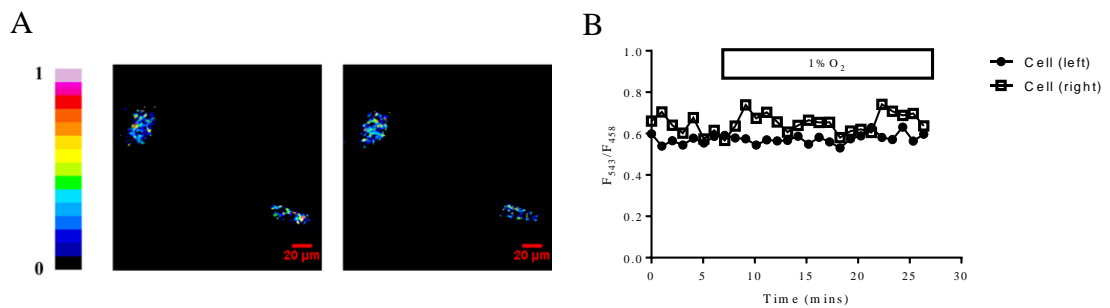


Figure 3.42: Effect of hypoxia on pHRed ratio fluorescence. (A) 2D ratio of 543 nm and 458 nm excitation from HCASMCs expressing pHRed before (left) and after (right) the exposure to 1% O₂. Images are pseudo-coloured with ratio of 0-1. (B) Time course of the pHRed ratiometric signal (F_{543 nm}/F_{458 nm}) for individual cells.

3.4.3.5 ATP:ADP ratio measurement with an improved biosensor, PercevalHR

PercevalHR is an improved biosensor where ATP:ADP ratio detection range is more suitable to mammalian cells [186]. Therefore, PercevalHR was used in our

project after it became available. Vehicle control with DMSO showed PercevalHR signal was stable over 20 mins (**Figure 3.43**). In cell culture medium, metabolic inhibition of oxidative phosphorylation reduced ATP:ADP ratio signal by $22.58 \pm 11.69\%$ (1 μM rotenone), $17.69 \pm 6.67\%$ (1 μM antimycin), $39.12 \pm 11.72\%$ (6 μM oligomycin), $32.85 \pm 1.73\%$ (1 μM CCCP, when measured at peak) and $9.49 \pm 4.10\%$ (1 μM CCCP, when measured at steady state) (**Figures 3.44, 3.45, 3.46 & 3.47**). Signal reduced by the application of rotenone was further decreased by application of antimycin (**Figure 3.48A**). On the other hand, rotenone had little effect in cells pre-treated with antimycin (**Figure 3.48B**). Transient hypoxia (1% O_2) induced a decrease in PercevalHR signal by $17.49 \pm 7.22\%$ in a reversible manner (**Figure 3.49**). Hypoxia (1% O_2) also decreased PercevalHR signal when cells were deprived of glucose or pre-treated with rotenone (**Figure 3.49**).

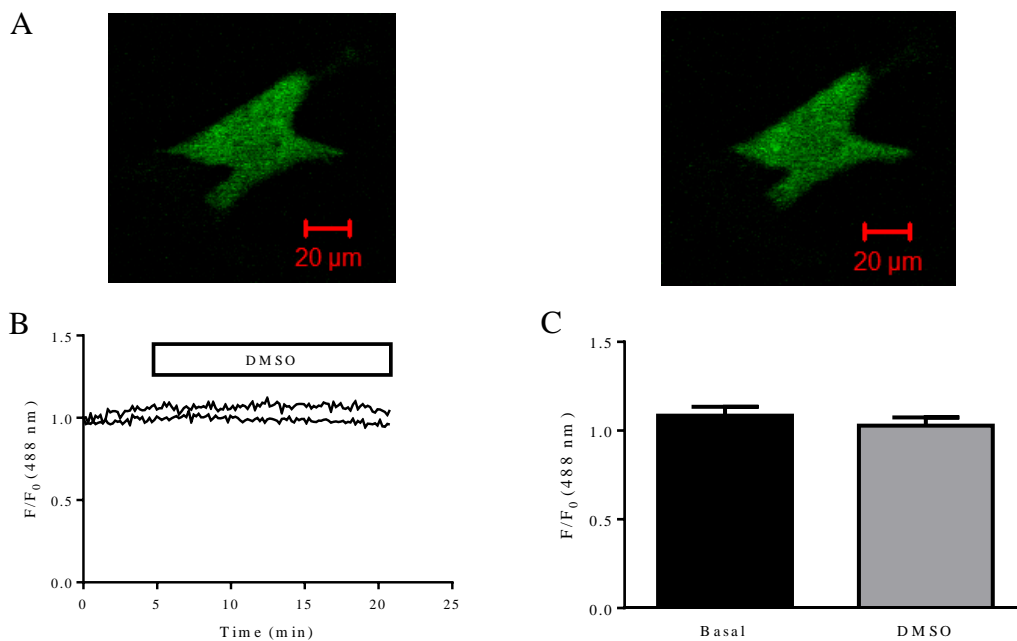


Figure 3.43: Vehicle control of PercevalHR fluorescence. (A) Images of PercevalHR transfected cell before (left) and after application of DMSO (right). (B) Time course of fractional fluorescence of PercevalHR during DMSO application at two regions of interest. (C) Mean \pm SEM of fractional fluorescence of PercevalHR before and after DMSO application (n=4).

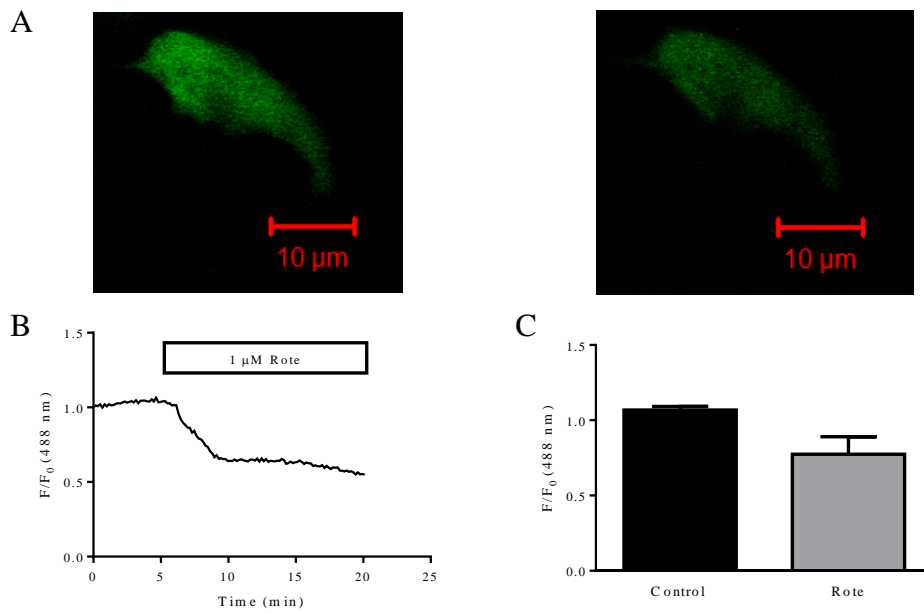


Figure 3.44: Effect of rotenone on ATP:ADP ratio signal. (A) Images of HCASMC expressing PercevalHR before (left) and after (right) application of 1 μM rotenone. (B) Time course of fractional fluorescence during rotenone application. (C) Mean \pm SEM of fractional fluorescence of PercevalHR before and after administration of rotenone ($P=0.111$, $n=3$).

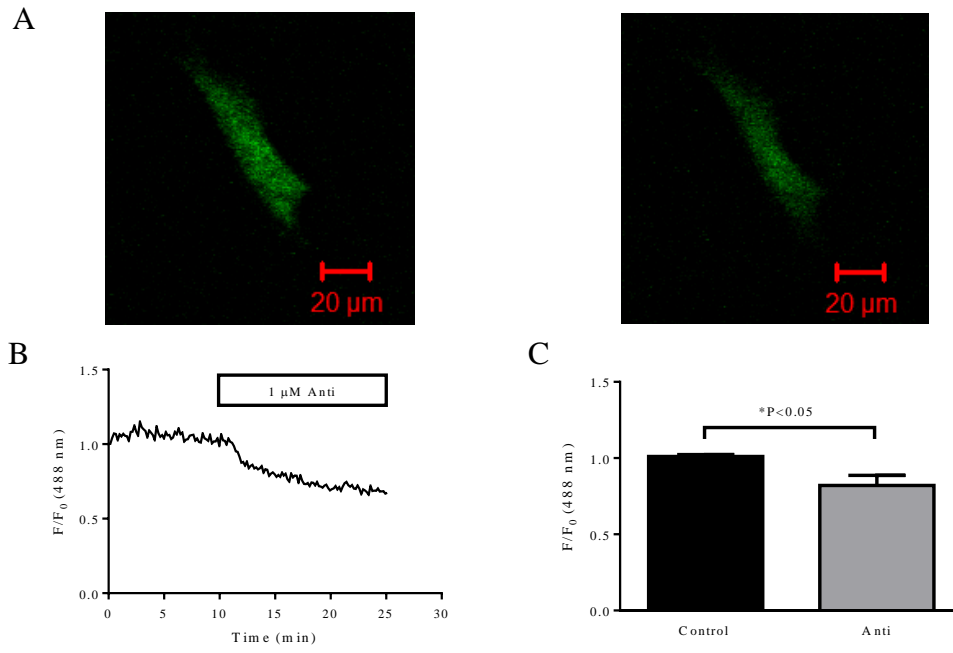


Figure 3.45: Effect of antimycin on ATP:ADP ratio signal. (A) Images of HCASMC expressing PercevalHR before (left) and after (right) application of 1 μM antimycin. (B) Time course of fractional fluorescence during antimycin application. (C) Mean \pm SEM of fractional fluorescence of PercevalHR before and after administration of antimycin (n=4).

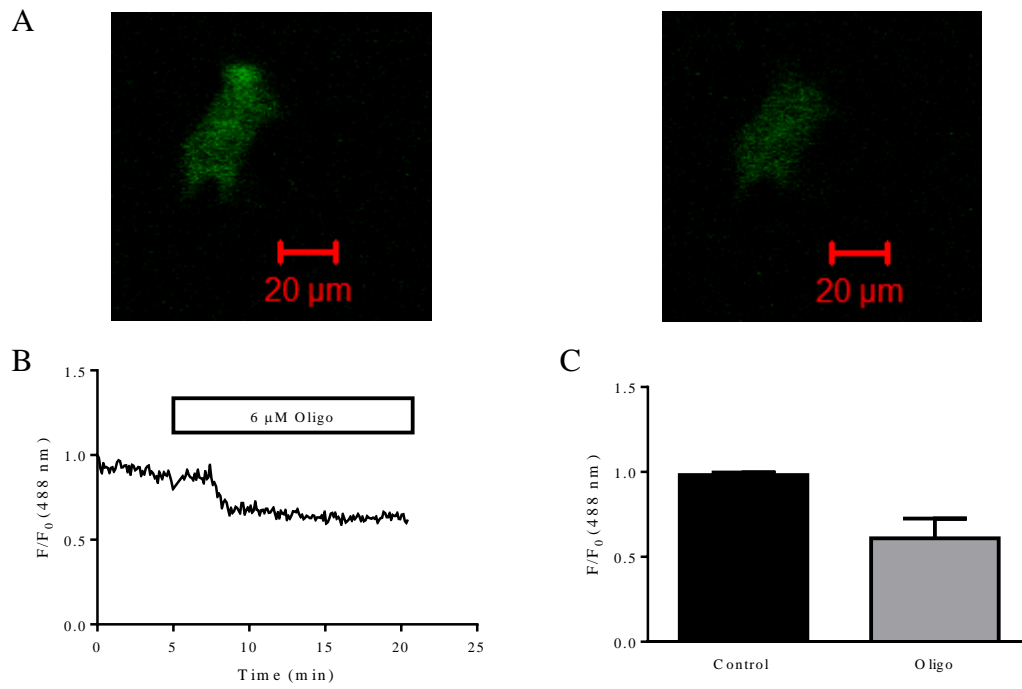


Figure 3.46: Effect of oligomycin on ATP:ADP ratio signal. (A) Images of HCASMC expressing PercevalHR before (left) and after (right) application of 6 μM oligomycin. (B) Time course of fractional fluorescence of the cell shown in (A). (C) Mean \pm SEM of fractional fluorescence of PercevalHR before and after administration of oligomycin (P=0.085, n=3).

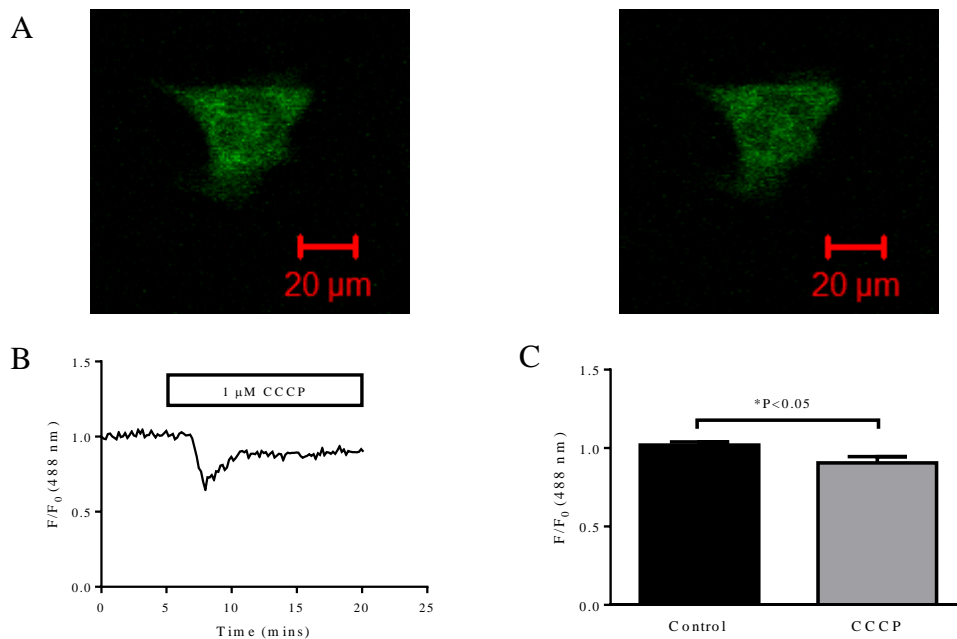


Figure 3.47: Effect of CCCP on ATP:ADP ratio signal. (A) Images of HCASMC before (left) and after (right) the application of 1 μM CCCP. (B) Time course of fractional fluorescence of the cell shown in (A). (C) Mean \pm SEM of fractional fluorescence before and after 15 mins administration of CCCP (n=3).

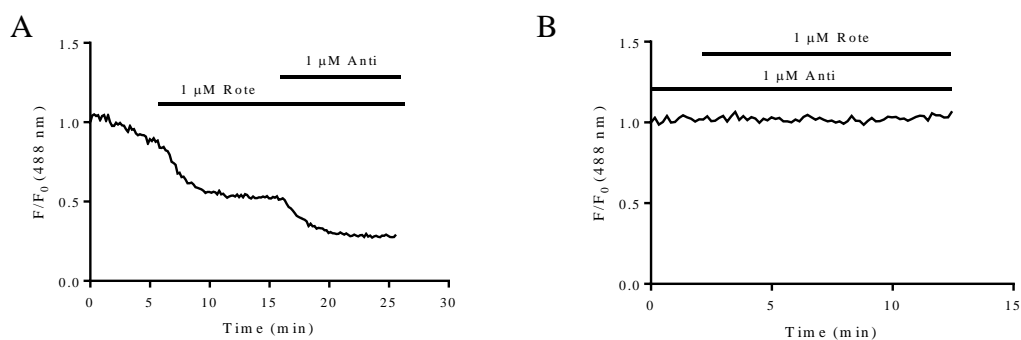


Figure 3.48: Effect of sequential application of rotenone and antimycin on ATP:ADP ratio signal. (A) Inhibiting complex I with rotenone then complex III with antimycin reduced the signal additively. This experiment was repeated twice (n=2). (B) The additive effect was not seen when the order was reversed. This experiment was repeated four times (n=4).

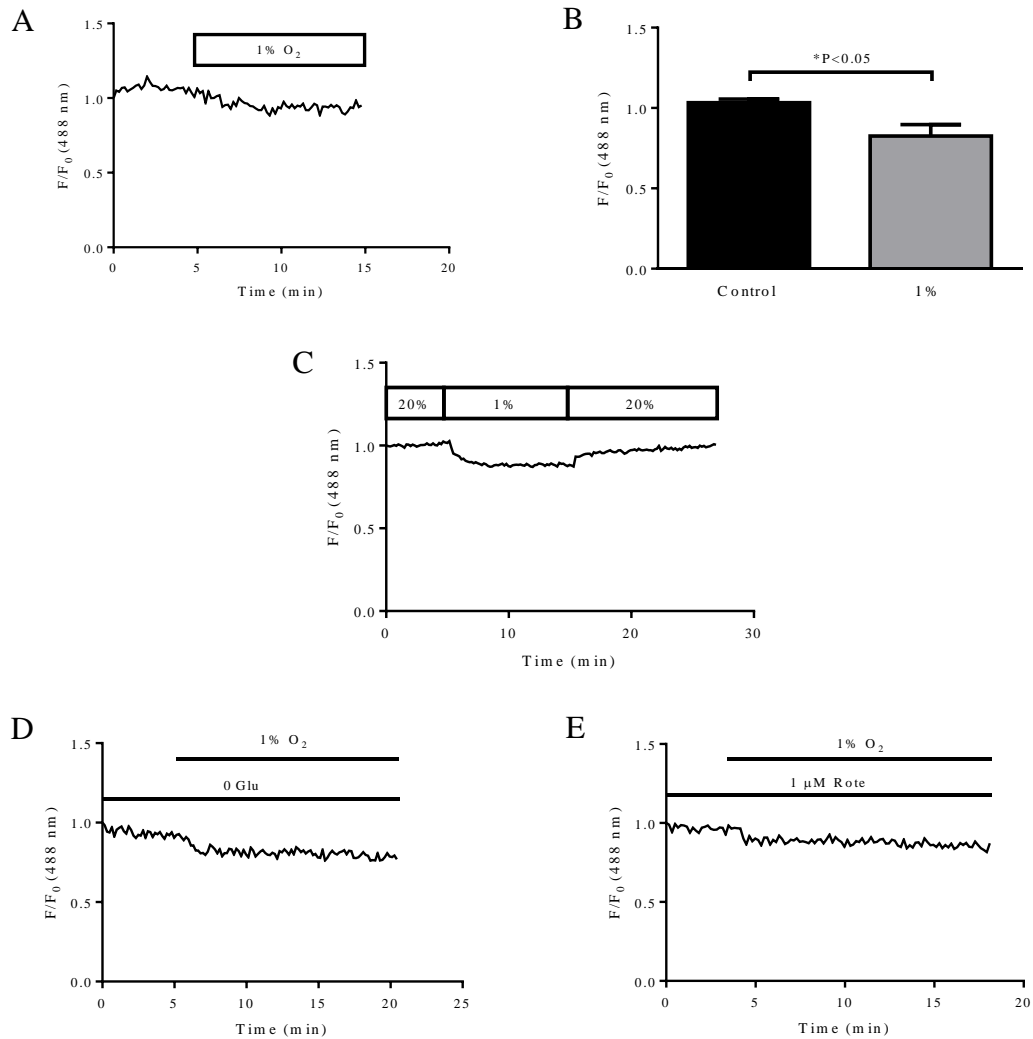


Figure 3.49: Effect of hypoxia on PercevalHR signal. Hypoxia decreased ATP:ADP ratio signal (A and B, n=4). The effect was reversible (C, n=3). Hypoxia (1% O₂) also caused a decrease in PercevalHR signal with 0 glucose (D, n=1) or cell pre-treated with rotenone (E, n=1).

3.4.4 Metabolic inhibition and mitochondrial membrane potential

3.4.4.1 Mitochondria and mitochondrial membrane potential

Mitochondria generate ATP by virtue of very negative mitochondrial inner membrane potential (~-200 mV). Thus, intervention that changes PercevalHR signal may do so by modulating mitochondrial membrane potential. Therefore, effect of hypoxia and metabolic inhibitors on mitochondrial membrane potential was investigated. First, the distribution pattern of mitochondria in HCASMCs was visualized using MitoTracker, a red-fluorescent dye that stains mitochondria in live

cells. Distribution of MitoTracker showed that HCASMCs are packed with mitochondria (**Figure 3.50**). As discussed earlier, ATP production by mitochondria is dependent on electrochemical motive force (ΔP). A compromised mitochondrial membrane potential will lead to the disruption of electron transport interrupting OXPHOS. Rhodamine123 was used to measure mitochondrial membrane potential. Rhodamine123 is a cell-permeant, cationic dye making it naturally accumulate in the mitochondria. Once accumulated, dye aggregation and quenching of the emission signal occurs. The release of the dye as a result of mitochondrial depolarization, on the other hand, results in unquenching and an increase in the fluorescence signal [195, 204, 205] (**Figure 3.51**). Therefore, the distribution of rhodamine123 closely correlates with the changes of the mitochondrial membrane potential. Except **Figure 3.51**, in which rhodamine123 signal in mitochondria and cytoplasm was measured separately, the changes of rhodamine123 signal in the rest of this chapter was measured by drawing a region of interest in the cells. Spontaneous oscillation of rhodamine123 signal in a very small number of HCASMCs was sometimes observed (data not shown).

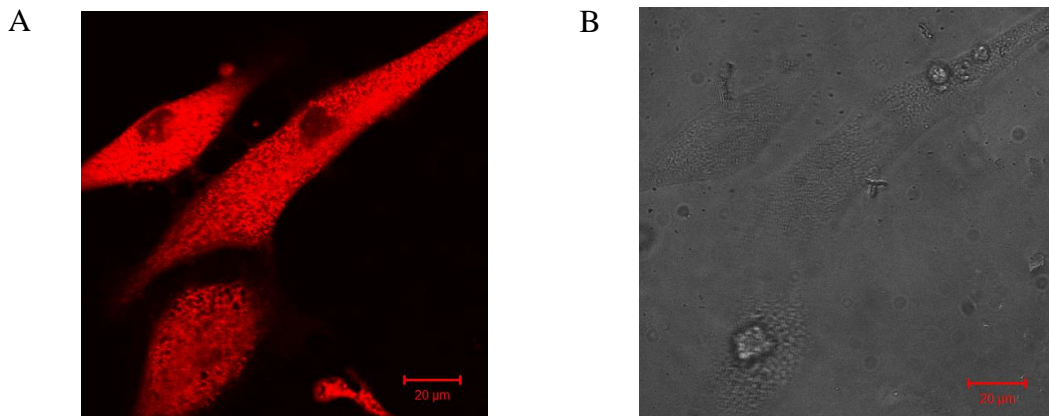


Figure 3.50: Staining mitochondrial with MitoTracker. (A) HCASMCs loaded with MitoTracker. (B) Brightfield.

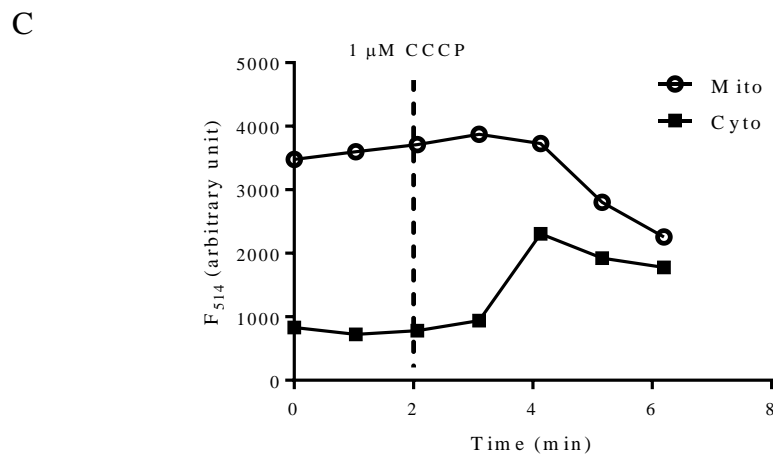
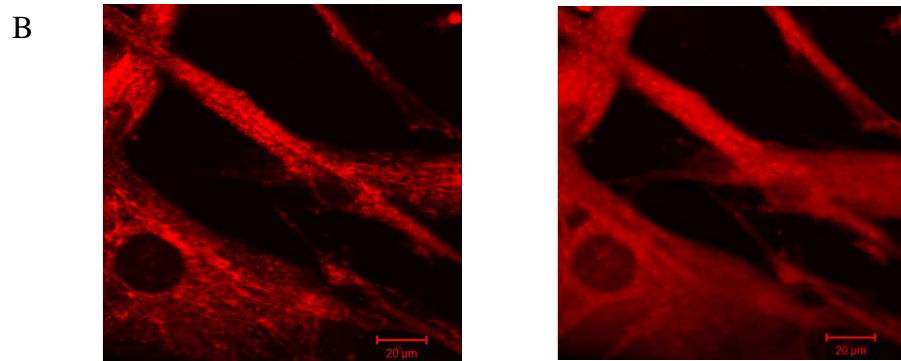
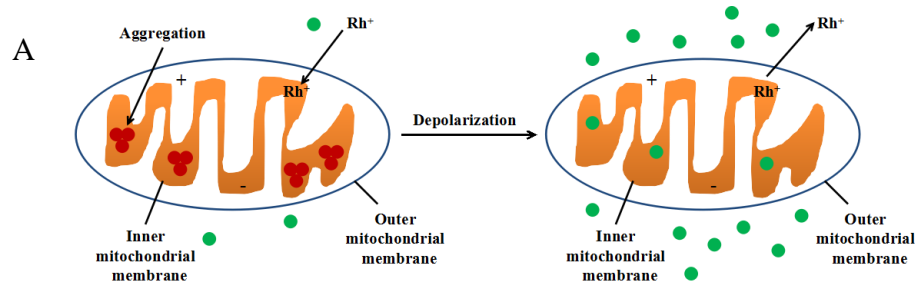


Figure 3.51: Measurement of mitochondrial membrane potential. (A) Schematic illustration of rhodamine123 aggregation in the mitochondria and its release due to mitochondrial depolarization (modified from: www.biotec.com). (B) 1 μ M CCCP caused depolarization of mitochondrial membrane potential, resulting in release of the dye from mitochondrial matrix (left image) to cytosol (right image) with subsequent unquenching of the dye and an increase in the signal. (C) Time course of rhodamine123 fluorescence intensity in cytosol and mitochondria matrix of the cell shown in (B).

3.4.4.2 Metabolic inhibition and mitochondrial membrane potential measured in 10 mM glucose PSS

Metabolic inhibition and hypoxia caused changes in cellular ATP:ADP ratio, this may be due to their effect on mitochondrial membrane potential. Therefore, we examined mitochondrial membrane potential during metabolic inhibition and hypoxia in PSS containing 10 mM glucose. DMSO induced little change in mitochondrial membrane potential (**Figure 3.52**). Rotenone was expected to increase rhodamine123 signal due to its inhibitory effect on mitochondrial complex I. However, application of 1 μM rotenone caused a decrease in rhodamine123 signal by $8.09 \pm 2.56\%$ (**Figure 3.53**). This change was unexpected (see discussion). 1 μM antimycin induced an increase in rhodamine123 signal by $66.52 \pm 16.57\%$ (**Figure 3.54**). 6 μM oligomycin increased rhodamine123 signal by $124.65 \pm 8.54\%$ (**Figure 3.55**). This unexpected change will be also discussed later. 1 μM CCCP increased signal by $176.76 \pm 13.28\%$ (**Figure 3.56**). Hypoxia (1% O₂) slightly increased rhodamine123 signal by $5.25 \pm 1.42\%$ (**Figure 3.57**). When two inhibitors were applied sequentially, antimycin depolarized mitochondrial membrane potential in the presence of rotenone, and rotenone slightly decreased rhodamine123 signal in the presence of oligomycin. Both antimycin and CCCP caused further mitochondrial membrane depolarization in the presence of oligomycin (**Figure 3.58**). Hypoxia had no effect on rhodamine123 signal in the presence of oligomycin, but it reduced rhodamine123 signal of the cells pre-treated with CCCP and CCCP plus oligomycin (**Figure 3.59**).

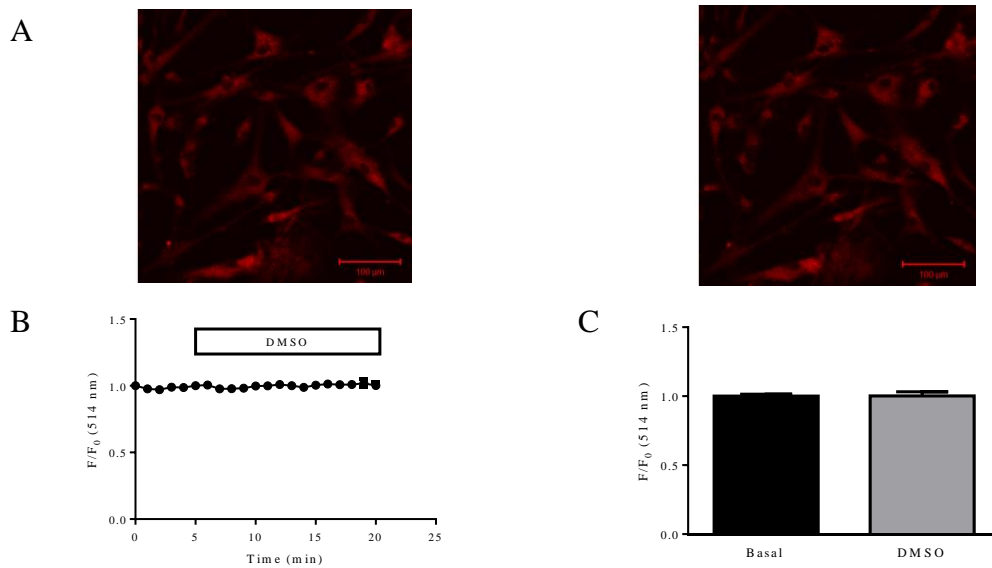


Figure 3.52: Effect of DMSO on mitochondrial membrane potential of cells kept in 10 mM glucose PSS. (A) Images of rhodamine123 signal in HCASMCs before (left) and after (right) application of DMSO. (B) Time course of fractional fluorescence. (C) Mean \pm SEM of fractional fluorescence before and after administration of DMSO (n=17).

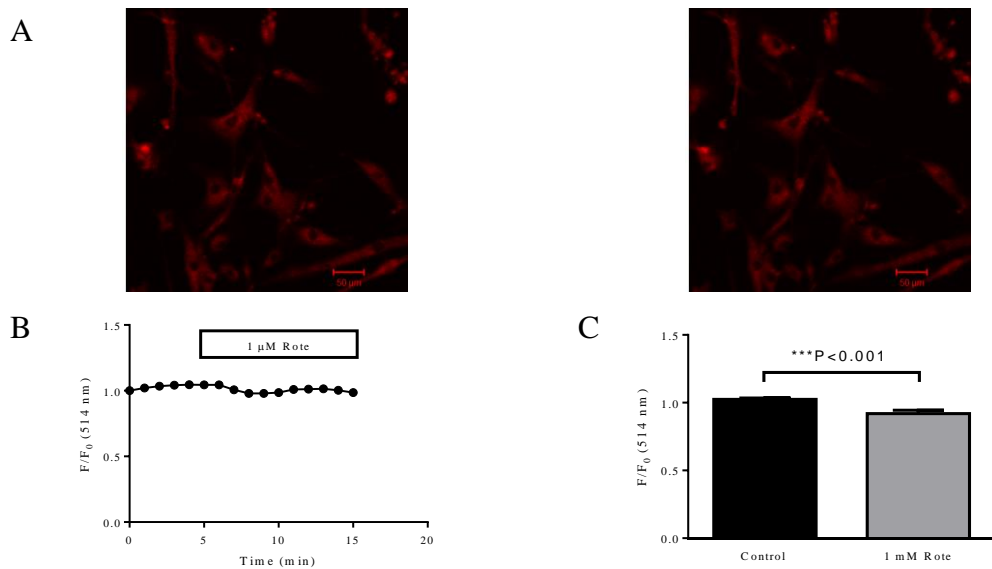


Figure 3.53: Effect of rotenone on mitochondrial membrane potential. (A) Images of rhodamine123 signal in HCASMCs before (left) and after (right) the application of rotenone. (B) Time course of fractional fluorescence of cells shown in (A). (C) Mean \pm SEM of fractional fluorescence of rhodamine123 before and after administration of rotenone (n=19).

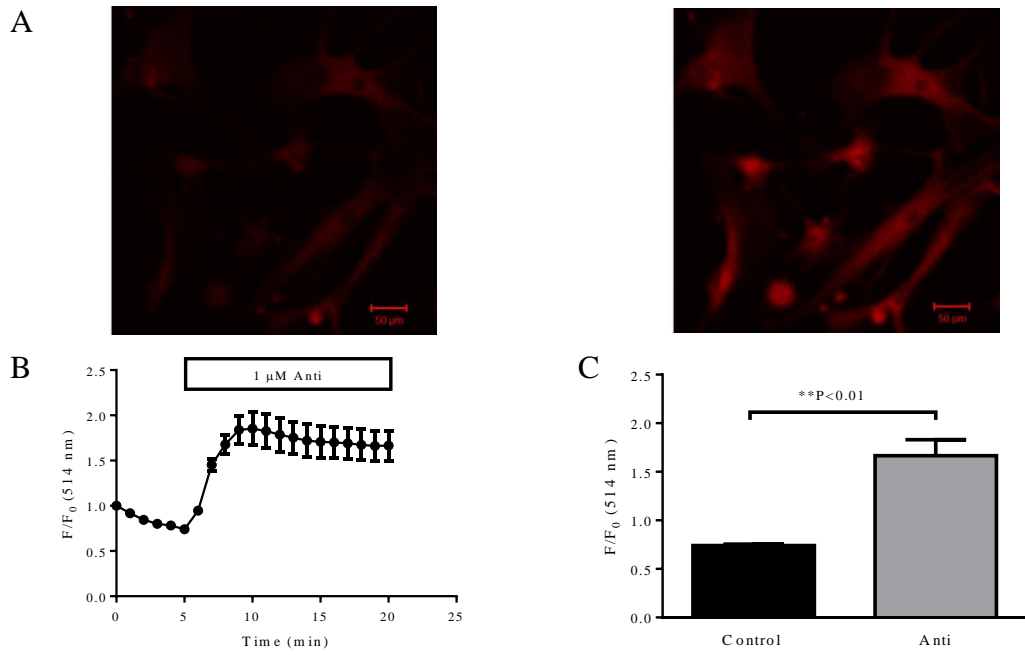


Figure 3.54: Effect of antimycin on mitochondrial membrane potential. (A) Images of rhodamine123 signal in HCASMCs before (left) and after (right) application of antimycin. (B) Time course of fractional fluorescence of cells shown in (A). (C) Mean \pm SEM of fractional fluorescence before and after administration of antimycin (n=9).

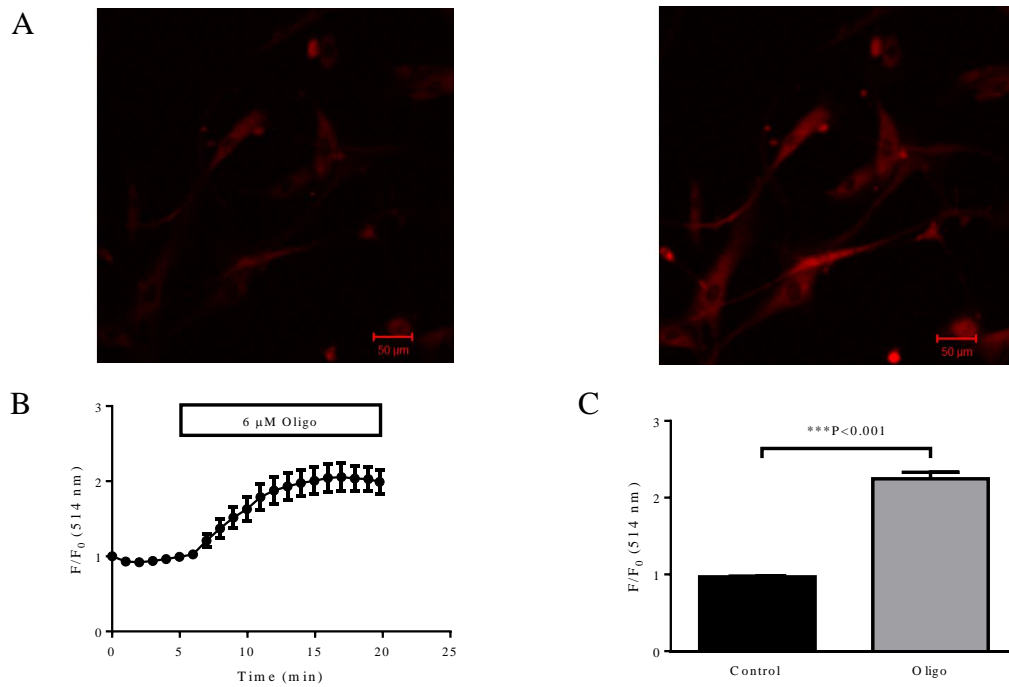


Figure 3.55: Effect of oligomycin on mitochondrial membrane potential. (A) Images of HCASMCs before (left) and after (right) the application of oligomycin. **(B)** Time course of fractional fluorescence of cells shown in (A). **(C)** Mean \pm SEM of fractional fluorescence before and after administration of oligomycin (n=81).

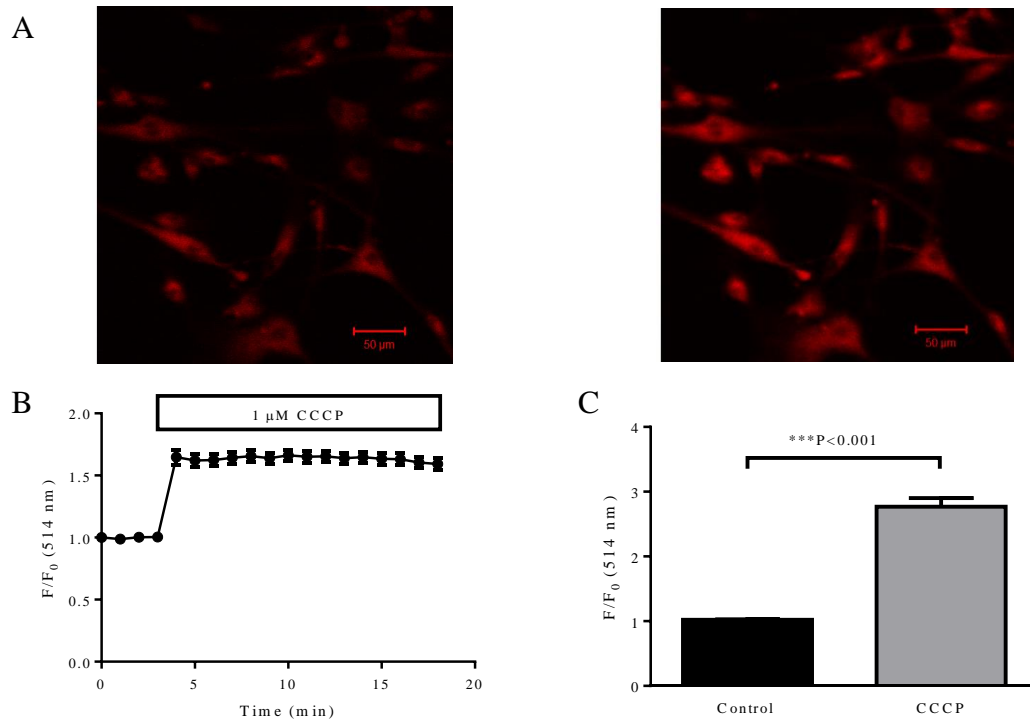


Figure 3.56: Effect of CCCP on mitochondrial membrane potential. (A) Images of HCASMCs before (left) and after (right) the application of CCCP. (B) Time course of fractional fluorescence of cells shown in (A). (C) Mean \pm SEM of fractional fluorescence before and after administration of CCCP (n=92).

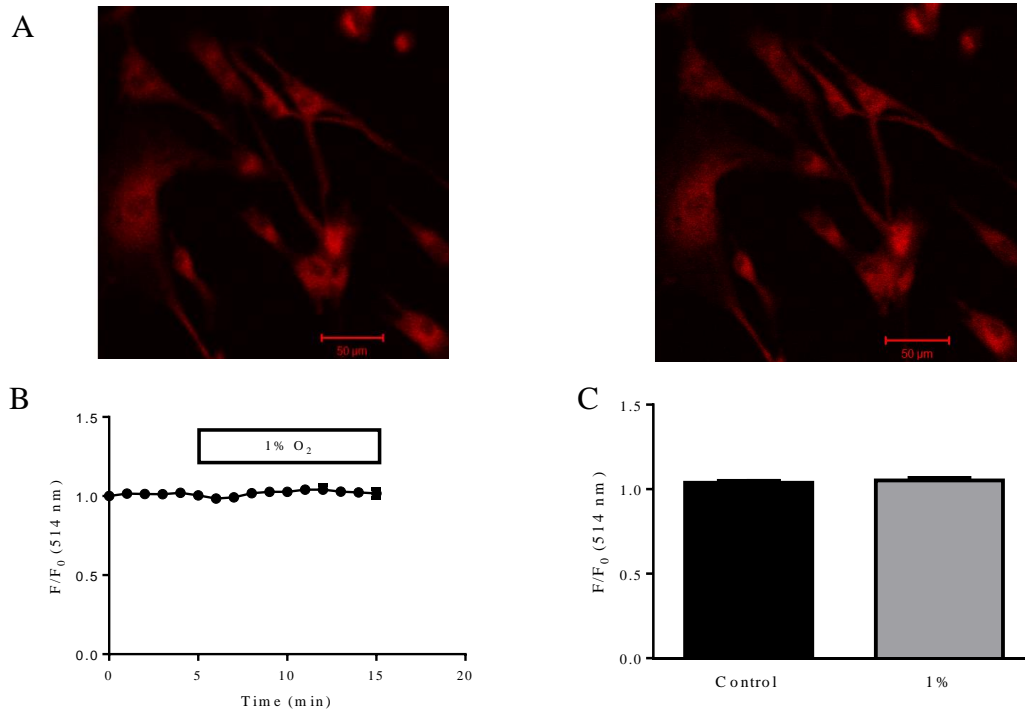


Figure 3.57: Effect of hypoxia on mitochondrial membrane potential. (A) Images of rhodamine123 signal in HCASMCs under control conditions (left) and exposure to hypoxia (right). (B) Time course of fractional fluorescence of cells shown in (A). (C) Mean \pm SEM of fractional fluorescence before and after hypoxia ($P=0.109$, $n=103$).

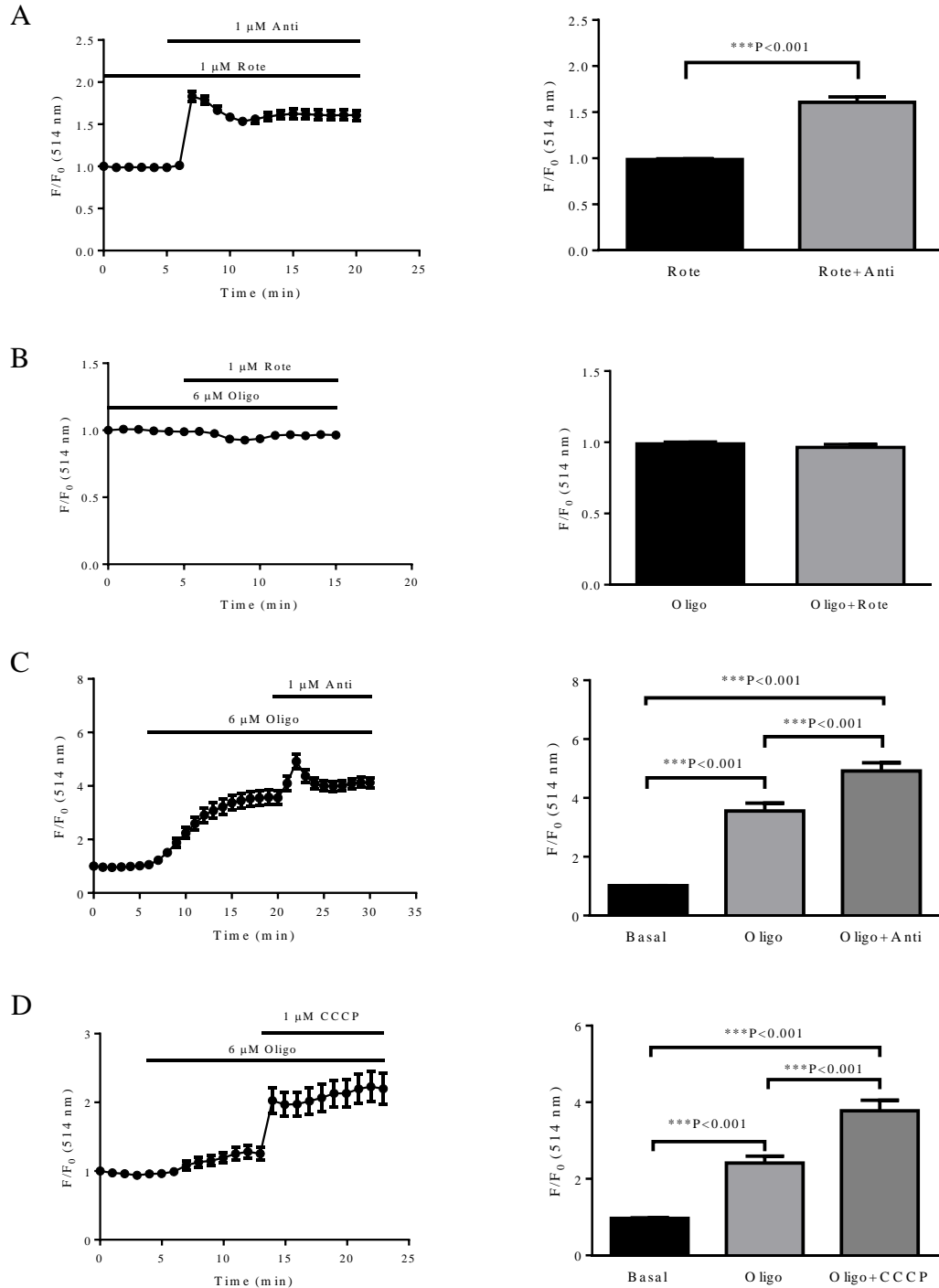


Figure 3.58: Effect of metabolic inhibitors on mitochondrial membrane potential. Application of antimycin in the presence of rotenone caused mitochondrial membrane potential depolarization (A, n=21). Effect of rotenone was inhibited in the presence of oligomycin (B, n=21). Antimycin and CCCP further depolarized mitochondrial membrane potential of the cells pre-treated with oligomycin (C and D, n=12 and 25 respectively).

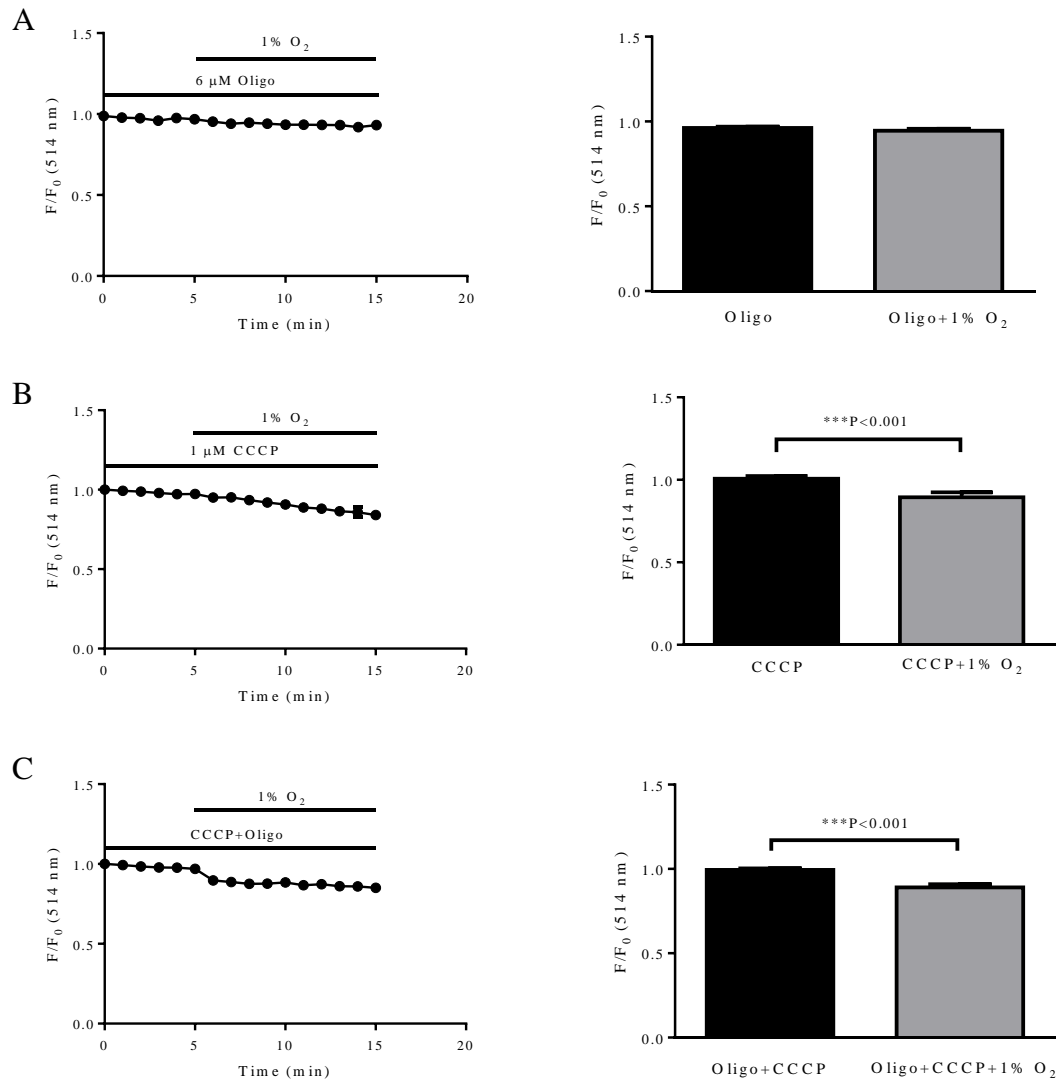


Figure 3.59: Effect of hypoxia on mitochondrial membrane potential in the presence of metabolic inhibitors. Hypoxia had no effect on mitochondrial membrane potential of the cells pre-treated with oligomycin (A, n=18). Hypoxia significantly reduced the fractional fluorescence in the presence of CCCP (B, n=17) and in the combination of CCCP and oligomycin (C, n=21).

3.4.4.2 Metabolic inhibition and mitochondrial membrane potential measured in $60K^+$ PSS

In the previous section, 1 μ M rotenone and 6 μ M oligomycin caused unexpected changes in rhodamine123 signal, and this may be due to an effect from plasma membrane potential. Previous studies have suggested that the uptake of mitochondrial membrane potential dyes including rhodamine123 is also dependent

on plasma membrane potential [206, 207]. If this is the case, then detected change in rhodamine123 signal may be due, in part, changes in plasma membrane potential. We therefore increased the extracellular K^+ concentration to 60 mM in order to largely eliminate the effect of plasma membrane potential. When $[K^+]_o$ is elevated from 5 mM to 60 mM by replacing equimolar Na^+ , potassium equilibrium potential (E_K) shifts from -88.7 mV to a more positive value of -21.1 mV. In 60 mM $[K^+]_o$ there is little net flux of K^+ across plasma membrane, eliminating possible influence of plasma membrane potential on rhodamine123 signal. Both time control and vehicle control showed no change in rhodamine123 signal in the presence of 60 mM K^+ (**Figure 3.60 and 3.61**). Rhodamine123 signal increased by $37.80 \pm 8.39\%$ after application of 1 μ M rotenone (**Figure 3.62**), $90.18 \pm 13.05\%$ after application of 1 μ M antimycin (**Figure 3.63**) and $108.29 \pm 18.63\%$ at the peak after treatment with 1 μ M CCCP (**Figure 3.65**). 6 μ M oligomycin caused a reduction in rhodamine123 signal by $11.81 \pm 4.44\%$ (**Figure 3.64**). Hypoxia (1% O_2) induced a negligible increase in rhodamine123 signal ($\sim 0.05\%$) in experiments from 4 dishes (**Figure 3.66**), but increased the signal from one dish by $17.99 \pm 2.34\%$ ($n=15$, data not shown). Inhibition of complex I with rotenone followed by inhibition of complex III with antimycin caused additive increase in rhodamine123 signal. Inhibition of complex III with antimycin in the presence of oligomycin still increased rhodamine123 signal (**Figure 3.67**). Rhodamine123 signal increase due to application of oligomycin and antimycin was additive regardless of the order of applications (**Figure 3.68**). So, the distribution of rhodamine123 was also affected by plasma membrane potential, and this effect could be eliminated by elevating $[K^+]_o$ to 60 mM.

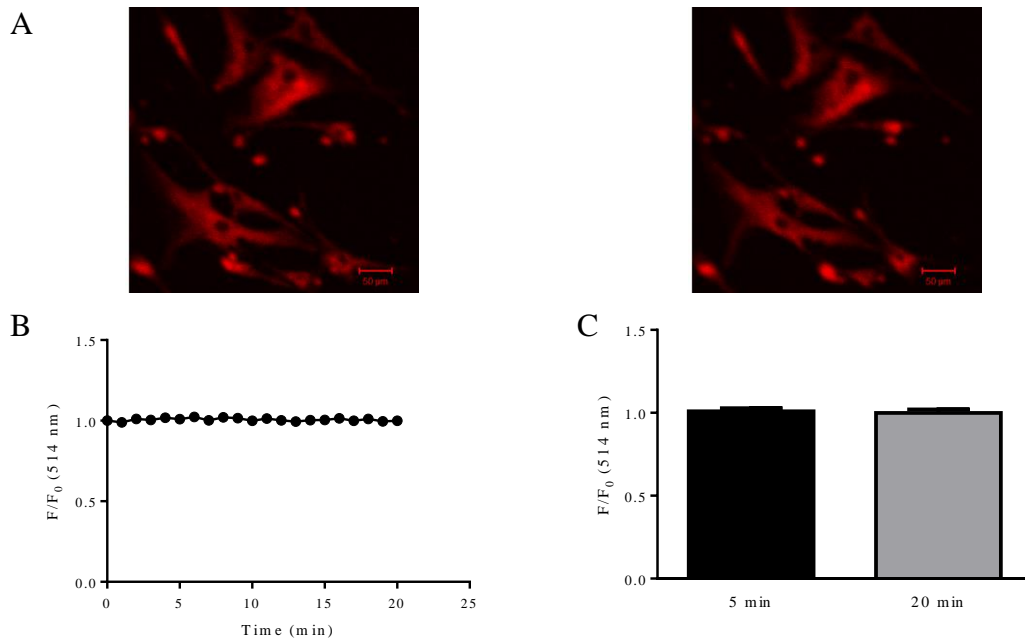


Figure 3.60: Time control of mitochondrial membrane potential signal in $60K^+$ PSS. Recording of 20 minutes showed no change in rhodamine123 signal (n=7).

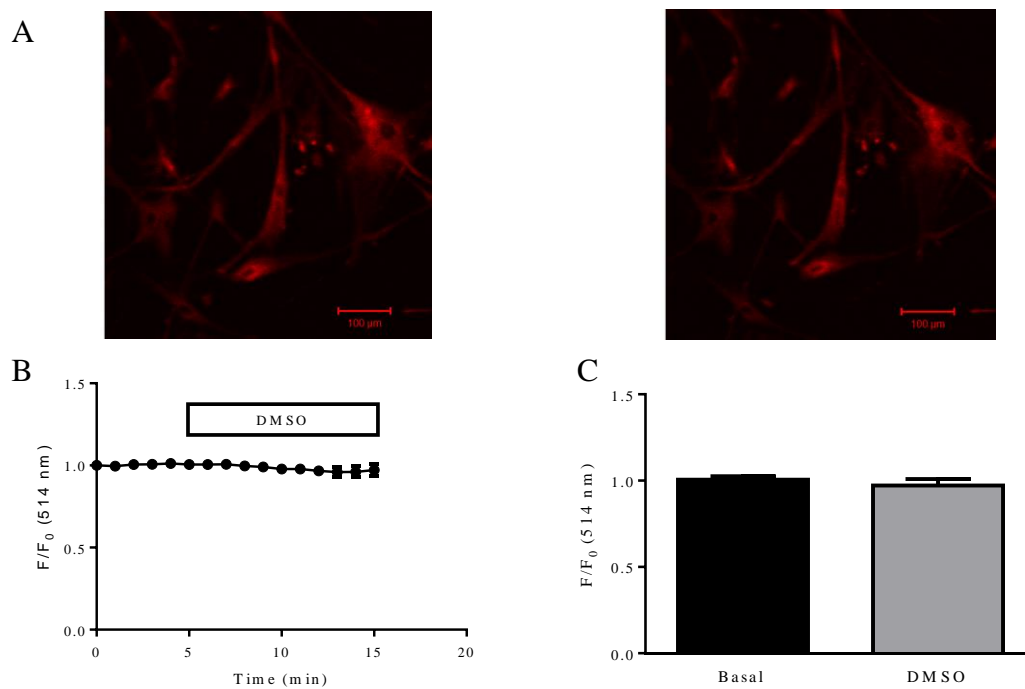


Figure 3.61: Vehicle control of mitochondrial membrane potential signal in $60K^+$ PSS. (A) Images of rhodamine123 signal in HCASMCs before (left) and after (right) the application of DMSO. (B) Time course of fractional fluorescence of the cells shown in (A). (C) Mean \pm SEM of fractional fluorescence of rhodamine123 before and after administration of DMSO (n=11).

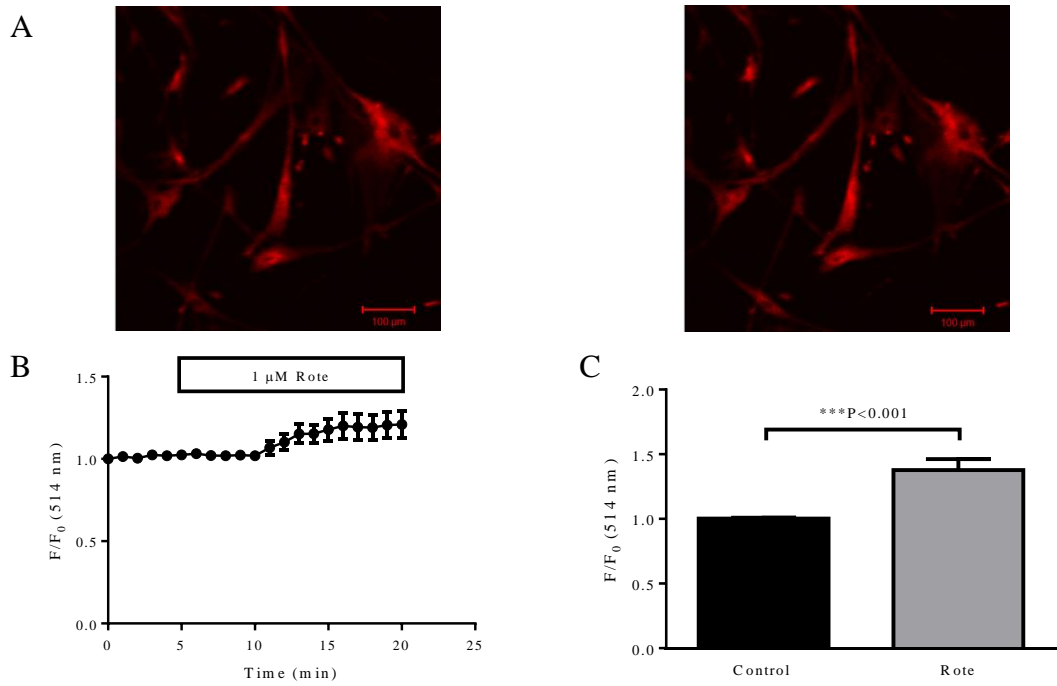


Figure 3.62: Effect of rotenone on mitochondrial membrane potential in 60K⁺ PSS. (A) Images of rhodamine123 signal in HCASMCs before (left) and after (right) the application of rotenone. (B) Time course of fractional fluorescence of the cells shown in (A). (C) Mean \pm SEM of fractional fluorescence of rhodamine123 before and after administration of rotenone (n=33).

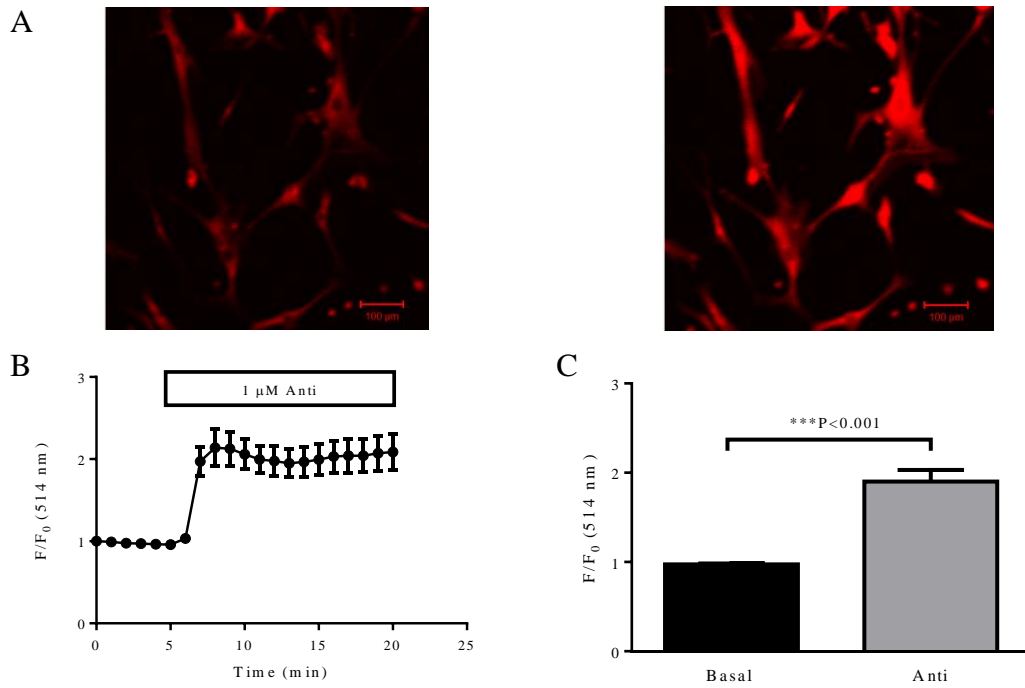


Figure 3.63: Effect of antimycin on mitochondrial membrane potential in 60K⁺ PSS. (A) Images of rhodamine123 signal in HCASMCs before (left) and after (right) the application of antimycin. (B) Time course of fractional fluorescence of the cells shown in (A). (C) Mean \pm SEM of fractional fluorescence of rhodamine123 before and after administration of antimycin (n=30).

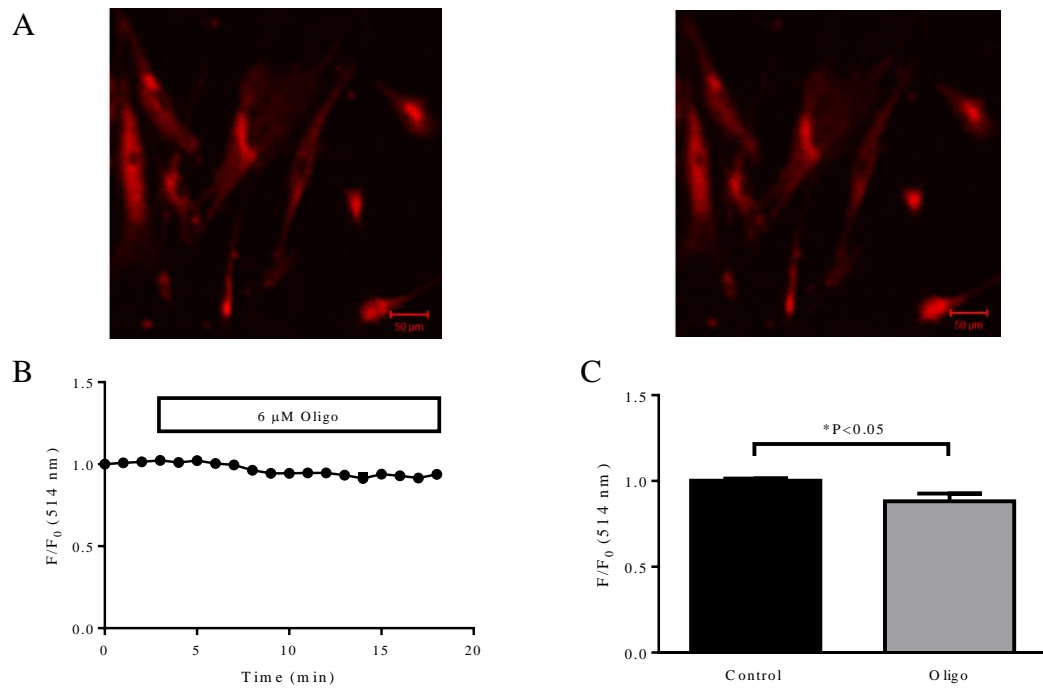


Figure 3.64: Effect of oligomycin on mitochondrial membrane potential in 60K⁺ PSS. (A) Images of rhodamine123 signal in HCASMCs before (left) and after (right) the application of oligomycin. (B) Time course of fractional fluorescence of the cells shown in (A). (C) Mean \pm SEM of fractional fluorescence of rhodamine123 before and after administration of oligomycin (n=16).

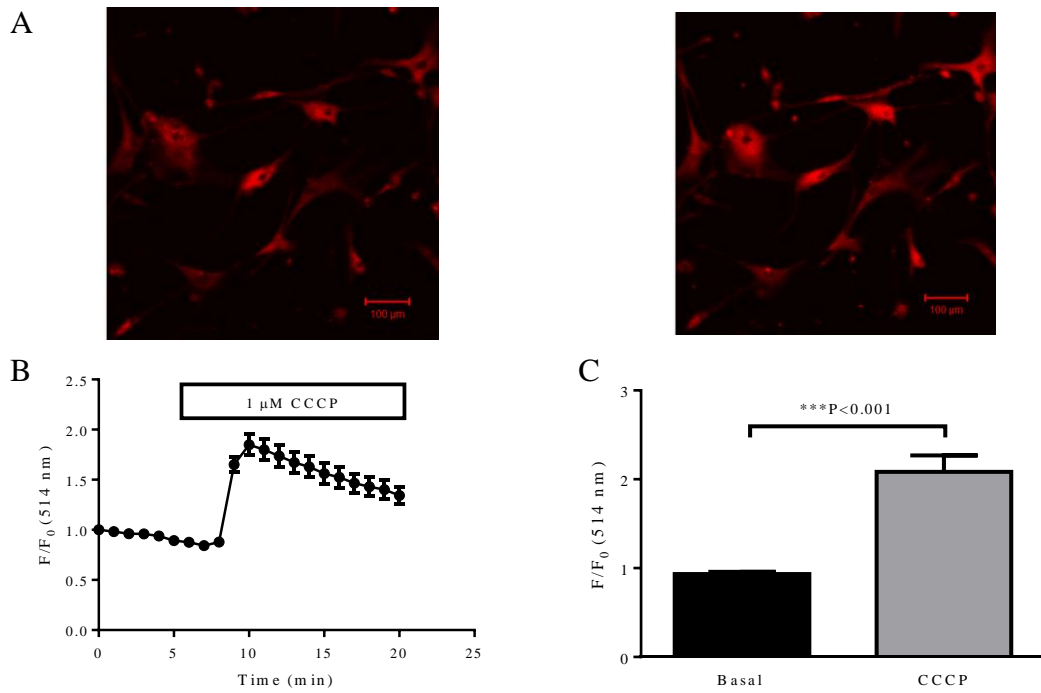


Figure 3.65: Effect of CCCP on mitochondrial membrane potential in 60K⁺ PSS.

(A) Images of rhodamine123 signal in HCASMCs before (left) and after (right) application of CCCP. (B) Time course of fractional fluorescence of the cells shown in (A). (C) Mean \pm SEM of fractional fluorescence of rhodamine123 before and at the peak after application of CCCP (n=17).

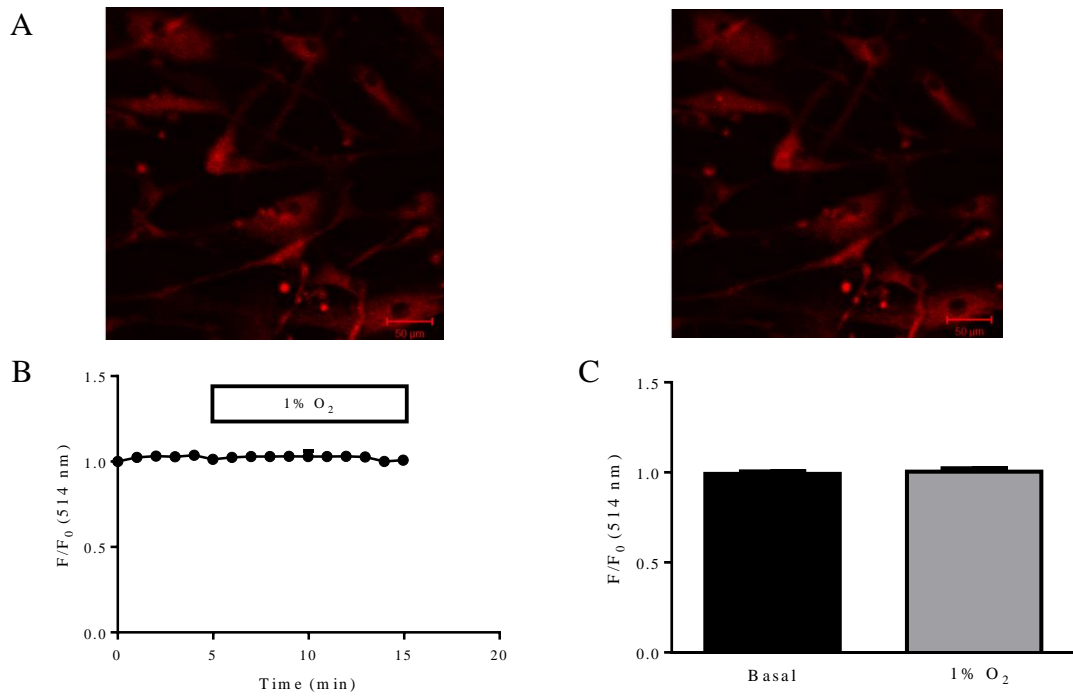


Figure 3.66: Effect of hypoxia on mitochondrial membrane potential in 60K⁺ PSS. (A) Images of rhodamine123 signal in HCASMCs under control condition (left) and hypoxia (right). (B) Time course of fractional fluorescence of the cells shown in (A). (C) Mean \pm SEM of fractional fluorescence of rhodamine123 before and after hypoxia (n=29).

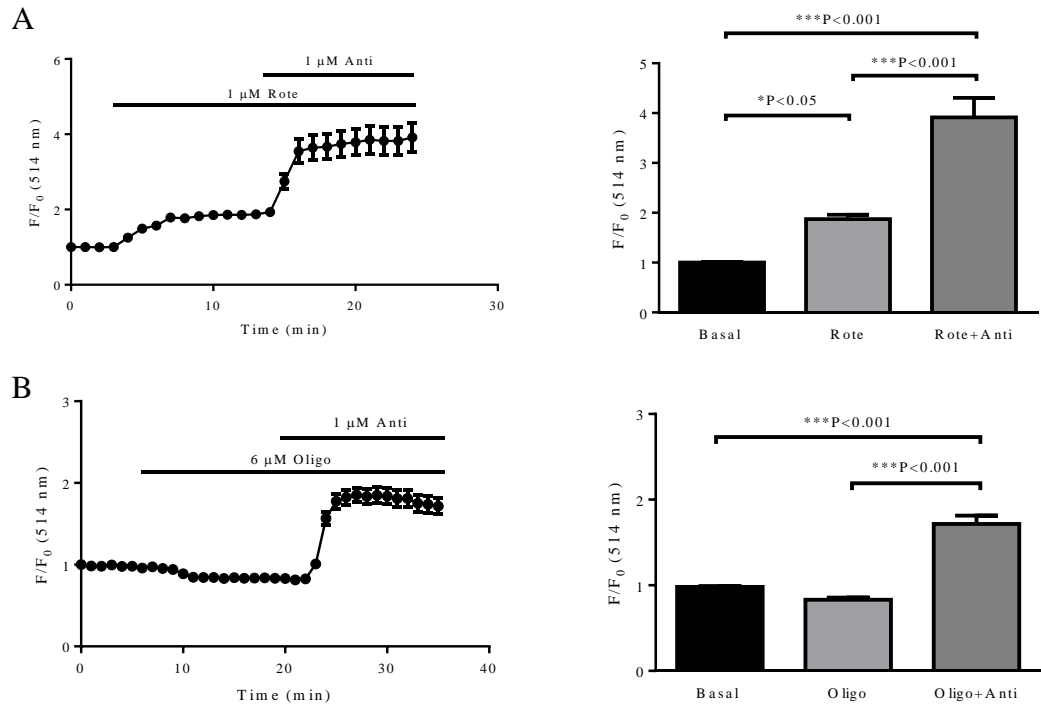


Figure 3.67: Effect of sequential application of metabolic inhibitors on mitochondrial membrane potential in $60K^+$ PSS. (A) Application of antimycin in the presence of rotenone caused a further increase in rhodamine123 signal (n=13). (B) In the cells pre-treated with oligomycin, antimycin increased the signal (n=18).

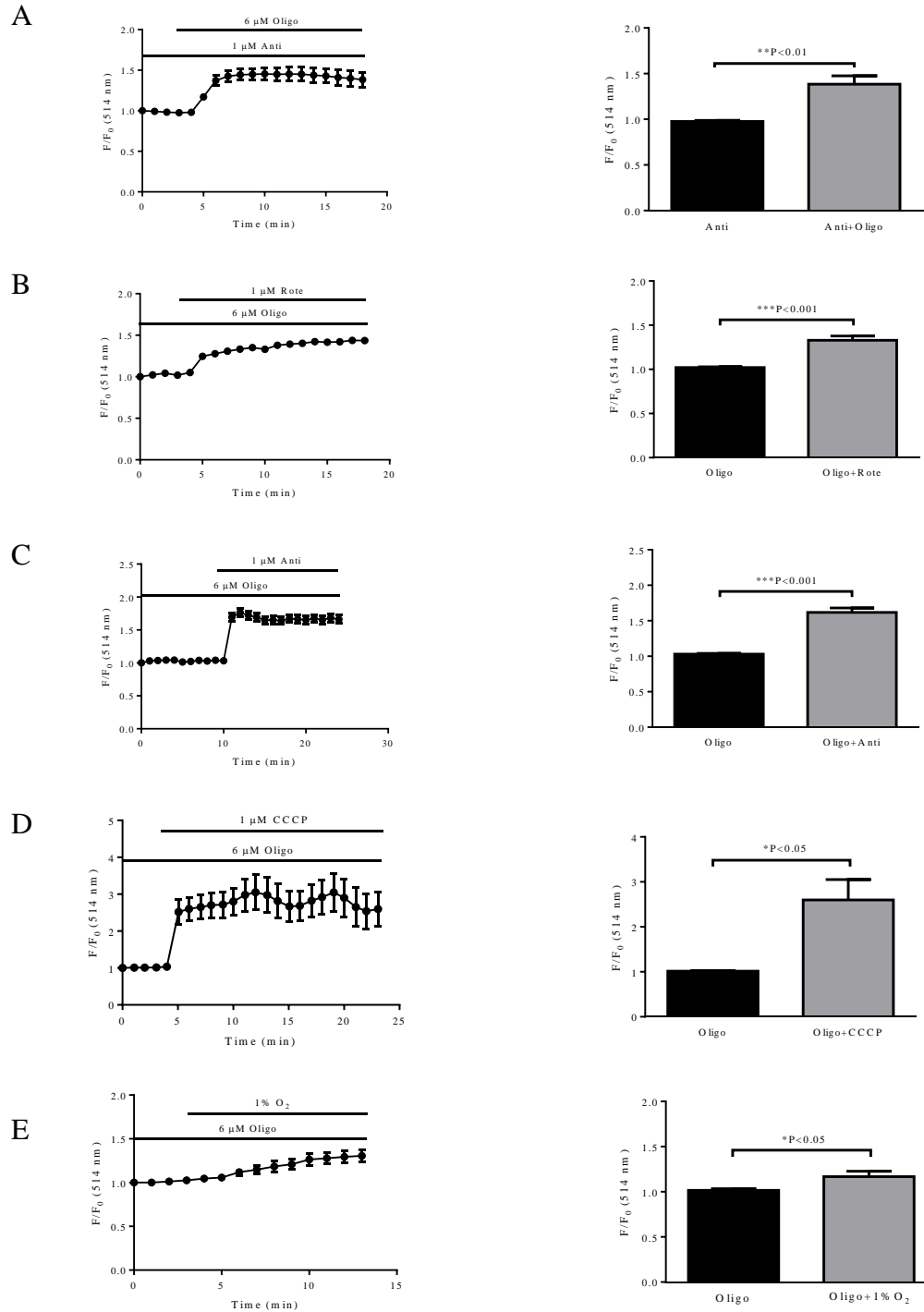


Figure 3.68: Effect of combined application of metabolic inhibitors on mitochondrial membrane potential signal in 60K⁺ PSS. Oligomycin caused an increase in mitochondrial membrane potential signal in the presence of antimycin (A, n=11). Rotenone (B, n=19), antimycin (C, n=14), CCCP (D, n=4) and hypoxia (E, n=17) caused an increase in rhodamine123 signal in the presence of oligomycin.

3.4.4.3 Metabolic inhibition and mitochondrial membrane potential measured in 0 mM glucose PSS

Removing glucose would reduce energy content of cells, so may unmask hypoxic/metabolic effects on mitochondrial membrane potential. Furthermore, hypoglycemia increases cardiovascular risks due to its effect on mitochondrial membrane potential and mitochondrial ROS production [208, 209]. We therefore characterized the effect of metabolic stress on mitochondrial membrane potential in the absence of extracellular glucose. Different from that in 10 mM glucose PSS, 1 μ M rotenone increased rhodamine123 signal by $35.03 \pm 6.35\%$ (**Figure 3.69**). 1 μ M antimycin increased rhodamine123 signal by $83.40 \pm 5.54\%$ (**Figure 3.70**). Different from the result using 10 mM glucose PSS, 6 μ M oligomycin decreased rhodamine123 signal by $29.34 \pm 3.86\%$ (**Figure 3.71**). 1 μ M CCCP increased signal by $115.18 \pm 14.73\%$ (**Figure 3.72**). Exposure to hypoxia (1% O₂) for 10 minutes increased rhodamine123 signal from $106.22 \pm 1.68\%$ to $110.25 \pm 3.38\%$ (**Figure 3.73**), suggesting an inhibition of electron transport chain. The data also showed that antimycin increased the signal in the presence of rotenone, and that hypoxia caused an increase and decrease in rhodamine123 signal in the presence of oligomycin and CCCP, respectively (**Figure 3.74**). All the results observed were as expected. The inconsistency of some effects from those in 10 mM glucose PSS could be explained by a glucose-dependent effect on the outside (plasma) membrane potential due to ATP depletion. These results also indirectly suggested HCASMCs used in the experiments rely largely on ATP generation through OXPHOS.

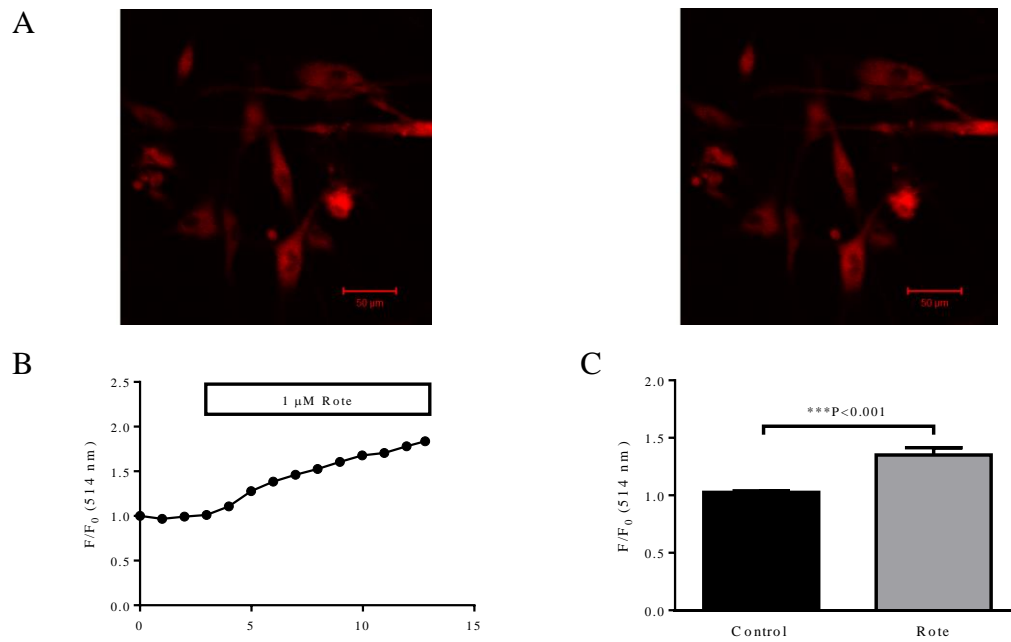


Figure 3.69: Depolarization of mitochondrial membrane potential by rotenone in 0 mM glucose PSS. (A) Images of HCASMCs before (left) and after (right) application of rotenone. (B) Time course of fractional fluorescence of cells shown in (A). (C) Mean \pm SEM of fractional fluorescence before and after rotenone (n=50).

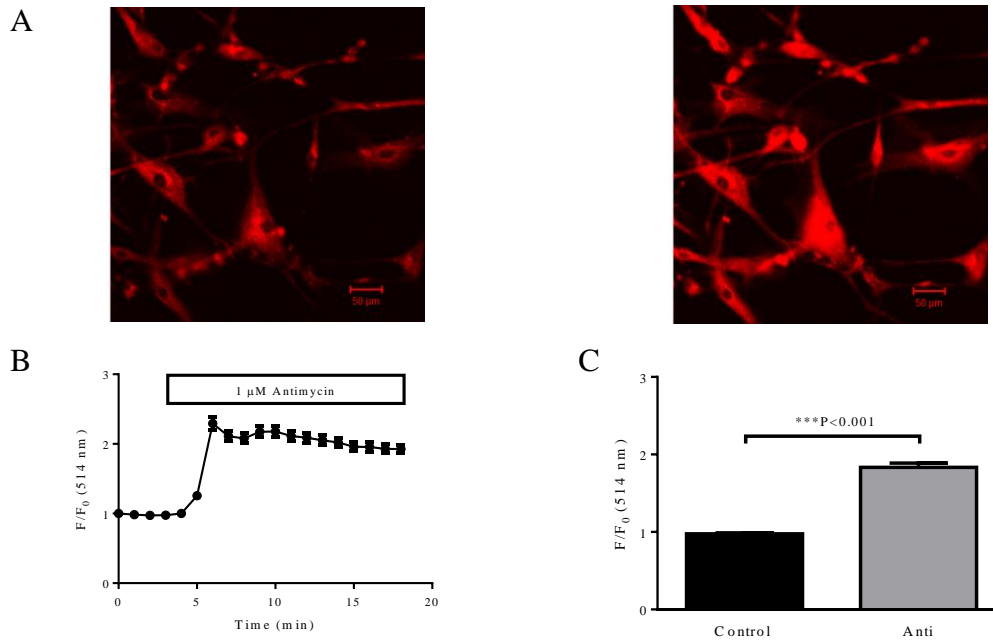


Figure 3.70: Depolarization of mitochondrial membrane potential by antimycin in 0 mM glucose PSS. (A) Images of HCASMCs before (left) and after (right) application of antimycin. (B) Time course of fractional fluorescence of cells shown in (A). (C) Mean \pm SEM of fractional fluorescence before and after antimycin (n=48).

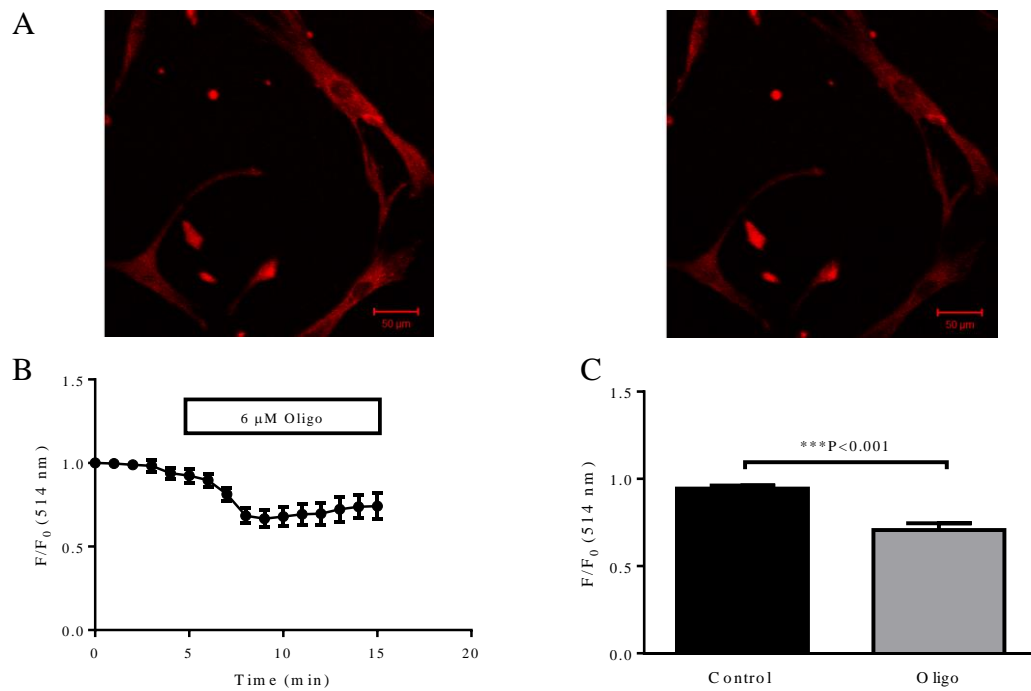


Figure 3.71: Hyperpolarization of mitochondrial membrane potential by oligomycin in 0 mM glucose PSS. (A) Images of HCASMCs before (left) and after (right) application of oligomycin. (B) Time course of fractional fluorescence of cells shown in (A). (C) Mean \pm SEM of fractional fluorescence before and after oligomycin (n=30).

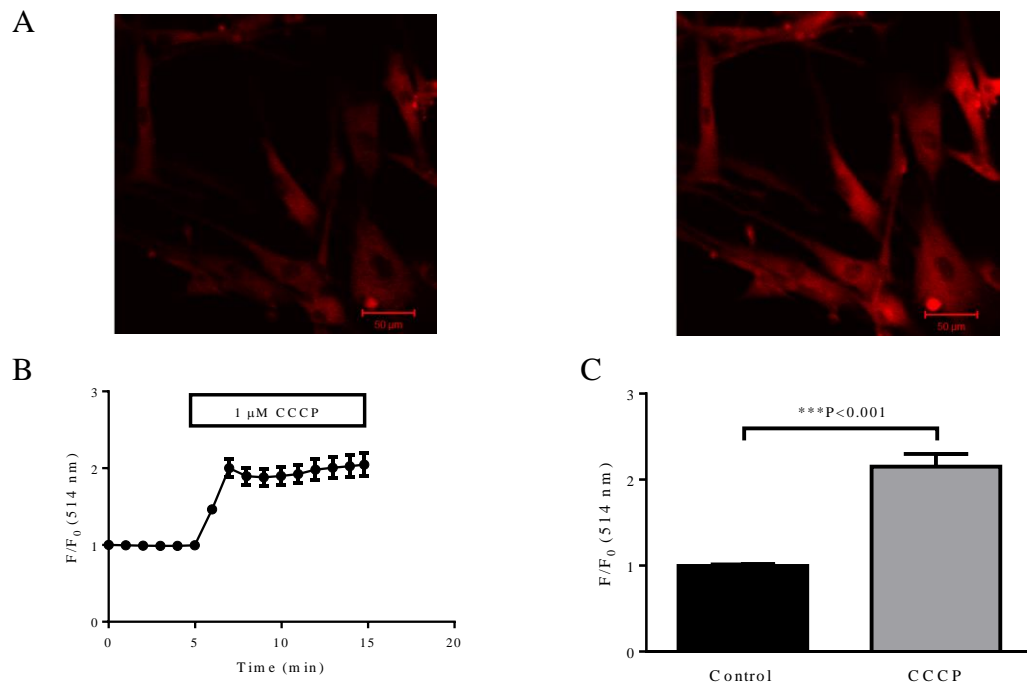


Figure 3.72: Depolarization of mitochondrial membrane potential by CCCP in 0 mM glucose PSS. (A) Images of HCASMCs before (left) and after (right) application of CCCP. (B) Time course of fractional fluorescence of cells shown in (A). (C) Mean \pm SEM of fractional fluorescence before and after CCCP (n=23).

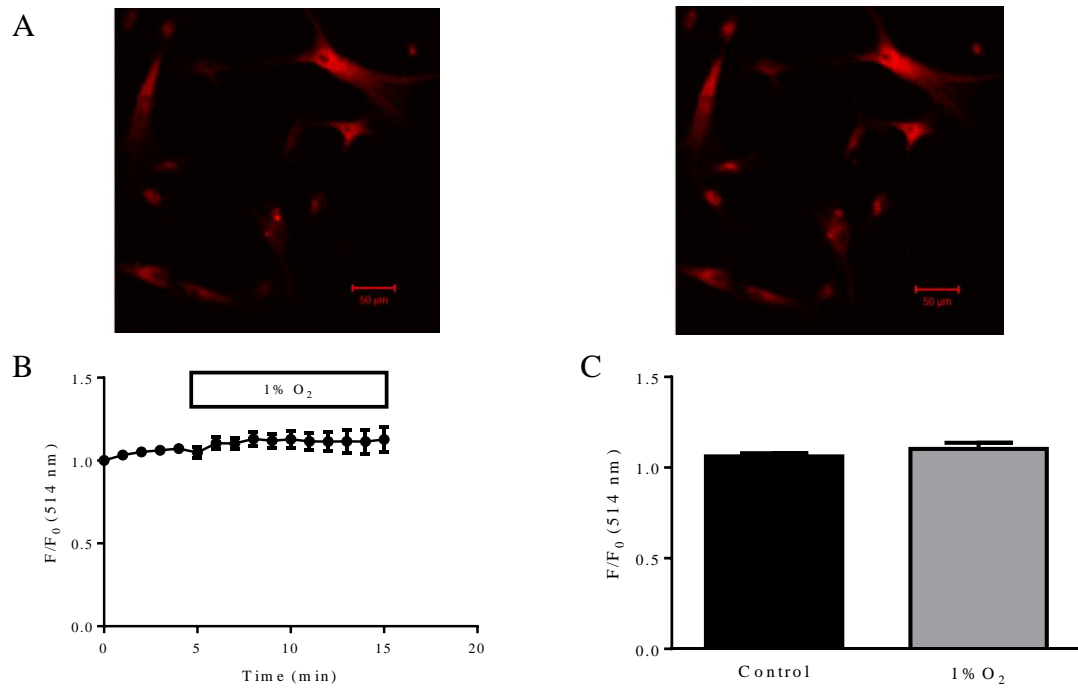


Figure 3.73: Effect of hypoxia on mitochondrial membrane potential in 0 mM glucose PSS. (A) Images of HCASMCs before (left) and during hypoxia (right). (B) Time course of fractional fluorescence of cells shown in (A). (C) Mean \pm SEM of fractional fluorescence before and after hypoxia (n=25).

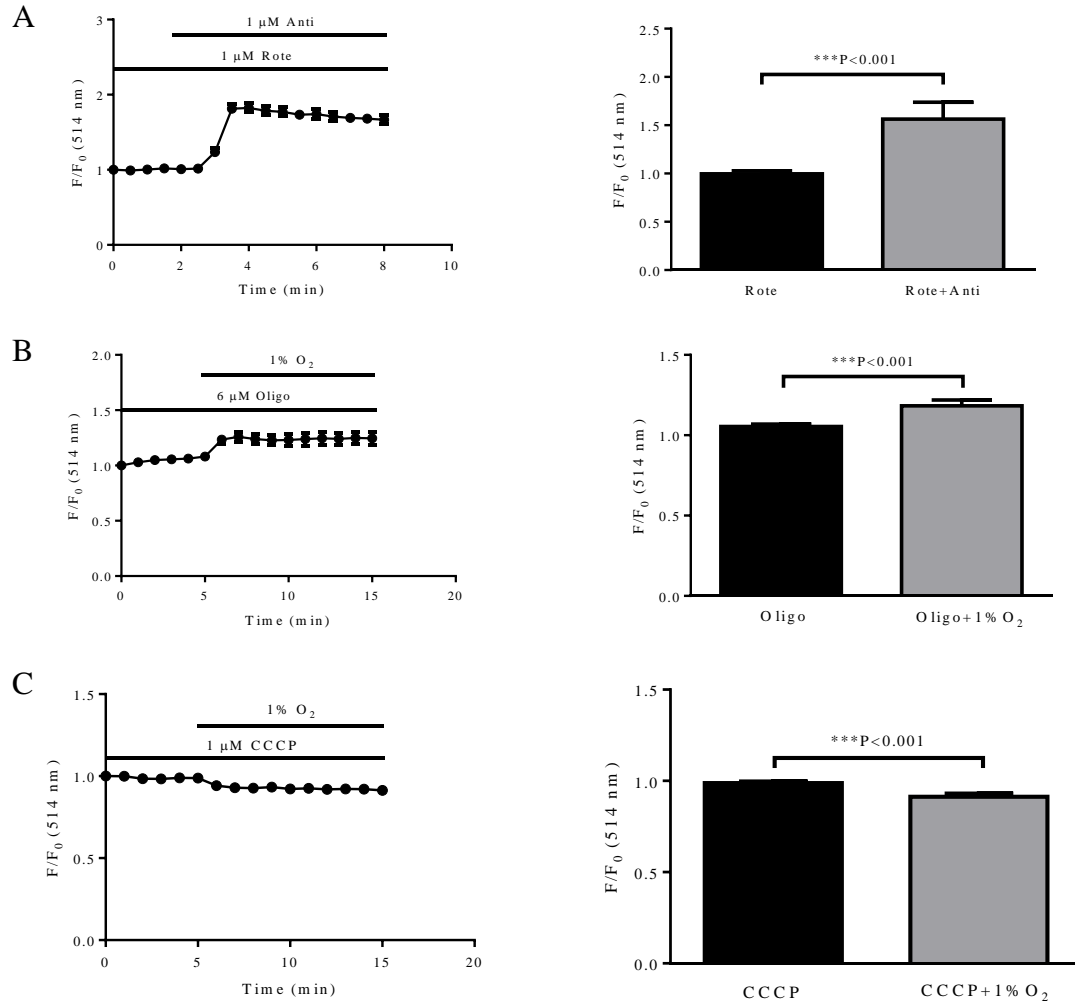


Figure 3.74: Effect of sequential application of metabolic inhibitors and hypoxia in 0 mM glucose PSS. (A) Antimycin caused an increase in rhodamine123 signal in the presence of rotenone (n=22). (B) Hypoxia increased rhodamine123 signal in the presence of oligomycin (n=40). (C) Hypoxia caused a decreased rhodamine123 signal in the presence of CCCP (n=18).

3.3.5 Microplate based ATP:ADP ratio measurement

Transduction of HCASMCs with 3rd generation lentivirus improved the efficiency to near 100% (see **section 4.4.2**) allowing ATP:ADP ratio to be measured on cell populations in multi-well plates. Hypoxia (1% O₂) treatment induced an initial increase in ATP:ADP ratio signal by $10.89 \pm 0.29\%$, followed by a recovery to the original level (**Figure 3.75**). Inhibition of glycolysis or/and OXPHOS using metabolic inhibitors for 15 minutes caused a significant change in the

FUGW-PercevalHR signal (**Figure 3.76**).

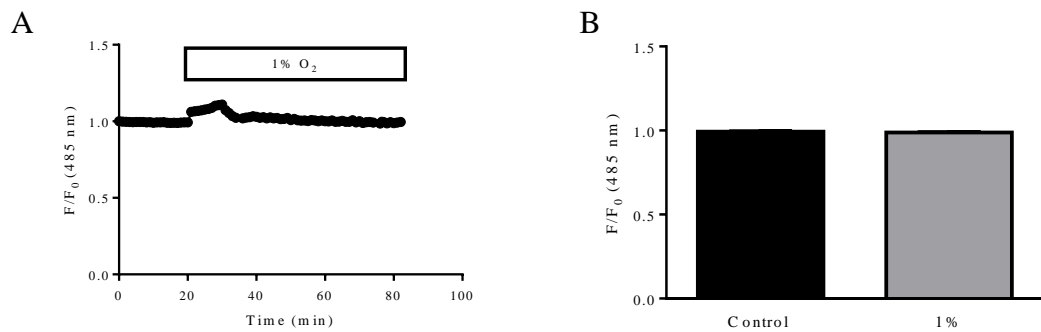


Figure 3.75: Microplate based ATP:ADP ratio measurement under hypoxia. (A) Fluorescence recording by microplate based assay showed a transient increase in ATP:ADP ratio signal followed by a complete recovery under hypoxia. (B) Mean \pm SEM of fractional fluorescence of FUGW-PercevalHR before and after 60 minutes exposure to hypoxia (n=29).

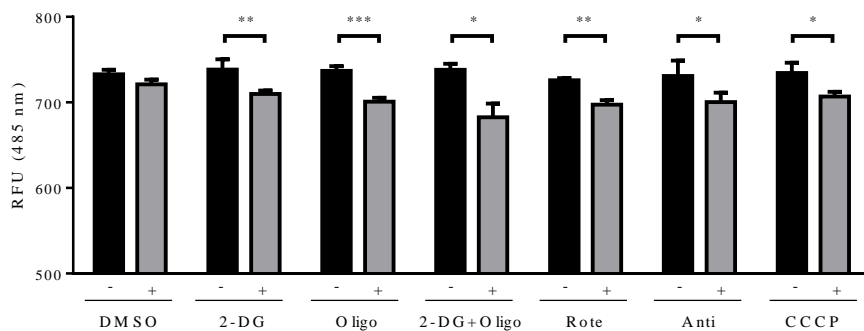


Figure 3.76: Metabolic inhibitors cause a decrease ATP:ADP ratio signal measured in microplate. In the microplate based ATP:ADP ratio measurement, metabolic inhibitors caused a decrease in FUGW-PercevalHR signal (n=4). RFU: relative fluorescence units.

3.4 Discussion

Cytosolic ATP, the primary energy currency of living cells, plays an important role in the modulation of ion channels and signaling pathways. However, there are few studies about bioenergetics of VSMCs, especially in human coronary vasculature. Furthermore, there is an increasing realization that it is necessary to monitor

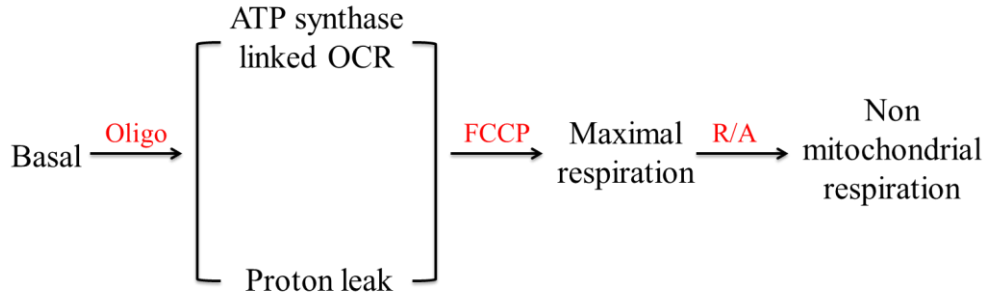
temporal and spatial changes of nucleotides within the microdomains of intracellular space. In this project, we examined the bioenergetic profile, ATP generation, and mitochondrial membrane potential of HCASMCs.

Cells produce ATP through glycolysis and OXPHOS, the latter requiring energized mitochondria. Normally, cells generate ATP primarily and preferentially via OXPHOS. However, cancer cells rely almost exclusively on glycolysis for energy production known as Crabtree Effect [210]. Because O₂ plays a vital role as the final electron acceptor in ETC, its levels in the vicinity of the cells can be used to evaluate the function of mitochondria. One of the classical methods is Clark type electrodes which measure O₂ on a catalytic platinum surface with a net reaction as $O_2 + 4e^- + 2H_2O \rightarrow 4OH^-$ [211]. More recently, Seahorse XF analyzer has made it possible to allow simultaneous measurement of OCR and ECAR in multi-well plate based methods, offering convenience and improved levels of sensitivity [180, 181, 183].

In order to obtain best results from Seahorse, we optimized cell seeding density and doses of oligomycin and FCCP as these are important parameters. For example, the stimulation of OCR with FCCP displayed bell-shaped concentration dependency as previously reported [180, 183]. Therefore, concentrations of pharmacological inhibitors must be chosen with care to avoid over estimation or under estimation of effects. In order to make our results comparable between different experiments, the reading was normalized to cell number and total protein.

In the mitochondrial stress test, addition of oligomycin induced a decrease in ATP synthase-linked oxygen consumption and ATP production from OXPHOS. When measured concurrently, ECAR and PPR increased immediately (**Figure 3.15**), suggesting that the rate of glycolysis increased above the baseline to maintain ATP production. On the other hand, increases in glycolysis resulted in a decrease in OCR (**Figure 3.14**). Therefore, glycolysis and OXPHOS are closely linked to each other to maintain the correct ATP production in HCASMCs. However, the ability of the cells to compensate for the reduction in ATP generation caused in one pathway by accelerating the other is not limitless, and spare capacities can be measured as

glycolysis reserve capacity and mitochondrial reserve capacity. Mitochondria have a spare capacity of ~2.49 fold of the ATP synthase-linked O₂ consumption (**Figure 2.4 & 3.12**). Inhibiting OXPHOS by oligomycin resulted in an increase by ~24% in the rate of glycolysis (**Figure 2.5 & 3.14**). High mitochondrial reserve capacity may play a crucial role in response to acute insults. However, if the cells are unable to increase the glycolysis sufficiently, or there is an excess demand of the energy when mitochondrial respiration is compromised, this will cause the cells to be more susceptible to various stresses [212]. In glucose free assay medium, adding 10 mM glucose decreased OCR from 76.89 ± 3.32 pmol/min per 2×10^4 cells to 51.32 ± 2.36 pmol/min per 2×10^4 cells and increased ECAR from 26.78 ± 1.50 mpH/min per 2×10^4 cells to 85.27 ± 3.22 mpH/min per 2×10^4 cells (n=8, **Figure 3.14**, OCR was not shown). In assay medium containing 25 mM glucose, cell OCR was 54.69 ± 4.56 pmol/min per 2×10^4 cells and ECAR was 85.44 ± 2.46 mpH/min per 2×10^4 cells (n=8, **Figure 3.12**, ECAR was not shown). These parallel studies indicated that assay medium containing 10 mM glucose is sufficient to support cellular metabolism, and an increase in glucose from 10 mM to 25 mM will not result in further effect on OCR, ECAR and ATP generation. A more detailed interpretation for mitochondrial bioenergetic profile was summarized by Hill et al [180] (**Figure 3.77**).



	High	Low
Basal OCR	(1) ATP turnover increased (2) Proton leak increased (3) Non mitochondrial ROS increased	(1) ATP demand decreased (2) Proton leak decreased (3) ETC or ATP synthase inhibited (4) Substrate supply decreased
ATP synthase linked OCR	(1) High ATP demand	(1) Low ATP demand (2) ETC damaged (3) Low substrate availability
Proton leak	(1) UCP activity increased (2) Inner membrane damaged (3) ETC complex damaged (4) Slippage of electrons	(1) UCP activity decreased (2) Good membrane and ETC integrity
Maximal OCR	(1) Substrate availability increased (2) Mitochondrial mass increased (3) Good ETC integrity	(1) Substrate availability decreased (2) Mitochondrial mass decreased (3) Poor ETC integrity
Non mitochondrial OCR	(1) Cytosolic ROS increased	(1) Low extramitochondrial ROS

Figure 3.77: Summary of mitochondrial bioenergetic profile. In different cell types, the contribution of mitochondria to the ATP generation could be different, and the function of mitochondria can be assessed by sequentially adding pharmacological inhibitors (Modified from Hill et al., 2012 [180]).

Are HCASMCs glycolytic or oxidative? In order to answer this question, ATP from both glycolysis and OXPHOS were calculated. In glycolysis, generation of two ATP from one molecular glucose releases 2 H⁺, so there is a 1:1 relationship between ATP and glycolytic PPR [201, 202], which is calculated in this study by subtracting non glycolytic PPR from PPR in glucose. Therefore, HCASMCs generate ATP at a rate of 115.87 ± 3.33 pmol/min per 2x10⁴ cells or 12.69 ± 0.50 pmol/min per µg protein from glycolysis. HCASMCs generate ATP at a rate of 138.93 ± 8.88 pmol/min per 2x10⁴ cells or 15.04 ± 0.59 pmol/min per µg protein from OXPHOS,

which is converted from ATP synthase-linked O₂ consumption at a ratio of 2.31 [173] (**Fig 3.15**). So mitochondrial OXPHOS is responsible for ~54.53% of the total ATP production, and HCASMCs are therefore more oxidative, but they also rely substantially on glycolysis. By comparing different passages of the cells during culture, ATP synthase linked OCR decreased as well as mitochondrial reserve capacity as passage number increased (**Figure 3.13**). Thus, the later passage cells seem to rely more on glycolysis and more susceptible to acute insults.

In addition to OCR and ECAR, Seahorse XF analyzer also allowed a broad investigation of the respiratory profile of HCASMCs, such as coupling efficiency, State_{apparent}, RCR_{basal}, RCR_{maximal}. All of these are internally normalized parameters that provide more consistent information of cell bioenergetics [180]. Coupling efficiency is calculated as 100*(ATP linked respiration)/basal, it can be used to estimate the percentage of basal O₂ consumption used to drive ATP synthesis. The coupling efficiency can also be presented as 1-(Proton leak+non-mitochondrial) respiration/basal respiration, it is therefore associated with proton leak related respiration. HCASMCs in culture had non-productive proton leak of about ~17% under physiological conditions (**Figure 3.12**). Others suggested that malfunction of OXPHOS will significantly increase proton leak [198]. HCASMCs have a relatively low leak when compared to approximately ~20% of proton leak reported for a range of vertebrate and invertebrate species [173]. State_{apparent} helps to simplify the different parameters acting together to contribute to the overall flux through respiratory chain. The changes in the value could then indicate the changes in activation or the expression level of metabolic proteins controlling the processes [180], and further studies therefore could be carried out to determine these proteins. RCR_{basal} and RCR_{maximal} are both useful in evaluating the oligomycin sensitive respiration. It is more informative to report the ratio of oligomycin insensitive respiration to maximal respiration when ATP turnover rate is low.

As discussed in **section 2.5.3**, outcome of Seahorse experiments can be classified into four bioenergetic phenotypes, aerobic, energetic, quiescent and glycolytic, by plotting OCR against ECAR. As shown in **Figure 3.19**, a change

caused by metabolic intervention can be displayed as a shift before and after the treatment. This simple analysis is useful in characterizing bioenergetics change not only as a result of metabolic insults, but also phenotype shift during cell proliferation and migration. The Seahorse results provided a clear overview of change in bioenergetics phenotype of HCASMCs caused by metabolic interventions, and detailed parameters including cellular ATP, ATP:ADP ratio and mitochondrial membrane potential can be investigated individually to further elucidate underlying mechanisms.

Examination of ATP content in HCASMCs was carried out by luciferase-based CellTiter-Glo assay. We estimated a relatively high ATP level ($\sim 1.48 \times 10^{-14}$ mole/cell) when compared to other somatic cell types ($\sim 10^{-15}$ mole/cell). We ascribe this to larger size of cells used. HCASMCs have an estimated cell volume of ~ 13.43 pL, more than 10 fold compared to that of single artery SMCs from rats [213]. Using this estimate, the ATP concentration in HCASMCs is calculated to be ~ 1.10 mM, a reasonable value expected in mammalian cells given the approximations involved in making this estimate. PDGF-BB and PGF2 α did not cause any change in cellular ATP level when cells were kept in 10 mM glucose PSS. However, PGF2 α caused a small decrease in ATP content of the cell in glucose free PSS (**Figure 3.22**). This may indicate that increase ATP utilization does not affect the cellular ATP concentration if there is enough extracellular substrate. Alternatively, the increased need in ATP generation could be met by the high reserve capacity (**Figure 3.12**). Blocking either glycolysis or oxidative phosphorylation decreased cellular ATP level, and a further effect was observed when inhibiting both pathways (**Figure 3. 26**).

Measurement of ATP content under various conditions is useful. However, as the absolute amount of cellular ATP and ADP level might vary widely among individual HCASMCs, the ratio of ATP:ADP may be a more informative indicator. Additionally, some metabolic sensitive proteins including K_{ATP} channels are known to be regulated not only by ATP but also ADP. Such dual regulation relying on ATP and ADP presumably is useful as perhaps finer tuning can be achieved. Perceval/PercevalHR is one such ATP:ADP ratio biosensor with several advantages

[194]. First, unlike luciferase, Perceval/PercevalHR does not consume ATP during measurements. Second, it senses not the absolute ATP, but the ratio of ATP:ADP [185-187]. Third, using Perceval or PercevalHR allows investigation of cellular metabolism at individual single cell level, not cell population. Finally, PercevalHR is well tuned to the level of ATP:ADP ratio expected in mammalian cells, making it a suitable ATP:ADP ratio sensor for HCASMCs.

When using fluorescent protein derived sensors, it is important to be aware that signal may also change in response to intracellular pH. We demonstrated that pHRed can be used with Perceval (**Figure 3.9D**). pHRed seems to be functioning correctly as it responded to 20 mM NH₄Cl, producing expected intracellular pH changes in a reversible manner (**Figure 3.35**). Metabolic inhibition of HCASMCs with 5 mM 2-DG or hypoxia induced no change in intracellular pH when measured in bicarbonate buffered PSS, and this is consistent with the results of other researchers [194]. Therefore, it seems safe to ascribe changes in Perceval/PercevalHR signal to true changes in ATP:ADP. Indeed, intracellular pH of HCASMCs is rather well maintained as cells can handle pH changes via ion transporters on the cell membrane [214, 215] (**Figure 3.78**). There is, however, reports showing that pH can change with metabolic inhibition [194]. In response to 2-DG, Kiang et al. (1990) reported a ~0.2 pH change in A-431 cells [216], and Brown et al. (1991) found the same degree of pH change in isolated epithelial cells [217]. It has been also reported that, in Neuro2A cells, metabolic inhibition by oligomycin and FCCP showed no effect on cytosol pH whilst complete withdrawal of glucose acidified the cytosol [197]. When estimated from ECAR change of our Seahorse result, application of 2-DG caused a decrease in ECAR by ~25.07 mpH/min, which may have an effect on extracellular and intracellular pH. Therefore, it is still important to monitor pH change in the cells while measuring ATP:ADP ratio changes in HCASMCs, and make adjustment if necessary.

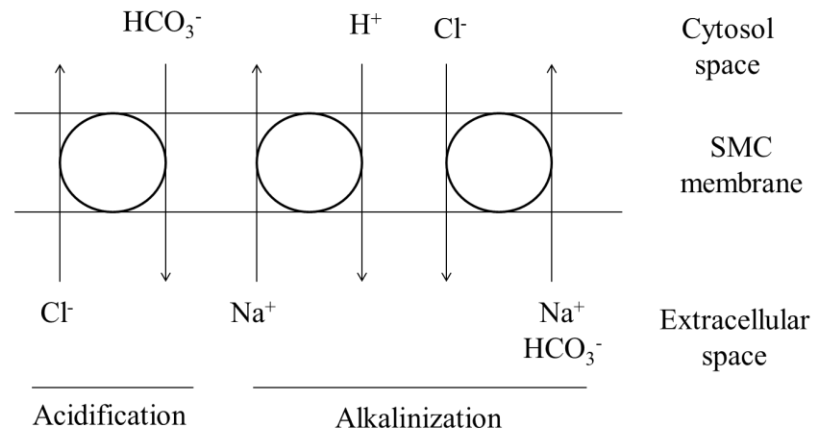


Figure 3.78: pH regulation by ion transporters in SMC. (Modified from Madden et al., 2000 [214])

One of the key roles of the mitochondria is to generate ATP through OXPHOS, a malfunction of which could be potentially catastrophic to the cell. As the electrons pass from one carrier to the next, complex I, III and IV pump positively charged H^+ to the intermembrane space from matrix. Resultant PMF across the inner membrane is used by ATP synthase to generate ATP. O_2 is the final electron acceptor, acting as a supplier of PMF and an indirect indicator of the process. Furthermore, ATP synthase can operate in reverse mode when ψ_m is depolarized where it consumes ATP. In this chapter, ψ_m was measured using rhodamine123. We observed spontaneous oscillation of rhodamine123 signal in several cells at rest or during pharmacological treatment (data not shown). Reason for this signal fluctuation is unknown. The majority of the cells did not oscillate and were used to study the effect of metabolic inhibitors and hypoxia on ψ_m . Metabolic inhibitors caused mitochondrial membrane potential depolarization by inhibition of ETC. CCCP induced mitochondrial membrane potential depolarization by dissipating H^+ gradient across the inner mitochondrial membrane (**Figures 3.56&3.72**). Although oligomycin induced an unexpected effect (depolarization) in 10 glucose PSS, application of oligomycin caused hyperpolarization of ψ_m in 0 glucose and 60 K^+ PSS. Oligomycin application is expected to cause mitochondrial membrane hyperpolarization due to blockade of proton re-entry into mitochondrial matrix that normally causes a small depolarization

(**Figures 3.55&3.71**). The fact that experiments using 60 K⁺ produced expected outcome suggests that plasma membrane potential change might have influenced rhodamine123 signal in PSS (see below). Hyperpolarizing effect of oligomycin was also observed in rat femoral arterial SMCs [218]. It was reported in cultured cerebellar granule cells, oligomycin caused a hyperpolarization of ~5-10 mV [219]. Hypoxia induced statistically non-significant increase in ψ_m in HCASMCs (**Figures 3.57&3.73**). It was previously shown hypoxia did not cause ψ_m depolarization in rat femoral artery SMCs [203].

Albeit it has been shown that there is a linear relationship between rhodamine123 fluorescence signal and ψ_m in cuvette study of mitochondria [220], it is necessarily the same in live cell imaging *in vivo*. Since the distribution of rhodamine123 follows the Nernst equation, it would be expected that there is a non-linear relationship between the two, especially when at very negative potentials (**Figure 3.51A**). Many studies also suggested that uptake of rhodamine123 by mitochondria is strongly plasma membrane potential dependent [207, 221], and it is difficult to ascertain whether rhodamine123 binds to mitochondria in an energy dependent or independent way. These might explain why we observed an unexpected effect from rotenone (hyperpolarization) which was predicted to depolarize ψ_m and oligomycin (depolarization) which was predicted to hyperpolarize ψ_m in PSS containing 10 mM glucose. In order to eliminate the possible effect from plasma membrane potential change, further experiments were carried out in extracellular solution containing 60 mM K⁺. Under 60 mM K⁺, inhibitors of ETC (rotenone, antimycin) and CCCP depolarized ψ_m (**Figure 3.62, 3.63&3.65**), oligomycin hyperpolarized ψ_m (**Figure 3.64**), but hypoxia had little effect on ψ_m (**Figure 3.66**).

Under some circumstances, for example dissipating ETC using CCCP, mitochondrial ATP synthase will work in a reverse mode in order to maintain the ψ_m at a cost of ATP consumption. Here, ATP synthase pumps out H⁺ from mitochondrial matrix using the energy from hydrolysis of ATP [179, 204, 222, 223]. The reverse mode of ATP synthase explains in some experiments we observed that mitochondria depolarization was transient and there was a partial repolarization of mitochondria

after depolarization by metabolic inhibitors, especially antimycin (**Figure 3.70**) and CCCP (**Figure 3.65**). When ATP synthase was blocked by oligomycin however, the repolarization was abolished. In the Seahorse experiments, oligomycin induced a decrease in ECAR after application of either R+A or FCCP, and this effect was diminished by the application of 2-DG before oligomycin, suggesting that ATP synthase was working in a reverse mode and caused a hydrolysis of ATP derived from glycolysis. 1% O₂ caused little change in rhodamine123 signal no matter which extracellular solution. When the cells were pretreated with oligomycin, exposure to hypoxia resulted in significant changes in rhodamine123, indicating ψ_m depolarization.

In summary, HCASMCs have a relative oxidative phenotype. When one energy production system is compromised, an alternative pathway can be called on to ensure continued supply of ATP.

One major limitation of this chapter is that the transfection efficiency of HCASMCs was very low (<1%). The low level of transfection not only makes the experiments generally difficult, but also raises the question as to whether the minority of cells transfected would represent the majority of non-transfected cells. There is also a concern that the low rate of transfection could be a result of transfected cells dying before experiments. Therefore a better transfection method should be used to elucidate the cellular metabolism and O₂ sensing of HCASMCs. This issue is addressed in **Chapter 4**.

Chapter 4
Using Lentivirus Based
Biosensors for Investigation of
Cellular Metabolism of
HCASMCs

4.1 Introduction

Transfection, a widely used technique to introduce genetic product into cells, traditionally relies on lipid-based transfecting agents. The protocol is simple and straight forward, and the large number of commercially available transfection agents reflects the importance of this technique. However, such gene delivery methods including transient transfection with LP2000 and Fugene6 are not always very efficient. This is particularly problematic with primary cells such as HCASMCs. Furthermore, these methods do not provide a reliable means to control protein expression level, leading to under expression or over expression. Perhaps the biggest disadvantage of conventional transfection methods, however, is cytotoxicity where successful transfection could potentially make cells unhealthy. In order to transfect a high proportion of primary cells without detrimental effects, various methods such as non-viral custom vectors, adenovirus (Ad), adeno-associated viruses (AAV), retroviral packaging systems and lentiviral packaging systems have become a preferred choice of gene delivery. Each method is described in more detail below.

4.1.1 PiggyBacTM transposon vector system

The PiggyBac (PB) DNA transposon technology, a method that utilizes custom vectors, has been successfully used in gene therapy, regenerative medicine, cell line engineering and animal model creation [[224-226](#)]. This system is supposed to be useful in altering the genomes of various animal species by simple transfection, reversing genomic modifications with footprint free transposon removal as well as helping to achieve highly efficient and cost-effective non-viral gene delivery. No cargo limit and reversible reactions are two unique features of the transposons. This means that re-transfection could be easily achieved with genomes containing an inserted PB vector using PB transposase expression vector. Moreover, the Super PB transposase expressing vector characterized by a strong cytomegalovirus (CMV) promoter offers very high level of expression of the transposase. With this system, high expression, stability and integration activity in many mammalian cells can be achieved by the optimized PB transposase coding sequence, a goal many researchers

wish to achieve. **Figure 4.1** shows how PB system works. With the purpose to improve the transfection efficiency, this vector was tried in HCASMCs.

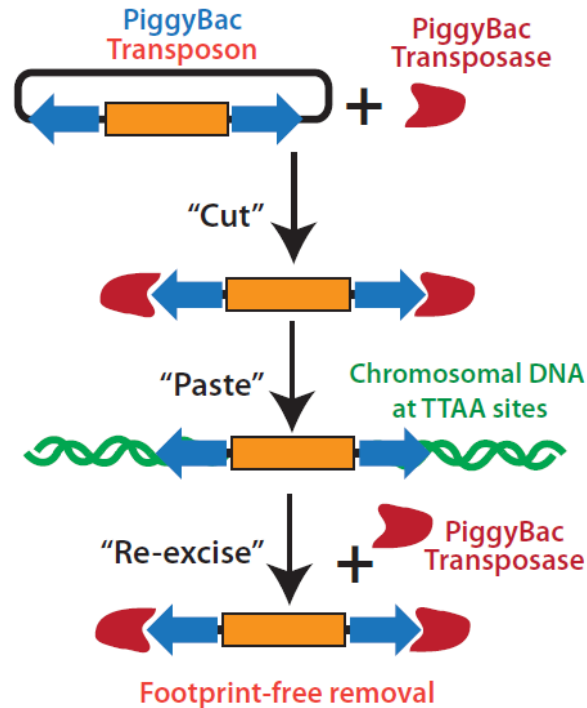


Figure 4.1 PiggyBacTM transposon vector systems. PB transposon is a mobile genetic element that efficiently transposes between vectors and chromosomes via a "cut and paste" mechanism. With this system, genes of interest between the two inverted terminal repeat sequences (ITRs) in the PB vector can be easily mobilized into target genomes. Moreover, transient re-transfection of genomes containing an inserted PB vector can be fulfilled with the PB transposase expression vector, in which transposons will be removed by transposase from the genome. (Reproduced from www.systembio.com/piggybac)

4.1.2 Lentivirus-mediated gene delivery

Although lentivirus remains less successful for gene therapy so far, some preclinical studies and clinical trials have demonstrated that lentivirus is emerging as a promising tool for a wide range of applications [227, 228]. A safe and stable lentiviral vector not only improves the efficiency of gene delivery, but also helps maintain normal tissue physiological function when compared to conventional ways

of gene delivery.

Lentiviruses are a subset of retroviruses (**Table 4.1**) which can transduce both dividing and non-dividing cells with little immune response. Because lentivirus also integrates into host cell genome, the long term gene expression can be achieved where a transfected cell will produce two daughter cells with modified gene (**Figure 4.2**). Due to these advantages, the 2nd and 3rd generation lentiviral systems (**Figure 4.3**) became important and popular tools both in gene editing and gene therapy. A comparison of 2nd and 3rd generation lentiviral systems is shown in **Table 4.2**.

The major aim of this chapter was to use lentivirus gene delivery system in order to bring reporter gene of interest to HCASMCs. Lentivirus transfection was more efficient and reliable and the changes of intracellular ATP:ADP ratio and pH were examined more successfully using lentivirus transfected HCASMCs.

Table 4.1: Retroviridae family

Retroviridae Subfamilies	Key Features
Alpharetrovirus	Type C morphology
Gammaretrovirus	<p>Mouse leukemia virus (MLV)</p> <p>Simple retrovirus: contains gag, pol, env</p> <p>Simple genome architecture makes this virus to be an attractive tool for gene delivery</p> <p>Infect dividing cells only</p> <p>The friend virus (FV) is a strain of MLV</p> <p>The friend virus has been used for both immunology and vaccines</p>
Lentivirus	<p>Human immunodeficiency virus (HIV)</p> <p>Complex retrovirus that causes acquired immunodeficiency syndrome (AIDS)</p> <p>Capable of infecting non-dividing cells</p> <p>Capable of integrating into relatively 'safe' areas within host genome</p> <p>When pseudotyped with VSV-G, can be used to infect practically any cell type</p> <p>Genome structure is well known, employed in gene delivery into dividing and non-diving cells</p>
Spumavirus	<p>The simian foamy virus (SFV)</p> <p>Complex retrovirus that closely related to HIV-1</p> <p>SFV is the oldest known vertebrate RNA viruses</p>
Betaretrovirus	<p>Mouse mammary tumor virus (MMTV)</p> <p>Encode accessory RNA export protein Rem, thus the first complex murine retrovirus to be documented</p> <p>Cause mammary tumor in mice</p> <p>Contains a glucocorticoid hormone response element in a tissue specific promoter with a LTR, promoter often used to construct mice which develop a breast cancer-like disease</p>
Deltaretrovirus	<p>Human T cell leukemia virus (HTLV-I, HTLV-II)</p> <p>First retrovirus to be unambiguously linked casually to the human cancer: adult T-cell like leukemia/lymphoma (ATL)</p> <p>Encodes an oncogenic protein, Tax, which plays a central role in transforming CD4⁺ T lymphocytes, and Rex involved in mRNA export</p>
Epsilonretrovirus	<p>Walleye dermal sarcoma virus (WDSV)</p> <p>Causes a formation of walleye dermal sarcomas in fish</p> <p>Encodes viral protein, rv-cyclin, involved in regulation of the cell cycle</p>

Adapted from Kantor et al., 2014 [229].

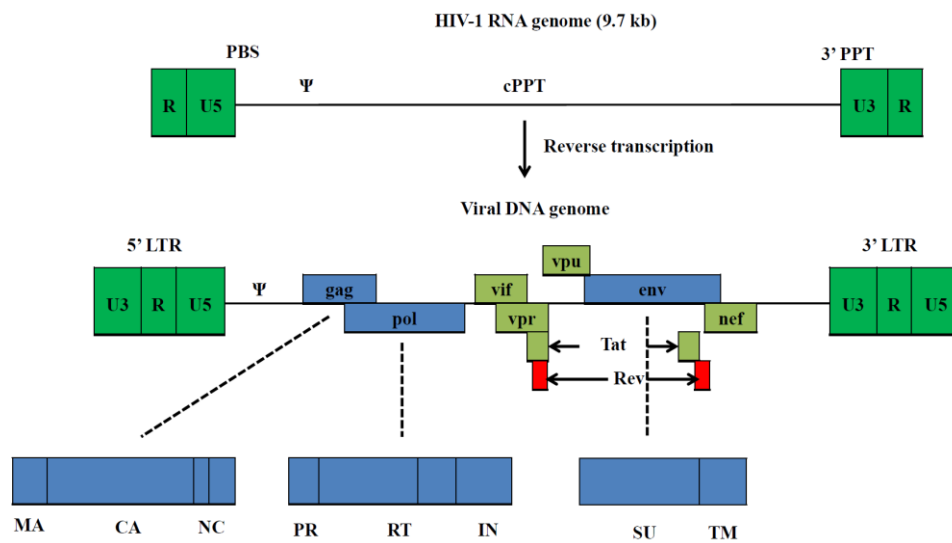


Figure 4.2: Schematic representation of HIV-1 genome. The HIV-1 virus has three gene regions (*gag*, *pol* and *env*), the accessory proteins and the flanking Long Terminal Repeats (LTR) (Modified from Shaw et al., 2014 and Yasutsugu et al., 2011 [230, 231]).

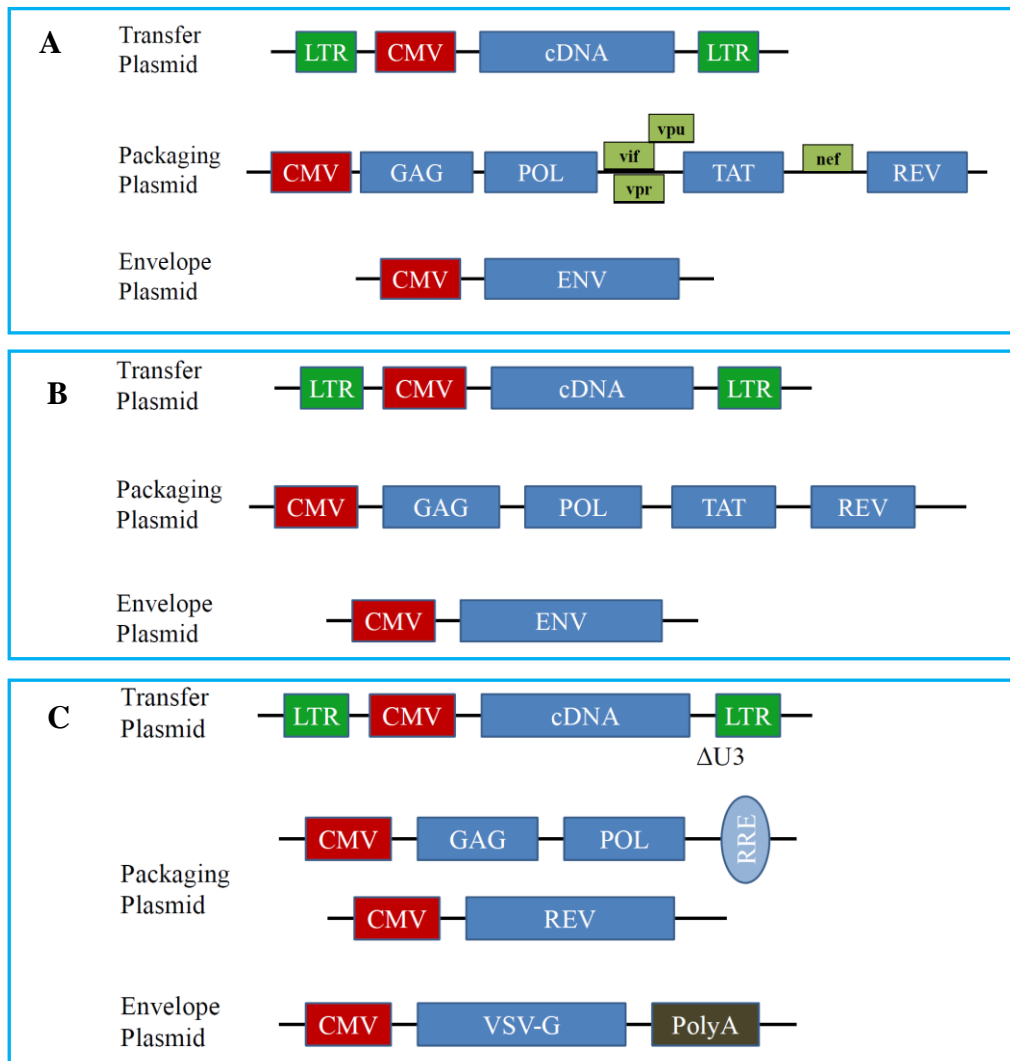


Figure 4.3: Schematic illustration of HIV-1 derived lentivirus. (A) First generation lentiviral vector: it is comprised of three separate plasmid DNAs encoding the vector genome, all HIV-1 gene except env, and Eve protein VSV-G. (B) Second generation lentiviral vector: this is also a three plasmids system, but with an improved safety by removing or mutating all accessory genes vif, vpr, vpu and nef from the packing plasmid. (C) The third generation lentiviral vector is designed to further reduce potential risk. It uses 4 plasmids instead of 3, and 5'LTR is partially deleted and fused to a heterologous enhancer/promoter such as CMV or RSV eliminating the requirement for Tat (Tat-independent). In addition, the enhancer/promoter is deleted from the U3 region of 3'LTR ($\Delta U3$) in the transfer vector plasmid (self-inactivating (SIN) vector). (Adapted from Shaw et al., 2014 and Yasutsugu et al., 2011 [230, 231])

Table 4.2: Comparison of 2nd and 3rd generation lentiviral systems

Feature	2 nd generation	3 rd generation
Transfer Plasmid	Can be packaged only by a second generation packaging system that includes TAT	Can be packaged by both 2nd and 3rd generation packaging systems
Packaging Plasmid	All on one plasmid: Gag, Pol, Rev, Tat	Two plasmids: one encoding Gag and Pol and another encoding Rev
Envelope Plasmid	Interchangeable: usually encodes for VSV-G	Interchangeable: usually encodes for VSV-G
Safety	Safe. Replication incompetent: Uses 3 separate plasmids encoding various HIV genes.	Safer. Replication incompetent and always SIN: Uses 4 plasmids instead of 3 and eliminates the requirement for Tat.
LTR Viral Promoter	Wild type	Hybrid: 5'LTR is partially deleted and fused to a heterologous enhancer/promoter such as CMV or RSV

Taken from: <https://www.addgene.org/viral-vectors/lentivirus/lenti-guide/>

4.1.3 Other alternatives

In addition to lentivirus, the most commonly used viral vectors for gene editing and delivery are based on Ads, AAVs and retrovirus. Nanoparticles have also been utilized as an efficient vector. The basic characteristics of different vectors are summarized in **Table 4.3**.

Ad is widely used for introduction of genetic material into host cells. It provides an efficient way to transduce mammalian cell types, both replicative and non-replicative. Viral DNA from Ad is maintained in episomal form in infected cells. Therefore it leads to transient transgene expression, and different from some other viral vectors capable of integrating into the host genome.

AAV is a small helper dependent and non-pathogenic parvoviruses found as a contaminant during the preparation of simian Ad [232, 233]. The majority of

recombinant AAV vectors are based on AAV serotype 2. There are a number of features inherent to their viral biology, making AAV a widely used gene transfer vector. AAV has not been linked with disease, has a broad cell and tissue tropisms, and triggers limited viral host response. These features proved AAV to be a good gene delivery vector.

A retrovirus is an enveloped, single-stranded RNA virus containing reverse transcriptase. As shown in **Table 4.1**, it comprises seven subfamilies. Generally, retrovirus vectors are replication-defective. Similar to AAV, retroviruses can provide long-term gene expression since it requires genome to be integrated in order to achieve gene expression. Amongst all viral vectors, oncoretroviruses were the first to be used as gene therapy vectors and subsequently contributed to many technical and conceptual advancements in the development of viral vectors.

Table 4.3: Basic properties of main viral vectors and non-viral vectors

	Adenovirus	AAV	Retrovirus	Lentivirus	Non-viral	Nanoparticle
Family	Adenovirus	Parvoviridae	Retroviridae	Retroviridae	-	-
Virion size	70-90 nm	18-26 nm	80-130 nm	80-130 nm	-	-
Genome size	38-39 kb	4.7 kb	3-9 kb	3-9 kb	-	-
Genome type	dsDNA	ssDNA	ssRNA	ssRNA	RNA or DNA	RNA or DNA
Host genome integration	No	No	Yes	Yes	No	No
Efficiency	Low-high	Moderate-high	Moderate-high	High	Poor	Poor-moderate
Transgene expression	Transient	long-term	long-term	long-term	Transient	Variable
Immunogenicity	High	Low	Low	Low	Low	Low-high
Infection/tropism	Dividing cells	Dividing and non-dividing	Dividing cells	Dividing and non-dividing	Dividing and non-dividing	Dividing and non-dividing
Packaging capacity	≤7.5 kb	≤1.8 kb	≤8 kb	≤8 kb	No limitation	No limitation

Modified from Mohan et al., 2013 [234].

4.2 Aims

The purpose of this chapter was to produce high yields of primary HCASMCs expressing the reporter genes PercevalHR and pHRed. As described previously, PercevalHR reports the cellular ATP:ADP ratio while pHRed reports pH. Furthermore, it is possible that K_{ATP} channels are regulated by the change of ATP:ADP ratio near plasma membrane microdomains. It follows that signal from PercevalHR diffused throughout the cytosol reporting the global change in the ratio may not be a good indicator. Thus, we also targeted PercevalHR to the lipid rafts of the cell membrane by adding a membrane targeting sequence derived from Lyn kinase.

4.3 Methods

4.3.1 Plasmid production, amplification and isolation

A conventional 3rd generation HIV-based lentivirus packaging system was used in this work. The plasmids (RRE, REV, VSVG) required for the production of lenti-psuedoviral particles carrying the expression construct were used to transduce competent *E.Coli* cells. A 3rd generation lentivirus vector with a conditional packaging system was used [235]. This system requires an envelope plasmid for the viral envelope, two packaging plasmids to produce the viral packaging proteins, and a transfer plasmid containing the gene of interest (**Figure 4.3**).

All plasmids contained an ampicillin resistance gene for selection of transformed *E.Coli*. Transformation of *E.Coli* was performed following the manufacturer's protocol involving heat shock. Growth of transformed cells and plasmid isolation were performed according to manufacturers' protocols (growth in LB broth containing ampicillin and plasmid isolation with commercially available mini-prep preparation of plasmid DNA). Successful transformation was confirmed by both restriction analysis and automated sequencing.

4.3.2 Production of lenti-psuedoviral particles

The purified plasmids were prepared with maxi-prep, then transfected transiently into the packaging cell line HEK293T cells, either by calcium precipitation or by using commercially available transfection reagents. The resulting lenti-psuedoviral particles were secreted into culture media and collected. Lenti-psuedoviral particles were frozen and stored in -80 °C freezer or used immediately (**Figure 4.4**).

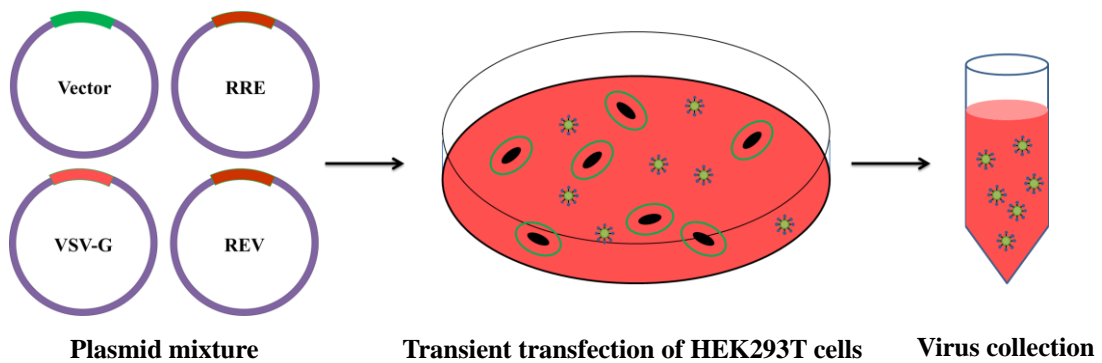


Figure 4.4: Production of lentivirus. Lentivirus were produced by introducing transfer plasmid, packaging plasmids and envelope plasmid into HEK293T cells transiently using calcium phosphate or transfection reagents. Maximal lentivirus generation usually occurred after 48-72 hours of transfection at which point viral particles were collected and clarified from cell debris. Vector particles can be further purified, concentrated and titrated before stored at -80°C . (Modified from Shaw et al., 2014 [[230](#)])

4.3.3 Transduction

The lenti-pseudoviral particles were used to transduce HCASMCs. Transduction was carried out following the protocols used by Kutner et al. (2009) and Li et al. (2012) with modifications [[236](#), [237](#)]. Transduction was performed on cells cultured for 3-21 DIV (days *in vitro*). The vector was added and incubated with the cells for 16-24 hours, then the media was completely removed, and fresh media was added. If treated with DNase, it can help to remove any remaining cDNA. The transduced cells will express the fluorescent reporter protein as a result of viral integration into the host genome, but incapable of generating new viral particles and infecting other cells as the envelope and packaging genes are no longer present. The cells were imaged at day 3 onwards after transduction by a confocal laser microscope located in the Center for Cell Imaging suite (CCI).

4.3.4 Cell permeabilisation

It is of high importance that the signals from biosensors are calibrated *in vivo*. In particular, although Perceval and PercevalHR are supposed to detect ATP:ADP ratio,

it has been also reported that their signals are independent of ADP [196]. Thus, attempts were made to calibrate the PercevalHR using standard solutions containing known concentration of ATP and ADP. To achieve this, HCASMCs have to be permeabilised in such a way that hydrophilic nucleotides can be introduced into the cells without loss of biosensor. Here permeabilisation with ESCIN or α -toxin was carried out for PercevalHR *in vivo* calibration.

4.3.4.1 Permeabilisation with ESCIN

Escin, a natural mixture of triterpenoid saponins isolated from horse chestnut (*Aesculus hippocastanum*) seeds, was first used to permeabilise HCASMCs.

Cells expressing PercevalHR were incubated with 20 μ M ESCIN (Sigma, E1378) in calibration solution containing [mM]: 140 KCl, 10 NaCl, 10 HEPES, 2 EGTA and 0.05 EDTA. After cells had been permeabilised, and the fluorescence of PercevalHR reached a steady state, cells were then perfused with calibration solution with different concentrations of ATP containing a free Mg^{2+} of 0.5 mM. Images were taken using LSM510 high speed confocal laser scanning microscope with a regular interval.

4.3.4.2 Permeabilisation with α -toxin

PercevalHR transfected cells were washed with PercevalHR calibration solution A then B (see below), then permeabilised with 200 μ l PercevalHR calibration solution B containing 200 μ g/ml α -toxin for ~1 hour. Cells were then washed with PercevalHR calibration solution B and replaced with PercevalHR calibration solution B containing required concentrations of nucleotides while keeping free Mg^{2+} constant at 0.5 mM (see the columns below. All calculations were done using MAXCHELATOR: <http://maxchelator.stanford.edu/>). Images were taken using LSM510 high speed multiphoton confocal laser scanning microscope.

PercevalHR calibration solution A		PercevalHR calibration solution B	
(pH 7.2)		(pH 7.2)	
NaCl	110 mM	KCl	140 mM
NaOH	30 mM	NaCl	10 mM
KCl	10 mM	HEPES	10 mM
HEPES	10 mM	EGTA	2 mM
EGTA	10 mM	EDTA	0.05 mM
EDTA	0.05 mM		

ATP (mM)	ADP (mM)	ATP:ADP	MgCl₂ (mM)
1	0.1	10	3.6
1	1	1	4.5
0	0	-	2.5
1	0	-	3.5
3	0	-	5.5
10	0	-	12.5

4.3.5 Making FUGW-pHRed and Lyn-FUGW-PercevalHR

FUGW-pHRed was constructed by inserting pHRed into the lentiviral vector from FUGW-PercevalHR. Lyn-FUGW-PercevalHR was made by inserting a 5' myristoylation and palmitoylation lipid modification sequence (GCIKSKRKDK) into FUGW-PercevalHR.

4.3.6 Analysis of cell morphology using Fiji

In order to characterize the morphology of the cells, images taken using LSM510 or LSM510 multiphoton confocal microscope were analyzed by the following parameters (Taken from Fiji manual):

Area Area of selection in square pixels or in calibrated square units (e.g., mm², μm², etc.) if Analyze >Set Scale. . . was used to spatially calibrate the image.

Major and Minor Primary (the longest) and secondary (the shortest) axis of the best fitting ellipse.

Shape descriptors Calculates and displays the following:

Circularity $4\pi \times [\text{Area}] / [\text{Perimeter}]^2$ with a value of 1.0 indicating a perfect circle. As the value approaches 0.0, it indicates an increasingly elongated shape. Values may not be valid for very small particles. Uses the heading Circ.

Aspect ratio The aspect ratio of the particle's fitted ellipse, i.e., [Major Axis]/[Minor Axis]. Uses the heading AR.

Roundness $4 \times [\text{Area}] / (\pi \times [\text{Major axis}]^2)$ or the inverse of Aspect Ratio. Uses the heading Round.

Solidity [Area]/[Convex area].

A representative analysis is shown in **Figure 4.5**. Dead cells and the cells those are cut off by the edge of the field are excluded.

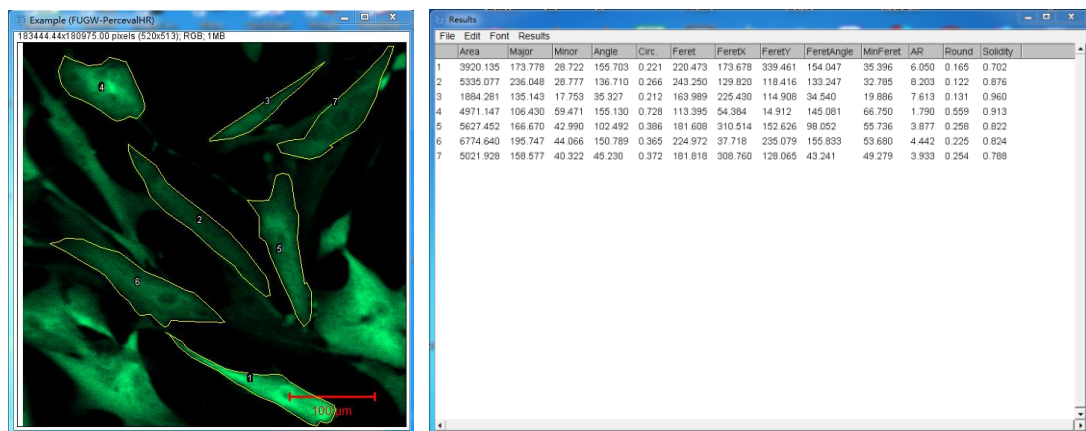


Figure 4.5: Analysis of cell morphology using Fiji. Cells were measured by drawing lines around the cell boundaries (left). All defined measurements are shown in the result table (right).

4.3.7 Cell volume measurement using Fiji

HCASMCs expressing Lyn-FUGW-PercevalHR were lifted with trypsin and suspended in cell culture medium. Images of the cells were taken using LSM510 multiphoton confocal microscope (examples: see **Figure 4.60 & 4.61**). After the

length of major and minor axis have been reported (see **4.3.6**), cell volume was estimated and calculated as: $V = (4/3) \times \pi \times ((\text{major axis}/2 + \text{minor axis}/2)/2)^3$.

4.3.8 Ratiometric image analysis using Fiji

Ratiometric analysis of confocal images was performed with Fiji software (**Figure 4.6**). Background was taken from the cell-free area and was subtracted from each channel before the image was processed. Ratio images for PercevalHR were obtained from pixel-by-pixel division of 488 nm excitation images with 458 nm excitation images, and ratio images of pHRed were produced from pixel-by-pixel division of 561 nm excitation images with 458 nm excitation images. A region of interest was drawn to analyze the changes of the ratio before and after treatment.

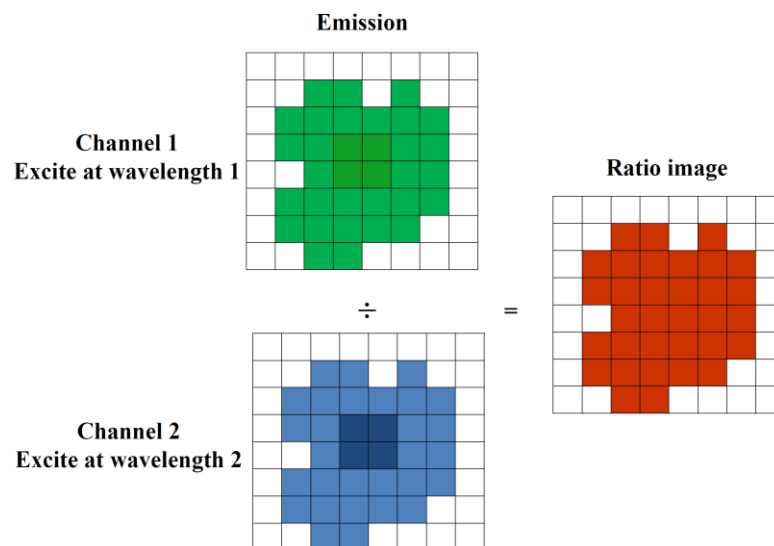


Figure 4.6: Modal for ratiometric image analysis of a cell expressing PercevalHR or pHRed. On the left are the pixelated cartoons of a fluorescent cell showing uneven distribution of fluorescence from two different excitation wavelengths indicated on top left (green) and bottom left (blue). Pixel-by-pixel division of the left two images results in a ratio image on the right (red). In this way, the image is normalized for biosensor concentration in the cell, and thus the final reading is independent of protein concentration (Modified from Tantama et al., 2014 [187]).

4.4 Results

4.4.1 PiggyBacTM transposon vector system

We first tried PiggyBacTM transposon vector system using vector (System Biosciences, Cat no. PB533A-2) containing anterior gradient protein 2 (AGR2) provided by Christopher Clarke (University of Liverpool). HCASMCs were labelled with anti-AGR2 primary antibody (Abcam, Cat no. ab56703) and visualized with AF488-conjugated goat anti-mouse secondary antibody (Molecular Probes, Cat no. A-11011). Overview of transfection images were taken by EVOS FL cell imaging system (Life Technologies). Although HCASMCs were transfected with PB vector, the efficiency was still very low and the fluorescent signal was weak (**Figure 4.7**). Therefore, we did not apply this vector for PercevalHR.

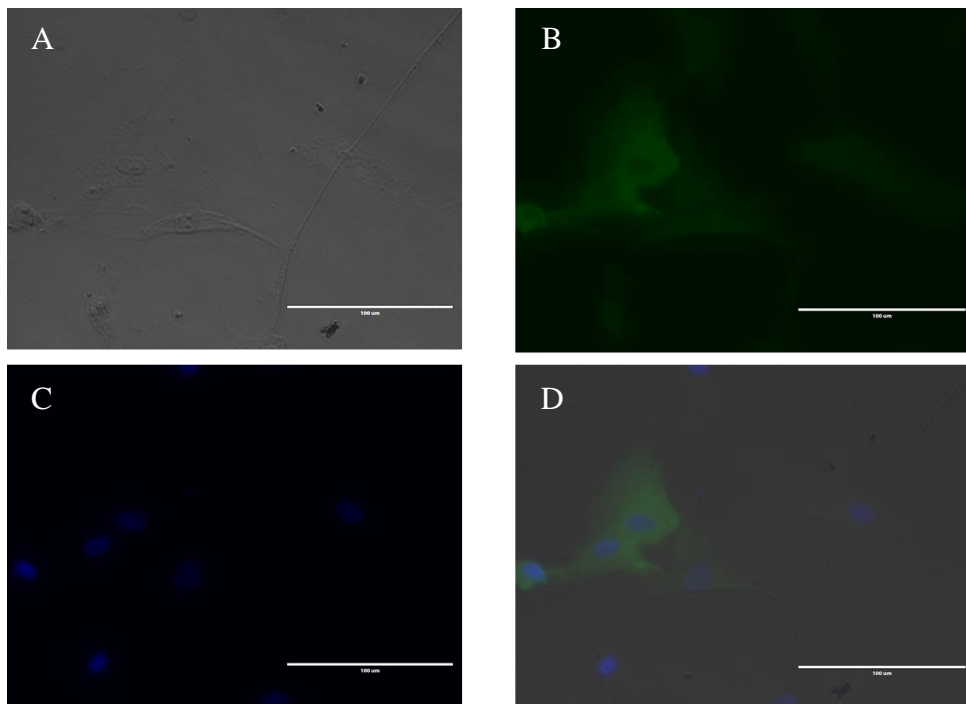


Figure 4.7: Transfection of PB vector containing AGR2. (A) Bright field. (B) Staining of AGR2. (C) DAPI staining of the nucleus. (D) Overlay of the channels. Scale bar is 100 μ m.

4.4.2 Transfection of HCASMCs with FUGW-PercevalHR

Figure 4.8 shows HCASMCs transfected with FUGW-PercevalHR using 3rd

generation lentivirus system viewed with EVOS FL cell imaging. Compared to transient transfection using reagents, infection with lentivirus brought the transfection efficiency to almost 100% where most of the cells were green.

For the rest of experiments, cells were plated into 35 mm glass-bottom dishes for confocal microscopy imaging.

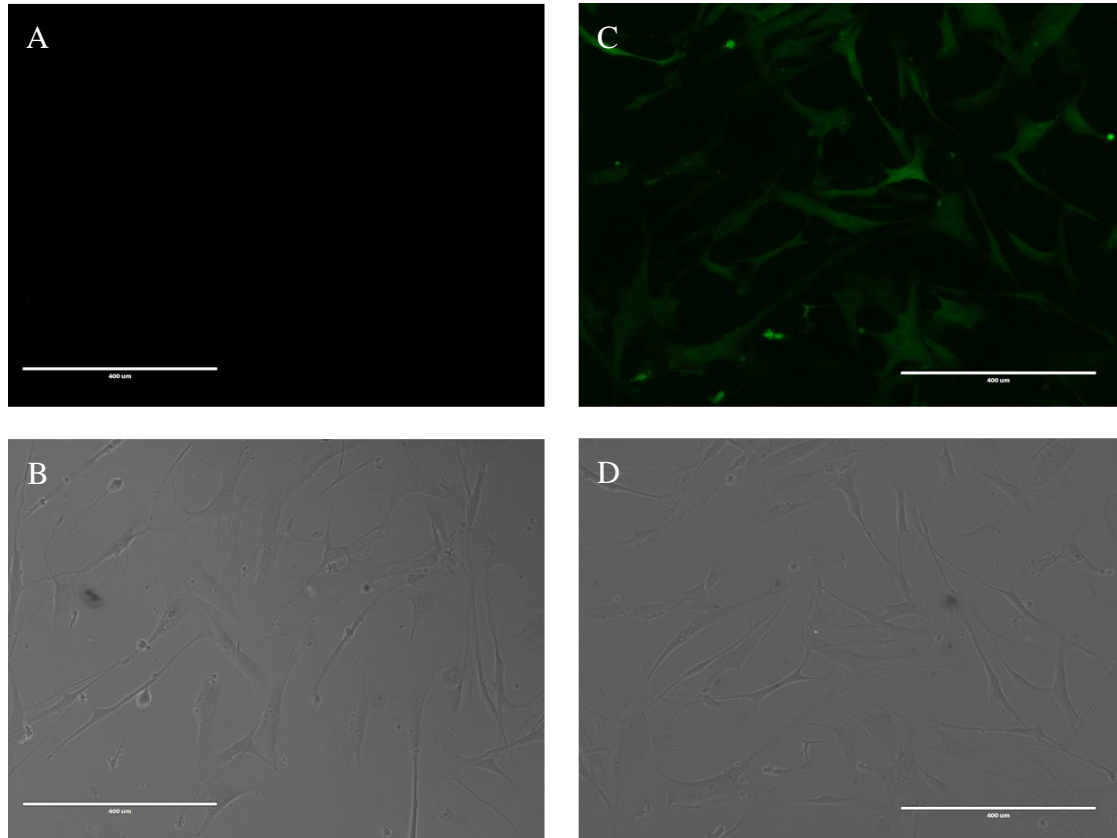


Figure 4.8: FUGW-PercevalHR transfected HCASMCs. (A) Green channel and (B) bright field images of negative control. (C) Green channel and (D) bright field images of HCASMCs transfected with FUGW-PercevalHR. Scale bar is 400 μm .

4.4.3 Morphological comparison between transfection with lentivirus and transfection reagents

It is commonly known that most of the transfection reagents are toxic to the cells to some extent. Detrimental effect is often indicated by changes in cell morphology as well as compromised function. Here we compared the cell morphology of transfected cells using reagents and lentivirus (**Figure 4.9**).

HCASMCs transfected using reagents had a shorter minor axis of $19.28 \pm 1.86 \mu\text{m}$, a major axis of $68.56 \pm 3.73 \mu\text{m}$, and an area of $988.46 \pm 88.10 \mu\text{m}^2$ respectively (n=20), compared to $36.99 \pm 2.94 \mu\text{m}$, $144.17 \pm 11.11 \mu\text{m}$ and $4356.67 \pm 503.19 \mu\text{m}^2$ of the cells infected with lentivirus (n=33) (**Figure 4.10**; $P < 0.001$ for all parameters). By comparing shape descriptors between the two groups (**Figure 4.11**; Group A: Transfection reagent, n=20; Group B: Lentivirus, n=33), there was no significant difference in Circ (A:B: 0.40 ± 0.04 vs 0.37 ± 0.03), AR (A:B: 4.61 ± 0.71 vs 4.58 ± 0.49), Round (A:B: 0.31 ± 0.04 vs 0.30 ± 0.03) and Solidity (A:B: 0.81 ± 0.03 vs 0.78 ± 0.03). The size of lentivirus transduced cells was closer to that of non-transfected cells (see **section 6.3.1**) while that of transfected cells using reagents was much smaller in both major and minor axis indicating an unhealthy state.

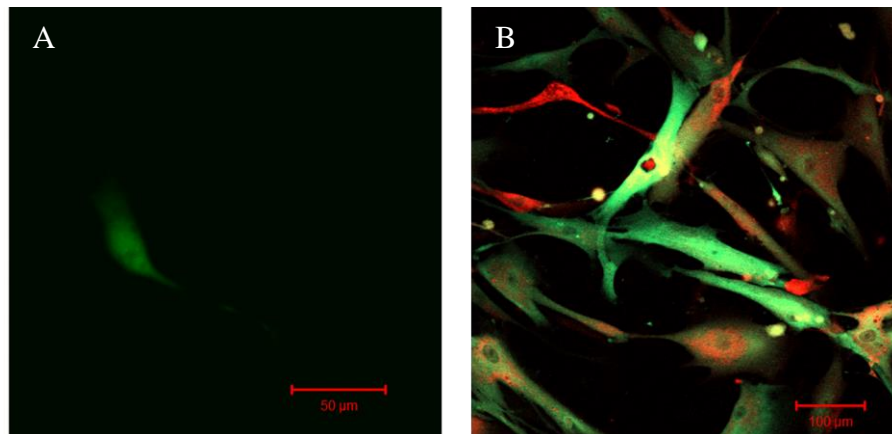


Figure 4.9: Cell transfection using different methods. (A) Cell transfected with Perceval using Fugene6. (B) Cell expressing FUGW-PercevalHR and FUGW-pHRed using 3rd generation lentivirus.

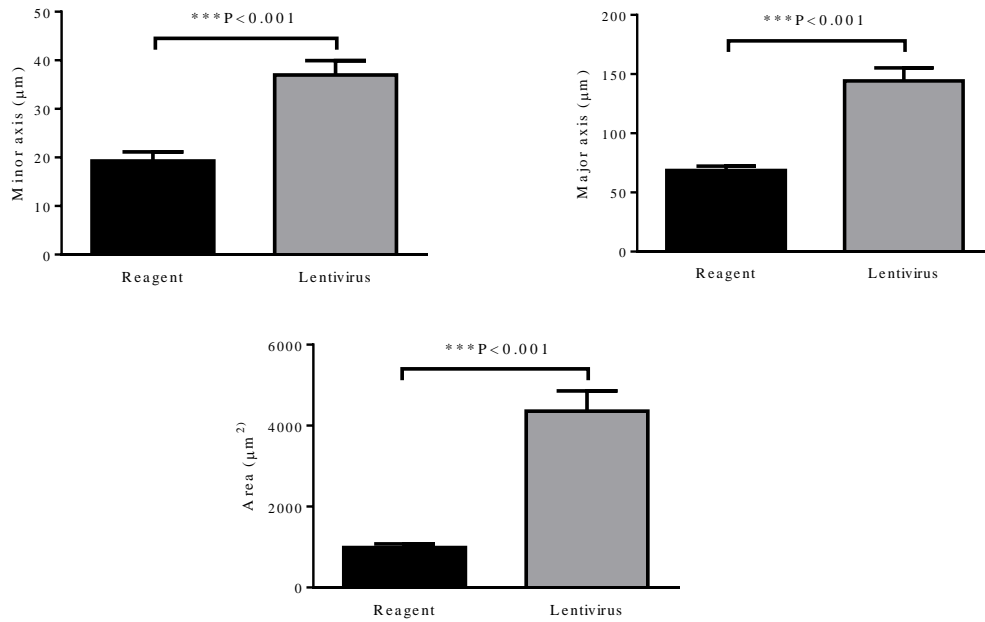


Figure 4.10: Comparison of cell size between different transfection methods with Fiji. Cells transfected using transfection reagents are smaller in size in terms of major axis, minor axis and area when compared to the cells infected with lentivirus.

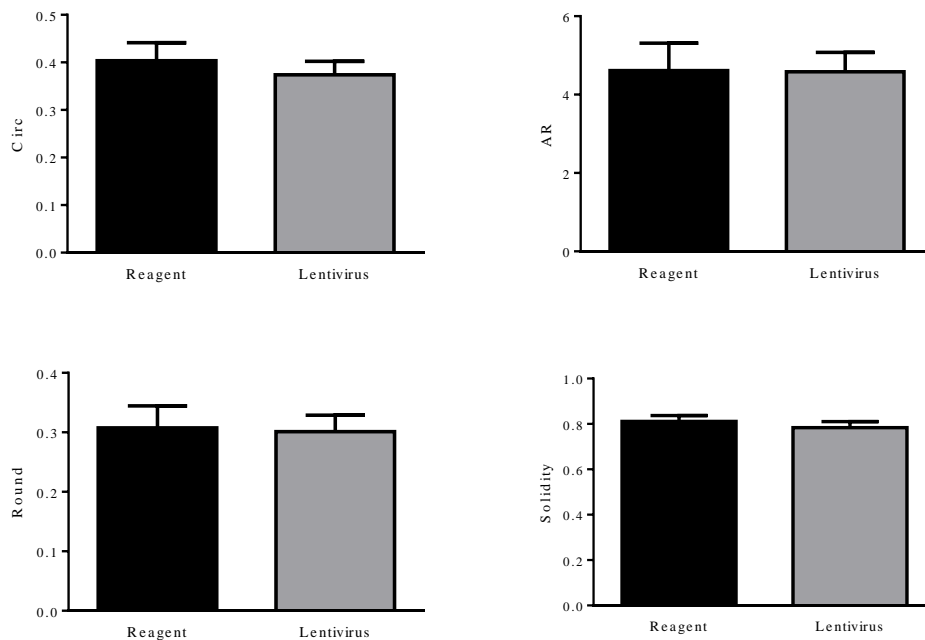


Figure 4.11: Comparison of cell morphology between different transfection methods using Fiji. Analysis of the shape descriptors showed that there is no significant difference in Circ, AR, Round and Solidity of cells using different transfection methods.

4.4.4 Intracellular calibration of FUGW-PercevalHR

4.4.4.1 Cell permeabilisation using ESCIN

In the first instance, ESCIN was applied to permeabilise HCASMCs expressing PercevalHR (**Figure 4.12**). Application of 20 μM ESCIN caused an immediate decrease in PercevalHR fluorescence. This could be due to the decrease in intracellular ATP by diffusion. However, PercevalHR signal did not recover when ATP concentration was raised to 10 mM. Likely explanation for this is that there was an escape of PercevalHR from HCASMCs following permeabilisation.

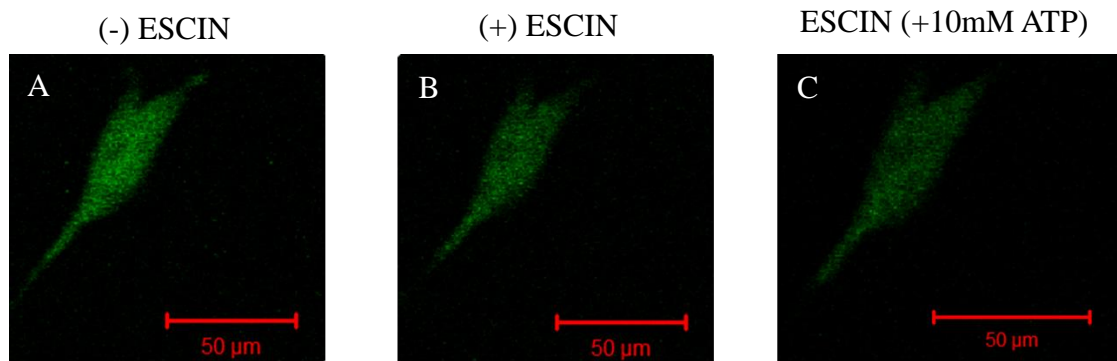


Figure 4.12: Cell permeabilisation with ESCIN. (A) HCASMC expressing PercevalHR. (B) Permeabilising with 20 μM ESCIN resulted in a decrease in PercevalHR signal. (C) PercevalHR fluorescence did not recover after 10 mM ATP was applied.

4.4.4.2 Cell permeabilisation using α -toxin

As shown above, permeabilisation with ESCIN appeared to be too harsh for *in vivo* calibration as membrane became too leaky so that not only ATP but also biosensor moved across the cell membrane. To circumvent this problem, α -Hemolysin from staphylococcus aureus (α -toxin, Sigma, Cat no. H9395) was used to permeabilise FUGW-PercevalHR transfected cells. Alpha toxin has previously been used in the Perceval calibration in MIN6 beta cells [196]. However, after incubation HCASMCs with α -toxin, the majority of the cells contracted, causing detachment of HCASMCs from the dish. This meant that cells were washed away

when solutions were exchanged (**Figure 4.13**). The contraction occurred even when the calcium was chelated using 10 mM EGTA. In order to minimize cell contraction and detachment, 35 mm glass-bottom dishes were coated with poly D-Lysine before the cells were seeded. This facilitated the attachment of cells. To prevent cell contraction, 10 μ M wortmannin (Sigma, Cat no. W1628) was added to PercevalHR calibration solution A (**Figure 4.14**). Wortmannin, a chemical primarily known as a phosphoinositide 3-kinases (PI3Ks) inhibitor, is also a potent inhibitor of smooth muscle MLCK [238]. Thus, wortmannin is routinely used for smooth muscle confocal imaging where movement of cells needs to be prevented. Surprisingly, wortmannin only slowed and did not completely prevent cell contraction. The reason for this is unknown, but wortmannin is a ‘dirty’ compound with multiple targets. Nonetheless, cell contraction and detachment was sufficiently less problematic in the presence of wortmannin, and *in vivo* calibration was possible.

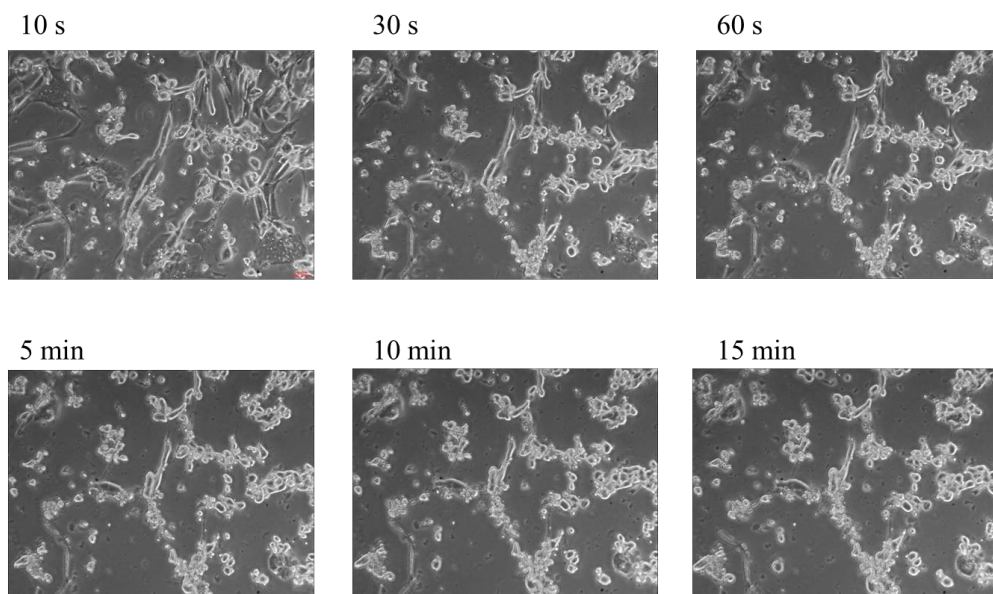


Figure 4.13: α -toxin causes SMC contraction. Time course of pictures taken by CMEX microscope (Euromex) showed that incubating the cells with α -toxin caused extensive HCASMCs contraction.

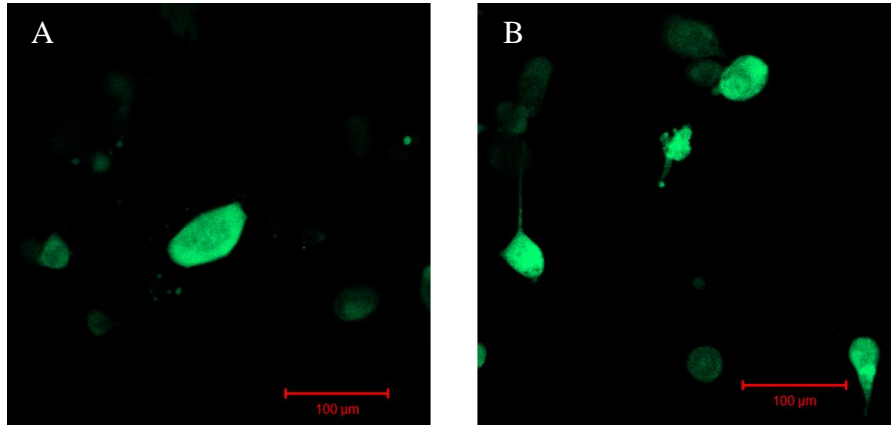


Figure 4.14: Poly D-Lysine coating helps cells adhere to the glass. (A) HCASMCs expressing PercevalHR after 1 hour permeabilisation with α -toxin. (B) Treating the glass bottom dishes with Poly D-Lysine helped cells to stick better. Note thread like structure of cells.

4.4.4.3 Cell permeabilisation for *in vivo* calibration

Permeabilised cells were washed with PercevalHR calibration solution B followed by PercevalHR calibration solution B containing 10 mM ATP (Sigma, Cat no. A2383). Images were taken with LSM510 multiphoton confocal microscope. After switching to PercevalHR calibration solution B containing 0 mM ATP, PercevalHR fluorescence decreased to its minimum. The signal remained stable and can be reversed between 10 ATP and 0 ATP for a relatively long period (**Figure 4.15**).

4.4.4.4 PercevalHR detects millimolar concentrations of ATP

In order to further investigate ATP sensitivity of PercevalHR, a concentration-response curve was constructed. Cells were imaged first with 10 and 0 mM MgATP. Next, cells were treated again with calibration solution B containing 10 mM ATP, and the extracellular solution was replaced with calibration solution B containing 3 mM ATP, 1 mM ATP and 0 mM ATP (**Figure 4.16**). PercevalHR fluorescence showed a concentration dependent decrease and recovered to original level when 10 mM ATP was re-administrated at the end of the experiment (**Figure**

4.16A). Plot of fractional fluorescence against time and curve fitting (hyperbolic function) showed a half maximal effect occurring at ~3.29 mM (**Figure 4.16B**).

4.4.4.5 PercevalHR detects intracellular ATP:ADP ratio

PercevalHR has been reported to be more sensitive to ATP:ADP ratio rather than ATP level alone. Moreover, it could be argued that ATP:ADP ratio is functionally more relevant parameter than absolute amount of ATP. However, it has been also reported that Perceval signal was not dependent on the level of ADP [196]. We therefore studied the influence of ADP on PercevalHR fluorescence using permeabilised HCASMCs (**Figure 4.17**).

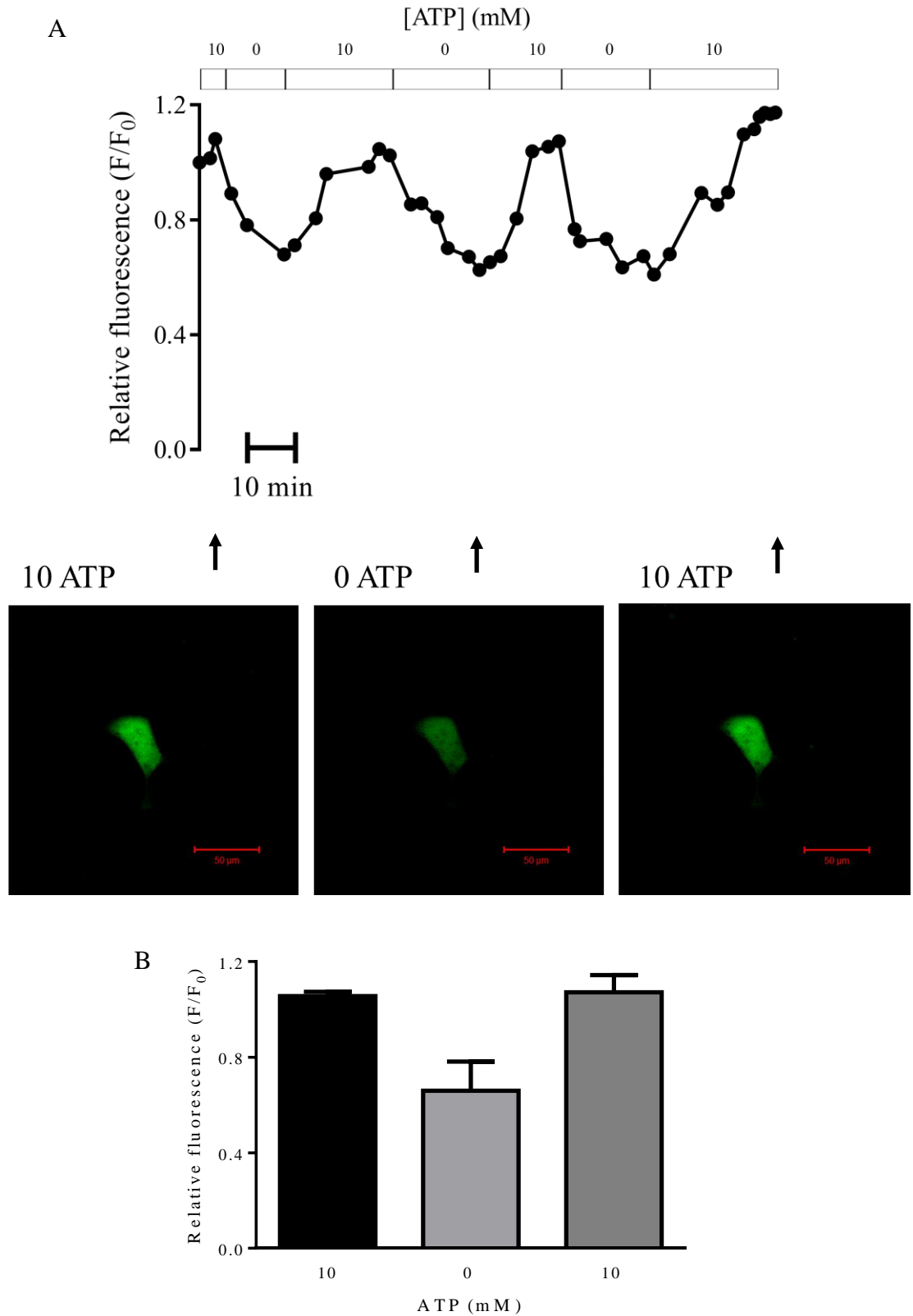


Figure 4.15: PercevalHR signal measured using α -toxin permeabilised

HCASMCs. (A) Confocal microscopy recording of PercevalHR fluorescence from a single HCASMC permeabilised with α -toxin. PercevalHR fluorescence decreased

when MgATP was removed, and recovered after re-administration of MgATP. Stable and predictable signal change indicates that *in vivo* calibration can be conducted over a long period of time. Confocal images of an individual HCASMC at three points of the study are shown. Scale bar is 50 μm . (B) Mean \pm SEM of PercevalHR fluorescence at 10 mM, 0 mM, and 10 mM of ATP (n=4).

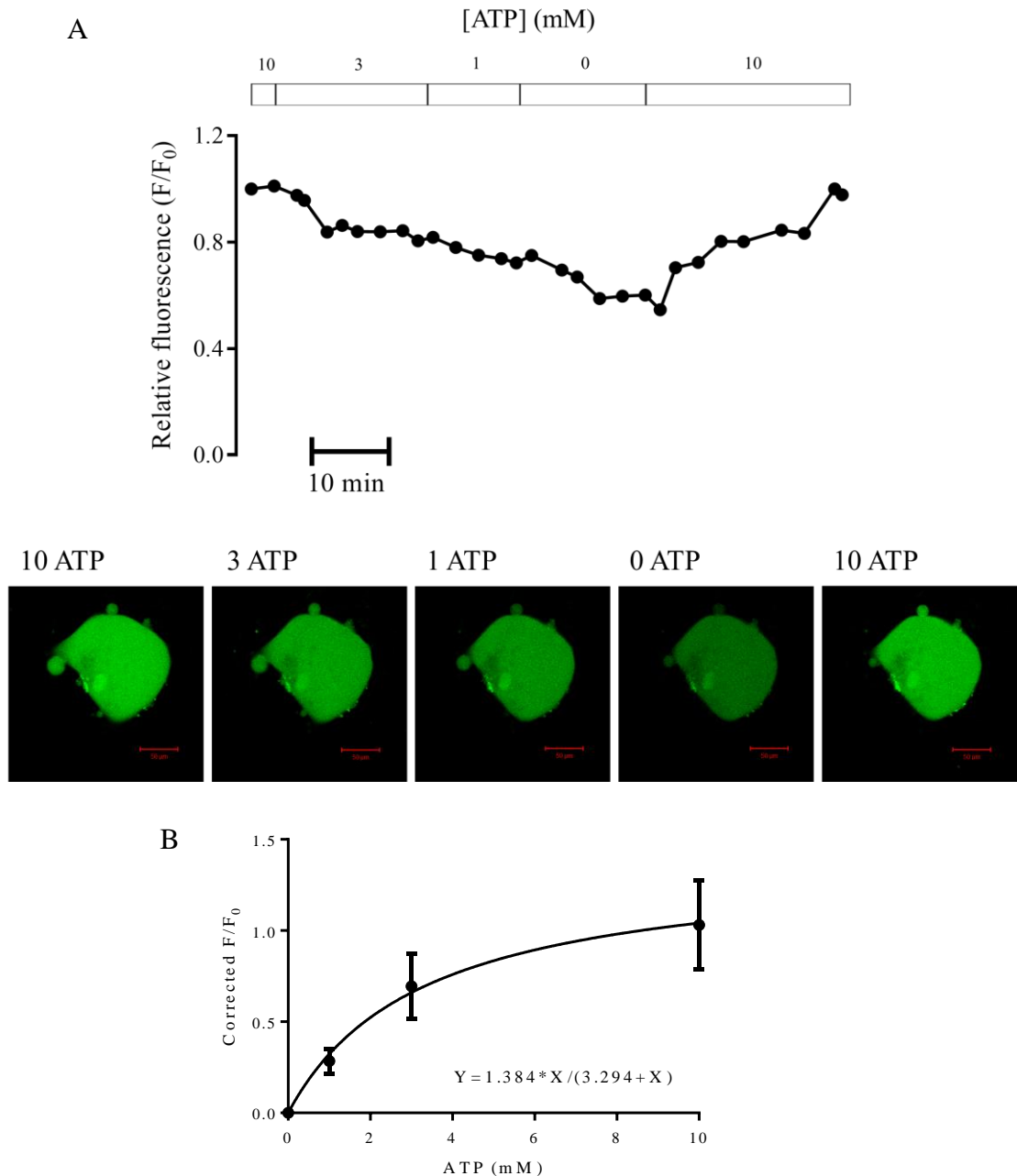


Figure 4.16: Dose-response curve of PercevalHR fluorescence as a function of ATP concentrations. (A) PercevalHR fluorescence determined over physiological range of ATP concentrations with corresponding confocal images of HCASMC. Scale bar is 50 μm . (B) Dose-response relationship between ATP concentration and FUGW-PercevalHR fluorescence (FUGW-PercevalHR fluorescence at 0 mM ATP was set as 0 here). Curve fitting of the data (hyperbolic function) shows a half maximal effect at ~ 3.29 mM ATP (n=4).

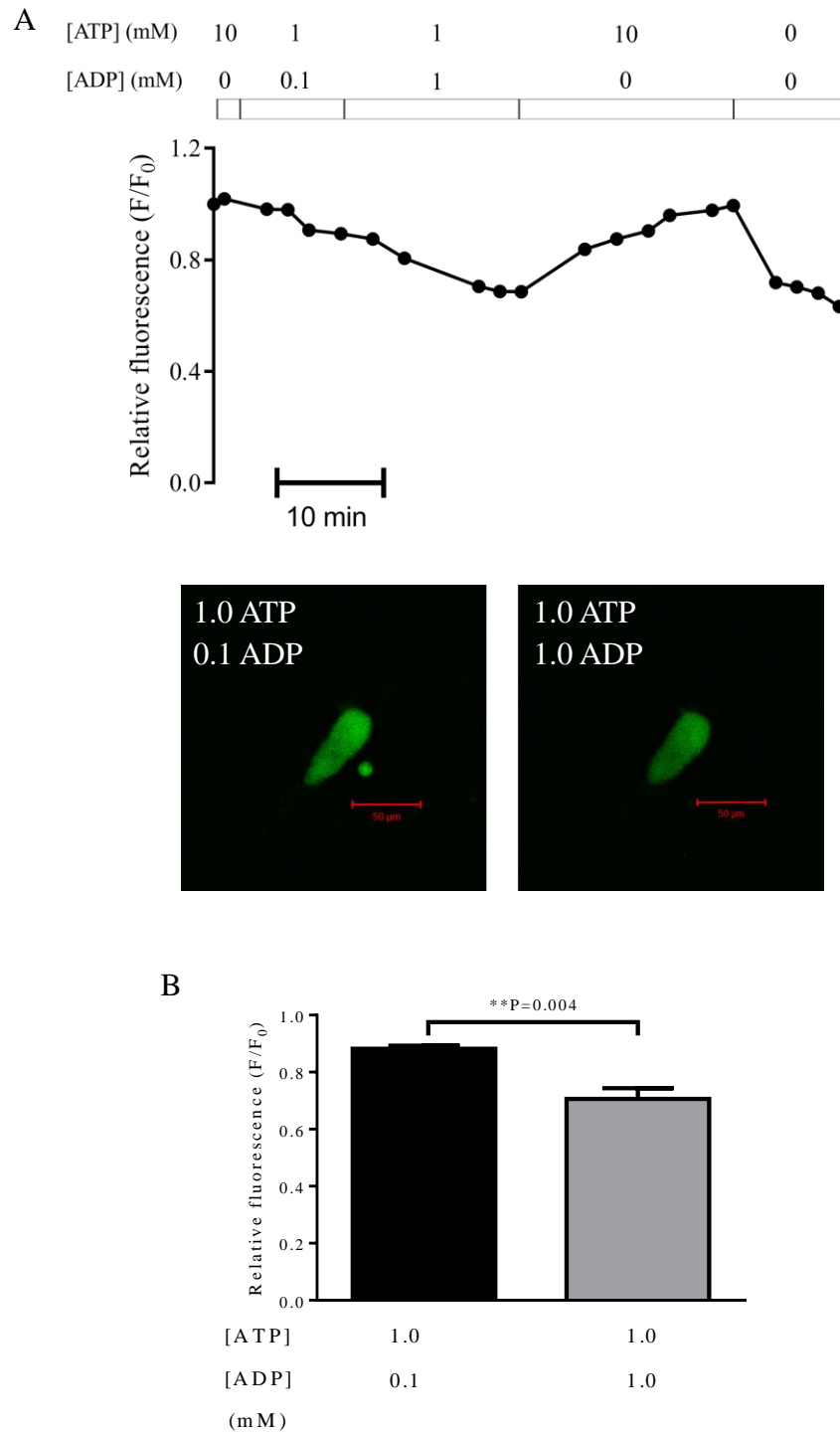


Figure 4.17: Effect of ADP on PercevalHR fluorescence. (A) Effect of ADP on PercevalHR signal in a single α -toxin permeabilised HCASMC. Confocal images of HCASMC with 0.1 (left) or 1.0 mM (right) ADP while ATP concentration was kept as 1.0 mM. Scale bar is 50 μ m. (B) Mean \pm SEM of PercevalHR fluorescence when α -toxin permeabilised cells were exposed to either 0.1 or 1 mM ADP when ATP was constant (1.0 mM) (n=5).

4.4.5 Metabolic inhibitors and intracellular ATP:ADP ratio

As mentioned earlier, chemical transfection efficiency with HCASMCs was very low. More importantly, the process seems to have detrimental effect on HCASMCs. This means that the effect of metabolic inhibitors and hypoxia evaluated with chemically transfected cells may not be reliable as metabolic state of the cells may not be physiological. Here, in order to overcome these problems, we repeated experiments using HCASMCs expressing PercevalHR by lentivirus transduction. In this part, the experiments with 2-DG and glucose deprivation were carried out with perfusion while test chemicals were added directly to the dish without perfusion for all other experiments.

4.4.5.1 Glycolytic inhibition with 2-DG

First, we examined the effect of glycolytic inhibitor, 2-DG, on PercevalHR signal. Cells were exposed to 5 mM 2-DG instead of 10 mM glucose. Upon application of 2-DG, PercevalHR fluorescence signal decreased by $42.37 \pm 4.11\%$ after 10 mins (**Figure 4.18**). There was no recovery in PercevalHR signal when 5 mM 2-DG was replaced by 10 mM glucose for 5 mins (data not shown).

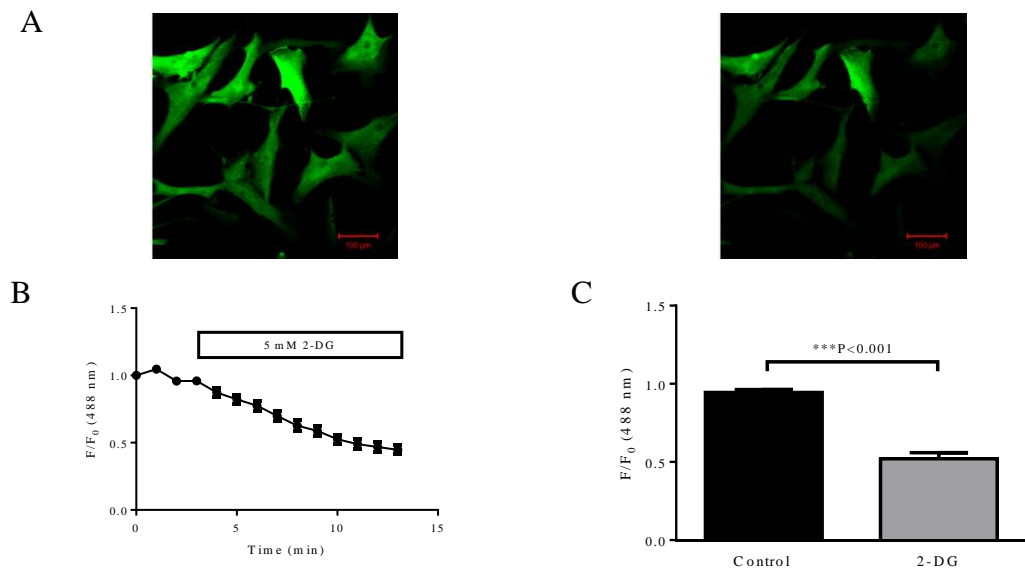


Figure 4.18: 2-DG caused decrease in PercevalHR signal. (A) Images of HCASMCs expressing PercevalHR before (left) and after (right) application of 5 mM 2-DG. (B) Time course of fractional fluorescence of cells shown in (A). (C) Mean \pm SEM of fractional fluorescence of PercevalHR before and after 5 mM 2-DG (n=18).

4.4.5.2 Effect of glucose removal on PercevalHR signal

Transient removal of glucose from extracellular solution caused about ~10% decrease in PercevalHR signal in 12 minutes, and it was reversed after glucose re-administration (**Figure 4.19**).

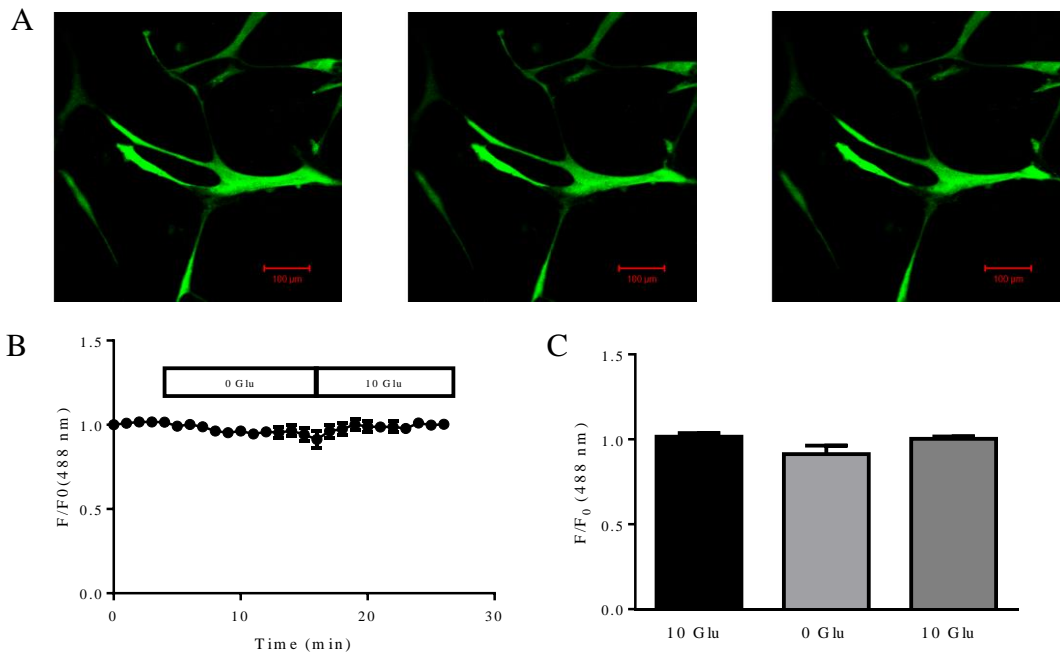


Figure 4.19: Transient glucose removal caused a transient decrease in PercevalHR signal. (A) Images of HCASMCs expressing PercevalHR under control condition (left), after 12 minutes of glucose removal (middle), and after glucose re-administration (right). (B) Time course of fractional fluorescence of the cells showed a ~10% decrease by glucose removal. Fluorescent signal recovered by glucose re-administration. (C) Mean \pm SEM of fractional fluorescence of PercevalHR measured with 10, 0 and 10 mM glucose (n=4, during this experiment several cells moved and contracted were excluded).

4.4.5.3 Time control and vehicle control of PercevalHR fluorescence

Prior to examining effect of metabolic inhibitors, control experiments were conducted to evaluate the possible bleaching of the fluorescence and drift in focal plane (time control, **Figure 4.20**) and the effect of DMSO on PercevalHR signal (vehicle control, **Figure 4.21**).

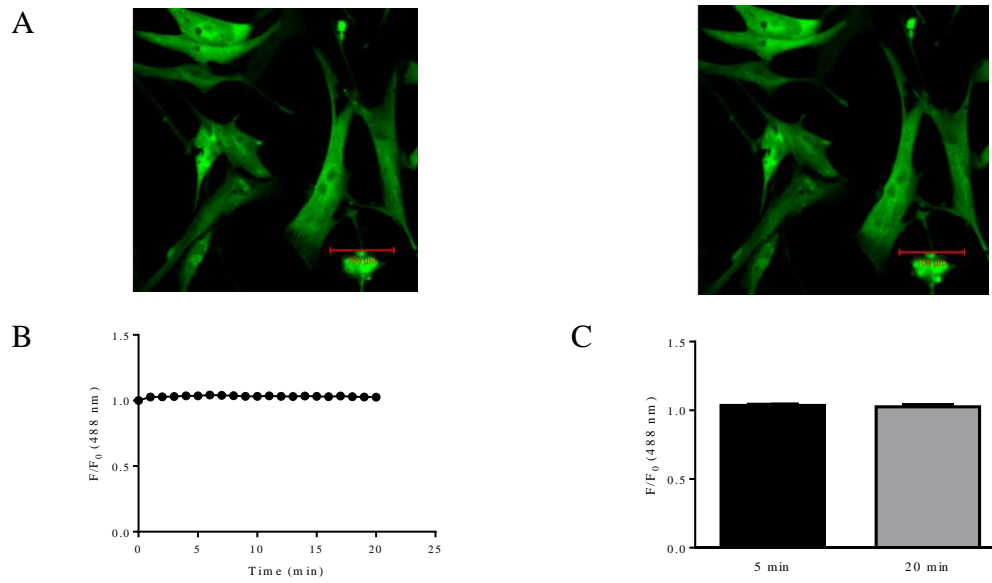


Figure 4.20: Time control of PercevalHR fluorescence. (A) Images of HCASMCs expressing PercevalHR at 5 min (left) and 20 min (right). (B) Time course of fractional fluorescence of the cells in (A). (C) Mean \pm SEM of fractional fluorescence of PercevalHR at 5 min and 20 min (n=63).

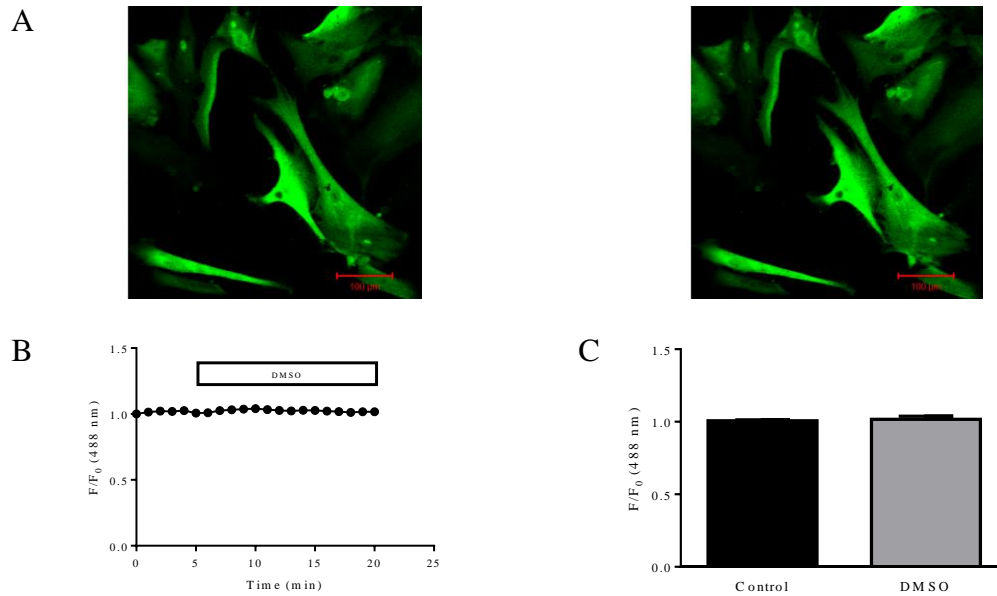


Figure 4.21: Vehicle control of PercevalHR fluorescence. (A) Images of HCASMCs expressing PercevalHR under control condition (left) and after 15 minutes application of DMSO (right). (B) Time course of fractional fluorescence of the cells in (A). (C) Mean \pm SEM of fractional fluorescence of PercevalHR before and after administration of DMSO (n=32).

4.4.5.4 Effects of inhibitors of oxidative phosphorylation on PercevalHR signal

Metabolic inhibition by blocking mitochondrial respiratory chain caused a significant decrease in the fractional fluorescence signal. Application of 1 μ M rotenone that blocks mitochondrial complex I caused a reduction by $16.36 \pm 2.32\%$ (**Figure 4.22**, n=58). Inhibiting mitochondrial complex III with 1 μ M antimycin reduced PercevalHR fluorescence by $53.92 \pm 2.38\%$ (**Figure 4.23**, n=41). An ATP synthase inhibitor, oligomycin (6 μ M), caused a decrease in PercevalHR signal by $37.97 \pm 2.17\%$ (**Figure 4.24**, n=71). 1 μ M CCCP, a proton ionophore, reduced PercevalHR signal by $33.14 \pm 2.76\%$ (**Figure 4.25**, n=54). However, hypoxia induced little change in PercevalHR fluorescence (**Figure 4.26**, n=5).

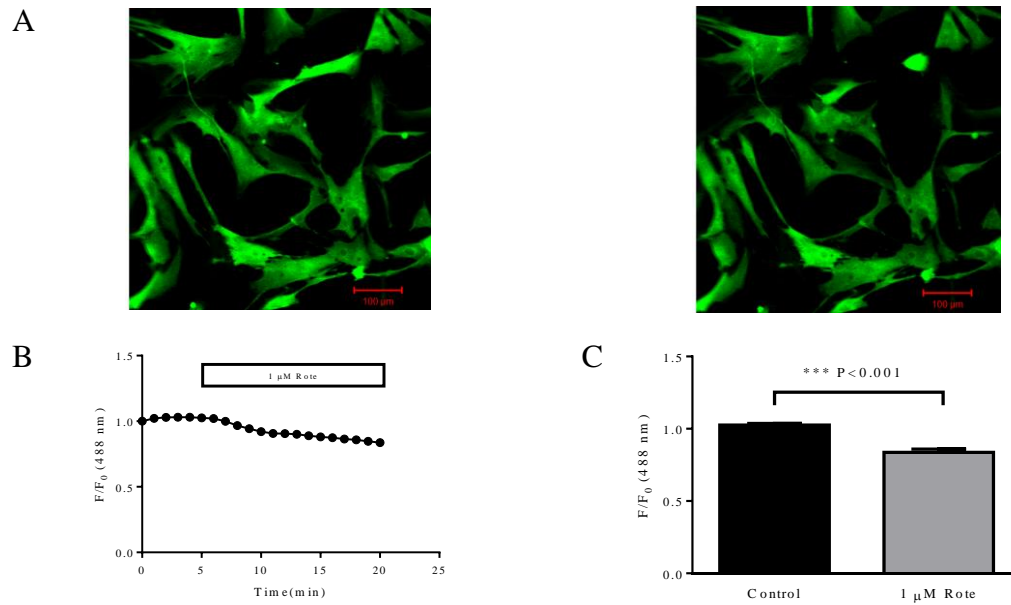


Figure 4.22: Metabolic inhibition of mitochondrial complex I caused a decrease in PercevalHR signal. (A) Images of HCASMCs expressing PercevalHR before (left) and after 15 minutes application of 1 μ M rotenone (right). (B) Time course of fractional fluorescence of the cells shown in (A). (C) Mean \pm SEM of fractional fluorescence of PercevalHR before and after administration of rotenone (n=58).

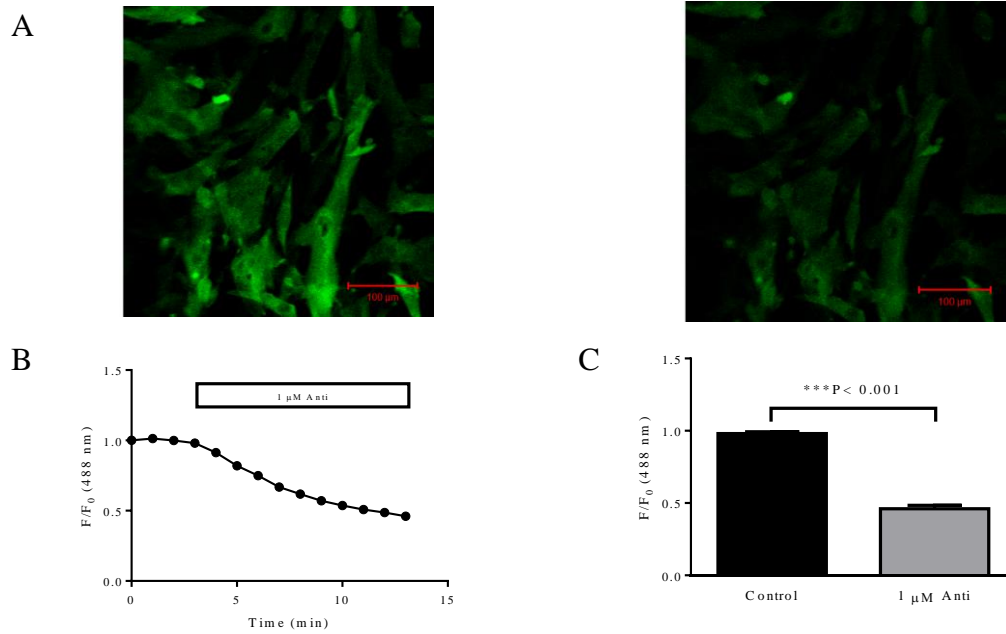


Figure 4.23: Metabolic inhibition of mitochondrial complex III caused a decrease in PercevalHR signal. (A) Images of HCASMCs expressing PercevalHR under control condition (left) and after 10 minutes application of 1 μM antimycin (right). (B) Time course of fractional fluorescence of the cells shown in (A). (C) Mean \pm SEM of fractional fluorescence of PercevalHR before and after administration of 1 μM antimycin (n=41).

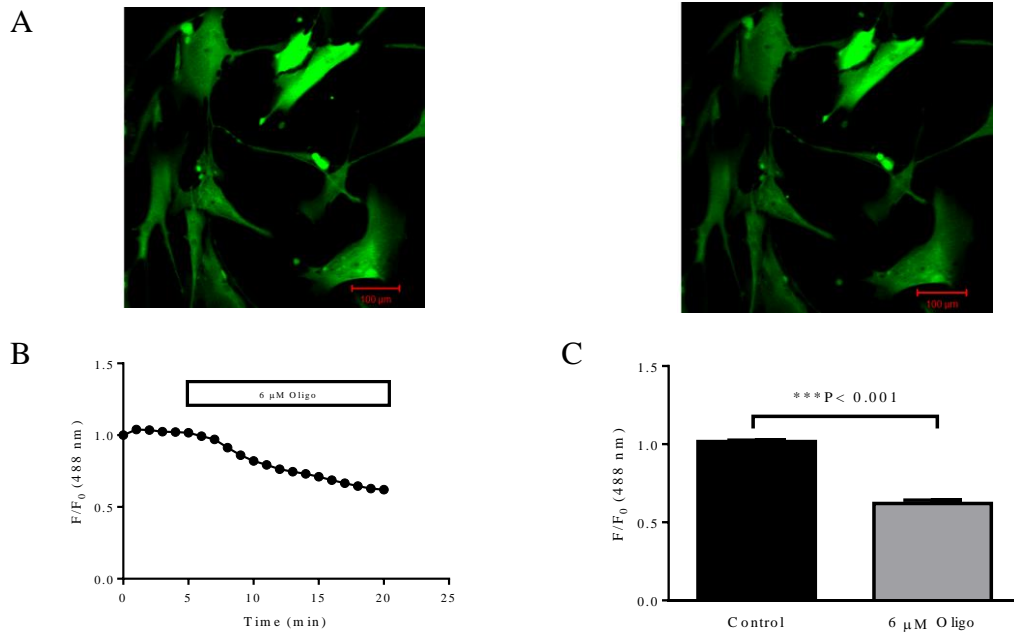


Figure 4.24: Blocking ATP synthase caused a decrease in PercevalHR signal. (A) Images of HCASMCs expressing PercevalHR under control condition (left) and after 15 minutes application of 6 μM oligomycin (right). (B) Time course of fractional fluorescence of the cells shown in (A). (C) Mean \pm SEM of fractional fluorescence of PercevalHR before and after administration of 6 μM oligomycin (n=71).

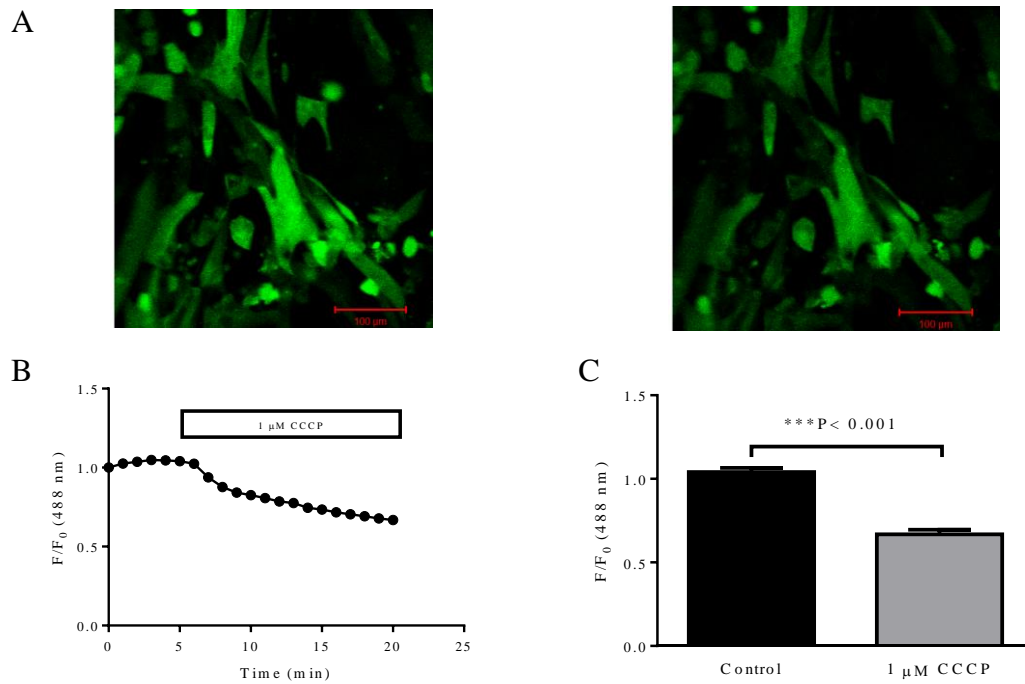


Figure 4.25: Application of proton ionophore resulted in a reduction in PercevalHR signal. (A) Images of HCASMCs expressing PercevalHR under control condition (left) and after 15 minutes application of 1 μ M CCCP (right). (B) Time course of fractional fluorescence of the cells shown in (A). (C) Mean \pm SEM of fractional fluorescence of PercevalHR before and after administration of 1 μ M CCCP (n=54).

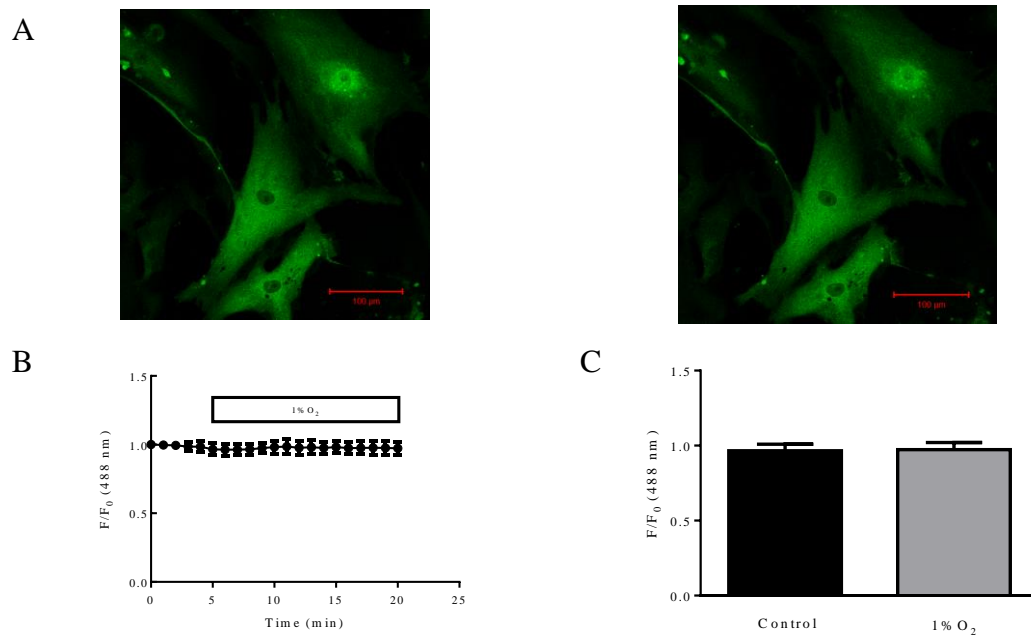


Figure 4.26: Effect of hypoxia on PercevalHR signal. (A) Images of HCASMCs expressing PercevalHR under control condition (left) and after 15 minutes exposure to 1% O₂ (right). (B) Time course of fractional fluorescence of the cells showed hypoxia caused little change in PercevalHR fluorescence. (C) Mean \pm SEM of fractional fluorescence of PercevalHR before and after exposure to hypoxia (n=5).

4.4.5.5 Interrelationship of the components in mitochondrial respiratory chain

The process taking place in mitochondria to generate ATP is complex. In order to further understand individual steps, metabolic inhibitors were sequentially applied to the cells. In order to test relationship between complex I and complex III, HCASMCs were first incubated with 1 μ M rotenone for 10 mins, then 1 μ M antimycin was applied. Antimycin caused a further decrease in PercevalHR fluorescence (**Figure 4.27**) indicating that blocking complex I did not abolish the effect of inhibiting downstream electron transport. We also tested the relationship between electron transport chain and ATP synthase by inhibiting ATP synthase with 6 μ M oligomycin in the presence of 1 μ M antimycin. 6 μ M oligomycin had no additional effect on PercevalHR fluorescence in the cells pre-treated with 1 μ M antimycin (**Figure 4.28**). Thus, ATP synthase appears to be tightly coupled with the mitochondrial inner membrane potential in HCASMCs.

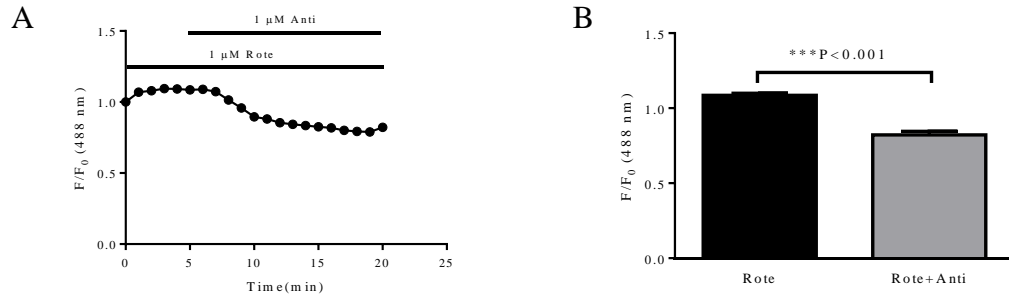


Figure 4.27: Interrelationship of mitochondrial complex I and complex III. (A) Time course of fractional fluorescence of the cells treated with 1 μM antimycin in the presence of 1 μM rotenone. Antimycin decreased PercevalHR fluorescence of the cells pre-treated with rotenone. (B) Mean \pm SEM of fractional fluorescence of PercevalHR before and after the application of 1 μM antimycin in the presence of rotenone. (n=11)

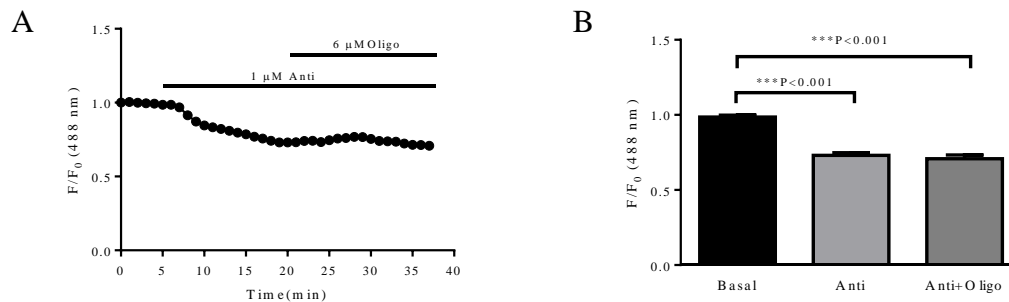


Figure 4.28: Interrelationship of ETC and ATP synthase. (A) Time course of fractional fluorescence of the cells treated with 1 μM antimycin followed by 6 μM oligomycin. (B) Mean \pm SEM of fractional fluorescence of PercevalHR at basal state and after application of 1 μM antimycin, then 6 μM oligomycin in the continued presence of antimycin (n=22).

4.4.5.6 Ratiometric measurement of PercevalHR signal

PercevalHR appeared to show non-uniform distribution in HCASMCs (e.g. **Figure 4.26**). This could be due to a true reflection of ATP:ADP gradient within a cell. However, this may be also due to the uneven distribution of the biosensor itself influenced by cell thickness and internal structure such as nucleus and sarcoplasmic reticulum [187]. PercevalHR can be used as a ratiometric biosensor, meaning the

intensity of the signal could be made concentration independent [186, 187]. This could be done as $F_{\text{high}}/F_{\text{low}}$ (F_{500}/F_{420}) or as $F_{\text{high}}/F_{\text{iso}}$ (F_{500}/F_{455}) using an isosbestic point at ~455 nm (**Figure 4.29**) [186]. Due to a lack of the exact wavelengths available, F_{488}/F_{458} was used instead of F_{500}/F_{455} in the experiment. A pixel-to-pixel ratiometric image showed that PercevalHR was unevenly distributed in HCASMCs with signal higher at peripheral region than inside the cell (**Figure 4.30A, 4.31A & 4.32A**). Changes in PercevalHR fluorescence were analyzed by drawing a region of interest inside the cell, and there was no obvious change in F_{488}/F_{458} signal of both time control and vehicle control (**Figure 4.30 & 4.31**). **Figure 4.32** shows the effect of rotenone on F_{488}/F_{458} ratio signal. The ratiometric 2D images before (left) and after (right) application of 1 μM rotenone showed that signal decrease occurred throughout the cell even though the biosensor distribution was uneven (**Figure 4.32A**). The time course of ratiometric measurement (**Figure 4.32B**, left panel) was essentially identical to that of 488 nm (**Figure 4.32B**, right top panel). Time course of 458 nm signal was not completely flat, perhaps reflecting it is not the true isosbestic point (**Figure 4.32B**, right bottom panel). Therefore, we feel safe that PercevalHR signal measured at 488 nm is reliable in reporting ATP:ADP changes.

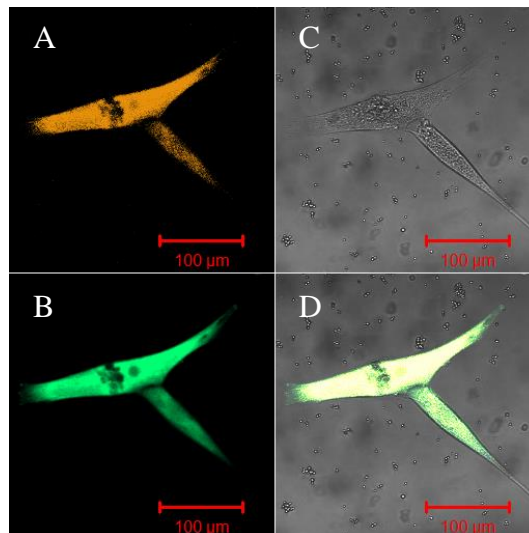


Figure 4.29: HCASMCs expressing FUGW-PercevalHR. (A) Cells excited at near isosbestic point of 458 nm. (B) Cells excited at 488 nm. (C) Brightfield image. (D) Overlay image.

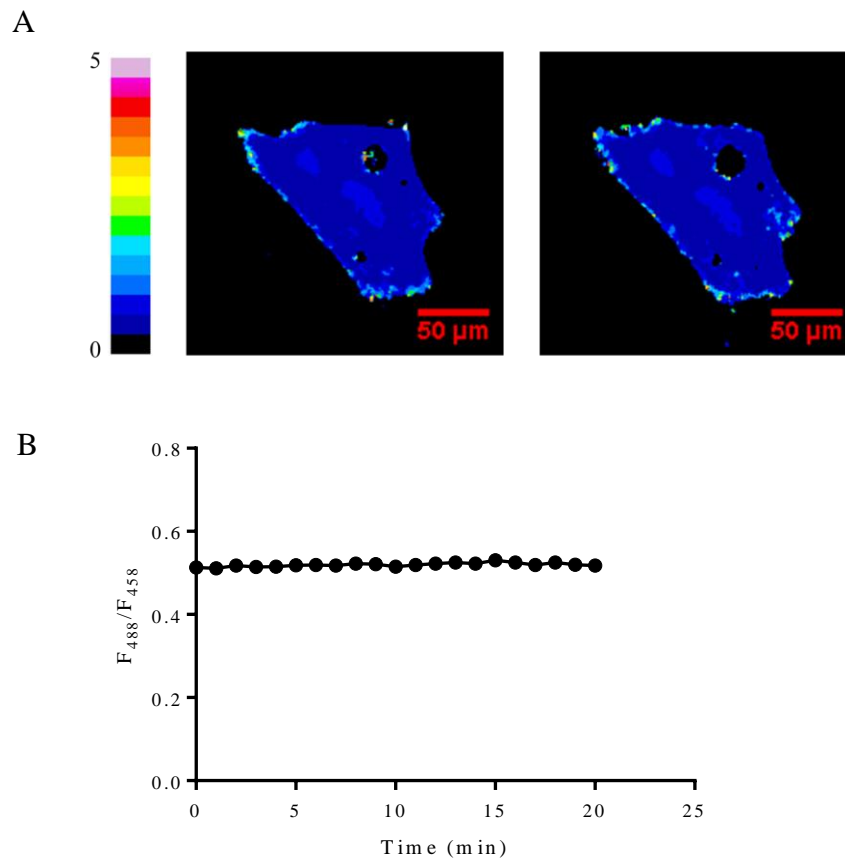


Figure 4.30: Time control of ratiometric imaging. (A) A pixel-to-pixel ratio of 488 nm excitation image divided with 458 nm excitation image from a single HCASMC at time 5 min (left) and 20 min (right) respectively. Images are pseudo-coloured with ratio of 0-5. (B) Time course of $F_{488\text{ nm}}/F_{458\text{ nm}}$ from a region of interest of the cell shown in (A).

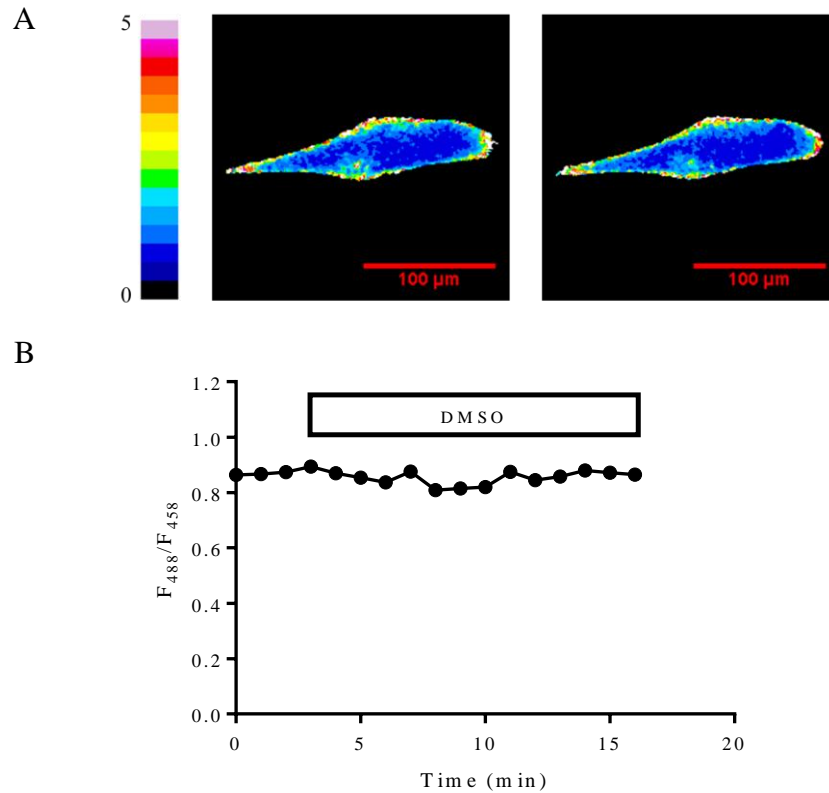


Figure 4.31: Vehicle control of ratiometric imaging. (A) A pixel-to-pixel ratio of 488 nm excitation image divided with 458 nm excitation image from an individual HCASMC before (left) and after application of DMSO (right). Images are pseudo-coloured with ratio of 0-5. (B) Time course of $F_{488\text{ nm}}/F_{458\text{ nm}}$ from a region of interest of the cell shown in (A).

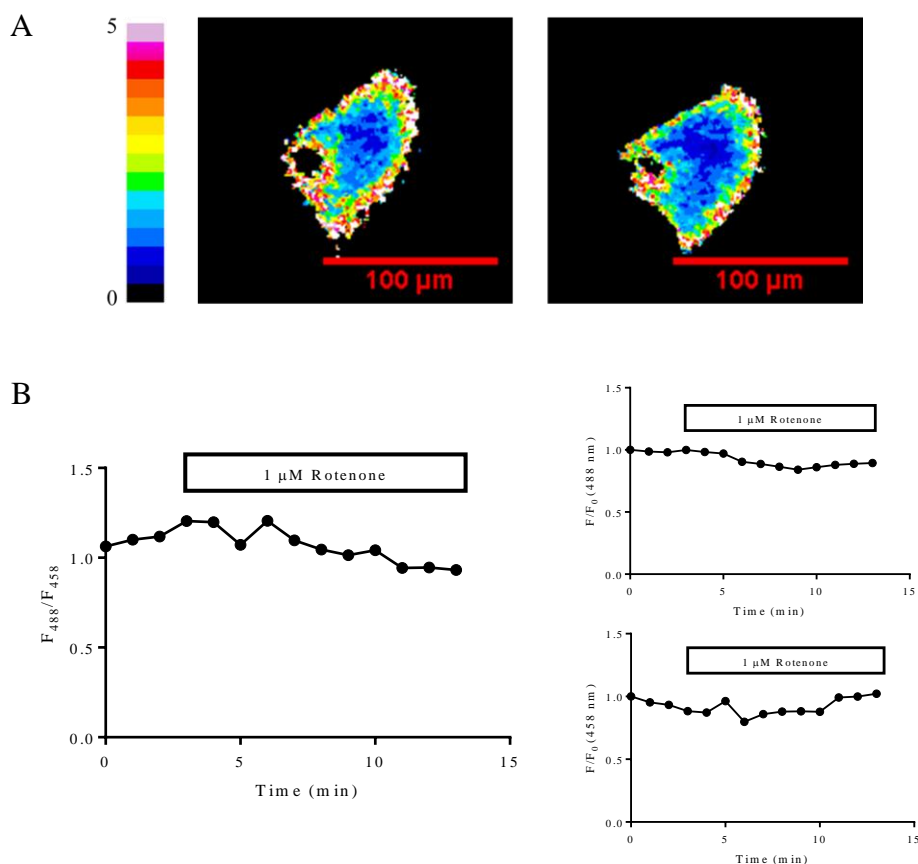


Figure 4.32: Effect of rotenone on PercevalHR ratiometric signal. (A) A pixel-to-pixel ratio of 488 nm excitation image divided with 458 nm excitation image from a single HCASMC during control condition (left) and after application of 1 μM rotenone (right). Images are pseudo-coloured with ratio of 0-5. (B) Time course of $F_{488 \text{ nm}}/F_{458 \text{ nm}}$ ratio showed a $\sim 23\%$ decrease after 10 minutes when compared to the time point just before the application of 1 μM rotenone. The right panels give the individual time course of 488 nm (top panel) and 458 nm (bottom panel) signals where the latter is near isosbestic point.

4.4.6 Constructing FUGW-pHRed

Lentivirus induction dramatically increased the transfection efficiency of PercevalHR while keeping HCASMCs in a better condition. Following this improvement, we constructed a lentivirus based FUGW-pHRed by inserting pHRed into the lentivirus vector made from FUGW-PercevalHR (**Figure 4.33**). The ligation product was verified by restriction analysis on an agarose gel (**Figure 4.34**) and DNA

sequencing.

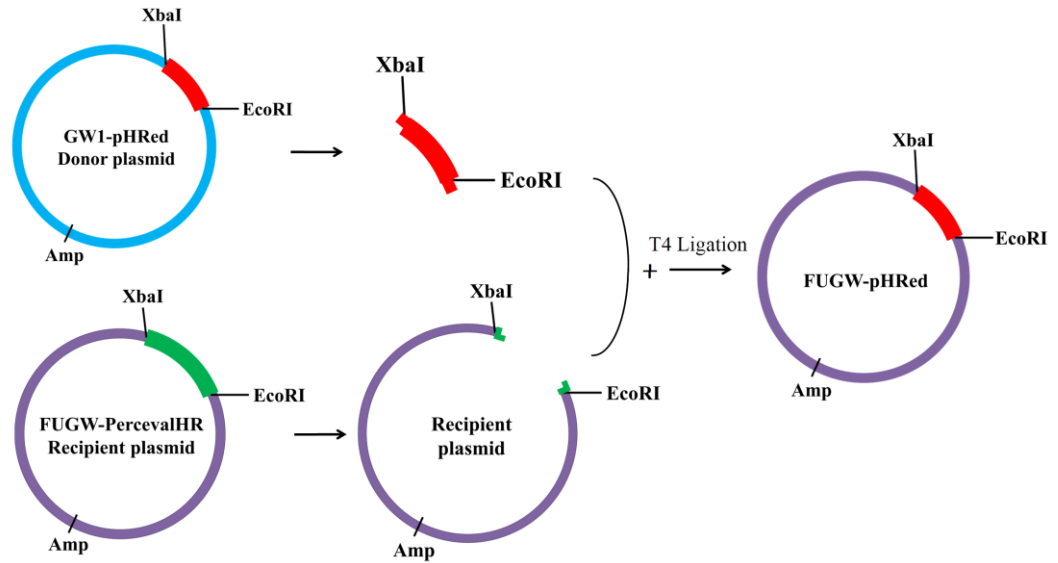


Figure 4.33: Schematic diagram of constructing FUGW-pHRed. Restriction digest was performed on both GW1-pHRed and FUGW-PercevalHR using XbaI and EcoRI. An agarose gel was run with the restriction mixture, and the insert and vector of interest were then isolated by gel extraction and purification. T4 ligation was performed in the end in order to ligate the insert with the vector.

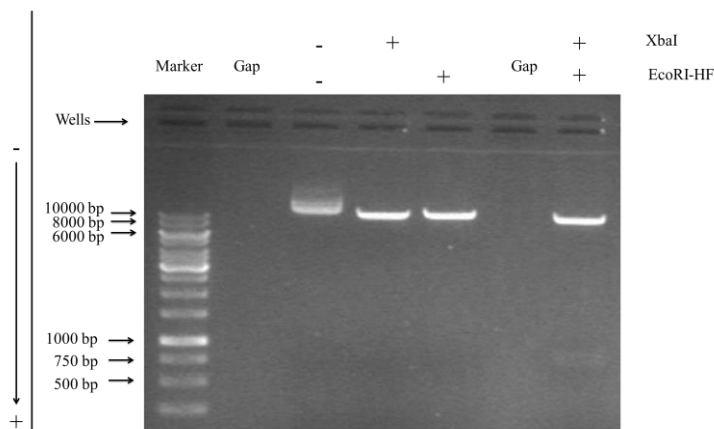


Figure 4.34: Agarose gel verification of FUGW-pHRed. Product of FUGW-pHRed digested with XbaI and EcoRI-HF was run on a 1% agarose gel. The DNA size marker is a commercial 1 kb gene ruler. The position of the wells and direction of DNA migration is noted.

4.4.7 Transfection of HCASMCs with FUGW-pHRed

HCASMCs transduced with FUGW-pHRed were checked after day 3 using EVOS FL cell imaging system (**Figure 4.35**).

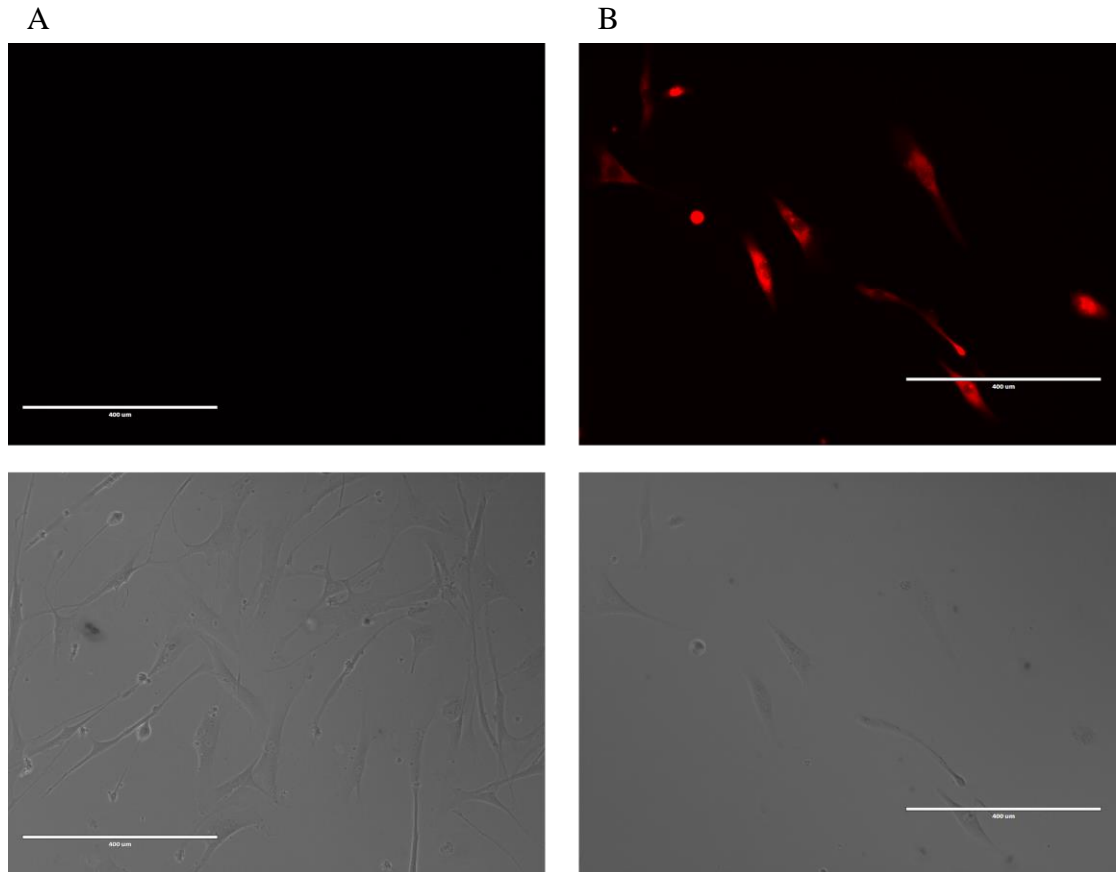


Figure 4.35: HCASMCs expressing FUGW-pHRed. (A) Negative control of the transfection. (B) HCASMCs infected with FUGW-pHRed. Scale bar is 400 μm .

4.4.8 Effect of metabolic inhibitors on intracellular pH

Time control and vehicle control were carried out first to ensure that FUGW-pHRed signal was stable during the course of experiments (**Figures 4.36 & 4.37**). We next tested the effects of metabolic inhibitors on pHRed signal. 1 μM rotenone or 6 μM oligomycin caused little change (**Figures 4.38 & 4.39**). 1 μM antimycin in the presence of 1 μM rotenone had little effect on pHRed signal (**Figure 4.40**). Because a sequential application of metabolic inhibitors was used in previous experiments with Perceval HR (e.g. **Figure 4.27**), we also examined effect of metabolic inhibitors on pH when applied sequentially. Application of 1 μM CCCP to

the cells pre-incubated with 6 μM oligomycin also showed little change in pHRed signal (**Figure 4.41**). These manipulations indicated that the changes in ATP:ADP signal recorded using PercevalHR were not caused by a change in cellular pH. Note that the positive control for pHRed using NH_4Cl was already provided (see **Figure 3.35**).

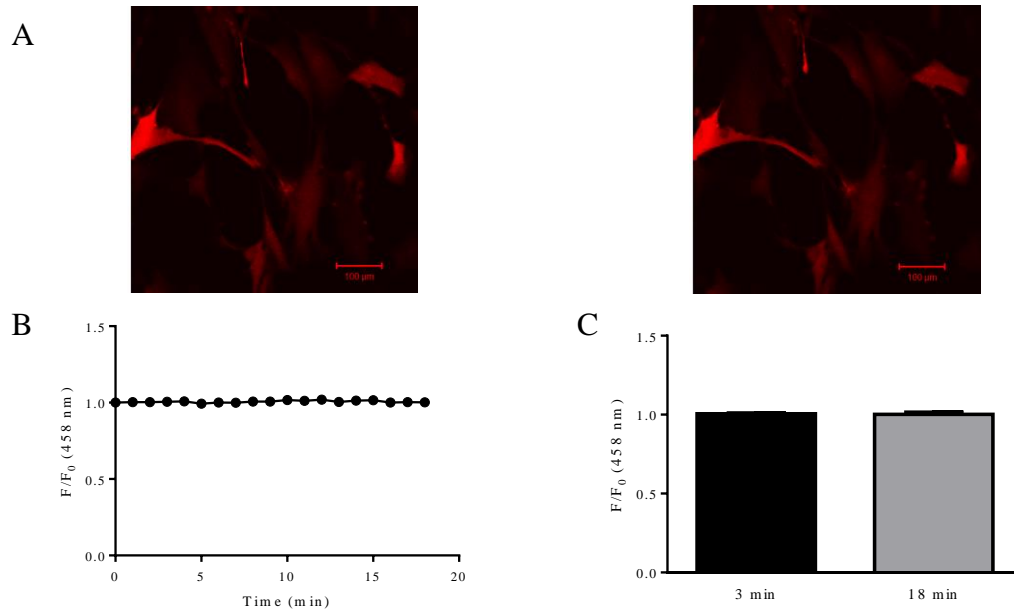


Figure 4.36: Time control of FUGW-pHRed fluorescence. (A) Images of FUGW-pHRed transfected cells at 3 min (left) and 18 min (right). (B) Time course of fractional fluorescence of the cells during a period of 18 mins. (C) Mean \pm SEM of fractional fluorescence of pHRed at 3 min and 18 min (n=35).

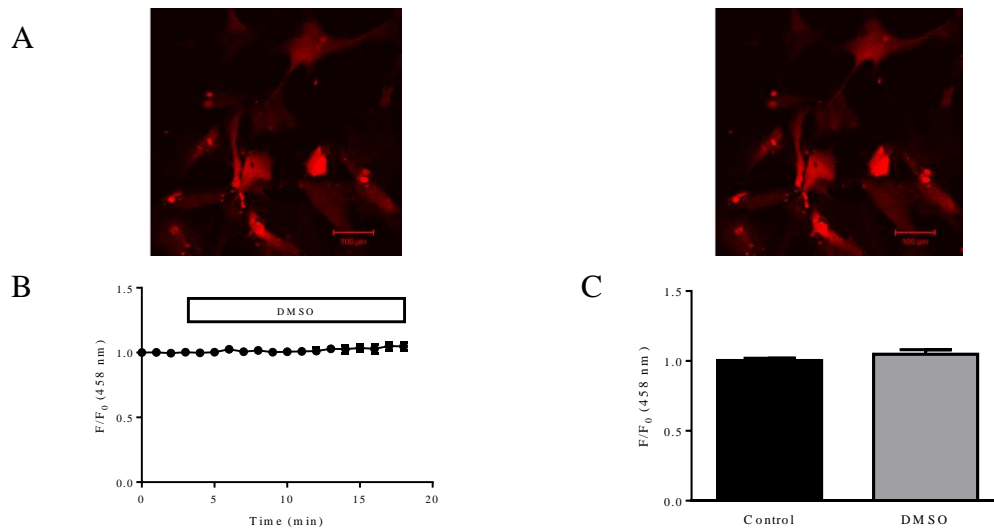


Figure 4.37: Vehicle control of FUGW-pHRed fluorescence signal. (A) Images of FUGW-pHRed transfected cells before (left) and after (right) application of DMSO. (B) Treating the cells with DMSO for 15 mins had little effect on pHRed fluorescence. (C) Mean \pm SEM of fractional fluorescence of pHRed before and after DMSO application (n=23).

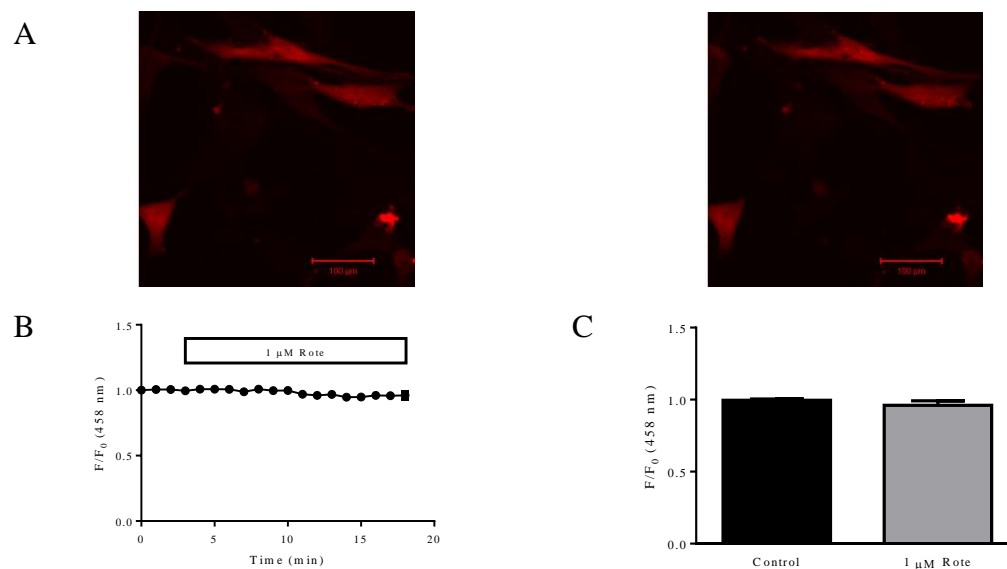


Figure 4.38: Effect of rotenone on pHRed signal. (A) Images of FUGW-pHRed transfected cells before (left) and after (right) application of 1 μ M rotenone. (B) pHRed reported little change after the application of 1 μ M rotenone. (C) Mean \pm SEM of fractional fluorescence of pHRed before and after 1 μ M rotenone application (n=5).

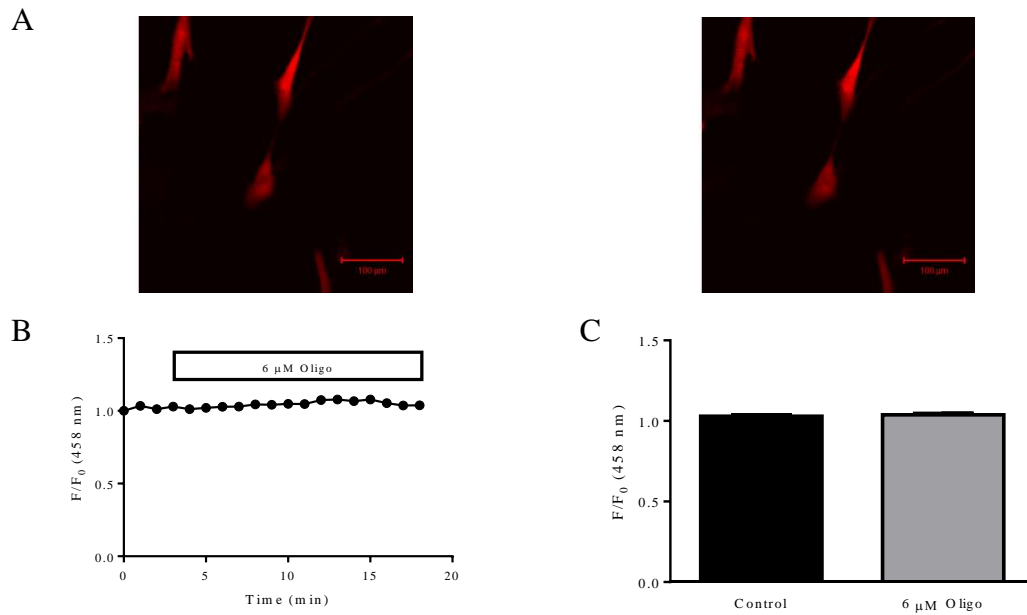


Figure 4.39: Effect of oligomycin on pHRed signal. (A) Images of FUGW-pHRed transfected cells before (left) and after (right) application of 6 μM oligomycin. (B) There was little change in pHRed signal after the application of 6 μM oligomycin. (C) Mean \pm SEM of fractional fluorescence of pHRed before and after application of 6 μM oligomycin (n=4).

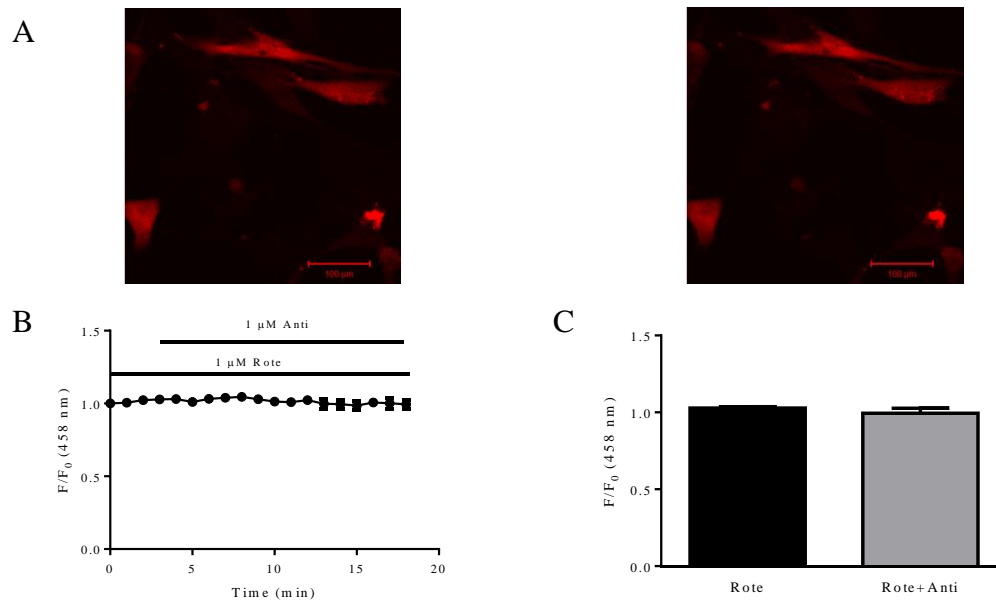


Figure 4.40: Effect of antimycin on cellular pH in the presence of rotenone. (A) Images of FUGW-pHRed transfected cells treated with 1 μM rotenone (left) and after subsequent application of 1 μM antimycin in the continued presence of rotenone (right). (B) 1 μM antimycin induced no change in pHRed signal in the presence of 1 μM rotenone. (C) Mean \pm SEM of fractional fluorescence of pHRed before and after application of 1 μM antimycin of the cells pre-treated with rotenone (n=5).

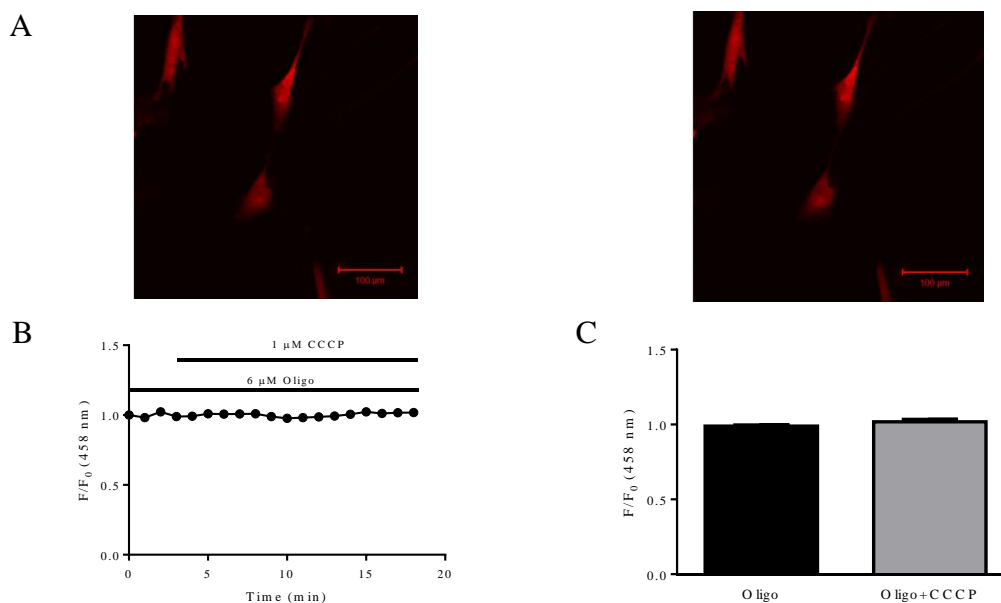


Figure 4.41: Effect of CCCP on pHRed signal in the presence of oligomycin. (A) Images of FUGW-pHRed transfected cells treated with 6 μM oligomycin (left) and after application of 1 μM CCCP in the continued presence of oligomycin (right). (B) Exposure to 1 μM CCCP to cells pre-incubated with 6 μM oligomycin showed little change in pHRed signal. (C) Mean \pm SEM for fractional fluorescence of pHRed before and after application of 1 μM CCCP in the presence of oligomycin (n=4).

4.4.9 Ratiometric measurement of intracellular pH

Like PercevalHR, pHRed can also be used for ratiometric imaging where signal can be made protein concentration independent. It exhibits dual excitation peaks at 440 and 585 nm, and emission peak at 610 nm [197]. Further experiments were carried out to measure intracellular pH ratiometrically. Cells expressing pHRed were excited at 458 and 561 nm, the closest wavelength options of LSM510 multiphoton confocal microscope (**Figure 4.42**). Blocking mitochondrial respiratory chain with a single inhibitor exerted little effect on intracellular pHRed signal (**Figures 4.43, 4.44, 4.45, 4.46, 4.47 & 4.48**). Application of 1 μM CCCP in the presence of 1 μM antimycin also showed little change in pHRed signal (**Figure 4.49**).

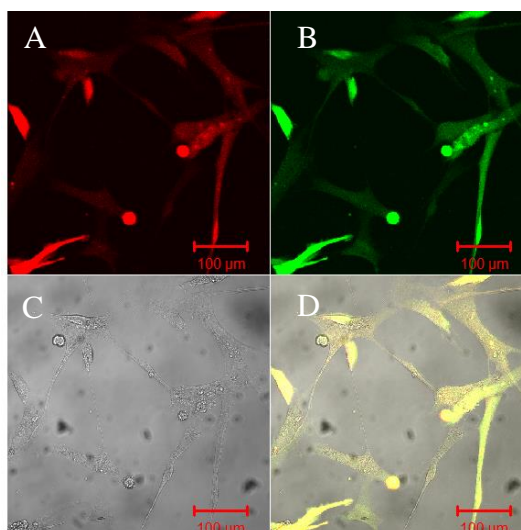


Figure 4.42: HCASMCs expressing FUGW-pHRed. (A) Cells expressing pHRed excited at 458 nm. (B) Cells expressing pHRed excited at 561 nm. (C) Brightfield image. (D) Overlay image.

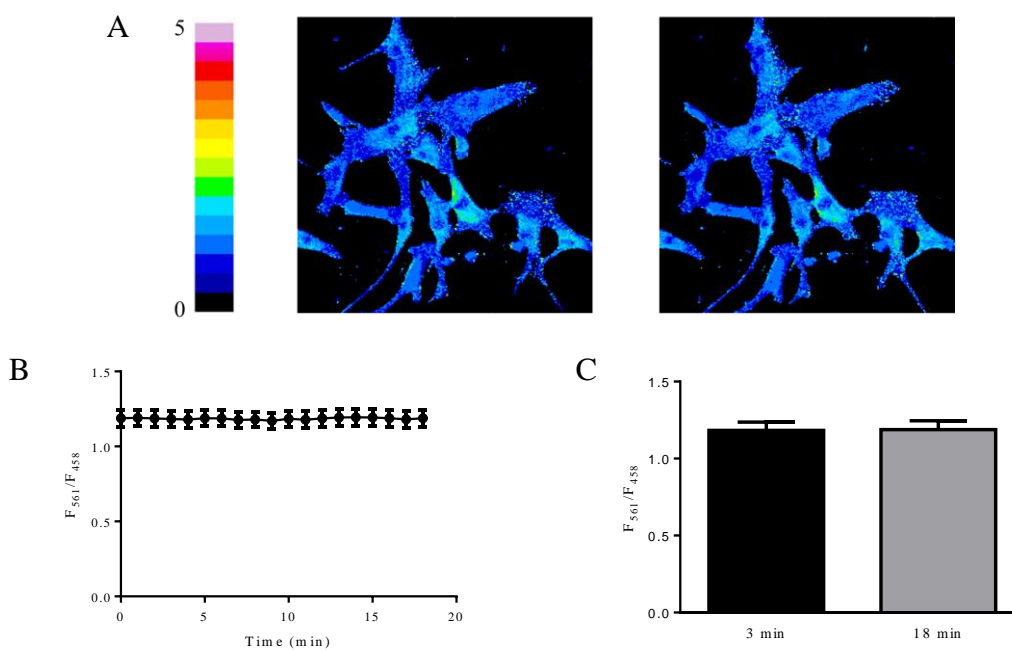


Figure 4.43: Time control of FUGW-pHRed fluorescence. (A) A pixel-to-pixel ratio of 561 nm excitation image divided by excitation image of 458 nm from HCASMCs expressing pHRed at 3 min and 18 min, respectively. Images are pseudo-coloured with ratio of 0-5. (B) Time course of $F_{561 \text{ nm}}/F_{458 \text{ nm}}$ ratio showed no change during 18 mins period. (C) Mean \pm SEM of ratio fluorescence of pHRed at time point 3 min and 18 min (n=54).

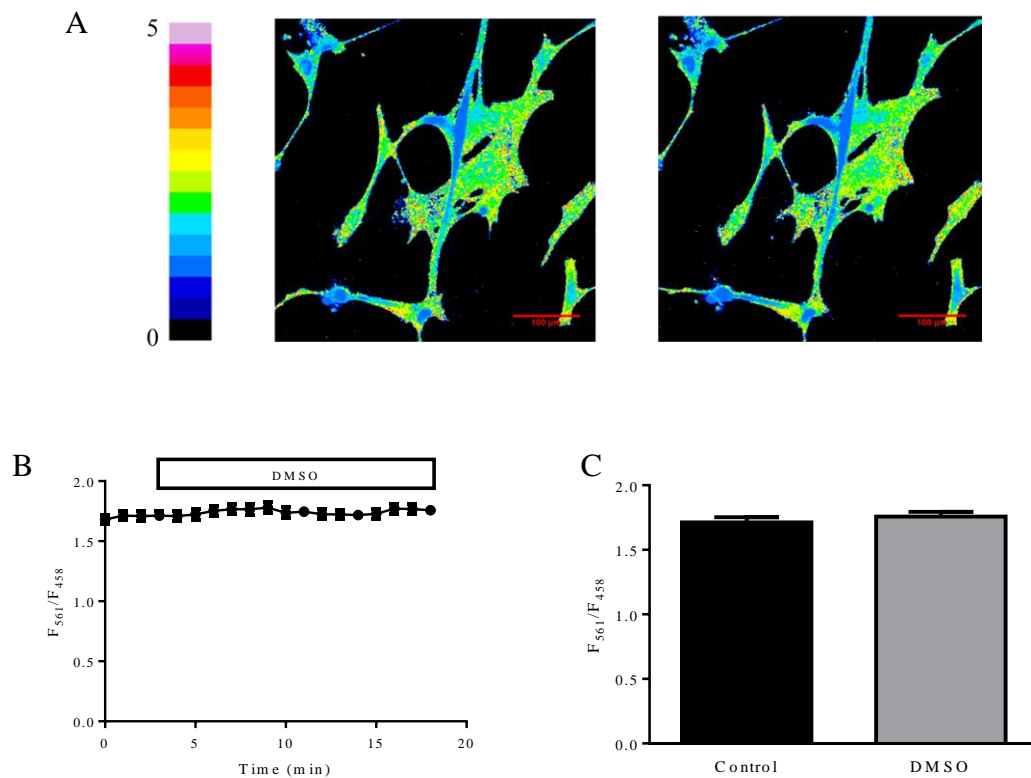


Figure 4.44: Vehicle control of FUGW-pHRed fluorescence. (A) A pixel-to-pixel ratio of 561 nm excitation image divided by excitation image of 458 nm from HCASMCs expressing pHRed before (left) and after (right) the application of DMSO. Images are pseudo-coloured with ratio of 0-5. (B) Time course of $F_{561\text{ nm}}/F_{458\text{ nm}}$ ratio showed no change after the application of DMSO. (C) Mean \pm SEM of ratio fluorescence of pHRed during control condition and after adding DMSO (n=11).

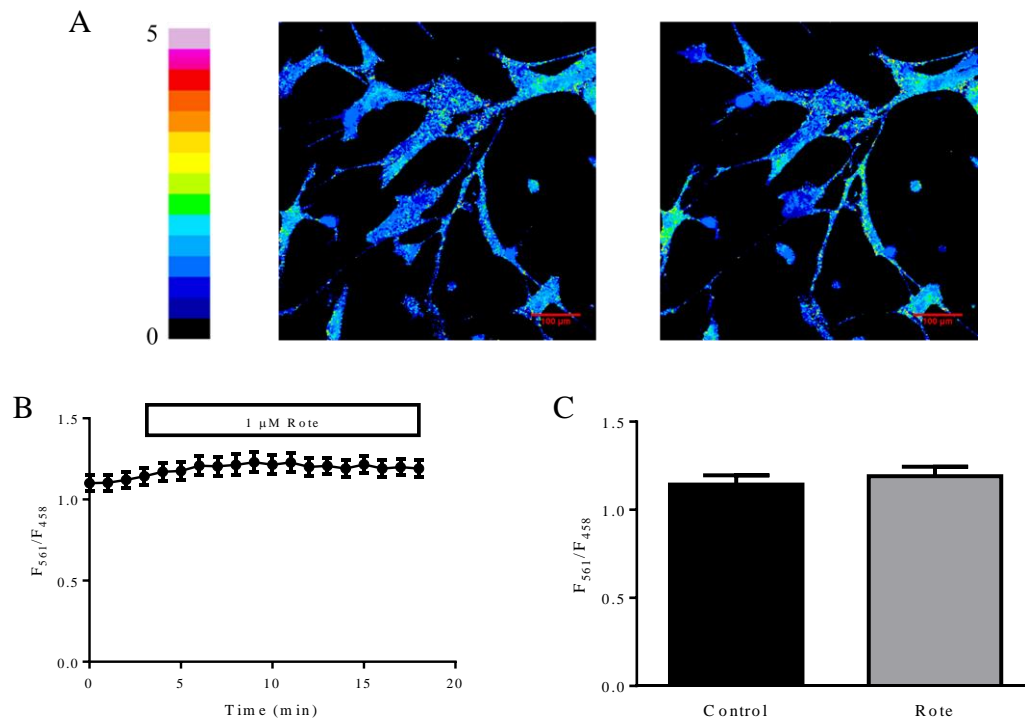


Figure 4.45: Effect of rotenone on FUGW-pHRed ratio fluorescence. (A) A pixel-to-pixel ratio of 561 nm excitation image divided by excitation image of 458 nm from HCASMCs expressing pHRed before (left) and after (right) the application of 1 μM rotenone. Images are pseudo-coloured with ratio of 0-5. (B) Time course of $F_{561 \text{ nm}}/F_{458 \text{ nm}}$ showed little change in the fluorescence ratio after application of 1 μM rotenone. (C) Mean \pm SEM of ratio fluorescence of pHRed during control condition and after adding 1 μM rotenone (n=13).

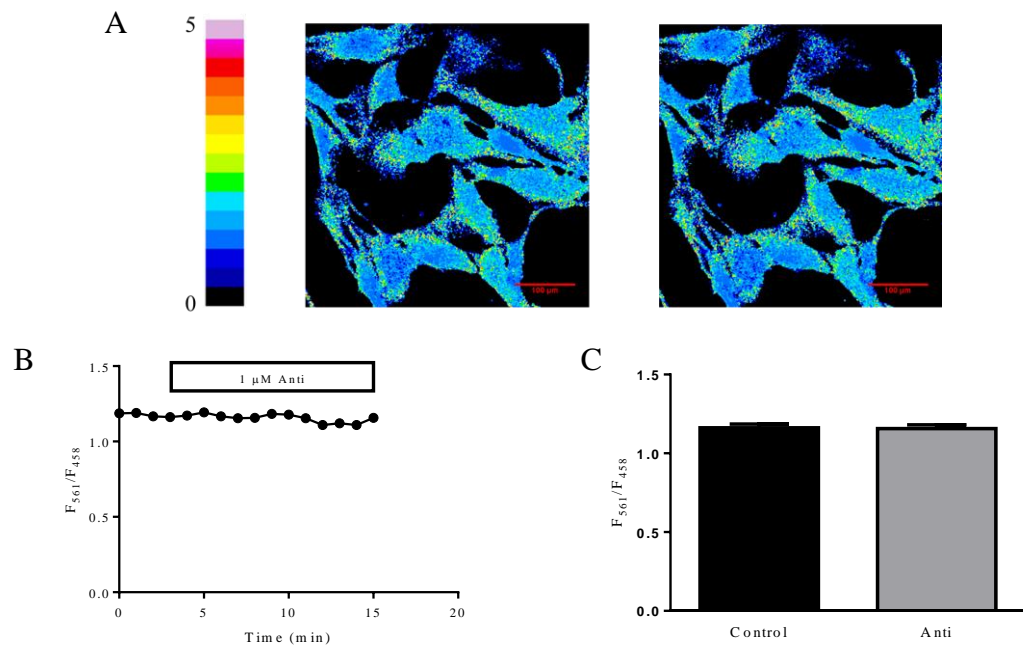


Figure 4.46: Effect of antimycin on FUGW-pHRed ratio fluorescence. (A) A pixel-to-pixel ratio of 561 nm excitation image divided by excitation image of 458 nm from HCASMCs expressing pHRed before (left) and after (right) the application of 1 μ M antimycin. Images are pseudo-coloured with ratio of 0-5. (B) Time course of $F_{561 \text{ nm}}/F_{458 \text{ nm}}$ showed little change in the fluorescence ratio after application of 1 μ M antimycin. (C) Mean \pm SEM of ratio fluorescence of pHRed during control condition and after adding 1 μ M antimycin (n=16).

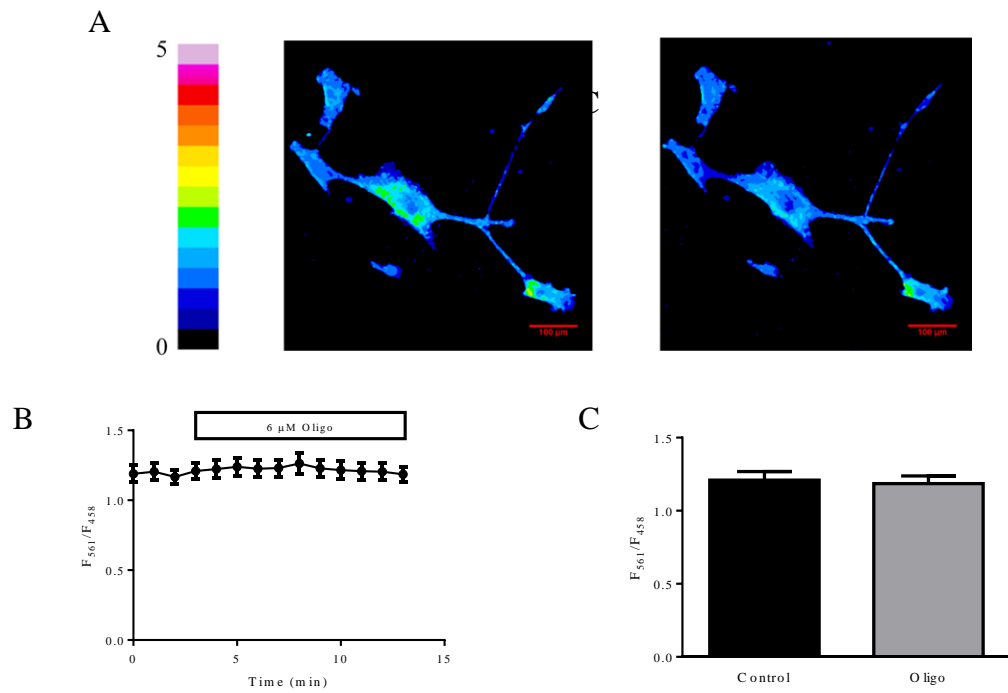


Figure 4.47: Effect of oligomycin on FUGW-pHRed ratio fluorescence. (A) A pixel-to-pixel ratio of 561 nm excitation image divided by excitation image of 458 nm from HCASMCs expressing pHRed before (left) and after (right) the application of 6 μM oligomycin. Images are pseudo-coloured with ratio of 0-5. (B) Time course of $F_{561\text{ nm}}/F_{458\text{ nm}}$ showed no change in the fluorescence ratio after application of 6 μM oligomycin. (C) Mean \pm SEM of ratio fluorescence of pHRed during control condition and after adding 6 μM oligomycin (n=4).

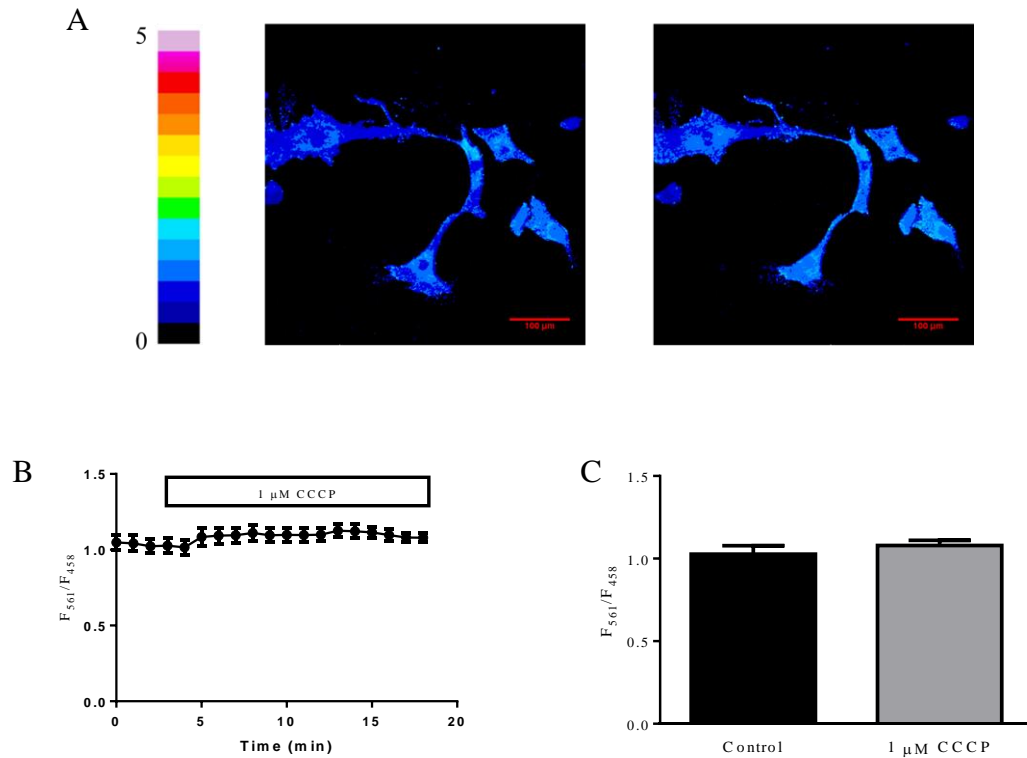


Figure 4.48: Effect of CCCP on FUGW-pHRed ratio fluorescence. (A) A pixel-to-pixel ratio of 561 nm excitation image divided by excitation image of 458 nm from HCASMCs expressing pHRed before (left) and after (right) the application of 1 μM CCCP. Images are pseudo-coloured with ratio of 0-5. (B) Time course of $F_{561\text{ nm}}/F_{458\text{ nm}}$ showed no change in the fluorescence ratio after application of 1 μM CCCP. (C) Mean \pm SEM for the ratio fluorescence of pHRed during control condition and after adding 1 μM CCCP (n=5).

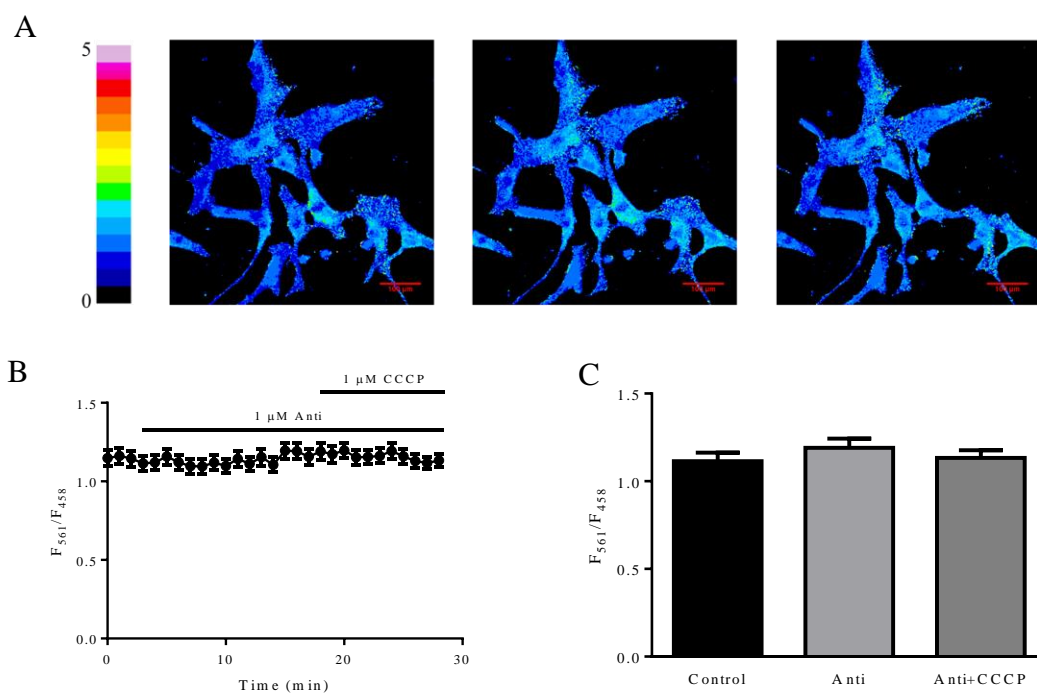


Figure 4.49: FUGW-pHRed ratio fluorescence in response to antimycin and subsequent application of CCCP. (A) A pixel-to-pixel ratio of 561 nm excitation image divided by excitation image of 458 nm from HCASMCs expressing pHRed under control condition (left), and after application of 1 μ M antimycin (middle) followed by application of 1 μ M CCCP (right). Images are pseudo-coloured with ratio of 0-5. (B) Time course of $F_{561\text{ nm}}/F_{458\text{ nm}}$ where neither 1 μ M antimycin nor 1 μ M CCCP affected cytosolic pH. (C) Mean \pm SEM of ratio fluorescence of pHRed during control condition and subsequent application of 1 μ M antimycin and 1 μ M CCCP (n=13)

4.4.10 Simultaneous imaging of intracellular ATP:ADP ratio and pH

So far, ATP:ADP ratio and pH signal were measured separately. Although it seems reasonable to suggest that changes seen in ATP:ADP ratio were real and not secondary to change in pH from those experiment (see **Sections 4.4.8 & 4.4.9**), ideally, it is better to conduct simultaneous measurement of intracellular ATP:ADP ratio and pH. In order to achieve this goal, we co-transfected HCASMCs with PercevalHR and pHRed.

4.4.10.1 Co-transfection of HCASMCs with FUGW-PercevalHR and FUGW-pHRed

HCASMCs co-transfected with FUGW-PercevalHR and FUGW-pHRed were checked after day 3 using EVOS FL cell imaging system, and well transfected cells were used for further experiments. **Figure 4.50** shows images of HCASMCs expressing both FUGW-PercevalHR and FUGW-pHRed.

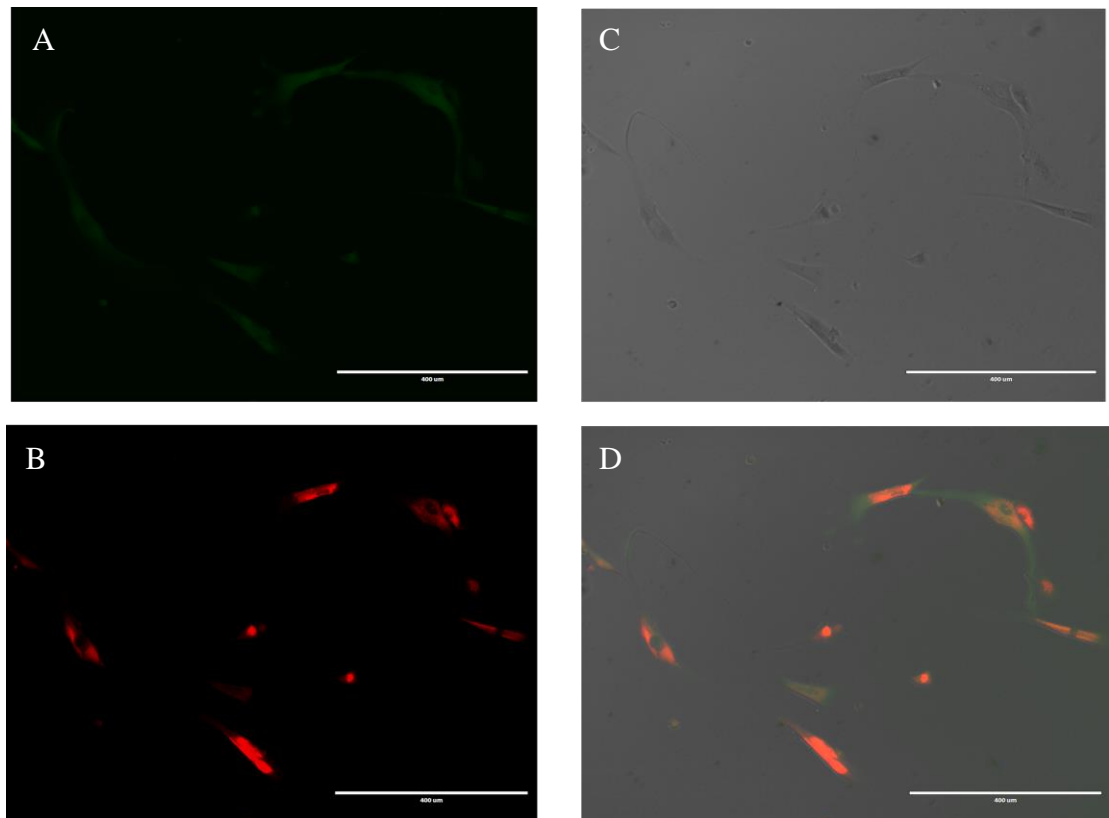


Figure 4.50: HCASMCs expressing both PercevalHR and pHRed. (A) PercevalHR fluorescence (488 nm excitation). (B) pHRed fluorescence (458 nm excitation). (C) Bright-field image. (D) Overlay image. Scale bar is 400 μm .

4.4.10.2 Simultaneous measurements of ATP:ADP ratio and pH using co-transfected HCASMCs

Metabolic inhibitors of mitochondrial respiratory chain reduced intracellular ATP:ADP ratio (**Figure 4.51**, green). There was little change in pH in most of the experiments, as assessed by concurrent measurement with pHRed (**Figure 4.51 A-E**,

red), but application of CCCP showed change in pH (**Figure 4.51 F**). Thus, the PercevalHR signal change caused by all metabolic inhibitors except CCCP is not secondary to intracellular pH change. Furthermore, time courses of PercevalHR and pHRed signal decrease caused by application of CCCP was not identical, suggesting that PercevalHR seems to report, at least in part, change in ATP:ADP ratio (**Figure 4.51F**).

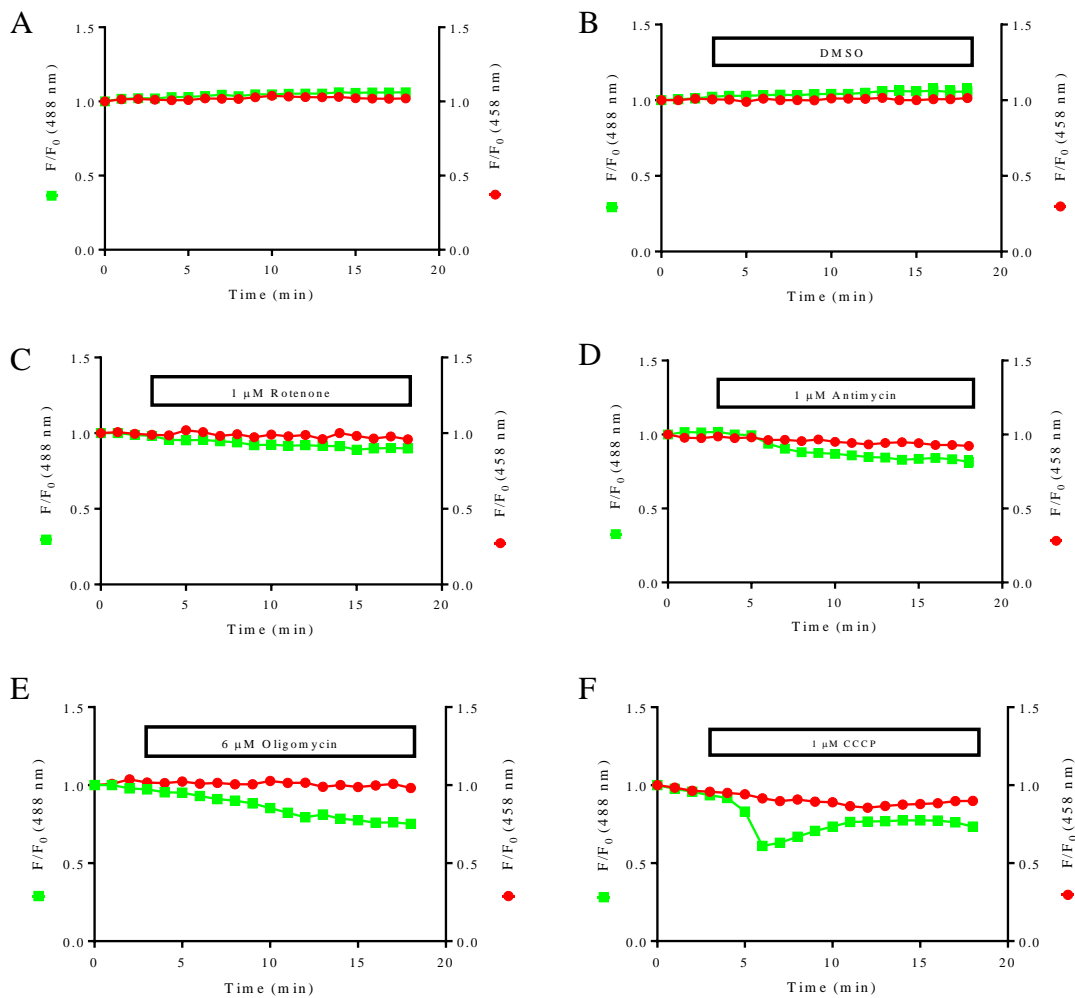


Figure 4.51: Concurrent measurement of intracellular ATP:ADP ratio and pH. Green squares and red circles show time course of PercevalHR and pHRed measurements for following conditions. (A) Time control (n=70). (B) Vehicle control (n=32). (C) 1 μM rotenone (n=12). (D) 1 μM antimycin (n=24). (E) 6 μM oligomycin (n=17). (F) 1 μM CCCP (n=27).

4.4.11 PercevalHR fluorescence and mitochondria

It has previously been reported that, although oligomycin and FCCP caused no change in cytosol pH, they caused acidification of mitochondrial matrix [197]. In order to elucidate the possibility if PercevalHR signal may be influenced by pH of mitochondrial matrix, MitoTracker was used to visualize mitochondria in cells expressing PercevalHR. Our results showed that there was no or little co-localization of the two signals as PercevalHR (green) did not overlap with pHRed (red) as shown the lack of yellow area (**Figure 4.52**). This indicates that PercevalHR signals do not originate from mitochondria matrix, and is therefore unlikely to be influenced by mitochondrial pH change.

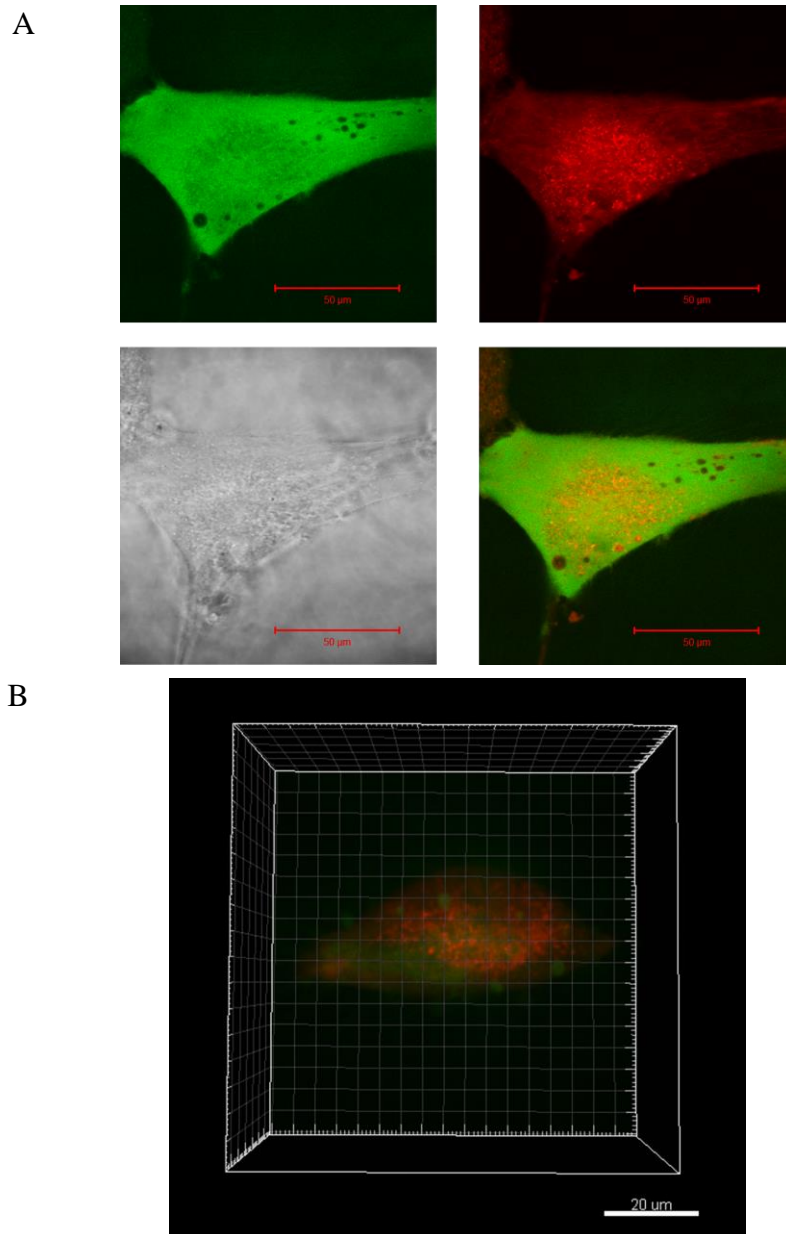


Figure 4.52: Distribution of PercevalHR and MitoTracker. (A) 2D images of PercevalHR (green) and MitoTracker (red) signal in HCASMC. Scale bar is 50 μm . (B) 3D reconstruction of the cell showing distribution of PercevalHR and MitoTracker. Both 2D and 3D images showed no co-localization of PercevalHR and MitoTracker.

4.4.12 Membrane targeting PercevalHR/Lyn-FUGW-PercevalHR

In later experiments, we observed membrane potential hyperpolarization with hypoxia, and this might be an effect through the activation of K_{ATP} channels in the cells membrane (see **Section 5.3.2.4**). However, hypoxia did not cause significant

change in intracellular ATP:ADP ratio when measured using FUGW-PercevalHR (**Figure 4.26**). The lack of effect, however, could be explained if FUGW-PercevalHR, which senses global ATP:ADP ratio, remains constant cannot detect change in near membrane ATP:ADP ratio. It is conceivable that K_{ATP} channels are regulated by ATP:ADP ratio in the plasma membrane micro-domains, not by change in bulk ATP:ADP ratio. With the purpose of addressing this problem, we next looked at the ATP:ADP ratio near the cell membrane in the following two ways: (i) Targeting FUGW-PercevalHR to the lipid rafts of cell membrane; (ii) TIRF imaging.

4.4.12.1 Designing of Lyn-FUGW-PercevalHR: Sub-cloning

A 5' myristoylation and palmitoylation lipid modification sequence (GCIKSKRKDK) derived from Lyn kinase has been previously applied to target proteins of interest to membrane lipid rafts [188]. Therefore, we next applied this sequence to FUGW-PercevalHR.

We first tried to introduce the targeting sequence into FUGW-PercevalHR with traditional PCR cloning without success (**Figure 4.53**). We then tried In-Fusion cloning method, and it proved to be successful (**Figure 4.54**). The cloning product was verified by restriction analysis (**Figure 4.55**) and DNA sequencing.

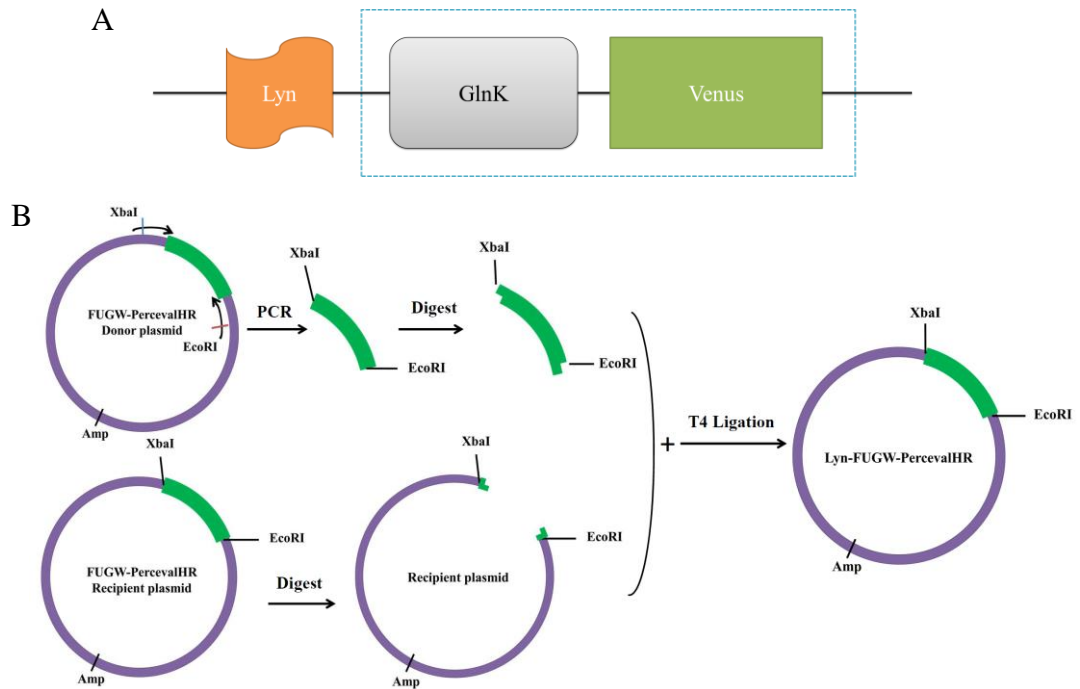


Figure 4.53: Designing of Lyn-FUGW-PercevalHR by PCR cloning. (A)

Schematic instruction of Lyn- FUGW-PercevalHR biosensor. **(B)** Targeting sequence was designed in the forward primer and cloned into PercevalHR by PCR with two blunt ends of XbaI and EcoRI. T4 ligation was performed with PCR product and lentiviral vector to produce Lyn-FUGW-PercevalHR.

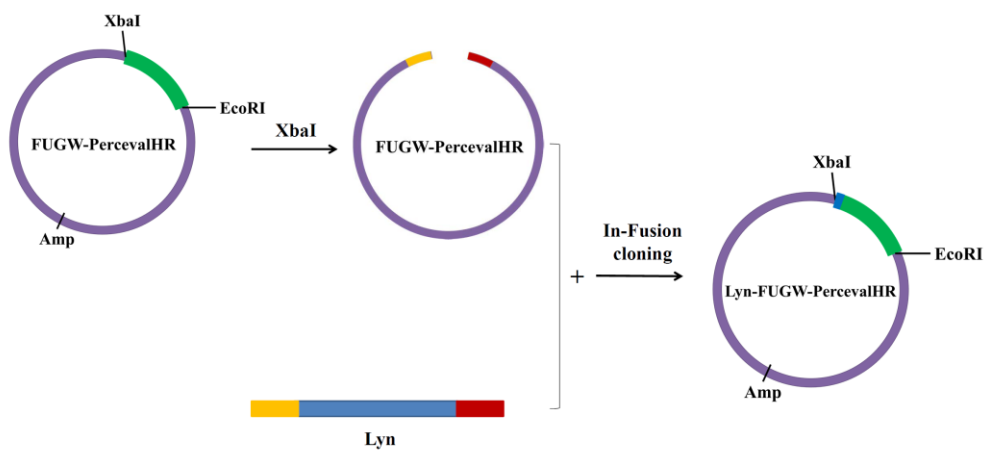


Figure 4.54: Designing of Lyn-FUGW-PercevalHR by In-Fusion cloning.

Linearized vector was first generated using restriction enzyme XbaI. Targeting sequencing (blue) was designed with bases of sequence homology at both 5' and 3' ends (yellow and red). In-Fusion cloning reaction was set according to manufacturer's protocol.

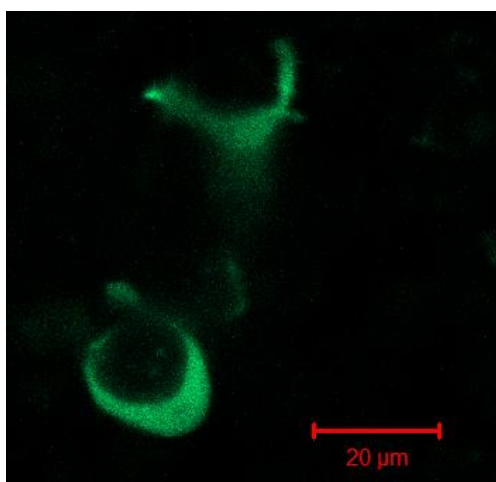


Figure 4.56: HEK293 cells transfected with Lyn-FUGW-PercevalHR. LSM510 multiphoton high speed laser scanning confocal microscope was used to collect Lyn-FUGW-PercevalHR signal at a signal z-plane.

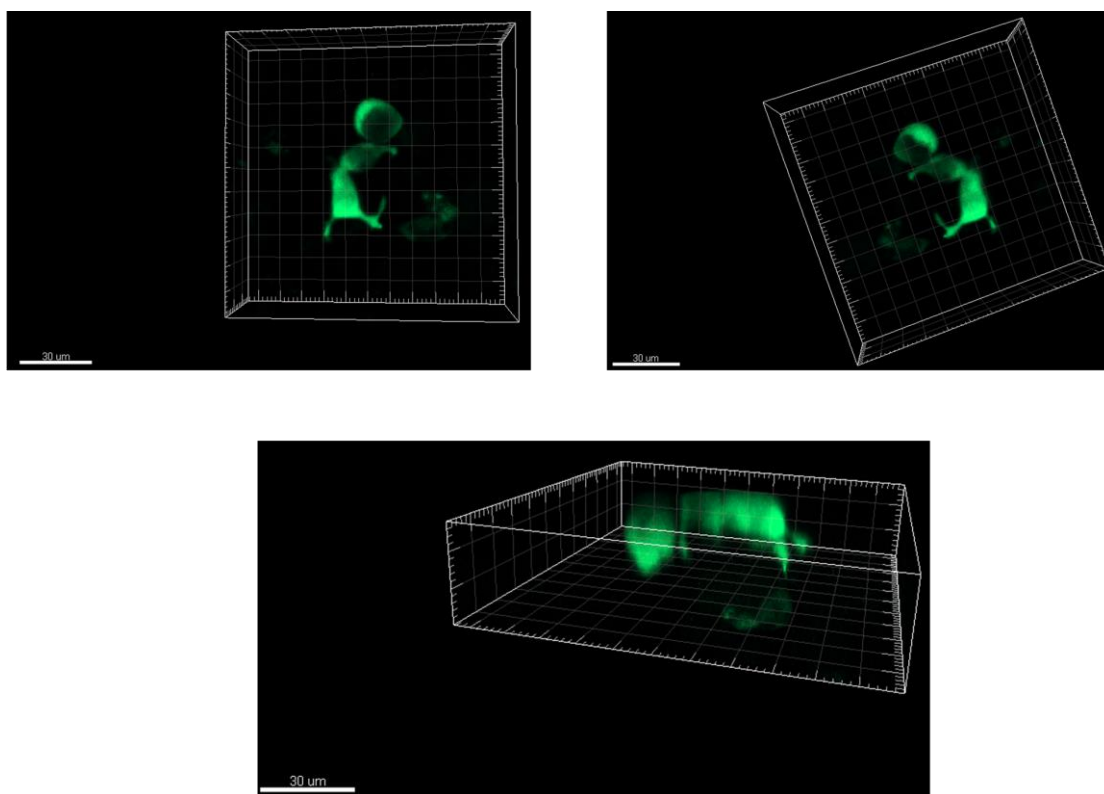


Figure 4.57: 3D reconstruction of HEK293 cells transfected with Lyn-FUGW-PercevalHR. Images from z-stacks taken by LSM510 multiphoton high speed laser scanning confocal microscope were reconstructed. Reconstructed images were shown with different angles. Scale bar is 30 μm.

4.4.12.3 HCASMC transfection with Lyn-FUGW-PercevalHR

We then moved to transfect HCASMCs with Lyn-FUGW-PercevalHR. Compared to global transfection with non-targeted PercevalHR, cell transfected with targeted PercevalHR showed higher expression and distribution of the fluorescent protein in the plasma membrane region (**Figure 4.58**). Because cultured HCASMCs are spread and thin, it was easier to observe the transfected cells by lifting them with trypsin where cells become spherical. Confocal images of lifted HCASMC expressing Lyn-FUGW-PercevalHR showed higher fluorescence in the cell membrane area (**Figure 4.59**).

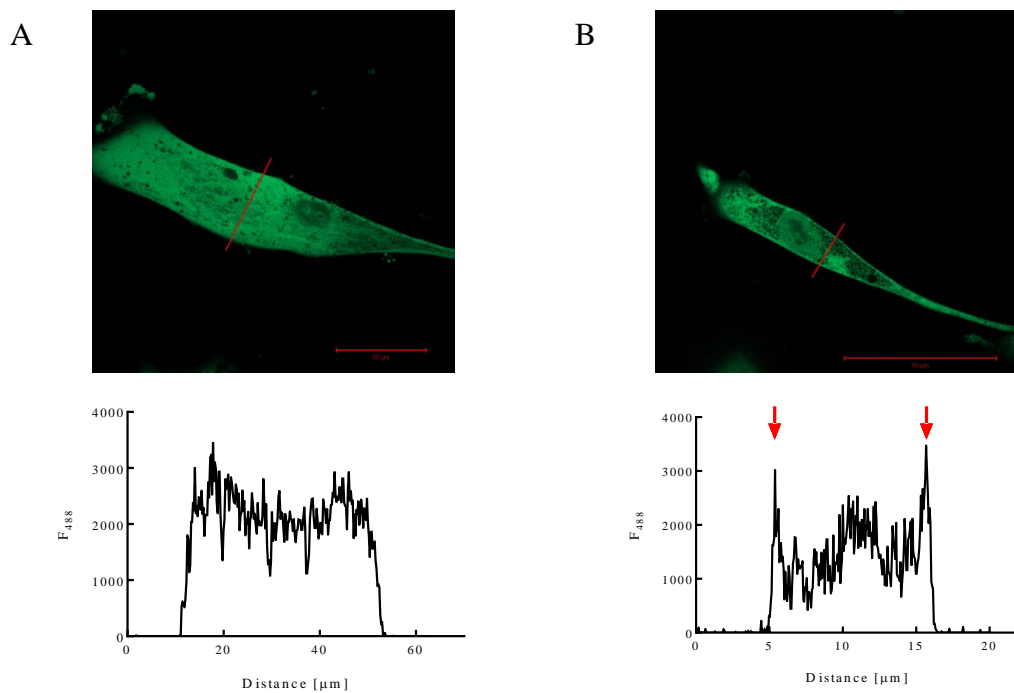


Figure 4.58: HCASMC transfected with Lyn-FUGW-PercevalHR. Compared to global transfection (A), cell transfected with membrane targeted PercevalHR showed higher expression of fluorescent protein in the cell plasma membrane (B).

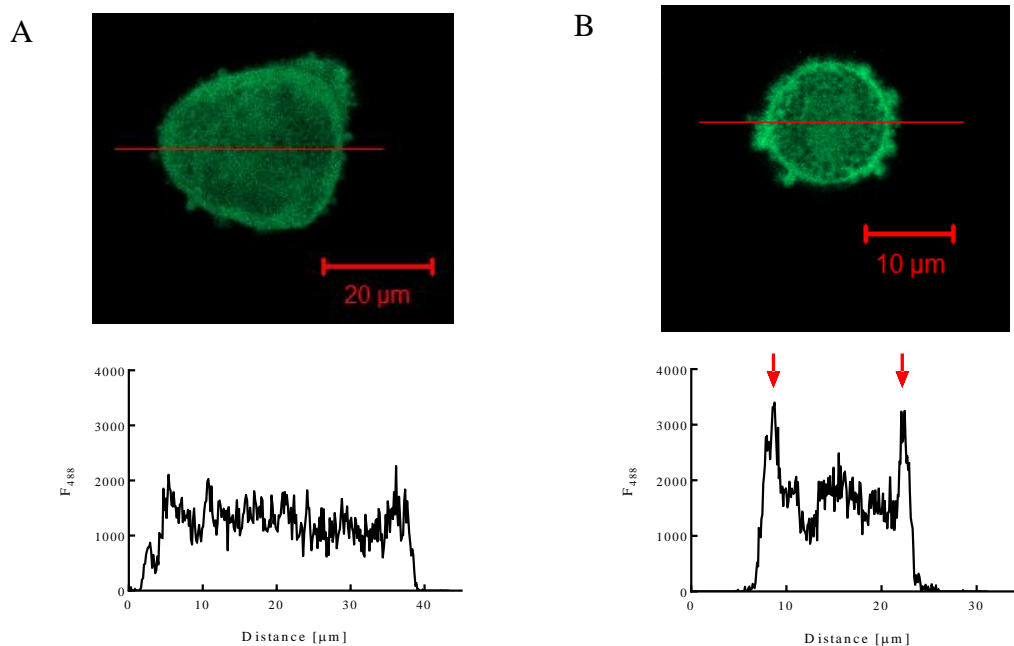


Figure 4.59: Lifted HCASMC expressing Lyn-FUGW-PercevalHR. Compared to global transfection (A), cell transfected with targeted PercevalHR showed higher expression of fluorescent protein in the cell plasma membrane (B).

4.4.12.4 Using Lyn-FUGW-PercevalHR to report ATP:ADP ratio in the plasma membrane microdomains

Using membrane targeted Lyn-FUGW-PercevalHR, changes of ATP:ADP ratio by a metabolic inhibitor was tested. Application of CCCP produced a decrease in Lyn-FUGW-PercevalHR emission fluorescence (**Figure 4.60**). Thus, although not tested in the current study, membrane targeted PercevalHR may be a useful tool in examining whether hypoxia can modify ATP:ADP ratio in near membrane area.

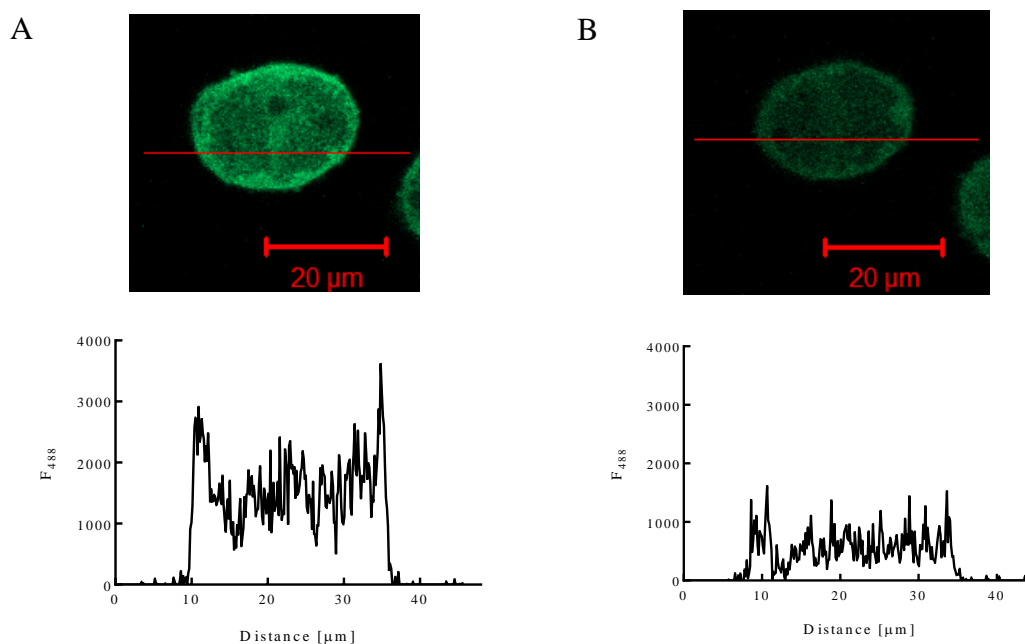


Figure 4.60: Metabolic inhibition lead to a change in Lyn-FUGW-PercevalHR signal. Images of Lyn-FUGW-PercevalHR in a single lifted HCASMC under control condition (A, top) and after application of 1 μM CCCP (B, top). Plot profile by drawing a line across the cell showed 1 μM CCCP decreased ATP:ADP ratio both in the membrane lipid raft microdomains and intracellular space.

4.4.13 TIRF imaging of FUGW-PercevalHR

Without targeting the plasmid to the membrane, TIRF analysis offers a direct way to look at the fluorescent molecules in the cell membrane and sub-plasmalemmal region (**Figure 4.61**) [190, 239]. Due to its advantages (i.e. spatial restriction and high signal-to-noise ratio of the excitation field), TIRF has been widely applied to study cell biological applications, especially spatial-temporal dynamics of molecules at or near the cell surface [190, 239]. In this study, we used TIRF technique to image HCASMCs expressing PercevalHR and pHRed (**Figure 4.62**). Real time imaging of FUGW-pHRed showed dynamic movement of the red fluorescence in the cell membrane area (data not shown). Preliminary studies indicated that application of metabolic inhibitor (1 μM antimycin) resulted in a decrease in FUGW-PercevalHR and Lyn-FUGW-PercevalHR signal in the near membrane area (**Figure 4.63**). Therefore TIRF imaging has the unique property to

directly look at fluorescent signals and their changes in the cell membrane area.

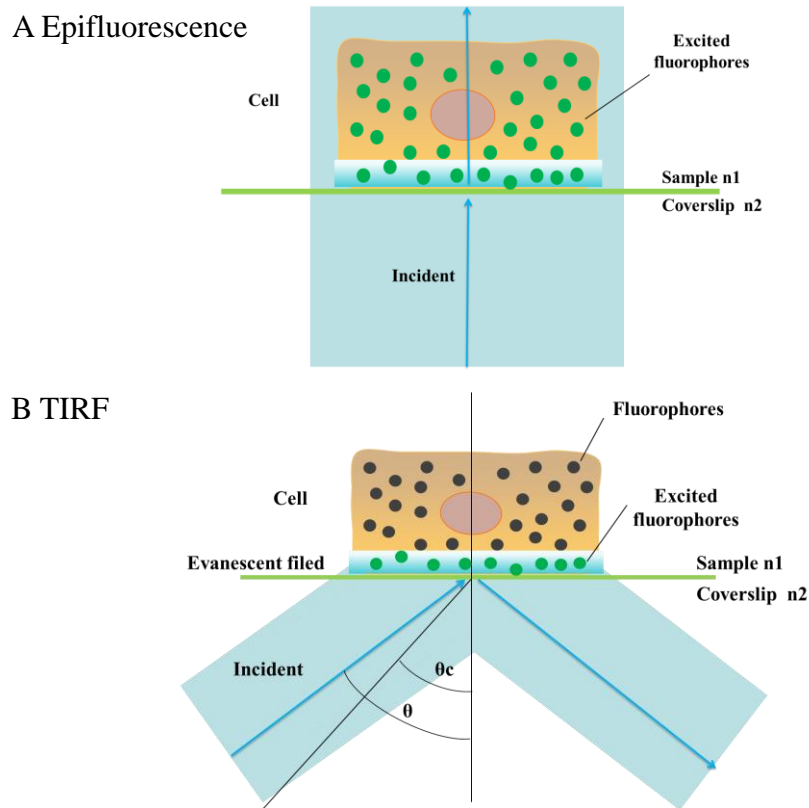


Figure 4.61: Diagram of TIRF imaging. (A) In epifluorescence, the excitation beam goes through directly and stimulates all fluorophores in the entire sample. (B) In TIRF imaging, the excitation beam enters the cover-slip-sample interface at an incidence angle greater than the critical angle (θ_c), and an evanescent field is generated when excitation light is internally reflected at the interface. The light in the evanescent field (evanescent wave) decays exponentially as the distance from the interface increases, so only the fluorophores and fluorescent-tagged proteins in close proximity to the coverslip are selectively excited. (Modified from Mattheyes et al., 2010 [191]).

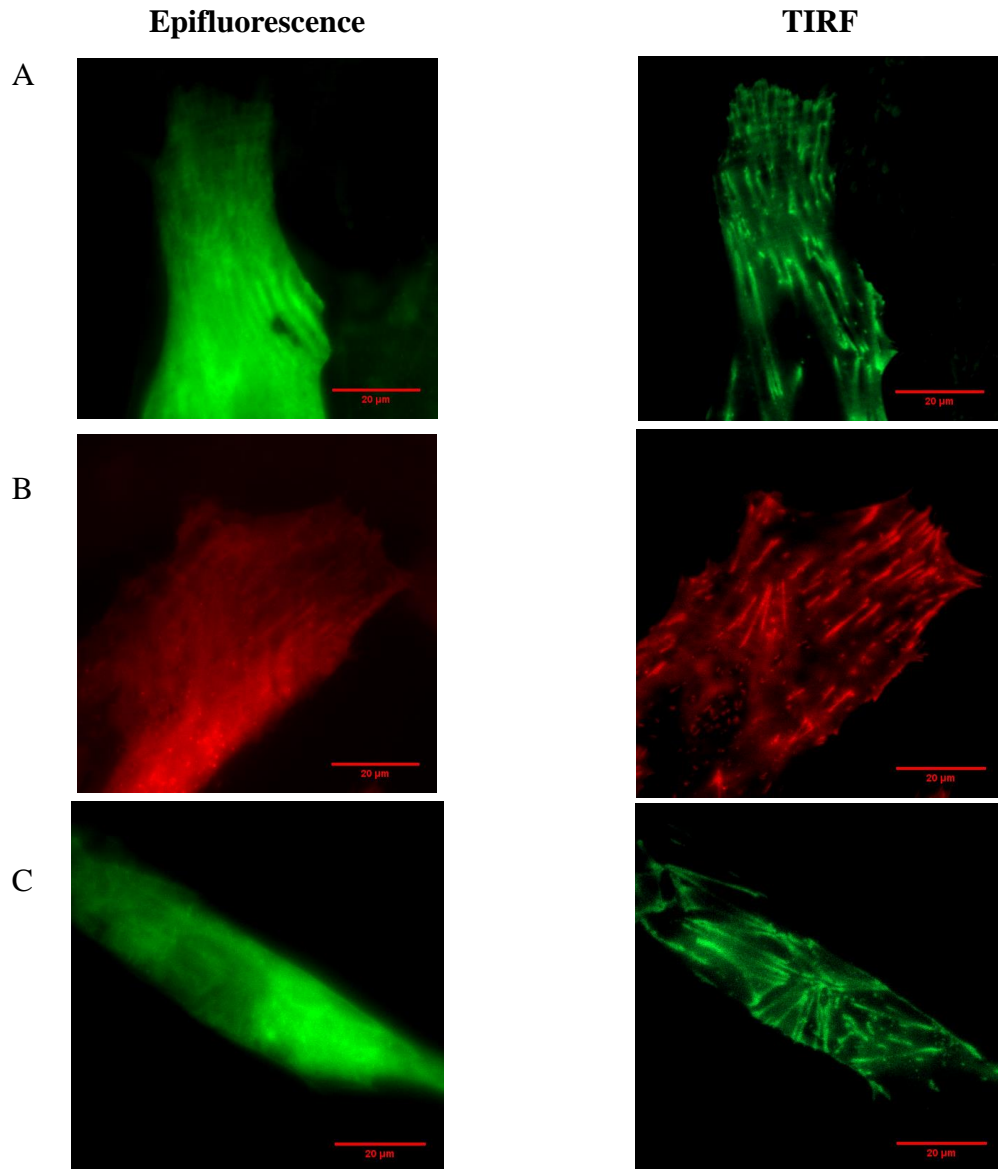


Figure 4.62: Images obtained using epifluorescence and TIRF. (A) HCASMC expressing FUGW-PercevalHR. (B) HCASMC expressing FUGW-pHRed. (C) HCASMC expressing Lyn-FUGW-PercevalHR. The microscope was focused at the adherent plasma membrane of HCASMC and the images were acquired with epifluorescence and TIRF, the latter clearly showed the detailed fluorescence signal at membrane area. Scale bar is 20 μm .

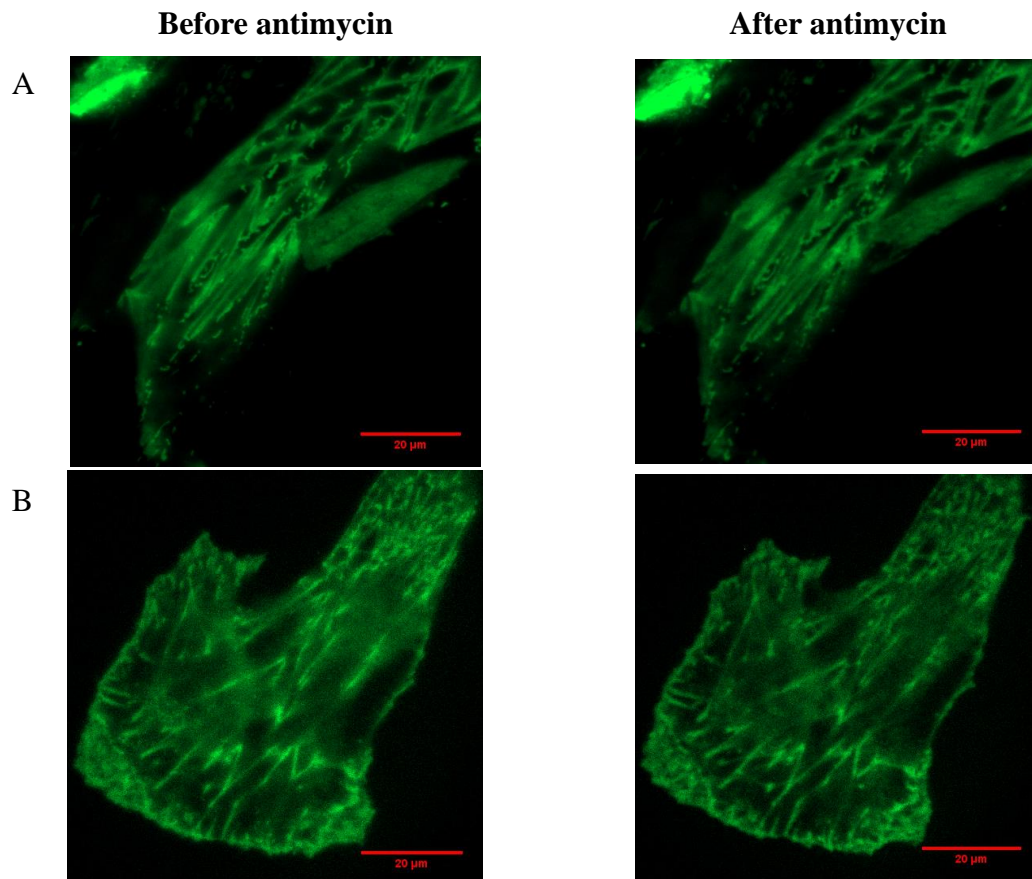


Figure 4.63: TIRF imaging of the effect of 1 μM antimycin on cellular metabolism. (A) Images of HCASMCs expressing FUGW-PercevalHR before (left) and after (right) the application of 1 μM antimycin. (B) Images of HCASMCs expressing Lyn-FUGW-PercevalHR before (left) and after (right) the application of 1 μM antimycin. Scale bar is 20 μm .

4.5 Discussion

4.5.1 Lentivirus transduction and other alternatives

Gene delivery vectors can be generally categorized into non-viral based vectors, viral vectors and combined hybrid systems (**Figures 4.64 & 4.65**). Non-viral systems can be further divided into two groups according to the way of preparation: chemical (synthetic vector-based gene delivery) and physical (carrier-free gene delivery) approaches. In terms of viral vectors, Ads, AAVs, retroviruses and lentiviruses are commonly used with different characteristics (**Table 4.4**) [240]. A lot of work has been focused on the development of vectors with improved efficiency, specificity and

safety. The modifications were made mainly with transfer vector by engineering a SIN lentiviral transfer vector or non-integrating lentivirus vectors (**Figure 4.3**), and other lentiviral components were also modified (**Table 4.5**).

Because of the low transfection efficiency of HCASMCs using non-viral vectors (see **section 3.3.2**), in this chapter we applied 3rd generation lentiviral gene delivery system which dramatically increased the efficiency to almost 100% for both PercevalHR and pHRed. The co-transfection, successfully achieved using lentivirus technique, was practically impossible with lipid-based transfection. One limitation that could affect the efficiency of transfection is that we did not titrate the virus. Therefore viral concentration in some batches could be lower than others, and this explains why transfection efficiency was not as consistent as it should have been. When lower concentration of virus was suspected, a second transfection was conducted, particularly for pHRed. By comparing cell morphology from non-viral and viral vectors transfected cells, we found that the latter maintained a significantly larger size, closer to the shape of normal cultured HCASMCs (**Figure 4.10 & 6.2**). We therefore conclude that HCASMC transfection using lentivirus maintained a better morphology and thus perhaps more physiological function. It should be noted that hypoxia caused a decrease in intracellular ATP:ADP ratio in HCASMCs transfected using the reagents (see **Section 3.4.3.4**) while there was no change in lentivirus transduced cells (**Figure 4.26**). The discrepancy could be due to the fact that condition of cells was compromised after transient transfection using reagents.

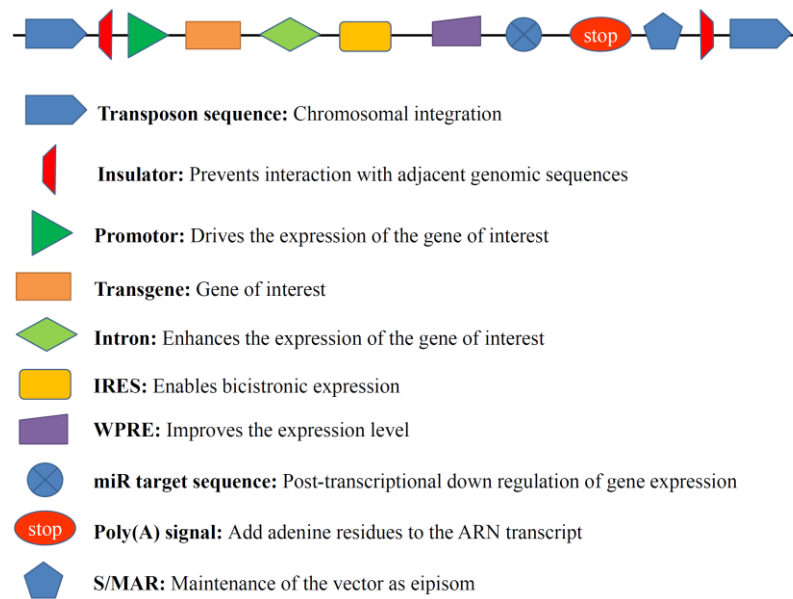


Figure 4.64: Representative components of a gene delivery vector. Expression of a gene of interest is driven by an upstream promoter. Inclusion of an intron into the expression cassette assures higher transcription level. The internal ribosome entry site (IRES) permits co-transcription of two genes from the same transcript in a bicistronic manner. A further enhancement of gene expression can be achieved by using the Woodchuck Hepatitis Virus Post-transcriptional Regulatory Element (WPRE) to increase the level and stability of the nuclear transcripts. The expression of a therapeutic gene can be spatially limited to a specific cell type by inclusion of a miR recognition sequence at the 3' end, which is recognized by its cognate miR transcript. The polyadenylation signal ensures properly sized transcripts. An optional element which can be included in the vector backbone is the scaffold matrix-associated region (S/MAR) which permits episomal replication and vector dilution in successive cell generations. An alternative to obtain stable and long term expression can be achieved by using transposon sequences for integration of the vector into the host genome. (Modified from Sergiu et al., 2015 [241])

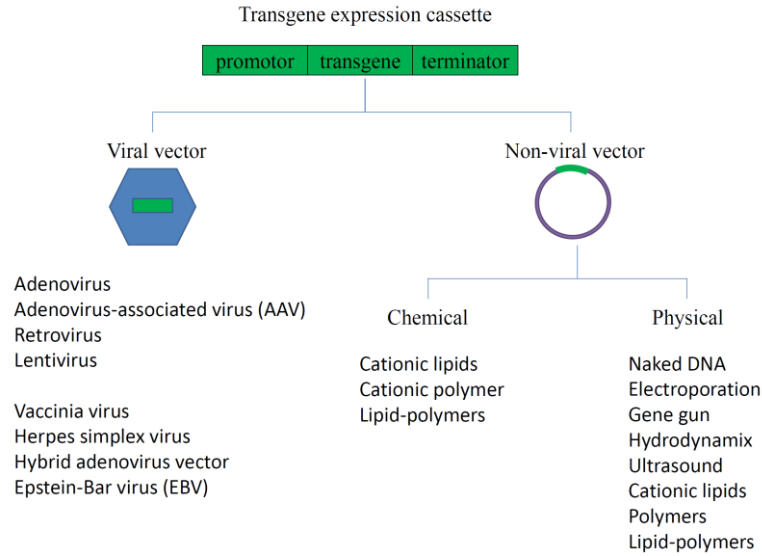
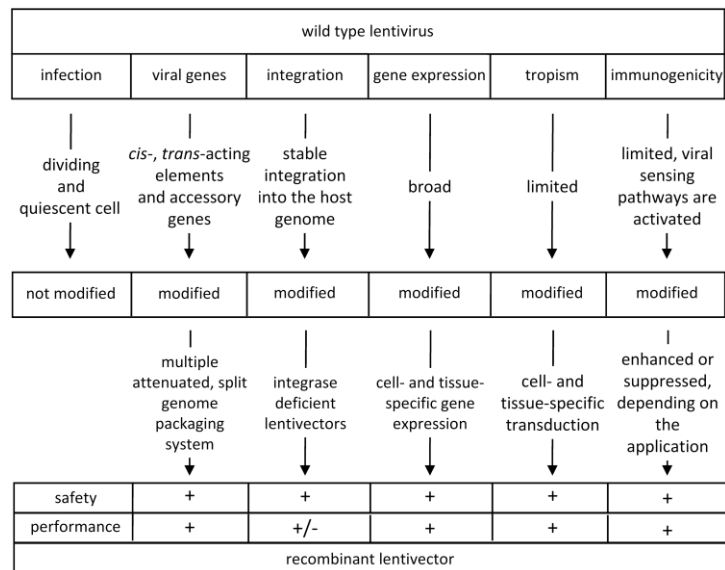


Figure 4.65: Schematic illustration of viral and non-viral delivery systems for gene delivery. Gene of interest can be delivered by a DNA vector or viral vector. (Modified from Nayerossadat et al., 2012 [242])

Table 4.4: Advantages and disadvantages of different gene delivery systems

Vector type	Description	Advantages	Limitations	Applications
Non-viral	Naked DNA or DNA complex with a chemical	Good safety; Easy to produce	Low transfection efficiency	Cancer; Cardiovascular disease; Cystic fibrosis
Adenoviral	Double strand DNA viruses; Genome of 36 kb; non-enveloped; Non-integrative; Over 50 serotypes	High titer production; Wide choice of serotypes; Insertion of large DNA fragments	Inflammatory and antigenic	Cancer; cardiovascular disease; Metabolic disorders; Diabetes; Neurodegenerative diseases; Angiogenesis induction; DNA vaccine production
AAV	Single stand DNA viruses; Genome of 4.8 kb; Non-enveloped; Integrative	Low immunogenicity; High titer production; Long term gene expression	Limited capacity for insertion of DNA;	Cancer; cardiovascular disease; Metabolic disorders; Hemophilia; Retinal diseases
Retroviral	Single stranded RNA viruses; Genome of 8-10 kb; Enveloped; Integrative	Low immunogenicity; Insertion of large DNA fragments	Insertional mutagenesis; Infect dividing cells only	Genetic diseases of T cells and hematological diseases
Lentiviral	Single stranded RNA viruses; Genome of 8-10 kb; Enveloped; Integrative	Low immunogenicity; Insertion of large DNA fragments; New generation are self inactivating for safety	Insertional mutagenesis	HIV/AIDS

Table 4.5: Development of improved recombinant lentivectors



Taken from Escor et al., 2010 [240].

4.5.2 Reporting intracellular ATP:ADP ratio using FUGW-PercevalHR

Compared to total ATP level, ATP:ADP ratio is arguably a more important element in cellular energy status. Perceval is originally constructed to monitor the changes in cellular ATP:ADP ratio [185, 196]. Although F_{488}/F_{405} or F_{488}/F_{435} ratiometric change in the excitation spectrum makes Perceval an ideal sensor, it saturates at low ATP:ADP ratio (ATP:ADP <5) and therefore was basically tuned to extreme metabolic inhibition [185]. However, mammalian ATP:ADP ratios are estimated to range from 1 to 100 in healthy conditions [243, 244]. The improved sensor PercevalHR meets the requirements to measure ATP:ADP ratio expected in mammalian cells [186, 187]. As it was shown in the previous chapter (section 3.3.2), the transient transfection efficiency of HCASMCs with PercevalHR was very low (<1%). Use of FUGW-PercevalHR, a lentivirus version of PercevalHR, increased the transfection efficiency to nearly 100% allowing previously difficult experiments to be carried out. For instance, *in vivo* calibration would not have been attempted due to the high wastage of cells during the course of experiments (and cost of α -toxin). One surprising problem was that, although, α -toxin has been successfully used for Perceval calibration with islet beta cells [196], it caused smooth muscle cell

contraction and cell detachment during treatment (**Figure 4.13**). By improving the efficiency of transfection, lentivirus transduction made the calibration of PercevalHR possible (**Figure 4.14**). Results showed that EC₅₀ of PercevalHR is suited to measure realistic ATP concentration in mammalian cells (**Figure 4.16**) and that PercevalHR signal is dependent not only ATP but also ADP (**Figure 4.17**). Taken together, PercevalHR is an excellent tool to explore changes in nucleotide concentrations in HCASMCs.

We then assessed the effect of metabolic inhibitors and hypoxia on intracellular ATP:ADP ratio. Both blocking glycolysis and mitochondrial respiratory chain caused a reduction in intracellular ATP:ADP ratio (**Figure 4.18 & 4.22-4.25**). Removal of glucose from extracellular solution lead to a small and reversible decrease in ATP:ADP ratio (**Figure 4.19**). These results were consistent with the effects observed from the transiently transfected cells (see **section 3.4.3**). However, hypoxia induced no change in cellular ATP:ADP ratio (**Figure 4.26**), in disagreement with the results from transiently transfected cells (see **Figure 3.38**). We deduce that the following two possible reasons might have contributed to this inconformity. First, the cells infected with lentivirus maintained a better physiological condition. Second, O₂ level used in the studies were not low enough to cause a change in intracellular energy in lentivirus infected cells. Further experiments will be required to address this issue in the future.

Vastly improved transfection made co-transfection of FUGW-pHRed and FUGW-PercevalHR possible. Generally, metabolic inhibitors and hypoxia had little effect in intracellular pH measured by FUGW-pHRed. Therefore, it is likely that observed changes in the ATP:ADP ratio reported with PercevalHR is not secondary to pH-induced changes. The exception to this was CCCP (**Figure 4.51**) that caused change in pHRed signal. Even in this experiment, however, it is highly unlikely that the observed change in PercevalHR was entirely due to pH as the time course of two biosensor signals were quite different (**Figure 4.51**). Mathew et al. showed in Neuro2A cells oligomycin and FCCP caused no change in intracellular pH, but when pHRed was targeted to the mitochondrial matrix by COX8, it was reported an

acidification of the mitochondrial matrix after the application of FCCP [197]. We have shown that there is no co-localization of PercevalHR and MitoTracker (**Figure 4.52**), suggesting that mitochondrial pH change is unlikely to influence the reading of PercevalHR. Simultaneous measurement of intracellular ATP:ADP ratio and pH will help to correct any changes in ATP:ADP ratio signal that may occur as a result of pH change [186, 197].

4.5.3 Investigation of cellular metabolism in plasma membrane microdomains

One of the major objectives of the project was to look at the role of K_{ATP} channels in hypoxic vasodilation. An exciting aspect is that live cell imaging can be combined with other techniques such as electrophysiology techniques. K_{ATP} channels have been found in the lipid rafts and caveolae of plasma membrane in the cardiovascular system although some suggest that they also exist in mitochondria [157, 164, 245, 246]. After having achieved targeting PercevalHR to lipid rafts of cell membrane, we could investigate the K_{ATP} channel physiology with further great detail in intact cells. As an alternative to membrane targeting, TIRF imaging system also opened the door for looking at the signal near the cell membrane with high resolution. Both a single- molecule TIRF analysis (e.g. dynamic movement of ion channels) and two single-molecule TIRF/FRET analysis (e.g. identification of molecules that interact with ion channels) have been described [190]. However TIRF imaging could not directly distinguish the signal from different compartments of the membrane if not using reporters containing specialized targeting sequence (e.g. lipid rafts and non-lipid rafts). In conclusion, membrane targeted PercevalHR and TIRF offer more spatially detailed information regarding ATP:ADP ratio change. Although the effect of hypoxia was not tested in the current study, these new tools offer an exciting opportunity for the future investigations.

4.5.4 Gene delivery in cardiovascular system

Gene delivery using viral vectors has been widely used in the labs and clinical trials, and using both viral and non-viral vectors have also become one of the most

promising fields for developing new treatments. The first gene therapy clinical trial was carried out in 1989 in patients with advanced melanoma, using tumor infiltrating lymphocytes modified by retroviral transduction [247]. Since then, more clinical trials were carried out, including viral vector application in cardiovascular system [227, 248, 249]. **Figure 4.66** shows the year for different gene delivery methods used in heart research and the trend in the total number of publications. Even though the therapeutic efficacy of gene delivery to date is not as good as originally hoped, further investigations are being carried out and may offer new area of treatments in the future.

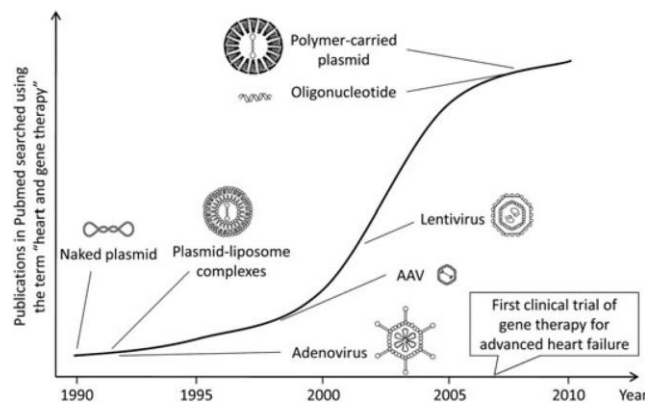


Figure 4.66: The evolution of heart gene delivery research. The number of publications is plotted against the year. A great increase in the number of heart gene delivery papers is noticed after AAV vector is introduced, which was first used in the clinical trial for advanced heart failure initiated in 2007. (Reproduced from Nalinda et al., 2011[227])

4.6 Conclusion

In conclusion, we successfully employed a 3rd generation lentiviral vector system. With this method, we were able to investigate intracellular ATP:ADP ratio and pH changes under desired environment. Targeting PercevalHR to lipid rafts of the cell membrane will further address the relationship between cellular ATP:ADP ratio and K_{ATP} channel activity under hypoxia in the future.

Chapter 5
Effect of Hypoxia and K⁺ Channel
Modulators on Ca²⁺ Homeostasis
and Membrane Potential of
HCASMCs

5.1 Introduction

In order for coronary hypoxic vasodilation to be physiological useful, several criteria have to be met. First, it must be sensitive to O_2 levels that occur during vasodilation in the intact heart [2]. Second, it must be a local event that does not require neuronal/circulating hormonal inputs. Third, it must respond to change in O_2 tension in a dynamic and timely manner so that the artery can respond promptly to the increased metabolic needs where supply can be matched to the demand. Finally, it must lead to lowering of $[Ca^{2+}]_i$ as this is the pre-requisite for vasorelaxation.

We hypothesize that hypoxia may regulate $[Ca^{2+}]_i$ by either directly modulating Ca^{2+} homeostasis or indirectly regulating K^+ channels and membrane potential. In order to evaluate the effect of hypoxia on Ca^{2+} homeostasis, it was necessary to elevate $[Ca^{2+}]_i$. The reduction in $[Ca^{2+}]_i$ will be more readily detected when $[Ca^{2+}]_i$ was increased, and arguably hypoxic vasodilation occurs when artery is already somewhat contracted and $[Ca^{2+}]_i$ elevated. PDGF-BB, an $\alpha 1$ -adrenergic agonist phenylephrine (PE), prostaglandin $F_{2\alpha}$ ($PGF_{2\alpha}$) and thromboxane A2 receptor (prostanoid TP receptor) agonist (U46619) are known vasoconstrictors which cause increases in $[Ca^{2+}]_i$ and smooth muscle contraction via the activation of second messenger signaling cascade [92, 112]. An increase in $[K^+]_o$ also results in increases in $[Ca^{2+}]_i$ due to membrane depolarization and opening of VDCCs without receptor activation. In this chapter, changes in $[Ca^{2+}]_i$ were reported using membrane permeable Ca^{2+} sensitive dyes, Fluo-4 AM and Fura-Red AM. A fluorescent membrane potential dependent dye, DiBAC4(3), was used to monitor changes in membrane potential [250]. Membrane hyperpolarization caused by activation of K^+ channels should be diminished when $[K^+]_o$ is elevated. The role of specific K^+ channel subtypes involved can be elucidated using specific pharmacological inhibitors. For instance, K_{ATP} channels are inhibited by the glibenclamide, BK_{Ca} channels are inhibited by penitrem A and iberitoxin, IK_{Ca} and SK_{Ca} channels are inhibited by tram34 and apamin, respectively, whilst K_{ir} channels are inhibited by low concentration of Ba^{2+} [251, 252]. Ultimately, the identity of K^+ channels involved in hypoxia, if any, could be examined using patch clamp technique [99, 203,

[252](#)].

5.2 Aims

The aim of this chapter is to evaluate the effect of hypoxia on $[Ca^{2+}]_i$ and membrane potential. Roles of different types of K^+ channels in setting HCASMC membrane potential were also investigated.

5.3 Results

5.3.1 Effect of hypoxia on Ca^{2+} homeostasis in single HCASMCs

5.3.1.1 Imaging with Ca^{2+} reporting fluorescent indicators

Fluo-4 AM and Fura-Red AM are both membrane permeable dyes which become Ca^{2+} sensitive when de-esterified and trapped within the cells. Binding to Ca^{2+} increases Fluo-4 fluorescence signal and decreases that of Fura-Red. **Figure 5.1** shows that application of 20 ng/ml PDGF-BB increased Ca^{2+} concentration in both cytosolic and nuclear region. Some cells showed spontaneous Ca^{2+} oscillations without vasoconstrictors. Representative Ca^{2+} oscillations occurring spontaneously or induced by vasoconstrictors are shown in **Figure 5.2**. Application of vasoconstrictors increased frequency of Ca^{2+} oscillations in the cells with spontaneous oscillations at rest and triggered Ca^{2+} oscillations in quiescent cells (**Figure 5.2A and 5.2B**). Increasing $[K^+]_o$ from 5 mM to 80 mM not only triggered Ca^{2+} oscillations in the cells, but also caused gradual elevation in the basal $[Ca^{2+}]_i$ (**Figure 5.2C**). These results suggest that Ca^{2+} homeostasis can be investigated using HCASMCs.

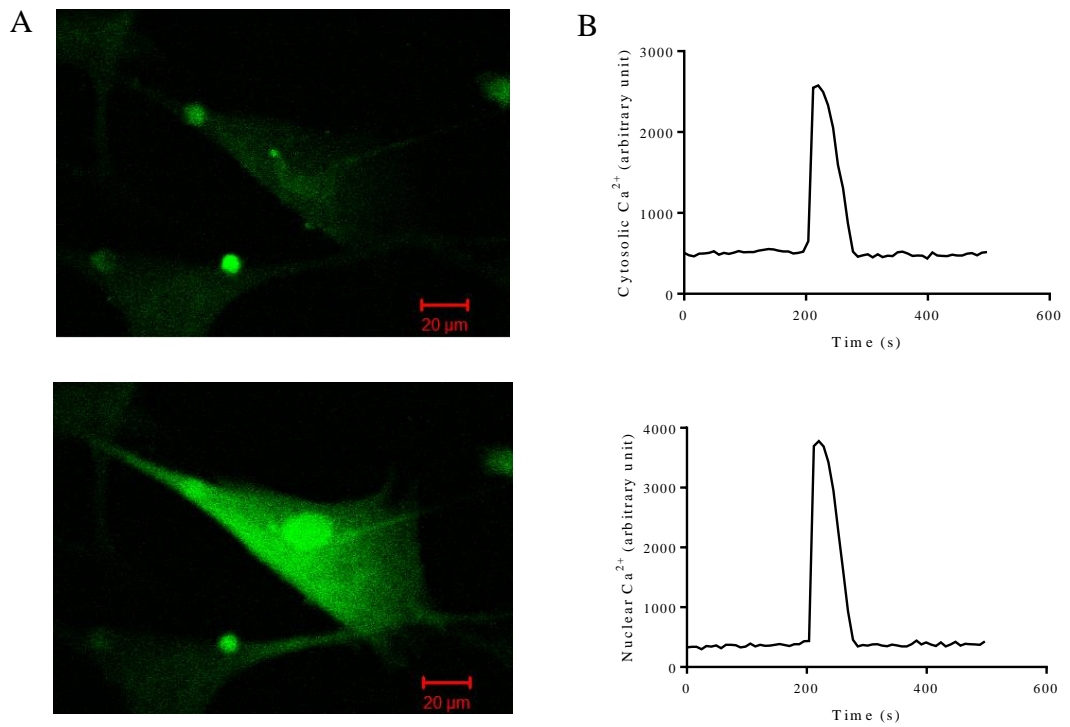


Figure 5.1: Ca²⁺ measurement with Fluo-4. (A) Images of HCASMCs loaded with Fluo-4 before (upper panel) and after (lower panel) treatment with 20 ng/ml PDGF-BB. (B) Time course of cytoplasmic (upper panel) and nuclear (lower panel) Ca²⁺ signal changes.

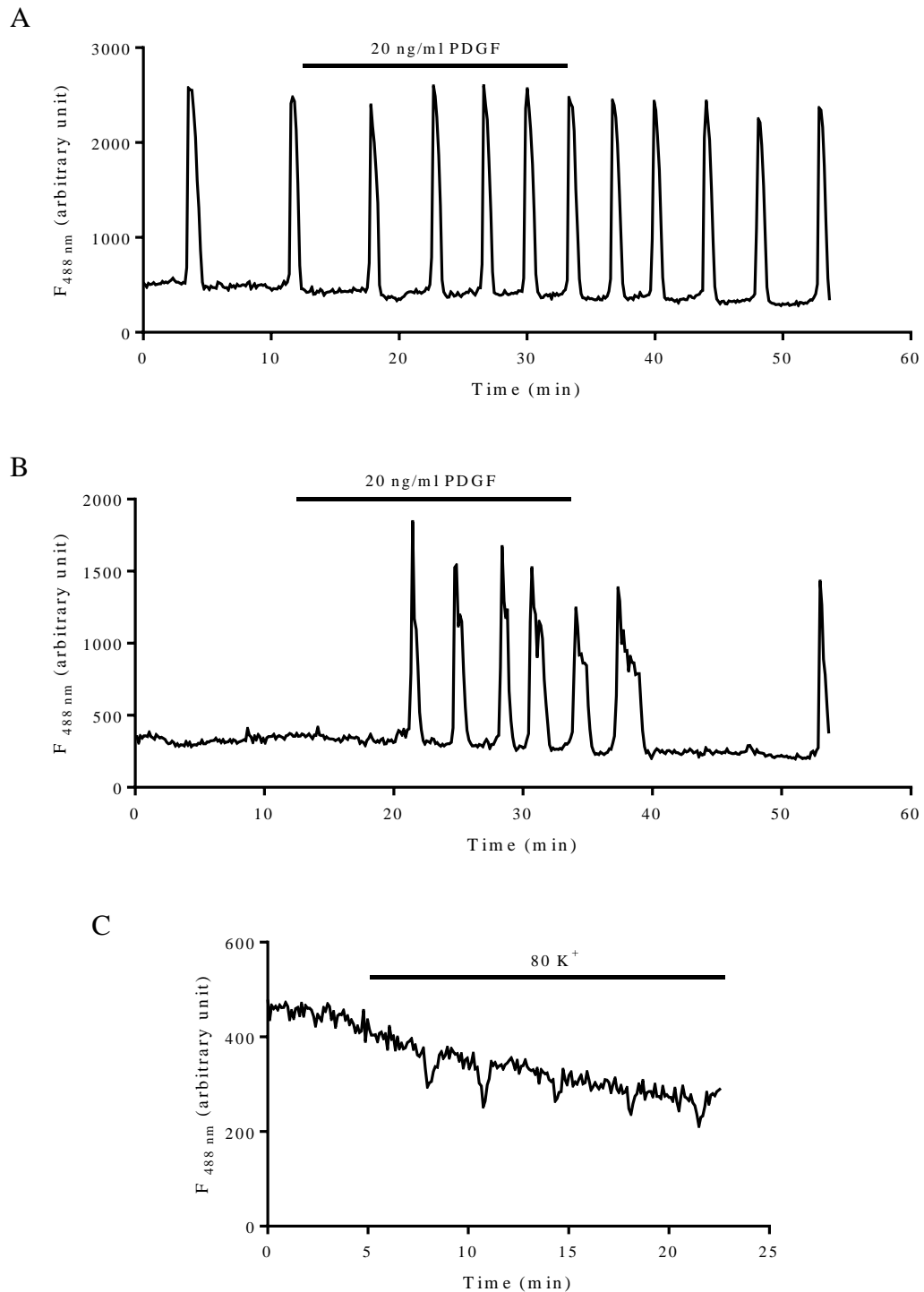


Figure 5.2: Ca²⁺ oscillations. (A) 20 ng/ml PDGF-BB increased Ca²⁺ oscillation frequency reported by Fluo-4. (B) 20 ng/ml PDGF-BB triggered Ca²⁺ oscillations in cell without spontaneous oscillations at rest. (C) Ca²⁺ oscillations and gradual [Ca²⁺]_i increase induced by 80 mM K⁺ reported by Fura-Red fluorescence. Note that Fura-Red signal decreases when [Ca²⁺]_i rises.

5.3.1.2 Analysis of Ca^{2+} measurements

In order to quantify Ca^{2+} oscillations, four basic parameters, amplitude (A), frequency (F), amplitude multiple frequency (AxF) and area under curve (AUC) were analyzed. Amplitude was corrected and calculated as $(F_p - F_0)/F_0$, where F_p is the measurement at the peak and F_0 is the nearest baseline measurement. Frequency was presented as the number of oscillations per hour (/hr), and AxF is the product of amplitude and frequency. AUC of Ca^{2+} oscillations was determined with Matalab software. After fractional fluorescence of Fluo-4 counts (F/F_0) was corrected for the drift in basal line, AUC of each oscillation was calculated by a trapezoid integration method. A representative analysis is shown in **Figure 5.3**.

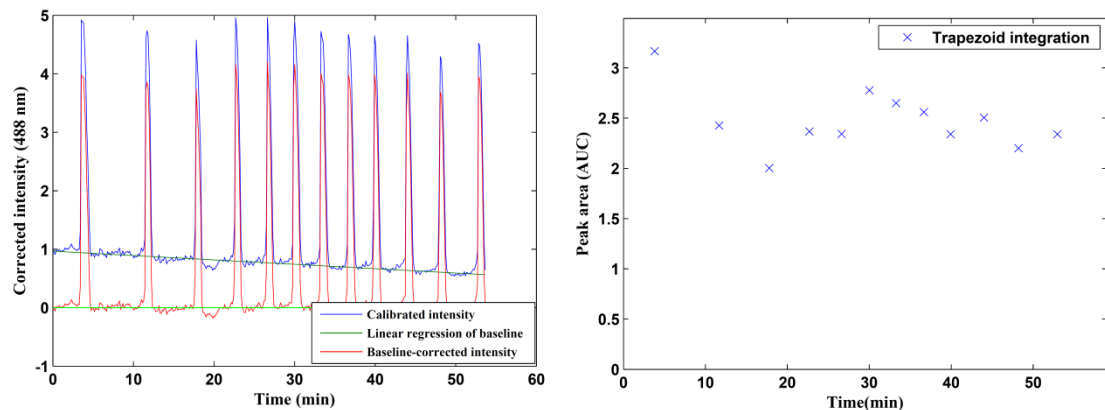


Figure 5.3: Analysis of Ca^{2+} oscillations with Matalab. Fractional fluorescence of Fluo-4 (blue) was corrected using the regression of basal line (dark green). The AUC of each oscillation was calculated with trapezoid integration method from the corrected curve (red) with horizontal new baseline (light green) and reported by the software (blue cross, right panel).

5.3.1.3 Effect of vasoconstrictors on $[\text{Ca}^{2+}]_i$

In order to study the effect of hypoxia on $[\text{Ca}^{2+}]_i$, we first aimed to elevate $[\text{Ca}^{2+}]_i$ using various vasoconstricting agents. Culturing of SMCs is known to change the phenotype including loss of receptors/signal transduction cascade that normally trigger elevation in $[\text{Ca}^{2+}]_i$ [253, 254]. A23187, a Ca^{2+} ionophore, was used first as positive control. Application of A23187 increased $[\text{Ca}^{2+}]_i$ immediately with the peak

reaching approximately 5 fold, and this is likely to be maximum fractional increase in single HCASMCs under our experimental condition (**Figure 5.4**). Next receptor-mediated vasoconstrictors, PDGF-BB, PE, PGF2 α and U46619, as well as high K⁺, were tested (**Figure 5.5-5.9**). PE had no effect on most of the cells. In cells that responded to PE (8 out of 34 cells), PE induced an increase in amplitude from 0.26 ± 0.17 to 2.29 ± 0.74 , frequency from 4.64 ± 3.05 to 11.75 ± 2.75 , AxF from 4.80 ± 3.15 to 19.83 ± 4.63 ; AUC from 0.13 ± 0.08 to 1.44 ± 0.36 , washing with PSS reduced amplitude to 1.25 ± 0.80 , frequency to 7.00 ± 2.67 , AxF to 9.30 ± 4.70 and AUC to 0.53 ± 0.28 respectively (**Figure 5.6**). The effects of other vasoconstrictors and high K⁺ were summarized in **Table 5.1**.

Table 5.1 The effects of vasoconstrictors and high K⁺ on [Ca²⁺]_i

	Amplitude (A)		Frequency (/hr, F)		AxF		Area under curve (AUC)	
	-	+	-	+	-	+	-	+
PDGF (n=18)	0.86 ± 0.35	2.39** ± 0.31	2.58 ± 0.95	10.40*** ± 1.03	6.89 ± 2.95	23.33** ± 3.56	0.49 ± 0.22	1.74*** ± 0.23
PGF2 α (n=10)	0	2.48 ± 0.45	0	14.80 ± 1.44	0	38.62 ± 10.19	0	1.30 ± 0.27
U46619 (n=11)	0.21 ± 0.10	1.69*** ± 0.29	4.73 ± 2.36	10.36 ± 2.54	2.34 ± 1.06	12.22*** ± 1.27	0.10 ± 0.05	0.94* ± 0.16
80 K ⁺ (n=9)	0.22 ± 0.12	0.67* ± 0.08	4.44 ± 2.42	16.40** ± 2.11	2.81 ± 1.49	11.16** ± 2.21	0.12 ± 0.06	0.30* ± 0.03

*For PE data, refer to the text.

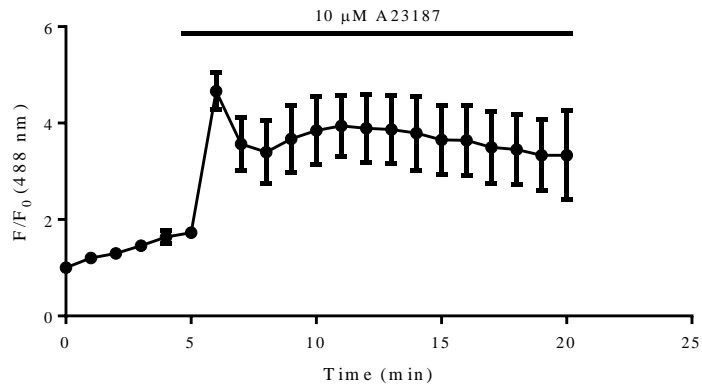


Figure 5.4: Effect of A23187 on intracellular Ca^{2+} . Application of 10 μM A23187 increased fractional fluorescence (F/F_0) of Fluo-4 ($n=3$).

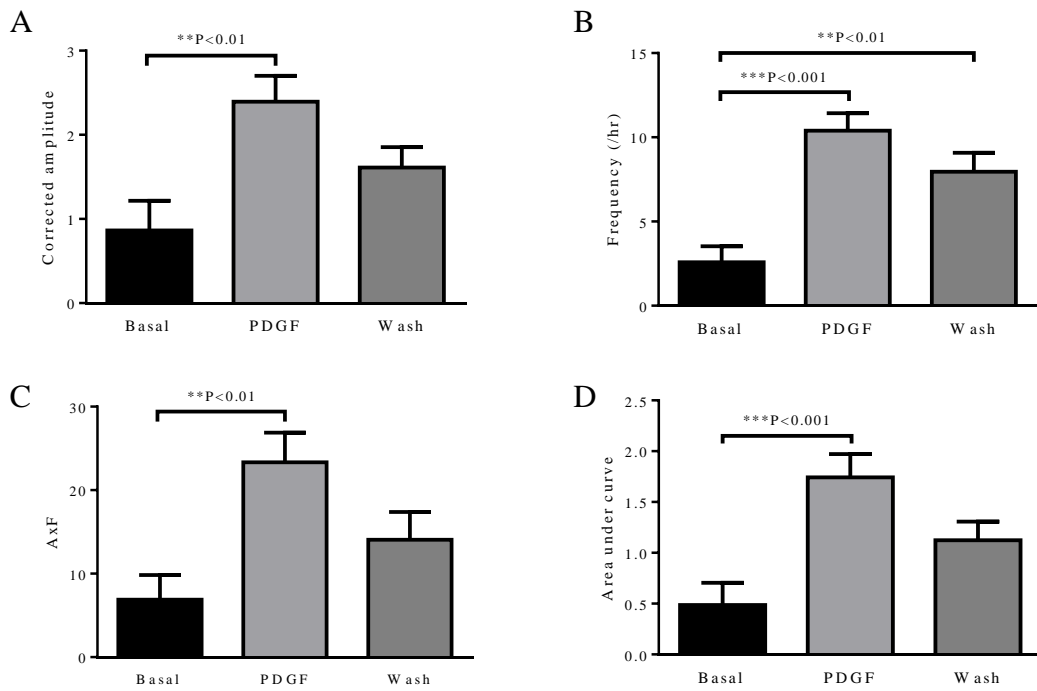


Figure 5.5: Effect of PDGF-BB on intracellular Ca^{2+} . Parameters of Ca^{2+} oscillations. Corrected amplitude (A), frequency (B), AxF (C) and AUC (D) under unstimulated (basal) conditions, following application of 20 ng/ml PDGF-BB and after wash with PSS ($n=18$, including 6 cells with spontaneous oscillations).

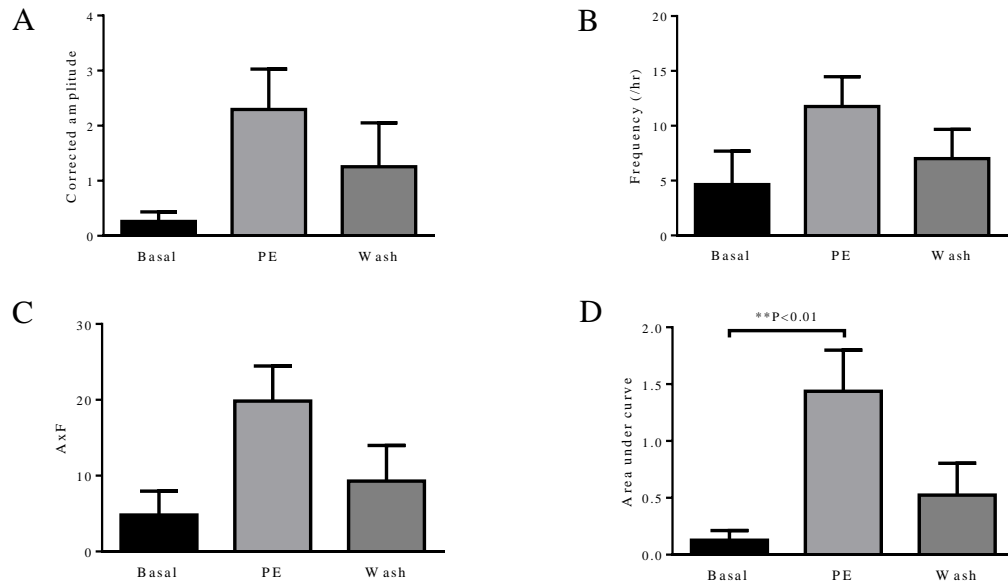


Figure 5.6: Effect of PE on intracellular Ca^{2+} . Parameters of Ca^{2+} oscillations.

Corrected amplitude (A), frequency (B), AxF (C) and AUC (D) under unstimulated (basal) conditions, following application of 10 μ M PE and after wash with PSS (n=8, including 2 cells with spontaneous oscillations).

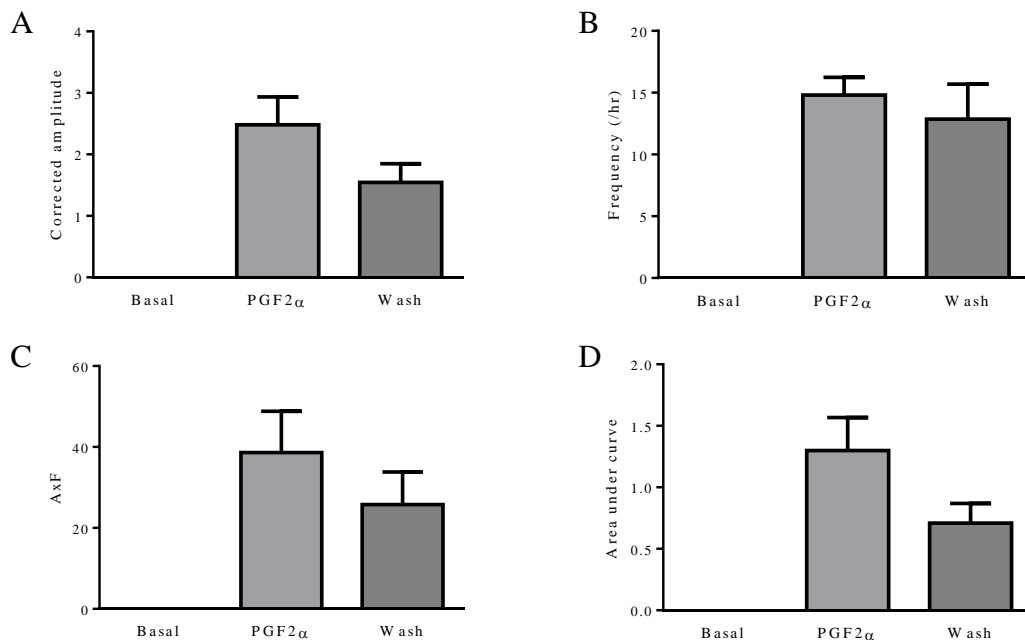


Figure 5.7: Effect of PGF2 α on intracellular Ca^{2+} . Parameters of Ca^{2+} oscillations.

Corrected amplitude (A), frequency (B), AxF (C) and AUC (D) under unstimulated (basal) conditions, following application of 10 μ M PGF2 α and after wash with PSS (n=10, all the cells without spontaneous oscillations).

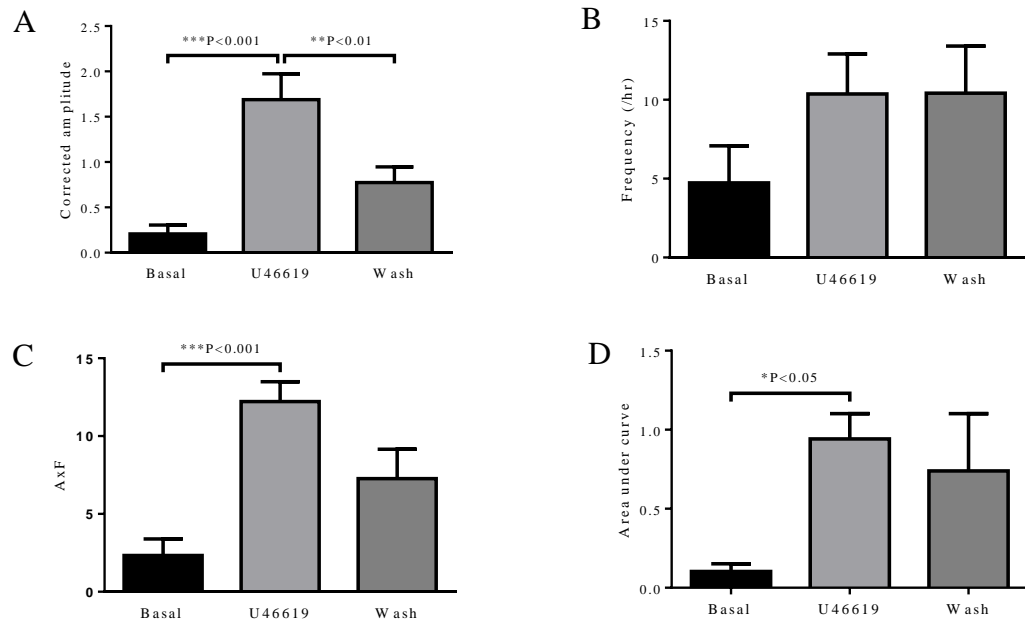


Figure 5.8: Effect of U46619 on intracellular Ca^{2+} . Parameters of Ca^{2+} oscillations. Corrected amplitude (A), frequency (B), AxF (C) and AUC (D) under unstimulated (basal) conditions, following application of 1 μM U46619 and after wash with PSS (n=11, including 4 cells with spontaneous oscillations).

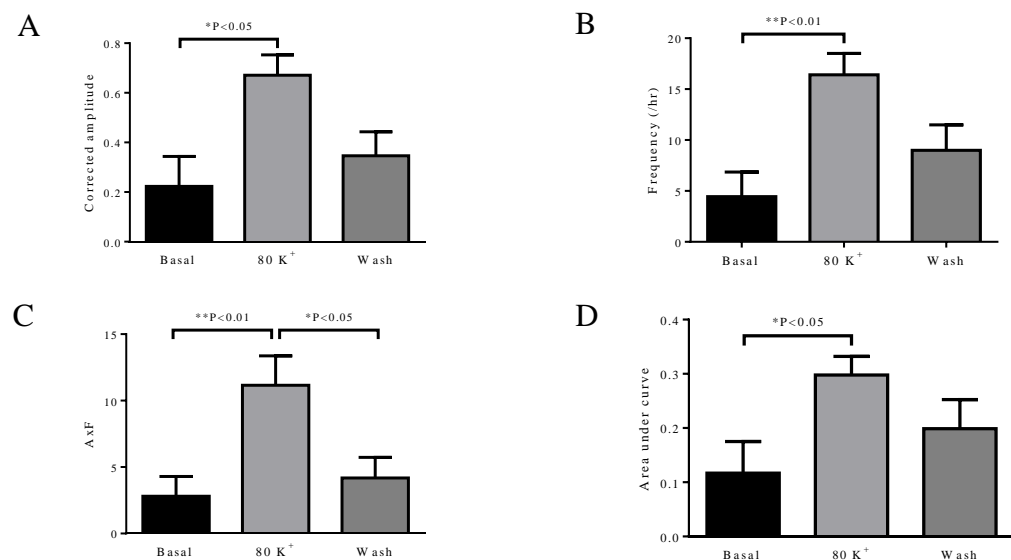


Figure 5.9: Effect of high K^+ on intracellular Ca^{2+} . Elevation of extracellular K^+ from 5 mM to 80 mM increased Ca^{2+} oscillations, indicated by corrected amplitude (A), frequency (B), AxF (C) and AUC (D) (n=9, including 3 cells with spontaneous oscillations).

5.3.1.4 Effect of hypoxia on intracellular Ca²⁺

Vasoconstrictors either triggered or enhanced Ca²⁺ oscillations in single HCASMCs suggesting that at least some of the Ca²⁺ handling mechanisms are still intact in those cells. Next, the effect of hypoxia was examined. **Figure 5.10A** shows that Ca²⁺ oscillations induced by application of 20 ng/ml PDGF-BB is stable although there was a small decrease in frequency and/or amplitude in some cells. Exposure to hypoxia caused a decrease in Ca²⁺ oscillations, and a representative example is shown in **Figure 5.10B**. In the presence of 20 ng/ml PDGF-BB, Ca²⁺ oscillations were observed with an amplitude of 1.34 ± 0.23 , a frequency (/hr) of 22.86 ± 2.86 , AxF of 31.20 ± 4.90 , and AUC of 0.53 ± 0.08 . Exposure to hypoxia (1% O₂) for 10 minutes caused decreases in amplitude to 0.78 ± 0.16 , frequency (/hr) to 17.14 ± 2.76 , AxF to 12.47 ± 2.96 , AUC to 0.46 ± 0.11 (**Figure 5.11**). Exposure to hypoxia for 30 minutes decreased 10 μM PGF2α induced Ca²⁺ oscillations with amplitude from 1.99 ± 0.49 to 1.37 ± 0.53 , frequency (/hr) from 15.56 ± 2.22 to 17.67 ± 3.40 , AxF from 29.31 ± 6.40 to 17.83 ± 2.44 , and AUC from 0.76 ± 0.22 to 0.47 ± 0.40 (**Figure 5.12**). Exposure to hypoxia for 25-30 minutes also decreased 1 μM U46619 induced Ca²⁺ oscillations with amplitude from 0.83 ± 0.28 to 0.65 ± 0.13 , frequency (/hr) from 25.89 ± 2.58 to 16.68 ± 3.25 , AxF from 33.74 ± 12.40 to 13.98 ± 5.02 , and AUC from 0.43 ± 0.08 to 0.21 ± 0.05 (**Figure 5.13**). Acute hypoxia had a minimum effect on basal Ca²⁺ of the cells without oscillations, but reduced Ca²⁺ oscillations of single HCASMC with spontaneous oscillations (**Figure 5.14**). Taken together, hypoxia significantly reduced amplitude/amplitude and frequency of Ca²⁺ oscillations in HCASMCs. Note that in some cells with spontaneous oscillations hypoxia not only reduced Ca²⁺ oscillations but also seemed to decrease basal Ca²⁺ (e.g. **Figure 5.14**).

In order to examine the role of VDCCs in Ca²⁺ responses, a dihydropyridine calcium channel blocker nimodipine was applied. When cells were preincubated with a K_{ATP} channel opener, pinacidil (10 μM) for 10 mins, 20 ng/ml PDGF-BB still caused a transient rise in intracellular Ca²⁺ (**Figure 5.15**). Blocking VDCCs by nimodipine (10 μM) for 10 minutes caused variable response. Application of

nimodipine induced no change or little change in basal Ca^{2+} or spontaneous Ca^{2+} oscillations in some cells (**Figure 5.16**). In another experiment, a decrease of $13.03 \pm 2.05\%$ in the basal fluorescence was observed in response to nimodipine ($n=7$, $p=0.001$). Hypoxia caused a decrease in high K^+ induced Ca^{2+} oscillations, but not significantly, indicating an effect, at least in part, independent of VDCCs (**Figure 5.17**). It should be emphasized that these experiments are preliminary, and more work is required to examine the role of VDCCs in hypoxia properly.

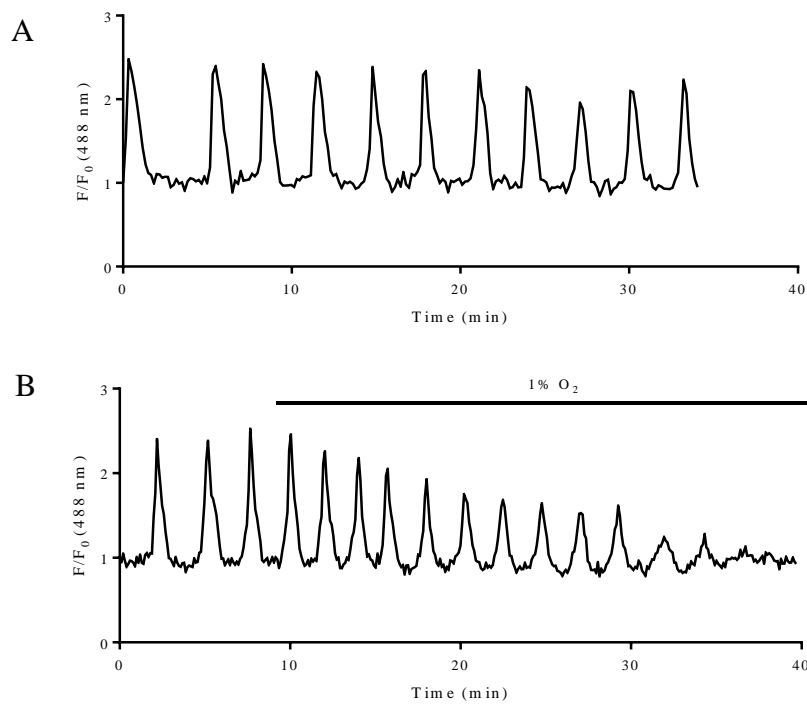


Figure 5.10: Effect of hypoxia on Ca^{2+} oscillations. (A) Ca^{2+} oscillations induced by 20 ng/ml PDGF-BB. (B) Hypoxia caused attenuation of Ca^{2+} oscillations induced by 10 μM PGF2 α .

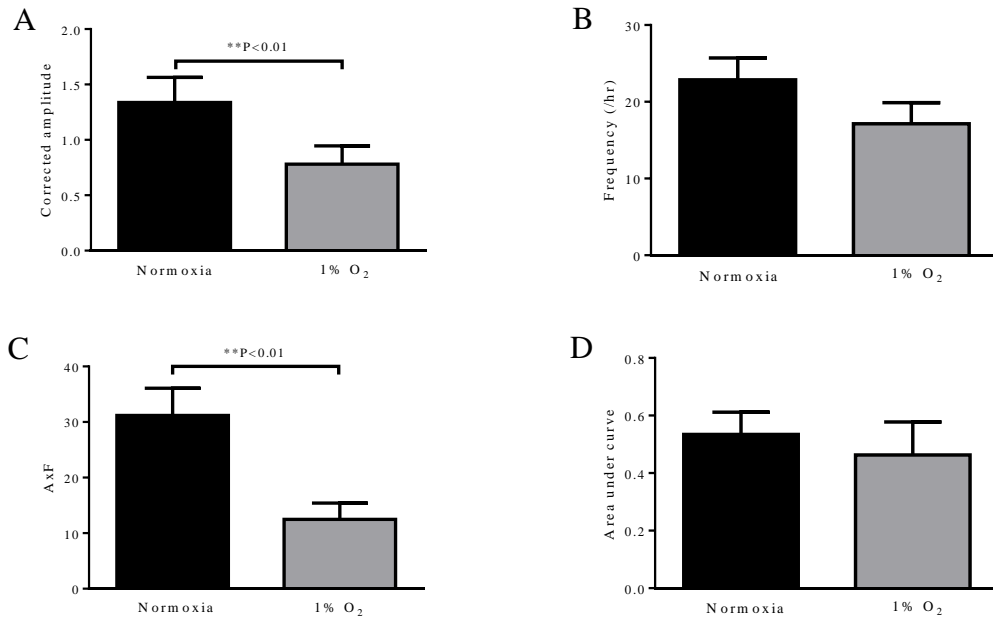


Figure 5.11: Effect of hypoxia on PDGF-BB induced Ca²⁺ oscillations. Effect of hypoxia (1% O₂) on amplitude (A), frequency (B), AxF (C), and AUC (D) of Ca²⁺ oscillations induced by PDGF-BB (n=7).

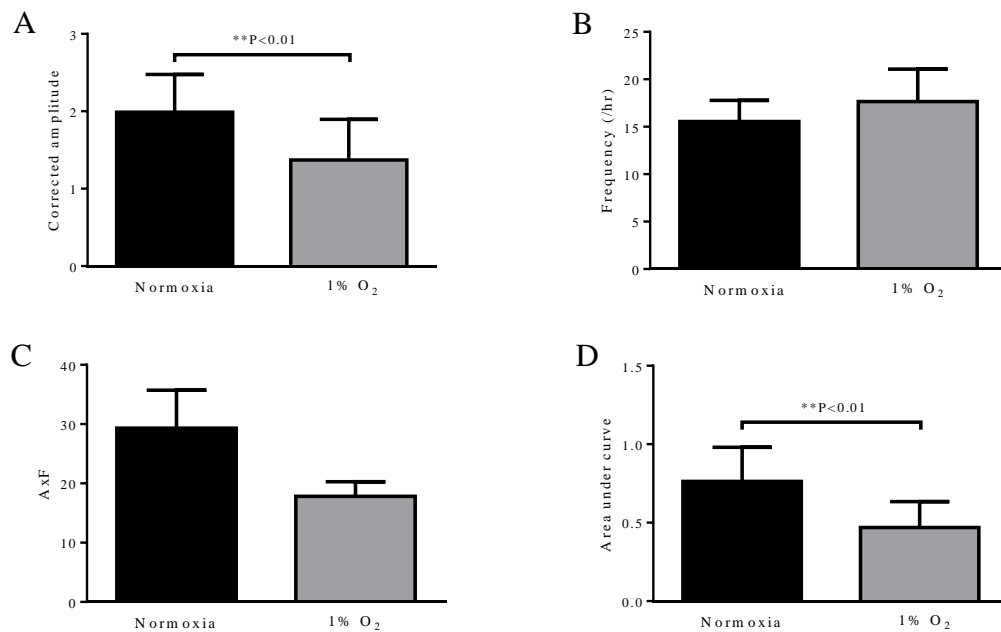


Figure 5.12: Effect of hypoxia on PGF2 α induced Ca²⁺ oscillations. Effect of hypoxia (1% O₂) on amplitude (A), frequency (B), AxF (C), and AUC (D) of Ca²⁺ oscillations induced by PGF2 α (n=6).

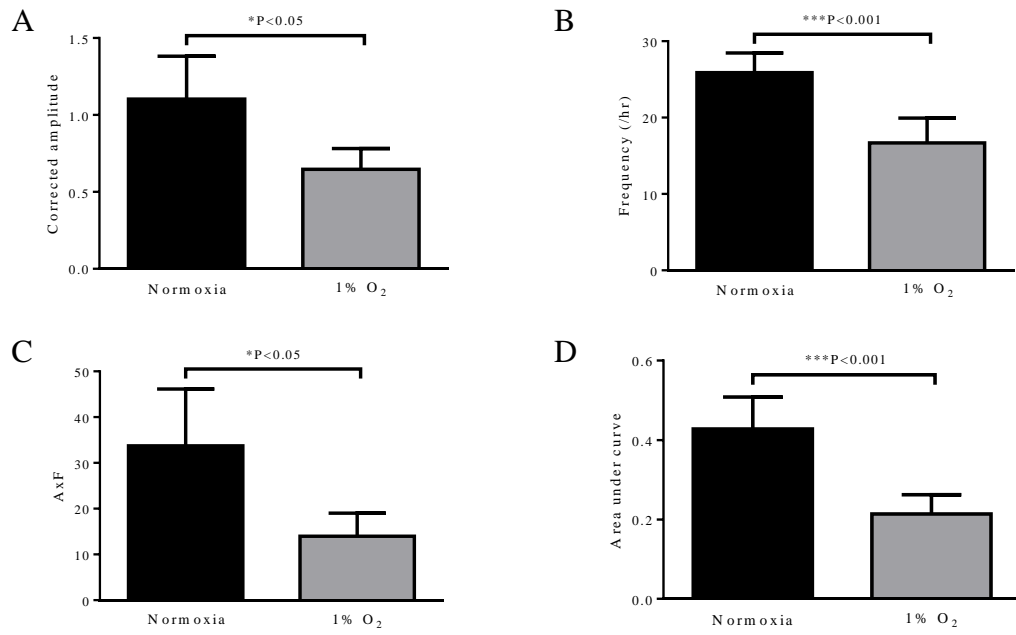


Figure 5.13: Effect of hypoxia on U46619 induced Ca²⁺ oscillations. Effect of hypoxia (1% O₂) on amplitude (A), frequency (B), AxF (C), and AUC (D) of Ca²⁺ oscillations induced by U46619 (n=17).

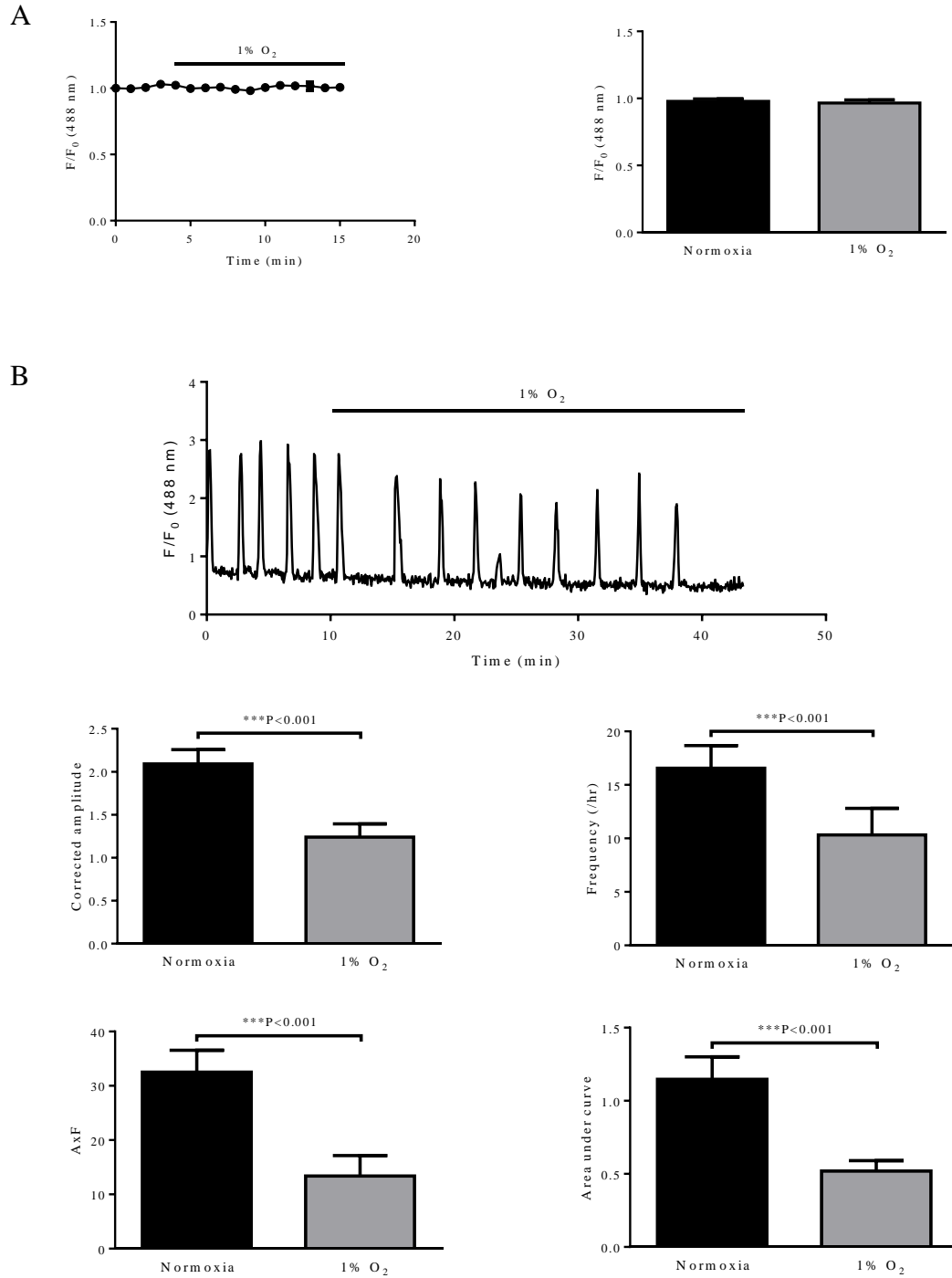


Figure 5.14: Effect of hypoxia on basal and spontaneous Ca^{2+} oscillations. (A) Exposure to hypoxia for 10 mins had little effect on basal Ca^{2+} of the cells without spontaneous oscillations (n=21). (B) Hypoxia reduced spontaneous Ca^{2+} oscillations of single HCASMCs (n=25).

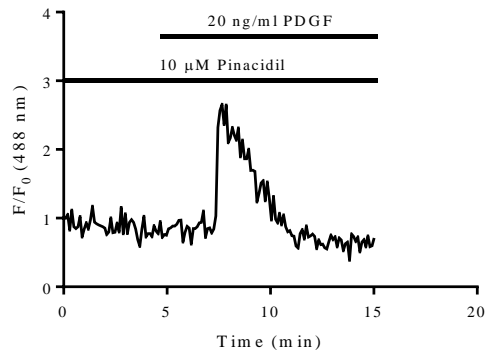


Figure 5.15: Effect of PDGF-BB on intracellular Ca^{2+} in the presence of pinacidil. Pinacidil ($10 \mu\text{M}$) was applied for 10 minutes before, and throughout application of PDGF-BB.

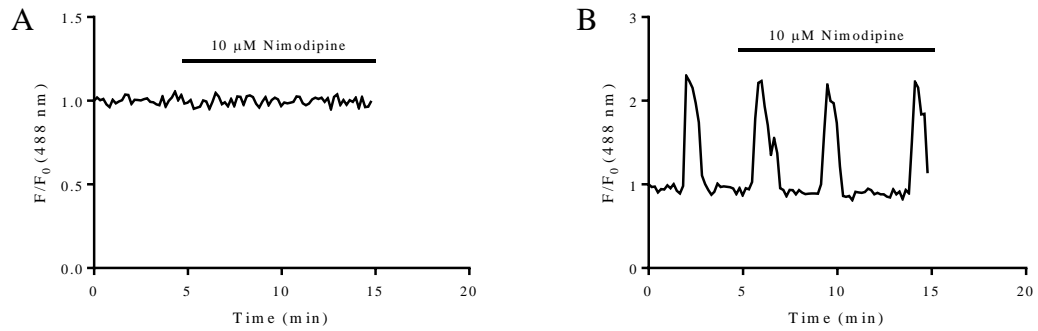


Figure 5.16: Effect of nimodipine on basal Ca^{2+} and spontaneous Ca^{2+} oscillations. (A) $10 \mu\text{M}$ nimodipine induced no change in basal Ca^{2+} level for a 10 mins period. (B) Spontaneous Ca^{2+} oscillations were not inhibited by $10 \mu\text{M}$ nimodipine for a 10 mins period.

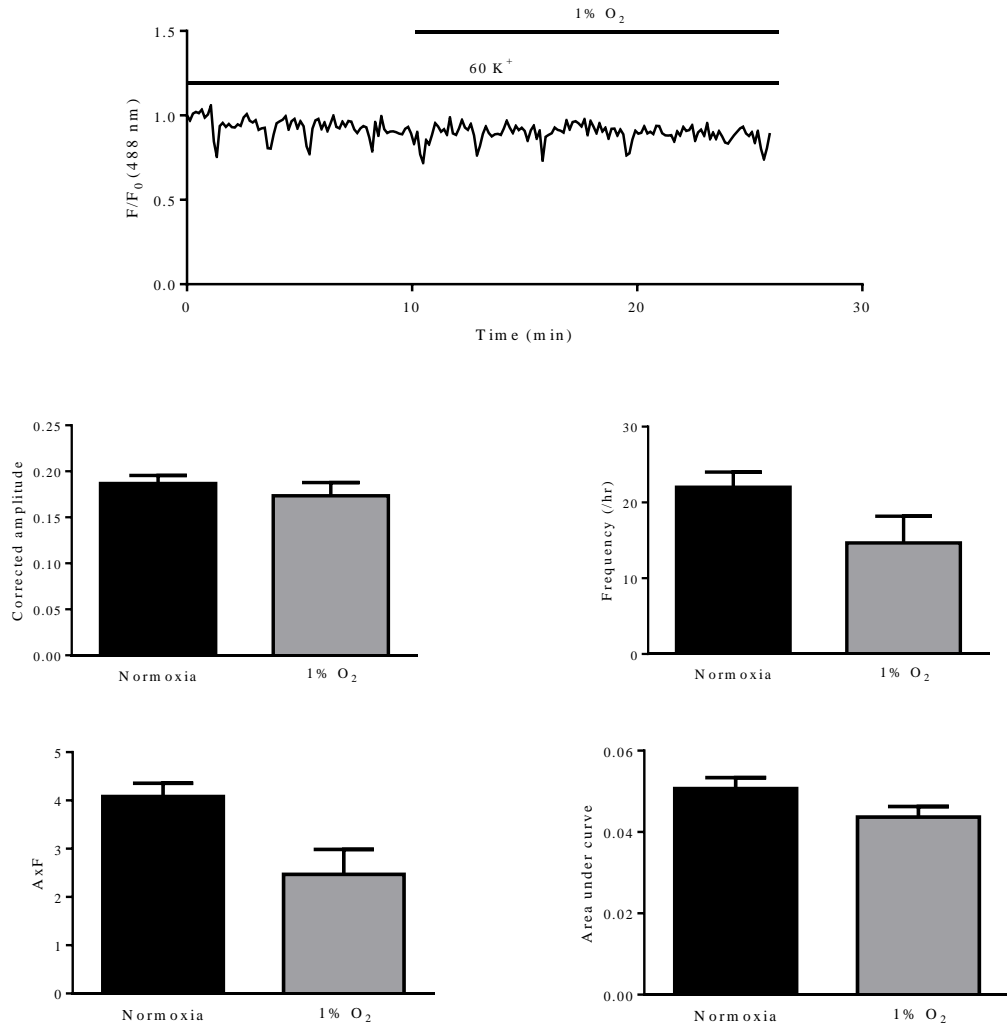


Figure 5.17: Effect of hypoxia on high K^+ induced Ca^{2+} oscillations. Exposure to hypoxia for 15 minutes caused a non-significant decrease in Ca^{2+} oscillations induced by high K^+ . The cells in this experiment were loaded with Fura-Red (n=3).

5.3.2 Effect of hypoxia on membrane potential of single HCASMCs

Hypoxia caused significant reduction in Ca^{2+} oscillations induced by vasoconstrictors. However, the inconsistency in cell response including presence or absence of spontaneous Ca^{2+} oscillations at rest made interpretation of the results difficult. Crucially, lack of nimodipine effect on Ca^{2+} oscillations strongly suggests that cyclic fluctuation in $[Ca^{2+}]_i$ may be explained by Ca^{2+} release from, and sequestration to, SR (**Figure 5.16**). It follows that the mechanisms by which hypoxia causes reduction in Ca^{2+} oscillations may be largely independent of membrane

hyperpolarization. That said, K^+ channels seem important in HCASMCs as elevation of $[K^+]_o$ not only induced Ca^{2+} oscillations but also gradual increase in basal $[Ca^{2+}]_i$ (**Figure 5.2C**). To further investigate the role of K^+ channels in HCASMCs, experiments were carried out to measure changes in membrane potential. Using a membrane potential-sensitive dye DiBAC4(3), we addressed the following questions: (i) Which K^+ channel(s) play a major role in setting resting membrane potential of HCASMCs? (ii) What are the effects of metabolic inhibitors/hypoxia on membrane potential? (iii) Which K^+ channels are involved in changes caused by metabolic inhibitors/hypoxia?

5.3.2.1 Measurement of membrane potential with DiBAC4(3)

DiBAC4(3) is a slow-response potential-sensitive fluorescent probe (**Figure 5.18 A**). It is an appropriate reporter of membrane potential change in HCASMCs where depolarization and hyperpolarization are expected to be slow and steady. It is permeable to plasma membrane, accumulating in the cytoplasm following a Nernst equilibrium distribution [255]. The anionic dye in the cell binds to intracellular proteins or membrane resulting in an enhanced fluorescence and also a red spectral shift [256, 257]. Depolarization of membrane potential causes additional entry of the anionic dye into the cell, increasing the fluorescence signal. Hyperpolarization, on the other hand, results in a decrease in the signal (**Figure 5.18 B**). Compared to cationic carbocyanines, DiBAC4(3) and related dyes are largely excluded from mitochondria due to their overall negative charge, making them primarily sensitive to plasma membrane potential. Initial experiments (n=3) characterized the correlation of the changes in the fluorescence (F/F_0) with the millivolt (mV) change in K^+ equilibrium potential, calculated with Nernst equation using various concentrations of $[K^+]_o$ (5, 30, and 80 mM). A representative characterization experiment is shown in **Figure 5.19**.

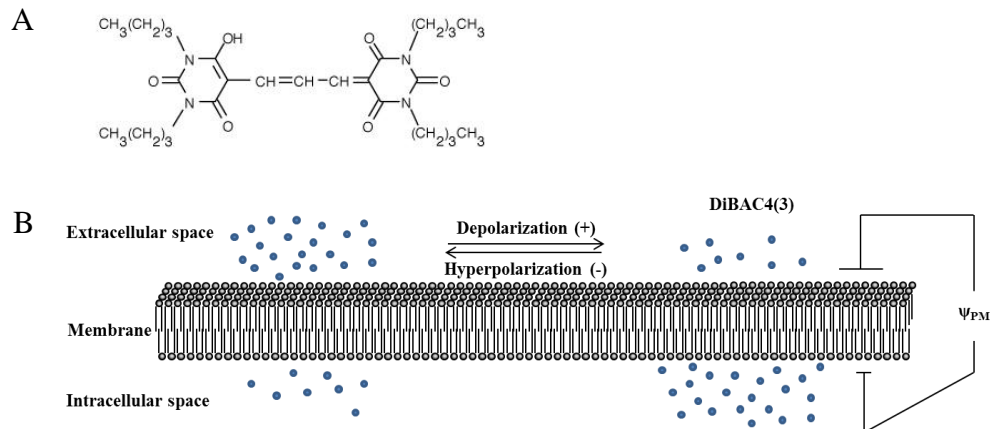


Figure 5.18: Distribution of DiBAC4(3) according to membrane potential. (A) Chemical structure of DiBAC4(3). (B) DiBAC4(3) molecules accumulate in cells following Nernst equilibrium distribution. Depolarization results in an additional accumulation of the dye and therefore an increase in fluorescence; conversely hyperpolarization causes a decrease in the fluorescence.

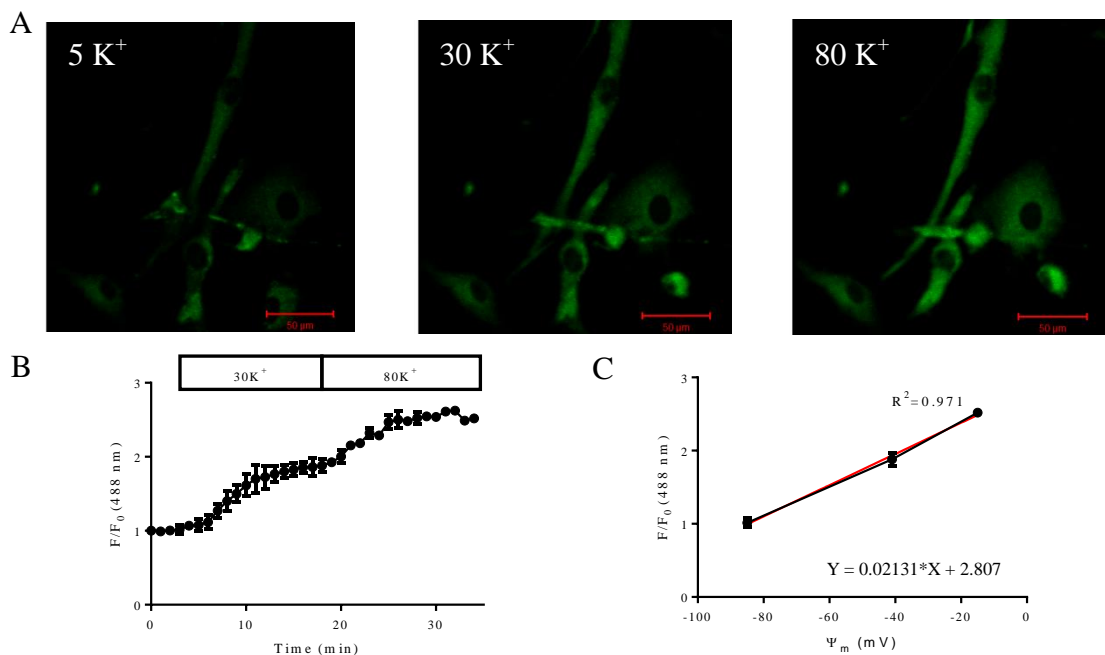


Figure 5.19: Characterization of DiBAC4(3) fluorescence. (A) Images of DiBAC4(3) loaded cells at 5 mM, 30 mM and 80 mM $[K^+]_o$. (B) DiBAC4(3) fluorescence changes upon increasing concentrations of $[K^+]_o$. (C) Relationship between changes in DiBAC4(3) fluorescence and E_K , calculated by Nernst equation. The slope of the regression line is $\sim 2.13\%/mV$ ($n=3$, cells contracted or moved were excluded).

5.3.2.2 Identification of K⁺ channels involved in resting membrane potential

Preliminary experiments using DiBAC4(3) clearly indicated that HCASMCs depolarize in a [K⁺]_o dependent manner, and therefore K⁺ channels are important in setting resting membrane potential. Next, a series of K⁺ channel inhibitors were applied to dissect which K⁺ channels are involved. Glibenclamide, penitrem A, tram34, apamin, BaCl₂ and XE991 are inhibitors of K_{ATP}, BK_{Ca}, IK_{Ca}, SK_{Ca}, K_{ir} and K_{v7} channels.

There was no change in DiBAC4(3) fluorescence in control studies where nothing, DMSO, or water was applied (**Figure 5.20**), suggesting membrane potential is stable. Application of K⁺ channel inhibitors for 10-15 minutes changed the fractional fluorescence of DiBAC4(3) by $54.94 \pm 8.18\%$ (10 μM glibenclamide, n=37, p=0.000), $1.10 \pm 2.69\%$ (200 nM penitrem A, n=18), -2.50 ± 2.08 (1 μM tram34, n=13), $0.08 \pm 0.48\%$ (200 nM apamin, n=32), $69.95 \pm 7.46\%$ (25 μM BaCl₂, n=26, p=0.000), and $3.87 \pm 1.40\%$ (10 μM XE991, n=14) respectively (**Figure 5.21**). Changes caused by glibenclamide and BaCl₂ are highly significant, suggesting that among all the K⁺ channels examined, K_{ATP} and K_{ir} channels play important roles in setting resting membrane potential of HCASMCs. BaCl₂ also caused an increase in the fluorescence in the presence of 10 μM glibenclamide (data not shown). At the concentration used, BaCl₂ should act as a specific blocker of K_{ir} channels [43, 252], and additive effect of glibenclamide and BaCl₂ further support the hypothesis that both K_{ATP} channels and K_{ir} channels regulate resting membrane potential in HCASMCs.

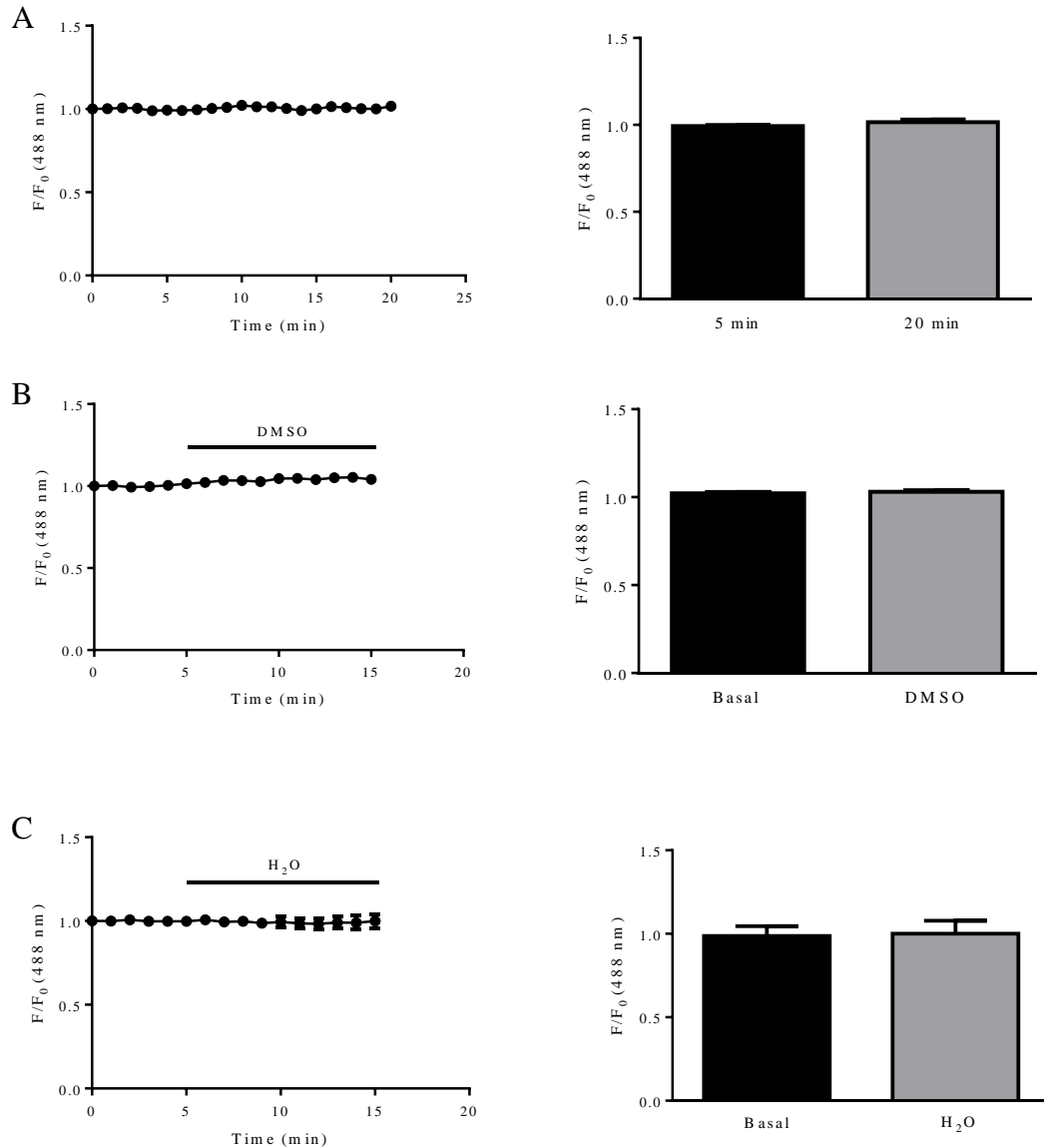


Figure 5.20: Changes of DiBAC4(3) fluorescence in control studies. (A) Imaging the cells for a period of 20 minutes had no effect on DiBAC4(3) fluorescence (n=42). (B) Application of DMSO for 10 minutes had no effect on DiBAC4(3) fluorescence (n=51). (C) Application of H₂O for 10 minutes had no effect on DiBAC4(3) fluorescence (n=17). Mean \pm SEM of DiBAC4(3) fluorescence just before the treatment and at the end point was shown in right panels.

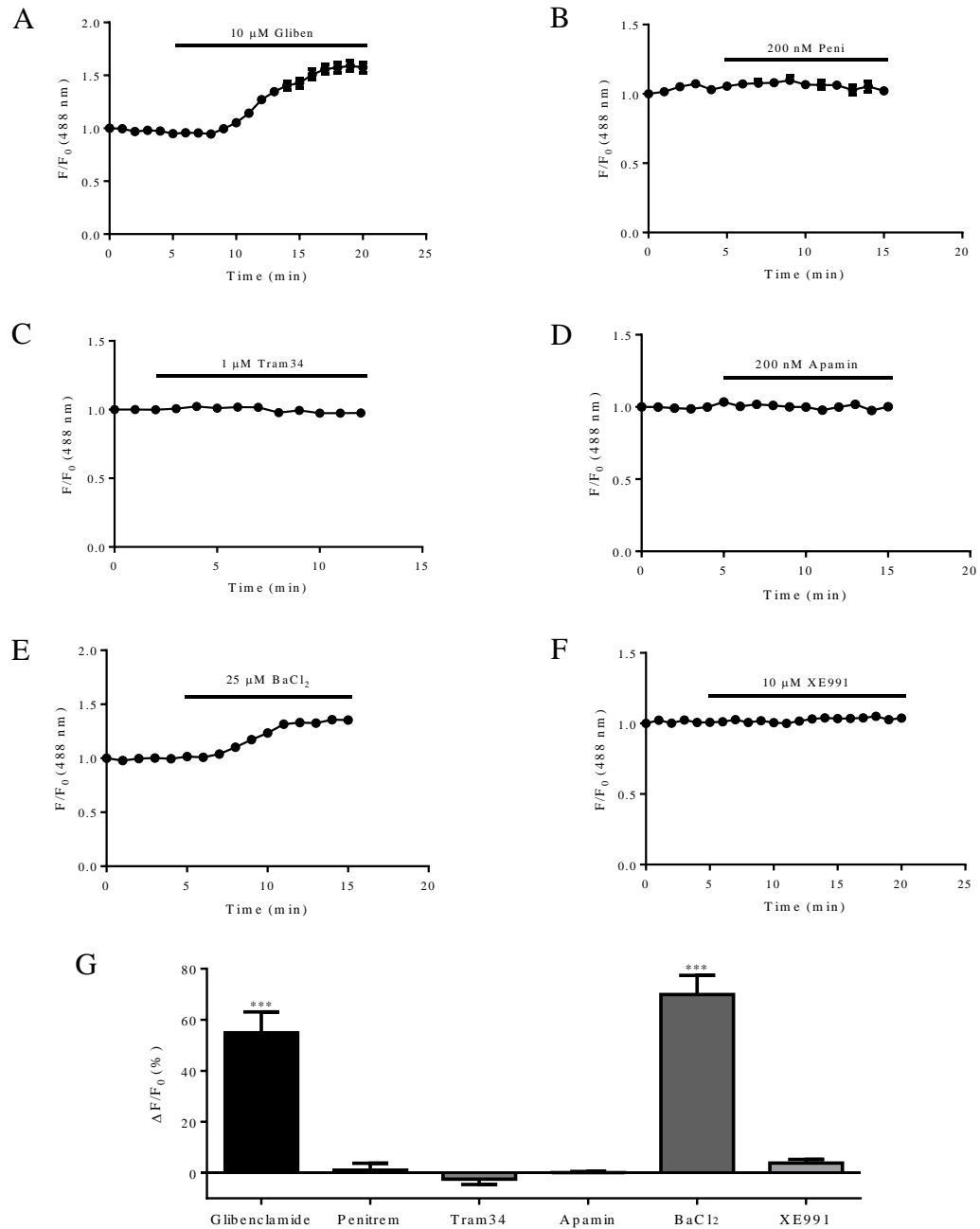


Figure 5.21: Effects of K^+ channels in regulating resting membrane potential of HCASMCs. (A) The effect of 10 μ M glibenclamide. (B) The effect of 200 nM penitrem A. (C) The effect of 1 μ M tram34. (D) The effect of 200 nM apamin. (E) The effect of 25 μ M $BaCl_2$. (F) The effect of 10 μ M XE991. (G) A summary of percent fold change of fractional fluorescence of DiBAC4(3) after application of K^+ channel inhibitors.

5.3.2.3 Pharmacological modulation of K⁺ channels

Response and sensitivity of K⁺ channels to pharmacological modulators can be different due to the origin of the artery. For example, the majority of HCASMC BK_{Ca} channels contain β1 subunit that is reported to have a high sensitivity to Ca²⁺ and little sensitivity to IbTX and penitrem A [258-261]. Thus, the changes in membrane potential of HCASMCs were further characterized in response to a variety of K⁺ channel agonists and antagonists. 10 μM adenosine, a physiological vasodilator thought to be important in coronary circulation, caused a reduction in DiBAC4(3) fluorescence by 30.88 ± 3.25% (**Figure 5.22**). K_{ATP} channel opener, pinacidil (10 μM) decreased DiBAC4(3) fluorescence by 31.62 ± 4.02% (n=14), and subsequent application of glibenclamide (10 μM) fully reversed the change (n=10). Note that higher signal after application of glibenclamide above base line indicates that K_{ATP} channels are open at rest (see **Figure 5.21**). Pinacidil was ineffective when cells were pre-incubated with 10 μM glibenclamide (n=17) (**Figure 5.23**). NS1619 (10 μM) caused a reduction in DiBAC4(3) fluorescence by 41.54 ± 2.01% (n=95). However, application of 200 nM penitrem A (n=68) or 100 nM IbTX (n=25) did not block NS1619 induced hyperpolarization. Pre-treating the cells with 100 nM IbTX for 10 mins also had no influence on the effect induced by NS1619 (n=18) (**Figure 5.24**). 1 μM NS11021, a potent BK_{Ca} channel activator, induced a decrease in DiBAC4(3) signal by 26.17 ± 7.16% (n=6). Higher concentration of NS11021 (10 μM) caused a larger effect on membrane potential, however this effect was also unaffected by 100 nM IbTX (64.74 ± 1.81% vs 66.47 ± 1.82%, NS11021 and NS11021 plus IbTX respectively, n=36) (**Figure 5.25**). Application of 1 μM SKA31, an activator of IK_{Ca}/SK_{Ca}, decreased DiBAC4(3) fluorescence by 30.46 ± 4.08% (n=31), and 10 μM SKA31 by 51.21 ± 1.55% (n=14). The effect from 1 μM SKA31 was not inhibited by 200 nM apamin alone (n=11), but by a combination of 200 nM apamin and 1 μM tram34 (n=15) (**Figure 5.26**).

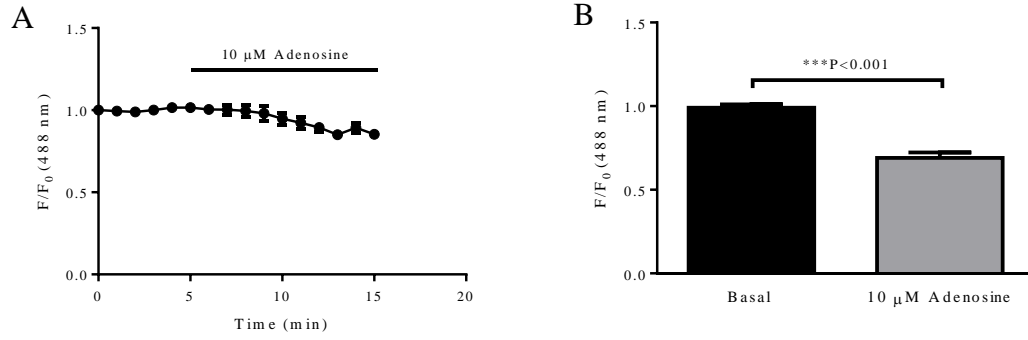


Figure 5.22: Effect of adenosine on plasma membrane potential. (A) Time course of fractional fluorescence of cells treated with 10 μ M adenosine. (B) Mean \pm SEM of DiBAC4(3) fluorescence during control condition (at 5 min) and after (at 15 min) application of 10 μ M adenosine (n=21).

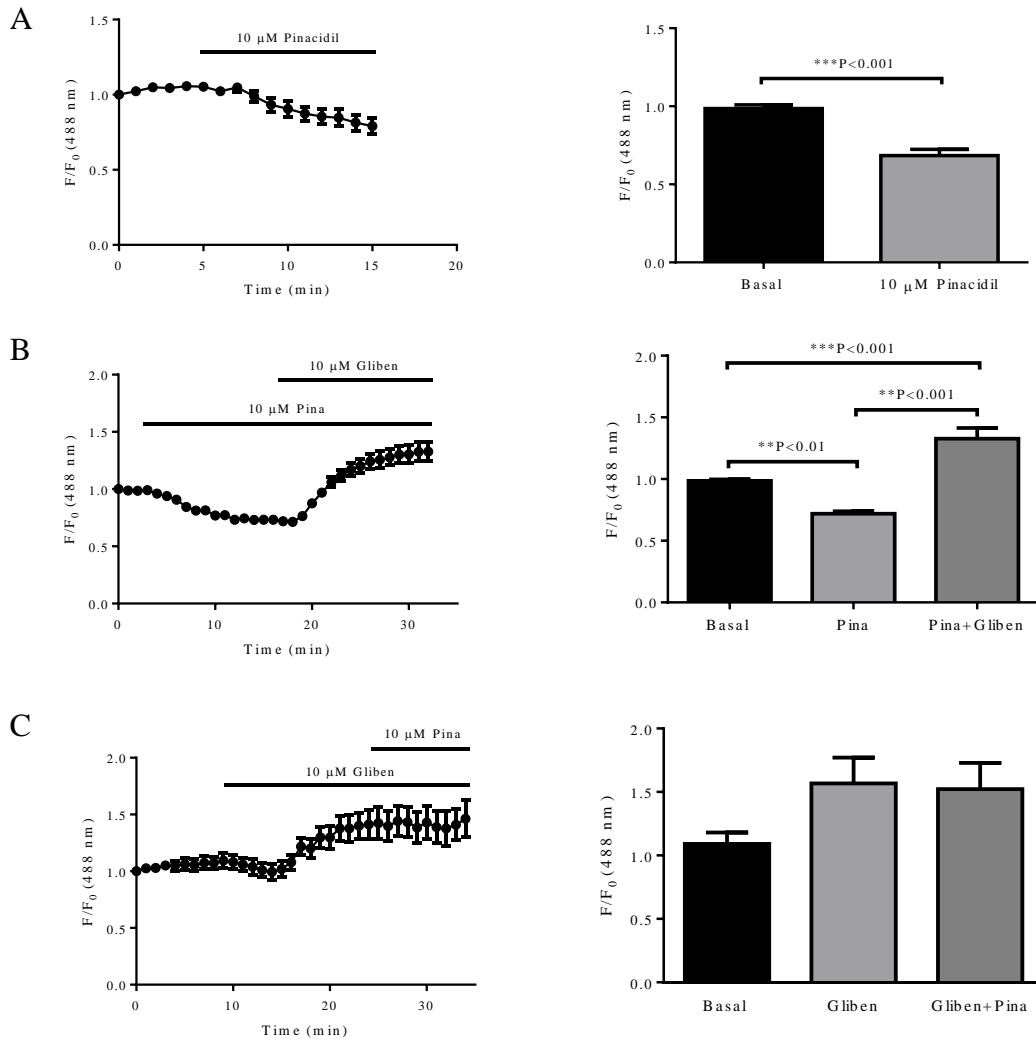


Figure 5.23: Effect of K_{ATP} channel modulators on membrane potential. (A) Application of 10 μ M pinacidil caused hyperpolarization of plasma membrane ($n=14$). (B) Subsequent addition of 10 μ M glibenclamide increased the signal above the basal level significantly ($n=10$). (C) 10 μ M glibenclamide caused an increase in DiBAC4(3) signal, and subsequent addition of 10 μ M pinacidil had no effect ($n=17$).

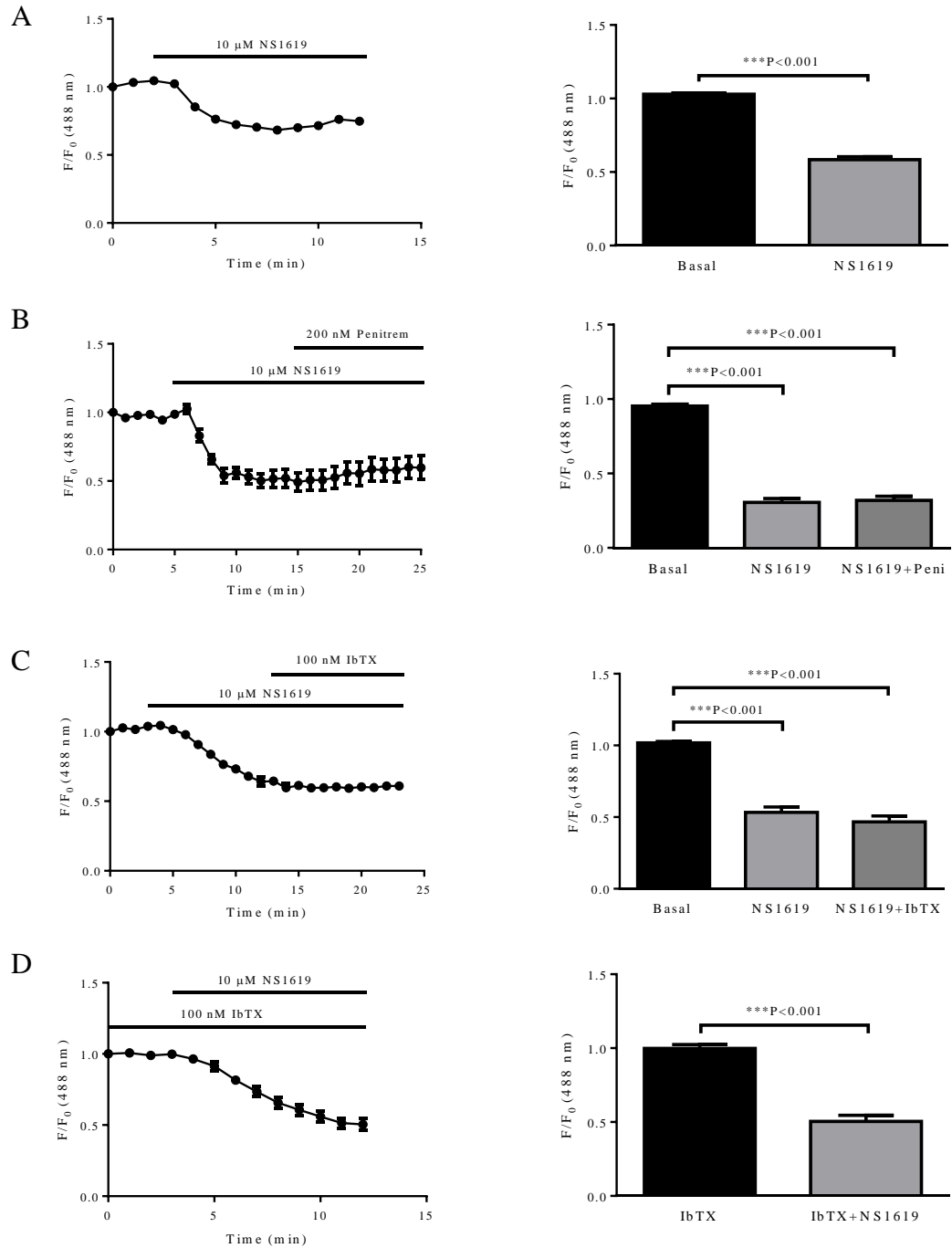


Figure 5.24: Effect of NS1619 on membrane potential. (A) Application of 10 μM NS1619 caused a rapid and sustained hyperpolarization ($n=95$). (B) Subsequent application of 200 nM penitrem A ($n=68$) or, (C) 100 nM IbTX after NS1619 ($n=25$) or, (D) pre-incubation with 100 nM IbTX for 10 mins did not alter the effect of NS1619 ($n=18$).

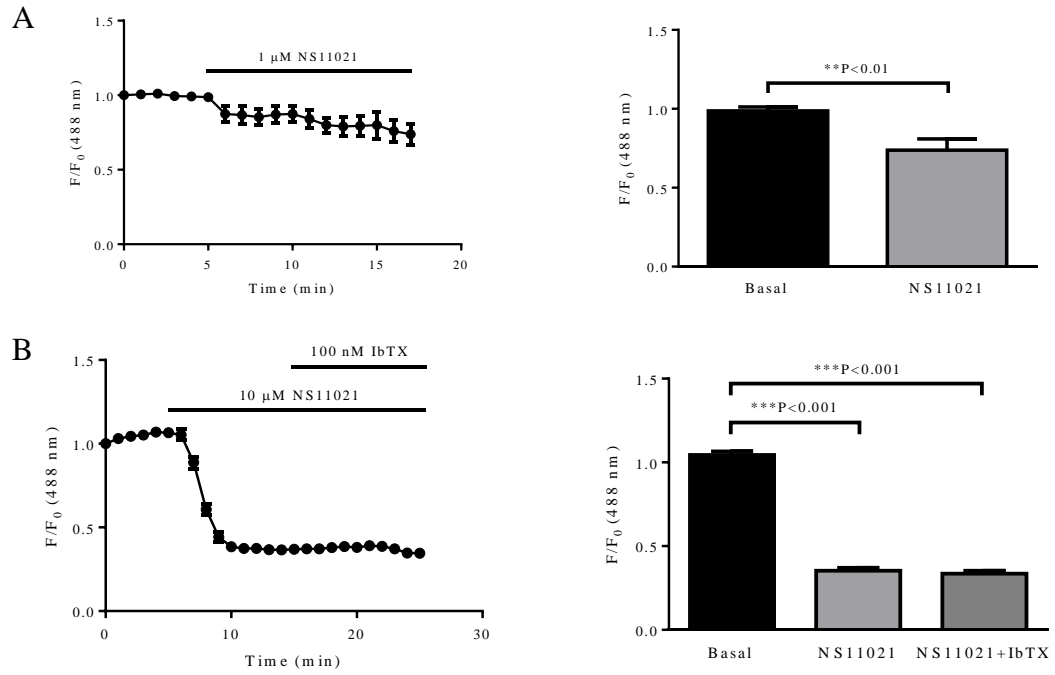


Figure 5.25: Effect of NS11021 on membrane potential. (A) Application of 1 μM NS11021 resulted in a decrease in fractional fluorescence of DiBAC4(3) ($n=6$). (B) The response of membrane potential to application of 10 μM NS11021 followed by 100 nM IbTX. 10 μM NS11021 caused a highly significant decrease in fluorescence, and the effect was not affected by application of 100 nM IbTX ($n=36$).

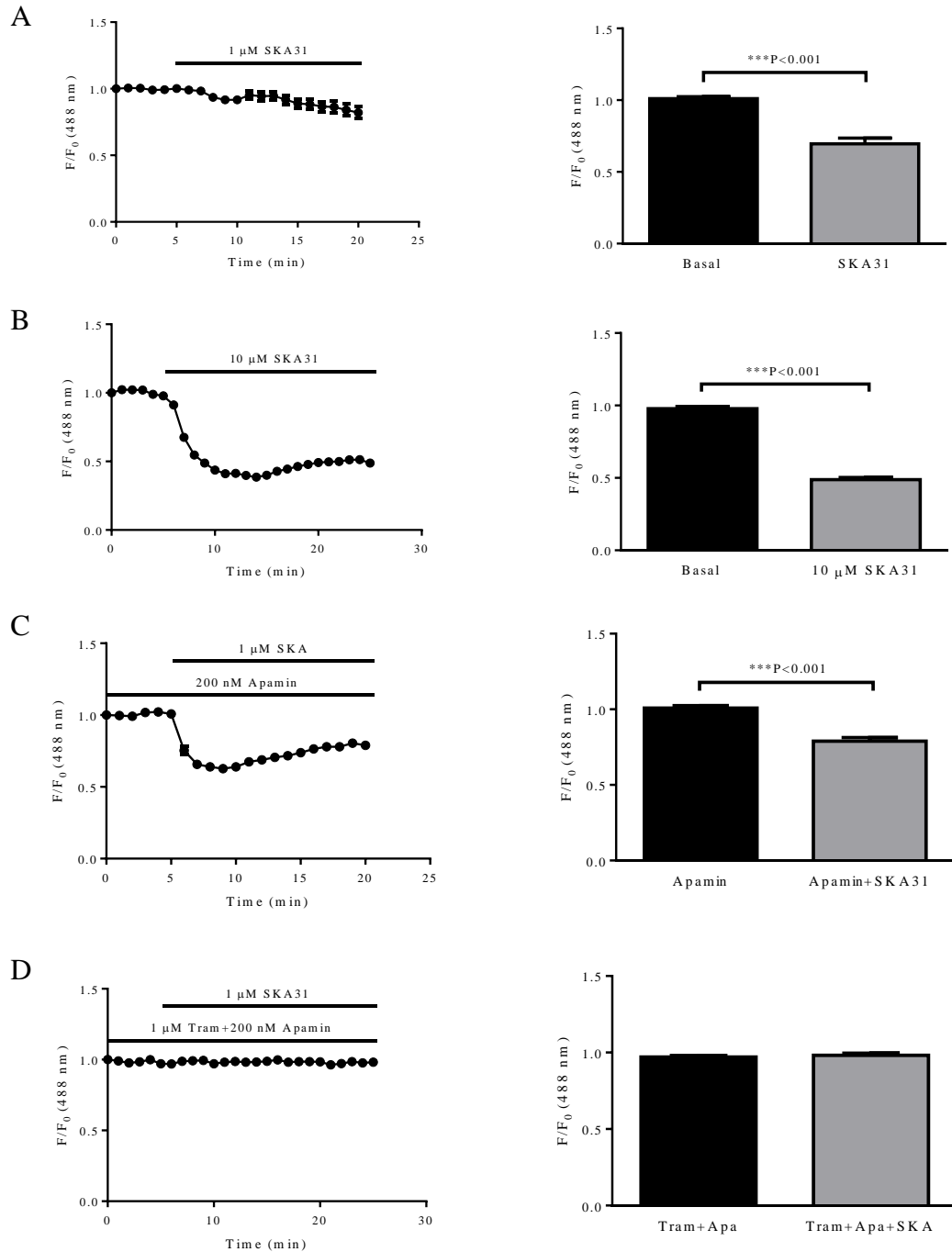


Figure 5.26: Effect of IK_{Ca} and SK_{Ca} channel modulators on membrane potential. (A) 1 μ M and (B) 10 μ M SKA31 (n= 31&14 respectively) caused a reduction in the fractional fluorescence of DiBAC4(3). (C) The effect of 1 μ M SKA31 was not inhibited by 200 nM apamin (n=11), but by 200 nM apamin plus 1 μ M tram34 (D, n=5).

5.3.2.4 Effect of metabolic inhibitors/hypoxia on membrane potential

In the previous chapters, we have reported the effect of metabolic inhibitors and hypoxia on cellular ATP and ATP:ADP ratio of HCASMCs. Here experiments were repeated to investigate the effects of metabolic inhibitors and hypoxia on membrane potential.

Application of 1 μM rotenone decreased DiBAC4(3) fluorescence signal by $34.44 \pm 1.29\%$ ($n=91$), and this effect was inhibited by high $[\text{K}^+]_o$ ($n=4$) (**Figure 5.27**), suggesting hyperpolarization depends on the opening of K^+ channels. Inhibiting mitochondrial complex III by 1 μM antimycin induced a decrease by $40.16 \pm 2.72\%$ in DiBAC4(3) fluorescence ($n=25$), which could be blocked by 10 μM glibenclamide or 60 K^+ (**Figure 5.28**), an indication that K_{ATP} channels may be involved. 6 μM oligomycin also caused a reduction in fluorescence signal by $41.67 \pm 3.05\%$ ($n=10$) (**Figure 5.29A**). However, addition of 1 μM CCCP caused a rise in DiBAC4(3) fluorescence ($n=23$) (**Figure 5.29B**). The possible explanation for this could be that application of CCCP resulted in an increase in DiBAC4(3) dye uptake by the cells [262].

Hypoxia (1% O_2) induced a decrease in DiBAC4(3) fluorescence by $12.37 \pm 1.31\%$ ($n=72$). The effect caused by hypoxia is reversible after re-administration of O_2 ($n=7$), and was blocked by 60 K^+ ($n=11$) (**Figure 5.30**), suggesting the involvement of K^+ channels. Exposure to hypoxia resulted in a decrease in DiBAC4(3) fluorescence by $13.74 \pm 3.12\%$ in the presence of 10 μM of pinacidil ($n=5$), by $11.21 \pm 1.43\%$ in the presence of 10 μM of glibenclamide ($n=36$), by $17.08 \pm 2.44\%$ in the presence of 25 μM BaCl_2 ($n=14$), by $11.70 \pm 2.14\%$ in the presence of 10 μM glibenclamide and 25 μM BaCl_2 ($n=25$), by $16.07 \pm 2.92\%$ in the presence of 100 nM IbTX ($n=17$), by $17.28 \pm 2.40\%$ in the presence of 200 nM penitrem ($n=14$) (**Figure 5.31**). These results indicate that K^+ channels are likely to be involved in hypoxia-induced membrane hyperpolarization reported by DiBAC4(3), but classic K^+ channel inhibitors, when applied singly, failed to block the effect of hypoxia.

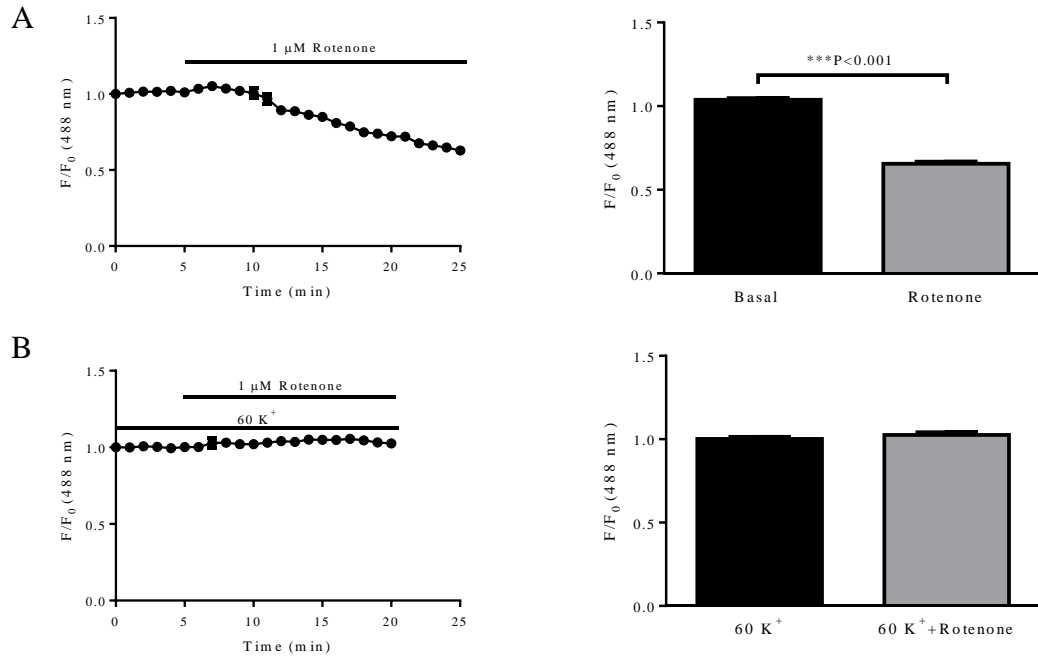


Figure 5.27: Effect of rotenone on membrane potential. (A) Application of 1 μM rotenone caused a decrease in DiBAC4(3) fluorescence (n=91). (B) Increasing K⁺ concentration of extracellular solution from 5 mM to 60 mM abolished the effect of rotenone (n=4).

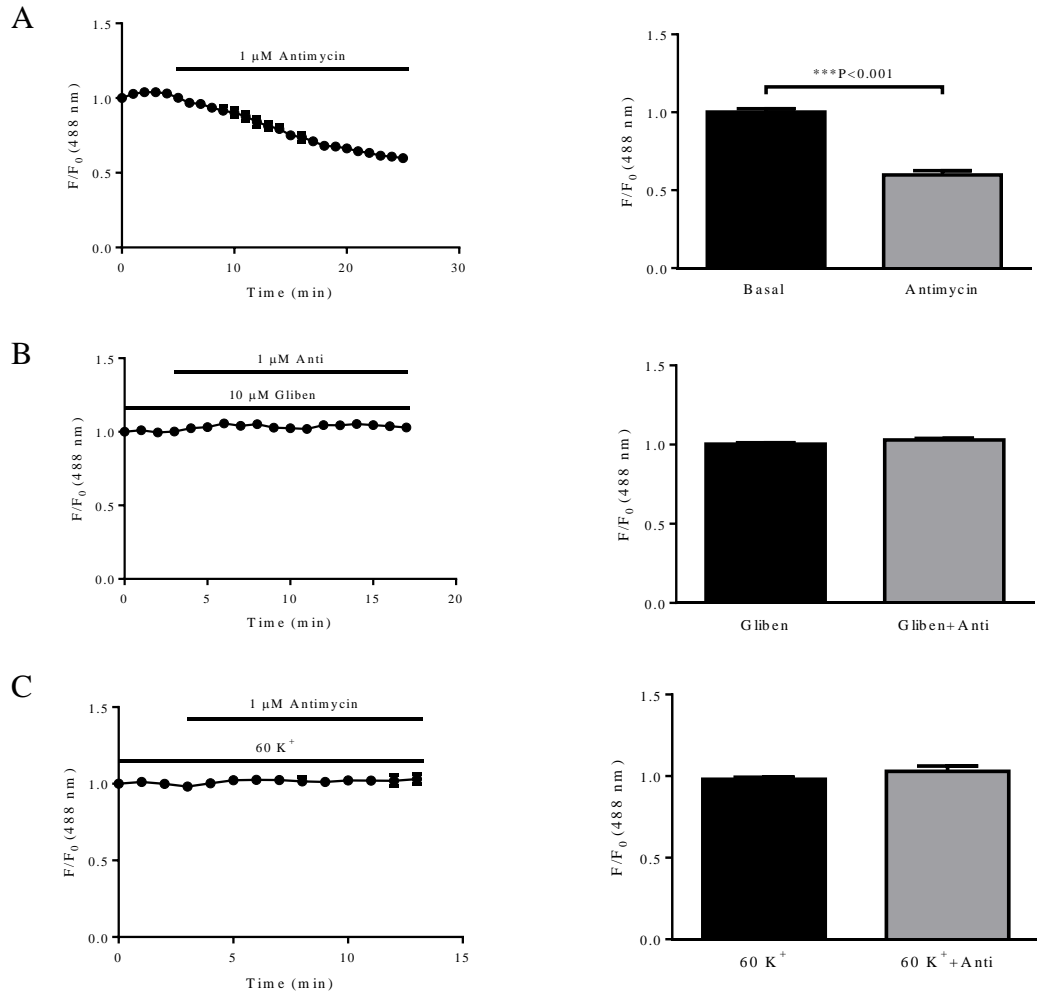


Figure 5.28: Effect of antimycin on membrane potential. (A) 1 μM antimycin caused membrane potential hyperpolarization (n=25). (B) 10 μM glibenclamide inhibited the effect of antimycin (n=22). (C) The effect of antimycin was inhibited by 60 K⁺ (n=6).

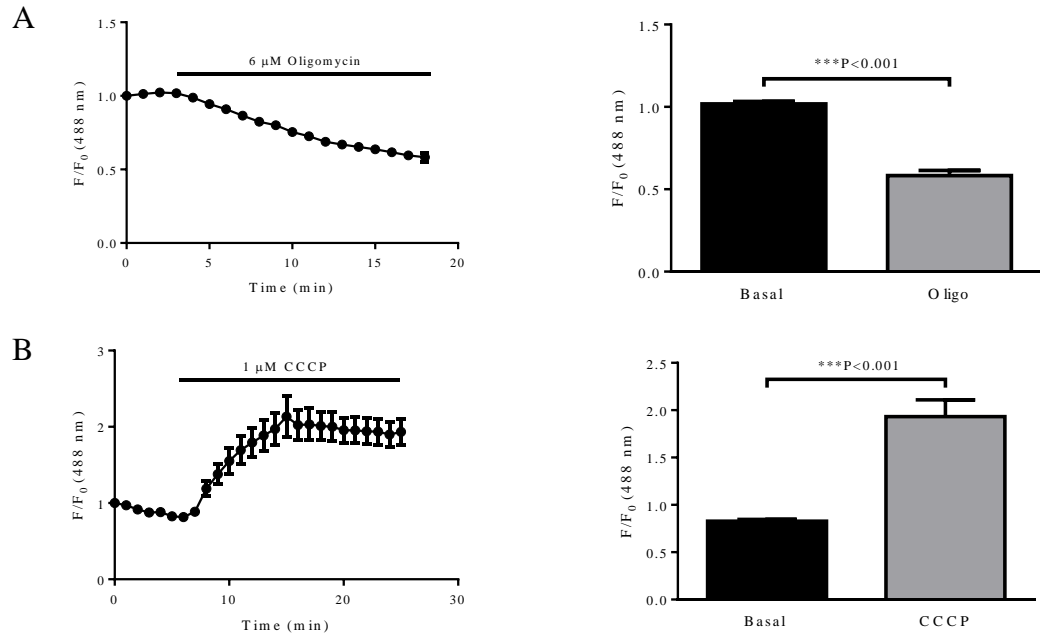


Figure 5.29: Effect of oligomycin and CCCP on membrane potential. (A) Application of 6 μ M oligomycin induced a decrease in fractional fluorescence of DiBAC4(3) (n=10). (B) 1 μ M CCCP caused an increase in DiBAC4(3) fluorescence (n=23).

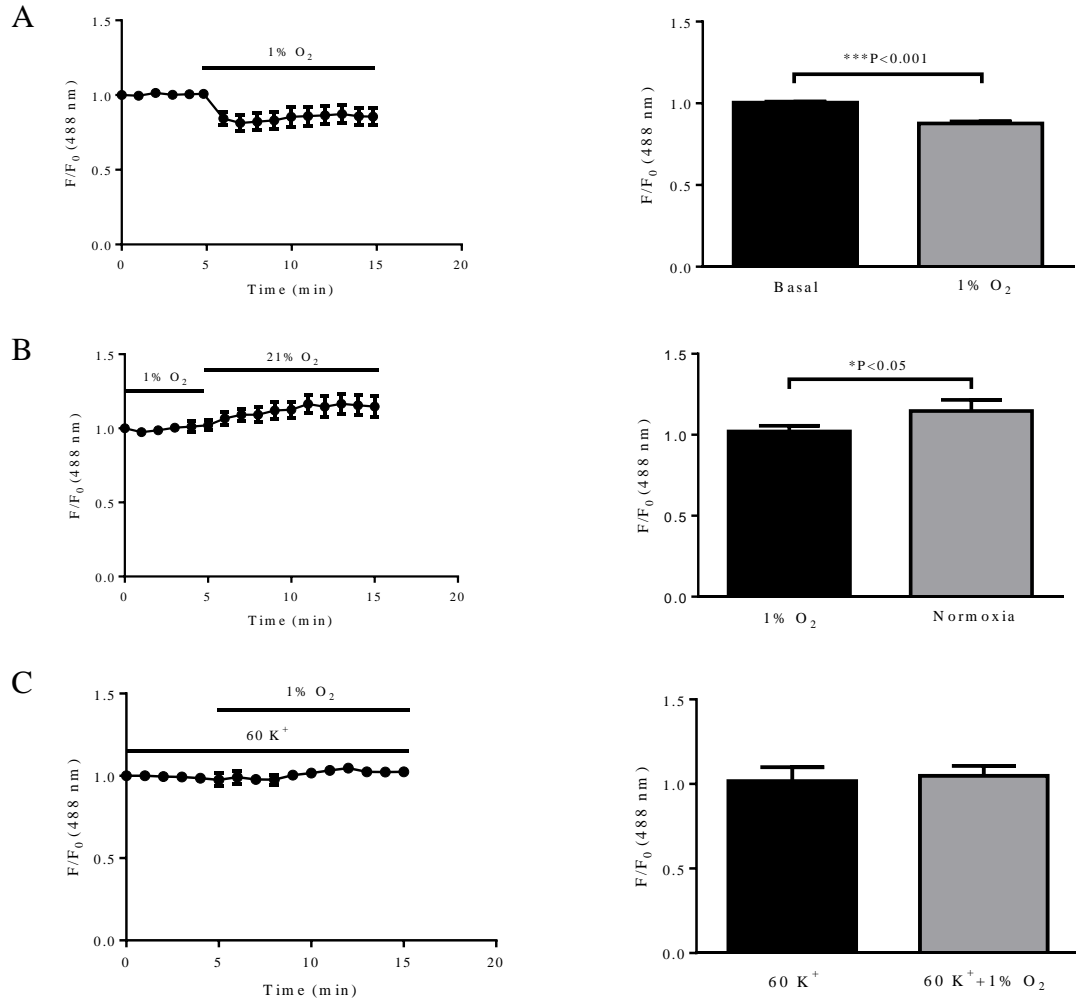


Figure 5.30: Effect of hypoxia on membrane potential. (A) Exposing the cells to hypoxia decreased fractional fluorescence of DiBAC4(3) (n=72). (B) Recovery of HCASMCs from hypoxia caused membrane potential depolarization (n=7). (C) The effect of hypoxia was inhibited by 60 K⁺ (n=11).

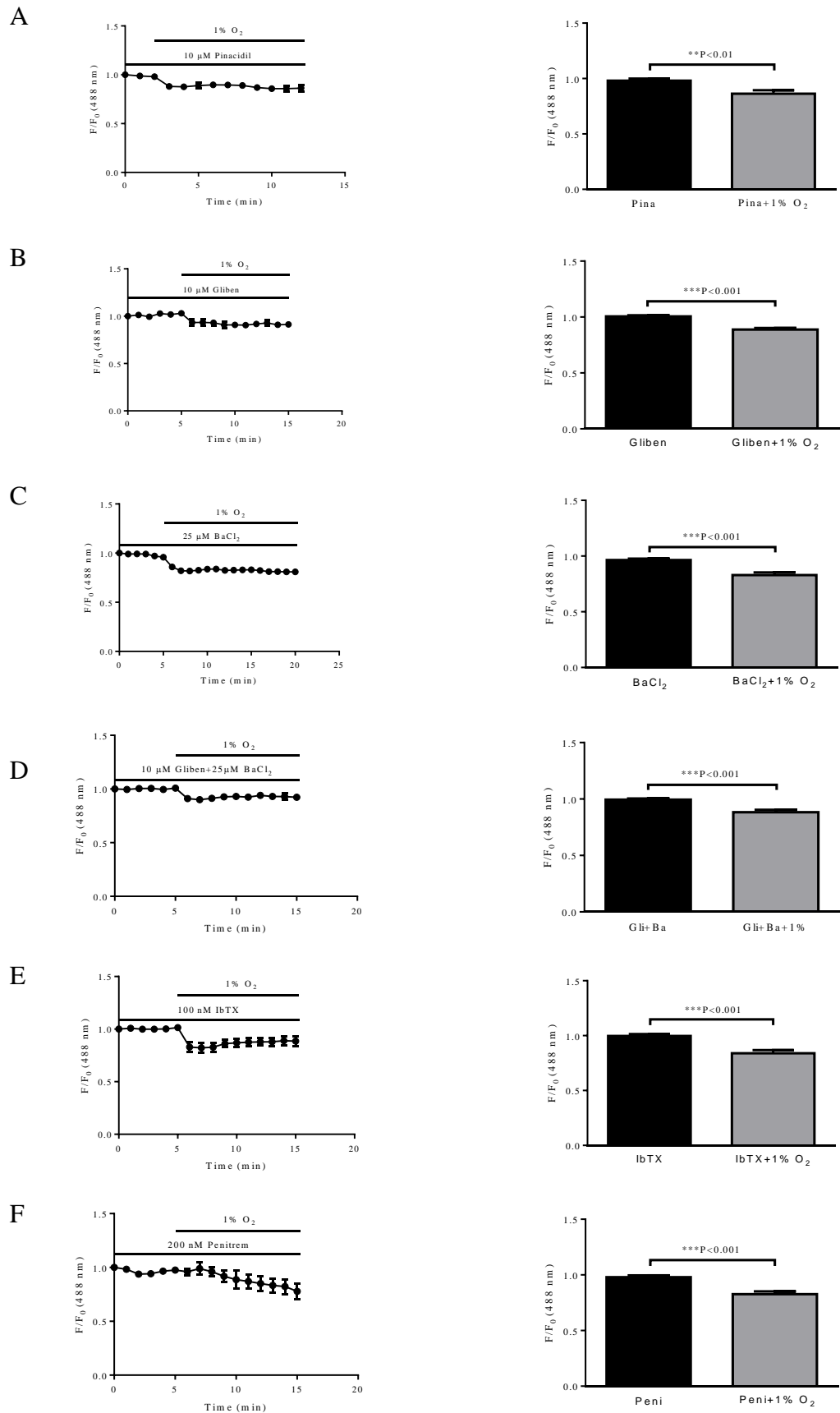


Figure 5.31: Role of K⁺ channels in hypoxia induced hyperpolarization. The effect of hypoxia on membrane potential in the presence of 10 μM pinacidil (A, n=5),

10 μM glibenclamide (B, n=36), 25 μM BaCl_2 (C, n=14), 10 μM glibenclamide plus 25 μM BaCl_2 (D, n=25), 100 nM IbTX (E, n=17), 200 nM penitrem A (F, n=14).

5.4 Discussion

Many studies suggested that hypoxia causes vasodilation by decreasing $[\text{Ca}^{2+}]_i$. Some investigations indicated that hypoxia has a direct effect on Ca^{2+} channels while others have shown that hypoxia causes membrane potential hyperpolarization and a closure of VDCCs [33, 34, 44, 45]. The observation that hypoxia inhibited Ca^{2+} oscillations in the presence of vasoconstrictors (**Figures 5.11, 5.12&5.13**) fits to the hypothesis that hypoxia causes coronary artery dilation by reducing $[\text{Ca}^{2+}]_i$. However, the application of nimodipine did not modify the Ca^{2+} oscillations, suggesting Ca^{2+} oscillations are largely independent of VDCCs (**Figure 5.16**). In the present study, however, the effect of nimodipine was not tested under hypoxic condition, and therefore we do not know whether nimodipine antagonizes inhibitory effect of hypoxia on Ca^{2+} oscillations. At this preliminary stage, we are far from providing cellular events underpinning the inhibition of Ca^{2+} oscillations by hypoxia, but it will be interesting to see whether hypoxia reduces SR Ca^{2+} content.

Even though results of Ca^{2+} measurements in the current work are very limited and Ca^{2+} handling of HCASMCs is far from clear, it seems useful to discuss Ca^{2+} homeostasis based on its central role in many type of cells. Ca^{2+} is a ubiquitous second messenger and the concentration difference between extracellular (in mM range) and intracellular spaces (in sub μM range) is the largest for Ca^{2+} . This allows Ca^{2+} to play spatially and temporally important roles in signal transduction cascade. As discussed above, the absolute value of $[\text{Ca}^{2+}]_i$ is important, but in some cases, activation of events may occur as a form of Ca^{2+} oscillations where the frequency, not just amplitude, may be an important form of signaling. This is an interesting form of carrying information as prolonged increase in $[\text{Ca}^{2+}]_i$ is generally harmful to the cells.

The phenomenon of Ca^{2+} oscillations was first observed in hepatocytes [263]. In HCASMCs, some cells were quiescent at rest while others exhibited spontaneous

Ca^{2+} oscillations. The selective $\alpha 1$ -adrenergic receptor agonist, PE, had no effect on most of the cells. This is likely to be due to loss of the receptors or a decrease in the sensitivity of the receptors. However, PDGF-BB, $\text{PGF}2\alpha$, U46619 and 80 mM K^+ all increased Ca^{2+} oscillations in the majority of HCASMCs. Combined with the results that hypoxia reliably inhibited Ca^{2+} oscillations, HCASMCs seem a good model to study Ca^{2+} handling and the effect of hypoxia in future.

Although not examined in the current study, the possibility that hypoxia may cause coronary artery relaxation independent of $[\text{Ca}^{2+}]_i$ should be also considered in the future. A basic model of receptor mediated increase in $[\text{Ca}^{2+}]_i$ and Ca^{2+} sensitization in HCASMCs is shown in **Figure 5.32**, both of them are possible controlling points for hypoxia. Hypoxia not only directly decreases $[\text{Ca}^{2+}]_i$, but also can cause Ca^{2+} desensitization in which way it induces vasodilation without a decrease in $[\text{Ca}^{2+}]_i$ [264, 265]. Furthermore, other studies provided the evidence that hypoxia directly modulates Ca^{2+} channels showing a reduction in O_2 rapidly inhibited I_{Ca} , and this effect was reversible [45, 266]. Further support for hypothesis that hypoxia directly modulates VDCC comes from the study where pretreating aortic rings with L-type VDCC blockers abolished hypoxia induced dilation [267]. In the current study, we also showed that hypoxia seem to decrease Ca^{2+} oscillations in the presence of high K^+ (60 mM), but the effect was not significant (**Figure 5.17**). However, this set of experiment consists of 3 cells, a number too small to be statistically reliable. Had a larger number of cells tested, it is conceivable that there was a statistically significant difference. If so, our result would have been consistent with the work of Smani et al. (2002), in which they demonstrated in isolated human and porcine myocytes, low O_2 tension decreased L-type Ca^{2+} current and reduced cytosolic $[\text{Ca}^{2+}]$ and this effect was independent of K^+ channel activation [77].

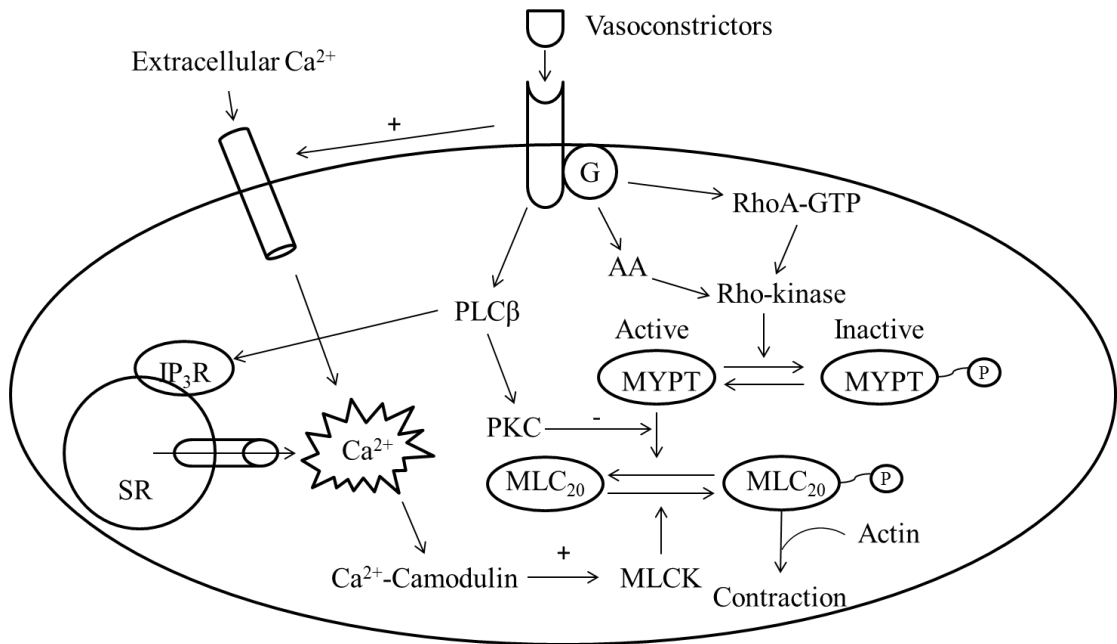


Figure 5.32 Mechanisms of VSMC contraction. AA, arachidonic acid; G, guanosine-5'-triphosphate-binding protein; IP₃R, inositol trisphosphate receptor; MLC₂₀, regulatory light chain of myosin (20 kDa); MLCK, myosin light chain kinase; MYPT, myosin phosphatase target subunit; SR, sarcoplasmic reticulum. (Modified from Akata, 2007 [92])

It is important to note that Ca²⁺ signaling in SMC is crucial not only for contraction but other functions including proliferation and bioenergetics. In this context, spatial compartmentalization of Ca²⁺ may play an important role. Apart from SR, nucleus and mitochondria are thought to be Ca²⁺ storage sites, and these organelles are often found to be close to each other. In Ca²⁺ oscillations of HCASMCs, we observed intracellular Ca²⁺ increase was always accompanied by an increase in nuclear Ca²⁺ (**Figure 5.1**). It has been suggested that the inner surface of nuclear envelop membrane of VSMCs contain IP₃ receptors [268, 269]. Changes in nuclear Ca²⁺ concentration may play a vital role in gene regulation, expression, and modulate transcription factors such as cAMP response element-binding protein (CREB) and nuclear factor of activated T-cells (NFAT) [270, 271]. However, there are very limited studies in this, and the mechanisms involved are controversial and still poorly understood.

Mitochondria have been suggested as a Ca^{2+} storage site in a wide range of cell types [272]. It is generally recognized that SERCA, sarcolemmal NCX and plasmalemmal Ca^{2+} ATPase are the main routes for cytosolic Ca^{2+} removal, and mitochondria Ca^{2+} uptake seems to account for a small proportion when compare with them [272]. It has been shown that mitochondrial Ca^{2+} plays an important role in many cell types including VSMCs, especially in local Ca^{2+} buffering and ATP synthesis [218, 273-275]. The latter may be particularly important in contracting SMCs where increase in mitochondrial Ca^{2+} affects enzymes involved in oxidative ATP production (i.e. PDH, G3PDH) [275]. Moreover, it has also been shown in rat aortic SMCs that there is a close relationship between mitochondria and SR, and application of FCCP completely abolished the large, transient mitochondrial Ca^{2+} increase induced by agonists [276].

K^+ channels are clearly involved in setting resting membrane potential in HCASMCs, as application of 10 μM glibenclamide and 25 μM BaCl_2 caused significant increase in DiBAC4(3) signal (**Figure 5.21**). 25 μM BaCl_2 also caused membrane potential depolarization in the presence of 10 μM glibenclamide. Therefore, we conclude both K_{ATP} and K_{ir} contribute to resting membrane potential of HCASMCs. Further characterization of K^+ channels using selective activators and inhibitors showed that HCASMCs functionally express K_{ATP} , BK_{Ca} , $\text{IK}_{\text{Ca}}/\text{SK}_{\text{Ca}}$ channels (**Figures 5.23, 5.24, 5.25&5.26**). In HCASMCs, changes in membrane potential caused by 10 μM NS1619 and 10 μM NS11021, activators of BK_{Ca} , were not inhibited by IbTX, and this could be due to the specific β subunit in human coronary BK_{Ca} channels. A total of four types of modulatory β subunits have been identified, and in HCASMCs the majority of BK_{Ca} channels contain $\beta 1$ subunit (KCNMB1) [258], which has higher sensitivity to Ca^{2+} and a lower sensitivity to IbTX [259].

Most puzzling results regarding hypoxia effects on membrane potential was that none of the traditional K^+ channel inhibitors eliminated the reduction in signal caused by hypoxia, although the effect of hypoxia was absent in high $[\text{K}^+]_o$ (**Figures 5.30 & 5.31**). Even if direct membrane potential measurement using current patch

clamp is preferable to DiBAC4(3) experiments, the fact that hypoxia reduced signal, and high $[K^+]_o$ prevented this effect strongly suggest hypoxia activates K^+ channels. The lack of effect of traditional K^+ channel inhibitors when applied singly may be explained by the hypothesis that more than one K^+ channels are involved, and so combination of antagonists are required to block hypoxia effect or K2P channels are important in hypoxic hyperpolarization studying of which is difficult due to a lack in specific channel inhibitors. These unresolved questions ultimately require current clamp experiments to be answered.

In conclusion, HCASMCs retaining functional Ca^{2+} handling mechanisms and K^+ channels that respond to hypoxia may be a useful model to examine further mechanisms by which $[Ca^{2+}]_i$ may be lowered when PO_2 is reduced. However, more work need to be done, ideally including patch clamp techniques.

Chapter 6
Effect of Hypoxia and K⁺ Channel
Modulators on HCASMCs
Proliferation and Migration

6.1 Introduction

HCASMCs obtained from Promocell originate from human coronary artery tunica media of RCA and LCA (LAD and LCX branches). Though cultured VSMCs are initially contractile phenotype, they undergo profound and reversible changes during cell culture as discussed earlier. This is because VSMCs maintain functional plasticity [277] and become synthetic phenotype triggered by local environmental stimuli [23, 278]. For example, physiological hypoxia induces erythropoiesis and angiogenesis, events useful in adaptive response for athletes [279-282]. More importantly in relation to this thesis, hypoxia results in contractile SMC dedifferentiation, migration and proliferation by re-entering cell cycle. This can be a pathological hypoxic response, causing atherosclerosis or vascular injury that may lead to cardiovascular malfunction and life-threatening outcomes [23, 24, 283].

Cell replication is a process highly energy dependent [284]. Hypoxia could regulate VSMC growth directly and indirectly via VSMC mitogens produced by ECs [285, 286]. Moreover, K^+ and Ca^{2+} channels, typically known for regulation of vascular tone [1, 92, 112, 287], are upregulated/downregulated during phenotype switching in VSMC including HCASMCs [288-291]. Evidence suggests K^+ channel activity is required in the initiation of G1 progression [291-293]. An increase in $[Ca^{2+}]_i$ was reported to be required in G0/G1 transition by regulating transcription of some early genes [294-298]. Although many hypotheses have been suggested, the mechanisms underlying hypoxic phenotype changes in VSMCs still remain obscure.

Because of the cell plasticity, it is necessary and important to characterize HCASMCs over passages to evaluate phenotype change that may occur during culture as this may have an unexpected influence on the results. Promocell suggests a maximum of 15 population doublings with monitoring of cell phenotype. We characterized HCASMCs at different passage points using WB and ICC with antibodies against three SMC specific markers: smooth muscle α -actin (α -SMC), an early-stage marker; calponin, a mid-stage marker; and smooth muscle myosin heavy chain (MHC), a late-stage marker [299, 300]. Multi-well plate based assays have been performed to evaluate cell proliferation and migration. Cell proliferation was

examined using MTT assay while cell migration was assessed using scratch wound assay and transwell assay. FACS analysis offers detailed information about the changes in cell cycle [301]. Pharmacological tools were used to address the potential roles of ion channels in phenotype change.

6.2 Aims

The time dependent changes in specific SMC markers in primary cultured HCASMCs were characterized in this chapter. The effect of hypoxia on HCASMC proliferation and migration and the possible roles of K⁺ channels were investigated.

6.3 Results

6.3.1 Cell growth and morphology

First, basic features of HCASMCs were characterized at different points of cell culture including cell growth rate and morphology. Bright field images of the cells were captured using a DC5000 CMEX microscope camera (Euromex) at x10 magnification. **Figure 6.1A** shows HCASMCs at P7, 10, 13 and 16 showing a stellate or spindle shape. In order to characterize the cell growth rate, the time taken for each passage to reach confluence was plotted (**Figure 6.1B**). The cell morphology measurement was carried out at confluence of ~50-60%. Albeit the size (minor axis, major axis and area) of HCASMCs increased during culture (**Figure 6.2**), there was no statistical difference in cell Circ, AR, Round and Solidity (see **Section 4.3.6** for details) (**Figure 6.3**). Analysis of these parameters indicates HCASMCs maintain an elongated spindle shaped morphology, typical for a differentiated phenotype, during the period passage used in this thesis.

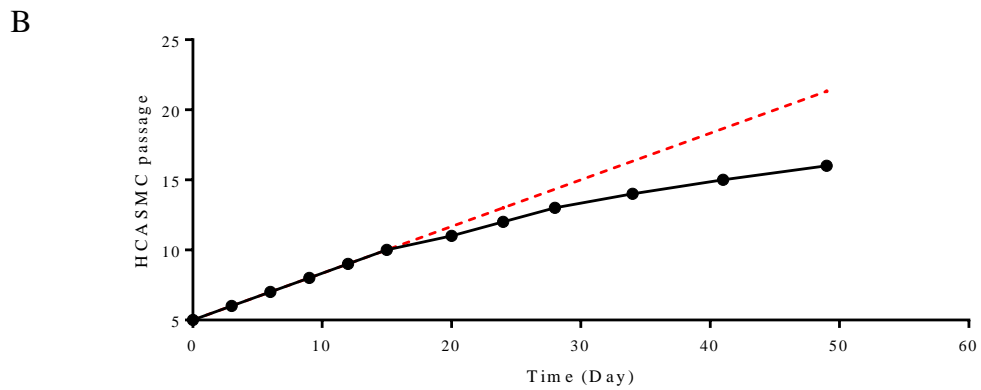
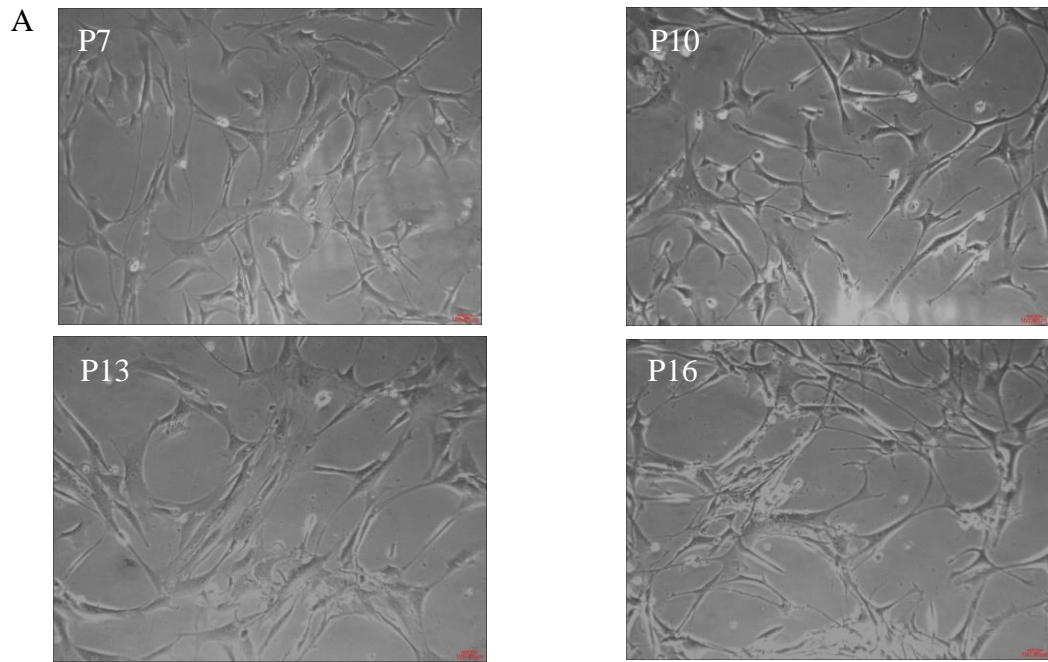


Figure 6.1: Morphology of HCASMCs. (A) Pictures of cultured HCASMCs between P7 and P16. (B) As cell passage number increased, the time for cells to reach confluence increased. Linear regression (red dotted line) of early passages (P7-P12) divergent from old passages (\geq P13).

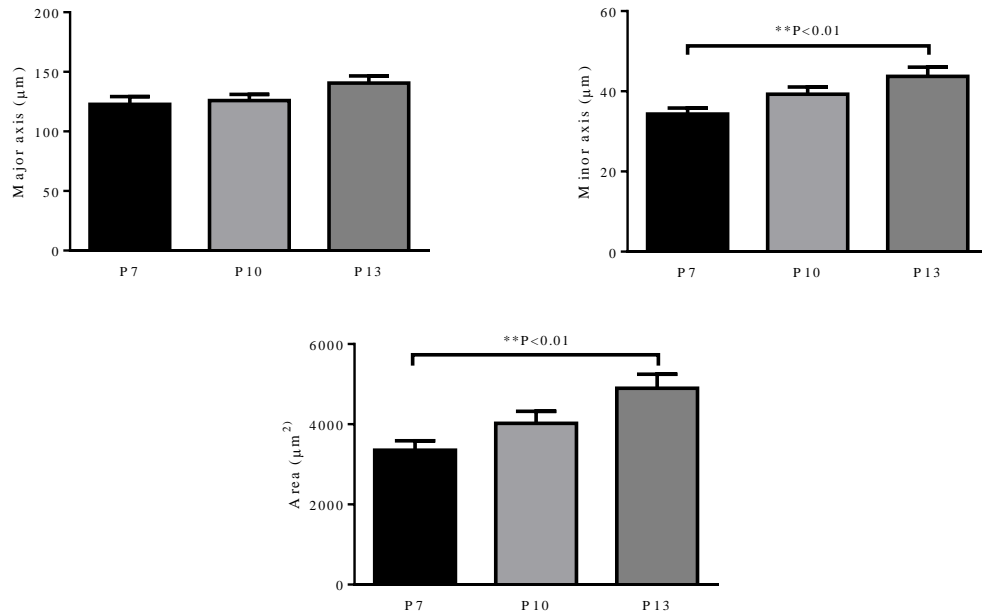


Figure 6.2: Comparison of cell size between different passages. The size of major axis, minor axis and area (calculated from major and minor axis) increased as the cell passage number increased during culture.

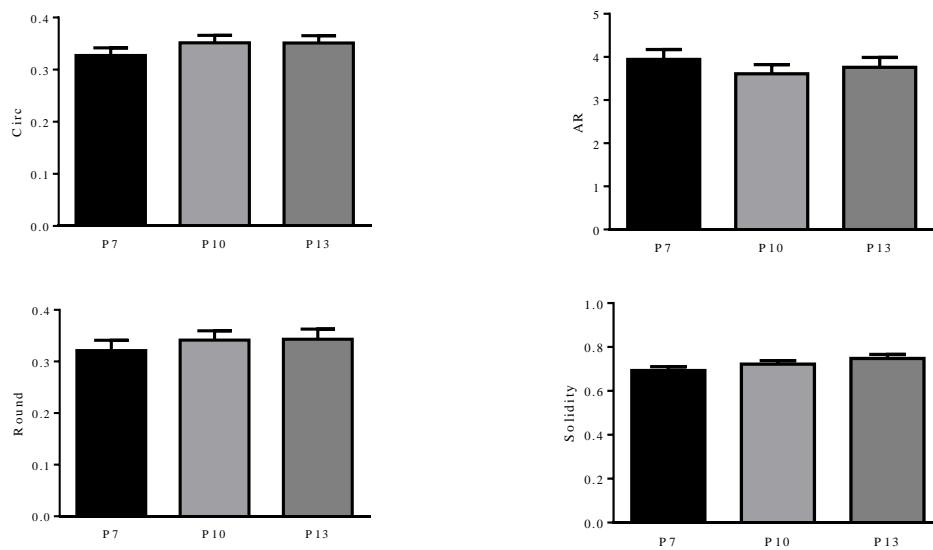


Figure 6.3: Comparison of cell morphology between different passages. Analysis of shape descriptors (Circ, AR, Round and Solidity) indicates there is no significant difference between different passages of cultured HCASMCs.

6.3.2 Coomassie blue staining

WB is an important procedure to detect specific proteins using antibodies [302]. In coomassie staining, the dye binds to all proteins, and its non-specific binding makes it a convenient and widely used overview of general protein expression. Coomassie staining can be used as loading control in WB analysis [303]. Therefore this procedure was used to compare the general distribution of proteins in HCASMC lysates across cell passages. Protein lysates from P7-P13 showed comparable distribution (**Figure 6.4**).

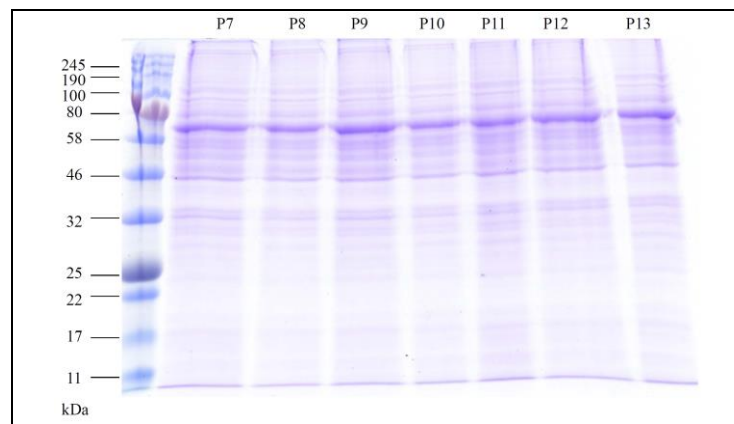


Figure 6.4: Coomassie blue staining of electrophoretically separated protein sample from P7-P13.

6.3.3 WB and ICC

In order to further characterize specific SMC proteins, Western blotting was applied [302]. α -SMA with a molecular weight of 42 kDa was identified as a single band in lysates from P7 to P13 (**Figure 6.5A**). Calponin, which has a molecular weight of 34 kDa, was also identified throughout the passages (**Figure 6.5B**). When compared to α -SMA, calponin was less specific, indicated by a larger size band in both SMC and EC lysates (**Figure 6.5B**). Re-blotting of actin showed a single band at 42 kDa (**Figure 6.5C**). In ICC, HCASMCs were labelled with anti- α -SMA, anti-calponin and anti-MHC antibodies, and visualized by AF488-conjugated secondary antibodies (**Figure 6.6**). EC markers CD31 and vWF were used as negative controls in ICC, and these EC markers were absent from HCASMCs (data

not shown). Taken together, WB and ICC results show that there is little change in the expression pattern of signature SMC proteins with few, if any, contaminating ECs. Although this still does not guarantee there are no functional changes during cell culture, it seems that later passage HCASMCs used in this thesis still retain at least some property of early passage cells.

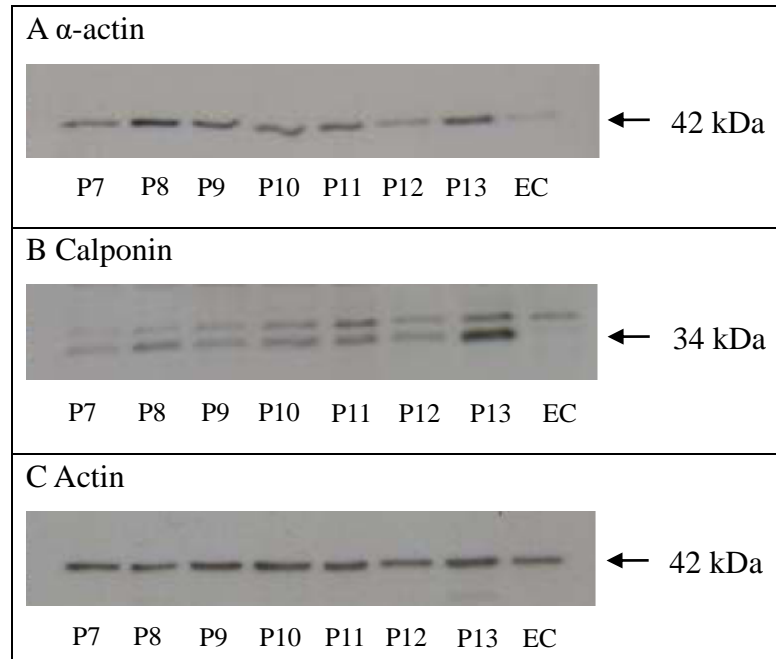


Figure 6.5: WB of α -SMA and calponin in HCASMCs. (A) α -SMA in HCASMC lysate from P7-P13, single band at 42 kDa, 20 minutes exposure. (B) Calponin in HCASMC lysate from P7-P13, with a primary band at 34 kDa, 20 minutes exposure. (C) Actin (re-blotting) in HCASMC lysate from P7-P13, single band at 42 kDa, 15 minutes exposure. All primary and secondary antibodies were diluted in TBST containing 5% non-fat powdered milk (**Section 2.1.2**). EC lysate was used as negative control.

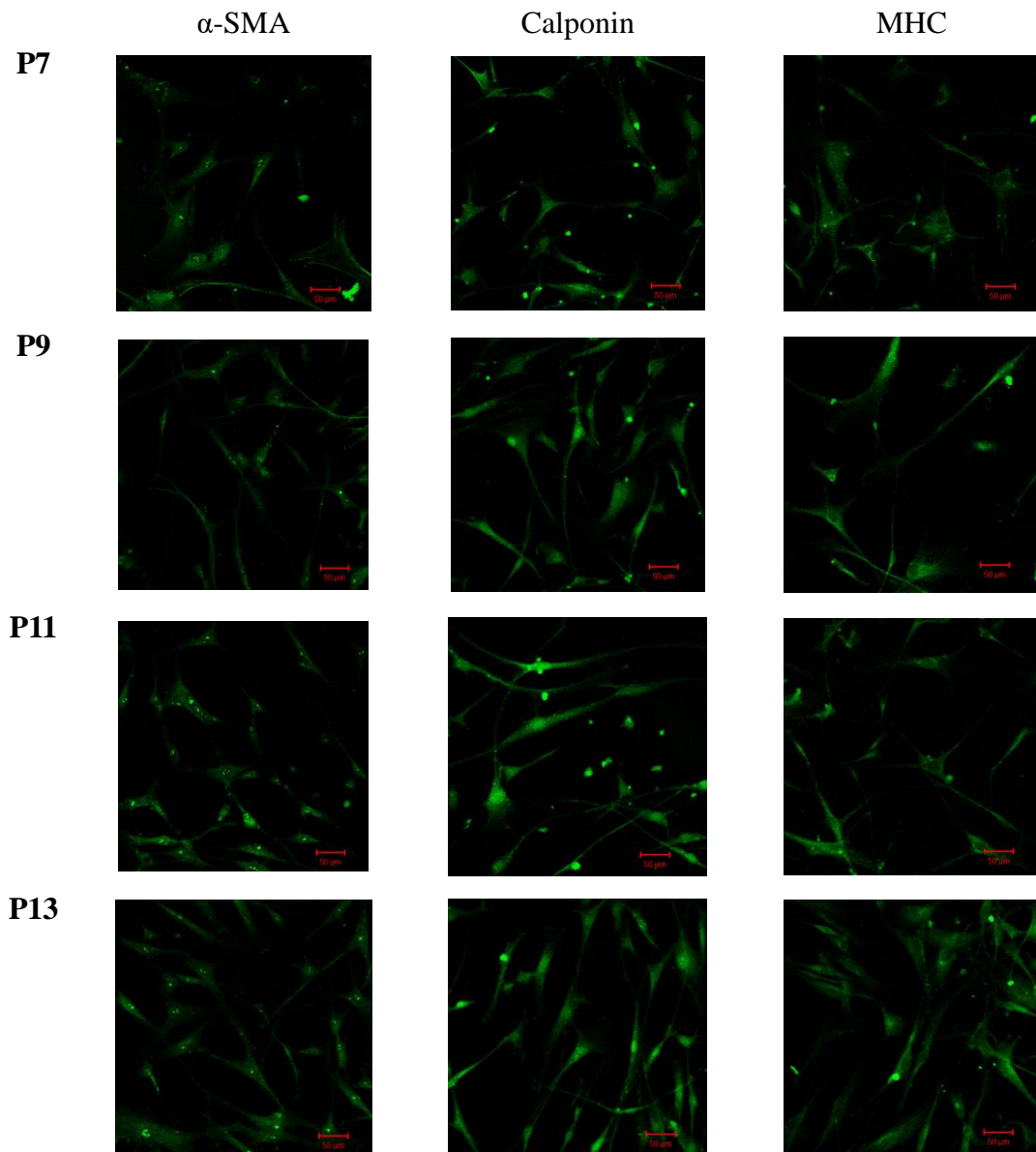


Figure 6.6: ICC of α -SMA, calponin and MHC expression. Confocal images of HCASMCs labelled with primary antibodies (anti- α -SMA, anti-calponin and anti-MHC) and AF488-conjugated secondary antibodies. Scale bar is 50 μ m.

6.3.4 Effect of hypoxia on cell number determined by cell counting

In order to assess the effect of hypoxia on cell growth, changes in cell number were first examined. HCASMCs were plated into 6-well or 24-well plate and incubated overnight. On the following day, cells were serum ‘starved’ with smooth muscle cell growth medium 2 containing 0.1% supplement (this low serum medium is indicated as SF medium in this chapter). Starved cells were then cultured using fully supplemented media under desired conditions. At the end of the experiment,

cells were lifted with trypsin and counted with Z1 Coulter particle counter. Serum deprivation halted the growth of HCASMCs, indicated by a smaller cell number in SF group (**Figure 6.7**). Inhibiting OXPHOS of HCASMCs with 6 μM oligomycin significantly reduced cell number after 6 hours, and the effect increased in a time dependent manner (**Figure 6.8**). Exposure to hypoxia (1% O_2) for 24 hours caused little change in cell number in medium containing supplement (FS medium) (**Figure 6.9A**). Treatment with high glucose (25 mM) for 48 hours in SF medium caused an increase in cell number (**Figure 6.9B**). Exposure to hypoxia for 48 hours in SF medium seemed to cause an increase in cell number, but the change is not significant. These preliminary results showed that adding high glucose to SF medium will increase cell number and inhibiting oxidative pathway in FS medium will decrease cell number. Exposure to hypoxia for a short term had no effect on cell number in both FS and SF medium, but hypoxia may require longer exposure time to be effective, and this will be addressed later in this chapter.

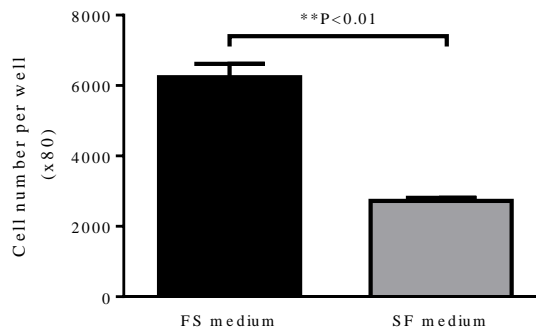


Figure 6.7: Effect of serum deprivation on cell number after 48 hours. 1.25×10^5 HCASMCs (initial count) were seeded into each well of 6-well plate (n=3). Number (x80) in the outline of Y axis indicates the diluting factor of cell suspension for counting purpose.

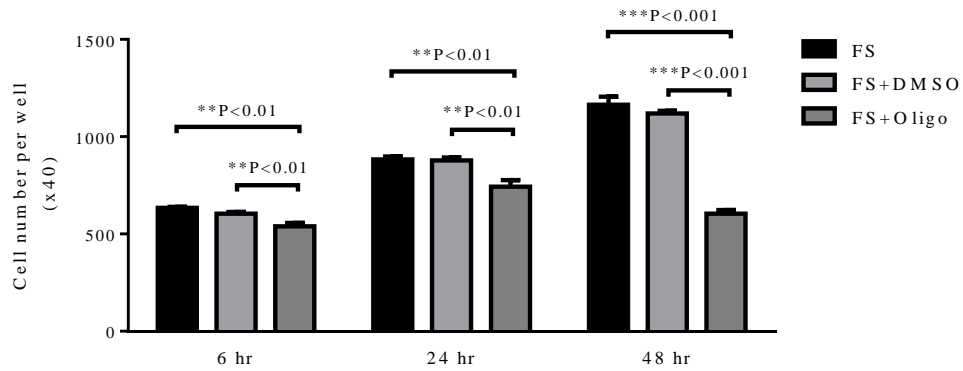


Figure 6.8: Effect of 6 μ M oligomycin on cell number. HCASMCs were seeded into 24-well plate at the density of 3×10^4 (initial count) (n=4).

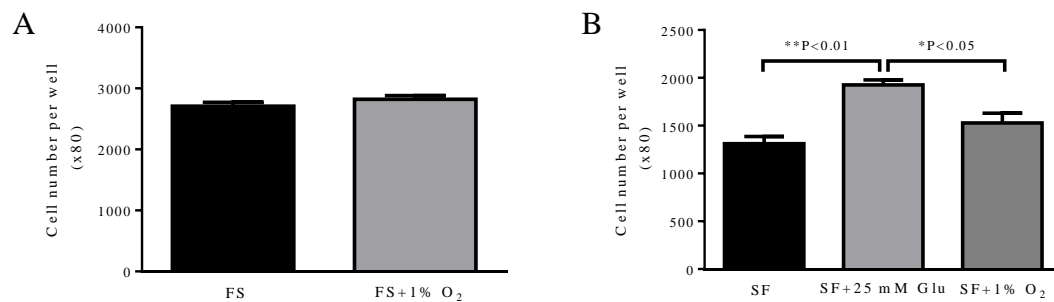


Figure 6.9: Effect of hypoxia and high glucose on cell number. (A) Cells were seeded into 6-well plate at a density of 1.0×10^5 cells per well (n=6). (B) Cells were seeded into 6-well plate at a density of 1.25×10^5 cells per well (n=3).

6.3.5 Assessing HCASMC proliferation with MTT assay

6.3.5.1 Overview

MTT assay, a colorimetric quantitative assay, is widely used to measure cytotoxicity [304] and proliferation of cells [305-307]. Its main advantages are rapidity, precision, convenience and safety [308]. The principle behind this method is that yellow MTT is reduced by active mitochondria dehydrogenases (i.e. living cells) by cleaving the tetrazolium ring, producing a purple product called formazan [307]. The formation of the colored product is proportional to mitochondrial activity, and therefore makes it ideal for measuring metabolically active cells. The reaction of MTT is shown in **Figure 6.10**. The plot showing background corrected absorbance (570 nm) as a function of the number of the cells yields a linear relationship, but the

signal saturates when there are too many cells (**Figure 6.11A**). Digitonin (200 $\mu\text{g/ml}$) and 35% ethanol (EtOH), both killing the cells, were used as negative controls (**Figure 6.11B**). Deprivation of serum slowed HCASMC growth significantly, indicated by a reduction in MTT absorbance at 570 nm to $85.26 \pm 3.57\%$ after 48 hours (**Figure 6.11C**, $n=6$).

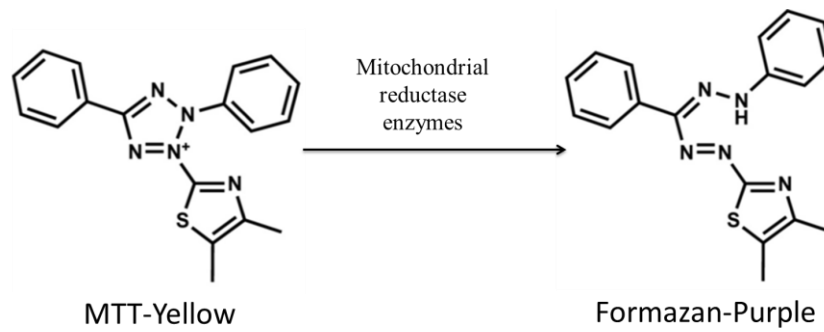


Figure 6.10: Colormetric change of MTT in reaction. Yellow MTT is reduced by mitochondria to produce a purple product, formazan.

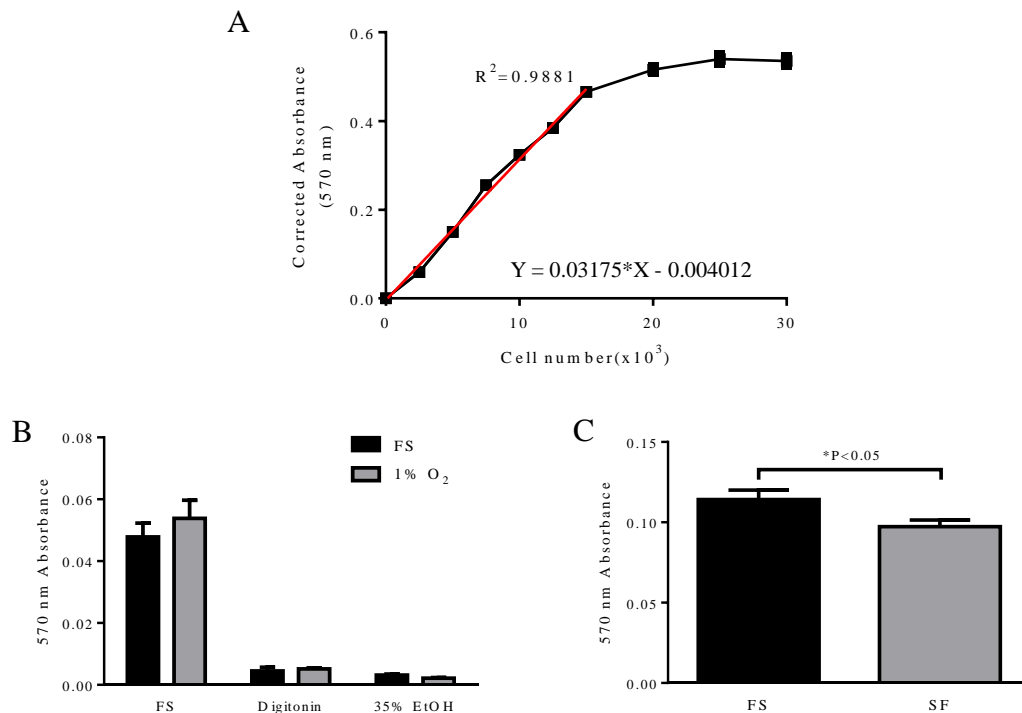


Figure 6.11: Cell number and 570 nm absorbance of MTT assay. (A) Background corrected absorbance at 570 nm against cell number ($n=6$). (B) Negative control for MTT assay in normoxia and hypoxia ($n=6$). (C) Deprivation of serum slowed cell growth ($n=6$). The absorbance at 570 nm was corrected for background.

6.3.5.2 Effect of PDGF-BB and high glucose on HCASMC proliferation

In FS medium, application of 20 ng/ml PDGF-BB seemed to increase MTT signal, but the effect was not significant ($100.36 \pm 3.22\%$ after 24 hours and $106.94 \pm 5.25\%$ after 48 hours) (**Figure 6.12A**). In SF medium, the change in MTT signal was statistically significant after the application of PDGF-BB ($119.80 \pm 6.65\%$ after 24 hours and $118.77 \pm 6.42\%$ after 48 hours) (**Figure 6.12B**). Compared to basal medium containing 5.55 mM glucose, high glucose (25 mM) induced significant changes in MTT signal in cell culture medium with and without supplement ($122.89 \pm 6.24\%$ in FS medium, $127.97 \pm 6.74\%$ in SF medium) (**Figure 6.13**).

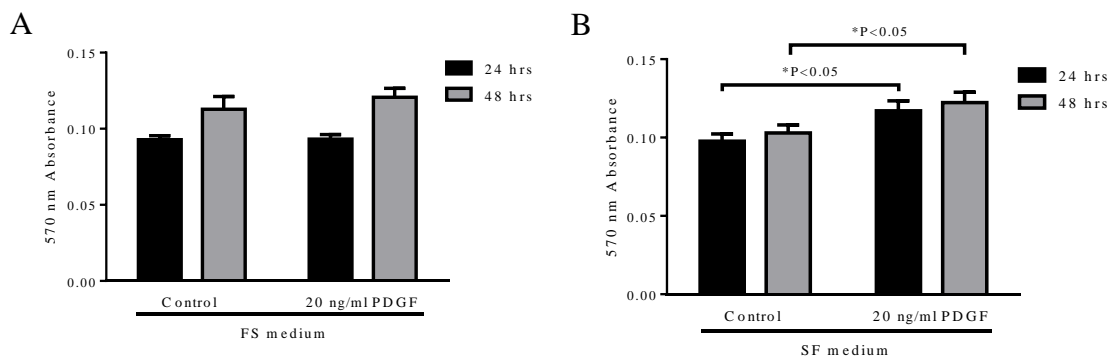


Figure 6.12: Effect of PDGF-BB on HCASMC proliferation. (A) Effect of PDGF-BB on HCASMC proliferation in FS medium (n=6). (B) Effect of PDGF-BB on HCASMC proliferation in SF medium (n=6).

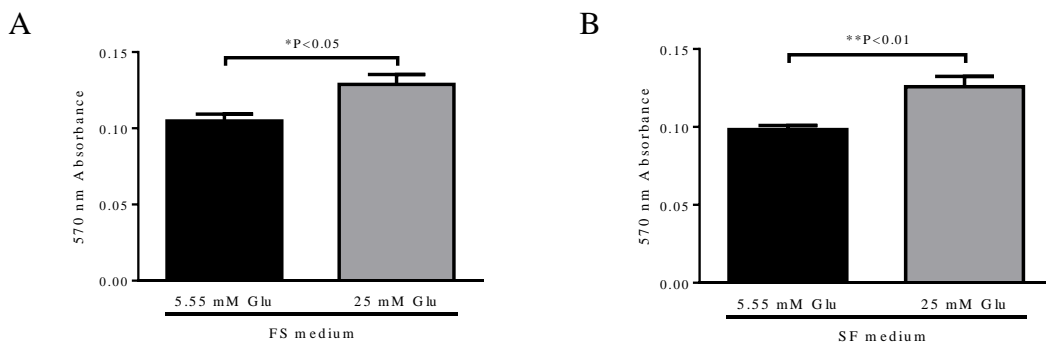


Figure 6.13: Effect of high glucose on HCASMC proliferation. (A) Effect of high glucose on cell proliferation in FS medium (n=6). (B) Effect of high glucose on cell proliferation in SF medium (n=6). Cells in this experiment were treated with high glucose for 48 hours without prior serum starving.

6.3.5.3 Effect of hypoxia on HCASMC proliferation

Next, experiments were carried out to examine whether hypoxia causes a change in HCASMC growth. We measured MTT signal from cells exposed to different concentrations of O₂ (normoxia, 5% and 1%). MTT absorbance signals were $114.79 \pm 3.96\%$ in 5% O₂ and $93.54 \pm 5.28\%$ in 1% O₂ after 2 days; to $150.41 \pm 1.29\%$ in 5% O₂ ($p < 0.01$) and $119.77 \pm 8.07\%$ in 1% O₂ after 4 days; $165.35 \pm 5.36\%$ in 5% O₂ ($p < 0.001$) and $123.84 \pm 2.18\%$ in 1% O₂ ($p < 0.01$) after 6 days in cell culture medium (**Figure 6.14**). These results suggest that exposure HCASMCs to both mild (5% O₂) and severe hypoxia (1% O₂) caused HCASMC proliferation. The cell number between 5% O₂ group and 1% O₂ group is highly significant after 6 days, this may be due to the fact that cell proliferation is energy dependent and the cells experience more severe energy crisis under 1% O₂ than in 5% O₂, thus severe hypoxia partially reversing the enhancing effect of mild hypoxia on cell proliferation.

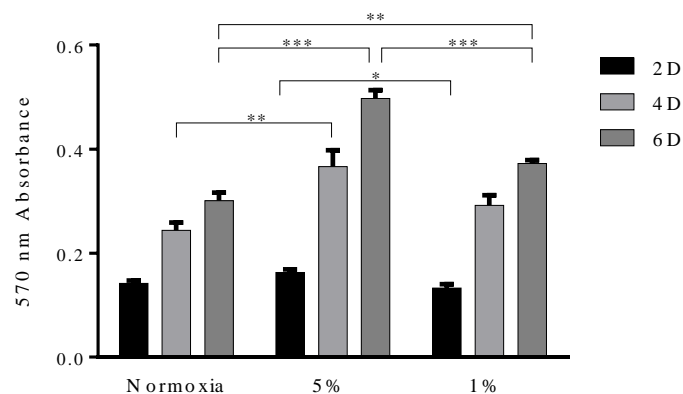


Figure 6.14: Effect of hypoxia on HCASMC proliferation. Exposure to hypoxia, both 5% and 1% O₂ induced HCASMC proliferation in FS medium (n=6). D: day.

6.3.5.4 Effect of K⁺ channel modulators on cell proliferation

In order to investigate whether K⁺ channels play a role in HCASMC proliferation, a wide range of K⁺ channel modulators were applied. K_{ATP} channel activator 10 μM pinacidil had no effect on MTT absorbance ($102.12 \pm 2.02\%$ after 24 hours and $99.63 \pm 2.52\%$ after 48 hours). Inhibition of K_{ATP} channels by 10 μM glibenclamide changed MTT absorbance to $91.01 \pm 1.97\%$ ($p < 0.05$) after 48 hours

(**Figure 6.15A**). In SF medium, application of 10 μM glibenclamide for 48 hours had little effect on cell proliferation, and this may not be surprising since cells are not growing (**Figure 6.15B**). In SF medium, BK_{Ca} channel opener (10 μM NS1619) and antagonist (100 nM IbTX) had little effect on MTT signals (**Figure 6.16A and B**). BK_{Ca} channel inhibitors, 100 nM IbTX and 200 nM penitrem A had no effects on MTT signals in FS medium (**Figure 6.16C and D**). In FS medium, $\text{IK}_{\text{Ca}}/\text{SK}_{\text{Ca}}$ activator and inhibitors had no effect on cell proliferation (**Figure 6.17A and B**). Inhibiting K_{ir} channel (25 μM BaCl_2) for 48 hours caused little change in both FS and SF medium (**Figure 6.18**). Application of K_{v} channel inhibitor XE991 (10 μM) had no effect on MTT absorbance (**Figure 6.19**). These results are preliminary but suggest that K_{ATP} channels that are open at rest may regulate cell proliferation.

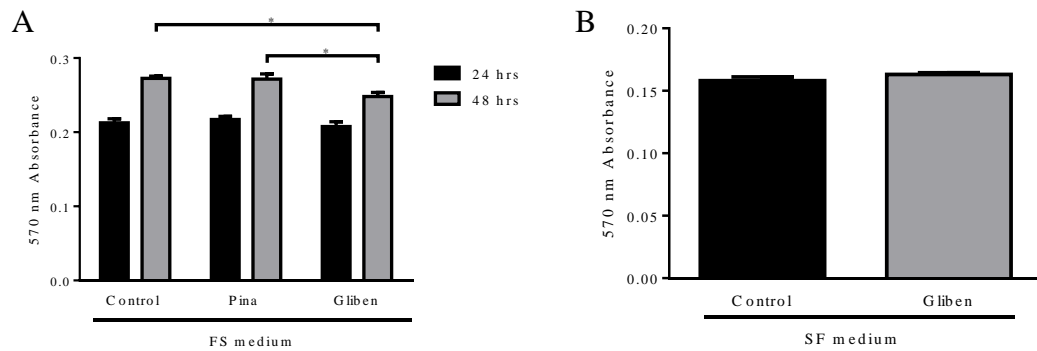


Figure 6.15: Effect of K_{ATP} channel modulators on HCASMC proliferation. (A) Effect of pinacidil and glibenclamide on HCASMC proliferation (n=6). Only the significance against the control was shown in the graph. (B) Effect of glibenclamide on HCASMC proliferation after 48 hours in SF medium (n=6).

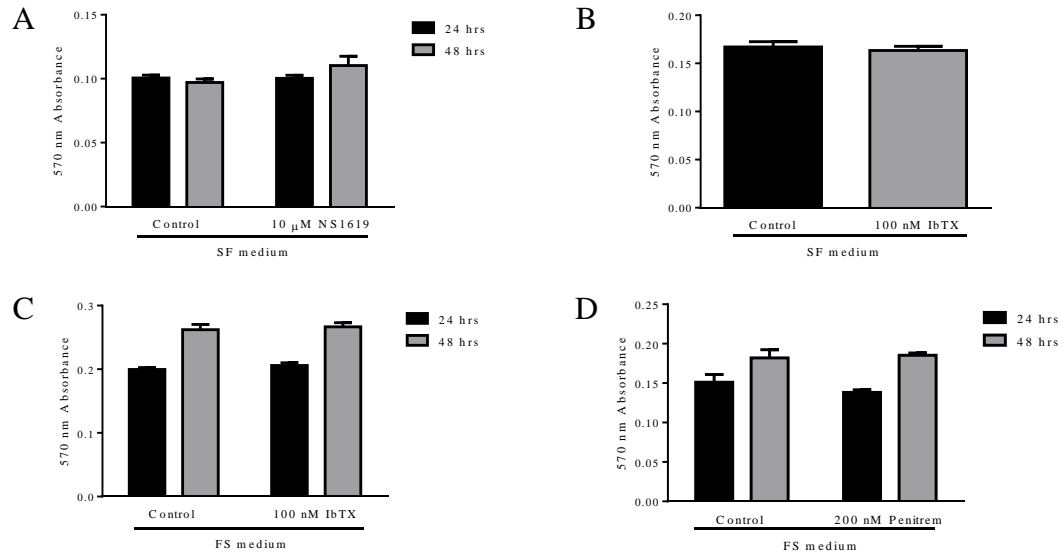


Figure 6.16: Effect of BK_{Ca} channel modulators on HCASMC proliferation. (A) Effect of NS1619 on cell proliferation in SF medium (n=4). (B) Effect of IbTX on cell proliferation in SF medium (n=6). (C) Effect of IbTX on cell proliferation in FS medium (n=6). (D) Effect of penitrem A on cell proliferation in FS medium (n=4).

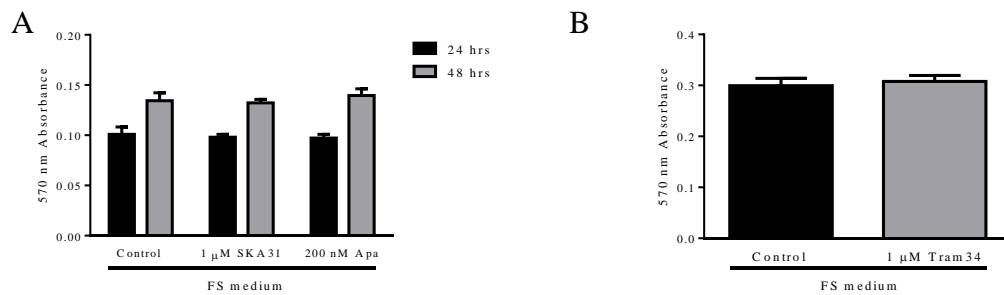


Figure 6.17: Effect of IK_{Ca}/SK_{Ca} channel modulators on HCASMC proliferation. (A) Effect of SKA31 and apamin on HCASMC proliferation (n=6). (B) Effect of Tram34 on HCASMC proliferation after 48 hours (n=4).

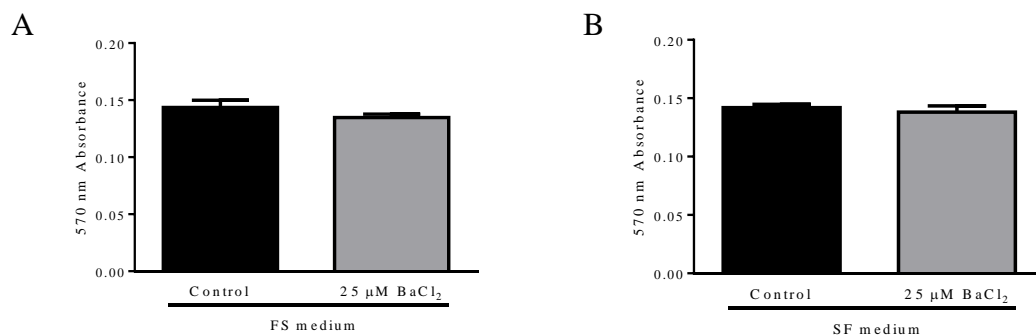


Figure 6.18: Effect of K_{ir} channel inhibitors on HCASMC proliferation. (A) Effect of BaCl₂ on HCASMC proliferation after 48 hours (n=6). (B) Effect of BaCl₂ on HCASMC proliferation in SF medium after 48 hours (n=6).

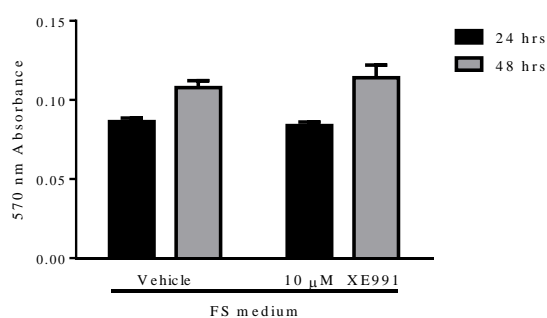


Figure 6.19: Effect of K_v channel inhibitor on HCASMC proliferation. XE991 had little effect on HCASMC proliferation for a period of 24 hours and 48 hours (n=4).

6.3.5.5 Effect of ion channel inhibitors on hypoxia induced HCASMC proliferation

Hypoxia caused HCASMCs proliferation, and ion channels maybe involved in this process. In this part, we further examined whether hypoxic proliferation is through, at least in part, an increase in K⁺ channel activity by using K⁺ channel inhibitors. In **Figure 6.14** we have shown that the effect of 1% O₂ on HCASMCs proliferation is time dependent. To see a maximal effect of K⁺ channel inhibitors, we chose to look at the effect 6 days after application of inhibitors. Hypoxia (1% O₂) induced increase in MTT absorbance was significantly reduced by 10 μM glibenclamide (p<0.001) and 10 μM XE991 (p<0.05). 100 nM IbTX, 1 μM tram 34,

200 nM apamin, 25 μM BaCl_2 and 10 μM nimodipine had little effect on cell proliferation (**Figure 6.20**). These results indicate that K_{ATP} and $\text{K}_{\text{V}7}$ channels maybe involved in hypoxia induced HCASMC proliferation.

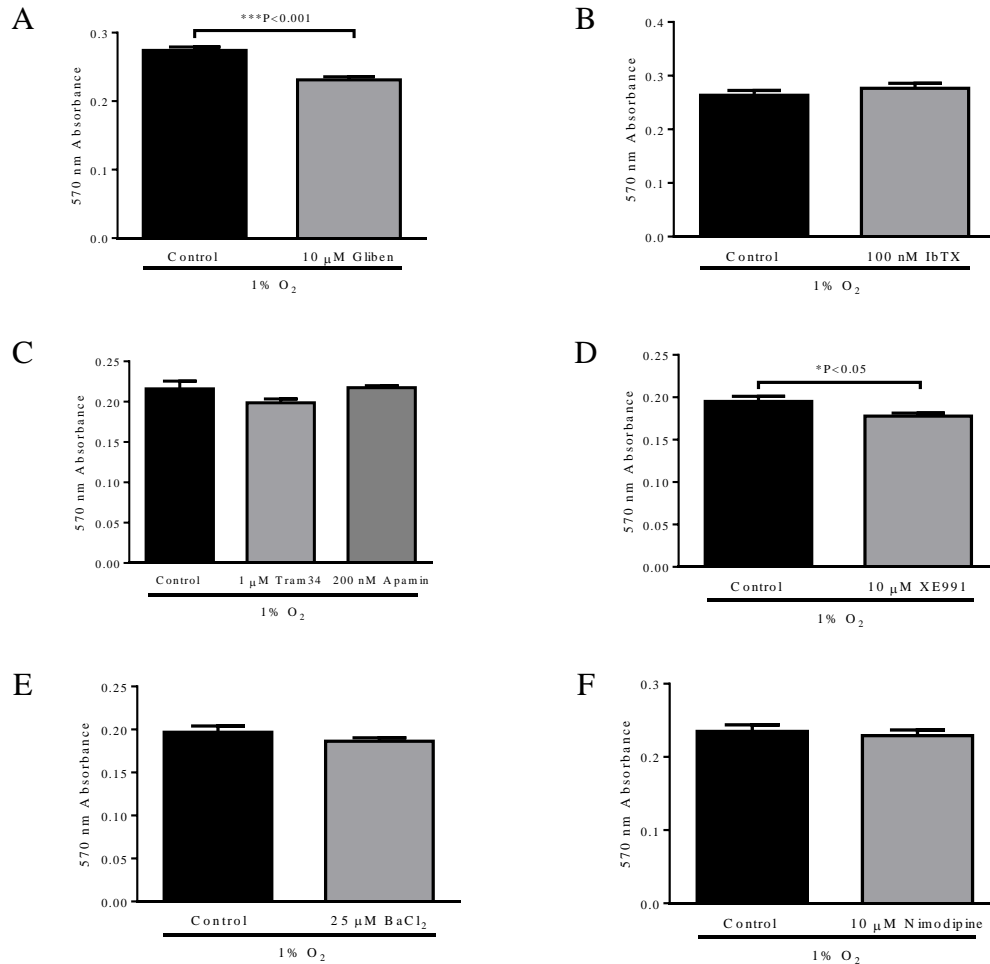


Figure 6.20: Effect of ion channel inhibitors on hypoxia induced HCASMC proliferation. The effect of glibenclamide (A, n=6), IbTX (B, n=6), tram34 and apamin (C, n=6), XE991 (D, n=6), BaCl_2 (E, n=6), nimodipine (F, n=6) on hypoxia induced HCASMC proliferation after 6 days.

6.3.6 Effect of hypoxia on HCASMC migration

We next studied the effect of hypoxia on cell migration by scratch wound assay and transwell migration assay. In scratch wound assay, the effect of 20 ng/ml PDGF-BB on HCASMC migration was assessed every 2 hours. Application of 20 ng/ml PDGF-BB seemed to cause cell migration, but the changes were not

significant within 10 hours. The changes may become greater if the time course was increased, but the limitation of this method did not allow us to examine the migration for a longer time because the wounds were closed after 12 hours (**Figure 6.21**). The difference in migration rate between groups with different O₂ levels was significant after 12 hours (normoxia vs 5% O₂ vs 1% O₂, 29.32 ± 1.34% vs 39.83 ± 1.94% vs 40.91 ± 3.52%, P<0.05) and 24 hours (normoxia vs 5% O₂ vs 1% O₂, 71.46 ± 4.44% vs 87.18 ± 2.24% vs 87.48 ± 3.09%, P<0.05) (**Figure 6.22**). These results indicate that hypoxia, both mild and severe, causes HCASMC migration.

In the transwell migration assay, cell seeding number was optimized first and a density of 2x10⁴ cells/well was chosen (data not shown). Hypoxia caused an increase in the number of migrated HCASMCs after 8 hours (normoxia vs 8% O₂ vs 1% O₂, 19.33 ± 0.88 vs 23.44 ± 1.70 vs 27.11 ± 1.16, P<0.01) (**Figure 6.23**). These observations further support the results from scratch wound assay by showing HCASMC migration increased under mild (8% O₂) and severe (1% O₂) hypoxia.

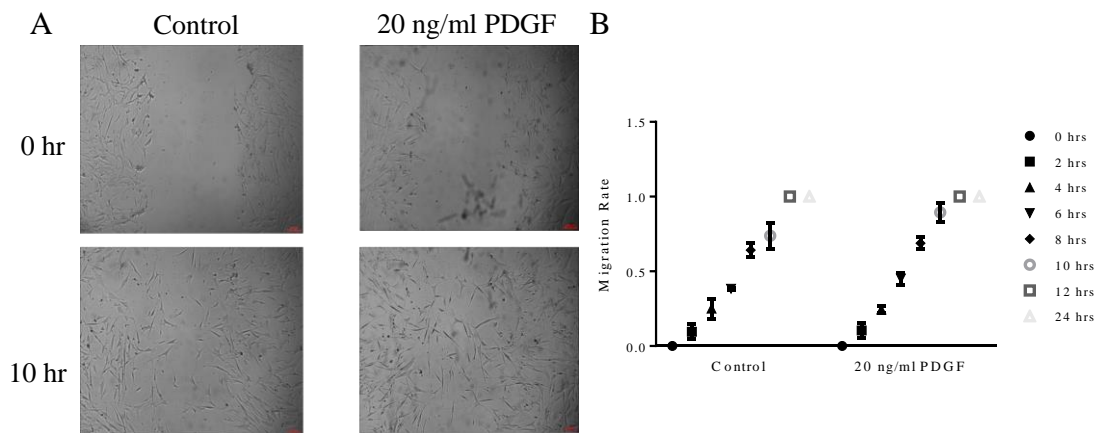


Figure 6.21: The effect of PDGF-BB on HCASMC migration. (A) Images of control and experimental groups before and after 10 hours of migration. (B) The migration rate of HCASMCs was assessed every 2 hours during cell migration (n=4).

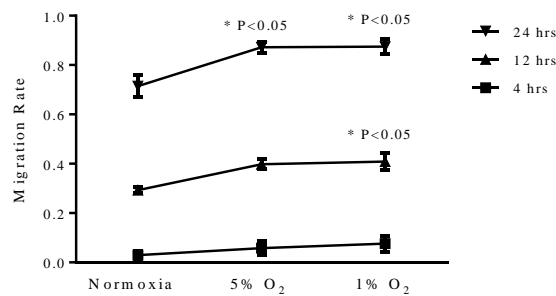


Figure 6.22: The effect of hypoxia on HCASMC migration. Migration rate of HCASMCs was assessed after 4 hours, 12 hours and 24 hours exposure to hypoxia (n=3). * indicates the significance against control (normoxia).

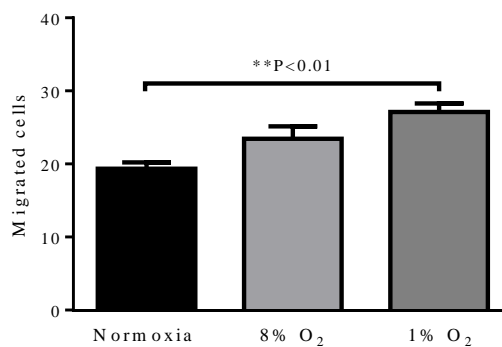


Figure 6.23: Hypoxia induces HCASMC migration in transwell assay. Mean ± SEM for the average of migrated cells over 8 hours exposure to different O₂ levels (n=9).

6.3.7 Effect of metabolic inhibitors and hypoxia on HCASM cell cycle

Cell proliferation is a process that produces two identical daughter cells from a mother cell, which generally comprises cell growth and cell division, and the latter requires a series of successful events during cell cycle. **Figure 6.24** gives an example of HCASMCs at different stages. Nowadays, revolutionary techniques employing flow cytometry and related software allow us to quantify and evaluate cell cycle processes and cell growth [301, 309].

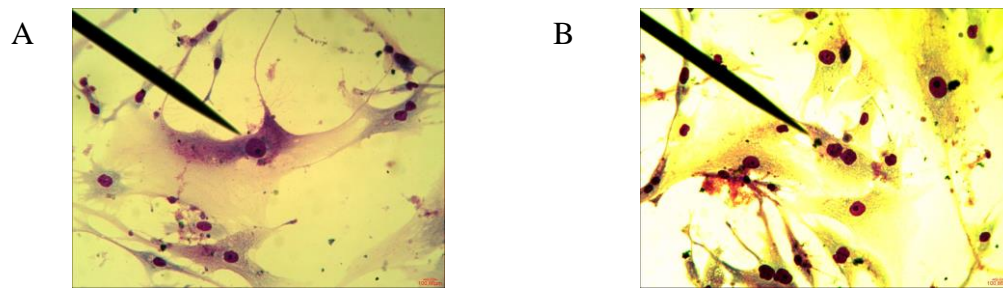


Figure 6.24: Staining of HCASMCs with Reastain Diff kit. (A) A typical cultured HCASMC. (B) HCASMC with two nuclei during cytokinesis.

6.3.7.1 Cell cycle analysis of HCASMCs using FACS

Cell cycle has two distinct processes, named interphase and mitotic phase (M), the former consists of Gap 1 (G1), synthesis (S), and Gap 2 (G2) (**Figure 6.25**). In this project, the distribution of these phases of HCASMCs was obtained by examining the intensity of DAPI incorporation using FACS [301]. With non-stained HCASMCs set as a negative control (**Figure 6.26**), a typical plot is shown in **Figure 6.27**, in which cell size is shown in forward scatter (FSC) and granularity in side scatter (SSC). The markers for each phase were added to cell cycle profile graph manually. The polygon drawn around the dot plot shows the cells considered for analysis, which defines the gate. Cells at different cell cycle phases have different amount of DNA copies, and the latter is directly related to DAPI intensity detected by FACS. Therefore, relative percentage of HCASMCs at each stage can be calculated from frequency histograms (**Figure 6.27C**). Cell cycle was synchronized before each treatment by deprivation of serum from cell culture medium. Cells serum free for 48 hours showed a larger proportion at G0/G1 phase ($P < 0.001$) and G2/M phase ($P < 0.05$), and smaller proportion at sub-G0/G1 phase ($P < 0.001$), than those for 24 hours. Therefore, the following experiments were done with the cells serum free for 48 hours prior to treatments (**Figure 6.28**).

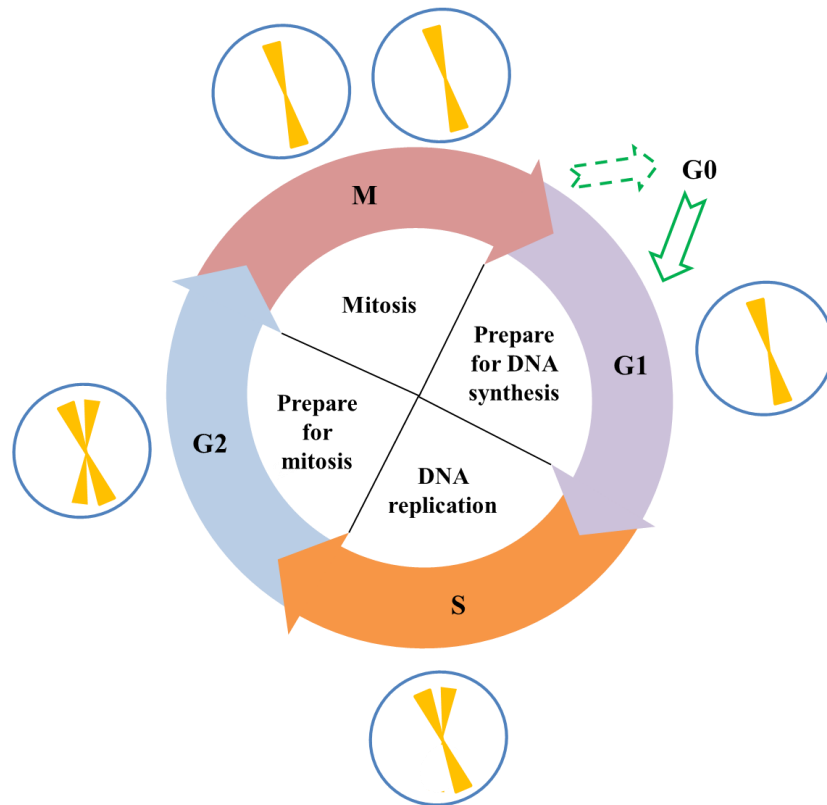


Figure 6.25: Schematic presentation of cell division cycle. A complete cell cycle is comprised of four distinct phases that are characterized by their different DNA content. Once the cell passes restriction point (R point), it progresses to gap phase 1 (G1) and begins DNA synthesis in S phase. Cells prepare to divide in gap phase 2 (G2) and then enter M phase, in which they divided into two daughter cells through mitosis and cytokinesis.

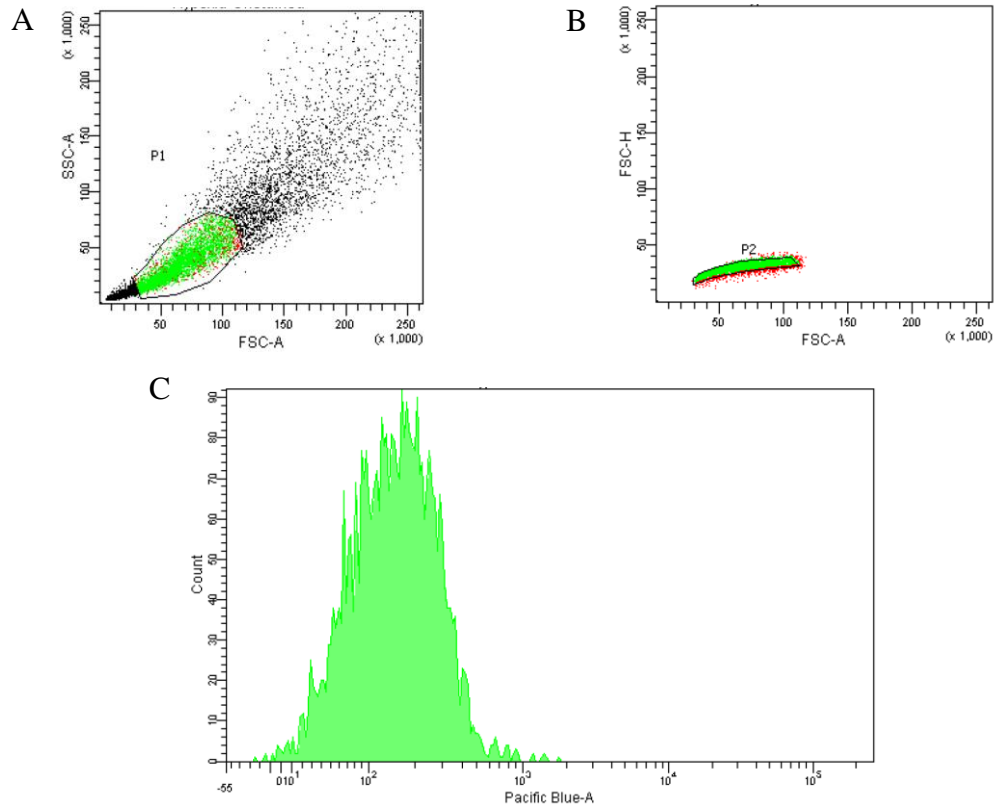


Figure 6.26: Negative control with unstained HCASMCs. (A) Scatter graph showing the size and granularity of HCASMCs. (B) Dot plot of background fluorescence of non-stained HCASMCs. (C) Profile graph of non-stained HCASMCs.

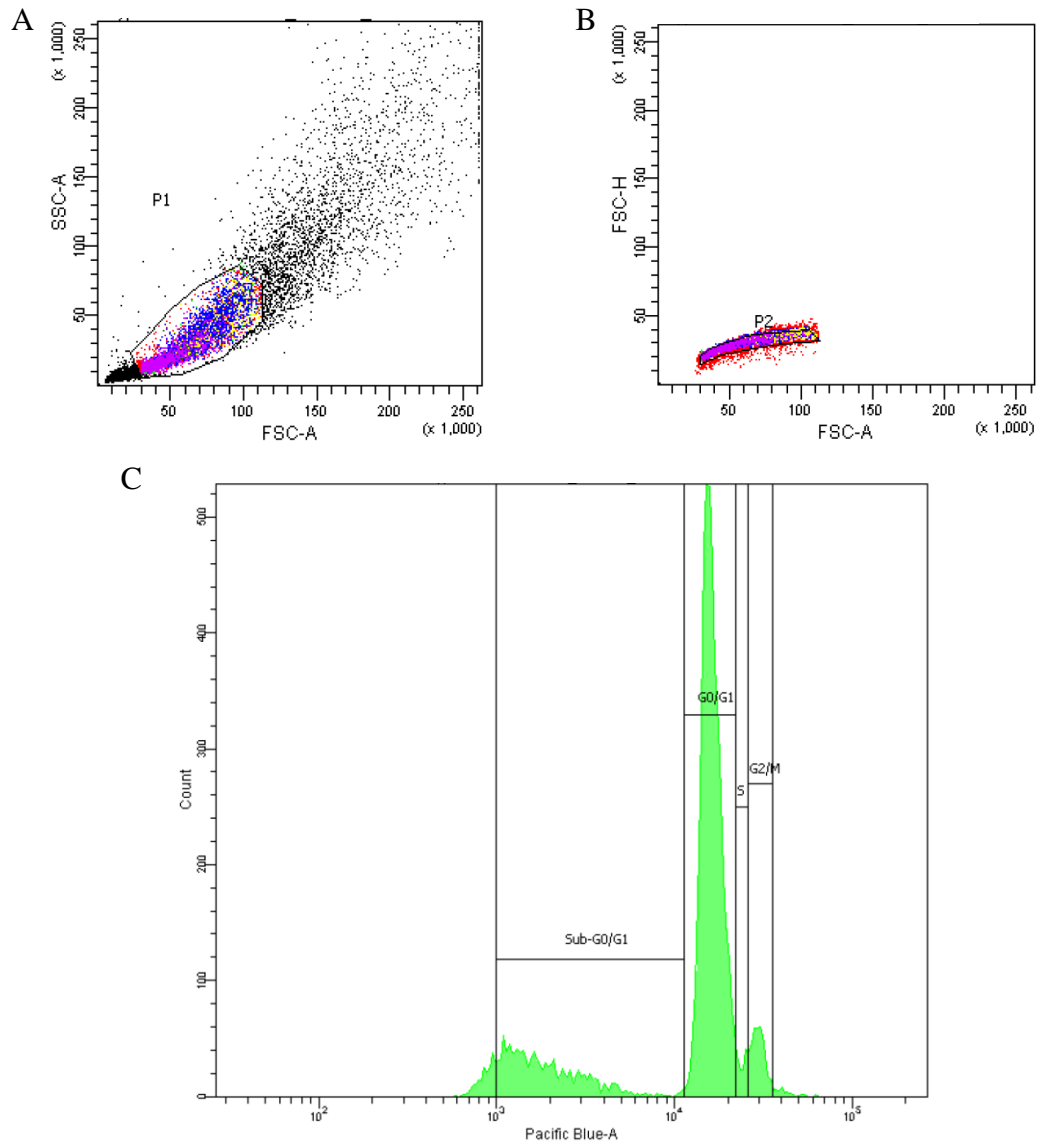


Figure 6.27: Cell cycle analysis. (A) Scatter graph showing the size and granularity of HCASMCs. (B) Dot plot of fluorescence signals of DAPI stained HCASMCs (fluorescence gate). (C) Cell cycle graph showing different phases of cell cycle stage.

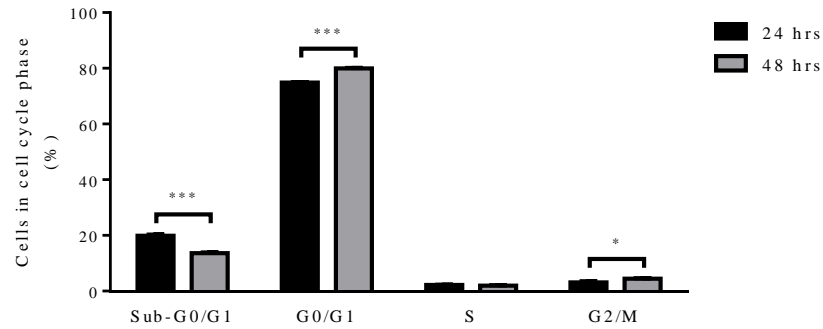


Figure 6.28: Effect of serum deprivation on HCASMC cell cycle. HCASMCs were synchronized before each experiment to induce quiescence (n=4).

6.3.7.2 Effect of hypoxia on HCASMCs cell cycle

To determine whether hypoxia induced HCASMC proliferation is through a general effect on cell cycle phase, DNA content was quantified. After exposure of HCASMCs to different levels of O₂, we found that the percentage of cells at sub-G0/G1 phase decreased and cell proportion at G0/G1 phase increased with a reduction in O₂ concentration (**Figure 6.29 & 6.30**). This suggests that hypoxia induced cell number increase is more likely due to decreased cell death rather than cell cycle arrest. Application of 10 μM glibenclamide showed little effect on cell cycle profile in normoxia and severe hypoxia, but resulted in a cell cycle profile with a smaller proportion of cells at sub-G0/G1 phase and a larger proportion at G0/G1 phase when compared to 5% O₂. These preliminary data suggests that a possible explanation for glibenclamide inhibition of hypoxia induced HCASMC proliferation, if cell cycle related, could be slowing the cell cycle. The experiments are preliminary, and further experiments are needed to provide solid evidence for the role of K⁺ channels in hypoxia induced cell proliferation.

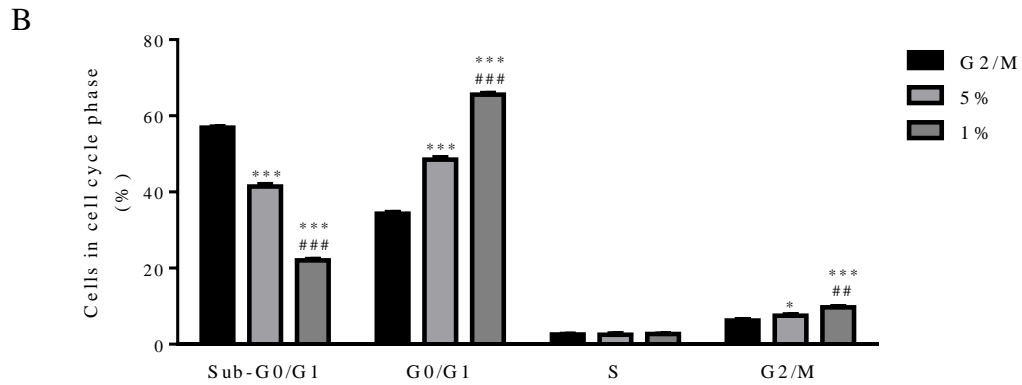
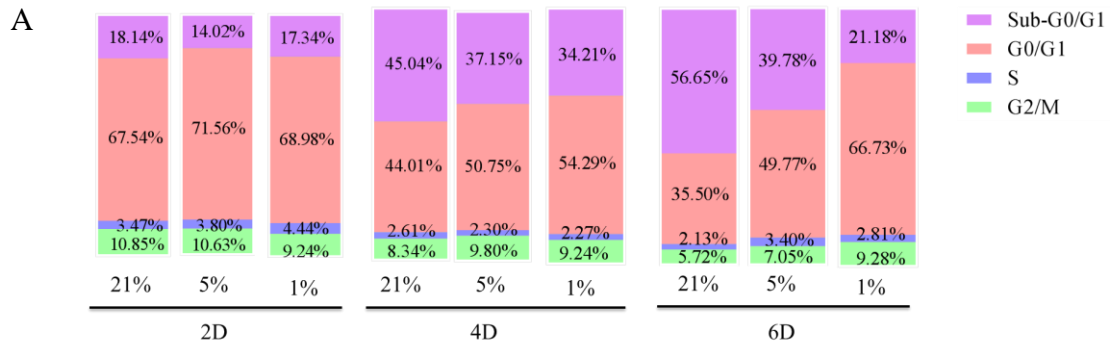


Figure 6.29 Cell cycle profiles of HCASMCs in hypoxia. (A) A representative cell cycle profile showing the percentage of cells at each cell cycle phase after exposure to various O₂ concentrations for 2D, 4D and 6D. (B) Mean \pm SEM for the average percentage of cells at each cell cycle phase after 6D exposure to normoxia, 5% and 1% O₂ (n=4). * indicates the statistics against normoxia, and # indicated the statistics between 5% and 1% O₂.

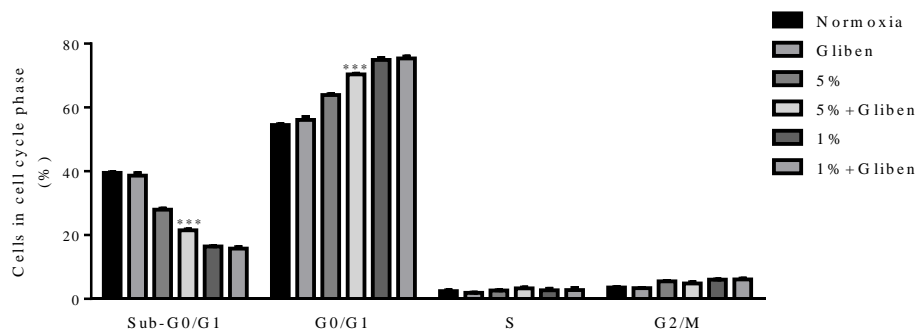


Figure 6.30 Effect of glibenclamide on HCASMCs cell cycle. HCASMCs were incubated in normoxia or hypoxia for 6D, and treated with 10 μ M glibenclamide. (n=4). Statistics was carried out as Normoxia vs Gliben, 5% vs 5%+Gliben and 1% vs 1%+Gliben.

6.4 Discussion

VSMC differentiation is essential during vascular development. It is well known that VSMCs can switch among a spectrum of phenotypes from a quiescent ‘contractile’ phenotype state to an active ‘synthetic’ state, in which SMCs can migrate from media to intima where the cells start to become more proliferative [23, 277, 310]. Therefore, a series of methods were used to characterize HCASMC phenotype throughout culture, and identify phenotype changes during treatments such as hypoxia.

As HCASMC passage increased, they became larger in size and slowed down in growth rate. There seems to be an increase in cell major axis and we observed a significant increase in cell minor axis during culture (**Figure 6.2**), but these are within the normal range suggested by Promocell (approximately ~120-240 μm in length including extensions and ~15-45 μm in width). There was no difference in cell shape parameters (Circ, AR, Round and Solidity) from P7 to P13. HCASMCs maintained an elongated spindle shaped morphology throughout culture, which is typical for differentiated SMCs [311]. Coomassie blue staining of electrophoretically separated total protein sample showed similar protein distribution across all the passages. More specifically, Western blotting analysis and immunofluorescence staining were applied to monitor the expression of SMC-specific markers α -SMA, calponin and MHC throughout culture. In Western blotting, α -SMA was identified as a single band at 42 kDa and calponin with a primary band at 34 kDa from P7 to P13. Actin was found to be present in both HCASMCs and HCAECs, but α -actin (42 kDa) and calponin (34 kDa) were not identified in ECs. All of the three SMC-specific markers (α -SMA, calponin, MHC) were identified in immunocytochemical staining of HCASMCs, but not of ECs. Moreover, a parallel experiment showed a lack of two EC makers (vWF and CD31), which were detected in HCAECs but not in HCASMCs. Taken together, our results indicate that elongated primary HCASMCs express SMC-specific markers from P7 to P13, and there is little contamination of HCAEC among commercially obtained HCASMCs. Therefore, HCASMCs used in this project kept at low passages (P7-P13) are deemed as acceptable model.

Cells can respond to prolonged hypoxia in many ways to survive. For example, HIF-1 is a master regulator of transcriptional response under hypoxia that mediates many crucial physiological responses to low O₂ concentrations including erythropoiesis, vascularization and anaerobic metabolism. However, VSMC proliferation and differentiation may also reflect the epidemic of many arterial diseases, in which development of a highly proliferative and synthetic phenotype of VSMCs plays a key pathogenic role [23, 312]. Because such phenotypic changes and cell replication are a highly energy dependent [284], we hypothesized that changes in cellular metabolism under hypoxia are likely to play a crucial role in regulating SMC plasticity.

It is clear that VSMC proliferation results in an increase in cell number, and causes atherosclerosis and neo-intimal hyperplasia. However, the overall number of cells is dependent not only on cell growth and proliferation, but also cell death which is caused by apoptosis and necrosis [312-314]. Therefore, it is the balance between the two that maintains tissue homeostasis. Our results suggested both 5% and 1% O₂ caused cell proliferation (**Figure 6.14**). HCASMCs exhibited higher proliferation under 5% than 1% O₂, we postulate that might be due to a shortage in energy for proliferation under severe hypoxia. When combined with cell cycle results, hypoxia induced cell number increase, maybe partly due to decreased cell death (**Figure 6.29**).

It is generally accepted K⁺ channels are necessary in the process of cell proliferation and migration. However, it is poorly understood in VSMCs how K⁺ channel expression both in amount and distribution may change during cell proliferation and migration. Since the pioneering work in lymphocytes [315], there has been increasing evidence suggesting a role of K⁺ channels in cell proliferation. It has been reported SK_{Ca}/IK_{Ca} channels are not or only poorly expressed in healthy and freshly isolated VSMCs, while they increase dramatically in proliferating cells as in culture or vascular injury [96, 97]. When the cells are exposed to prolonged hypoxia, the expression of a wide range of O₂ sensitive ion channels will increase [21]. It is reported that K⁺ channels are required in the initiation of G1 progression [291-293],

and electrical properties of the cells are regulated by K^+ channels which will subsequently induce spatial and temporal organization of Ca^{2+} signaling. Meanwhile, Ca^{2+} is involved in G0/G1 transition [294-298]. Therefore, it is very likely that various K^+ channels are involved in the process of VSMC proliferation [316]. Based on these, inhibition of K^+ channels will result in a decrease in VSMC proliferation both under normoxia and hypoxia.

Although many K^+ channels are suggested as candidates in regulating VSMC growth, the unique gating properties of some channels (e.g. K_{Ca} channels) make them more likely to be important determinants in VSMC proliferation. The changes in K^+ channel function cause temporal organization of Ca^{2+} signaling, and thus lead to activation of gene expression and cell growth [316] (**Figure 6.31**). It was found that there is an increase in $K_{Ca3.1}$ channels in coronary vessels from patients with coronary artery disease, and pharmacological blockade or gene silencing of $K_{Ca3.1}$ channel suppressed human VSMC proliferation and migration [317]. In HCASMCs, PDGF-BB induced cell proliferation was attenuated by lowering $[Ca^{2+}]_i$ and enhanced by elevating $[Ca^{2+}]_i$, and $K_{Ca3.1}$ was found to be involved in PDGF-induced rise in $[Ca^{2+}]_i$ which can be suppressed by A23187 in a dose dependent manner [318] (**Figure 6.31**). Our preliminary results suggest K_{ATP} channels may be important in cell proliferation, and K_{ATP} and K_v7 channels may be involved in hypoxia induced HCASMC proliferation. However, more studies are required to provide further evidence to these observations in the future.

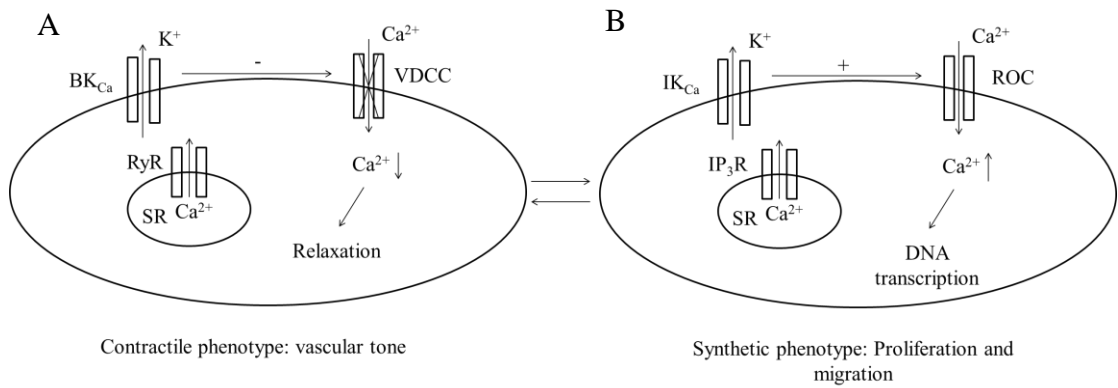


Figure 6.31: The role that K_{Ca} channels play in regulating SMC plasticity. (A) In contractile SMCs, activation of BK_{Ca} channels by Ca^{2+} sparks results in decrease in vascular tone, and therefore vessel dilation. (B) Transition to synthetic phenotype is associated with a loss of BK_{Ca} and upregulation of IK_{Ca} and ROCs. (Modified from Neylon, 2002 [316])

In conclusion, cultured HCASMCs express characteristic markers specific to VSMCs, and these findings are of great relevance since the cells are from human coronary arteries. Our results suggest that at least during the passages relevant to this project, HCASMC did not experience a large shift in phenotype and maintained at least some native characteristics. Growth factors, hypoxia, as well as ion channels play crucial roles in HCASMC phenotype switch, and therefore may constitute a new therapeutic target for cardiovascular diseases [318, 319].

Chapter 7

Discussion

7.1 Introduction

It was first described by Roy and Brown that when O₂ supply cannot meet the demand of metabolically active tissues, the cardiovascular system responded with vasodilation and a subsequent increase in local blood flow [320]. The coronary circulation is adapted to provide high rates of flow to meet basal metabolic demand, coupled with an ability to further increase flow more than ~5 fold in response to increased cardiac work, for example during exercise [1, 2] (Figure 7.1). This direct link between blood supply and metabolic demand is a hallmark of coronary circulation. A number of parallel mechanisms to achieve this may exist, and interpretation of studies where only one of these pathways was blocked has been problematic due to this redundancy [2]. Thus, lack of effect in inhibiting one mechanism does not automatically prove it is not important as the true effect could be masked by alternative pathways picking up what is eliminated. Presumably the multiple mechanisms acts as a safety net, ensuring supply of blood is guaranteed and must not fail, and this is a reflection of the absolute importance of coronary metabolic vasodilation. With this caveat, broadly two major hypotheses have been advanced to account for coronary metabolic vasodilation: (i) the release of vasodilator metabolites from cardiac myocytes (e.g. adenosine, K⁺ and H⁺), and (ii) the direct vasodilatory effects of hypoxia on VSMCs. This project investigated the possible cellular mechanisms underlying direct hypoxic vasodilation of HCASMCs, with particular emphasis on the role of K⁺ channels. In addition to the acute effect on vascular tone, we also looked at the effect of prolonged hypoxia on HCASMC proliferation and migration. Many studies have reported that hypoxia activates various K⁺ channels in systemic arteries at different locations and of different species [21, 34, 38, 321]. However, this is the first study to specifically look at the role of K⁺ channels as targets of hypoxic vasodilation in human coronary vasculature at cellular level. Furthermore, the use of human cells can provide a more direct and relevant way of studying human pathophysiological settings than use animal cells.

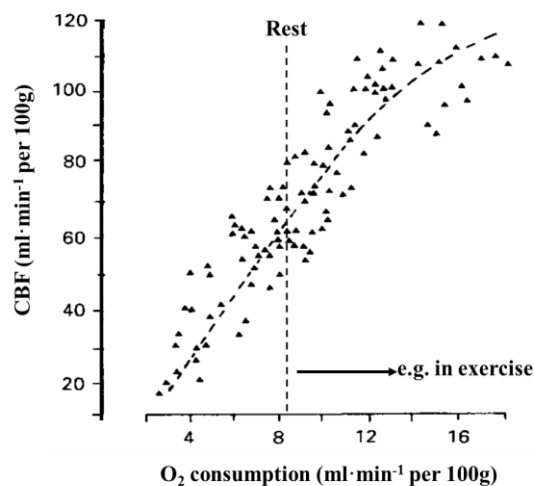


Figure 7.1: Relationship between O₂ consumption and coronary blood flow. The diagram shows that coronary blood flow increases when there is a growing cardiac work, shown as a rise in O₂ consumption in dog (Reproduced from Berne and Sprekalis, 1979 [322]).

7.2 K⁺ channels as cellular targets in hypoxic vasodilation

It has been reported that K_{ATP} and K_{ir} channels, along with the "leak" channels, are involved in establishing the resting membrane potential of VSMCs [1, 43, 90, 91, 323]. Glibenclamide and Ba²⁺ caused membrane potential depolarization, indicating that K_{ATP} and K_{ir} channels are playing the major roles in setting resting membrane potential of HCASMCs (Figure 5.21). Reverse transcription polymerase chain reaction (RT-PCR) and electrophysiological experiments showed the expression of K_{Ca} and K_{ATP} channel subunits in HCASMCs (work by M Yang and Megan Kitching, data not shown). Pharmacological modulation of K⁺ channels also corroborated the evidence of these channels in coronary artery SMCs as shown by previous work from others [34, 73, 99, 324-326]. K_{ATP} channels were activated by pinacidil and inhibited by glibenclamide (Figure 5.23). BK_{Ca} channels showed acute and large responses to various channels openers, including NS1619 and NS11021 (Figure 5.24&5.25). Addition of SKA31 caused membrane potential hyperpolarization, and this effect is fully abolished by tram34 plus apamin (Figure 5.26), suggesting a role of SK_{Ca}/IK_{Ca}

in HCASMCs. Thus, HCASMCs functionally express K_{ATP} , BK_{Ca} and SK_{Ca}/IK_{Ca} channels, and any of these could be potentially activated by hypoxia. Since the first study demonstrated that K^+ currents in carotid body type I cells were reversibly reduced by 25 to 50 percent in hypoxia (PO_2 from 150 to 10 millimeters of mercury) [32], O_2 sensitivity of ion channels, particularly K^+ channels received more attention and studies were carried out in various tissues which response to hypoxia [34, 38, 39].

Initially, it was uncertain whether cultured HCASMCs had a capacity to sense and respond to hypoxic insults. If these cells do not respond to low O_2 level, it could be argued that whole project does not make sense. Our $[Ca^{2+}]_i$ measurement results showed that reducing O_2 tension from 20% to 1% resulted in decreases in Ca^{2+} oscillations in HCASMCs (Section 5.3.1.4). We also found that membrane potential, measured by DiBAC4(3) hyperpolarized with hypoxia (1% O_2) (Figure 5.30). Taken together, HCASMCs can respond to hypoxia, and these results suggest that hypoxia vasodilation of human coronary smooth muscle may be caused by a direct effect on $[Ca^{2+}]_i$ as well as indirectly through the change of membrane potential. The change in membrane potential under hypoxia could be blocked by high K^+ (60 mM) solution, but inhibiting K^+ channels including K_{ATP} channels (glibenclamide), K_{ir} channels ($BaCl_2$), BK_{Ca} channels (IbTX or Penitrem A), or K_{ATP} plus K_{ir} channels (glibenclamide plus $BaCl_2$) did not completely inhibit hypoxia induced hyperpolarization. This suggested that more than one K^+ channels may be involved in this phenomenon. Also, K_2P channels were not investigated in this thesis as there are not specific inhibitors that can be used to dissect out the role of these channels. Moreover, the sensitivity of K^+ channels to inhibitors may be reduced during hypoxia [327]. Knocking down individual K^+ channels using techniques including KO mice and siRNA might be useful to address some of these unanswered questions.

7.3 K_{ATP} channels in hypoxic vasodilation

K_{ATP} channels are inhibited by intracellular ATP and activated by intracellular ADP, making them uniquely placed to couple cellular metabolic state to membrane

excitability. For example, these channels are responsible for glucose sensation in pancreatic β -cells where an increase in blood glucose causes channel closure through cellular ATP production (or, more precisely, via a change in the ATP:ADP ratio). The resulting β -cell membrane depolarization triggers Ca^{2+} entry through opening of VDCCs and so insulin secretion. The anti-diabetic sulphonylurea drugs such as glibenclamide cause insulin secretion by directly inhibiting K_{ATP} channels in β -cells.

In the cardiovascular system, K_{ATP} channels have multiple functions. In cardiac myocytes, the channel opens during severe and prolonged anoxia due to reduced ATP and increased ADP levels. This reduces cellular excitability, so preventing action potential generation and cell contraction [33]. Ultimately this protects the myocardium from damage by preventing complete depletion of intracellular ATP, which would trigger cell death. In the vasculature, K_{ATP} channels have diverse functions (summarized in reviews referenced) [33, 132] (**Figure 7.2**). K_{ATP} channels are activated by vasodilators coupled to cAMP-dependent protein kinase and are inhibited by vasoconstrictors coupled to PKC [328]. The resulting membrane potential changes are important in the actions of vasodilators and vasoconstrictors. Co-localization of K_{ATP} channels and protein kinases within specific plasma membrane microdomains, termed caveolae, appears important for modulation [157, 165, 245]. Most recently, we have shown that the novel cellular cAMP sensor, EPAC, causes channel inhibition via Ca^{2+} -dependent protein phosphatase 2B [329]. Importantly, vascular K_{ATP} channels are activated by the anti-anginal compound nicorandil, and are inhibited by the sulphonylureas.

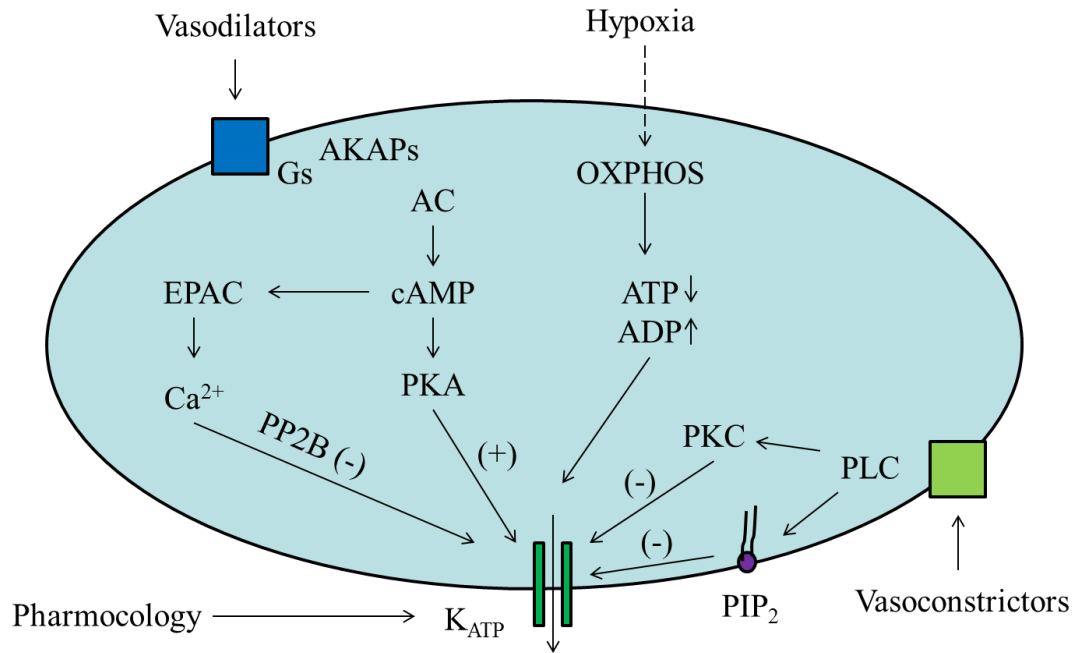


Figure 7.2: Regulation of vascular K_{ATP} channels. AC, adenylyl cyclase; AKAP, A-kinase anchor protein; cAMP, cyclic AMP; EPAC, exchange protein activated by cAMP; G_s, G-protein (stimulatory); OXPHOS, oxidative phosphorylation; PIP₂, phosphatidylinositol (4,5)-bisphosphate; PKC, protein kinase C; PLC, phospholipase C; PP2B, protein phosphatase 2B.

Although K_{ATP} channel is regulated by vasoconstrictors and vasodilators acting through second messengers and enzymes, it is the nucleotide sensitivity of the channel itself that has made it an obvious target for metabolic regulation of blood flow. The hypothesis is that hypoxia would cause a fall in cellular ATP and a rise in ADP, both of which would lead to activation of K_{ATP} channels and so membrane hyperpolarization and vasodilation. Many studies have addressed this issue at the level of intact coronary artery or heart in animal models, and many, though certainly not all, have provided evidence for a role of K_{ATP} channels in hypoxic vasodilation. The first report was made by Daut et al in 1990, in which vasodilation induced by hypoxia was inhibited by glibenclamide in intact guinea-pig heart [330]. Using a Langendorff heart preparation it was suggested that hypoxic vasodilation occurred via activation of coronary artery K_{ATP} channels in guinea-pig, probably as a consequence

of the effect on cellular nucleotide levels [331]. The results of a large number of functional studies in animal models are summarized in recent reviews [2, 21, 33]. However, we know of only two attempts to address this issue in human coronary arteries. In arteries isolated from the right atrial appendage hypoxia caused dilation that was not dependent on surrounding cardiac myocytes or the presence of the endothelium [332, 333]. In one study pharmacological inhibition of K_{ATP} channels using a sulphonylurea (glibenclamide) blunted the hypoxic response [332], whilst in the other study glibenclamide was without effect [333]. K_{ATP} channels have been identified in cultured HCASMCs but there have been no studies looking at metabolic or other regulation of these channels in single cells [334]. Regarding the physiological role of the K_{ATP} channel in the coronary circulation, it is of interest that genetic knockout in mice results in hypertension, coronary artery vasospasm and sudden cardiac death [335, 336]. The effects of knockout have been linked to Prinzmetal angina, although it is not known if K_{ATP} channel mutations cause this disease in humans.

Despite the functional studies cited above, the apparently simple hypothesis that hypoxia changes cellular nucleotide levels to a degree sufficient to activate vascular K_{ATP} channels has proved to be very difficult to address [33]. Thus K_{ATP} channels appear to be closed at levels of ATP normally encountered in cells, and cytochrome oxidase, the key O_2 sensitive enzyme involved in mitochondrial ATP generation, is fully O_2 saturated unless O_2 drops to very low levels (<1 mmHg, essentially equivalent to anoxia). In contrast, hypoxic vasodilation can occur at much higher oxygen levels (~30 mmHg) [2]. Indeed, a major recent review on the subject states that it remains unclear what the adenosine nucleotide levels are in the VSM myocytes and whether cellular metabolism changes sufficiently to dynamically regulate VSM K_{ATP} channel activity under physiological condition [33]. K_{ATP} currents in pig coronary artery are activated by hypoxia (PO_2 ~35 mmHg) [34]. In contrast, K_{ATP} currents in rat femoral artery are not activated by hypoxia but are activated during anoxia (PO_2 < 1 mmHg) [203]. This difference may reflect origin of artery (i.e. species, vascular bed, small vs large).

In order to answer the question whether hypoxia changes cellular nucleotide levels to a degree sufficient to activate K_{ATP} channels, a series of experiments were designed to investigate the cellular metabolism of HCASMCs during metabolic inhibition and hypoxia. Bioenergetic profile of HCASMCs was characterized by Seahorse technique, in which it showed that the cells rely on ~54.53% of ATP production from OXPHOS (138.93 ± 8.88 mol/min per 2×10^4 cells or 15.04 ± 0.59 pmol/min per μg protein) (**Figure 3.15**). In aerobic respiration, O_2 is the final electron acceptor of ETC during OXPHOS, in which free energy is generated for various cell functions. When cell OCR was compartmentalized by a sequential application of metabolic inhibitors, we found that basal OCR encompasses 72.6% of mitochondrial O_2 consumption and 27.40% of non-mitochondrial O_2 consumption. In mitochondrial O_2 consumption, 23.91% is due to proton leak, which is consistent with previous report showing proton leak from a range of vertebrate and invertebrate species is approximately ~20% [[173](#), [177](#)]. In our experimental conditions, switching off one metabolic pathway caused cells to resort to increase ATP production rate from the other. The changes in bioenergetic phenotype after the application of a drug can be used to predict the cellular energy status and explain some of the malfunctions in pathology.

After the bioenergetic profile of the cells has been determined, we then measured the changes in cellular nucleotides under metabolic inhibitors and hypoxia. In the extracellular solution containing 10 mM glucose, inhibiting either glycolysis (2-DG) or OXPHOS (oligomycin) caused a small change in $[\text{ATP}]_i$, but blocking both pathways induced significant changes in $[\text{ATP}]_i$ (**Figure 3.26**). In the absence of glucose, either inhibiting glycolysis or OXPHOS resulted in significant changes in $[\text{ATP}]_i$, and an even larger effect was observed when 2-DG and oligomycin were co-applied (**Figure 3.26**). Because the absolute amount of ATP, ADP and AMP can vary widely among cells, measurement of intracellular ATP:ADP and ATP:AMP ratios will provide more reliable information of cellular metabolism [[185](#), [187](#)]. Hydrolysis of one molecular ATP produces one molecular diphosphate ADP and one molecular inorganic phosphate (P_i), making ATP:ADP ratio a direct indicator of

cellular energy charge and phosphorylation potential. Using transient transfection, Perceval/PercevalHR, were introduced to the cells to report intracellular ATP:ADP ratio. Removal of substrate (glucose) and inhibition of either glycolysis or OXPHOS with metabolic inhibitors all resulted in decreases in cellular ATP:ADP ratio (**Section 3.4.3**). Hypoxia also induced a decrease in cellular ATP:ADP ratio (**Section 3.4.3.4**).

When cells were transfected using lentivirus technique, however, hypoxia caused no change in ATP:ADP ratio. These contradictory results from cells expressing reporter genes may be due to the different methods used for gene delivery. The cells transfected with lentivirus may be in a more physiological and healthier condition compared to the ones transiently transfected. The morphology of the former was more closely matched to the untransfected cells (**Figure 4.10&6.2**), and this may indicate that lentivirus transfected cells are more resilient to hypoxic insult. That said, it may be also possible to argue that those cells need to be “working” in order to examine the effect of hypoxia. Although cells require ATP to be just alive, somewhat contracting cells that would be seen in the artery with tone need substantially more ATP, and thus hypoxia challenge need to be investigated using working cells. In any case, the change seen in Perceval/PercevalHR signals are unlikely to be artifact as inhibiting glycolysis or OXPHOS induced no change or a small change in $[pH]_i$ in cell culture medium or HCO_3^- buffered PSS in the majority of the cell, reported by pHRed [197]. Therefore, the changes in Perceval/PercevalHR fluorescence are true changes owing to changes of intracellular ATP:ADP ratio. At the same time, if K_{ATP} channels are activated, the effect due to a change in pH could be ruled out.

It has been reported that ATP binding site on $K_{ir}6.2$ subunit is estimated to be ~2 nm below the membrane and at the interface between adjacent $K_{ir}6.2$ [166]. Therefore, the ATP:ADP ratio in the plasma membrane microdomains will be more relevant and important in K_{ATP} channel gating. Even within a single cell, ATP:ADP ratio is very likely to be distinctive due to ATP compartmentalization and localized energy production and consumption. Evidence has suggested that local nucleotide

level is modified when bulk ATP was transmitted over the diffusional barrier into the sub-membrane space due to the effect from metabolic enzymes [33, 123, 167]. AMP is suggested to regulate ATP:ADP ratio in the near membrane area by being involved in the phosphotransfer reactions mediated by AK, resulting in a change sufficient to cause K_{ATP} channel opening [168]. Meanwhile, ATP is largely consumed by many physiological processes in the cell membrane, for example, the pumps work as ATPases while the ions and small molecules are moved across cell membrane against a chemical concentration gradient or electric potential. Given the importance of ATP:ADP ratio in the immediate vicinity of K_{ATP} channels in controlling channel activity, further experiments were designed to assess ATP:ADP ratio in K_{ATP} channel microdomains. This aim was attempted in this project by either adding a membrane targeting sequence to PercevalHR or TIRF imaging. Preliminary studies with both methods showed successful measurement of ATP:ADP ratio and detection of its changes in the sub-membrane area. Due to the time limitation, we just proved the application of these methods and showed some promising preliminary results at this stage.

To summarize, metabolic inhibitors (e.g. antimycin) caused membrane hyperpolarization by activating K_{ATP} channels. Exposing cells to hypoxia also resulted in membrane potential hyperpolarization through the activation of K^+ channels since this effect could be abolished with high K^+ (60 mM). However, it is not known whether hypoxia affects ATP:ADP ratio to a level low enough in the sub-membrane area to stimulate K_{ATP} channel activity.

7.4 Other K^+ channels in hypoxic vasodilation

Although the nucleotide sensitivity of K_{ATP} channel makes it an obvious target for regulation by cellular metabolism, both BK_{Ca} and K_{ir} channels have also been reported to be activated during hypoxia in the vasculature [38, 321]. K_{ir} channels are activated by hypoxia in rabbit coronary VSMCs, and this underlies hypoxic vasodilation in these vessels [321, 337]. We were the first group to record K_{ir} channels in single VSMCs, initially in rat cerebral arteries and later in pig coronary

arteries [99, 252]. An interesting feature of these channels in the coronary circulation is that they are expressed only in arteries < 200 μm in diameter [99]. These small or resistance-sized arteries are responsible for the majority of resistance to blood flow and are therefore key to understanding hypoxic vasodilation [2]. K_{ir} channels are activated by extracellular K^+ , and this triggers membrane potential hyperpolarization and relaxation of VSMCs in response to elevated $[\text{K}^+]_{\text{o}}$ [73]. K^+ is released from cardiac myocytes during cardiac action potential and also proposed as a metabolic vasodilator in the coronary circulation. Accumulation of extracellular K^+ , for instance during ischemia, is pro-arrhythmic, and vascular K_{ir} channel may limit local K^+ accumulation in the myocardium through increased blood flow. Whether K_{ir} or BK_{Ca} channels are activated by hypoxia in human coronary arteries is currently unknown.

7.5 VDCCs in hypoxic vasodilation

VDCCs are the major route of Ca^{2+} entry into SMCs and Ca^{2+} channels blockers are routinely used to lower BP and to treat angina. Hypoxia directly inhibits VDCCs in the cells isolated from systemic arteries, including human coronary arteries [77, 203]. Interestingly, hypoxia activates VDCCs in pulmonary artery myocytes, where a fall in O_2 leads to hypoxic pulmonary vasoconstriction, which serves to balance ventilation to perfusion in the lung [338]. It has been suggested that this reflects a fundamental difference between mitochondria in systemic arteries and pulmonary arteries [64]. Although the principle of hypoxic inhibition of VDCCs in VSMCs from systemic arteries has been established, the mechanism is unclear. Our data in HCASMCs further corroborated the evidence that hypoxia caused changes in $[\text{Ca}^{2+}]_{\text{i}}$ independent of K^+ channel activation, in which the changes in E_{m} was abolished by high $[\text{K}^+]_{\text{o}}$. It has been suggested that the direct inhibitory effect on VDCCs from hypoxia is through the modulation of cysteine residues in the pore forming $\alpha 1$ -subunit which is redox sensitive [339-341]. The decrease in $[\text{Ca}^{2+}]_{\text{i}}$ of the coronary was also ascribed by a mechanism in which metabotropic CCICR was inhibited by hypoxia [79].

7.6 Limitations and future work

The major limitation of this study is that it was conducted on cultured cells. Even though the signature SMC proteins were not fundamentally changing during the course of cell culture (**Figure 6.5 and 6.6**), we are aware that this does not mean cultured cells would behave the same way seen *in vivo*, and this might affect the results. However, apart from it is not practical to dissociate SMCs from cadaver for every experiment, culturing is currently the only way to introduce biosensors such as PercevalHR. Another important limitation of the current work is that HCASMCs were examined in isolation. It is very likely that even hypoxic vasodilation is a local event, contractile state of a SMC may be influenced by cardiac cells, ECs and even other SMCs. Such cell to cell interactions and communications are lost in cultured dish, and ultimately any results obtained from single cells studies need to be placed into a bigger picture.

In this study, we investigated the possible roles of K^+ channels and VDCCs as O_2 sensors in hypoxic vasodilation. Our findings have suggested that hypoxia causes membrane potential hyperpolarization, which can be abolished by high $[K^+]_o$, suggesting a role of K^+ channels. However, this effect is not fully blocked by inhibiting single K^+ channel or both K_{ATP} and K_{ir} channels. Thus, currently the identity of K^+ channels that underlies the hypoxia induced hyperpolarization in HCASMCs is unknown. Of course, one must be careful in interpreting the data obtained from fluorescent probe experiments as ultimately the hyperpolarizing effect of hypoxia must be examined using current clamp technique (or sharp microelectrode membrane potential measurement using tissues). Future studies measuring electrical conductance through whole cell patch clamp recording of currents will provide more detailed information and allow the examination in the role of a specific K^+ channel in hypoxic vasodilation, using appropriate voltage protocols and pharmacological tools [[99](#), [203](#), [252](#)].

Preliminary studies have shown that hypoxia had no effect on bulk ATP:ADP ratio measured in HCASMCs expressing FUGW-PercevalHR, and hypoxia caused no change in mitochondrial membrane potential in the majority of the experiments (4

in 5 experiments). It is not known whether a much lower oxygen concentration will result in a change in ATP:ADP ratio sufficient to stimulate K_{ATP} channels in HCASMCs. The standard criticism is that the key O_2 sensitive enzyme cytochrome c has an extremely low O_2 affinity thus it is fully saturated at physiological hypoxia. K_{ATP} channels in rat femoral artery were shown to be activated only when O_2 drops to less than 1 mmHg, which is equivalent to anoxia [203]. It would be interesting to see whether decreasing O_2 to anoxia will cause changes in ATP:ADP ratio and mitochondrial membrane potential in HCASMCs.

Due to the nucleotide compartmentalization, there is a difference between global and local concentrations of ATP/ ATP:ADP ratio. In order to further examine the potential link between cellular metabolism and K_{ATP} channel activity, it is more relevant to examine the ATP:ADP ratio levels in the channel microenvironment. Both membrane targeted PercevalHR and TIRF imaging are exciting tools to continue the work in this area. The compatibility of live cell imaging with other techniques, such as electrophysiology will allow cellular energy and channel activity to be determined at the same time, providing a direct relationship and valuable detailed information. In this way, we will be able to better characterize the possible roles of K_{ATP} channels in hypoxic vasodilation of coronary arteries with different sizes [186]. More importantly, these techniques involved in this project are valuable tools in study various biological and pathophysiological functions of the cells, therefore can be widely applied for future work.

7.7 Conclusion remarks

Hypoxic vasodilation is crucial to the regulation of human coronary blood flow and the cellular and molecular mechanisms involved in are beginning to come out about what happened (**Figure 7.3**). Previous work from our lab and others suggested that the vasodilator effects of hypoxia are transduced by actions on Ca^{2+} and K^+ channels in SMCs. The data within this thesis further corroborated this hypothesis. However, more work is needed to show which K^+ channels are involved and play a major role in acute O_2 sensing in human coronary vasculature. Because altered Ca^{2+}

and K^+ channel function may be important in the coronary artery vascular changes seen in angina, diabetes and metabolic syndrome [287, 332, 335, 336, 342], this study therefore provided a basis for understanding these disease states. The application of some vasodilatory substrates may provide beneficial effects and reveal potential therapeutic strategies to treat diseases associated with hypoxia/ischemia by inducing local vasodilation.

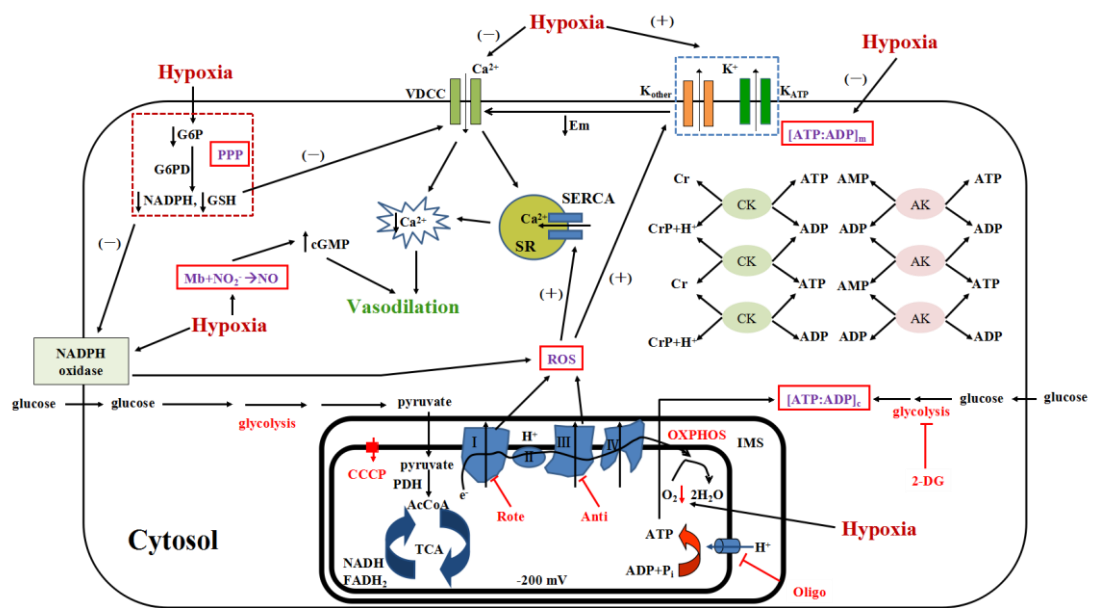


Figure 7.3: Hypothesised mechanisms of metabolic/hypoxic vasodilation of HCASMCs. The schematic diagram shows the cellular and molecular mechanisms proposed for metabolic/hypoxic vasodilation. Metabolic inhibitors cause vasodilation by decreasing intracellular ATP:ADP ratio to a level sufficient to activate K_{ATP} channels. Hypoxia does not reduce global ATP:ADP ratio, but it may cause a decrease in ATP:ADP ratio in the vicinity of the channels and lead to channel open. Metabolic enzymes such as AK and CK may play a role and make K_{ATP} channels more sensitive to small changes of ATP:ADP ratio in the channel microdomains. Diminished ROS production from both mitochondria and NADPH oxidase during hypoxia leads to smooth muscle relaxation through the enhanced K^+ channel activity, thus subsequent membrane hyperpolarization and a decrease in $[Ca^{2+}]_i$ [64, 343, 344]. A decrease in the flux of PPP under hypoxia results in decreased NADPH and $[Ca^{2+}]_i$ which is due to both of reduced extracellular Ca^{2+} influx and enhanced ER Ca^{2+}

uptake [61]. The reduction in $[Ca^{2+}]_i$ could also be a direct inhibitory effect on VDCCs from hypoxia through the modulation of cysteine residues in the pore forming $\alpha 1$ -subunit which is redox sensitive [339-341]. The decrease in $[Ca^{2+}]_i$ subsequently initiates relaxation. A recent study suggested that heme-protein myoglobin in VSMCs produces NO through the reduction of endogenous nitrite under hypoxia and leads to vasodilation, which is independent of the well-known endothelial NO synthase (eNOS) [345]. A direct effect of hypoxia on K^+ channels cannot be excluded, and perhaps hypoxic relaxation of the VSMCs is through an intrinsic O_2 sensor which is a part of the K^+ channel subunits. (Modified from Larsen et al., 2006 and Flagg et al., 2010 [33, 61])

References

1. Levick, J.R., *An introduction to cardiovascular physiology*. 2010: London : Hodder Arnold, 2010. 5th ed.
2. Duncker, D.J. and R.J. Bache, *Regulation of coronary blood flow during exercise*. *Physiol Rev*, 2008. **88**(3): p. 1009-86.
3. Grover, R.F., *Mechanisms augmenting coronary arterial oxygen extraction*. *Adv Cardiol*, 1973. **9**: p. 89-98.
4. Wolff, C.B., *Normal cardiac output, oxygen delivery and oxygen extraction*. *Adv Exp Med Biol*, 2007. **599**: p. 169-82.
5. Tomanek, R.J., *Coronary vasculature. [e;ectronic book] : development, structure-function, and adaptations*. Online access with purchase: Springer. 2013: New York : Springer Science+Business Media, ©2013.
6. Franco, R.S., *Measurement of Red Cell Lifespan and Aging*. *Transfusion Medicine and Hemotherapy*, 2012. **39**(5): p. 302-307.
7. Sherwood, L., *Human physiology : from cells to systems*. 2013: Belmont, CA : Brooks/Cole, Cengage Learning 2013. 8th ed.
8. Kiefer, C.R. and L.M. Snyder, *Oxidation and erythrocyte senescence*. *Curr Opin Hematol*, 2000. **7**(2): p. 113-6.
9. Wood, B.R., B. Tait, and D. McNaughton, *Micro-Raman characterisation of the R to T state transition of haemoglobin within a single living erythrocyte*. *Biochim Biophys Acta*, 2001. **1539**(1-2): p. 58-70.
10. Berg, J.M., J.L. Tymoczko, and L. Stryer, *Biochemistry*. 5th ed. 2002: New York: W H Freeman.
11. Ward, J.P., *Oxygen sensors in context*. *Biochim Biophys Acta*, 2008. **1777**(1): p. 1-14.
12. Clanton, T.L., M.C. Hogan, and L.B. Gladden, *Regulation of cellular gas exchange, oxygen sensing, and metabolic control*. *Compr Physiol*, 2013. **3**(3): p. 1135-90.
13. Pittman, R.N., *Oxygen gradients in the microcirculation*. *Acta Physiol (Oxf)*, 2011. **202**(3): p. 311-22.
14. Tsai, A.G., P.C. Johnson, and M. Intaglietta, *Oxygen gradients in the microcirculation*. *Physiol Rev*, 2003. **83**(3): p. 933-63.
15. Pittman, R.N., *Oxygen transport and exchange in the microcirculation*. *Microcirculation*, 2005. **12**(1): p. 59-70.
16. Bentley, T.B. and R.N. Pittman, *Influence of temperature on oxygen diffusion in hamster retractor muscle*. *Am J Physiol*, 1997. **272**(3 Pt 2): p. H1106-12.
17. Takahashi, E., et al., *Direct observation of radial intracellular PO₂ gradients in a single cardiomyocyte of the rat*. *Am J Physiol*, 1998. **275**(1 Pt 2): p. H225-33.
18. Richardson, R.S., et al., *Human skeletal muscle intracellular oxygenation: the impact of ambient oxygen availability*. *J Physiol*, 2006. **571**(Pt 2): p. 415-24.
19. Richardson, R.S., S.C. Newcomer, and E.A. Noyszewski, *Skeletal muscle intracellular PO₂ assessed by myoglobin desaturation: response to graded exercise*. *J Appl Physiol (1985)*, 2001. **91**(6): p. 2679-85.
20. Semenza, G.L., *Oxygen sensing, homeostasis, and disease*. *New England Journal of Medicine*, 2011. **365**(6): p. 537-547 11p.

21. Shimoda, L.A. and J. Polak, *Hypoxia. 4. Hypoxia and ion channel function.*
22. Chan, C.K. and P.M. Vanhoutte, *Hypoxia, vascular smooth muscles and endothelium.* Acta Pharmaceutica Sinica B, 2013. **3**(1): p. 1-7.
23. Owens, G.K., M.S. Kumar, and B.R. Wamhoff, *Molecular regulation of vascular smooth muscle cell differentiation in development and disease.* Physiol Rev, 2004. **84**(3): p. 767-801.
24. Fong, G.H., *Potential contributions of intimal and plaque hypoxia to atherosclerosis.* Curr Atheroscler Rep, 2015. **17**(6): p. 510.
25. Reglin, B. and A.R. Pries, *Metabolic control of microvascular networks: oxygen sensing and beyond.* J Vasc Res, 2014. **51**(5): p. 376-92.
26. Weir, E.K., et al., *Acute oxygen-sensing mechanisms.* N Engl J Med, 2005. **353**(19): p. 2042-55.
27. Fujishiro, N., et al., *Mechanisms for hypoxia detection in O₂-sensitive cells.* Jpn J Physiol, 2004. **54**(2): p. 109-23.
28. Lopez-Barneo, J., et al., *Oxygen-sensing by arterial chemoreceptors: Mechanisms and medical translation.* Mol Aspects Med, 2016. **47-48**: p. 90-108.
29. Heeringa, J., et al., *Relative contribution of central and peripheral chemoreceptors to the ventilatory response to CO₂ during hyperoxia.* Respir Physiol, 1979. **37**(3): p. 365-79.
30. Lopez-Barneo, J., et al., *Carotid body oxygen sensing and adaptation to hypoxia.* Pflugers Arch, 2016. **468**(1): p. 59-70.
31. Buckler, K.J., *A novel oxygen-sensitive potassium current in rat carotid body type I cells.* J Physiol, 1997. **498 (Pt 3)**: p. 649-62.
32. Lopez-Barneo, J., et al., *Chemotransduction in the carotid body: K⁺ current modulated by PO₂ in type I chemoreceptor cells.* Science, 1988. **241**(4865): p. 580-2.
33. Flagg, T.P., et al., *Muscle KATP channels: recent insights to energy sensing and myoprotection.* Physiol Rev, 2010. **90**(3): p. 799-829.
34. Dart, C. and N.B. Standen, *Activation of ATP-dependent K⁺ channels by hypoxia in smooth muscle cells isolated from the pig coronary artery.* J Physiol, 1995. **483 (Pt 1)**: p. 29-39.
35. Jiang, C. and G.G. Haddad, *A direct mechanism for sensing low oxygen levels by central neurons.* Proc Natl Acad Sci U S A, 1994. **91**(15): p. 7198-201.
36. Patel, A.J. and E. Honore, *Molecular physiology of oxygen-sensitive potassium channels.* Eur Respir J, 2001. **18**(1): p. 221-7.
37. Riesco-Fagundo, A.M., et al., *O₂ modulates large-conductance Ca²⁺-dependent K⁺ channels of rat chemoreceptor cells by a membrane-restricted and CO-sensitive mechanism.* Circ Res, 2001. **89**(5): p. 430-6.
38. Gebremedhin, D., K. Yamaura, and D.R. Harder, *Role of 20-HETE in the hypoxia-induced activation of Ca²⁺-activated K⁺ channel currents in rat cerebral arterial muscle cells.* Am J Physiol Heart Circ Physiol, 2008. **294**(1): p. H107-20.
39. Buckler, K.J. and P.J. Turner, *Oxygen sensitivity of mitochondrial function in rat arterial chemoreceptor cells.* J Physiol, 2013. **591**(14): p. 3549-63.
40. Vadula, M.S., J.G. Kleinman, and J.A. Madden, *Effect of hypoxia and norepinephrine on cytoplasmic free Ca²⁺ in pulmonary and cerebral arterial myocytes.* Am J Physiol, 1993. **265**(6 Pt 1): p. L591-7.
41. Nelson, M.T., et al., *Calcium channels, potassium channels, and voltage dependence of arterial smooth muscle tone.* Am J Physiol, 1990. **259**(1 Pt 1): p. C3-18.

42. Nelson, M.T., et al., *Noradrenaline contracts arteries by activating voltage-dependent calcium channels*. *Nature*, 1988. **336**(6197): p. 382-5.
43. Nelson, M.T. and J.M. Quayle, *Physiological roles and properties of potassium channels in arterial smooth muscle*. *Am J Physiol*, 1995. **268**(4 Pt 1): p. C799-822.
44. Welsh, D.G., W.F. Jackson, and S.S. Segal, *Oxygen induces electromechanical coupling in arteriolar smooth muscle cells: a role for L-type Ca²⁺ channels*. *Am J Physiol*, 1998. **274**(6 Pt 2): p. H2018-24.
45. Franco-Obregon, A., J. Urena, and J. Lopez-Barneo, *Oxygen-sensitive calcium channels in vascular smooth muscle and their possible role in hypoxic arterial relaxation*. *Proc Natl Acad Sci U S A*, 1995. **92**(10): p. 4715-9.
46. McBride, H.M., M. Neuspiel, and S. Wasiak, *Mitochondria: More Than Just a Powerhouse*. *Current Biology*. **16**(14): p. R551-R560.
47. Duchen, M.R., *Contributions of mitochondria to animal physiology: from homeostatic sensor to calcium signalling and cell death*. *J Physiol*, 1999. **516** (Pt 1): p. 1-17.
48. Gnaiger, E., et al., *Mitochondrial oxygen affinity, respiratory flux control and excess capacity of cytochrome c oxidase*. *J Exp Biol*, 1998. **201**(Pt 8): p. 1129-39.
49. Chandel, N.S., G.R. Budinger, and P.T. Schumacker, *Molecular oxygen modulates cytochrome c oxidase function*. *J Biol Chem*, 1996. **271**(31): p. 18672-7.
50. Chance, B. and G.R. Williams, *Respiratory enzymes in oxidative phosphorylation. I. Kinetics of oxygen utilization*. *J Biol Chem*, 1955. **217**(1): p. 383-93.
51. Turrens, J.F., *Mitochondrial formation of reactive oxygen species*. *J Physiol*, 2003. **552**(Pt 2): p. 335-44.
52. Loboda, A., A. Jozkowicz, and J. Dulak, *HIF-1 and HIF-2 transcription factors — Similar but not identical*. *Molecules and Cells*, 2010. **29**(5): p. 435-442.
53. Semenza, G.L., *Hypoxia-inducible factors in physiology and medicine*. *Cell*, 2012. **148**(3): p. 399-408.
54. Wenger, R.H., D.P. Stiehl, and G. Camenisch, *Integration of oxygen signaling at the consensus HRE*. *Sci STKE*, 2005. **2005**(306): p. re12.
55. Ran, R., et al., *Hypoxia preconditioning in the brain*. *Dev Neurosci*, 2005. **27**(2-4): p. 87-92.
56. Cummins, E.P. and C.T. Taylor, *Hypoxia-responsive transcription factors*. *Pflügers Archiv*, 2005. **450**(6): p. 363-371.
57. Ausserer, W.A., et al., *Regulation of c-jun expression during hypoxic and low-glucose stress*. *Mol Cell Biol*, 1994. **14**(8): p. 5032-42.
58. Semenza, G.L., L.A. Shimoda, and N.R. Prabhakar, *Regulation of gene expression by HIF-1*. *Novartis Found Symp*, 2006. **272**: p. 2-8; discussion 8-14, 33-6.
59. Yeom, C.J., et al., *Strategies To Assess Hypoxic/HIF-1-Active Cancer Cells for the Development of Innovative Radiation Therapy*. *Cancers (Basel)*, 2011. **3**(3): p. 3610-31.
60. Cavadas, M.A., L.K. Nguyen, and A. Cheong, *Hypoxia-inducible factor (HIF) network: insights from mathematical models*. *Cell Commun Signal*, 2013. **11**(1): p. 42.
61. Larsen, B.T. and D.D. Gutterman, *Hypoxia, coronary dilation, and the pentose phosphate pathway*. *Am J Physiol Heart Circ Physiol*, 2006. **290**(6): p. H2169-71.
62. Morio, Y. and I.F. McMurtry, *Ca(2+) release from ryanodine-sensitive store contributes to mechanism of hypoxic vasoconstriction in rat lungs*. *J Appl Physiol* (1985), 2002. **92**(2): p. 527-34.

63. Shibahara, S., et al., *Hypoxia and heme oxygenases: oxygen sensing and regulation of expression*. *Antioxid Redox Signal*, 2007. **9**(12): p. 2209-25.
64. Michelakis, E.D., et al., *Diversity in mitochondrial function explains differences in vascular oxygen sensing*. *Circ Res*, 2002. **90**(12): p. 1307-15.
65. Pittman, R.N., *Regulation of tissue oxygenation*. [electronic book]. Colloquium series on integrated systems physiology, from molecule to function: 17. 2011: San Rafael, Calif. : Morgan & Claypool, 2011.
66. Roy, C.S. and J.G. Brown, *The Blood-Pressure and its Variations in the Arterioles, Capillaries and Smaller Veins*. *J Physiol*, 1880. **2**(5-6): p. 323-446.1.
67. Aaronson, P.I., et al., *Hypoxic pulmonary vasoconstriction: mechanisms and controversies*. *The Journal of Physiology*, 2006. **570**(Pt 1): p. 53-58.
68. Tune, J.D., M.W. Gorman, and E.O. Feigl, *Matching coronary blood flow to myocardial oxygen consumption*. *J Appl Physiol* (1985), 2004. **97**(1): p. 404-15.
69. Nakhostine, N. and D. Lamontagne, *Contribution of prostaglandins in hypoxia-induced vasodilation in isolated rabbit hearts. Relation to adenosine and KATP channels*. *Pflugers Arch*, 1994. **428**(5-6): p. 526-32.
70. Edlund, A., et al., *Release of two vasodilators, adenosine and prostacyclin, from isolated rabbit hearts during controlled hypoxia*. *The Journal of Physiology*, 1983. **340**: p. 487-501.
71. Crawford, J.H., et al., *Hypoxia, red blood cells, and nitrite regulate NO-dependent hypoxic vasodilation*. *Blood*, 2006. **107**(2): p. 566-574.
72. Dart, C. and N.B. Standen, *Adenosine-activated potassium current in smooth muscle cells isolated from the pig coronary artery*. *J Physiol*, 1993. **471**: p. 767-86.
73. Knot, H.J., P.A. Zimmermann, and M.T. Nelson, *Extracellular K(+)-induced hyperpolarizations and dilatations of rat coronary and cerebral arteries involve inward rectifier K(+) channels*. *J Physiol*, 1996. **492 (Pt 2)**: p. 419-30.
74. Vanhoutte, P.M., *Endothelium and control of vascular function. State of the Art lecture*. *Hypertension*, 1989. **13**(6 Pt 2): p. 658-67.
75. Vanhoutte, P.M. and H. Shimokawa, *Endothelium-derived relaxing factor and coronary vasospasm*. *Circulation*, 1989. **80**(1): p. 1-9.
76. Spilk, S., et al., *Endothelium-derived hyperpolarizing factor contributes to hypoxia-induced skeletal muscle vasodilation in humans*. *Am J Physiol Heart Circ Physiol*, 2013. **305**(11): p. H1639-45.
77. Smani, T., et al., *Reduction of Ca(2+) channel activity by hypoxia in human and porcine coronary myocytes*. *Cardiovasc Res*, 2002. **53**(1): p. 97-104.
78. Kwan, Y.W., R.M. Wadsworth, and K.A. Kane, *Hypoxia- and endothelium-mediated changes in the pharmacological responsiveness of circumflex coronary artery rings from the sheep*. *British Journal of Pharmacology*, 1989. **96**(4): p. 857-863.
79. Calderon-Sanchez, E., et al., *Hypoxia inhibits vasoconstriction induced by metabotropic Ca2+ channel-induced Ca2+ release in mammalian coronary arteries*. *Cardiovasc Res*, 2009. **82**(1): p. 115-24.
80. Bayliss, W.M., *On the local reactions of the arterial wall to changes of internal pressure*. *J Physiol*, 1902. **28**(3): p. 220-31.
81. Fedele, F., et al., *Role of ion channels in coronary microcirculation: a review of the literature*. *Future Cardiol*, 2013. **9**(6): p. 897-905.

82. Meininger, G.A. and M.J. Davis, *Cellular mechanisms involved in the vascular myogenic response*. Am J Physiol, 1992. **263**(3 Pt 2): p. H647-59.
83. Webb, R.C., *SMOOTH MUSCLE CONTRACTION AND RELAXATION*. Advances in Physiology Education, 2003. **27**(4): p. 201-206.
84. Hughes, A.D., *Calcium channels in vascular smooth muscle cells*. J Vasc Res, 1995. **32**(6): p. 353-70.
85. Korthuis, R.J., *Skeletal muscle circulation*. [electronic book]. Colloquium series on integrated systems physiology, from molecule to function: 23. 2011: San Rafael, Calif. : Morgan & Claypool, 2011.
86. Spudich, J.A., *The myosin swinging cross-bridge model*. Nat Rev Mol Cell Biol, 2001. **2**(5): p. 387-92.
87. Lai, A. and W.H. Frishman, *Rho-kinase inhibition in the therapy of cardiovascular disease*. Cardiol Rev, 2005. **13**(6): p. 285-92.
88. Standen, N.B. and J.M. Quayle, *K⁺ channel modulation in arterial smooth muscle*. Acta Physiol Scand, 1998. **164**(4): p. 549-57.
89. Moudgil, R., E.D. Michelakis, and S.L. Archer, *The role of k⁺ channels in determining pulmonary vascular tone, oxygen sensing, cell proliferation, and apoptosis: implications in hypoxic pulmonary vasoconstriction and pulmonary arterial hypertension*. Microcirculation, 2006. **13**(8): p. 615-32.
90. Goldstein, S.A., et al., *International Union of Pharmacology. LV. Nomenclature and molecular relationships of two-P potassium channels*. Pharmacol Rev, 2005. **57**(4): p. 527-40.
91. Lloyd, E.E., S.P. Marrelli, and R.M. Bryan, *cGMP does not activate two-pore domain K⁺ channels in cerebrovascular smooth muscle*. American Journal of Physiology - Heart and Circulatory Physiology, 2009. **296**(6): p. H1774-H1780.
92. Akata, T., *Cellular and molecular mechanisms regulating vascular tone. Part 2: regulatory mechanisms modulating Ca²⁺ mobilization and/or myofilament Ca²⁺ sensitivity in vascular smooth muscle cells*. J Anesth, 2007. **21**(2): p. 232-42.
93. Brayden, J.E., *Potassium channels in vascular smooth muscle*. Clin Exp Pharmacol Physiol, 1996. **23**(12): p. 1069-76.
94. Ko, E.A., et al., *Physiological roles of K⁺ channels in vascular smooth muscle cells*. J Smooth Muscle Res, 2008. **44**(2): p. 65-81.
95. Ghatta, S., et al., *Large-conductance, calcium-activated potassium channels: structural and functional implications*. Pharmacol Ther, 2006. **110**(1): p. 103-16.
96. Fédou, M., *Calcium-activated potassium channels and endothelial dysfunction: therapeutic options?* British Journal of Pharmacology, 2009. **156**(4): p. 545-562.
97. Fédou, M., *The endothelium*. [electronic book]. Colloquium series on integrated systems physiology, from molecule to function: 19. 2011: San Rafael, Calif. : Morgan & Claypool, 2011.
98. Noma, A., *ATP-regulated K⁺ channels in cardiac muscle*. Nature, 1983. **305**(5930): p. 147-8.
99. Quayle, J.M., C. Dart, and N.B. Standen, *The properties and distribution of inward rectifier potassium currents in pig coronary arterial smooth muscle*. J Physiol, 1996. **494** (Pt 3): p. 715-26.
100. Es-Salah-Lamoureux, Z., D.F. Steele, and D. Fedida, *Research into the therapeutic roles of*

- two-pore-domain potassium channels*. Trends Pharmacol Sci, 2010. **31**(12): p. 587-95.
101. Standen, N.B. and J.M. Quayle, *K⁺ channel modulation in arterial smooth muscle*. Acta Physiologica Scandinavica, 1998. **164**(4): p. 549-557.
 102. Purves, G.I., et al., *Exchange protein activated by cAMP (Epac) mediates cAMP-dependent but protein kinase A-insensitive modulation of vascular ATP-sensitive potassium channels*. The Journal of Physiology, 2009. **587**(14): p. 3639-3650.
 103. Sargent, C.A., et al., *The cardioprotective, vasorelaxant and electrophysiological profile of the large conductance calcium-activated potassium channel opener NS-004*. J Pharmacol Exp Ther, 1993. **266**(3): p. 1422-9.
 104. Edwards, G., et al., *Ion channel modulation by NS 1619, the putative BKCa channel opener, in vascular smooth muscle*. Br J Pharmacol, 1994. **113**(4): p. 1538-47.
 105. Bentzen, B.H., et al., *The small molecule NS11021 is a potent and specific activator of Ca²⁺-activated big-conductance K⁺ channels*. Mol Pharmacol, 2007. **72**(4): p. 1033-44.
 106. Blatz, A.L. and K.L. Magleby, *Calcium-activated potassium channels*. Trends in Neurosciences, 1987. **10**(11): p. 463-467.
 107. Wulff, H. and N.A. Castle, *Therapeutic potential of KCa3.1 blockers: an overview of recent advances, and promising trends*. Expert Review of Clinical Pharmacology, 2010. **3**(3): p. 385-396.
 108. Gluais, P., et al., *Role of SK(Ca) and IK(Ca) in endothelium-dependent hyperpolarizations of the guinea-pig isolated carotid artery*. British Journal of Pharmacology, 2005. **144**(4): p. 477-485.
 109. Mackie, A.R. and K.L. Byron, *Cardiovascular KCNQ (Kv7) Potassium Channels: Physiological Regulators and New Targets for Therapeutic Intervention*. Molecular Pharmacology, 2008. **74**(5): p. 1171-1179.
 110. Owsianik, G., et al., *Permeation and selectivity of TRP channels*. Annu Rev Physiol, 2006. **68**: p. 685-717.
 111. Bourinet, E., et al., *Calcium-permeable ion channels in pain signaling*. Physiol Rev, 2014. **94**(1): p. 81-140.
 112. Akata, T., *Cellular and molecular mechanisms regulating vascular tone. Part 1: basic mechanisms controlling cytosolic Ca²⁺ concentration and the Ca²⁺-dependent regulation of vascular tone*. J Anesth, 2007. **21**(2): p. 220-31.
 113. Cribbs, L.L., *Vascular Smooth Muscle Calcium Channels: Could "T" Be a Target?* Circulation Research, 2001. **89**(7): p. 560-562.
 114. Akaike, N., et al., *Low-voltage-activated calcium current in rat aorta smooth muscle cells in primary culture*. J Physiol, 1989. **416**: p. 141-60.
 115. Bean, B.P., et al., *Calcium channels in muscle cells isolated from rat mesenteric arteries: modulation by dihydropyridine drugs*. Circulation Research, 1986. **59**(2): p. 229-35.
 116. Ganitkevich, V. and G. Isenberg, *Contribution of two types of calcium channels to membrane conductance of single myocytes from guinea-pig coronary artery*. J Physiol, 1990. **426**: p. 19-42.
 117. Gollasch, M., et al., *L-type calcium channel expression depends on the differentiated state of vascular smooth muscle cells*. The FASEB Journal, 1998. **12**(7): p. 593-601.
 118. Yamamura, A., et al., *Dihydropyridine Ca(2+) channel blockers increase cytosolic [Ca(2+)] by activating Ca(2+)-sensing receptors in pulmonary arterial smooth muscle cells*. Circ Res,

2013. **112**(4): p. 640-50.
119. Ferrante, J., et al., *Binding of a 1,4-dihydropyridine calcium channel activator, (-) S bay K 8644, to cardiac preparations*. Biochemical and Biophysical Research Communications, 1989. **158**(1): p. 149-154.
 120. Hool, L.C., *What cardiologists should know about calcium ion channels and their regulation by reactive oxygen species*. Heart Lung Circ, 2007. **16**(5): p. 361-72.
 121. Isomoto, S. and Y. Kurachi, *Function, regulation, pharmacology, and molecular structure of ATP-sensitive K⁺ channels in the cardiovascular system*. J Cardiovasc Electrophysiol, 1997. **8**(12): p. 1431-46.
 122. Zhuo, M.L., et al., *KATP channel: relation with cell metabolism and role in the cardiovascular system*. Int J Biochem Cell Biol, 2005. **37**(4): p. 751-64.
 123. Foster, M.N. and W.A. Coetzee, *KATP Channels in the Cardiovascular System*. Physiol Rev, 2016. **96**(1): p. 177-252.
 124. Zhang, C., et al., *Identification and characterization of a novel member of the ATP-sensitive K⁺ channel subunit family, Kir6.3, in zebrafish*. Physiol Genomics, 2006. **24**(3): p. 290-7.
 125. Babenko, A.P., L. Aguilar-Bryan, and J. Bryan, *A view of sur/KIR6.X, KATP channels*. Annu Rev Physiol, 1998. **60**: p. 667-87.
 126. Tinker, A., Q. Aziz, and A. Thomas, *The role of ATP-sensitive potassium channels in cellular function and protection in the cardiovascular system*. Br J Pharmacol, 2014. **171**(1): p. 12-23.
 127. Mikhailov, M.V., et al., *3-D structural and functional characterization of the purified KATP channel complex Kir6.2-SUR1*. Embo j, 2005. **24**(23): p. 4166-75.
 128. Inagaki, N., et al., *A family of sulfonylurea receptors determines the pharmacological properties of ATP-sensitive K⁺ channels*. Neuron, 1996. **16**(5): p. 1011-7.
 129. Seino, S., *ATP-sensitive potassium channels: a model of heteromultimeric potassium channel/receptor assemblies*. Annu Rev Physiol, 1999. **61**: p. 337-62.
 130. Ashcroft, F.M. and F.M. Gribble, *New windows on the mechanism of action of K(ATP) channel openers*. Trends Pharmacol Sci, 2000. **21**(11): p. 439-45.
 131. Quayle, J.M. and N.B. Standen, *KATP channels in vascular smooth muscle*. Cardiovasc Res, 1994. **28**(6): p. 797-804.
 132. Quayle, J.M., M.T. Nelson, and N.B. Standen, *ATP-sensitive and inwardly rectifying potassium channels in smooth muscle*. Physiol Rev, 1997. **77**(4): p. 1165-232.
 133. Tucker, S.J., et al., *Truncation of Kir6.2 produces ATP-sensitive K⁺ channels in the absence of the sulfonylurea receptor*. Nature, 1997. **387**(6629): p. 179-83.
 134. Ashcroft, F.M. and P. Rorsman, *Electrophysiology of the pancreatic β -cell*. Progress in Biophysics and Molecular Biology, 1989. **54**(2): p. 87-143.
 135. Nichols, C.G., et al., *Adenosine diphosphate as an intracellular regulator of insulin secretion*. Science, 1996. **272**(5269): p. 1785-7.
 136. Babenko, A.P. and J. Bryan, *Sur domains that associate with and gate KATP pores define a novel gatekeeper*. J Biol Chem, 2003. **278**(43): p. 41577-80.
 137. Bienengraeber, M., et al., *ATPase activity of the sulfonylurea receptor: a catalytic function for the KATP channel complex*. Faseb j, 2000. **14**(13): p. 1943-52.
 138. Zingman, L.V., et al., *Signaling in channel/enzyme multimers: ATPase transitions in SUR module gate ATP-sensitive K⁺ conductance*. Neuron, 2001. **31**(2): p. 233-45.
 139. Ueda, K., N. Inagaki, and S. Seino, *MgADP antagonism to Mg²⁺-independent ATP binding*

- of the sulfonylurea receptor SUR1. *J Biol Chem*, 1997. **272**(37): p. 22983-6.
140. Ortiz, D., et al., *Reinterpreting the action of ATP analogs on K(ATP) channels*. *J Biol Chem*, 2013. **288**(26): p. 18894-902.
 141. Ueda, K., et al., *Cooperative binding of ATP and MgADP in the sulfonylurea receptor is modulated by glibenclamide*. *Proc Natl Acad Sci U S A*, 1999. **96**(4): p. 1268-72.
 142. Koster, J.C., et al., *Targeted overactivity of β cell K(ATP) channels induces profound neonatal diabetes*. *Cell*, 2000. **100**(6): p. 645-654.
 143. Koster, J.C., et al., *Tolerance for ATP-Insensitive KATP Channels in Transgenic Mice*. *Circulation Research*, 2001. **89**(11): p. 1022-1029.
 144. Mislser, S., et al., *Electrophysiology of stimulus-secretion coupling in human beta-cells*. *Diabetes*, 1992. **41**(10): p. 1221-8.
 145. Carmeliet, E., *Cardiac ionic currents and acute ischemia: from channels to arrhythmias*. *Physiol Rev*, 1999. **79**(3): p. 917-1017.
 146. Suzuki, M., et al., *Functional roles of cardiac and vascular ATP-sensitive potassium channels clarified by Kir6.2-knockout mice*. *Circ Res*, 2001. **88**(6): p. 570-7.
 147. Murry, C.E., R.B. Jennings, and K.A. Reimer, *Preconditioning with ischemia: a delay of lethal cell injury in ischemic myocardium*. *Circulation*, 1986. **74**(5): p. 1124-36.
 148. Nichols, C.G. and W.J. Lederer, *The regulation of ATP-sensitive K⁺ channel activity in intact and permeabilized rat ventricular myocytes*. *J Physiol*, 1990. **423**: p. 91-110.
 149. Brayden, J.E., *Functional roles of KATP channels in vascular smooth muscle*. *Clin Exp Pharmacol Physiol*, 2002. **29**(4): p. 312-6.
 150. Kovalev, H., et al., *Molecular analysis of the subtype-selective inhibition of cloned KATP channels by PNU-37883A*. *Br J Pharmacol*, 2004. **141**(5): p. 867-73.
 151. Meisheri, K.D., et al., *4-morpholinecarboximidine-N-1-adamantyl-N'-cyclohexylhydrochloride (U-37883A): pharmacological characterization of a novel antagonist of vascular ATP-sensitive K⁺ channel openers*. *J Pharmacol Exp Ther*, 1993. **266**(2): p. 655-65.
 152. Wellman, G.C., et al., *Inhibition of vascular K(ATP) channels by U-37883A: a comparison with cardiac and skeletal muscle*. *Br J Pharmacol*, 1999. **128**(4): p. 909-16.
 153. Findlay, I., *Sulphonylurea drugs no longer inhibit ATP-sensitive K⁺ channels during metabolic stress in cardiac muscle*. *J Pharmacol Exp Ther*, 1993. **266**(1): p. 456-67.
 154. Ripoll, C., W.J. Lederer, and C.G. Nichols, *On the mechanism of inhibition of KATP channels by glibenclamide in rat ventricular myocytes*. *J Cardiovasc Electrophysiol*, 1993. **4**(1): p. 38-47.
 155. Binder, W.H., V. Barragan, and F.M. Menger, *Domains and rafts in lipid membranes*. *Angew Chem Int Ed Engl*, 2003. **42**(47): p. 5802-27.
 156. Simons, K. and E. Ikonen, *Functional rafts in cell membranes*. *Nature*, 1997. **387**(6633): p. 569-72.
 157. Sampson, L.J., et al., *Caveolae localize protein kinase A signaling to arterial ATP-sensitive potassium channels*. *Circ Res*, 2004. **95**(10): p. 1012-8.
 158. Maguy, A., T.E. Hebert, and S. Nattel, *Involvement of lipid rafts and caveolae in cardiac ion channel function*. *Cardiovasc Res*, 2006. **69**(4): p. 798-807.
 159. Dart, C., *Lipid microdomains and the regulation of ion channel function*. *J Physiol*, 2010. **588**(Pt 17): p. 3169-78.

160. Singer, S.J. and G.L. Nicolson, *The fluid mosaic model of the structure of cell membranes*. Science, 1972. **175**(4023): p. 720-31.
161. Levitan, I., et al., *Cholesterol and ion channels*. Subcell Biochem, 2010. **51**: p. 509-49.
162. Enkvetchakul, D. and C.G. Nichols, *Gating mechanism of KATP channels: function fits form*. J Gen Physiol, 2003. **122**(5): p. 471-80.
163. Zerangue, N., et al., *A new ER trafficking signal regulates the subunit stoichiometry of plasma membrane K(ATP) channels*. Neuron, 1999. **22**(3): p. 537-48.
164. Garg, V., J. Jiao, and K. Hu, *Regulation of ATP-sensitive K⁺ channels by caveolin-enriched microdomains in cardiac myocytes*. Cardiovasc Res, 2009. **82**(1): p. 51-8.
165. Davies, L.M., et al., *Interaction with caveolin-1 modulates vascular ATP-sensitive potassium (KATP) channel activity*. J Physiol, 2010. **588**(Pt 17): p. 3255-66.
166. Antcliff, J.F., et al., *Functional analysis of a structural model of the ATP-binding site of the KATP channel Kir6.2 subunit*. Embo j, 2005. **24**(2): p. 229-39.
167. Selivanov, V.A., et al., *Nucleotide-gated K(ATP) channels integrated with creatine and adenylate kinases: Amplification, tuning and sensing of energetic signals in the compartmentalized cellular environment*. Molecular and cellular biochemistry, 2004. **256-257**(1-2): p. 243-256.
168. Carrasco, A.J., et al., *Adenylate kinase phosphotransfer communicates cellular energetic signals to ATP-sensitive potassium channels*. Proc Natl Acad Sci U S A, 2001. **98**(13): p. 7623-8.
169. Crawford, R.M., et al., *Creatine kinase is physically associated with the cardiac ATP-sensitive K⁺ channel in vivo*. Faseb j, 2002. **16**(1): p. 102-4.
170. Crawford, R.M., et al., *M-LDH serves as a sarcolemmal K(ATP) channel subunit essential for cell protection against ischemia*. Embo j, 2002. **21**(15): p. 3936-48.
171. Weiss, J.N. and S.T. Lamp, *Glycolysis preferentially inhibits ATP-sensitive K⁺ channels in isolated guinea pig cardiac myocytes*. Science, 1987. **238**(4823): p. 67-9.
172. Berg, J.M., et al., *Biochemistry*. 2015: New York : W.H. Freeman, [2015]. 8th ed.
173. Brand, M.D., *The efficiency and plasticity of mitochondrial energy transduction*. Biochem Soc Trans, 2005. **33**(Pt 5): p. 897-904.
174. Umbrello, M., et al., *The Key Role of Nitric Oxide in Hypoxia: Hypoxic Vasodilation and Energy Supply-Demand Matching*.
175. Rolfe, D.F. and G.C. Brown, *Cellular energy utilization and molecular origin of standard metabolic rate in mammals*. Physiol Rev, 1997. **77**(3): p. 731-58.
176. Liemburg-Apers, D.C., et al., *Quantitative glucose and ATP sensing in mammalian cells*. Pharm Res, 2011. **28**(11): p. 2745-57.
177. Divakaruni, A.S. and M.D. Brand, *The Regulation and Physiology of Mitochondrial Proton Leak*. Physiology, 2011. **26**(3): p. 192-205.
178. Nicholls, D.G. and S.J. Ferguson, *Bioenergetics*. Online access with subscription: Elsevier (Sciencedirect Freedom Collection). 2013: Amsterdam : Academic Press, 2013. Fourth edition.
179. Campanella, M., et al., *IF(1): setting the pace of the F(1)F(o)-ATP synthase*. Trends Biochem Sci, 2009. **34**(7): p. 343-50.
180. Hill, B.G., et al., *Integration of cellular bioenergetics with mitochondrial quality control and autophagy*. Biological Chemistry, 2012. **393**(12): p. 1485-1512.

181. Divakaruni, A.S., et al., *Analysis and interpretation of microplate-based oxygen consumption and pH data*. Methods in Enzymology. Vol. 547. 2014: Academic Press Inc. 275-307.
182. Kennedy, H.J., et al., *Glucose generates sub-plasma membrane ATP microdomains in single islet beta-cells. Potential role for strategically located mitochondria*. J Biol Chem, 1999. **274**(19): p. 13281-91.
183. Dranka, B.P., et al., *Assessing bioenergetic function in response to oxidative stress by metabolic profiling*. Free Radical Biology and Medicine, 2011. **51**(9): p. 1621-1635.
184. Voronina, S.G., et al., *Dynamic changes in cytosolic and mitochondrial ATP levels in pancreatic acinar cells*. Gastroenterology, 2010. **138**(5): p. 1976-87.
185. Berg, J., Y.P. Hung, and G. Yellen, *A genetically encoded fluorescent reporter of ATP:ADP ratio*. Nat Methods, 2009. **6**(2): p. 161-6.
186. Tantama, M., et al., *Imaging energy status in live cells with a fluorescent biosensor of the intracellular ATP-to-ADP ratio*. Nat Commun, 2013. **4**: p. 2550.
187. Tantama, M. and G. Yellen, *Imaging Changes in the Cytosolic ATP-to-ADP Ratio*. METHODS IN ENZYMOLOGY, 2014. **547**: p. 355-372.
188. Depry, C., M.D. Allen, and J. Zhang, *Visualization of PKA activity in plasma membrane microdomains*. Mol Biosyst, 2011. **7**(1): p. 52-8.
189. Zacharias, D.A., et al., *Partitioning of lipid-modified monomeric GFPs into membrane microdomains of live cells*. Science, 2002. **296**(5569): p. 913-6.
190. Yamamura, H., Y. Suzuki, and Y. Imaizumi, *New light on ion channel imaging by total internal reflection fluorescence (TIRF) microscopy*. J Pharmacol Sci, 2015. **128**(1): p. 1-7.
191. Mattheyses, A.L., S.M. Simon, and J.Z. Rappoport, *Imaging with total internal reflection fluorescence microscopy for the cell biologist*. J Cell Sci, 2010. **123**(Pt 21): p. 3621-8.
192. Yarrow, J.C., et al., *A high-throughput cell migration assay using scratch wound healing, a comparison of image-based readout methods*. BMC Biotechnology, 2004. **4**: p. 21-9.
193. Friedl, P., Y. Hegerfeldt, and M. Tusch, *Collective cell migration in morphogenesis and cancer*. Int J Dev Biol, 2004. **48**(5-6): p. 441-9.
194. Imamura, H., et al., *Visualization of ATP levels inside single living cells with fluorescence resonance energy transfer-based genetically encoded indicators*. Proc Natl Acad Sci U S A, 2009. **106**(37): p. 15651-6.
195. Perry, S.W., et al., *Mitochondrial membrane potential probes and the proton gradient: a practical usage guide*. Biotechniques, 2011. **50**(2): p. 98-115.
196. Li, J., et al., *Oscillations of sub-membrane ATP in glucose-stimulated beta cells depend on negative feedback from Ca(2+)*. Diabetologia, 2013. **56**(7): p. 1577-86.
197. Tantama, M., Y.P. Hung, and G. Yellen, *Imaging intracellular pH in live cells with a genetically encoded red fluorescent protein sensor*. J Am Chem Soc, 2011. **133**(26): p. 10034-7.
198. Divakaruni, A.S. and M.D. Brand, *The regulation and physiology of mitochondrial proton leak*. Physiology (Bethesda), 2011. **26**(3): p. 192-205.
199. Herst, P.M. and M.V. Berridge, *Cell surface oxygen consumption: a major contributor to cellular oxygen consumption in glycolytic cancer cell lines*. Biochim Biophys Acta, 2007. **1767**(2): p. 170-7.
200. Wu, M., et al., *Multiparameter metabolic analysis reveals a close link between attenuated mitochondrial bioenergetic function and enhanced glycolysis dependency in human tumor*

- cells. *Am J Physiol Cell Physiol*, 2007. **292**(1): p. C125-36.
201. Shen, Y., et al., *Carnosine inhibits the proliferation of human gastric cancer SGC-7901 cells through both of the mitochondrial respiration and glycolysis pathways*. *PLoS One*, 2014. **9**(8): p. e104632.
 202. Robergs, R.A., F. Ghasvand, and D. Parker, *Biochemistry of exercise-induced metabolic acidosis*. *Am J Physiol Regul Integr Comp Physiol*, 2004. **287**(3): p. R502-16.
 203. Quayle, J.M., et al., *Effects of hypoxia, anoxia, and metabolic inhibitors on KATP channels in rat femoral artery myocytes*. *Am J Physiol Heart Circ Physiol*, 2006. **291**(1): p. H71-80.
 204. Nicholls, D.G. and S.L. Budd, *Mitochondria and neuronal survival*. *Physiol Rev*, 2000. **80**(1): p. 315-60.
 205. Skulachev, V.P., *Mitochondrial filaments and clusters as intracellular power-transmitting cables*. *Trends Biochem Sci*, 2001. **26**(1): p. 23-9.
 206. Chen, L.B., *Fluorescent labeling of mitochondria*. *Methods Cell Biol*, 1989. **29**: p. 103-23.
 207. Davis, S., et al., *Mitochondrial and plasma membrane potentials cause unusual accumulation and retention of rhodamine 123 by human breast adenocarcinoma-derived MCF-7 cells*. *J Biol Chem*, 1985. **260**(25): p. 13844-50.
 208. Wang, J., et al., *Acute Exposure to Low Glucose Rapidly Induces Endothelial Dysfunction and Mitochondrial Oxidative Stress: Role for AMP Kinase*. *Arteriosclerosis, Thrombosis, and Vascular Biology*, 2012. **32**(3): p. 712-720.
 209. Marambio, P., et al., *Glucose deprivation causes oxidative stress and stimulates aggresome formation and autophagy in cultured cardiac myocytes*. *Biochimica et Biophysica Acta (BBA) - Molecular Basis of Disease*, 2010. **1802**(6): p. 509-518.
 210. Moreno-Sanchez, R., et al., *Energy metabolism in tumor cells*. *Febs j*, 2007. **274**(6): p. 1393-418.
 211. Diepart, C., et al., *Comparison of methods for measuring oxygen consumption in tumor cells in vitro*. *Anal Biochem*, 2010. **396**(2): p. 250-6.
 212. Nadanaciva, S., et al., *Assessment of drug-induced mitochondrial dysfunction via altered cellular respiration and acidification measured in a 96-well platform*. *J Bioenerg Biomembr*, 2012. **44**(4): p. 421-37.
 213. Kamishima, T. and J.G. McCarron, *Regulation of the cytosolic Ca²⁺ concentration by Ca²⁺ stores in single smooth muscle cells from rat cerebral arteries*. *J Physiol*, 1997. **501** (Pt 3): p. 497-508.
 214. Madden, J.A., P.A. Keller, and J.G. Kleinman, *Changes in smooth muscle cell pH during hypoxic pulmonary vasoconstriction: a possible role for ion transporters*. *Physiol Res*, 2000. **49**(5): p. 561-6.
 215. Boedtkjer, E., J. Praetorius, and C. Aalkjaer, *NBCn1 (slc4a7) mediates the Na⁺-dependent bicarbonate transport important for regulation of intracellular pH in mouse vascular smooth muscle cells*. *Circ Res*, 2006. **98**(4): p. 515-23.
 216. Kiang, J.G., L.C. McKinney, and E.K. Gallin, *Heat induces intracellular acidification in human A-431 cells: role of Na⁽⁺⁾-H⁺ exchange and metabolism*. *Am J Physiol*, 1990. **259**(5 Pt 1): p. C727-37.
 217. Brown, S.E., et al., *ATP-sensitive Na⁽⁺⁾-H⁺ antiport in type II alveolar epithelial cells*. *Am J Physiol*, 1991. **261**(6 Pt 1): p. C954-63.
 218. Kamishima, T. and J.M. Quayle, *Mitochondrial Ca²⁺ uptake is important over low [Ca²⁺]_i*

- range in arterial smooth muscle. *Am J Physiol Heart Circ Physiol*, 2002. **283**(6): p. H2431-9.
219. Ward, M.W., et al., *Mitochondrial membrane potential and glutamate excitotoxicity in cultured cerebellar granule cells*. *J Neurosci*, 2000. **20**(19): p. 7208-19.
220. Emaus, R.K., R. Grunwald, and J.J. Lemasters, *Rhodamine 123 as a probe of transmembrane potential in isolated rat-liver mitochondria: spectral and metabolic properties*. *Biochimica et Biophysica Acta (BBA) - Bioenergetics*, 1986. **850**(3): p. 436-448.
221. Wang, Y.-L. and D.L. Taylor, *Fluorescence microscopy of living cells in culture*. *Methods in cell biology*: 29, 30. 1989: San Diego: Academic Press, 1989.
222. Oropesa, M., et al., *Apoptotic microtubule network organization and maintenance depend on high cellular ATP levels and energized mitochondria*. *Apoptosis*, 2011. **16**(4): p. 404-24.
223. Domenis, R., et al., *Mitochondrial bioenergetic profile and responses to metabolic inhibition in human hepatocarcinoma cell lines with distinct differentiation characteristics*. *J Bioenerg Biomembr*, 2011. **43**(5): p. 493-505.
224. Saridey, S.K., et al., *PiggyBac Transposon-based Inducible Gene Expression In Vivo After Somatic Cell Gene Transfer*. *Mol Ther*, 2009. **17**(12): p. 2115-2120.
225. Inada, E., et al., *PiggyBac transposon-mediated gene delivery efficiently generates stable transfectants derived from cultured primary human deciduous tooth dental pulp cells (HDDPCs) and HDDPC-derived iPS cells*. In *J Oral Sci*, 2015. **7**(3): p. 144-154.
226. Ivics, Z. and Z. Izsvák, *The expanding universe of transposon technologies for gene and cell engineering*. *Mobile DNA*, 2010. **1**: p. 25-25.
227. Wasala, N.B., J.H. Shin, and D. Duan, *The evolution of heart gene delivery vectors*. *J Gene Med*, 2011. **13**(10): p. 557-65.
228. Di Pasquale, E., et al., *Lentiviral vectors and cardiovascular diseases: a genetic tool for manipulating cardiomyocyte differentiation and function*. *Gene Ther*, 2012. **19**(6): p. 642-648.
229. Kantor, B., et al., *Methods for gene transfer to the central nervous system*. *Adv Genet*, 2014. **87**: p. 125-97.
230. Shaw, A. and K. Cornetta, *Design and Potential of Non-Integrating Lentiviral Vectors*. *Biomedicines*, 2014. **2**(1): p. 14.
231. Yasutsugu, S. and S. Youichi, *Gene Regulatable Lentiviral Vector System*. 2011: InTech. 285-308.
232. Atchison, R.W., B.C. Casto, and W.M. Hammon, *ADENOVIRUS-ASSOCIATED DEFECTIVE VIRUS PARTICLES*. *Science*, 1965. **149**(3685): p. 754-6.
233. Fields, B.N., D.M. Knipe, and P.M. Howley, *Fields virology*. 2007, Philadelphia: Wolters Kluwer Health/Lippincott Williams & Wilkins.
234. Mohan, R.R., J.T. Rodier, and A. Sharma, *Corneal gene therapy: basic science and translational perspective*. *Ocul Surf*, 2013. **11**(3): p. 150-64.
235. Dull, T., et al., *A third-generation lentivirus vector with a conditional packaging system*. *J Virol*, 1998. **72**(11): p. 8463-71.
236. Kutner, R.H., X.Y. Zhang, and J. Reiser, *Production, concentration and titration of pseudotyped HIV-1-based lentiviral vectors*. *Nat Protoc*, 2009. **4**(4): p. 495-505.
237. Li, M., et al., *Production of lentiviral vectors for transducing cells from the central nervous system*. *J Vis Exp*, 2012(63): p. e4031.
238. Nakanishi, S., et al., *Wortmannin, a microbial product inhibitor of myosin light chain kinase*.

- J Biol Chem, 1992. **267**(4): p. 2157-63.
239. Mattheyses, A.L., S.M. Simon, and J.Z. Rappoport, *Imaging with total internal reflection fluorescence microscopy for the cell biologist*. Journal of Cell Science, 2010. **123**(21): p. 3621-3628.
 240. Escors, D. and K. Breckpot, *Lentiviral vectors in gene therapy: their current status and future potential*. Arch Immunol Ther Exp (Warsz), 2010. **58**(2): p. 107-19.
 241. Chira, S., et al., *Progresses towards safe and efficient gene therapy vectors*. Oncotarget, 2015. **6**(31): p. 30675-703.
 242. Nayerossadat, N., T. Maedeh, and P.A. Ali, *Viral and nonviral delivery systems for gene delivery*. Adv Biomed Res, 2012. **1**: p. 27.
 243. Veech, R.L., et al., *Cytosolic phosphorylation potential*. J Biol Chem, 1979. **254**(14): p. 6538-47.
 244. Traut, T.W., *Physiological concentrations of purines and pyrimidines*. Mol Cell Biochem, 1994. **140**(1): p. 1-22.
 245. Sampson, L.J., et al., *Angiotensin II-activated protein kinase C targets caveolae to inhibit aortic ATP-sensitive potassium channels*. Cardiovasc Res, 2007. **76**(1): p. 61-70.
 246. Liu, Y., et al., *Mitochondrial ATP-Dependent Potassium Channels*. Novel Effectors of Cardioprotection?, 1998. **97**(24): p. 2463-2469.
 247. Rosenberg, S.A., et al., *Gene transfer into humans--immunotherapy of patients with advanced melanoma, using tumor-infiltrating lymphocytes modified by retroviral gene transduction*. N Engl J Med, 1990. **323**(9): p. 570-8.
 248. Katz, M.G., et al., *Gene therapy delivery systems for enhancing viral and nonviral vectors for cardiac diseases: current concepts and future applications*. Hum Gene Ther, 2013. **24**(11): p. 914-27.
 249. Asokan, A. and R.J. Samulski, *An emerging adeno-associated viral vector pipeline for cardiac gene therapy*. Hum Gene Ther, 2013. **24**(11): p. 906-13.
 250. Mustafa, A.K., et al., *Hydrogen sulfide as endothelium-derived hyperpolarizing factor sulfhydrates potassium channels*. Circ Res, 2011. **109**(11): p. 1259-68.
 251. Quayle, J.M., et al., *Pharmacology of ATP-sensitive K⁺ currents in smooth muscle cells from rabbit mesenteric artery*. Am J Physiol, 1995. **269**(5 Pt 1): p. C1112-8.
 252. Quayle, J.M., et al., *Inward rectifier K⁺ currents in smooth muscle cells from rat resistance-sized cerebral arteries*. Am J Physiol, 1993. **265**(5 Pt 1): p. C1363-70.
 253. Chamley-Campbell, J., G.R. Campbell, and R. Ross, *The smooth muscle cell in culture*. Physiol Rev, 1979. **59**(1): p. 1-61.
 254. Mitchell, R.W., et al., *Selective restoration of calcium coupling to muscarinic M(3) receptors in contractile cultured airway myocytes*. Am J Physiol Lung Cell Mol Physiol, 2000. **278**(5): p. L1091-100.
 255. Apell, H.J. and B. Bersch, *Oxonol VI as an optical indicator for membrane potentials in lipid vesicles*. Biochim Biophys Acta, 1987. **903**(3): p. 480-94.
 256. Klapperstück, T., et al., *Methodological aspects of measuring absolute values of membrane potential in human cells by flow cytometry*. Cytometry Part A, 2009. **75A**(7): p. 593-608.
 257. Epps, D.E., M.L. Wolfe, and V. Groppi, *Characterization of the steady-state and dynamic fluorescence properties of the potential-sensitive dye bis-(1,3-dibutylbarbituric acid)trimethine oxonol (Dibac4(3)) in model systems and cells*. Chem Phys Lipids, 1994.

- 69(2): p. 137-50.
258. Tanaka, Y., et al., *Molecular constituents of maxi KCa channels in human coronary smooth muscle: predominant alpha + beta subunit complexes*. J Physiol, 1997. **502** (Pt 3): p. 545-57.
259. Dworetzky, S.I., et al., *Phenotypic alteration of a human BK (hSlo) channel by hSlobeta subunit coexpression: changes in blocker sensitivity, activation/relaxation and inactivation kinetics, and protein kinase A modulation*. J Neurosci, 1996. **16**(15): p. 4543-50.
260. Hill, M.A., et al., *Large Conductance, Ca(2+)-Activated K(+) Channels (BK(Ca)) and Arteriolar Myogenic Signaling*. FEBS letters, 2010. **584**(10): p. 2033-2042.
261. Maher, J., et al., *Smooth muscle relaxation and activation of the large conductance Ca(++) – activated K(+) (BK(Ca)) channel by novel oestrogens*. British Journal of Pharmacology, 2013. **169**(5): p. 1153-1165.
262. Bushnell, W.R., K. Mendgen, and Z. Liu, *Accumulation of potentiometric and other dyes in haustoria of Erysiphe graminis in living host cell*. Physiological and Molecular Plant Pathology, 1987. **31**(2): p. 237-250.
263. Woods, N.M., K.S. Cuthbertson, and P.H. Cobbold, *Repetitive transient rises in cytoplasmic free calcium in hormone-stimulated hepatocytes*. Nature, 1986. **319**(6054): p. 600-2.
264. Taggart, M.J. and S. Wray, *Hypoxia and smooth muscle function: key regulatory events during metabolic stress*. J Physiol, 1998. **509** (Pt 2): p. 315-25.
265. Gu, M., et al., *Ca2+-independent hypoxic vasorelaxation in porcine coronary artery*. J Physiol, 2005. **562**(Pt 3): p. 839-46.
266. Urena, J., A. Franco-Obregon, and J. Lopez-Barneo, *Contrasting effects of hypoxia on cytosolic Ca2+ spikes in conduit and resistance myocytes of the rabbit pulmonary artery*. J Physiol, 1996. **496** (Pt 1): p. 103-9.
267. Herrera, G.M. and B.R. Walker, *Involvement of L-type calcium channels in hypoxic relaxation of vascular smooth muscle*. J Vasc Res, 1998. **35**(4): p. 265-73.
268. Gerasimenko, O.V., et al., *ATP-dependent accumulation and inositol trisphosphate- or cyclic ADP-ribose-mediated release of Ca2+ from the nuclear envelope*. Cell, 1995. **80**(3): p. 439-44.
269. Esfandiarei, M., et al., *Waves of calcium depletion in the sarcoplasmic reticulum of vascular smooth muscle cells: an inside view of spatiotemporal Ca2+ regulation*. PLoS One, 2013. **8**(2): p. e55333.
270. Cartin, L., K.M. Lounsbury, and M.T. Nelson, *Coupling of Ca(2+) to CREB activation and gene expression in intact cerebral arteries from mouse : roles of ryanodine receptors and voltage-dependent Ca(2+) channels*. Circ Res, 2000. **86**(7): p. 760-7.
271. Dolmetsch, R.E., K. Xu, and R.S. Lewis, *Calcium oscillations increase the efficiency and specificity of gene expression*. Nature, 1998. **392**(6679): p. 933-936.
272. Williams, G.S., et al., *Mitochondrial calcium uptake*. Proc Natl Acad Sci U S A, 2013. **110**(26): p. 10479-86.
273. Chalmers, S. and J.G. McCarron, *The mitochondrial membrane potential and Ca2+ oscillations in smooth muscle*. J Cell Sci, 2008. **121**(Pt 1): p. 75-85.
274. Palty, R., M. Hershinkel, and I. Sekler, *Molecular identity and functional properties of the mitochondrial Na+/Ca2+ exchanger*. J Biol Chem, 2012. **287**(38): p. 31650-7.
275. Glancy, B. and R.S. Balaban, *Role of mitochondrial Ca2+ in the regulation of cellular*

- energetics*. *Biochemistry*, 2012. **51**(14): p. 2959-73.
276. Szado, T., et al., *Agonist-induced mitochondrial Ca²⁺ transients in smooth muscle*. *FASEB J*, 2003. **17**(1): p. 28-37.
277. Worth, N.F., et al., *Vascular smooth muscle cell phenotypic modulation in culture is associated with reorganisation of contractile and cytoskeletal proteins*. *Cell Motil Cytoskeleton*, 2001. **49**(3): p. 130-45.
278. Campbell, G.R. and J.H. Campbell, *Smooth muscle phenotypic changes in arterial wall homeostasis: implications for the pathogenesis of atherosclerosis*. *Exp Mol Pathol*, 1985. **42**(2): p. 139-62.
279. Guillemin, K. and M.A. Krasnow, *The hypoxic response: huffing and HIFing*. *Cell*, 1997. **89**(1): p. 9-12.
280. Marzo, F., et al., *Erythropoietin in heart and vessels: focus on transcription and signalling pathways*. *J Thromb Thrombolysis*, 2008. **26**(3): p. 183-7.
281. Lorier, G., C. Tourino, and R.A. Kalil, *Coronary angiogenesis as an endogenous response to myocardial ischemia in adults*. *Arq Bras Cardiol*, 2011. **97**(6): p. e140-8.
282. Michiels, C., *Physiological and Pathological Responses to Hypoxia*. *The American Journal of Pathology*, 2004. **164**(6): p. 1875-1882.
283. Takahashi, M., et al., *[Role of thrombospondin-1 in hypoxia-induced migration of human vascular smooth muscle cells]*. *Yakugaku Zasshi*, 2008. **128**(3): p. 377-83.
284. Wieser, W. and G. Krumschnabel, *Hierarchies of ATP-consuming processes: direct compared with indirect measurements, and comparative aspects*. *Biochem J*, 2001. **355**(Pt 2): p. 389-95.
285. Kourembanas, S., et al., *Hypoxic responses of vascular cells*. *Chest*, 1998. **114**(1 Suppl): p. 25s-28s.
286. Minamino, T., S.A. Mitsialis, and S. Kourembanas, *Hypoxia extends the life span of vascular smooth muscle cells through telomerase activation*. *Mol Cell Biol*, 2001. **21**(10): p. 3336-42.
287. Dick, G.M. and J.D. Tune, *Role of potassium channels in coronary vasodilation*. *Exp Biol Med (Maywood)*, 2010. **235**(1): p. 10-22.
288. Beech, D.J., *Ion channel switching and activation in smooth-muscle cells of occlusive vascular diseases*. *Biochem Soc Trans*, 2007. **35**(Pt 5): p. 890-4.
289. Berra-Romani, R., et al., *Ca²⁺ handling is altered when arterial myocytes progress from a contractile to a proliferative phenotype in culture*. *Am J Physiol Cell Physiol*, 2008. **295**(3): p. C779-90.
290. Munoz, E., et al., *Intracellular Ca(2+) remodeling during the phenotypic journey of human coronary smooth muscle cells*. *Cell Calcium*, 2013. **54**(5): p. 375-85.
291. Miguel-Velado, E., et al., *Cell cycle-dependent expression of Kv3.4 channels modulates proliferation of human uterine artery smooth muscle cells*. *Cardiovasc Res*, 2010. **86**(3): p. 383-91.
292. Gavrilova-Ruch, O., et al., *Effects of imipramine on ion channels and proliferation of IGR1 melanoma cells*. *J Membr Biol*, 2002. **188**(2): p. 137-49.
293. Wonderlin, W.F. and J.S. Strobl, *Potassium channels, proliferation and G1 progression*. *J Membr Biol*, 1996. **154**(2): p. 91-107.
294. Takuwa, N., W. Zhou, and Y. Takuwa, *Calcium, calmodulin and cell cycle progression*. *Cell Signal*, 1995. **7**(2): p. 93-104.

295. Ono, T., et al., *Broad antiproliferative effects of benidipine on cultured human mesangial cells in cell cycle phases*. Am J Nephrol, 2002. **22**(5-6): p. 581-6.
296. Ahmed, A., et al., *Differential effects of Ca²⁺ channel blockers on Ca²⁺ transients and cell cycle progression in vascular smooth muscle cells*. Eur J Pharmacol, 1998. **344**(2-3): p. 323-31.
297. Lepple-Wienhues, A., et al., *K⁺ channels and the intracellular calcium signal in human melanoma cell proliferation*. J Membr Biol, 1996. **151**(2): p. 149-57.
298. Lu, K.P. and A.R. Means, *Regulation of the cell cycle by calcium and calmodulin*. Endocr Rev, 1993. **14**(1): p. 40-58.
299. Owens, G.K., *Regulation of differentiation of vascular smooth muscle cells*. Physiological Reviews, 1995. **75**(3): p. 487-517.
300. Wang, Z.-y., et al., *Enhancing mesenchymal stem cell response using uniaxially stretched poly(ϵ -caprolactone) film micropatterns for vascular tissue engineering application*. Journal of Materials Chemistry B, 2014. **2**(35): p. 5898-5909.
301. Pozarowski, P. and Z. Darzynkiewicz, *Analysis of Cell Cycle by Flow Cytometry*. 2004. p. 301-311.
302. Kurien, B.T. and R.H. Scofield, *Western blotting: an introduction*. Methods Mol Biol, 2015. **1312**: p. 17-30.
303. Welinder, C. and L. Ekblad, *Coomassie staining as loading control in Western blot analysis*. J Proteome Res, 2011. **10**(3): p. 1416-9.
304. Sumantran, V.N., *Cellular chemosensitivity assays: an overview*. Methods Mol Biol, 2011. **731**: p. 219-36.
305. Hoshi, S., et al., *Regulation of vascular smooth muscle cell proliferation by nuclear factor-kappaB and its inhibitor, I-kappaB*. J Biol Chem, 2000. **275**(2): p. 883-9.
306. Huang, F., et al., *Leptin-induced vascular smooth muscle cell proliferation via regulating cell cycle, activating ERK1/2 and NF-kappaB*. Acta Biochim Biophys Sin (Shanghai), 2010. **42**(5): p. 325-31.
307. Liu, Y., et al., *Mechanism of cellular 3-(4,5-dimethylthiazol-2-yl)-2,5-diphenyltetrazolium bromide (MTT) reduction*. J Neurochem, 1997. **69**(2): p. 581-93.
308. Mosmann, T., *Rapid colorimetric assay for cellular growth and survival: application to proliferation and cytotoxicity assays*. J Immunol Methods, 1983. **65**(1-2): p. 55-63.
309. Darzynkiewicz, Z., H.D. Halicka, and H. Zhao, *Analysis of cellular DNA content by flow and laser scanning cytometry*. Adv Exp Med Biol, 2010. **676**: p. 137-47.
310. Rensen, S.S., P.A. Doevendans, and G.J. van Eys, *Regulation and characteristics of vascular smooth muscle cell phenotypic diversity*. Neth Heart J, 2007. **15**(3): p. 100-8.
311. Neylon, C.B., et al., *Different electrical responses to vasoactive agonists in morphologically distinct smooth muscle cell types*. Circulation Research, 1994. **75**(4): p. 733-41.
312. Rudijanto, A., *The role of vascular smooth muscle cells on the pathogenesis of atherosclerosis*. Acta Med Indones, 2007. **39**(2): p. 86-93.
313. Clarke, M.C.H., et al., *Apoptosis of vascular smooth muscle cells induces features of plaque vulnerability in atherosclerosis*. Nat Med, 2006. **12**(9): p. 1075-1080.
314. Son, D.J., et al., *Melittin Inhibits Vascular Smooth Muscle Cell Proliferation through Induction of Apoptosis via Suppression of Nuclear Factor- κ B and Akt Activation and Enhancement of Apoptotic Protein Expression*. Journal of Pharmacology and Experimental

- Therapeutics, 2006. **317**(2): p. 627-634.
315. DeCoursey, T.E., et al., *Voltage-gated K⁺ channels in human T lymphocytes: a role in mitogenesis?* Nature, 1984. **307**(5950): p. 465-8.
316. Neylon, C.B., *Potassium channels and vascular proliferation.* Vascul Pharmacol, 2002. **38**(1): p. 35-41.
317. Toyama, K., et al., *The intermediate-conductance calcium-activated potassium channel KCa3.1 contributes to atherogenesis in mice and humans.* J Clin Invest, 2008. **118**(9): p. 3025-37.
318. Bi, D., et al., *The intermediate conductance calcium-activated potassium channel KCa3.1 regulates vascular smooth muscle cell proliferation via controlling calcium-dependent signaling.* J Biol Chem, 2013. **288**(22): p. 15843-53.
319. Olschewski, A., *Blocking potassium channels: a new principle for treating restenosis?* Cardiovasc Res, 2011. **89**(2): p. 255-7.
320. Roy, C.S. and J.G. Brown, *The Blood-Pressure and its Variations in the Arterioles, Capillaries and Smaller Veins.* The Journal Of Physiology, 1880. **2**(5-6): p. 323-446.1.
321. Park, W.S., et al., *Activation of inward rectifier K⁺ channels by hypoxia in rabbit coronary arterial smooth muscle cells.* Am J Physiol Heart Circ Physiol, 2005. **289**(6): p. H2461-7.
322. Berne, R.M. and N. Sprekalis, *Handbook of Physiology, Section 2: The Cardiovascular System.* Vol. 1, The Heart. 1979. p.873-952.
323. Chilton, L., et al., *K⁺ currents regulate the resting membrane potential, proliferation, and contractile responses in ventricular fibroblasts and myofibroblasts.* Am J Physiol Heart Circ Physiol, 2005. **288**(6): p. H2931-9.
324. Hedegaard, E.R., et al., *KV 7 channels are involved in hypoxia-induced vasodilatation of porcine coronary arteries.* Br J Pharmacol, 2014. **171**(1): p. 69-82.
325. Wiecha, J., et al., *Ca²⁺-activated K⁺ channels in human smooth muscle cells of coronary atherosclerotic plaques and coronary media segments.* Basic Res Cardiol, 1997. **92**(4): p. 233-9.
326. Gollasch, M., et al., *K⁺ currents in human coronary artery vascular smooth muscle cells.* Circ Res, 1996. **78**(4): p. 676-88.
327. Venkatesh, N., S.T. Lamp, and J.N. Weiss, *Sulfonylureas, ATP-sensitive K⁺ channels, and cellular K⁺ loss during hypoxia, ischemia, and metabolic inhibition in mammalian ventricle.* Circ Res, 1991. **69**(3): p. 623-37.
328. Kubo, M., J.M. Quayle, and N.B. Standen, *Angiotensin II inhibition of ATP-sensitive K⁺ currents in rat arterial smooth muscle cells through protein kinase C.* J Physiol, 1997. **503** (Pt 3): p. 489-96.
329. Purves, G.I., et al., *Exchange protein activated by cAMP (Epac) mediates cAMP-dependent but protein kinase A-insensitive modulation of vascular ATP-sensitive potassium channels.* J Physiol, 2009. **587**(Pt 14): p. 3639-50.
330. Daut, J., et al., *Hypoxic Dilation of Coronary Arteries is Mediated by ATP-Sensitive Potassium Channels.* 1990, American Society for the Advancement of Science. p. 1341.
331. von Beckerath, N., et al., *Hypoxic vasodilatation in isolated, perfused guinea-pig heart: an analysis of the underlying mechanisms.* J Physiol, 1991. **442**: p. 297-319.
332. Miura, H., et al., *Diabetes mellitus impairs vasodilation to hypoxia in human coronary arterioles: reduced activity of ATP-sensitive potassium channels.* Circ Res, 2003. **92**(2): p.

- 151-8.
333. Lynch, F.M., et al., *Adenosine- and hypoxia-induced dilation of human coronary resistance arteries: evidence against the involvement of K(ATP) channels*. *Br J Pharmacol*, 2006. **147**(4): p. 455-8.
334. Yoshida, H., et al., *K ATP channels of primary human coronary artery endothelial cells consist of a heteromultimeric complex of Kir6.1, Kir6.2, and SUR2B subunits*. *J Mol Cell Cardiol*, 2004. **37**(4): p. 857-69.
335. Chutkow, W.A., et al., *Episodic coronary artery vasospasm and hypertension develop in the absence of Sur2 K(ATP) channels*. *J Clin Invest*, 2002. **110**(2): p. 203-8.
336. Miki, T., et al., *Mouse model of Prinzmetal angina by disruption of the inward rectifier Kir6.1*. *Nat Med*, 2002. **8**(5): p. 466-72.
337. Park, W.S., et al., *Acute hypoxia induces vasodilation and increases coronary blood flow by activating inward rectifier K(+) channels*. *Pflugers Arch*, 2007. **454**(6): p. 1023-30.
338. Franco-Obregon, A. and J. Lopez-Barneo, *Differential oxygen sensitivity of calcium channels in rabbit smooth muscle cells of conduit and resistance pulmonary arteries*. *J Physiol*, 1996. **491 (Pt 2)**: p. 511-8.
339. Grlach, A., et al., *Calcium and ROS: A mutual interplay*. *Redox Biology*, 2015. **6**: p. 260-271.
340. Campbell, D.L., J.S. Stamler, and H.C. Strauss, *Redox modulation of L-type calcium channels in ferret ventricular myocytes. Dual mechanism regulation by nitric oxide and S-nitrosothiols*. *The Journal of General Physiology*, 1996. **108**(4): p. 277-293.
341. Fearon, I.M., et al., *Modulation of recombinant human cardiac L-type Ca²⁺ channel alpha1C subunits by redox agents and hypoxia*. *J Physiol*, 1999. **514 (Pt 3)**: p. 629-37.
342. Borbouse, L., et al., *Metabolic syndrome reduces the contribution of K⁺ channels to ischemic coronary vasodilation*. *Am J Physiol Heart Circ Physiol*, 2010. **298**(4): p. H1182-9.
343. Gutterman, D.D., H. Miura, and Y. Liu, *Redox modulation of vascular tone: focus of potassium channel mechanisms of dilation*. *Arterioscler Thromb Vasc Biol*, 2005. **25**(4): p. 671-8.
344. Wolin, M.S., T.M. Burke-Wolin, and H.K. Mohazzab, *Roles for NAD(P)H oxidases and reactive oxygen species in vascular oxygen sensing mechanisms*. *Respir Physiol*, 1999. **115**(2): p. 229-38.
345. Hendgen-Cotta, U.B., M. Kelm, and T. Rassaf, *Myoglobin's novel role in nitrite-induced hypoxic vasodilation*. *Trends Cardiovasc Med*, 2014. **24**(2): p. 69-74.